REPORT DOCUMENTATION PAGE

Form Approved OMB NO. 0704-0188

1. REPORT DATE (DD-MM-YYYY)	2. REPORT TYPE	3. DATES COVERED (From - To)
01-02-2011	Final Report	19-Mar-2007 - 18-Mar-2010

4. TITLE AND SUBTITLE
Final Report on "Bioremediation Using Dehaloperoxidase"

5a. CONTRACT NUMBER
W911NF-07-1-0119

5b. GRANT NUMBER

5c. PROGRAM ELEMENT NUMBER
611102

6. AUTHORS
Franzen

5d. PROJECT NUMBER

5e. TASK NUMBER

5f. WORK UNIT NUMBER

7. PERFORMING ORGANIZATION NAMES AND ADDRESSES
North Carolina State University
Office of Contract and Grants
Leazar Hall Lower Level- MC
Raleigh, NC 27695 -7214

8. PERFORMING ORGANIZATION REPORT NUMBER

9. SPONSORING/MONITORING AGENCY NAME(S) AND ADDRESS(ES)
U.S. Army Research Office
P.O. Box 12211
Research Triangle Park, NC 27709-2211

10. SPONSOR/MONITOR'S ACRONYM(S)
ARO

11. SPONSOR/MONITOR'S REPORT NUMBER(S)
52278-LS.1

12. DISTRIBUTION AVAILIBILITY STATEMENT
Approved for Public Release; Distribution Unlimited

13. SUPPLEMENTARY NOTES
The views, opinions and/or findings contained in this report are those of the author(s) and should not contrued as an official Department of the Army position, policy or decision, unless so designated by other documentation.

14. ABSTRACT
The project addresses the need to develop biological approaches to detoxifiy the environment. We have studied the first known hemoglobin that has a natural peroxidase function. The hemoglobin was first isolated from the marine worm (terebellid polychaete) Amphitrite ornata, but has been cloned and expressed in E. coli bacteria. During the grant period we discovered a principle of action of such peroxidases, namely internal inhibition by para-halophenols. This information permits further progress to be made in cloning and expressing bioremediation

15. SUBJECT TERMS
bioremediation, peroxidase, oxidation, enzyme, chlorinated phenol, quinone, structure, function

16. SECURITY CLASSIFICATION OF:			17. LIMITATION OF ABSTRACT	15. NUMBER OF PAGES	19a. NAME OF RESPONSIBLE PERSON
a. REPORT	b. ABSTRACT	c. THIS PAGE			Stefan Franzen
UU	UU	UU	UU		19b. TELEPHONE NUMBER: 919-515-8915

Report Title

Final Report on "Bioremediation Using Dehaloperoxidase"

ABSTRACT

The project addresses the need to develop biological approaches to detoxifiy the environment. We have studied the first known hemoglobin that has a natural peroxidase function. The hemoglobin was first isolated from the marine worm (terebellid polychaete) Amphitrite ornata, but has been cloned and expressed in E. coli bacteria. During the grant period we discovered a principle of action of such peroxidases, namely internal inhibition by para-halophenols. This information permits further progress to be made in cloning and expressing bioremediation enzymes capable of degrading environmental pollutants such as 2,4-dichlorophenol, which is a byproduct of the insecticide 2,4-D and a precursor to highly toxic dioxins. We have published numerous X-ray crystal structures and nuclear magnetic resonance data to support the conclusions. We have carried out extensive enzymatic kinetic assays to demonstrate the utility of dehaloperoxidase for bioremediation applications.

List of papers submitted or published that acknowledge ARO support during this reporting period. List the papers, including journal references, in the following categories:

(a) Papers published in peer-reviewed journals (N/A for none)

1. de Serrano, V.S.; Chen, Z.; Davis, M. F.; Franzen, S. "X-ray Crystal Structural Analysis of the Binding Site in the Ferric and Oxyferrous Forms of the Recombinant Heme Dehaloperoxidase Cloned from Amphitrite ornata" Acta Cryst. D 2007, 63, 1094-1101

2. Smirnova, T.I., Weber, R.T., Davis, M.F., Franzen, S. "Substrate binding triggers a switch in the iron coordination in dehaloperoxidase from Amphitrite ornata: HYSCORE experiments" J. Am. Chem. Soc. 2008, 130, 2128-2129

3. Feducia, J.; Dumarieh, R.; Gilvey, L.B.G.; Smirnova, T.; Franzen, S.; Ghiladi, R.A. "Characterization of Dehaloperoxidase Compound ES and its Reactivity with Trihalophenols" Biochemistry, 2009, 48, 995-1005

4. Chen, Z.; de Serrano, V.S.; Betts, L.; Franzen, S. "Distal Histidine Conformational Flexibility in Dehaloperoxidase from Amphitrite ornata" Acta Cryst. D 2009, 65, 34-40

5. Davis, M.F.; Gracz, H.; Vendeix, F.A.P.; Gilvey, L.B.; Somasundaram, A.; Decatur, S.M.; Franzen, S. "Internal Structural Changes Induced by the Binding of Substrates to the Hemoglobin Dehaloperoxidase from Amphitrite ornata" Biochemistry, 2009, 48, 2164-2172

6. Davis, M.F.; Bobay, B.G.; Franzen, S. "Determination of Separate Inhibitor and Substrate Binding Sites in the Dehaloperoxidase-Hemoglobin from Amphitrite ornata" Biochemistry 2010, 49, 1199-1206

7. Nicoletti, F.P.; Thompson, M.K.; Howes, B.D.; Franzen, S.; Smulevich, G. "New Insights into the Role of Distal Histidine Flexibility in Ligand Stabilization of Dehaloperoxidase-Hemoglobin from Amphitrite ornata" Biochemistry, 2010, 49, 1903-1912

8. de Serrano, V.S.; Davis, M.F.; Gaff, J.F.; Zhang, Q.; Chen, Z.; D'Antonio, E.L. ; Bowden, E.F.; Rose, R.; Franzen, S. "X-ray structure of the metcyano form of dehaloperoxidase from Amphitrite ornata: Evidence for photoreductive dissociation of the iron-cyanide bond" Acta Cryst. D 2010, 66, 770-782

9. de Serrano, V.; D'Antonio, J.; Thompson, M.K.; Franzen, S.; Ghiladi, R.A. "Crystal Structure of Dehaloperoxidase B at 1.58 Å and Structural Characterization of the A/B Dimer from Amphitrite ornata Acta Cryst. D, 2010, 66, 529-538

10. D'Antonio, J.; D'Antonio, E.L.; Bowden, E.F.; Smirnova, T.; Franzen, S.; Ghiladi, R.A. "Spectroscopic and Mechanistic Investigations of Dehaloperoxidase B from Amphitrite ornata" Biochemistry, 2010, 49, 6600-6616

11. Thompson, M.K.; Davis, M.F.; de Serrano, V.' Nicoletti, F.P.; Howes, B.D.' Smulevich, G.; Franzen, S. "Two-site competitive inhibition in dehaloperoxidase-hemoglobin" Biophys. J. 2010, 99, 1586-1599

12. Ma, H.; Thompson, M.K.; Gaff, J.; Franzen, S. "Kinetic analysis of a naturally occurring bioremediation enzyme: Dehaloperoxidase-hemoglobin from Amphitrite ornata"
J. Phys. Chem. B, 2010, 114, 11283-11289

13. Thompson, M.K.; Franzen,S.; Ghiladi, R.A.; Reeder, B.J.; Svistunenko, D.A. "Free radical mechanism of hydrogen peroxide induced activation of dehaloperoxidase-hemoglobin from Amphitrite ornata" J. Am. Chem. Soc., 2010, 132, 17501,17510

Number of Papers published in peer-reviewed journals: 13.00

(b) Papers published in non-peer-reviewed journals or in conference proceedings (N/A for none)

Number of Papers published in non peer-reviewed journals: 0.00

(c) Presentations

A. International Conference on Bioinorganic Chemistry, Nagoya, Japan 2009

Franzen, S.; de Serrano, V.S.; Davis, M.F.; Thompson, M.K. "Two-site competitive inhibition in dehaloperoxidase-hemoglobin from Amphitrite ornata" J. Biol. Inorg. Chem., 2009, 14, S34

B. Biophysical Society Meeting, Boston, MA 2009

Franzen, S.; de Serrano, V.; Davis, M.F.; Thompson, M.K. Structural Probes Of Reactive Intermediates Of Dehaloperoxidase From Amphitrite ornata Biophys. J. 2009, 96, 558A

Thompson, M.K.; Davis,M.F.; Franzen, S. Resonance Raman Probes of the Internal Binding Pocket of Dehaloperoxidase from Amphitrite ornata Biophys J. 2009, 96, 437A

Ghiladi, R.A.; Dumarieh, R.; Thompson, M.K.; Wang, Z.; Smirnova, T.; Franzen, S. Spectroscopic Probes of the Reactive Intermediates of Dehaloperoxidase from Amphitrite ornata Biophys J. 2009, 96, 437A

Smirnova, T.I.; Davis, M.F.; Weber, R.T.; Franzen, S. Substrate binding triggers a switch in the iron coordination in dehaloperoxidase from Amphitrite Ornata Biophys J. 2009, 96, 437A

C. Biophysical Society Meeting, San Francisco, CA 2010

Thompson, M.K.; Parnel, J.; Franzen, S. Blocking the Inhibitor Binding Site in the Interior of Dehaloperoxidase from Amphitrite Ornata Biophys J. 2010, 98, 641A

Franzen, S; de Serrano, V.; Oliver, R.C.; Krueger, J.. Experimental and Computational Study of the Monomer-Dimer Equilibrium in Dehaloperoxidase from Amphitrite Ornata Biophys J. 2010, 98, 640A

Number of Presentations: 7.00

Non Peer-Reviewed Conference Proceeding publications (other than abstracts):

Number of Non Peer-Reviewed Conference Proceeding publications (other than abstracts): 0

Peer-Reviewed Conference Proceeding publications (other than abstracts):

Number of Peer-Reviewed Conference Proceeding publications (other than abstracts): 0

(d) Manuscripts

Number of Manuscripts: 2.00

Patents Submitted

Patents Awarded

Awards

Graduate Students

NAME	PERCENT_SUPPORTED
Matthew Thompson	1.00
Michael Davis	1.00
FTE Equivalent:	**2.00**
Total Number:	**2**

Names of Post Doctorates

NAME	PERCENT_SUPPORTED
Vesna de Serrano	0.50
FTE Equivalent:	**0.50**
Total Number:	**1**

Names of Faculty Supported

NAME	PERCENT_SUPPORTED	National Academy Member
Stefan Franzen	0.05	No
FTE Equivalent:	**0.05**	
Total Number:	**1**	

Names of Under Graduate students supported

NAME	PERCENT_SUPPORTED
Jonathan Parnell	0.05
FTE Equivalent:	**0.05**
Total Number:	**1**

Student Metrics

This section only applies to graduating undergraduates supported by this agreement in this reporting period

The number of undergraduates funded by this agreement who graduated during this period:	1.00
The number of undergraduates funded by this agreement who graduated during this period with a degree in science, mathematics, engineering, or technology fields:.....	1.00
The number of undergraduates funded by your agreement who graduated during this period and will continue to pursue a graduate or Ph.D. degree in science, mathematics, engineering, or technology fields:.....	1.00
Number of graduating undergraduates who achieved a 3.5 GPA to 4.0 (4.0 max scale):	1.00
Number of graduating undergraduates funded by a DoD funded Center of Excellence grant for Education, Research and Engineering:	0.00
The number of undergraduates funded by your agreement who graduated during this period and intend to work for the Department of Defense	0.00
The number of undergraduates funded by your agreement who graduated during this period and will receive scholarships or fellowships for further studies in science, mathematics, engineering or technology fields:	0.00

Names of Personnel receiving masters degrees

NAME
Wang Zao
Zuxu Chen
Total Number: 2

Names of personnel receiving PHDs

NAME
Michael Davis
Matthew Thompson
Total Number: 2

Names of other research staff

NAME	PERCENT_SUPPORTED
FTE Equivalent:	
Total Number:	

Sub Contractors (DD882)

Inventions (DD882)

Scientific Progress

Our proposed research consists of four aims:
1. To determine the range of substrates that can be oxidized by DHP.
2. To determine the conditions that favor quinone vs. polymer products.
3. To determine the nature of crucial mutations that allow the Hb to function as DHP.
4. To determine whether a flavoprotein plays a role in the activation of DHP.

In pursuit of the objectives of the grant we discovered that dehaloperoxidase-hemoglobin (DHP) has both an inhibitor and substrate binding site. This unexpected discovery is summarized in Figure 1 below. Figure 1 shows a switch between an inhibited state (1a) and a substrate-bound active state (1c). Both X-ray crystal structures and correlated resonance Raman spectra show a coupling of the histidine (H55) and the inhibitor or substrate. This discovery cuts across objectives 1, 2 and 3 and has bearing on each of them. Clearly 4-bromophenol is not a substrate, since it is an inhibitor (Objective 1). Thus, from these studies we concluded that the series 4-iodo-, 4-bromo-, 4-chloro- and 4-fluorophenol are all inhibitors, although the binding constant in the internal pocket decreases as the halogen atom in the 4-position decreases in radius. 2,4-dihalophenols are intermediate in their reactivity. They enter the pocket partially as determined by NMR spectroscopy. Finally, all of the 2,4,6-trihalophenols are excellent substrates, with the exception of 2,4,6-trifluorophenol, which also can enter the pocket and therefore can self-inhibit.

We studied the project distribution (Objective 2) and discovered that DHP makes almost exclusively quinone products. The reason is that polymer products are formed from the 4-XPs (X = I, Br, Cl or F), which are inhibitors. Perhaps this is the physiological reason for inhibition. Polymer formation may be harmful to the organism. Thus, from a practical viewpoint we would like to mutate the inhibitor binding site to relieve the inhibition. These studies were initiated and it was found that L100T is a mutant that has activity with little or no inhibition. The reason for this is that the binding pocket that stabilizes the halogen atom is enlarged to the point that inhibitor binding is not highly stable.

Objective 3 was addressed in a series of mutants of the distal (H55D, H55V, H55R) and proximal (H89G) histidines. Clearly, the distal histidine is key for function. It acts as the acid-base catalyst that activates bound hydrogen peroxide.

Objective 4 was addressed by isolation of the flavin-containing protein that is found in the coelom of A. ornata along with DHP. Although we attempted to purify the yellow-colored fraction, we were not successful during this grant period.

Technology Transfer

Final Report to the Army Research Office
Proposal Number: 52278-LS
Agreement Number: W911NF-07-1-0119
Proposal Title: Bioremediation Using Dehaloperoxidase

Grant period: from March 19, 2007 to March 18, 2010.

Foreword

The 13 peer-reviewed publications, 2 PhD dissertations and 7 meeting abstracts summarized in this document show the progress made towards developing a new type of bioremediation enzyme. Dehaloperoxidase-hemoglobin is a naturally occurring enzymes that can degrade chlorinated and brominated pollutants. The major breakthrough in understanding the internal binding site function shows that DHP has the potential for artificial or bioremediation applications. We have shown that we can eliminate the internal binding site, and use DHP on the relevant substrate, 2,4-dichlorophenol, which is a breakdown product of 2,4-D and other herbicides used in the field.

Table of contents

Statement of the Problem to be Studied

The project addresses the need to develop new biological approaches to detoxification both in the environment and in human beings. We propose to study the first known hemoglobin that has evolved to adopt an additional peroxidase function. The dehaloperoxidase-hemoglobin (DHP) was first isolated from the marine worm (terebellid polychaete) *Amphitrite ornata*, but has been cloned and expressed in *E. coli* bacteria. Our goal is to understand the mechanism of this cloned protein and to use the information to develop a novel protein for bioremediation applications. We believe that DHP has the capability to degrade chlorinated and brominated phenols in the environment without the need to add any exogenous agent. This hypothesis was tested by structural and kinetic studies during the three-year grant period.

Summary of the Most Important Results

Our proposed research consists of four aims:

1. To determine the range of substrates that can be oxidized by DHP.
2. To determine the conditions that favor quinone vs. polymer products.
3. To determine the nature of crucial mutations that allow the Hb to function as DHP.
4. To determine whether a flavoprotein plays a role in the activation of DHP.

In pursuit of these goals we discovered that dehaloperoxidase-hemoglobin (DHP) has both an inhibitor and substrate binding site. This unexpected discovery is summarized in Figure 1 below. Figure 1 shows a switch between an inhibited state (1a) and a substrate-bound active state (1c). Both X-ray crystal structures and correlated resonance Raman spectra show a coupling of the histidine (H55) and the inhibitor or substrate. This discovery cuts across objectives 1, 2 and 3 and has bearing on each of them. Clearly 4-bromophenol is not a substrate, since it is an inhibitor (Objective 1). Thus, from these studies we concluded that the series 4-iodo-, 4-bromo-, 4-chloro- and 4-fluorophenol are all inhibitors, although the binding constant in the internal pocket decreases as the halogen atom in the 4-position decreases in radius. 2,4-dihalophenols are intermediate in their reactivity. They enter the pocket partially as determined by NMR spectroscopy. Finally, all of the 2,4,6-trihalophenols are excellent substrates, with the exception of 2,4,6-trifluorophenol, which also can enter the pocket and therefore can self-inhibit.

We studied the project distribution (Objective 2) and discovered that DHP makes almost exclusively quinone products. The reason is that polymer products are formed from the 4-XPs (X = I, Br, Cl or F), which are inhibitors. Perhaps this is the physiological reason for inhibition. Polymer formation may be harmful to the organism. Thus, from a practical viewpoint we would like to mutate the inhibitor binding site to relieve the inhibition. These studies were initiated and it was found that L100T is a mutant that has activity with little or no inhibition. The reason for this is that the binding pocket that stabilizes the halogen atom is enlarged to the point that inhibitor binding is not highly stable.

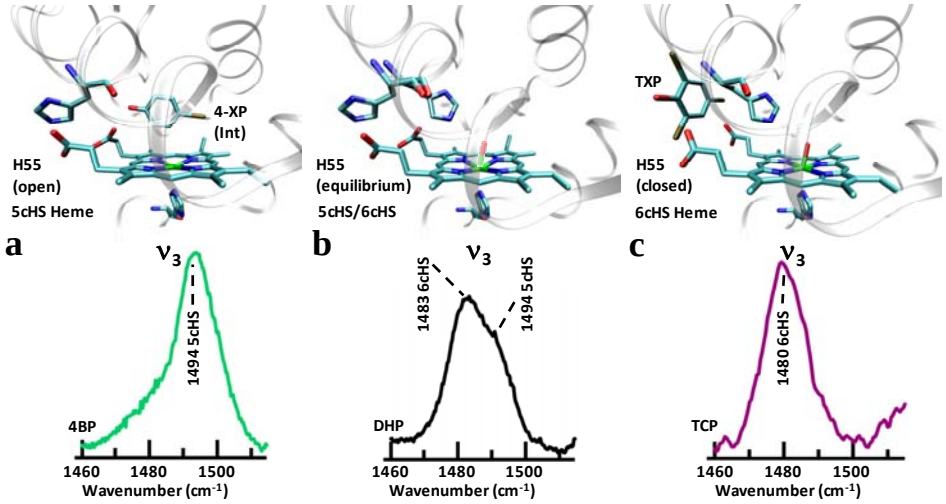

Figure 1. Model representations of internal and external binding in DHP. (a.) The distal H55 is forced into the solvent exposed (open) position by the internally bound 4-XP inhibitor. (b.) The room temperature X-ray crystal structure of WT DHP the H55 open (5cHS) and closed (6cHS) states in equilibrium. (c.) Depiction of tri-halogenated phenol forcing the distal H55 into the closed position. PDB accession numbers are 2QFK, 3DR9, 3BL1, 3BL2, 3BL3, and 3BL4.

Objective 3 was addressed in a series of mutants of the distal (H55D, H55V, H55R) and proximal (H89G) histidines. Clearly, the distal histidine is key for function. It acts as the acid-base catalyst that activates bound hydrogen peroxide.

Objective 4 was addressed by isolation of the flavin-containing protein that is found in the coelom of A. ornata along with DHP. Although we attempted to purify the yellow-colored fraction, we were not successful during this grant period.

Bibiography

Publications from this grant period

1. de Serrano, V.S.; Chen, Z.; Davis, M. F.; Franzen, S. "X-ray Crystal Structural Analysis of the Binding Site in the Ferric and Oxyferrous Forms of the Recombinant Heme Dehaloperoxidase Cloned from *Amphitrite ornata*" Acta Cryst. D **2007**, 63, 1094-1101

2. Smirnova, T.I., Weber, R.T., Davis, M.F., Franzen, S. "Substrate binding triggers a switch in the iron coordination in dehaloperoxidase from Amphitrite ornata: HYSCORE experiments" J. Am. Chem. Soc. **2008**, 130, 2128-2129

3. Feducia, J.; Dumarieh, R.; Gilvey, L.B.G.; Smirnova, T.; Franzen, S.; Ghiladi, R.A. "Characterization of Dehaloperoxidase Compound ES and its Reactivity with Trihalophenols" Biochemistry, **2009**, 48, 995-1005

4. Chen, Z.; de **Serrano, V.S.; Betts, L.; Franzen, S.** "Distal Histidine Conformational Flexibility in Dehaloperoxidase from *Amphitrite ornata*" Acta Cryst. D **2009**, 65, 34-40

5. Davis, M.F.; Gracz, H.; Vendeix, F.A.P.; Gilvey, L.B.; Somasundaram, A.; Decatur, S.M.; Franzen, S. "Internal Structural Changes Induced by the Binding of Substrates to the Hemoglobin Dehaloperoxidase from *Amphitrite ornata*" Biochemistry, **2009**, 48, 2164-2172

6. Davis, M.F.; Bobay, B.G.; Franzen, S. "Determination of Separate Inhibitor and Substrate Binding Sites in the Dehaloperoxidase-Hemoglobin from *Amphitrite ornata*" Biochemistry **2010**, 49, 1199-1206

7. Nicoletti, F.P.; Thompson, M.K.; Howes, B.D.; Franzen, S.; Smulevich, G. "New Insights into the Role of Distal Histidine Flexibility in Ligand Stabilization of Dehaloperoxidase-Hemoglobin from *Amphitrite ornata*" Biochemistry, **2010**, 49, 1903-1912

8. de Serrano, V.S.; Davis, M.F.; Gaff, J.F.; Zhang, Q.; Chen, Z.; D'Antonio, E.L. ; Bowden, E.F.; Rose, R.; Franzen, S. "X-ray structure of the metcyano form of dehaloperoxidase from *Amphitrite ornata*: Evidence for photoreductive dissociation of the iron-cyanide bond" Acta Cryst. D **2010**, 66, 770-782

9. de Serrano, V.; D'Antonio, J.; Thompson, M.K.; Franzen, S.; Ghiladi, R.A. "Crystal Structure of Dehaloperoxidase B at 1.58 Å and Structural Characterization of the A/B Dimer from *Amphitrite ornata* Acta Cryst. D, **2010**, 66, 529-538

10. D'Antonio, J.; D'Antonio, E.L.; Bowden, E.F.; Smirnova, T.; Franzen, S.; Ghiladi, R.A. "Spectroscopic and Mechanistic Investigations of Dehaloperoxidase B from *Amphitrite ornata*" Biochemistry, **2010**, 49, 6600-6616

11. Thompson, M.K.; Davis, M.F.; de Serrano, V.' Nicoletti, F.P.; Howes, B.D.' Smulevich, G.; Franzen, S. "Two-site competitive inhibition in dehaloperoxidase-hemoglobin" Biophys. J. **2010**, 99, 1586-1599

12. Ma, H.; Thompson, M.K.; Gaff, J.; Franzen, S. "Kinetic analysis of a naturally occurring bioremediation enzyme: Dehaloperoxidase-hemoglobin from *Amphitrite ornata*" J. Phys. Chem. B, **2010**, 114, 11283-11289

13. Thompson, M.K.; Franzen,S.; Ghiladi, R.A.; Reeder, B.J.; Svistunenko, D.A. "Free radical mechanism of hydrogen peroxide induced activation of dehaloperoxidase-hemoglobin from *Amphitrite ornata"* J. Am. Chem. Soc., **2010**, 132, 17501,17510

Meeting Abstracts

A. International Conference on Bioinorganic Chemistry, Nagoya, Japan 2009

Franzen, S.; de Serrano, V.S.; Davis, M.F.; Thompson, M.K. "Two-site competitive inhibition in dehaloperoxidase-hemoglobin from *Amphitrite ornata*" J. Biol. Inorg. Chem., **2009**, 14, S34

B. Biophysical Society Meeting, Boston, MA 2009

Franzen, S.; de Serrano, V.; Davis, M.F.; Thompson, M.K. Structural Probes Of Reactive Intermediates Of Dehaloperoxidase From Amphitrite ornata Biophys. J. **2009**, 96, 558A

Thompson, M.K.; Davis,M.F.; Franzen, S. Resonance Raman Probes of the Internal Binding Pocket of Dehaloperoxidase from *Amphitrite ornata* Biophys J. **2009**, 96, 437A

Ghiladi, R.A.; Dumarieh, R.; Thompson, M.K.; Wang, Z.; Smirnova, T.; Franzen, S. Spectroscopic Probes of the Reactive Intermediates of Dehaloperoxidase from *Amphitrite ornata* Biophys J. **2009**, 96, 437A

Smirnova, T.I.; Davis, M.F.; Weber, R.T.; Franzen, S. Substrate binding triggers a switch in the iron coordination in dehaloperoxidase from *Amphitrite Ornata* Biophys J. **2009**, 96, 437A

C. Biophysical Society Meeting, San Francisco, CA 2010

Thompson, M.K.; Parnel, J.; Franzen, S. Blocking the Inhibitor Binding Site in the Interior of **Dehaloperoxidase** from *Amphitrite Ornata* Biophys J. **2010**, 98, 641A

Franzen, S; de Serrano, V.; Oliver, R.C.; Krueger, J.. Experimental and Computational Study of the Monomer-Dimer Equilibrium in Dehaloperoxidase from *Amphitrite Ornata* Biophys J. **2010**, 98, 640A

Theses

1. MS Thesis, Zuxu Chen, Nov. 2007
"Distal Histidine Conformational Flexibility in Dehaloperoxidase from Amphitrite Ornata"

2. MS Thesis, Wang Zao, July, 2009
"Spectroscopic Studies of Activation of Dehaloperoxidase by Hydrogen Peroxide**"**

3. PhD Dissertation, Michael Davis, August, 2009
"Structural Studies of Inhibitor and Substrate Binding in the Hemoglobin Dehaloperoxidase**"**

4. PhD Dissertation, Matthew Thompson (anticipated July 2011)

Acta Crystallographica Section D
Biological Crystallography
ISSN 0907-4449

X-ray crystal structural analysis of the binding site in the ferric and oxyferrous forms of the recombinant heme dehaloperoxidase cloned from *Amphitrite ornata*

Vesna de Serrano,* Zuxu Chen, Michael F. Davis and Stefan Franzen*

Department of Chemistry, North Carolina State University, Raleigh, NC, USA

Correspondence e-mail: vsserran@ncsu.edu, stefan_franzen@ncsu.edu

Received 29 June 2007
Accepted 4 September 2007

PDB References: wild-type DHP, 2qfk, r2qfksf; C73S mutant DHP, 2qfn, r2qfnsf.

The dehaloperoxidase (DHP) from the terebellid polychaete *Amphitrite ornata* is an enzyme that converts *para*-halogenated phenols to the corresponding quinones in the presence of hydrogen peroxide. Its enzymatic activity is similar to that of heme peroxidases such as horseradish peroxidase, yet it has the structural characteristics of the globin family of proteins, the main functions of which are oxygen transport and storage. In order to investigate the dual function of this hemoglobin peroxidase, the enzyme was expressed in *Escherichia coli* as a recombinant protein in its wild-type form and as a mutant protein in which Cys73 was replaced by a serine residue (C73S). Both the wild-type and mutant proteins were crystallized and their structures were determined at 100 K to a resolution of 1.62 Å. The structure of the wild-type protein demonstrated that it was in the metaquo form, with the heme iron in the ferric oxidation state and the bound water lying 2.2 Å from the heme iron. The structure of the C73S mutant protein was shown to contain a ferrous heme iron with a bound oxygen molecule. The bent bonding geometry of the Fe–O(1)–O(2) adduct results in a hydrogen bond of length 2.8 Å between the second O atom, O(2), of molecular oxygen and $N^{\varepsilon 2}$ of the distal histidine residue (His55) in both subunits contained within the asymmetric unit. This hydrogen-bonding interaction between His55 and the bound diatomic oxygen molecule provides new insight into the catalytic activation of H_2O_2, which is essential for peroxidase activity.

1. Introduction

The enzyme dehaloperoxidase (DHP), first isolated from the terebellid polychaete *Amphitrite ornata*, is a heme-containing peroxidase. Genetic analysis corroborates that DHP is encoded by a gene that has significant sequence homology to the globins of the annelid family (Bailly *et al.*, 2007). Like hemoglobins, DHP is capable of binding diatomic ligands such as molecular oxygen, carbon monoxide and nitric oxide, which bind to the ferrous form of the heme group. In addition, DHP has catalytic properties that are similar to those of horseradish peroxidase (HRP; Ferrari *et al.*, 1999). Quantitative comparisons of the catalytic degradation of halogenated phenols (Belyea *et al.*, 2005; Franzen, Belyea *et al.*, 2006; Franzen, Jasaitis *et al.*, 2006; Chen *et al.*, 1996) demonstrate that DHP has a turnover number that is 12 times lower than HRP, but 13 times greater than myoglobin (Mb) at pH 5.0. HRP is a secretory peroxidase that displays optimal activity at pH < 6.0. DHP, on the other hand, is found in the coelom (fluidic compartment) of *A. ornata* and has a pH optimum of 7.5 (Franzen *et al.*, 2007). Although the different environments complicate comparison, HRP and DHP can both accept a range of halogenated phenols as substrates.

It is not presently understood how DHP switches between its oxygen-binding hemoglobin function and its peroxidase activity. Indeed, this combination of functions is unprecedented in the heme-protein family. Whereas oxygen binding is a reversible process that is common to all ferrous hemoglobins, peroxidase activity requires a ferric resting state. Accordingly, for peroxidase activity, hydrogen peroxide (H_2O_2) binds to ferric heme iron (Fe) to yield compound I according to the reaction

$$P\text{–}Fe^{III}\text{–}H_2O_2 \rightarrow P^{+\cdot}\text{–}Fe^{IV}{=}O + H_2O,$$

where P is the protoporphyrin IX moiety of the heme shown in Fig. 1. Compound I is the oxo heme iron radical cation, $P^{+\cdot}$, that can act as a two-electron oxidant for phenolic substrates according to the overall reaction shown in Fig. 2 at a pH greater than the pK_a of the substrate. We have shown elsewhere that the phenolate form of the substrate is relevant at physiological pH (Franzen *et al.*, 2007).

The X-ray crystallographic structure of DHP isolated from *A. ornata*, first determined by LaCount *et al.* (2000) (PDB code 1ew6), reveals that it has a globin fold but that its heme moiety is located approximately 1.5 Å deeper in the protein than that observed in Mb. The distal histidine is in the same orientation, but is 1.2 Å further from the heme iron than in the Mb structure deposited under PDB code 1a6k (Vojtechovsky *et al.*, 1999). Fig. 1, which is derived from this first structural analysis, displays the heme moiety, the iron, the distal histidine (residue His55) located above the heme plane and the proximal histidine (His89) located below the heme plane. A second DHP structure in complex with the substrate analog 4-iodophenol (PDB code 1ewa) revealed that the substrate analog is bound in an internal binding pocket (LaCount *et al.*, 2000). Given that substrate localization in an internal binding site is unprecedented in globins, this structure suggested that ligand binding might serve as a trigger to switch the protein from its oxygen-carrying role to a catalytic function (Belyea *et al.*, 2005). However, the substrate does not interact strongly with the amino-acid residues of the distal pocket. All the residues in the distal pocket are hydrophobic (Phe21, Val59, Phe35, Phe60), with the exception of the distal histidine His55 and a tyrosine, Tyr38. The hydroxyl group of Tyr38 is sufficiently close to the substrate to form a hydrogen bond with the hydroxyl group of 4-iodophenol.

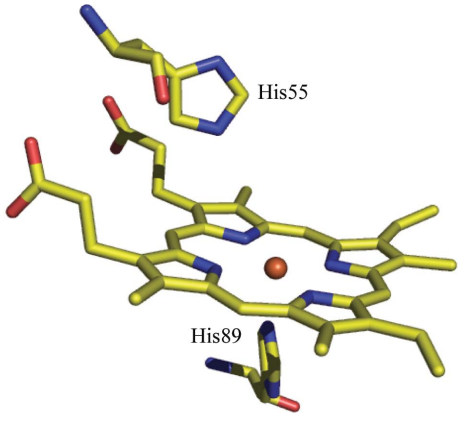

Figure 1
Structure of the heme prosthetic group of DHP relative to the position of the proximal histidine (His89) and distal histidine (His55) located below and above the heme plane, respectively.

The present structural analysis focuses specifically on the ligation of the heme iron in DHP. As is well known, hemoglobins bind oxygen in their ferrous form and are inactive in the ferric oxidation state. Additionally, the ferric irons in methemoglobin and metmyoglobin are six-coordinate when the distal residue (E10) is a histidine (Katz *et al.*, 1994; Royer, 1994; Liu *et al.*, 2001; Vojtechovsky *et al.*, 1999; Yang & Phillips, 1996; Nardini *et al.*, 1995; Della Longa *et al.*, 2003). Ferric peroxidases, which also have a histidine as the distal residue, are usually five-coordinate and thus lack the water molecule bound to the heme iron (Hashimoto *et al.*, 1986; Chouchane *et al.*, 2000; Cheek *et al.*, 1999; Yonetani & Anni, 1987; de Ropp *et al.*, 1991; Andersson *et al.*, 1987; Kuila *et al.*, 1985; Yamazaki *et al.*, 1981; Wang *et al.*, 1990; Kunishima *et al.*, 1996). Strikingly, in the resting state of DHP the ferric form of the heme iron is observed and initial X-ray analysis of native DHP indicated that a water molecule was present in the distal pocket, but it did not appear to be located within bonding distance of the heme iron center (LaCount *et al.*, 2000). Specifically, the Fe—O distances in the A and B subunits were 3.3 and 2.5 Å, respectively. However, spectroscopic experiments (Osborne *et al.*, 2006; Belyea *et al.*, 2006; Nienhaus *et al.*, 2006) suggest that water is bound to the heme iron in the ferric resting state of DHP. Hence, the ligation of the heme in the ferric resting state is still unresolved.

The published X-ray structure of DHP shows the distal histidine residue (His55) in two conformations with nearly equal populations (LaCount *et al.*, 2000). In one of the two conformations His55 is located in the distal cavity, whereas in the second conformation it is positioned away from the distal pocket towards the solvent. This type of conformational variability has precedence in myoglobin, where the distal histidine (His64) assumes the solvent-exposed conformation upon protonation at acidic pH (Yang & Phillips, 1996). Importantly, however, the myoglobin structures that exhibit a solvent-exposed conformation of the distal histidine were obtained below pH 4.5 (Yang & Phillips, 1996), whereas the solvent-exposed conformation of His55 in native DHP was observed at pH 6.5. In addition, the DHP–4-iodophenol complex model shows that His55 is displaced to the solvent-exposed position when the substrate is bound in the distal cavity. Thus, the observation of His55 in a solvent-exposed position and water in the distal pocket, but not bound to the heme iron, may be related.

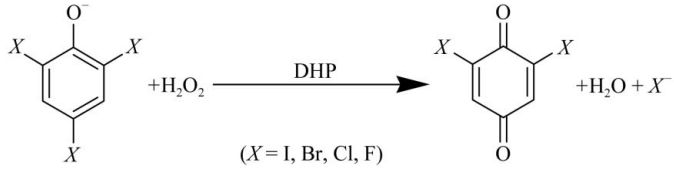

Figure 2
The reaction catalyzed by DHP.

To gain further insight into these issues, we crystallized and solved the structures of wild-type recombinant DHP and the C73S variant. This mutant form of DHP photoreduced in the X-ray beam and thus we were able to obtain a structure of the oxy form of DHP, which yielded further insight into the hydrogen-bonding pattern surrounding His55.

2. Materials and methods

2.1. Purification of recombinant DHP

The C73S mutant DHP was obtained by substituting a serine for a cysteine residue at position 73 using a mutagenesis primer of sequence (5′→3′) GTCGGACGCAAGGGGTAC-CGAATCGGTGGCTCGGTCCGC and its reverse complement. The mutation was generated on the DNA background of four mutated arginine codons in the DNA sequence of DHP, which were introduced to improve expression of the protein in *Escherichia coli* (Belyea *et al.*, 2005). Site-directed mutagenesis was performed using the QuickChange Multi Site-Directed Mutagenesis Kit (Stratagene), as described previously (Belyea *et al.*, 2005).

Genes encoding the wild-type and mutant forms of DHP were cloned into a pET-16b expression vector (Belyea *et al.*, 2005), which was subsequently used to express protein in Rosetta(DE3)pLysS cells. For protein purification, a 50 g cell pellet was resuspended in 100 ml 50 m*M* Tris buffer pH 8.0 supplemented with 100 m*M* NaCl, 1 m*M* EDTA and a protease-inhibitor cocktail (Boehringer Mannheim). The cell suspension was incubated with lysozyme, sonicated and submitted to one cycle of freezing and thawing. After centrifugation to remove cellular debris, the crude extract was subjected to ammonium sulfate fractionation. DHP was precipitated from 50–95% ammonium sulfate. The precipitate was recovered by centrifugation, resuspended in a minimum volume of 20 m*M* Tris pH 8.0 and subjected to dialysis against two changes of the same buffer in order to remove the remaining ammonium sulfate. After subsequent dialysis against 20 m*M* sodium phosphate buffer pH 4.8, followed by brief centrifugation to remove precipitated material, the solution was applied onto an SP Sepharose Fast Flow cation-exchange column using a GE-Pharmacia FPLC system. Protein was eluted with a linear gradient of 0–250 m*M* NaCl in buffer containing 20 m*M* sodium phosphate pH 4.8, 5 m*M* NaN_3 and 5% glycerol. Fractions containing DHP were pooled, concentrated using Millipore centrifugal concentrators and applied onto a HiPrep Sephacryl S-200 column equilibrated with buffer consisting of 50 m*M* Tris pH 5.0, 150 m*M* NaCl and 5% glycerol. The purity of the eluted fractions of DHP was analyzed by SDS–PAGE. The homogeneous fractions were pooled, concentrated and buffer-exchanged to 20 m*M* sodium cacodylate buffer pH 6.5. The protein purity was also assessed by using the ratio of the Soret absorbance at 406 nm to the protein (mostly tryptophan) at 280 nm and DHP protein preparations with A_{406}/A_{280} greater than 3.2 were considered to be pure. UV–visible spectroscopy (UV–Vis) measurement of the Soret band λ_{max} at 406 nm confirmed that both the wild-type enzyme and the C73S mutant protein were isolated in the ferric state (Belyea *et al.*, 2005; Osborne *et al.*, 2006). The integrity of the two proteins was further analyzed by assessing their enzymatic activities toward 2,4,6-tribromophenol (TBP), a natural substrate of DHP (Belyea *et al.*, 2005; Franzen, Belyea *et al.*, 2006; Franzen, Jasaitis *et al.*, 2006).

2.2. Crystallization

The two proteins were crystallized in the ferric form and initial crystallization screening was conducted using commercially available crystal screening kits (Crystal Screens I and II and PEG/Ion Screen; Hampton Research). Both the sitting-drop and hanging-drop methods of vapor diffusion were initially employed at temperatures of 293 and 277 K. After identifying the best conditions, crystals were grown by the hanging-drop method at 277 K. A total drop volume of 6 µl was set up with a 1:1 protein:reservoir solution ratio and the drop was equilibrated against reservoir solution containing 0.2 *M* ammonium sulfate and 26–34% polyethylene glycol 4000. The starting protein concentration was 8 mg ml^{-1}. The pH of the drop solution was 5.9. Diffraction-quality crystals were obtained within one week and ranged in size from 0.2 to 0.7 mm in the largest dimension. They belonged to space group $P2_12_12_1$, with unit-cell parameters a = 60.7, b = 67.6, c = 67.6 Å for the recombinant wild-type protein and a = 57.9, b = 67.1, c = 68.4 Å for the C73S mutant protein. The solvent content for both crystalline lattices was ∼50% and the asymmetric units contained two subunits (Matthews, 1968). For X-ray data collection at low temperatures, the crystals were cryoprotected by brief equilibration in 10 µl 0.2 *M* ammonium sulfate solution containing 32% polyethylene glycol 4000 and 15% polyethylene glycol 400, mounted in a nylon loop and rapidly cryocooled in liquid nitrogen.

2.3. X-ray data collection and structure refinement

X-ray diffraction data for both the wild-type and C73S mutant forms of DHP were collected using a Rigaku RUH3R copper rotating-anode generator (λ = 1.5418 Å) operated at 50 kV and 100 mA with Osmic optics and a Rigaku R-AXIS IV^{++} image-plate detector at the Biomolecular X-ray Crystallography Core Facility, University of North Carolina at Chapel Hill. A full X-ray data set from a single crystal was collected at 100 K using a crystal-to-detector distance of 100 mm and exposure times of 10 min per frame covering 1° oscillations and spanning a range of 150°. All data were processed using the *HKL*-2000 program suite (Otwinowski & Minor, 1997). Each data set extended to a nominal resolution of 1.62 Å. The structures were solved by molecular replacement with the program *Phaser* (McCoy *et al.*, 2005) at 3 Å resolution, using as a search model two polypeptide chains and two heme molecules from the asymmetric unit of the native DHP structure (PDB entry 1ew6; LaCount *et al.*, 2000). In order to eliminate model bias, OMIT maps were constructed with *CNS* (Brünger *et al.*, 1998). Approximately 20 residues in each chain in both the wild-type and C73S mutant structures

Table 1
Data-collection and refinement statistics.

Values in parentheses are for the highest resolution shell.

	Wild-type, recombinant mixed (H_2O, O_2)†	C73S mutant O_2 adduct
Data collection		
Wavelength (Å)	1.5418	1.5418
Space group	$P2_12_12_1$	$P2_12_12_1$
Unit-cell parameters (Å)		
a	60.7	57.9
b	67.6	67.1
c	67.6	68.4
Resolution (Å)	25.62–1.62 (1.66–1.62)	35.0–1.62 (1.68–1.62)
Unique reflections	34161 (2461)	34429 (2289)
Completeness (%)	99.88 (98.66)	99.63 (96.49)
R_{merge}‡ (%)	4.4 (29.5)	5.8 (53.1)
$I/\sigma(I)$	47.7 (6.5)	34.0 (3.0)
Redundancy	5.7	5.7
Refinement		
R_{work}§ (%)	19.1	17.0
R_{free}¶ (%)	23.8	22.4
No. of protein atoms	2391	2434
No. of solvent atoms	275	292
R.m.s.d. from ideal geometry		
Bond lengths (Å)	0.012	0.011
Bond angles (°)	1.3	1.2
Ramachandran plot†† (%)		
Most favored region	94.0	94.8
Additional allowed region	6.0	5.2

† The sixth coordination ligand of the heme Fe is a mixture of water and O_2 in an approximate ratio of 0.75:0.3. ‡ $R_{merge} = \sum_h \sum_i [|I_i(h) - \langle I(h)\rangle|/\sum_h \sum_i I(h)] \times 100$, where $I_i(h)$ is the ith measurement and $\langle I(h)\rangle$ is the weighted mean of all measurements of $I(h)$. § $R_{work} = \sum |F_o - F_c|/\sum F_o \times 100$, where F_o are the observed and F_c the calculated structure factors, respectively. ¶ R_{free} is the R factor for the subset (5%) of reflections selected before and not included in the refinement. †† Calculated using *PROCHECK* (Laskowski *et al.*, 1993).

could be modeled in two conformations and their occupancies were adjusted until there was no significant $F_o - F_c$ density. Using $F_o - F_c$ density contoured at 3σ, 275 water molecules were added to the wild-type model and 292 water molecules were positioned into the mutant structure using *Coot* (Emsley & Cowtan, 2004). The final models were obtained by iterative cycles of model building in *Coot* (Emsley & Cowtan, 2004) and positional and isotropic *B*-factor refinement using *REFMAC*5 (Murshudov *et al.*, 1997) from the *CCP*4 suite of programs (Collaborative Computational Project, Number 4, 1994) and *CNS* (Brünger *et al.*, 1998). Simulated-annealing and composite OMIT maps were constructed using *CNS*. All figures (except Fig. 2) were prepared using *PyMOL* (DeLano, 2002).

The final model for the wild-type structure contained two protein molecules in the asymmetric unit, three sulfate ions, four ammonium ions and 275 water molecules. The final model for the C73S mutant protein structure contained two polypeptide chains, three sulfate ions, two ammonium ions and 292 water molecules. Relevant X-ray data-collection and refinement statistics are summarized in Table 1.

3. Results and discussion

Wild-type DHP expressed in *E. coli* as a recombinant protein produces insoluble precipitates upon prolonged incubation. To test whether the sole surface cysteine (Cys73) plays a role in protein aggregation, it was mutated to a serine residue. Cys73 is located at a distance of approximately 20 Å from the heme iron. This distance was deemed to be sufficiently far that the mutation would not cause significant perturbations in the catalytic properties of the enzyme. Indeed, the C73S mutant protein retained the substrate-binding and catalytic properties of the recombinant wild-type protein (data not shown).

The crystal structures of both the wild-type and C73S mutant forms of DHP were determined for proteins in the Fe^{III} oxidation state as determined by UV–Vis spectra with Soret maxima at 406 nm. Each diffraction data set was collected at 100 K using Cu $K\alpha$ radiation and both structures were refined to a resolution of 1.62 Å, with R factors of 19.1% for the wild-type protein (PDB code 2qfk) and 17.0% for the C73S mutant protein (PDB code 2qfn; Table 1). Both proteins crystallized with two molecules in the asymmetric unit as observed in the original structural analysis of DHP (Zhang *et al.*, 1996). The two subunits have slightly different geometries. For the wild-type enzyme they superimpose with a root-mean-square deviation of 0.27 Å and for the mutant protein structure they superimpose with a root-mean-square deviation of 0.45 Å for all backbone atoms.

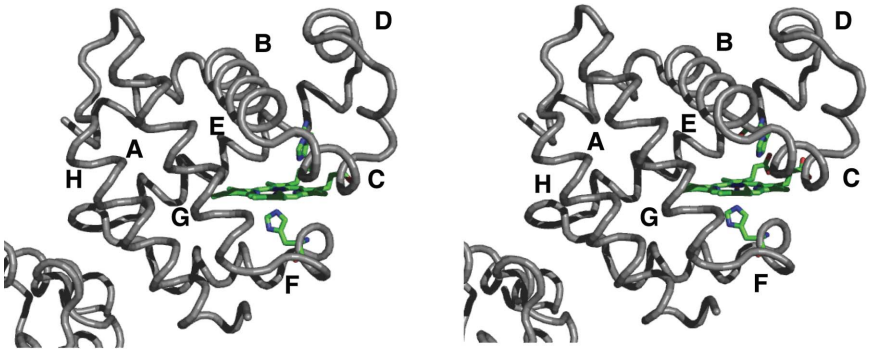

Figure 3
Stereoview of the backbone trace of the wild-type DHP subunit A, shown in ribbon rendering. The eight helices of the structure are labeled A–H according to the globin-fold topology convention. The active-site heme group and the proximal and distal histidine residues are also shown, drawn as green-colored sticks.

3.1. Overall structure of the wild-type and C73S mutant proteins

The structure of the recombinant wild-type DHP consists of a standard myoglobin fold with eight helices (Kendrew *et al.*, 1960). The helical segment, helix C, spanning residues Pro29–Tyr34, adopts a 3_{10}-helical conformation. A backbone trace of the structure of the wild-type protein is presented in Fig. 3, where the eight helices are identified by the letter codes A–H, analogous to the nomenclature for myoglobin (Kendrew *et al.*, 1960). Helix D is two residues shorter in the present structure than that previously reported. As a consequence, the position of His55 in the wild-

Table 2
Comparison of heme-ligand parameters.

The values are tabulated for subunit A of the asymmetric unit.

	Protein form		
	Wild type† (2qfk)	C73S (2qfn)	Original‡ (1ew6)
Fe—His89 $N^{\varepsilon 2}$ (Å)	2.1	2.2	2.3
Fe—His55 $N^{\varepsilon 2}$§ (Å)	4.8	5.1	5.5
Fe—O¶ (Å)	2.2/2.2	2.4/2.2	3.3/2.5
Ligand–His55 (Å)	3.1	O(1) 3.2, O(2) 2.8††	3.6
Fe to pyrrole N plane (Å)	0.04	0.09	0.20
Fe—ligand bend angle‡‡ (°)	—	167.9§§	—
Fe—ligand tilt angle¶¶ (°)	10.9	11	18.3

† Values for the recombinant wild-type DHP structure at 100 K, where the sixth coordination ligand of the heme iron is mixture of water (75%) and O_2 (25%), the mixture being a consequence of partial reduction of the heme iron during X-ray data collection; only parameters for the water ligand are listed in the table. ‡ Compiled from the published structure of DHP determined at room temperature (PDB code 1ew6). § Distance to the His55 conformer located inside the distal cavity. ¶ Fe—O is the distance between the heme iron and ligand oxygen, the ligand being a water molecule in the wild-type and native proteins and an oxygen molecule in the C73S mutant; the two values listed for each structure refer to the distances in subunit A and subunit B, respectively. †† O(1) is the O atom closer to Fe and O(2) is the O atom further from Fe. ‡‡ In subunit B this angle is 145°. §§ The bend angle is the Fe—O—O angle. ¶¶ The tilt angle is the angle between the heme perpendicular and Fe—O (Vangberg *et al.*, 1997).

type metaquo structure solved here is closer to that observed in other hemoglobins and is significantly closer to the heme iron than in the previously solved structure of native DHP (LaCount *et al.*, 2000).

As would be expected, the wild-type and the C73S mutant structures of DHP are nearly identical in the region of the heme-binding site. There are small differences in the two structures, primarily in the subunit-interface region of the molecule, which includes the EF loop where the C73S mutation is located. Both proteins undergo X-ray-induced reduction of the heme iron, but to a different extent. The wild type is reduced only slightly and the structure refines well with a water molecule as a sixth heme iron ligand. The heme center of the C73S mutant undergoes complete reduction, permitting oxygen to bind to its iron.

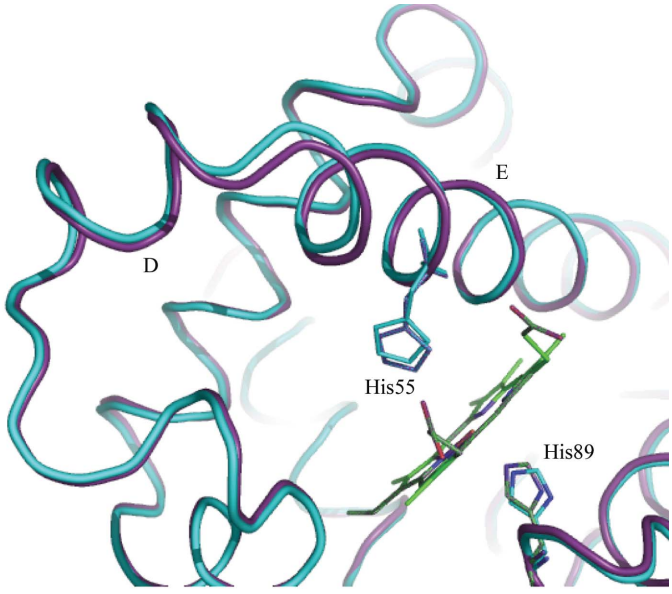

Figure 4
C^{α}-trace superposition of the wild-type DHP (colored purple) and original DHP (colored cyan) structures. Helices D and E are indicated in the figure and the superimposed His55 and His89 residues that illustrate subtle structural differences are shown in stick representation.

3.2. Distal and proximal histidine positions in the structures

Ligands bind to the heme iron of DHP in the distal pocket. Residue His55, referred to as the distal histidine, potentially stabilizes ligands bound to the heme iron through the formation of hydrogen bonds. In the original structure of DHP, His55 was displaced from the distal pocket when the substrate bound in the internal binding site (LaCount *et al.*, 2000). In the structures presented here, the conformation of His55 is closer to the heme iron. Indeed, in our structure of the wild-type metaquo DHP form, the distal histidine is located 0.75 Å closer to the heme iron (Table 2 and Fig. 4). The distance from the distal histidine to the heme iron in the structure presented here is close to the distance observed in myoglobin at neutral pH (PDB entry 1a6k; Vojtechovsky *et al.*, 1999). In the structure of the C73S mutant protein (PDB code 2qfn), which has an oxygen molecule bound in the distal pocket, the His55 residue is a little further removed from the heme iron, as shown in the superimposed active sites of the two proteins in Fig. 5. As a consequence, there is a hydrogen bond between His55 $N^{\varepsilon 2}$ and the O(2) atom of the oxygen molecule (see below). The distal histidine does not exhibit a solvent-exposed conformation based on OMIT maps where His55 is removed from the calculations. The electron density observed in the OMIT map could accommodate only one water molecule instead of a histidine residue. Under the present crystallization conditions, His55 exhibits a single conformation, which is inside the distal pocket in both the wild-type and C73S mutant protein structures.

The proximal histidine His89 is the fifth coordination ligand of the heme iron in DHP and is positioned at a distance of 2.1 Å from the heme iron in the wild-type protein and at a distance of 2.2 Å in the C73S mutant protein (Table 2 and Fig. 5). In the original structure of DHP, the bond length of the proximal histidine $N^{\varepsilon 2}$ to the iron was observed to be 2.3 Å (Table 2). It is believed that the protein environment on the proximal side of the heme influences the reactivity of the heme iron towards *trans* ligands. The distances observed in the structures presented here agree with those found in globins (Vojtechovsky *et al.*, 1999). The Fe–His distance can be shorter in peroxidases (Bonagura *et al.*, 2003), which may arise from strong hydrogen bonding of a neighboring aspartate to the proximal histidine (Spiro *et al.*, 1990), leading to an Asp-His-Fe triad on the proximal side (Goodin & McRee, 1993). This interaction leads to an even shorter Fe—$N^{\varepsilon 2}$ bond length of 2.1 Å in cytochrome *c* peroxidase (Bonagura *et al.*, 2003).

3.3. Coordination geometries of the ligands in the two forms of DHP

The differences in the distal and proximal histidine positions discussed above appear to correlate with a six-coordinate

heme iron in both the wild-type and C73S protein structures. In the wild-type model, shown in Fig. 6(*a*), a water molecule is positioned in the distal pocket at a coordination distance of 2.2 Å from the heme iron in both the A and B subunits. In the original DHP structure, the waters present in the distal pocket are at nonbonding distances of 3.3 and 2.5 Å, respectively, in subunits A and B (Table 2). This Fe—O distance is most likely to arise from subtle variations in crystallization conditions that affect the distal pocket. The Fe—O bond length of 2.2 Å in the wild-type structure presented here is consistent with a chemical bond, while the longer distance in the first DHP structure is most likely to indicate that water is trapped in the distal pocket but not bound to the heme iron. The six-coordinate metaquo adduct observed here is consistent with the structures of all ferric myoglobins and hemoglobins that have a distal histidine. Moreover, magnetic circular dichroism (Osborne *et al.*, 2006), resonance Raman spectroscopy (Belyea *et al.*, 2006) and UV–Vis titrations (Nienhaus *et al.*, 2006) are also consistent with the coordination of water as observed in this investigation.

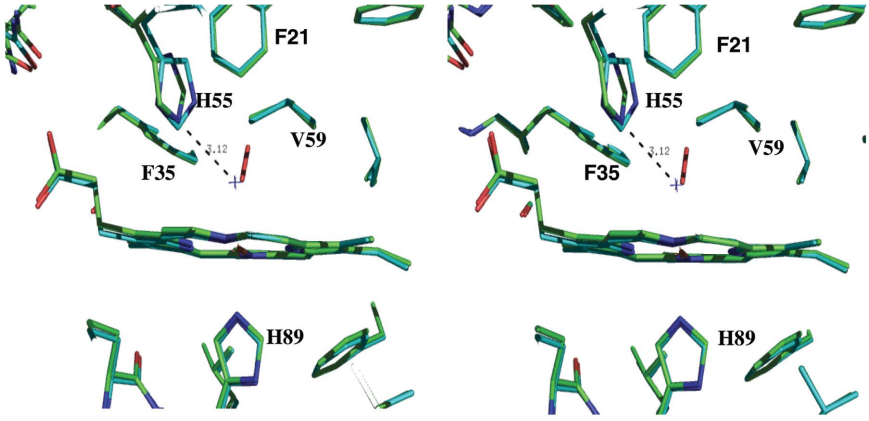

Figure 5
Stereoview of an overlay of the distal pocket region for the wild-type recombinant enzyme (colored green) and the O_2-ligated form of the C73S mutant protein (colored cyan). The figure emphasizes the differences in the conformation of His55 in the two superimposed structures of subunit A. The indicated hydrogen bond between His55 $N^{\epsilon 2}$ and the water molecule bound to the heme iron in the wild-type protein has an N—O distance of 3.1 Å.

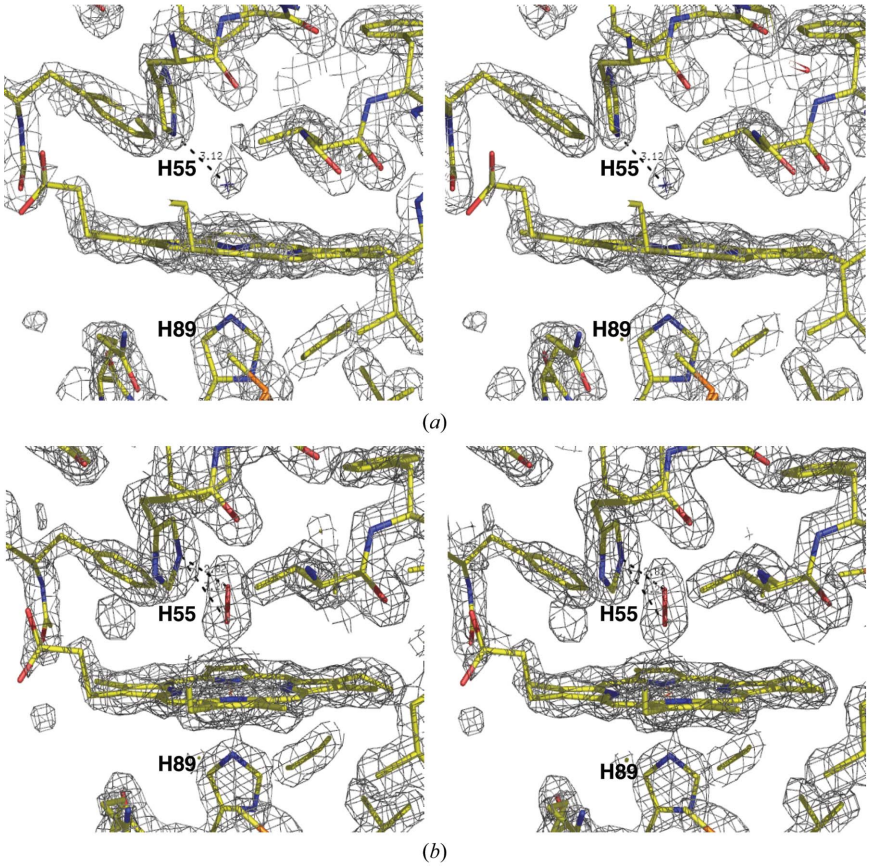

Figure 6
Stereo representation of electron-density maps ($2F_o - F_c$) for the wild-type protein (*a*) and the O_2 complex of the C73S mutant form of DHP (*b*). The maps were contoured at 1.5σ for the wild-type enzyme and at 1.7σ for the C73S–oxygen complex. The coordinates shown correspond to subunit A.

There was clearly more electron density observed above the heme iron in the distal pocket in the C73S mutant protein compared with the wild-type structure. It is most likely that the C73S mutant protein was photoreduced during X-ray data collection (Berglund *et al.*, 2002; de Sanctis *et al.*, 2004; Schlichting *et al.*, 2000; Sjorgren & Hajdu, 2001; Fedorov *et al.*, 2003; Bolognesi *et al.*, 1999). While the wild-type enzyme had a minority population of reduced heme iron, reduction was virtually complete in the C73S mutant protein (Table 1). Composite OMIT $2F_o - F_c$ maps were calculated in *CNS* by omitting 5% of the model for 20 cycles of simulated-annealing refinement steps with a starting temperature of 4000 K. These maps revealed differences in the ligation geometries between the wild-type and C73S mutant proteins. The results shown in Fig. 6(*b*) indicate that diatomic oxygen is ligated to the heme iron in the C73S mutant protein structure.

3.4. Mechanistic significance of distal histidine hydrogen bonding

The distal histidine His55 forms hydrogen bonds to both water and O_2 in the structures reported here. In the wild-type model, His55 forms a weak hydrogen bond to the water ligand bound to the heme iron such that $N^{\delta 1}$ is positioned at a hydrogen-bonding distance of 3.0 Å from the hydroxyl of the Tyr38 residue. This hydrogen bond might be important for reactivity since it may regulate H_2O displacement from the heme iron when either substrate or H_2O_2 binds as part of the

Table 3
Comparison of the distances of His55 to the heme Fe ligand and the hydroxyl group of Tyr38 in the wild-type and C73S mutant protein structures.

Values in bold emphasize relevant hydrogen-bonding distances; values are listed for subunit A.

	His55 distances (Å)			
	Wild-type (2qfk)		C73S (2qfn)	
	$N^{\delta1}$	$N^{\varepsilon2}$	$N^{\delta1}$	$N^{\varepsilon2}$
Ligand†	4.9	**3.1**	O(1) 4.5, O(2) 4.6	O(1) **3.2**, O(2) **2. 8**
Tyr38 OH	**3.0**	4.8	4.4	4.7

† For the wild-type recombinant structure the values are listed for water as a ligand; for the C73S mutant of DHP the sixth coordination ligand of the heme iron is O_2.

peroxidase catalytic cycle. For example, if the substrate binds first then it could displace His55 to the solvent-exposed conformation observed in the original DHP structure, thereby allowing the binding of H_2O_2. It is possible that H_2O is a gatekeeper that regulates the initiation of the catalytic cycle. This behavior would be analogous to the displacement of water in the catalytic cycle of cytochrome $P450_{cam}$ (Sligar & Gunsalas, 1976).

The hydrogen bond to the diatomic oxygen in the C73S structure is stronger than the hydrogen bond to water. The oxygen molecule is bent and the Fe—O(1)—O(2) angle is 168° in subunit A and 144° in subunit B. There is also a small tilt angle [defined as the angle between the heme perpendicular and the Fe—O(1) bond (Vangberg *et al.*, 1997)] of 11° and 6°, respectively. Both O atoms of the molecule can form hydrogen bonds to $N^{\varepsilon2}$ of the distal histidine His55, with distances of 2.8 Å for O(2) and a weaker 3.2 Å bond distance for O(1) in subunit A (Table 2). In this orientation, His55 $N^{\delta1}$ is no longer within hydrogen-bonding distance of Tyr38, but instead faces the solvent. In mechanistic terms, this new interaction of His55 (by analogy, also likely to occur with H_2O_2) could facilitate closer contacts of Tyr38 with the substrate in the course of the enzymatic activity of DHP, while at the same time allowing His55 to move into a position that straddles the two O atoms of bound H_2O_2. This conformation of His55 is consistent with its role as an acid/base catalyst needed for the activation of H_2O_2 to form compound I (Poulos & Kraut, 1980). The catalytic step involves abstracting a hydrogen from O(1) and transferring it to O(2) as indicated below:

$$\begin{aligned} &P\text{–}Fe^{III}\text{–}H\text{–}O(1)\text{–}O(2)\text{–}H + His\text{–}N^{\varepsilon2} \\ &\quad\rightarrow P\text{–}Fe^{III}\text{–}O(1)\text{–}O(2)\,\text{–}H^{-} + His\text{–}N^{\varepsilon2}\text{–}H^{+} \\ &\quad\rightarrow P\text{–}Fe^{III}\text{–}O(1)\,\text{–}O(2)\,\text{–}H_2 + His\text{–}N^{\varepsilon2} \\ &\quad\rightarrow P^{+\cdot}\text{–}Fe^{IV}{=}O(1) + O(2)\text{–}H_2 + His\text{–}N^{\varepsilon2}. \end{aligned}$$

The transfer leads to heterolytic bond cleavage and the formation of compound I. The distances from both Tyr38 and the heme iron ligand to the distal histidine His55 are listed in Table 3 to emphasize the differences between the wild-type and C73S mutant protein structures.

Normally, peroxidases have an arginine residue that resides near the distal histidine that acts to stabilize the proton transfer required to promote heterolytic bond cleavage. Since this arginine is missing in DHP, the observed hydrogen bond may account for the activation of the peroxy intermediate to form compound I. We can infer that Tyr38 is a critical residue in this process since it changes from hydrogen bonding to His55 (substrate-free) to hydrogen bonding to the substrate itself (substrate-bound) as evident in the first DHP crystal structure (LaCount *et al.*, 2000). Both the strong hydrogen bond in the oxy form and the water bound in the ferric form, which is the peroxidase resting state, are new features that have not been observed previously for this enzyme.

4. Conclusion

The hypothesis that His55 activates bound H_2O_2 in DHP is strengthened by the structural data presented here. However, there is an apparent contradiction in this hypothesis if one considers both solution reactivity and the X-ray crystal structures. The first DHP structure showed that His55 was displaced to a solvent-exposed conformation more than 9 Å from the heme iron when the substrate was bound in the distal pocket (LaCount *et al.*, 2000). However, mechanistic data indicate that the enzyme is inactivated if H_2O_2 is added more than 30 s prior to the substrate (Belyea *et al.*, 2005). In order for His55 to catalyze the formation of compound I it must be in the distal pocket, yet according to the original model it will be displaced when substrate is bound. There are three possibilities that can account for this apparent inconsistency. The first possibility is that His55 does not activate H_2O_2, but rather the phenolate oxygen activates bound H_2O_2 (Franzen *et al.*, 2007). However, this hypothesis can only explain the reactivity when the pH is greater than the pK_a, which is not relevant for the crystallization conditions of the structures presented here. Stopped-flow data show that DHP has significant peroxidase activity even when the pH is less than the pK_a of the substrate (Belyea *et al.*, 2005). The second possibility is that the substrate always binds to the enzyme within 30 s of activation. This seems unlikely unless the substrate first interacts on the exterior of the enzyme in a priming step that serves as a trigger for the onset of peroxidase function. Without such a step DHP would wastefully bind H_2O_2 and be rapidly inactivated. The third possibility is that the substrate binds to an external site. This binding could either be a priming event as suggested above or it could be that oxidation takes place at an external binding site near the heme edge as observed for other heme peroxidases (Ator & de Montellano, 1987). The present structure shows the possible interactions of His55 with a bound diatomic molecule and thus our current data support the third hypothesis at low pH and perhaps more generally. The resolution of these issues will require additional NMR and X-ray crystallographic studies, which are presently under way.

We acknowledge financial support for this work from Army Research Office Grant 52278-LS. We thank Dr Robert Rose, Department of Molecular and Structural Biochemistry at NCSU for his help, guidance and discussions during this

project. We also thank Dr Laurie Betts of the UNC Biomolecular X-ray Crystallography Core Facility for assistance in the X-ray data collection and analysis. We thank Dr David Lambright for essential advice on crystallization conditions and analysis.

References

Andersson, L. A., Renganathan, V., Loehr, T. M. & Gold, M. H. (1987). *Biochemistry*, **26**, 2258–2263.

Ator, M. A. & de Montellano, P. R. O. (1987). *J. Biol. Chem.* **262**, 1542–1551.

Bailly, X., Chabasse, C., Hourdez, S., Dawilde, S., Martial, S., Moens, L. & Zal, F. (2007). *FEBS J.* **274**, 2641–2652.

Belyea, J., Belyea, C. M., Lappi, S. & Franzen, S. (2006). *Biochemistry*, **45**, 14275–14284.

Belyea, J., Gilvey, L. B., Davis, M. F., Godek, M., Sit, T. L., Lommel, S. A. & Franzen, S. (2005). *Biochemistry*, **44**, 15637–15644.

Berglund, G. I., Carlsson, G. H., Smith, A. T., Szoke, H., Henriksen, A. & Hajdu, J. (2002). *Nature (London)*, **417**, 463–468.

Bolognesi, M., Rosano, C., Losso, R., Borassi, A., Rizzi, M., Wittenberg, J. B., Boffi, A. & Ascenzi, P. (1999). *Biophys. J.* **77**, 1093–1099.

Bonagura, C. A., Bhaskar, B., Shimizu, H., Li, H. Y., Sundaramoorthy, M., McRee, D. E., Goodin, D. B. & Poulos, T. L. (2003). *Biochemistry*, **42**, 5600–5608.

Brünger, A. T., Adams, P. D., Clore, G. M., DeLano, W. L., Gros, P., Grosse-Kunstleve, R. W., Jiang, J.-S., Kuszewski, J., Nilges, M., Pannu, N. S., Read, R. J., Rice, L. M., Simonson, T. & Warren, G. L. (1998). *Acta Cryst.* D**54**, 905–921.

Cheek, J., Mandelman, D., Poulos, T. L. & Dawson, J. (1999). *J. Biol. Inorg. Chem.* **4**, 64–72.

Chen, Y. P., Woodin, S. A., Lincoln, D. E. & Lovell, C. R. (1996). *J. Biol. Chem.* **271**, 4609–4612.

Chouchane, S., Lippai, I. & Magliozzo, R. S. (2000). *Biochemistry*, **39**, 9975–9983.

Collaborative Computational Project, Number 4 (1994). *Acta Cryst.* D**50**, 760–763.

DeLano, W. L. (2002). *The PyMOL Molecular Graphics System.* DeLano Scientific, San Carlos, CA, USA.

Della Longa, S., Arcovito, A., Benefatto, M., Congiu-Castellano, A., Girasole, M., Hazemann, J. L. & Lo Bosco, A. (2003). *Biophys. J.* **85**, 549–558.

Emsley, P. & Cowtan, K. (2004). *Acta Cryst.* D**60**, 2126–2132.

Fedorov, R., Ghosh, D. K. & Schlichting, I. (2003). *Arch. Biochem. Biophys.* **409**, 25–31.

Ferrari, R. P., Laurenti, E. & Trotta, F. (1999). *J. Biol. Inorg. Chem.* **4**, 232–237.

Franzen, S., Belyea, J., Gilvey, L. B., Davis, M. F., Chaundhary, C. E., Sit, T. L. & Lommel, S. (2006). *Biochemistry*, **45**, 9085–9094.

Franzen, S., Gilvey, L. B. & Belyea, J. (2007). *Biochim. Biophys. Acta*, **1774**, 121–130.

Franzen, S., Jasaitis, A., Belyea, J., Brewer, S. H., Casey, R., MacFarlane, A., W., Stanley, R. J., Vos, M. H. & Martin, J.-L. (2006). *J. Phys. Chem. B*, **110**, 14483–14493.

Goodin, D. B. & McRee, D. E. (1993). *Biochemistry*, **32**, 3313–3324.

Hashimoto, S., Teraoka, J., Inubushi, T., Yonetani, T. & Kitagawa, T. (1986). *J. Biol. Chem.* **261**, 11110–11118.

Katz, D. S., White, S. P., Huang, W., Kumar, R. & Christianson, D. W. (1994). *J. Mol. Biol.* **244**, 541–553.

Kendrew, J. C., Dickerson, R. E., Strandberg, B. E., Hart, R. G., Davies, D. R., Phillips, D. C. & Shore, V. C. (1960). *Nature (London)*, **185**, 422–427.

Kuila, D., Tien, M., Fee, J. A. & Ondrias, M. R. (1985). *Biochemistry*, **24**, 3394–3397.

Kunishima, N., Amada, F., Fukujama, K., Kawamoto, M., Maesunaga, T. & Matsubara, H. (1996). *FEBS Lett.* **378**, 291–294.

LaCount, M. W., Zhang, E., Chen, Y. P., Han, K., Whitton, M. M., Lincoln, D. E., Woodin, S. A. & Lebioda, L. (2000). *J. Biol. Chem.* **275**, 18712–18716.

Laskowski, R. A., MacArthur, M. W., Moss, D. S. & Thornton, J. M. (1993). *J. Appl. Cryst.* **26**, 283–291.

Liu, X.-Z., Li, S.-L., Jing, H., Liang, Y.-H., Hua, Z.-Q. & Lu, G.-Y. (2001). *Acta Cryst.* D**57**, 775–783.

McCoy, A. J., Grosse-Kunstleve, R. W., Storoni, L. C. & Read, R. J. (2005). *Acta Cryst.* D**61**, 458–464.

Matthews, B. W. (1968). *J. Mol. Biol.* **33**, 491–497.

Murshudov, G. N., Vagin, A. A. & Dodson, E. J. (1997). *Acta Cryst.* D**53**, 240–255.

Nardini, M., Tarricone, C., Rizzi, M., Lania, A., Desideri, A., De Sanctis, G., Coletta, M., Petruzzelli, R., Ascenzi, P., Coda, A. & Bolognesi, M. (1995). *J. Mol. Biol.* **247**, 459–465.

Nienhaus, K., Deng, P., Belyea, J., Franzen, S. & Nienhaus, G. U. (2006). *J. Phys. Chem. B*, **110**, 13264–13276.

Osborne, R. L., Sumithran, S., Coggins, M. K., Chen, Y.-P., Lincoln, D. E. & Dawson, J. H. (2006). *J. Inorg. Biochem.* **100**, 1100–1108.

Otwinowski, Z. & Minor, W. (1997). *Methods Enzymol.* **276**, 307–326.

Poulos, T. L. & Kraut, J. (1980). *J. Biol. Chem.* **255**, 575–580.

Ropp, J. S. de, LaMar, G. N., Wriishi, H. & Gold, M. H. (1991). *J. Biol. Chem.* **266**, 15001–15008.

Royer, W. E. Jr (1994). *J. Mol. Biol.* **235**, 657–681.

Sanctis, D. de, Dewilde, S., Pesce, A., Moens, L., Ascenzi, P., Hankeln, T., Burmester, T. & Bolognesi, M. (2004). *J. Mol. Biol.* **336**, 917–927.

Schlichting, I., Berendzen, J., Chu, K., Stock, A. M., Maves, S. A., Benson, D. E., Sweet, R. M., Ringe, D., Petsko, G. A. & Sligar, S. G. (2000). *Science*, **287**, 1615–1622.

Sjorgren, T. & Hajdu, J. (2001). *J. Biol. Chem.* **276**, 13072–13076.

Sligar, S. G. & Gunsalas, I. C. (1976). *Proc. Natl Acad. Sci. USA*, **73**, 1078–1081.

Spiro, T. G., Smulevich, G. & Su, G. (1990). *Biochemistry*, **29**, 4497–4508.

Vangberg, T., Bocian, D. F. & Ghosh, A. (1997). *J. Biol. Inorg. Chem.* **2**, 526–530.

Vojtechovsky, J., Chu, K., Berendzen, J., Sweet, R. M. & Schlichting, I. (1999). *Biophys. J.* **77**, 2153–2174.

Wang, J., Mauro, M., Edwards, S. L., Oatley, S. J., Fishel, L. A., Ashford, V. A., Xuong, N.-H. & Krout, J. (1990). *Biochemistry*, **29**, 7160–7173.

Yamazaki, I., Tamura, M. & Nakajima, R. (1981). *Mol. Cell. Biochem.* **40**, 143–153.

Yang, F. & Phillips, G. N. (1996). *J. Mol. Biol.* **256**, 762–774.

Yonetani, T. & Anni, H. (1987). *J. Biol. Chem.* **262**, 9547–9554.

Zhang, E., Chen, Y. P., Roach, M. P., Lincoln, D. E., Lovell, C. R., Woodin, S. A., Dawson, J. H. & Lebioda, L. (1996). *Acta Cryst.* D**52**, 1191–1193.

J|A|C|S
COMMUNICATIONS

Published on Web 01/25/2008

Substrate Binding Triggers a Switch in the Iron Coordination in Dehaloperoxidase from *Amphitrite ornata*: HYSCORE Experiments

Tatyana I. Smirnova,*,† Ralph T. Weber,‡ Mike F. Davis,† and Stefan Franzen†

Department of Chemistry, North Carolina State University, 2620 Yarbrough Drive, Raleigh, North Carolina 27695, and Bruker BioSpin Corporation, EPR Division, Billerica, Massachusetts 10821

Received September 20, 2007; E-mail: tatyana_smirnova@ncsu.edu

We have explored the effect of substrate binding on the heme iron conformation in the enzyme dehaloperoxidase (DHP) that was first isolated from the terebellid polychaete *Amphitrite ornata* and is now expressed in *Escherichia coli*.[1−3] DHP is a dimeric hemoglobin[4] that also has significant peroxidase activity under physiological conditions.[5] Since hemoglobins and peroxidases require ferrous and ferric oxygen, respectively, one can hypothesize that substrate binding causes a change in protein conformation that affects the spin state of the heme iron. A recent X-ray crystal structure of metaquo DHP resting state[6] shows that water is indeed bound to the heme iron as predicted by spectroscopic measurements.[7−9] In attempting to understand the role of substrate binding, we obtained an indication from hyperfine-shifted NMR that the substrate enters the distal pocket at pH < 7.0. At pH < 7.0, the enzyme turnover is rapid and so is the inactivation of DHP.[2,3] Above pH 7.0, the turnover is significantly slower, but substantially more product is formed. Although an X-ray crystal structure[10] shows a substrate analogue, 4-iodophenol, to be bound in the distal pocket of the hemoglobin, stopped-flow experiments (not shown) indicate that DHP can function without the substrate bound to the internal binding site. The ∼23% occupancy of the substrate analogue 4-iodophenol in the X-ray structure 1EWA[10] suggests a function for the substrate interaction in the distal pocket but is inconclusive whether the distal pocket is an active site of the enzyme. We have advanced a hypothesis that substrate binding acts as a trigger event in the switch from the oxygen binding to the peroxidase function.[1−3] An experimental test correlating changes in the ligation state with the coordination of the ferric heme iron upon substrate binding is considered to be critical for verification of our hypothesis.

Herein we report on continuous wave (CW) EPR and hyperfine sublevel correlation spectroscopic (HYSCORE) analysis of the ferric form of DHP that was undertaken to characterize effects of the binding of 2,4,6-trifluorophenol (TFP) on heme iron coordination. HYSCORE experiments that correlate nuclear frequencies in the two manifolds of the electronic spin are informative for studying the hyperfine interactions of the heme iron with the surrounding nuclei.

Experimental X-band (9.5 GHz) CW EPR spectra of DHP in the absence (dotted line) and the presence (solid line) of a 10-fold excess of TFP at pH 6.0 are shown in Figure 1. The characteristic $g_{\perp}$= 6 and $g_{||}$ = 2 features of the EPR spectra show that the iron exists in a high spin (HS, $S = {}^5/_2$) state in both the absence and presence of the substrate.[14,19] In this respect, DHP resembles metmyoglobin, a known HS ferric heme protein having a six-coordinate ligation. At pH 6.0, there is no change in the spin state; however, the coordination sphere of the heme iron is clearly affected by substrate binding (Figure 1 inset).

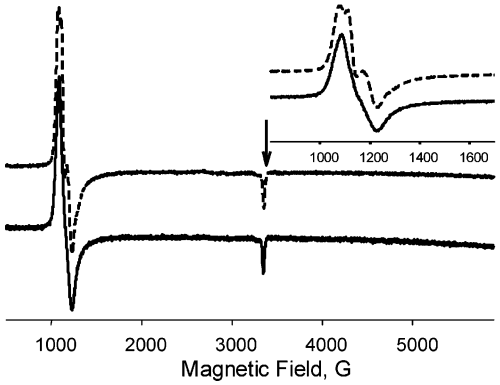

Figure 1. CW X-band (9.5 GHz) EPR spectra of DHP in the absence (dotted line) and in the presence (solid line) of 10-fold excess of TFP at pH 6.0 and T = 4 K. Arrow indicates the field of HYSCORE experiment.

Figure 2 shows HYSCORE spectra of DHP at pH = 6.0 in an H_2O buffer (A), a D_2O (99%) buffer (B), and an H_2O buffer with 10-fold excess of TFP relative to DHP (C). The spectrum of DHP in the second quadrant reveals the signals from strongly coupled nitrogen nuclei at (−9.5, 5.54) MHz that are assigned to a double quantum ($\Delta m_I = \pm 2$, dq) transition. Two less intense peaks at (−4.98, 2.95) and (−4.45, 3.15) MHz arise from single quantum ($\Delta m_I = \pm 1$, sq) transitions. These signals were assigned to four approximately equivalent nitrogen nuclei of the porphyrin ring and another nitrogen of the proximal His89.[11,12] The first quadrant revealed proton signals at 14.8 MHz that span about 6.2 MHz frequency range with a well-defined strong intensity characterized by weaker interactions of 2.5 MHz and lower.

To better understand the origin of the proton signals, a spectrum of DHP prepared in pH 6.0 D_2O buffer was obtained (Figure 2B). For this sample preparation, all of the spectral features in both quadrants remained the same, except the signals corresponding to strongly coupled (6 MHz) proton(s) that disappeared. This indicates that the signal from the weakly coupled proton(s) with interaction of about 2.5 MHz originates from nonexchangeable protein protons. Hyperfine interactions of similar magnitude have been observed for hydrogen atoms in the heme and proximal histidine.[13,14] The disappearance of the strongly coupled 6 MHz proton signal in D_2O buffer (Figure 2B) is attributed to exchangeable hydrogen atom-(s). Previous ENDOR studies of metmyoglobin reported a 6.1 ± 0.1 MHz hyperfine coupling for the protons of a water molecule coordinated to the iron as the sixth ligand,[15,16] which is essentially the same as the 6 MHz signal observed for DHP. Following buffer exchange, we have observed an additional intensity in the first quadrant at (1.83, 2.63) MHz that is consistent with the deuteron signals (ν_D = 2.3 MHz). Unfortunately, for DHP, in both H_2O and D_2O buffers, this quadrant contains a strong spectral feature, extending from 1.5 to 3.8 MHz that prohibits unambiguous

† North Carolina State University.
‡ Bruker BioSpin Corporation.

10.1021/ja0772952 CCC: $40.75

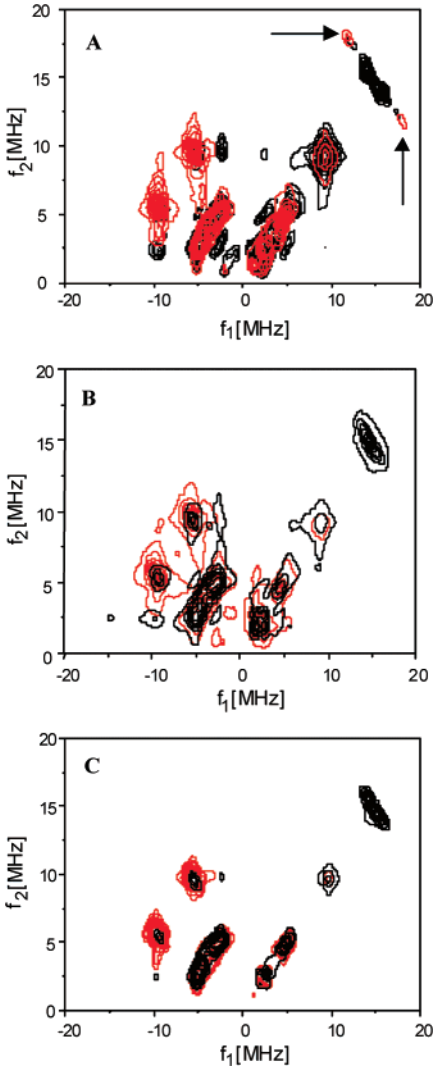

Figure 2. HYSCORE spectra of DHP in pH = 6.0 buffers prepared from H_2O (A) and D_2O (B) and DHP in H_2O buffer with 10-fold excess of TFP (C). The spectra were recorded at magnetic field of 346 mT with τ =128 ns (red trace) and 100 ns (black trace) at T = 4.5 K.

determination of the deuteron nuclei coupling constant. The assignment of the 6 MHz protons to heme-bound water agrees with the X-ray crystal structure[6] and other spectroscopic data.[7−9]

The major change in the pH 6.0 DHP HYSCORE spectra upon TFP substrate binding is the disappearance of the signal from the strongly coupled protons (Figure 2C). We have also observed changes in the positions of nitrogen resonance lines corresponding to a small but measurable increase in the hyperfine coupling constant from approximately 7.5 to 7.7 MHz. On the other hand, although the line shape of the signals from the weakly coupled nonexchangeable protons alters slightly in the presence of TFP, the maximum hyperfine splitting remained similar in all three spectra. The changes in strongly coupled protons demonstrate that the binding of TFP at pH 6.0 results in a displacement of the water molecule and transition from five- to six-coordinated iron. Increase in the hyperfine coupling of nitrogen nuclei of the heme is consistent with the change in the iron coordination.[13] Since no spectral features from ^{19}F were observed, the TFP substrate does not appear to ligate to the heme iron in this process.

The reported HYSCORE data provide information on the molecular mechanism by which substrate binding can alter the function of DHP. The data indicate that the heme-bound water molecule in the resting state of the ferric form is displaced when the substrate binds, at least under the conditions of the experiment. Such behavior can be compared to the effect observed in cytochrome P450cam, where the transition from the low-spin $S = {}^1/_2$ to the high-spin state, observed upon substrate binding, is associated with displacement of a water molecule from the axial ligand position.[17−19] However, in contrast to cytochrome P450cam, displacement of a water molecule from the heme iron of DHP at pH 6.0 does not result in a change of the spin state since the iron is initially in the HS state. Thus, in DHP, the EPR data show a change in rhombicity that is consistent with a change in the coordination without affecting the spin state. The power of HYSCORE is that it shows changes in the coupling of protons on the heme-bound water that further substantiate the hypothesis that substrate binding displaces the water from the heme iron.

Acknowledgment. The work at NCSU was supported by the NSF Grant MCB-0451510 to T.I.S. and ARO Grant 52278-LS to S.F.

Supporting Information Available: Experimental procedures and HYSCORE spectra. This material is available free of charge via the Internet at http://pubs.acs.org.

References

(1) Franzen, S.; Chaudhary, C.; Belyea, J.; Gilvey, L.; Davis, M. F.; Sit, T. L.; Lommel, S. A. *Biochemistry* **2006**, *45*, 9085−9094.
(2) Belyea, J.; Gilvey, L. B.; Davis, M. F.; Godek, M.; Sit, T. L.; Lommel, S. A.; Franzen, S. *Biochemistry* **2005**, *44*, 15637−15644.
(3) Franzen, S.; Gilvey, L. B.; Belyea J. *Biochim. Biophys. Acta* **2007**, *1775*, 121−130.
(4) Weber, R. E.; Magnum, C. P.; Steinman, H.; Bonaventura, C.; Sullivan, B.; Bonaventura, J. *Comp. Biochem. Physiol.* **1977**, *56A*, 179−187.
(5) Chen, Y. P.; Woodin, S. A.; Lincoln, D. E.; Lovell, C. R. *J. Biol. Chem.* **1996**, *271*, 4609−4612.
(6) de Serrano, V.; Chen, Z.; Davis, M. F.; Franzen, S. *Acta Crystallogr.* **2007**, *D63*, 1094−1101.
(7) Nienhaus, K.; Deng, P. C.; Belyea, J.; Franzen, S.; Nienhaus, G. U. *J. Phys. Chem. B* **2006**, *110*, 13264−13276.
(8) Belyea, J.; Belyea, C. M.; Lappi, S.; Franzen, S. *Biochemistry* **2006**, *45*, 14275−14284.
(9) Osborne, R. L.; Surnithran, S.; Coggins, M. K.; Chen, Y. P.; Lincoln, D. E.; Dawson, J. H. *J. Inorg. Biochem.* **2006**, *100*, 1100−1108.
(10) Zhang, E.; Chen, Y. P.; Roach, M. P.; Lincoln, D. E.; Lovell, C. R.; Woodin, S. A.; Dawson, J. H.; Lebioda, L. *Acta Crystallogr.* **1996**, *D52*, 1191−1193.
(11) Scholes, C.; Lapidot, A.; Mascarenhas, R.; Inubushi, T.; Isaacson, R.; Feher, G. *J. Am. Chem. Soc.* **1982**, *104*, 2724−2735.
(12) Garcia-Rubio, I.; Broun, M.; Gromov, I.; Thony-Meyer, L.; Schweiger, A. *Biophys. J.* **2007**, *92*, 1361−1373.
(13) Usov, O. M.; Choi, P. S.-T.; Shapleigh, J. P.; Scholes, C. P. *J. Am. Chem. Soc.* **2005**, *127*, 9485−9494.
(14) Fahnenschmidt, M.; Rau, H. K.; Bittl, R.; Haehnel, W.; Lubitz, W. *Chem.−Eur. J.* **1999**, *5*, 2327−2334.
(15) Mulks, C. F.; Scholes, C. P.; Dickinson, L. C.; Lapidot, A. *J. Am. Chem. Soc.* **1979**, *101*, 1645−1654.
(16) Veselov, A. V.; Osborne, J. P.; Gennis, R. B.; Scholes, C. P. *J. Am. Chem. Soc.* **2000**, *122*, 8712−8716.
(17) Tsai, R.; Yu, C. A.; Gunsalus, I. C.; Peisach, J.; Blumberg, W.; Orme-Johnson, W. H.; Beinert, H. *Proc. Natl. Acad. Sci. U.S.A.* **1970**, *66*, 1157−1163.
(18) Sligar, S. G.; Gunsalas, I. C. *Proc. Natl. Acad. Sci. U.S.A.* **1976**, *73*, 1078−1081.
(19) Poulos, T. L.; Raag, R. *FASEB J.* **1992**, *6*, 674−679.

JA0772952

BIOCHEMISTRY
including biophysical chemistry & molecular biology

Article

Characterization of Dehaloperoxidase Compound ES and Its Reactivity with Trihalophenols

Jeremiah Feducia, Rania Dumarieh, Lauren B. G. Gilvey, Tatyana Smirnova, Stefan Franzen, and Reza A. Ghiladi

Biochemistry, **2009**, 48 (5), 995-1005• DOI: 10.1021/bi801916j • Publication Date (Web): 15 January 2009

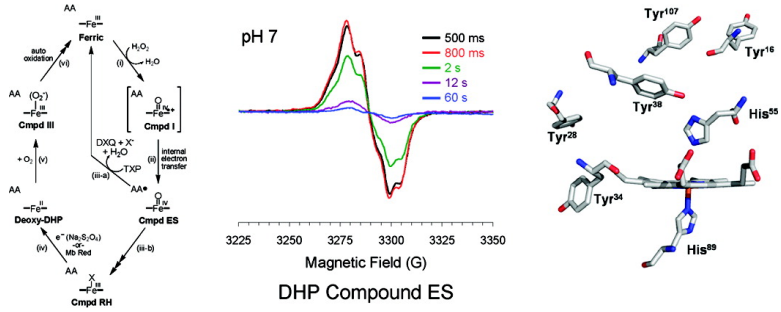

More About This Article

Additional resources and features associated with this article are available within the HTML version:

- Supporting Information
- Access to high resolution figures
- Links to articles and content related to this article
- Copyright permission to reproduce figures and/or text from this article

View the Full Text HTML

Characterization of Dehaloperoxidase Compound ES and Its Reactivity with Trihalophenols[†]

Jeremiah Feducia, Rania Dumarieh, Lauren B. G. Gilvey, Tatyana Smirnova, Stefan Franzen,* and Reza A. Ghiladi*

Department of Chemistry, North Carolina State University, Raleigh, North Carolina 27695

Received October 12, 2008; Revised Manuscript Received November 18, 2008

ABSTRACT: Dehaloperoxidase (DHP), the oxygen transport hemoglobin from the terebellid polychaete *Amphitrite ornata*, is the first globin identified to possess a biologically relevant peroxidase activity. DHP has been shown to oxidize trihalophenols to dihaloquinones in a dehalogenation reaction that uses hydrogen peroxide as a substrate. Herein, we demonstrate that the first detectable intermediate following the addition of hydrogen peroxide to ferric DHP contains both a ferryl heme and a tyrosyl radical, analogous to Compound ES of cytochrome *c* peroxidase. Furthermore, we provide a detailed kinetic description for the reaction of preformed DHP Compound ES with the substrate 2,4,6-trichlorophenol and demonstrate the catalytic competency of this intermediate in generating the product 2,4-dichloroquinone. Using rapid-freeze-quench electron paramagnetic resonance spectroscopy, we detected a $g \approx 2.0058$ signal confirming the presence of a protein radical in DHP Compound ES. In the absence of substrate, DHP Compound ES evolves to a new species, Compound RH, which is functionally unique to dehaloperoxidase. We propose that this intermediate plays a protective role against heme bleaching. While unreactive toward further oxidation, Compound RH can be reduced and subsequently bind dioxygen, generating oxyferrous DHP, which may represent the catalytic link between peroxidase and oxygen transport activities in this bifunctional protein.

The terebellid polychaete *Amphitrite ornata* contains an abundant coelomic hemoglobin (*1*) that has been named dehaloperoxidase (DHP)[1] (*2*). In the presence of hydrogen peroxide, this globin catalyzes the two-electron oxidation of a trihalophenol substrate to yield a dihaloquinone (Scheme 1). Although DHP is dependent upon the pH and substrate employed, kinetic assays demonstrate that DHP is 1−2 orders of magnitude faster than myoglobin (Mb) in its ability to dehalogenate substrate (*3*), and only 1 order of magnitude slower than horseradish peroxidase (HRP) (*4*). Thus, DHP is an anomaly: it functions as the oxygen transport protein in *A. ornata* despite having a low degree of sequence homology with other hemoglobins (*5*−*8*) yet exhibits significant peroxidase activity approaching that of HRP even though it possesses neither structural nor sequence homology with any known peroxidase.

Scheme 1: Reaction of DHP with Trihalogenated Phenolate and Hydrogen Peroxide Yields Quinone Products

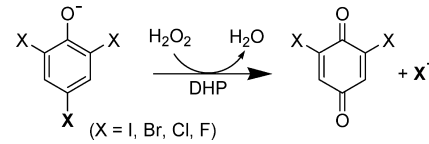

Despite a number of studies on DHP, how this bifunctional protein can act as both a hemoglobin and a peroxidase is still not understood (*1, 2, 4*). Peroxidases generally function via the Poulos−Kraut mechanism (*9*) in which H_2O_2 reacts with a ferric heme to form Compound I, the iron(IV)−oxo porphyrin π-cation radical species that is formally oxidized by two electrons relative to the ferric resting state. The majority of peroxidases regenerate the resting form of the enzyme via two sequential one-electron substrate oxidations ($2AH + H_2O_2 \rightarrow 2A^{\bullet} + 2H_2O$), proceeding through Compound II, an iron(IV)−oxo species that is one-electron-oxidized when compared to the ferric state. Furthermore, DHP (and HRP) has been shown to perform the net two-electron oxidation of phenols ($X-A-OH + H_2O_2 \rightarrow O=A=O + HX + H_2O$) to yield the corresponding quinones, again consistent with the formation of a two-electron-oxidized intermediate (*10*−*12*). However, the reaction of

[†] This project was supported by Army Research Office Grant 52278-LS.

* To whom correspondence should be addressed. S.F.: Department of Chemistry, North Carolina State University, Raleigh, NC 27695; phone, (919) 515-8915; fax, (919) 515-8920; e-mail, Stefan_Franzen@ncsu.edu. R.A.G.: Department of Chemistry, North Carolina State University, Raleigh, NC 27695; phone, (919) 513-0680; fax, (919) 515-8920; e-mail, Reza_Ghiladi@ncsu.edu.

[1] Abbreviations: DHP, dehaloperoxidase; Hb, hemoglobin; HRP, horseradish peroxidase; Mb, myoglobin; 4IP, 4-iodophenol; 4BP, 4-bromophenol; DCP, 2,4-dichlorophenol; TBP, 2,4,6-tribromophenol; TCP, 2,4,6-trichlorophenol; TFP, 2,4,6-trifluorophenol; TXP, trihalophenol; DXQ, dihalophenol; RFQ-CW-EPR, rapid-freeze-quench continuous wave electron paramagnetic resonance; Compound I, two-electron-oxidized heme center when compared to the ferric form, commonly as an $Fe^{IV}=O$ porphyrin π-cation radical; Compound II, one-electron-oxidized heme center when compared to the ferric form, commonly as an $Fe^{IV}=O$ or $Fe^{IV}-OH$; Compound III, oxyferrous [$Fe^{II}-O_2$ or $Fe^{III}-(O_2^-)$] state of the enzyme; Compound ES, two-electron-oxidized state containing both a ferryl center ($Fe^{IV}=O$) and an amino acid (tryptophanyl or tyrosyl) radical, analogous to Compound ES in cytochrome *c* peroxidase; Compound RH, "reversible heme" state of dehaloperoxidase, formed from the decay of Compound ES in the absence of substrate.

10.1021/bi801916j CCC: $40.75
Published on Web 01/15/2009

DHP with its physiological oxidant, H_2O_2, yields what has been characterized to date as Compound II (*7*), which is formally a one-electron-oxidized heme center. Thus, the question of how DHP oxidizes its phenol substrates by two electrons when it appears to form only a one-electron oxidized intermediate needs to be addressed.

Several possible mechanisms for a net two-electron oxidation exist, including the simplest notion that two sequential one-electron oxidations are required for DHP to oxidize a trihalophenol, the first generating a trihalophenoxy radical intermediate and the second yielding a trihalocyclohexanedienone cation which reacts with a solvent water molecule to yield the dihaloquinone product. These intermediates have been proposed by Osborne et al. to form during the oxidation of trichlorophenol to dichloroquinone by horse heart myoglobin (*3*). Another option is that DHP oxidizes trihalophenols by only one electron, forming a trihalophenoxy radical intermediate, which can undergo disproportionation with a second radical species, giving both trihalophenol and dihaloquinone. This proposed mechanism is reminiscent of ascorbate peroxidase (APX), which has been shown to oxidize ascorbate via a one-electron process to monohydroascorbate, the latter undergoing disproportionation to yield ascorbate and dehydroascorbate (*13*). A third possibility is that the intermediate in DHP formed from the reaction of the ferric enzyme with hydrogen peroxide is electronically similar to that of Compound ES in CcP, which has been shown to be isoelectronic with Compound I but in addition to the ferryl moiety also possesses a protein radical as the second oxidizing equivalent rather than a porphyrin-based one. This may be the favored mechanism, as it would allow for product formation via either (i) a direct two-electron oxidation (direct formation of the trihalocyclohexanedienone cation) without generating radical intermediates (which could be potentially harmful if formed in the coelom of *A. ornata*) or (ii) two sequential one-electron oxidations via a transiently formed trihalophenoxy radical that would be further oxidized to the dienone cation (*3*), potentially without first diffusing out of the active site pocket.

To explore mechanistic hypotheses, we have undertaken a comprehensive UV−visible and electron paramagnetic spectroscopic study of the DHP intermediate formed from the reaction of the ferric enzyme with hydrogen peroxide under a variety of conditions using both stopped-flow and rapid-freeze-quench methods and have determined this intermediate to be DHP Compound ES. We have further explored the stability of this Compound ES and demonstrated the existence of a competitive pathway between product formation and decay to a novel species, termed Compound RH, which possesses attenuated levels of dehaloperoxidase activity. Our experimental design reveals mechanistic insights and kinetic descriptions of the intermediates in DHP, which have not been previously reported. We propose an updated catalytic cycle which provides a clearer understanding of the link between peroxidase and oxygen transport activities unique to this bifunctional enzyme.

MATERIALS AND METHODS

Buffer salts and acetonitrile (HPLC-grade) were purchased from Fisher Scientific. All other reagents and biochemicals, unless otherwise specified, were of the highest grade available from Sigma-Aldrich. Solutions of 2,4,6-trichlorophenol (TCP) were freshly prepared daily in 100 mM potassium phosphate (KP_i) buffer (variable pH) and kept at 4 °C. UV−visible spectra were recorded periodically to ensure that the TCP substrate had not degraded (molar absorptivity listed in Table S1 of the Supporting Information). Hydrogen peroxide solutions were also freshly made prior to each experiment. Initially, a 10 mM stock solution of H_2O_2 was prepared and maintained at 4 °C (typically less than 15 min), during which all other protein/substrate solutions were loaded into the stopped-flow apparatus. When prepared in this manner, the stock H_2O_2 solution did not exhibit any degradation over this time period as determined by UV−visible spectroscopic analysis of the hydrogen peroxide absorbance at 240 nm ($\varepsilon_{240} = 43.6\ M^{-1}\ cm^{-1}$) (*18*). The stock H_2O_2 solution was then diluted to the appropriate premixing concentration and immediately loaded into the stopped-flow apparatus. Wild-type (WT) DHP (six-His-tagged protein) expression and purification procedures were preformed as previously described (*4*). TCP (4.05 mM maximum solubility) (*14*) was employed throughout this study due to the low solubility (0.355 mM) of TBP in aqueous solution (*15*).

Spectroscopic Studies. Optical spectra were recorded on either an Agilent 8453 diode array spectrophotometer or a Cary 50 UV−visible spectrophotometer, both equipped with thermostated cell holders at 25 °C. The protoheme content was measured by the pyridine hemochrome assay using a $\Delta\varepsilon_{557}$ of 20.7 $mM^{-1}\ cm^{-1}$ (reduced − oxidized) for iron protoporphyrin IX (*16, 17*).

Enzyme Assays. All measurements were performed in octiplet using a SpectraMax Plus384 UV−visible plate reader equipped with 96-well plates. Assays were carried out at 25 °C in 100 mM KP_i buffer (pH 7.5) containing 5 μM EDTA (total volume of 200 μL). Catalase activity was measured spectrophotometrically by following the decrease over 60 s (linear least-squares fittings) of the hydrogen peroxide concentration (1.5, 30, and 60 mM) at 240 nm ($\varepsilon_{240} = 43.6\ M^{-1}\ cm^{-1}$), in the presence of 1 μM DHP (*18*).

Preparation of Ferric DHP. DHP was incubated with a 1.7-fold molar excess of potassium ferricyanide for 2 min at room temperature. Excess ferricyanide was removed using a Sephadex G-25 gel-filtration column. The protein was concentrated using an Amicon Ultra centrifugal filter equipped with a 10000 kDa molecular mass membrane, and the purity of DHP was determined as previously described (*4*). Only DHP samples that exhibited Reinheitzahl values (RZ) greater than 4.0 were utilized in this study. The concentration of DHP was determined spectrophotometrically ($\varepsilon_{406} = 116.4\ mM^{-1}\ cm^{-1}$) (*19*).

Stopped-Flow UV−Visible Spectrophotometric Studies. Experiments were performed on a Bio-Logic SFM-400 triple-mixing stopped-flow instrument equipped with a diode array UV−visible spectrophotometer and were carried out at 20 °C in 100 mM KP_i buffer (pH 5.0 and 7.0). A constant temperature was maintained using a circulating water bath. Data were collected (900 scans total) over a three-time domain regime (2.5, 25, and 250 ms; 300 scans each) using Bio Kinet32 (Bio-Logic). Experiments were performed in double-mixing mode using an aging line prior to the second mixing step. The design of the experiments allowed for the mixing of DHP with either TCP or H_2O_2 followed by an aging time of 1.5, 30, or 60 s, followed by the second mix

with the remaining (co-) substrate: (i) DHP + TCP → delay → + H_2O_2 or (ii) DHP + H_2O_2 → delay → + TCP. Concentrations after mixing were as follows: $[DHP]_f = 10$ μM, $[H_2O_2]_f = 100$ μM, and $[TCP]_f = 300$ μM. All data were evaluated using Specfit Global Analysis System (Spectrum Software Associates) as pseudo-first-order reactions and fit with SVD analysis from one to three exponential curves where applicable. Kinetic data were baseline corrected using the Specfit autozero function.

Preparation of Reaction Intermediates by Freeze-Quench Methods. Rapid-freeze-quench experiments were performed with a BioLogic SFM 400 freeze-quench apparatus by mixing a 50 μM enzyme solution (final concentration) with a 10-fold excess of H_2O_2 solution in 100 mM potassium phosphate buffer (pH 5 and 7) at 25 °C. Reaction times were as follows: pH 5, 100 ms, 400 ms, 3.6 s, 36 s, and 60 s; and pH 7, 100 ms, 500 ms, 800 ms, 2 s, 12 s, and 60 s. A standard 4 mm outside diameter quartz EPR tube was connected to a Teflon funnel, and both the tube and the funnel were completely immersed in an isopentane bath at −110 °C. The reactions were quenched by spraying the mixtures into the cold isopentane, and the frozen material so obtained was packed at the bottom of the quartz tube using a packing rod equipped with a Teflon plunger. Samples were then transferred to a liquid nitrogen storage dewar until they were analyzed.

X-Band EPR Spectroscopy. EPR spectra were recorded with an X-band (9 GHz) Varian E-9 EPR spectrometer (Varian, El Palo, CA). A standard 3 mm × 4 mm quartz EPR tube was filled with a sample and placed into a quartz finger dewar insert filled with liquid nitrogen. The temperature of the samples was kept at 77 K for the duration of the data acquisition, which required periodic refilling of the dewar due to the evaporation of the liquid nitrogen during longer acquisition runs. The typical spectrometer settings were as follows: field sweep, 200 G; scan rate, 3.33 G/s; modulation frequency, 100 kHz; modulation amplitude, 4.0 G; and microwave power, 2 mW. The exact resonant frequency of each EPR experiment was measured by an EIP-578 (PhaseMatrix, San Jose, CA) in-line microwave frequency counter and is indicated in the figure captions. Typically, 20 and 200 individual scans were averaged to achieve sufficient signal to noise for the spectra obtained at short quench and long quench times, respectively.

RESULTS

UV−Visible Spectroscopic Studies of Ferric DHP in the Presence of TCP. The electronic absorption spectra of ferric metaquo DHP at pH 5 and 7 are presented in Figure 1. TCP exhibits absorbance maxima at 285 and 311 nm at pH 5.0 (Figure 1A) and pH 7.0 (Figure 1B), respectively. Although there is evidence for binding of substrate at an internal site in an X-ray crystal structure (*8*), there is also evidence for an external (*20, 21*) binding site. The spectra in Figure 1 show that TCP has a minimal effect on the heme spectra, and it is believed that TCP binds at an external binding site in the stopped-flow studies reported here.

Stopped-Flow UV−Visible Characterization of Compound ES in DHP. Single-mixing stopped-flow UV−visible spectroscopic methods were employed to detect DHP Compound ES. At pH 7, when a solution of ferric DHP [UV−visible spectrum, 407 (Soret), 504, 538, 635 nm] was rapidly mixed (2 ms) with H_2O_2, a transient species was observed (Figure 2 and Table 1), the spectral features of which [UV−visible, 420 (Soret), 545, 585 nm] we ascribe to a ferryl-containing DHP intermediate based upon previous characterization (*4, 7, 22*) and comparison to other known Fe(IV)−oxo species-containing hemoproteins (*11, 12*). As the ferryl intermediate of Compound ES is likely indistinguishable from that of Compound II by UV−visible spectroscopy, we assign this intermediate here as DHP Compound ES on the basis of these results and those of our EPR spectroscopic study (vide infra). Values of k_{obs} for formation of this new species were linearly dependent on H_2O_2 concentration (2.5−10-fold excess per heme), giving a bimolecular rate constant of (3.56 ± 0.02) × 10^4 M^{-1} s^{-1}. Under these conditions, and in the absence of substrate, DHP Compound ES decays to a stable species [UV−visible, 411 (Soret), 530, 564 nm; $k_{obs} = 0.0167 \pm 0.0003$ s^{-1}], which we have termed Compound RH.

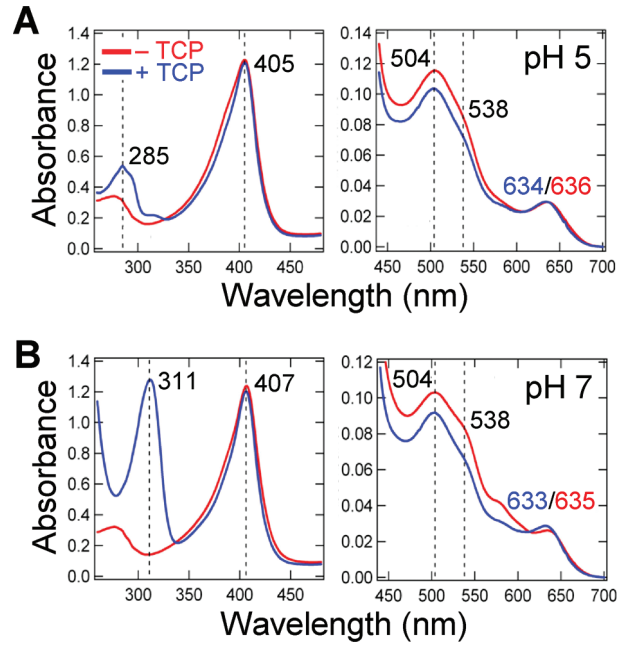

FIGURE 1: UV−visible spectra of ferric DHP (10 μM) in the presence (blue) and absence (red) of TCP (300 μM) at pH 5.0 (A) and pH 7.0 (B).

Similar reactivity is observed at pH 5. Ferric DHP [UV−visible, 405 (Soret), 504, 538, 636 nm] is converted to Compound ES [UV−visible, 419 (Soret), 545, 585 nm; $k_{obs} = (2.78 \pm 0.01) \times 10^4$ M^{-1} s^{-1}], which further decays to Compound RH [UV−visible, 410 (Soret), 530, 590 nm; $k_{obs} = 0.0701 \pm 0.0001$ s^{-1}] (Figure S1 of the Supporting Information). Hence, the rate of Compound RH formation is ~4 times greater at pH 5 than at pH 7.

Reaction of Preformed Compound ES with TCP Substrate. Stopped-flow UV−visible spectroscopy was employed to monitor the reaction between preformed DHP Compound ES and TCP. In a double-mixing experiment, 10 μM DHP was first reacted with a 10-fold excess of H_2O_2, allowed to incubate for 1.5 or 0.9 s, corresponding to the maximum accumulation of DHP Compound ES at pH 7 or 5, respectively, and then subsequently mixed with a 30-fold excess of TCP, which resulted in the regeneration of ferric (resting) DHP (Figure 3 and Figure S2 of the Supporting Information).

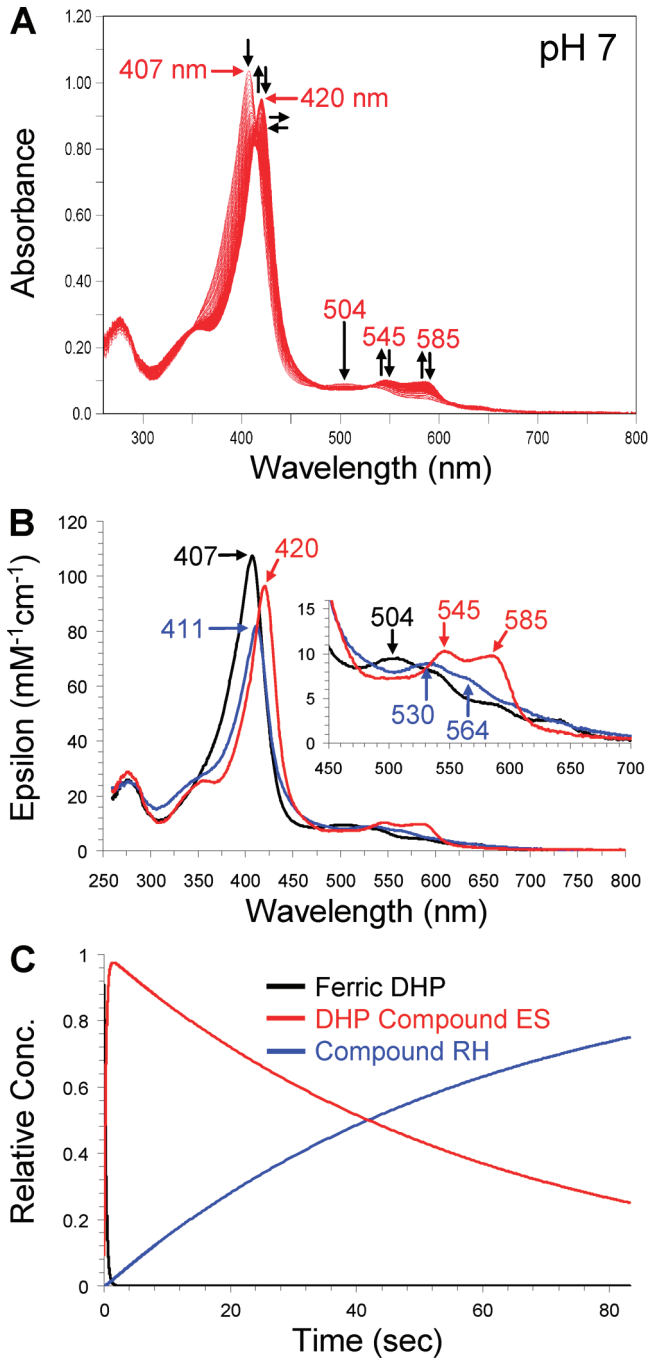

FIGURE 2: (A) Stopped-flow UV−visible spectroscopic monitoring of the reaction (900 scans, 85 s) between DHP (10 μM) and a 10-fold excess of H_2O_2 at pH 7.0. See Materials and Methods for details. (B) Calculated UV−visible spectra for resting (black), Compound ES (red), and Compound RH (blue) DHP are shown; the rapid-scanning data from panel A were compiled and fitted to a double-exponential reaction model using the Specfit global analysis program. (C) Relative concentration profile determined from the three-component fit used in panel B.

Under these conditions, nearly identical quantities of the DCQ product are formed at both pH values (Figure 4). However, it is interesting to note that at pH 5.0, the disappearance of Compound ES and the return of the enzyme to its resting state (8.47 ± 0.05 s^{-1}) are not directly coupled with product formation, which occurs subsequent to that process (0.13 ± 0.01 s^{-1}). On the other hand, at pH 7.0 the disappearance of DHP Compound ES (0.11 s^{-1}) is concomitant with the appearance of product (0.14 s^{-1}), although this observation does not prove that they are coupled. Nonenzymatic control experiments confirmed the necessity for DHP at both pH values, as no DCQ product was observed in the absence of the enzyme.

When the double-mixing experiments described above were repeated with longer incubation times that permitted Compound ES to completely decay to Compound RH prior to mixing with TCP, neither substrate loss (311 nm) nor product formation (275 nm) was observed during the 85 s time scale of these stopped-flow experiments. Specifically, at pH 5, Compound RH is nearly fully formed after 30 s (Figure S1c of the Supporting Information), with little to no Compound ES present, and neither the 30 nor 60 s incubation time exhibited product formation at this pH (Figure 4), indicating that Compound RH possesses a much lower catalytic activity than ferric DHP (vide infra). At pH 7, a 30 s incubation time results in a partial mixture of Compounds ES and RH being observed (Figure 2C), concomitant with partial substrate oxidation, whereas the 60 s incubation period led to no product formation, consistent with the nearly complete decay of Compound ES to Compound RH observed in the single-mixing experiments during this time frame. Thus, the extent of product formation is directly correlated with the amount of Compound ES present, strongly indicative that this intermediate is an active oxidant in DHP.

In Situ Compound ES Formation in the Presence of TCP. In contrast to the experiments described above in which preformed Compound ES was reacted with TCP, we employed double-mixing stopped-flow UV−visible spectroscopic methods to examine if preincubation of ferric DHP with TCP, followed by the addition of a 10-fold excess of H_2O_2, led to the formation of DCQ product (275 nm) via a transiently formed Compound ES intermediate. Under these conditions, the yield of DCQ product was nearly identical with that found for the reaction of fully preformed Compound ES with TCP (vide supra), at both pH 7 (Figure 5) and pH 5 (Figure S3 of the Supporting Information). When TCP was preincubated with DHP, there was no dependence on the delay time (1.5−60 s) prior to addition of H_2O_2 (Figure 6 and Figure S4 of the Supporting Information for pH 7 and 5, respectively). DCQ product formation had pseudo-first-order constants (k_{obs}) of 0.11 and 0.22 s^{-1} for pH 7.0 and 5.0, respectively. DCQ was also observed to be unstable under these conditions, undergoing side reaction(s) leading to its slow loss at longer time periods which were more apparent at pH 5 than at pH 7, but this chemistry was not further explored.

We also did note a pH-dependent difference with respect to the heme species observed. At pH 7.0, Compound ES [UV−visible, 420 (Soret), 545, 585 nm] is distinctly formed, with approximately the same rate [$k_{obs} = (3.11 \pm 0.02) \times 10^4$ M^{-1} s^{-1}] as when TCP was absent [$k_{obs} = (3.56 \pm 0.02) \times 10^4$ M^{-1} s^{-1}], and returns to the ferric state (UV−visible, 407, 504, 538, 578, 633 nm) with approximately the same rate ($k_{obs} = 0.12$ s^{-1}) as product formation (0.11 s^{-1}). At pH 5.0, no distinct Compound ES spectrum is observed upon reaction of hydrogen peroxide with DHP incubated in the presence of TCP; the UV−visible features [406 (Soret), 504, 538, and 635 nm] match those of the resting (ferric) enzyme, with the caveat that a minor broadening on the red side may be indicative of Compound ES formation and disappearance within the stopped-flow mixing time (2 ms).

Table 1: UV−Visible Spectroscopic Data and Kinetic Parameters for the Oxidized Intermediates of DHP

	pH 7		pH 5	
	λ_{max} (nm)	k_{obs} (M^{-1} s^{-1})	λ_{max} (nm)	k_{obs} (M^{-1} s^{-1})
ferric	407, 504, 538, 635	not applicable	405, 504, 538, 636	not applicable
Compound ES	420, 545, 585	$(3.56 \pm 0.02) \times 10^4$ M^{-1} s^{-1}	419, 545, 585	$(2.78 \pm 0.01) \times 10^4$ M^{-1} s^{-1}
Compound RH	411, 530, 564	0.0167 ± 0.0003 s^{-1}	410, 530, 590	0.0701 ± 0.0001 s^{-1}
Compound III	417, 542, 578	not determined	417, 542, 578	not determined

Characterization of Protein Radicals in DHP Compound ES. Rapid-freeze-quench methods were employed to stabilize intermediates of the reaction between DHP (final concentration of 50 μM) and a 10-fold excess of hydrogen peroxide at both pH 7 and 5 for consequent characterization by continuous wave (CW) EPR. X-Band CW EPR spectra of DHP samples recorded at pH 7.0 with various quench times are shown in Figure 7. The shapes of all the EPR spectra measured from the samples collected with quenching times of 500 ms, 800 ms, and 2 s were found to be identical, the only difference being in the signal intensities. The maximal concentration of the radical is observed over the period of Compound ES formation (Figure 2C). The position of the signal is characterized by an average g factor of 2.0058. The shape of the signal is best described by an anisotropic quintet. On the basis of the signal g factor and a partially resolved hyperfine structure with a peak-to-peak line width of ~21 G, this EPR signal was assigned to a tyrosyl radical (*23*). Samples with longer incubation times of 12 and 60 s have similar average g factors ($g \approx 2.005$) and the same peak-to-peak line width of 21 G; however, they do not exhibit resolved hyperfine structure and have much lower intensity [concomitant with the loss of the ferryl UV−visible spectrum in our component analysis (Figure 2C)].

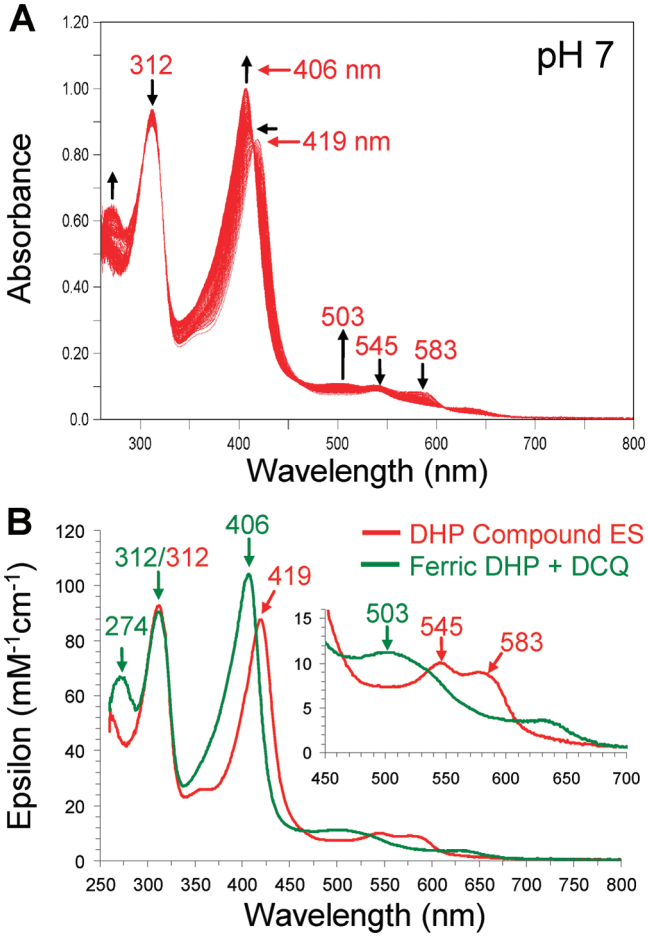

FIGURE 3: (A) Stopped-flow UV−visible spectroscopic monitoring of the double-mixing reaction (900 scans, 85 s) between preformed DHP Compound ES (10 μM) and TCP (300 μM) at pH 7. See Materials and Methods for details. (B) Calculated UV−visible spectra for both DHP Compound ES (red) and ferric DHP regenerated upon product formation (green); the rapid-scanning data from panel A were compiled and fitted to a single-exponential reaction model using the program Specfit.

The EPR spectrum of Compound ES was similarly recorded at various quench times at pH 5 (Figure 8). The spectrum is centered at $g = 2.0058$ and shows a partially resolved hyperfine splitting described as an "anisotropic septet" (*29*). A very weak shoulder is observed at $g = 2.035$ (Figure S5 of the Supporting Information) that could be an indication of the formation of a peroxyl radical since the samples were prepared under aerobic conditions (*30*), but the signal intensity is too low to warrant further speculation about its origin. At longer quench times when the component analysis indicates little to no remaining Compound ES by UV−visible spectroscopy (Figure S1c of the Supporting Information), the line shape of the EPR signal is drastically different, its signal intensity has dropped considerably, and the hyperfine splitting features are lost. Specifically, the signal has a very broad spectral feature in the $g \approx 2.04$ region and sharper features at $g = 2.0085$ and $g = 1.995$.

Unfortunately, the low g factor spectral resolution of these CW X-band experiments does not permit unambiguous identification of the radical species on the basis of magnetic parameters alone. This ambiguity could be resolved by high-field (95 GHz) EPR experiments coupled with mutagenesis studies that are planned for the near future.

Formation and Reactivity of Compound RH. As described above, in the absence of reducing substrate, a new, unique species of DHP, termed Compound RH to denote that is a reversible heme intermediate, is formed upon the decay of Compound ES. Compound RH was found to be robust to size-exclusion chromatography, protein concentration, and other sample preparation procedures. While its UV−visible features remained constant, we did observe that some protein

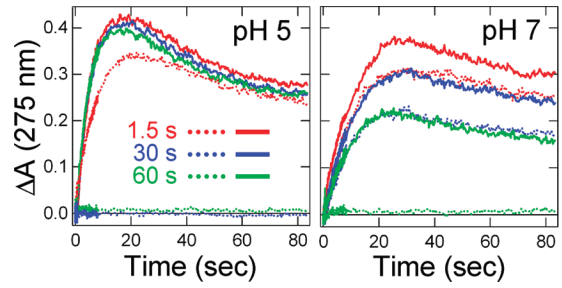

FIGURE 4: DCQ product formation (ΔA_{275}) as a function of pH for the following reaction conditions: preformed Compound ES with TCP (dotted lines) and TCP-preincubated DHP with H_2O_2 (solid lines). Both the aging time of Compound ES and the substrate preincubation period were varied (1.5, 30, and 60 s).

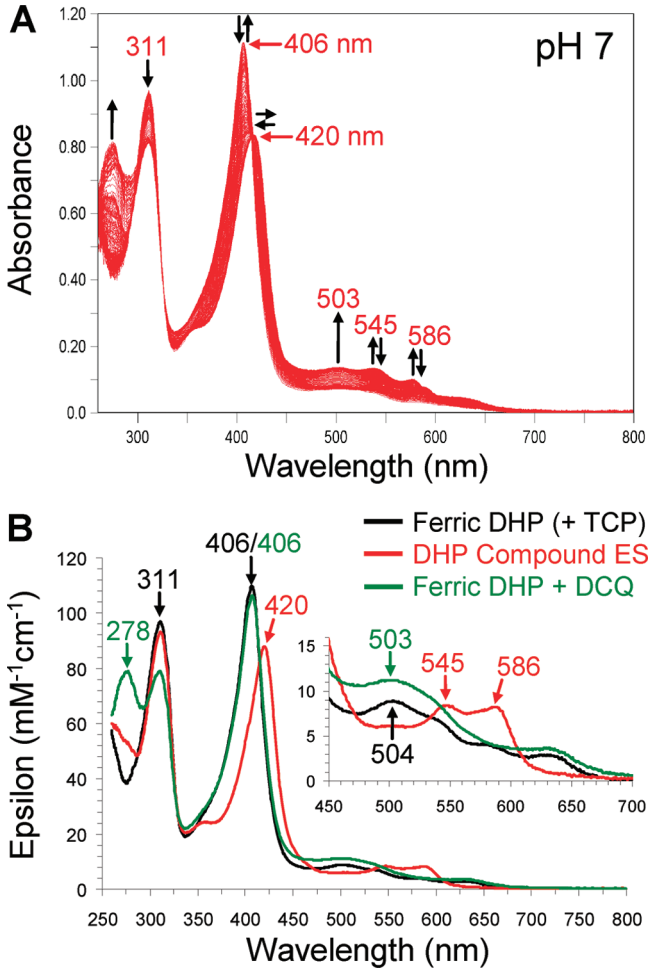

FIGURE 5: (A) Stopped-flow UV−visible spectroscopic monitoring of the double-mixing reaction (900 scans, 85 s) of ferric DHP (10 μM) preincubated with TCP (300 μM) for 1.5 s prior to its reaction with a 10-fold excess of H_2O_2 at pH 7. See Materials and Methods for details. (B) Calculated UV−visible spectra for ferric DHP incubated with TCP (black), the Compound ES intermediate formed (red), and ferric DHP regenerated upon product formation (green); the rapid-scanning data from panel A were compiled and fitted to a double-exponential reaction model using Specfit.

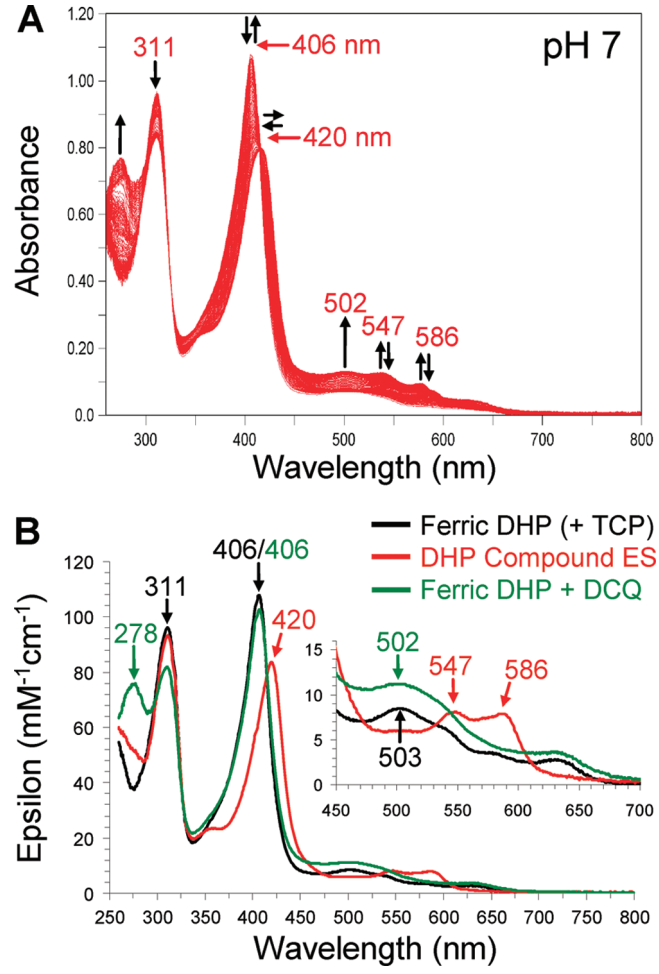

FIGURE 6: (A) Stopped-flow UV−visible spectroscopic monitoring of the double-mixing reaction (900 scans, 85 s) of ferric DHP (10 μM) preincubated with TCP (300 μM) for 60 s prior to its reaction with a 10-fold excess of H_2O_2 at pH 7. See Materials and Methods for details. (B) Calculated UV−visible spectra for ferric DHP incubated with TCP (black), the Compound ES intermediate formed (red), and ferric DHP regenerated upon product formation (green); the rapid-scanning data from panel A were compiled and fitted to a double-exponential reaction model using Specfit.

precipitation occurred when the long-term (several hours) room temperature stability of the Compound RH species was investigated. Addition of excess potassium cyanide (600 mM) to Compound RH resulted in a new UV−visible spectrum observed [421 (Soret), 545, 575 (sh) (data not shown)], consistent with the formation of a DHP ferricyanide adduct (*31*), providing further evidence that Compound RH is a single species.

To test the reactivity of the Compound RH species, single-mixing stopped-flow UV−visible spectroscopy was used to monitor the reaction between Compound RH (10 μM) and either a 10- or 100-fold molar excess of H_2O_2. In both cases, no reaction was observed [both pH 5 and 7 were investigated (data not shown)]. In spite of its inability to form high-valent iron−oxo intermediates, Compound RH still possesses attenuated levels of dehaloperoxidase activity, exhibiting a 6-fold lower reactivity with TCP as a substrate when compared to ferric DHP.

While Compound RH displays a lack of reactivity with H_2O_2 by stopped-flow UV−visible spectroscopy, it is readily reduced with sodium dithionite at either pH 5 or 7 to yield ferrous (deoxy) DHP [UV−visible, 432 (Soret), 557, 626 nm], which upon exposure to dioxygen led to formation of oxyferrous DHP [UV−visible, 417 (Soret), 542, 578 nm]. Further oxidation with potassium ferricyanide, followed by

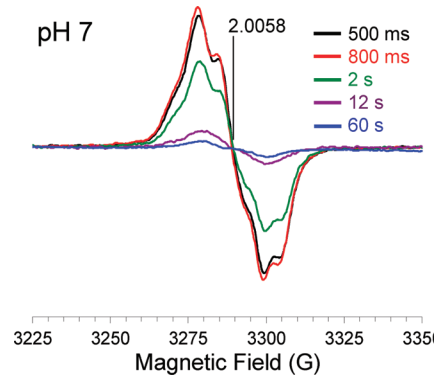

FIGURE 7: EPR spectra of the radical(s) in DHP Compound ES at pH 7. Rapid-freeze-quench samples were prepared from the reaction of DHP (final concentration of 50 μM) with a 10-fold molar excess of H_2O_2 at 25 °C and rapidly frozen in an isopentane slurry. Spectra were recorded at 77 K using the spectrometer settings described in Materials and Methods. The frequency of the experiments was 9.2330 GHz.

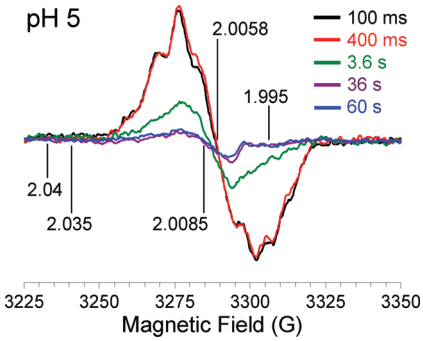

FIGURE 8: EPR spectra of the radical(s) in DHP Compound ES at pH 5. Rapid-freeze-quench samples were prepared from the reaction of DHP (final concentration of 50 μM) with a 10-fold molar excess of H_2O_2 at 25 °C and rapidly frozen in an isopentane slurry. Spectra were recorded at 77 K using the parameters described in Materials and Methods.

desalting, allowed for the reisolation of ferric DHP [UV−visible, 407 (Soret), 504, 538, 635 nm]. The activity of this "regenerated" ferric DHP was found to be nearly identical to that of as-isolated ferric DHP for TCP oxidation, suggesting that a pathway through Compound RH does not have any deleterious effect on dehaloperoxidase activity.

DISCUSSION

DHP has been shown to perform the net two-electron oxidation of phenol (X−A−OH + H_2O_2 → O=A=O + HX + H_2O) to yield the corresponding quinone, consistent with the reactive species being a two-electron-oxidized intermediate such as Compound I or Compound ES (*10*−*12*). However, the reaction of DHP with its physiological oxidant, H_2O_2, yields what had been characterized to date as Compound II, which is formally a one-electron-oxidized heme center. Thus, the question of how DHP oxidizes its phenol substrates by two electrons when it has been shown to only form a one-electron-oxidized intermediate needs to be addressed. This study provides further characterization of the intermediate formed from the reaction of ferric dehaloperoxidase with hydrogen peroxide, which suggests that this species is similar to the two-electron-oxidized Compound ES of CcP.

We employed stopped-flow UV−visible spectroscopic methods to monitor the reaction of ferric DHP with its physiological oxidant, H_2O_2. The first intermediate observed had spectral features which unequivocally match those for a ferryl-containing species lacking a porphyrin π-cation radical, such as Compound ES or Compound II. This implies either that Compound I is not formed by this reaction or more likely that it is formed transiently but undergoes rapid reduction to the observed Compound ES intermediate (vide infra). Interestingly, in the absence of a reducing substrate, the Compound ES intermediate was found to be unstable and converted to a new, stable species which we have termed Compound RH on the basis of the fact that it is a reversibly formed heme intermediate (RH, reversible heme). In the presence of substrate, however, Compound ES returned to the resting state, concomitant with formation of the quinone product. We examined this reaction with TCP using both preformed and in situ-generated Compound ES, and in both cases, the amount and rate of DCQ product generated were identical and independent of pH. The implication is that Compound ES is likely the actual species which is catalyzing TCP oxidation, rather than Compound I. If this were not the case, then one might expect different results between the amount and rate of product formation for in situ versus preformed Compound ES reactions. While this does not absolutely preclude a transiently formed Compound I species from oxidizing TCP, it strongly suggests that Compound ES is the active oxidant. Dichloroquinone product formation may result from either a single two-electron oxidation of the trichlorophenol substrate by Compound ES or two sequential one-electron oxidations, both pathways being indistinguishable under the multiple-turnover conditions examined in this study.

Stopped-flow UV−visible and rapid-freeze-quench EPR spectroscopic studies were employed to follow the formation of the high-valent iron(IV)−oxo and protein radical species, respectively, for the reaction of DHP with H_2O_2 leading to Compound ES. The UV−visible spectroscopic data indicate the direct formation of a classical ferryl-containing species, similar to that formed in HRP and Mb. Moreover, a recent ENDOR study by Hoffman and co-workers (*32*) supports the assignment as Fe(IV)=O, and not the protonated analogue Fe(IV)−OH (as in chloroperoxidase). The lack of an observable Compound I species suggested the presence of an endogenous reducing agent. As the crystal structure of DHP does not show any other redox capable cofactor (e.g., flavin, another metal center, etc.), we investigated by RFQ-CW-EPR spectroscopy whether a protein side chain could be responsible for the rapid reduction of a transiently formed Compound I species to the observed Compound ES intermediate, resulting in the formation of a protein radical. Indeed, we have identified the presence of a protein radical whose maximal concentration is observed over the period of Compound ES formation identified from UV−visible spectroscopy. As a result, we present here for the first time clear evidence of DHP Compound ES as a two-electron-oxidized intermediate, with one oxidation equivalent centered on the ferryl moiety and the second oxidation equivalent located on a protein side chain as a radical. Thus, DHP Compound ES bears a strong resemblance to CcP Compound ES, which has been extensively studied and shown to possess both a ferryl heme center and a radical on Trp^{191}.

Analysis of the signal *g* factor and the partially resolved hyperfine structure present in our EPR data, with a peak-to-peak line width of ~21 G, suggests that the radical in DHP Compound ES likely resides on a tyrosine residue initially (*23*). The longer incubation times of 12 and 60 s exhibit a similar average *g* factor ($g \approx 2.005$) and the same peak-to-peak line width of 21 G; however, they do not show resolved hyperfine structure and have much lower intensity [concomitant with the loss of the ferryl UV−visible spectrum in our component analysis (Figure 2C)]. Thus, it is difficult to comment extensively on the origin of these signals observed at later times. These spectra could be attributed to a different Tyr-based radical than the one initially observed, or the signal could also be an admixture of Tyr- and Trp-based radicals (*24*). Another option to consider is a radical originating from a cysteine residue, which is usually characterized by high *g* factor anisotropy that would be resolved in the X-band spectra (*25*−*27*). Although Cys-based radicals have been accepted as intermediates in metalloprotein cycles, they are not commonly observed by freeze-quench EPR

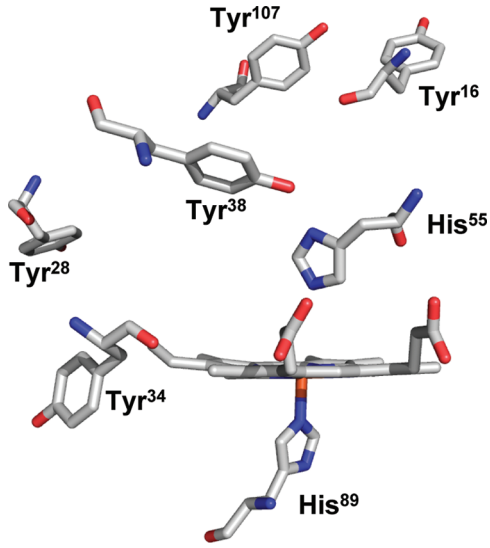

FIGURE 9: Active site of DHP showing all tyrosine residues present in the enzyme. The proximal and distal histidines, His^{89} and His^{55}, respectively, are provided for orientation. Coordinates (2QFK) were obtained from the Protein Data Bank and displayed using Pymol.

spectroscopy. However, Cys-based radicals should not be completely ruled out as intermediates at the quenching times of 12 and 60 s as they have been shown to form in human Mb under similar conditions (*28*).

Of the five tyrosine residues which DHP possesses [Tyr^{16}, Tyr^{28}, Tyr^{34}, Tyr^{38}, and Tyr^{107} (Figure 9)], only two are reasonably close to the heme prosthetic group to be considered likely candidates for reducing Compound I initially, Tyr^{34} and Tyr^{38}; the closest contact between Tyr^{34} and the heme edge is 5.56 Å (Tyr Cγ), whereas Tyr^{38} is 7.54 Å distant (phenolic oxygen). The three remaining tyrosine residues are more than 10 Å (Tyr^{28}) or 15 Å (Tyr^{16} and Tyr^{107}) from the heme edge. Furthermore, the closest heme edge to Trp^{120} (10.53 Å) and Cys^{73} (16.29 Å) contacts are similarly distant, making them unlikely candidates for the residues responsible for the initial reduction of the transiently formed Compound I intermediate. Thus, on the basis of both the available structural studies of DHP and our spectroscopic analysis presented here, we suggest that the initial site of radical formation in DHP Compound ES is either Tyr^{34} or Tyr^{38}.

While the definitive identification of the specific residue that gives rise to the initial protein radical in DHP Compound ES will be the subject of future high-field EPR investigations coupled with mutagenesis studies, the time-dependent changes observed in the protein radical signal suggest either a change in the local electronic structure of the radical or a migration of the radical out of the active site to other redox active protein side chains upon decay of Compound ES. This latter conjecture is interesting, given that the reaction of sperm whale Mb with hydrogen peroxide yields covalent dimers that arise from the coupling of surface tyrosyl radicals (Tyr^{151}), which results from a radical migration out of the Mb active site (*33*). Similarly, it has been demonstrated that human Mb also forms a covalent dimer (*34*), but through surface cysteines (Cys^{110}) forming a disulfide link, consistent with our putative radical observed at long quench times at pH 5 possessing a similar radical migration pathway, with surface radicals leading to the oxidation of TCP that binds to DHP through a hypothesized external binding pocket. This would not be unlike that of CcP, whose initial Trp^{191} radical in Compound ES leads to a radical migration which is ultimately responsible for oxidizing substrate (cytochrome *c*) at the surface of the peroxidase (protein−protein interface) (*35*). Thus, as CcP may have evolved from traditional (heme edge electron transfer) peroxidases an external binding interface for oxidizing cytochrome *c*, DHP may also similarly have evolved from Mb an external binding pocket for oxidizing trihalophenols. In accord with this hypothesis, tyrosine has been proposed to play a role in the peroxidase mechanism of Mb (*36*). This hypothesis will be particularly interesting if our supposition is that Tyr^{34} is the site of the radical in DHP Compound ES, as this residue is located at the surface of DHP yet is also in the proximity of the heme (Figure 9), and thus could serve as a redox conduit between the hypothesized external binding pocket and the active site.

From the initial observation in the X-ray crystal structure that 4-iodophenol (4IP) binds at an internal site in the distal pocket of DHP (*8*), the possibility of substrate binding to both internal and external binding pockets has been investigated with a number of techniques, including Fourier transform infrared (FTIR) (*20*), electron paramagnetic resonance (EPR) (*37*), nuclear magnetic resonance (NMR) (*21*), and resonance Raman experiments (Thompson and S. Franzen, unpublished results). Solution studies (*21*) and cryogenic studies (*20, 37*) have been carried out using 2,4,6-trifluorophenol (TFP) as a model of the native substrate 2,4,6-tribromophenol (TBP), which is relatively insoluble. EPR and HYSCORE experiments (*37*) are consistent with a change from six-coordinate high-spin to five-coordinate high-spin upon TFP binding at pH 6.0. TFP was used in those experiments because of its relatively high solubility, which facilitates detection under the conditions of the EPR experiment (4 K). FTIR experiments conducted on the carbonmonoxy form of DHP (DHP−CO) at cryogenic temperature (*20*) show that there is a large effect of TFP binding on the CO stretching frequency and rebinding kinetics at pH 5.5, but not at pH 7.0. However, near ambient temperature and physiological pH, TFP does not bind to DHP−CO (*20*). On the basis of the binding of 4IP in the distal pocket of DHP in the X-ray crystal structure, one hypothesis is that TFP is bound in the distal pocket of DHP−CO at low pH and at low temperatures. Hyperfine ^{1}H NMR experiments show that 4-bromophenol (4BP) and 2,4-dichlorophenol (DCP) interact with the metcyano form (DHP−CN) at ambient temperature through changes in the position of the internal heme edge Phe^{97} residue and the 3-CH_3 heme methyl (*21*). TFP does not produce these changes at ambient temperature, but there are shifts in ^{19}F resonances of the substrate when it interacts with DHP, which can be detected by ^{19}F NMR. From these data, one can further hypothesize that there is an external binding site (*21*) as well as the internal binding site observed by X-ray crystallography (*8*). Further confirmation can be found in resonance Raman experiments on 4IP and 4BP, which also show a change in core size marker modes when substrate binds (S. Franzen and Thompson, unpublished results). These experiments confirm that there is a change from six-coordinate high-spin in the resting metaquo form of DHP to five-coordinate high-spin when 4IP and 4BP bind. Thus, while 4IP and 4BP appear to bind inside the distal

Scheme 2: Proposed Catalytic Cycle for Dehaloperoxidase

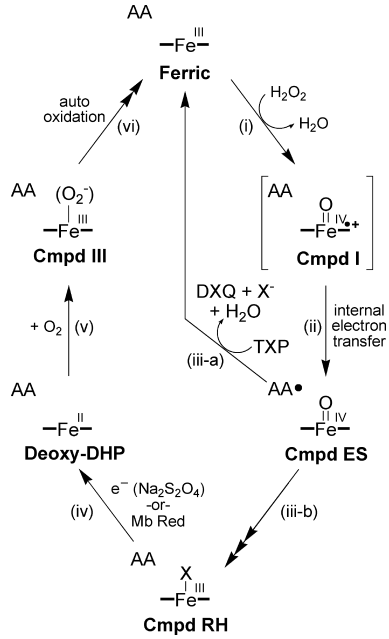

pocket, there are several observations that suggest that the external binding pocket is the active site.

In the absence of substrate, we observed that DHP Compound ES forms a new, stable species, termed Compound RH, which is unreactive toward H_2O_2 and, as a consequence, possesses attenuated levels of dehaloperoxidase activity. While peroxidase inactivation is a known phenomenon in HRP or CcP, where heme bleaching is the primary culprit (*38*), Compound RH is still active and can reversibly return to the deoxy ferrous state under mild reduction conditions. Furthermore, Compound RH has not been reported in myoglobin or hemoglobin previously, and is therefore unique to DHP (*33, 39*−*42*). Thus, as it is not found in either the monofunctional peroxidases or the O_2 transport globins, DHP Compound RH represents a novel species which may be a result of the bifunctional nature of DHP: the inactivated (dehalo)peroxidase can be regenerated back to an active oxygen transport protein via a reduction pathway that is specific for globins, but not peroxidases. When DHP is functioning as a peroxidase, its inactivation is necessary to prevent nonspecific oxidation of other metabolites from occurring when trihalophenol substrate is absent. However, while heme bleaching is a normal route for peroxidase inactivation, this could be metabolically costly for DHP, given that it is the hemoglobin in *A. ornata*. Thus, formation of Compound RH allows dehaloperoxidase to be inactivated without sacrificing the protein to heme bleaching while at the same time allowing for its functional switch back to an oxygen transport protein upon reduction. While the exact nature of the Compound RH species will require further study, it nevertheless represents an interesting and novel observation in this study.

A catalytic cycle can be proposed on the basis of the reversible formation of Compound RH. The catalytic cycle shown in Scheme 2 confers "hydrogen peroxide reductase" activity to dehaloperoxidase. The use of reducing agents to scavenge reactive oxygen species enzymatically is not unprecedented, with members of the peroxiredoxin family (Prx, also termed the thioredoxin peroxidases and alkylhydroperoxide-reductase-C22 proteins) and superoxide reductase (SOR) being perhaps the most well-known examples for H_2O_2 and superoxide reduction, respectively (*43, 44*). While disproportionation of H_2O_2 may be preferable over its reduction from a metabolic viewpoint, DHP does not exhibit significant catalase activity, although myoglobin has been shown to consume (noncatalytic) up to 8 equiv of H_2O_2 (*33, 41, 42*). Overall, should a partner reductase similar to Mb reductase be identified for DHP, the door for DHP to be considered a trifunctional protein capable of peroxidase, O_2 transport, and H_2O_2 scavenging activities would be opened.

On the basis of the results obtained from these stopped-flow UV−visible and RFQ-EPR spectroscopic experiments, and through modification of previously established mechanisms for the general function of peroxidases (*45*), we propose the following catalytic cycle for the in vitro peroxide-dependent oxidation of ferric DHP from *A. ornata* in the presence and absence of trihalophenol (Scheme 2). Ferric DHP reacts with 1 equiv of H_2O_2, transiently forming Compound I (step i), which then undergoes rapid endogenous electron transfer to generate the observed Compound ES intermediate and protein radical (step ii). A bifurcation in the mechanism occurs which is dependent upon substrate. In the presence of trihalophenol, DHP Compound ES is reduced by two electrons, thereby regenerating the ferric state of the enzyme, and forming the dihaloquinone product (step iii-a). In the absence of substrate, however, Compound RH is formed (iii-b) by a not-yet-understood process and can subsequently be reduced to the ferrous enzyme (iv) and bind dioxygen to form the oxyferrous intermediate (v). Autoxidation of oxyferrous DHP leads to the formation of the ferric enzyme (vi). The existence, and by extension identity, of a possible sixth ligand in Compound RH is unknown at this time, and this ambiguity is represented by the bound X in Scheme 2. We tentatively assign the oxidation state of Compound RH as a ferric heme on the basis of the evidence that (i) Compound RH exhibits a "ferric-like" heme spectrum that matches neither the ferryl nor the ferrous spectra of DHP (Table 1), (ii) Compound RH forms from the decay of an iron(IV)−oxo species, which for most heme proteins yields a ferric enzyme, and (iii) Compound RH can be reduced to the ferrous enzyme, implying that it does not start as a ferrous heme. Further studies will be necessary to definitively assign the oxidation state of the heme in Compound RH.

CONCLUSION

This study addresses a number of key questions pertaining to the nature and catalytic competency of the Compound ES intermediate in DHP. Our spectroscopic and biochemical characterization of DHP Compound ES suggests that this species is similar to the two-electron-oxidized Compound ES of CcP in that it possesses both a ferryl heme center and a protein radical. Furthermore, our results are consistent with Compound ES being an active species responsible for trihalophenol oxidation, as opposed to Compound I. The data support the hypothesis that there is an external substrate binding pocket in DHP, in which case the data reported here indicate that there may be a radical migration pathway in DHP analogous to that in CcP. A peroxidase-attenuated species unique to DHP, namely Compound RH, was also

identified, and a role for its formation as a protective species against unwanted oxidation chemistry was hypothesized. As Compound RH is unreactive toward further oxidation, it was found that reduction of Compound RH regenerates oxyferrous DHP, and this suggests that the recovery of the oxygen transport function from an attenuated peroxidase species via reduction (possibly globin reductase) is a consequence of the bifunctional nature of this protein and may represent the chemical process that links the oxygen transport and peroxidase activities in dehaloperoxidase.

SUPPORTING INFORMATION AVAILABLE

Molar absorbances for 2,4,6-trichlorophenol at pH 5, 6, 7, and 7.5 (Table S1), stopped-flow UV−visible spectroscopic monitoring of the reaction between DHP and a 10-fold molar excess of H_2O_2 at pH 5.0 (Figure S1), stopped-flow UV−visible spectroscopic monitoring of the double-mixing reaction between preformed DHP Compound ES and TCP at pH 5 (Figure S2), stopped-flow UV−visible spectroscopic monitoring of the double-mixing reaction of ferric DHP preincubated with TCP for 1.5 s prior to its reaction with H_2O_2 at pH 5 (Figure S3), stopped-flow UV−visible spectroscopic monitoring of the double-mixing reaction of ferric DHP preincubated with TCP for 60 s prior to its reaction with H_2O_2 at pH 5 (Figure S4), and rapid-freeze-quench data at pH 5 (Figure S5). This material is available free of charge via the Internet at http://pubs.acs.org.

REFERENCES

1. Weber, R. E., Magnum, C. P., Steinman, H., Bonaventura, C., Sullivan, B., and Bonaventura, J. (1977) Hemoglobins of two terebellid polychaetes: *Enoplobranchus sanuigneus* and *Amphitire ornata*. *Comp. Biochem. Phys. 56A*, 179–187.
2. Chen, Y. P., Woodin, S. A., Lincoln, D. E., and Lovell, C. R. (1996) An unusual dehalogenating peroxidase from the marine terebellid ploychaete *Amphitrite ornata*. *J. Biol. Chem. 271*, 4609–4612.
3. Osborne, R. L., Coggins, M. K., Walla, M., and Dawson, J. H. (2007) Horse heart myoglobin catalyzes the H_2O_2-dependent oxidative dehalogenation of chlorophenols to DNA-binding radicals and quinones. *Biochemistry 46*, 9823–9829.
4. Belyea, J., Gilvey, L. B., Davis, M. F., Godek, M., Sit, T. L., Lommel, S. A., and Franzen, S. (2005) Enzyme function of the globin dehaloperoxidase from *Amphitrite ornata* is activated by substrate binding. *Biochemistry 44*, 15637–15644.
5. Hardison, R. (1998) Hemoglobins from bacteria to man: Evolution of different patterns of gene expression. *J. Exp. Biol. 201*, 1099–1117.
6. Bailly, X., Chabasse, C., Hourdez, S., Dewilde, S., Martial, S., Moens, L., and Zal, F. (2007) Globin gene family evolution and functional diversification in annelids. *FEBS J. 274*, 2641–2652.
7. Franzen, S., Gilvey, L. B., and Belyea, J. L. (2007) The pH dependence of the activity of dehaloperoxidase from *Amphitrite ornata*. *Biochim. Biophys. Acta 1774*, 121–130.
8. LaCount, M. W., Zhang, E. L., Chen, Y. P., Han, K. P., Whitton, M. M., Lincoln, D. E., Woodin, S. A., and Lebioda, L. (2000) The crystal structure and amino acid sequence of dehaloperoxidase from *Amphitrite ornata* indicate common ancestry with globins. *J. Biol. Chem. 275*, 18712–18716.
9. Poulos, T. L., and Kraut, J. (1980) The structure of cytochrome c peroxidase at 2.5 Å resolution. *J. Biol. Chem. 255*, 575–580.
10. Akita, M., Tsutsumi, D., Kobayashi, M., and Kise, H. (2001) Structural change and catalytic activity of horseradish peroxidase in oxidative polymerization of phenol. *Biosci., Biotechnol., Biochem. 65*, 1581–1588.
11. Laurenti, E., Ghibaudi, E., Todaro, G., and Ferrari, R. P. (2002) Enzymatic degradation of 2,6-dichlorophenol by horseradish peroxidase: UV-visible and mass spectrophotometric characterization of the reaction products. *J. Inorg. Biochem. 92*, 75–81.
12. Laurenti, E., Ghibaudi, E., Ardissone, S., and Ferrari, R. P. (2003) Oxidation of 2,4-dichlorophenol catalyzed by horseradish peroxidase: Characterization of the reaction mechanism by UV-visible spectroscopy and mass spectrometry. *J. Inorg. Biochem. 95*, 171–176.
13. Raven, E. L. (2000) Peroxidase-Catalyzed Oxidation of Ascorbate. In *Subcellular Chemistry, Volume 35: Enzyme-Catalyzed Electron and Radical Transfer* (Holzenburg, A., and Scrutton, N., Eds.) pp 317−349, Kluwer Academic/Plenum Publishers, New York.
14. Neely, W. B. (1984) An Analysis of Aquatic Toxicity Data: Water Solubility and Acute Lc50 Fish Data. *Chemosphere 13*, 813–819.
15. Dannenfelser, R. M., and Yalkowsky, S. H. (1991) Data-Base of Aqueous Solubility for Organic Nonelectrolytes. *Sci. Total Environ. 109*, 625–628.
16. Falk, J. E. (1964) Haems. I. Determination as pyridine hemochromes. *Porphyrins and Metalloporphyrins: Their General, Physical, and Coordination Chemistry and Laboratory Methods*, pp 181−188, Elsevier Publishing, New York.
17. Fuhrhop, J. H., and Smith, K. M. (1975) Laboratory Methods. In *Porphyrins and Metalloporphyrins* (Smith, K. M., Ed.) pp 804−807, Elsevier Publishing, New York.
18. Beers, R. F., Jr., and Sizer, I. W. (1952) A spectrophotometric method for measuring the breakdown of hydrogen peroxide by catalase. *J. Biol. Chem. 195*, 133–140.
19. Osborne, R. L., Taylor, L. O., Han, K. P., Ely, B., and Dawson, J. H. (2004) *Amphitrite ornata* dehaloperoxidase: Enhanced activity for the catalytically active globin using MCPBA. *Biochem. Biophys. Res. Commun. 324*, 1194–1198.
20. Nienhaus, K., Deng, P. C., Belyea, J., Franzen, S., and Nienhaus, G. U. (2006) Spectroscopic study of substrate binding to the carbonmonoxy form of dehaloperoxidase from *Amphitrite ornata*. *J. Phys. Chem. B 110*, 13264–13276.
21. Davis, M. F., Gracz, H., Vendeix, F. A. P., Gilvey, L. B., Somasundaram, A., Decatur, S. M., and Franzen, S. (2009) Different Binding Modes of Mono-, Di- and Trihalogenated Phenols to the Hemoglobin Dehaloperoxidase from *Amphitrite ornata*. *Biochemistry* . (submitted for publication).
22. Franzen, S., Chaudhary, C., Belyea, J., Gilvey, L., Davis, M. F., Sit, T. L., and Lommel, S. A. (2006) Proximal cavity, distal histidine and substrate hydrogen-bonding mutations modulate the activity of *Amphitrite ornata* dehaloperoxidase. *Biochemistry 45*, 9085–9094.
23. Svistunenko, D. A., and Cooper, C. E. (2004) A new method of identifying the site of tyrosyl radicals in proteins. *Biophys. J. 87*, 582–595.
24. Svistunenko, D. A., Dunne, J., Fryer, M., Nicholls, P., Reeder, B. J., Wilson, M. T., Bigotti, M. G., Cutruzzola, F., and Cooper, C. E. (2002) Comparative study of tyrosine radicals in hemoglobin and myoglobins treated with hydrogen peroxide. *Biophys. J. 83*, 2845–2855.
25. Lawrence, C. C., Bennati, M., Obias, H. V., Bar, G., Griffin, R. G., and Stubbe, J. (1999) High-field EPR detection of a disulfide radical anion in the reduction of cytidine 5′-diphosphate by the E441Q R1 mutant of *Escherichia coli* ribonucleotide reductase. *Proc. Natl. Acad. Sci. U.S.A. 96*, 8979–8984.
26. Hoffman, M. Z., and Hayon, E. (1972) One-Electron Reduction of Disulfide Linkage in Aqueous-Solution: Formation, Protonation, and Decay Kinetics of $RSSR^-$ Radical. *J. Am. Chem. Soc. 94*, 7950–7957.
27. Chan, P. C., and Bielski, B. H. J. (1973) Pulse-Radiolysis Study of Optical-Absorption and Kinetic Properties of Dithiothreitol Free-Radical. *J. Am. Chem. Soc. 95*, 5504–5508.
28. Witting, P. K., Douglas, D. J., and Mauk, A. G. (2000) Reaction of human myoglobin and H_2O_2: Involvement of a thiyl radical produced at cysteine 110. *J. Biol. Chem. 275*, 20391–20398.
29. Svistunenko, D. A. (2005) Reaction of haem containing proteins and enzymes with hydroperoxides: The radical view. *Biochim. Biophys. Acta 1707*, 127–155.
30. Lund, M. N., Luxford, C., Skibsted, L. H., and Davies, M. J. (2008) Oxidation of myosin by haem proteins generates myosin radicals and protein cross-links. *Biochem. J. 410*, 565–574.
31. Roach, M. P., Chen, Y. P., Woodin, S. A., Lincoln, D. E., and Dawson, J. H. (1997) *Notomastus lobatus* chloroperoxidase and *Amphitrite ornata* dehaloperoxidase both contain histidine as their proximal heme iron ligand. *Biochemistry 36*, 2197–2202.
32. Davydov, R., Osborne, R. L., Kim, S. H., Dawson, J. H., and Hoffman, B. M. (2008) EPR and ENDOR studies of cryoreduced compounds II of peroxidases and myoglobin. Proton-coupled electron transfer and protonation status of ferryl. *Biochemistry 47*, 5147–5155.

33. Fenwick, C. W., and English, A. M. (1996) Trapping and LC-MS identification of protein radicals formed in the horse heart met-myoglobin-H_2O_2 reaction. *J. Am. Chem. Soc. 118*, 12236–12237.
34. Hirota, S., Azuma, K., Fukuba, M., Kuroiwa, S., and Funasaki, N. (2005) Heme reduction by intramolecular electron transfer in cysteine mutant myoglobin under carbon monoxide atmosphere. *Biochemistry 44*, 10322–10327.
35. Smith, A. T., and Veitch, N. C. (1998) Substrate binding and catalysis in heme peroxidases. *Curr. Opin. Chem. Biol. 2*, 269–278.
36. Witting, P. K., Mauk, A. G., and Lay, P. A. (2002) Role of tyrosine-103 in myoglobin peroxidase activity: Kinetic and steady-state studies on the reaction of wild-type and variant recombinant human myoglobins with H_2O_2. *Biochemistry 41*, 11495–11503.
37. Smirnova, T. I., Weber, R. T., Davis, M. F., and Franzen, S. (2008) Substrate binding triggers a switch in the iron coordination in dehaloperoxidase from *Amphitrite ornata*: HYSCORE experiments. *J. Am. Chem. Soc. 130*, 2128–2129.
38. Gajhede, M. (2001) Horseradish Peroxidase. In *Handbook of Metalloprotein* (Messerschmidt, A., Huber, R., Poulos, T. L., and Weighardt, K., Eds.) pp 195−210, John Wiley & Sons, Inc., Chichester, U.K.
39. Keilin, D., and Hartree, E. F. (1950) Reaction of Methaemoglobin with Hydrogen Peroxide. *Nature 166*, 513–514.
40. George, P., and Irvine, D. H. (1951) Reaction of Metmyoglobin with Hydrogen Peroxide. *Nature 168*, 164–165.
41. Giulivi, C., and Cadenas, E. (1998) Heme protein radicals: Formation, fate, and biological consequences. *Free Radical Biol. Med. 24*, 269–279.
42. Alayash, A. I., Ryan, B. A. B., Eich, R. F., Olson, J. S., and Cashon, R. E. (1999) Reactions of sperm whale myoglobin with hydrogen peroxide: Effects of distal pocket mutations on the formation and stability of the ferryl intermediate. *J. Biol. Chem. 274*, 2029–2037.
43. Wood, Z. A., Schroder, E., Harris, J. R., and Poole, L. B. (2003) Structure, mechanism and regulation of peroxiredoxins. *Trends Biochem. Sci. 28*, 32–40.
44. Niviere, V., and Fontecave, M. (2004) Discovery of superoxide reductase: An historical perspective. *J. Biol. Inorg. Chem. 9*, 119–123.
45. Dunford, H. B. (1999) *Heme Peroxidases*, Wiley-VCH, New York (and references cited therein).

BI801916J

Acta Crystallographica Section D
Biological Crystallography
ISSN 0907-4449

Distal histidine conformational flexibility in dehaloperoxidase from *Amphitrite ornata*

Zuxu Chen,[a] Vesna de Serrano,[a] Laurie Betts[b] and Stefan Franzen[a]*

[a]Department of Chemistry, North Carolina State University, Raleigh, NC 27695, USA, and [b]Biomolecular X-ray Structure Facility, University of North Carolina School of Medicine, Chapel Hill, NC 27599, USA

Correspondence e-mail: stefan_franzen@ncsu.edu

Received 5 August 2008
Accepted 6 November 2008

PDB Reference: deoxy dehaloperoxidase, 3dr9, r3dr9sf.

The enzyme dehaloperoxidase (DHP) from the terebellid polychaete *Amphitrite ornata* is a heme protein which has a globin fold but can function as both a hemoglobin and a peroxidase. As a peroxidase, DHP is capable of converting 2,4,6-trihalophenols to the corresponding 2,6-dihaloquinones in the presence of hydrogen peroxide. As a hemoglobin, DHP cycles between the oxy and deoxy states as it reversibly binds oxygen for storage. Here, it is reported that the distal histidine, His55, exhibits conformational flexibility in the deoxy form and is consequently observed in two solvent-exposed conformations more than 9.5 Å away from the heme. These conformations are analogous to the open conformation of sperm whale myoglobin. The heme iron in deoxy ferrous DHP is five-coordinate and has an out-of-plane displacement of 0.25 Å from the heme plane. The observation of five-coordinate heme iron with His55 in a remote solvent-exposed conformation is consistent with the hypothesis that His55 interacts with heme iron ligands through hydrogen bonding in the closed conformation. Since His55 is also displaced by the binding of 4-iodophenol in an internal pocket, these results provide new insight into the correlation between heme iron ligation, molecular binding in the distal pocket and the conformation of the distal histidine in DHP.

1. Introduction

The enzyme dehaloperoxidase (DHP), which was first isolated from the terebellid polychaete *Amphitrite ornata*, is a heme-containing peroxidase which functions as both a globin and a peroxidase. While all hemoglobins possess some peroxidase activity, the activity of DHP is significantly greater than that of any known native hemoglobin. As is well known, oxygen binding is a reversible process that is common to all ferrous hemoglobins, whereas peroxidase activity requires a ferric resting state. The enzymatic activity of DHP is most similar to that of cytochrome *c* peroxidase. Hydrogen peroxide (H_2O_2) binds to ferric heme iron to yield Compound II and a protein radical according to the reaction $AA + P{-}Fe^{III}{-}H_2O_2 \rightarrow AA^{+\cdot} + P{-}Fe^{IV}{=}O + H_2O$, where P is the protoporphyrin IX moiety of the heme and AA is an amino acid. The combination of Compound II and the radical cation $AA^{+\cdot}$ can act as a two-electron oxidant for phenolic substrates, as shown in mechanistic studies (Franzen *et al.*, 2007). We have shown elsewhere that the relevant form of the substrate is the phenolate form at physiological pH (Franzen *et al.*, 2007). However, the nature of substrate binding is complex and there is evidence for both internal and external binding interactions. When crystals of native DHP were soaked in a solution containing 4-iodophenol, the X-ray structure (PDB code

1ewa) revealed that the phenol binds in an internal binding pocket (LaCount *et al.*, 2000). However, both kinetic analyses and NMR data indicated that the substrate-binding site is on the exterior of DHP (Franzen *et al.*, 2007; Davis *et al.*, 2008). Although it is not presently understood how DHP switches between its hemoglobin (dioxygen-binding) and peroxidase (dioxygen-cleaving) functions, substrate localization in the distal pocket has not been previously observed in globins and may play a regulatory role (Belyea *et al.*, 2005).

It is important to understand the ligation of the heme iron in DHP in light of its bifunctional nature. The ferric iron in methemoglobin and metmyoglobin is six-coordinate (Katz *et al.*, 1994; Royer, 1994; Liu *et al.*, 2001;Vojtechovsky *et al.*, 1999; Yang & Phillips, 1996; Nardini *et al.*, 1995; Della Longa *et al.*, 2003). In contrast, the heme iron is usually five-coordinate in ferric heme peroxidases (Hashimoto *et al.*, 1986; Chouchane *et al.*, 2000; Cheek *et al.*, 1999; Yonetani & Anni, 1987; de Ropp *et al.*, 1991; Andersson *et al.*, 1987; Kuila *et al.*, 1985; Yamazaki *et al.*, 1981; Wang *et al.*, 1990; Kunishima *et al.*, 1996), although it can be six-coordinate provided that the sixth heme iron ligand is sufficiently labile (Badyal *et al.*, 2006). The first published structure of native DHP, determined at room temperature, showed a water molecule in the distal pocket which was not located within bonding distance of the heme iron (PDB code 1ew6; LaCount *et al.*, 2000). In contrast, in structures determined at 100 K the ligands bound to the heme iron are stabilized by hydrogen bonding to the distal histidine His55 (Serrano *et al.*, 2007). A strong interaction of His55 with heme iron ligands is observed in the ferric metaquo form and oxy ferrous form of the C73S mutant. These structures have PDB codes 2qfk and 2qfn, respectively (Serrano *et al.*, 2007).

The hydrogen bonding of His55 to heme iron ligands, such as H_2O or O_2, may play a significant role in the peroxidase reactivity of DHP because it potentially regulates H_2O or O_2 displacement from the heme iron when the substrate interacts with the protein as required for peroxidase catalysis (Serrano *et al.*, 2007). The displacement of H_2O or O_2 from the heme iron is required for H_2O_2 binding, which is the first step of the catalytic cycle. However, the hypothesis that the distal histidine conformation is related to heme iron ligation must be reconciled with the observation of two conformations of His55 in the room-temperature X-ray crystal structure (LaCount *et al.*, 2000). The distal His55 residue was observed in both a closed conformation in the distal pocket and an open solvent-exposed conformation in the 1ew6 structure determined at room temperature. The correlation of these conformations with heme ligation is still not clear. In this report, we address the issue by determining the X-ray crystal structure of the deoxy form of DHP at 100 K.

The existence of multiple conformations of the distal histidine is a key structural feature that is common to both DHP and sperm whale myoglobin (SWMb; Tian *et al.*, 1993; Nienhaus *et al.*, 2006; Yang & Phillips, 1996). Although DHP is a dimeric hemoglobin, its subunits appear to act with relative independence. No cooperativity has so far been observed in any binding studies of substrate or heme iron ligand. Moreover, the intersubunit contacts consist of two salt bridges and are consequently relatively weak. In SWMb, a local conformational equilibrium between the open and closed distal pocket states can be triggered by pH variation (Morikis *et al.*, 1989; Tian *et al.*, 1993; Yang & Phillips, 1996). When the pH is lowered, the distal histidine HisE7 becomes protonated and rotates about the $C^{\alpha}-C^{\beta}$ bond towards the solvent (Morikis *et al.*, 1989; Tian *et al.*, 1993; Yang & Phillips, 1996). In the native DHP structure, His55 is displaced from the distal pocket when the a substrate analog 4-iodophenol binds in the internal binding site (LaCount *et al.*, 2000). In the metaquo structure of the recombinant wild-type DHP, the distal His55 is only observed in the closed conformation (Serrano *et al.*, 2007; Saga *et al.*, 1991; Tian *et al.*, 1993). Based on these observations, it appears that His55 is stabilized by hydrogen bonding to heme ligands and is observed in the open conformation when the heme is five-coordinate (*i.e.* when no ligand is present to act as a hydrogen-bond partner with His55) or on binding of 4-iodophenol in the distal pocket. The room-temperature DHP X-ray crystal structure shows that the distal histidine has significant conformational flexibility compared with ferric (metaquo) SWMb at pH $\simeq$ 6 (Kachalova *et al.*, 1999). Since the open conformation of SWMb is observed at pH 4 but not at pH 6 (at 277 K; Yang & Phillips, 1996), there is clearly a difference in the pK_a of the histidine of DHP relative to SWMb that requires explanation.

A number of heme proteins undergo conformational rearrangements, which can be triggered by a change in pH, in the oxidation state of the iron (Williams *et al.*, 1997; Badyal *et al.*, 2006) or by substrate binding. For example, a ligand switch in the refolding of mitochondrial cytochrome *c* involves a displacement of His by Met in a His–His coordinated heme *c* in the last stage of the folding process near neutral pH (Elove *et al.*, 1994; Colon *et al.*, 1996; Takahashi *et al.*, 1997; Yeh *et al.*, 1997). A similar change of ligation takes place in cytochrome cd_1 at the *c* heme during catalysis of the conversion of nitrite to nitric oxide (Williams *et al.*, 1997). An intrinsic mobility of the distal histidine was observed in the structure of the W41A mutant of ascorbic peroxidase. In the mutant, the distal histidine His42 binds to ferric heme iron (Badyal *et al.*, 2006). Binding of the substrate triggers a conformational change in which His42 dissociates from the heme. A similar conformational rearrangement occurs upon reduction of the heme iron, so that His42 dissociates from the iron in the ferrous form of W41A (Badyal *et al.*, 2008). The structure of deoxy DHP presented here shows that His55 is quite flexible when the heme is five-coordinate. The flexibility of the distal histidine in the deoxy DHP structure presents a contrast with the six-coordinate form where His55 is clearly in the distal pocket and is strongly associated with the sixth ligand, whether it is H_2O or O_2.

2. Material and methods

2.1. Protein purification, characterization and crystallization

Recombinant wild-type DHP was prepared and purified in the ferric form as described previously (Serrano *et al.*, 2007).

Table 1
Data-collection and refinement statistics for deoxy ferrous wild-type DHP.

Values in parentheses are for the highest resolution shell.

Data collection	
Wavelength (Å)	1.0000
Space group	$P2_12_12_1$
Unit-cell parameters (Å)	a = 57.5, b = 67.2, c = 69.1
Resolution (Å)	35.00–1.26 (1.29–1.26)
Unique reflections	68067 (4982)
Completeness (%)	98.43 (98.27)
$R_{\rm merge}$† (%)	0.057 (0.411)
$I/\sigma(I)$	18.3 (2.1)
Redundancy	3.5 (3.2)
Refinement	
$R_{\rm work}$‡ (%)	17.6 (24.7)
$R_{\rm free}$§ (%)	19.7 (28.1)
No. of protein atoms	2768
No. of solvent atoms	296
R.m.s.d. from ideal geometry	
Bond lengths (Å)	0.007
Bond angles (°)	1.208
Ramachandran plot¶ (%)	
Most favored region	94.8
Additional allowed region	5.2

† $R_{\rm merge} = \sum_{hkl}\sum_i |I_i(hkl) - \langle I(hkl)\rangle|/\sum_{hkl}\sum_i I_i(hkl)$, where $I_i(hkl)$ is the ith measurement and $\langle I(hkl)\rangle$ is the weighted mean of all measurements of $I(hkl)$. ‡ $R_{\rm work} = \sum |F_{\rm o} - F_{\rm c}|/\sum |F_{\rm o}|$, where $F_{\rm o}$ are observed and $F_{\rm c}$ are calculated structure factors. § $R_{\rm free}$ is the R factor for a subset (5%) of reflections selected previously and not included in refinement. ¶ Calculated using *PROCHECK* (Laskowski *et al.*, 1993).

The integrity of the protein was analyzed by assessing its enzymatic activity toward 2,4,6-tribromophenol (TBP), a natural substrate of DHP (Belyea *et al.*, 2005; Franzen *et al.*, 2006). Crystals were grown by the hanging-drop vapor-diffusion method from 0.2 *M* ammonium sulfate and 26–34% polyethylene glycol 4000 at 277 K. The starting protein concentration was 8 mg ml^{-1}. The pH of the drop solution was 5.9. Diffraction-quality crystals were obtained within one week and ranged in size from 0.2 to 0.7 mm in the largest dimension. The crystals grown in the ferric form were reduced in 20 m*M* sodium dithionite solution/mother liquor for 20 min under anaerobic conditions. For X-ray data collection at low temperatures, the crystals were removed from the reducing solution and cryoprotected by brief immersion in 10 µl 0.2 *M* ammonium sulfate solution containing 32% polyethylene glycol 4000 and 15% polyethylene glycol 400, mounted in a nylon loop and rapidly cryocooled in liquid nitrogen. The crystals belonged to space group $P2_12_12_1$, with unit-cell parameters a = 57.5, b = 67.2, c = 69.1 Å. The solvent content of the crystal was about 50% and the asymmetric unit contained two subunits.

2.2. X-ray data collection and structure refinement

X-ray diffraction data for deoxy wild-type DHP were collected at 100 K using a MAR 225 detector at the Advanced Photon Source (Argonne, Illinois, USA) using an X-ray wavelength of λ = 1.0 Å. The crystals diffracted to 1.22 Å resolution. The data were processed using the *HKL*-2000 program suite (Otwinowski & Minor, 1997). The structure was solved by molecular replacement with the program *Phaser* (McCoy *et al.*, 2005) at 3 Å resolution, using as a search model two polypeptide chains and two heme molecules from the asymmetric unit of the native DHP structure (PDB code 1ew6; LaCount *et al.*, 2000). In order to eliminate model bias, OMIT maps were constructed with *CNS* (Brünger *et al.*, 1998).

Table 2
Comparison of heme iron and distal and proximal histidine parameters.

The values are tabulated for subunit *A* of the asymmetric unit. Heme restraints are derived from the monomer library of the *REFMAC*5 program from the *CCP*4 suite (Collaborative Computational Project, Number 4, 1994), with no restraints on Fe axial-ligand bond lengths.

	Protein form		
	Deoxy ferrous wild type	Metaquo wild type† (2qfk)	Oxy ferrous C73S† (2qfn)
Fe—His89 N$^{\varepsilon 2}$ (Å)	2.18	2.09	2.15
Fe—His55 N$^{\varepsilon 2}$‡ (Å)	—	4.75	5.13
Fe to porphyrin plane (Å)	0.25	0.04	0.09

† Compiled from the published structures of DHP at 100 K (PDB codes 2qfk and 2qfn). ‡ Distance to the His55 conformer located inside the distal cavity.

Approximately 20 residues in each chain in the deoxy wild-type DHP could be modeled in alternative conformations and their occupancies were adjusted until there was no significant $F_{\rm o} - F_{\rm c}$ density. Using $F_{\rm o} - F_{\rm c}$ electron density contoured at 3σ, 290 water molecules were positioned into the structure using *Coot* (Emsley & Cowtan, 2004). The final model was obtained by iterative positional and isotopic *B*-factor refinement using *REFMAC*5 (Murshudov *et al.*, 1997) from the *CCP*4 suite of programs (Collaborative Computational Project, Number 4, 1994). Simulated-annealing and composite OMIT maps were constructed using *CNS*. The final model of the deoxy wild-type DHP structure contained two protein molecules in the asymmetric unit, three sulfate ions and 290 water molecules. Relevant X-ray data-collection and refinement statistics are summarized in Table 1.

3. Results and discussion

Crystals of recombinant wild-type DHP were produced as previously described (Serrano *et al.*, 2007) using protein in the ferric (Fe$^{\rm III}$) oxidation state as determined by UV–Vis spectroscopy (Soret maximum at 406 nm). Preparation of crystals of the deoxy ferrous form of wild-type DHP was attempted using two different methods. In the first method, DHP was reduced using sodium dithionite and set up for crystallization in an anaerobic atmosphere. However, no diffraction-quality crystals grew under these conditions. In the second method, crystals of DHP were reduced by soaking in sodium dithionite dissolved in the mother liquor. The second method produced diffraction-quality crystals. A diffraction data set was collected at 100 K on the SER-CAT 22-BM beamline at the Advanced Photon Source (Argonne, Illinois, USA) and the structure was refined to a resolution of 1.22 Å with an R factor of 18.5% (Table 1). The deoxy wild-type DHP crystallized with two molecules in the asymmetric unit, as observed in the original structural analysis of DHP (Zhang *et al.*, 1996).

3.1. Heme iron ligation in the structure

The proximal histidine His89 is the fifth coordination ligand of the heme iron in DHP. The Fe—N^{ε} bond length refines to 2.18 Å. The heme Fe atom is displaced 0.25 Å below the porphyrin plane on the proximal side (Table 2). The doming of the heme iron can be seen in the $2F_o - F_c$ electron-density map shown in Fig. 1. In the metaquo ferric and oxy ferrous DHP structures, the six-coordinate Fe atom is positioned at a distance of 0.04 and 0.09 Å below the porphyrin plane, respectively (Serrano *et al.*, 2007). The iron displacement in the deoxy form is similar to observations in SWMb (Cameron *et al.*, 1993) and is attributable to the change in spin state and coordination geometry. The heme iron in DHP behaves like SWMb in that it moves out of the heme plane in response to dissociation of a ligand from the six-coordinate low-spin heme to form a five-coordinate high-spin heme (Schlichting *et al.*, 1994; Hartmann *et al.*, 1996; Chu *et al.*, 2000). The core-size expansion drives the iron out of the heme plane and serves as a trigger for the protein-structure change that gives rise to the cooperative oxygen binding observed in the human hemoglobin tetramer (Hoffman *et al.*, 1972; Perutz, 1970; Brucker *et al.*, 1996; Franzen *et al.*, 1994).

3.2. Distal histidine conformations in DHP

His55 is observed in two conformations in the structure of deoxy wild-type DHP, both of which correspond to the solvent-exposed or open position (Fig. 2). Based on OMIT maps, it was possible to place the distal histidine in a third conformation in the distal pocket (not shown) with an occupancy of 44% (46% in chain *B*). However, this structure was deemed to be inappropriate based on the lack of electron density in four atom positions on the side of the imidazole ring closest to the heme. The alternative model with water instead of His55 in the distal pocket resulted in a poorer fit to the electron-density map. Since His55 ring electron density is missing for the lower portion of the ring in the best-fit model, we concluded that the density corresponds to a water atom. Fig. 1 shows that the two His55 conformations in the solvent-exposed open conformation are clearly well represented by the electron density, but there is not sufficient electron density in the internal or closed position to justify placement of His55. The difficulty in fitting the region of the density in the distal pocket is likely to arise from ring torsional dynamics of the histidine that are responsible for the lack of observable density in this portion of the structure.

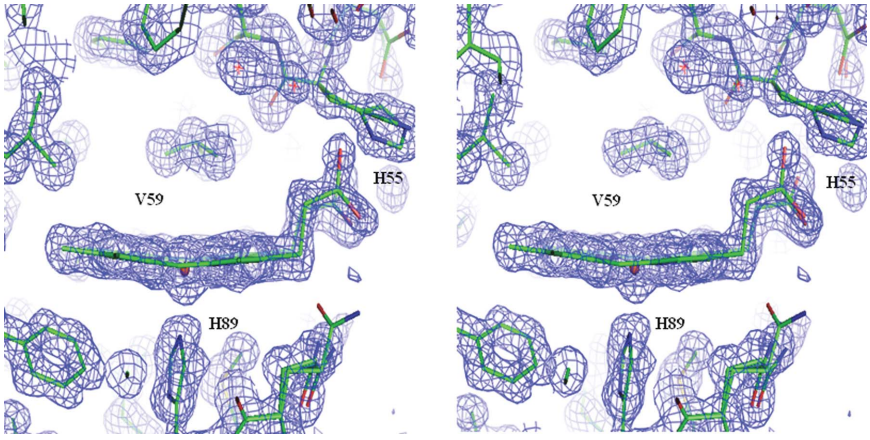

Figure 1
Stereo drawing of the $2F_o - F_c$ electron-density map for deoxy ferrous DHP. The map was contoured at 1.3σ and the coordinates shown correspond to chain *A*.

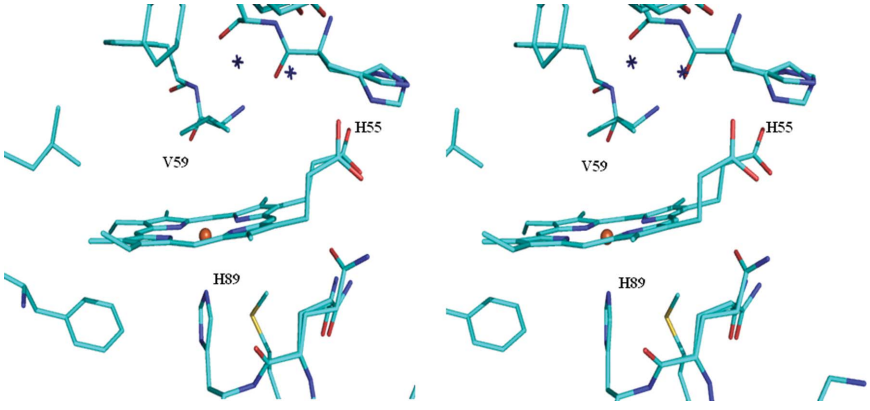

Figure 2
Stereoview of the distal-pocket region of deoxy ferrous DHP.

There are two well defined conformations of His55 that are located in a solvent-exposed site that is more than 9.5 Å away from the heme plane. The two solvent-exposed conformations of His55 are not completely separated and their occupancies are 70 and 30%, respectively (87 and 13% in chain *B*). The C^{α}, C^{β} and C^{γ} atoms of those two conformations overlap, but the imidazole planes have different rotation angles around the C^{β}—C^{γ} bond. The N^{δ} atom in the conformation with 70% occupancy (chain *A*) is positioned at a hydrogen-bonding distance (2.85 Å) from heme propionate 6.

The deoxy ferrous DHP structure differs from those of metaquo ferric DHP and oxy ferrous DHP, as shown in Figs. 3 and 4, respectively (Serrano *et al.*, 2007). There is no water or other ligand in the vicinity of the heme iron in the deoxy structure. The solvent-exposed conformations of the distal histidine in the deoxy structure can be contrasted with the internal conformation of the distal histidine in the metaquo DHP (2qfk) and oxy ferrous C73S (2qfn) structures (Serrano *et al.*, 2007). These differences are of great interest because of the key role played by the distal histidine in both globin oxygen binding and in peroxidase catalysis.

Although the enzymatic activity of DHP is similar to that of heme peroxidases, it has the structural characteristics of the globin

protein family. The conformation of the distal histidine in the six-coordinate metaquo adduct of DHP is consistent with the structures of ferric myoglobins and hemoglobins (Serrano *et al.*, 2007). Likewise, the distal histidine of DHP in the oxy ferrous form is analogous to the structure of oxy ferrous SWMb (Phillips, 1980; Brucker *et al.*, 1996). However, the conformation of the distal histidine in the deoxy DHP structure is unique in terms of its conformational flexibility.

In the deoxy SWMb structure (Cameron *et al.*, 1993), there is a noncoordinated water molecule in the distal pocket that is in a position to form strong hydrogen bonds to N^{ε} of the distal histidine. In SWMb, the distal-pocket water of the deoxy form is eliminated in the H64L mutant (Christian *et al.*, 1997). Elsewhere, we have shown the similarity of the H64V heme environment to DHP in the context of NO recombination kinetics (Franzen *et al.*, 2006). Replacement of the histidine with an aliphatic amino acid makes the distal pocket more hydrophobic in both H64L and H64V SWMb. Comparison with the SWMb mutants leads to the conclusion that the hydrophobic nature of the distal pocket in DHP (Serrano *et al.*, 2007) may contribute to the absence of a water molecule in this pocket in the deoxy structure.

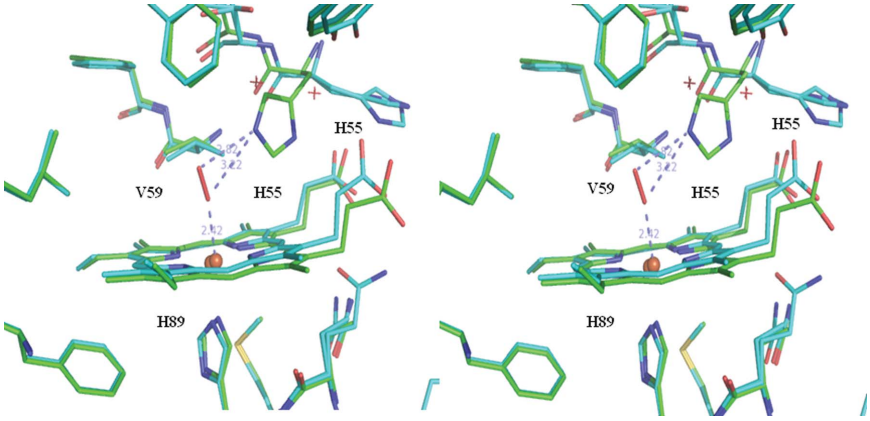

Figure 3
Stereoview of an overlay of the distal-pocket region of deoxy ferrous DHP (colored blue) and oxy ferrous DHP (PDB code 2qfn, colored green).

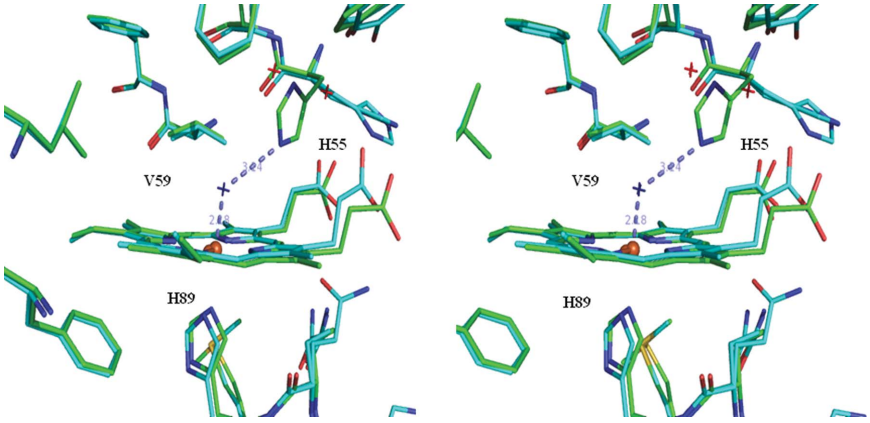

Figure 4
Stereoview of an overlay of the distal-pocket region of deoxy ferrous DHP (colored cyan) and metaquo ferric DHP (PDB code 2qfn, colored green).

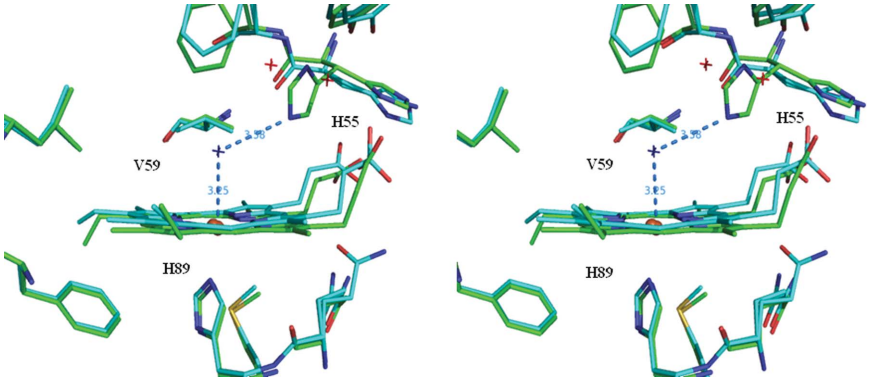

Figure 5
Stereoview of an overlay of the distal-pocket region of deoxy ferrous DHP (colored cyan) and the ferric form of native DHP at room temperature (PDB code 1ew6, colored green).

Based on the deoxy structure, we can begin to understand the origin of the two conformations of His55 in the room-temperature X-ray structure of ferric DHP (LaCount *et al.*, 2000). An overlay of the 100 K deoxy DHP structure with the room-temperature ferric DHP structure (1ew6) in Fig. 5 shows subtle differences in the open His55 conformations. The most obvious difference is that there is essentially no well defined conformation for His55 in the internal or closed conformation. There appear to be even greater dynamics of His55 in the deoxy structure than in the room-temperature ferric DHP structure. Based on previous work, we hypothesized that the ligation state of the water in the ferric form of DHP depends on temperature (Serrano *et al.*, 2007). Fig. 4 shows a water molecule bound to the heme iron in ferric (metaquo) DHP that forms a strong hydrogen bond to His55. As a consequence, His55 is observed only in the closed conformation in the metaquo DHP structure at 100 K (Serrano *et al.*, 2007). We hypothesize that at ambient temperature the ferric heme iron adduct consists of an equilibrium between five-coordinate and six-coordinate metaquo forms. If the His55 conformation is coupled to the heme iron ligand by hydrogen bonding, then both open and closed conformations would be expected in the room-temperature structure corresponding to the five- and six-coordinate adducts, respectively.

The hypothesis of stabilization by the heme iron ligand must also take into

account the protonation state of the distal histidine. The solvent-exposed conformation of the distal histidine is analogous to the open conformation of His64 in SWMb that was observed in a low-pH (pH 4.0) environment (Sage *et al.*, 1991; Tian *et al.*, 1996). The solvent-exposed or open conformation observed by X-ray crystallography is likely to be associated with the protonation of His64 in SWMb (Yang & Phillips, 1996). At low pH the oxygen-dissociation rate increases dramatically, suggesting that the hydrogen bond between the distal histidine and the bound O_2 is important for the stabilization of bound oxygen in the closed conformation and is disrupted in the open conformation. According to this hypothesis, the open form of deoxy ferrous DHP would also provide an open channel that allows ligand diffusion between the solution and the heme. According to this hypothesis, the distal histidine stabilizes the oxygen on the heme iron by hydrogen-bond formation, which is consistent with the X-ray structure (Serrano *et al.*, 2007)

The difference between room-temperature and 100 K crystal structures may depend on the temperature-dependence of the pK_a of the distal histidine (Braunstein *et al.*, 1993; Nienhaus *et al.*, 2008). The distal histidine of SWMb, His64, has a pK_a of $\sim$4.5 at room temperature, which implies that His64 will be in the closed conformation at pH 6, which was used for crystallization. FTIR spectroscopy of SWMb indicates that the fraction of the open conformation increases as the temperature is lowered (Braunstein *et al.*, 1993; Nienhaus *et al.*, 2008). In DHP there is the additional factor that binding of a substrate analog in the internal binding site can force the distal histidine into the open or solvent-exposed conformation (LaCount *et al.*, 2000), but this effect may also be coupled with protonation of the distal histidine. Since molecular binding in the internal site also displaces His55 (Smirnova *et al.*, 2008), conformational flexibility may also be associated with the lack of a hydrogen-bond partner in the substrate-bound form. Thus, the conformation of the distal histidine of DHP has been shown to be determined by interrelated interactions between the protonation state, the heme iron ligand and the presence of substrate.

4. Conclusion

The X-ray crystal structure of deoxy DHP strongly resembles the X-ray crystal structures of deoxy SWMb in the geometry of the heme iron, but shows a greater conformational flexibility of the distal histidine His55. The heme iron is significantly displaced out of the porphyrin plane compared with six-coordinate ferric adducts and this heme doming is comparable to that of deoxy SWMb (Vojtechovsky *et al.*, 1999; Kachalova *et al.*, 1999). The comparison with myoglobin is relevant since the intersubunit interactions of the DHP dimer are relatively weak. Most X-ray crystal structures of SWMb have been obtained at pH 6, which is also the pH that is optimal for crystallization of DHP. The observation of His55 in the open conformation at pH 6 may be a consequence of the temperature-dependence of the pK_a of the distal histidine (Braunstein *et al.*, 1993; Nienhaus *et al.*, 2008). As the temperature is lowered, the pK_a of the distal histidine increases and the greater population of the protonated imidazolium ring leads to a larger population of the solvent-exposed conformation. The only deoxy SWMb X-ray crystal structure at cryogenic temperature was obtained at pH 7, which was necessary to ensure that the distal histidine remained in the closed conformation (Vojtechovsky *et al.*, 1999). The systematic study of histidine conformation in SWMb as a function of pH conducted by Yang & Phillips (1996) at 277 K shows a difference from DHP. While SWMb requires a pH of $\sim$4.5 to show a significant fraction of distal histidine (His64) residues in the open conformation, the room-temperature DHP structure shows 50% of the His55 residues in the open conformation at pH 6 (LaCount *et al.*, 2000). These results suggest that the conformational rearrangements of His55 are intrinsically different in DHP. One possible difference is the fact that the heme is buried 1.5 Å more deeply in the globin relative to SWMb (Serrano *et al.*, 2007). The displacement of the heme deeper into the globin implies that the histidine is more distant from the heme iron in DHP and therefore more labile. On the other hand, the lability of the distal histidine is restricted by hydrogen-bonding interactions with ligands bound to the heme iron, which are strong in the metaquo DHP and oxy ferrous C73S structures at 100 K (Serrano *et al.*, 2007). Thus, it is suggested that a combination of the ligation state of the iron and the protonation state of the histidine determine the His55 conformation.

The structure presented here represents an important aspect of coupling of a protein motion with heme ligation that is likely to be associated with both the hemoglobin and peroxidase functions of DHP. The flexibility of His55 accounts for the high escape rate for carbon monoxide (CO) in photolyzed DHP–CO and therefore with the ease of ligand exchange at the heme iron that is required for activation by H_2O_2 (Nienhaus *et al.*, 2006). The coupled motion of His55 with the substrate analog 4-iodophenol, which binds in an unusual internal binding site, must also depend on the flexibility of the distal histidine (LaCount *et al.*, 2000). Since the binding of substrate analogs in the internal pocket also displaces bound water in the metaquo form (Smirnova *et al.*, 2008), the displacement of His55 to the open form observed in the deoxy DHP structure is driven both by steric interactions and by loss of stabilization owing to hydrogen bonding. These features are likely to regulate the activity of the two functions of DHP.

We acknowledge financial support for this work from Army Research Office Grant 52278-LS. We thank Dr Zhongmin Jin at SER-CAT (Advanced Photon Source) for synchrotron data collection. The Advanced Photon Source is supported by the US Department of Energy, Office of Science, Office of Basic Energy Sciences under Contract No. W-31-109-End-38. We thank Dr Robert Rose, Department of Molecular and Structural Biochemistry at NCSU for insightful discussions.

References

Andersson, L. A., Renganathan, V., Loehr, T. M. & Gold, M. H. (1987). *Biochemistry*, **26**, 2258–2263.

Badyal, S. K., Joyce, M. G., Sharp, K. H., Seward, H. E., Mewies, M., Basran, J., Macdonald, I. K., Moody, P. C. E. & Raven, E. L. (2006). *J. Biol. Chem.* **281**, 24512–24520.

Belyea, J., Belyea, C. M., Lappi, S. & Franzen, S. (2006). *Biochemistry*, **45**, 14275–14284.

Belyea, J., Gilvey, L. B., Davis, M. F., Godek, M., Sit, T. L., Lommel, S. A. & Franzen, S. (2005). *Biochemistry*, **44**, 15637–15644.

Braunstein, D. P., Chu, K., Egeberg, K. D., Frauenfelder, H., Mourant, J. R., Nienhaus, G. U., Ormos, P., Sligar, S. G., Springer, B. A. & Young, R. D. (1993). *Biophys. J.* **65**, 2447–2454.

Brucker, E. A., Olson, J. S. & Phillips, G. N. Jr (1996). *J. Biol. Chem.* **271**, 25419–25422.

Brünger, A. T., Adams, P. D., Clore, G. M., DeLano, W. L., Gros, P., Grosse-Kunstleve, R. W., Jiang, J.-S., Kuszewski, J., Nilges, M., Pannu, N. S., Read, R. J., Rice, L. M., Simonson, T. & Warren, G. L. (1998). *Acta Cryst.* D**54**, 905–921.

Cameron, A. D., Smerdon, S. J., Wilkinson, A. J., Habash, J., Helliwell, J. R., Li, T. & Olson, J. S. (1993). *Biochemistry*, **32**, 13061–13070.

Cheek, J., Mandelman, D., Poulos, T. L. & Dawson, J. (1999). *J. Biol. Inorg. Chem.* **4**, 64–72.

Chouchane, S., Lippai, I. & Magliozzo, R. S. (2000). *Biochemistry*, **39**, 9975–9983.

Christian, J. F., Unno, M., Sage, J. T., Champion, P. M., Chien, E. & Sligar, S. G. (1997). *Biochemistry*, **36**, 11198–11204.

Chu, K., Vojtchovsky, J., McMahor, B., Sweet, R., Berendzen, J. & Schlichting, I. (2000). *Nature (London)*, **403**, 921–923.

Collaborative Computational Project, Number 4 (1994). *Acta Cryst.* D**50**, 760–763.

Colon, W., Elove, G. A., Wakem, L. P., Sherman, F. & Roder, H. (1996). *Biochemistry*, **35**, 5538–5549.

Davis, M. F., Gracz, H., Vendeix, F. A. P., Gilvey, L. B., Somasundaram, A., Decatur, S. M. & Franzen, S. (2008). In the press.

Della Longa, S., Arcovito, A., Benefatto, M., Congiu-Castellano, A., Girasole, M., Hazemann, J. L. & Lo Bosco, A. (2003). *Biophys. J.* **85**, 549–558.

Elove, G. A., Bhuyan, A. K. & Roder, H. (1994). *Biochemistry*, **33**, 6925–6935.

Emsley, P. & Cowtan, K. (2004). *Acta Cryst.* D**60**, 2126–2132.

Franzen, S., Gilvey, L. B. & Belyea, J. (2007). *Biochim. Biophys. Acta*, **1774**, 121–130.

Franzen, S., Jasaitis, A., Belyea, J., Brewer, S. H., Casey, R., MacFarlane, A. W. IV, Stanley, R., Vos, M. H. & Martin, J.-L. (2006). *J. Phys. Chem. B*, **110**, 14483–14493.

Franzen, S., Lambry, J.-C., Bohn, B., Poyart, C. & Martin, J.-L. (1994). *Nature Struct. Biol.* **1**, 230–233.

Hartmann, H., Zinser, S., Komninos, P., Schneider, R. T., Nienhaus, G. U. & Parak, F. (1996). *Proc. Natl. Acad. Sci. USA*, **93**, 7013–7016.

Hashimoto, S., Teraoka, J., Inubushi, T., Yonetani, T. & Kitagawa, T. (1986). *J. Biol. Chem.* **261**, 11110–11118.

Hoffman, B. M., Spilburg, C. A. & Petering, D. H. (1972). *Cold Spring Harbor Symp. Quant. Biol.* **36**, 343–348.

Kachalova, G. S., Popov, A. N. & Bartunik, H. D. (1999). *Science*, **284**, 473–476.

Katz, D. S., White, S. P., Huang, W., Kumar, R. & Christianson, D. W. (1994). *J. Mol. Biol.* **244**, 541–553.

Kuila, D., Tien, M., Fee, J. A. & Ondrias, M. R. (1985). *Biochemistry*, **24**, 3394–3397.

Kunishima, N., Amada, F., Fukujama, K., Kawamoto, M., Maesunaga, T. & Matsubara, H. (1996). *FEBS Lett.* **378**, 291–294.

LaCount, M. W., Zhang, E., Chen, Y. P., Han, K., Whitton, M. M., Loncoln, D. E., Woodin, S. A. & Lebioda, L. (2000). *J. Biol. Chem.* **275**, 18712–18716.

Laskowski, R. A., MacArthur, M. W., Moss, D. S. & Thornton, J. M. (1993). *J. Appl. Cryst.* **26**, 283–291.

Liu, X.-Z., Li, S.-L., Jing, H., Liang, Y.-H., Hua, Z.-Q. & Lu, G.-Y. (2001). *Acta Cryst.* D**57**, 775–783.

McCoy, A. J., Grosse-Kunstleve, R. W., Storoni, L. C. & Read, R. J. (2005). *Acta Cryst.* D**61**, 458–464.

Morikis, D., Champion, P. M., Springer, B. A. & Sligar, S. G. (1989). *Biochemistry*, **28**, 4791–4800.

Murshudov, G. N., Vagin, A. A. & Dodson, E. J. (1997). *Acta Cryst.* D**53**, 240–255.

Nardini, M., Tarricone, C., Rizzi, M., Lania, A., Desideri, A., De Danctie, G., Coletta, M., Petruzzeli, R., Ascenzi, P., Coda, A. & Bolognesi, M. (1995). *J. Mol. Biol.* **247**, 459–465.

Nienhaus, K., Deng, P., Belyea, J., Franzen, S. & Nienhaus, G. U. (2006). *J. Phys. Chem. B*, **110**, 13264–13276.

Nienhaus, K., Palladino, P. & Nienhaus, G. U. (2008). *Biochemistry*, **47**, 935–948.

Otwinowski, Z. & Minor, W. (1997). *Methods Enzymol.* **276**, 307–326.

Perutz, M. F. (1970). *Nature (London)*, **228**, 726–734.

Phillips, S. E. V. (1980). *J. Mol. Biol.* **142**, 531–554.

Ropp, J. S. de, La Mar, G. N., Wariishi, H. & Gold, M. H. (1991). *J. Biol. Chem.* **266**, 15001–15008.

Royer, W. E. Jr (1994). *J. Mol. Biol.* **235**, 657–681.

Sage, J. T., Morikis, D. & Champion, P. M. (1991). *Biochemistry*, **30**, 1227–1237.

Schlichting, I., Berendzen, J., Phillips, G. & Sweet, R. (1994). *Nature (London)*, **137**, 808–812.

Serrano, V. de, Chen, Z., Davis, M. F. & Franzen, S. (2007). *Acta Cryst.* D**63**, 1094–1101.

Smirnova, T. I., Weber, R. T., Davis, M. F. & Franzen, S. (2008). *J. Am. Chem. Soc.* **130**, 2128–2129.

Takahashi, S., Yeh, S.-R., Das, T. K., Chan, C.-K., Gottfried, D. S. & Rousseau, D. L. (1997). *Nature Struct. Biol.* **4**, 44–50.

Tian, W., Saga, J. & Champion, P. (1993). *J. Mol. Biol.* **233**, 155–156.

Tian, W., Saga, J., Champion, P., Chien, E. & Sligar, S. (1996). *Biochemistry*, **35**, 3487–3502.

Vojtechovsky, J., Chu, K., Berendzen, J., Sweet, R. M. & Schlichting, I. (1999). *Biophys. J.* **77**, 2153–2174.

Wang, J., Mauro, M., Edwards, S. L., Oatley, S. J., Fishel, L. A., Ashford, V. A., Xuong, N.-H. & Kraut, J. (1990). *Biochemistry*, **29**, 7160–7173.

Williams, P. A., Fülöp, V., Garman, E. F., Saunders, N. F. W., Ferguson, S. J. & Hajdu, J. (1997). *Nature (London)*, **389**, 406–412.

Yamazaki, I., Tamura, M. & Nakajima, R. (1981). *Mol. Cell. Biochem.* **40**, 143–153.

Yang, F. & Phillips, G. N. (1996). *J. Mol. Biol.* **256**, 762–774.

Yeh, S.-R., Takahashi, S., Fan, B. & Rousseau, D. L. (1997). *Nature Struct. Biol.* **4**, 51–56.

Yonetani, T. & Anni, H. (1987). *J. Biol. Chem.* **262**, 9547–9554.

Zhang, E., Chen, Y. P., Roach, M. P., Lincoln, D. E., Lovell, C. R., Woodin, S. A., Dawson, J. H. & Lebioda, L. (1996). *Acta Cryst.* D**52**, 1191–1193.

Different Modes of Binding of Mono-, Di-, and Trihalogenated Phenols to the Hemoglobin Dehaloperoxidase from *Amphitrite ornata*[†]

Michael F. Davis,[‡] Hanna Gracz,[‡] Franck A. P. Vendeix,[§] Vesna de Serrano,[‡] Aswin Somasundaram,[‡] Sean M. Decatur,[||] and Stefan Franzen*[,‡]

Department of Chemistry, North Carolina State University, Raleigh, North Carolina 27606, Department of Molecular and Structural Biochemistry, North Carolina State University, Raleigh, North Carolina 27606, and Chemistry Department, Oberlin College, Oberlin, Ohio 44074

Received August 20, 2008; Revised Manuscript Received January 6, 2009

ABSTRACT: The hemoglobin dehaloperoxidase (DHP), found in the coelom of the terebellid polychaete *Amphitrite ornata*, is a dual-function protein that has the characteristics of both hemoglobins and peroxidases. In addition to oxygen transport function, DHP readily oxidizes halogenated phenols in the presence of hydrogen peroxide. The peroxidase activity of DHP is high relative to that of wild-type myoglobin or hemoglobin, but the most definitive difference in DHP is a well-defined substrate-binding site in the distal pocket, which was reported for 4-iodophenol in the X-ray crystal structure of DHP. The binding of 2,4,6-trihalogenated phenols is relevant since 2,4,6-tribromophenol is considered to be the native substrate and 2,4,6-trichlorophenol also gives high turnover rates in enzymatic studies. The most soluble trihalogenated phenol, 2,4,6-trifluorophenol, acts as a highly soluble structural analogue to the native substrate 2,4,6-tribromophenol. To improve our understanding of substrate binding, we compared the most soluble substrate analogues, 4-bromophenol, 2,4-dichlorophenol, and 2,4,6-trifluorophenol, using ^{1}H and ^{19}F NMR to probe substrate binding interactions in the active site of the low-spin metcyano adduct of DHP. Both mono- and dihalogenated phenols induced changes in resonances of the heme prosthetic group and an internal heme edge side chain, while ^{1}H NMR, ^{19}F NMR, and relaxation data for a 2,4,6-trihalogenated substrate indicate a mode of binding on the exterior of DHP. The differences in binding are correlated with differences in enzymatic activity for the substrates studied.

The terebellid polychaete *Amphitrite ornata* inhabits estuarine mudflats with other marine annelids, such as *Notomastus lobatus*, *Saccoglossus kowalevskii*, and *Thelepus crispus*, which secrete brominated aromatic compounds as a means of territorial protection (*1*−*3*). While such repellents would be deterrents for some organisms, *A. ornata* has developed a novel defense mechanism in the hemoglobin dehaloperoxidase (DHP).[1] DHP is found in the coelom of *A. ornata* and is one of two hemoglobins in the organism (*4*). Structurally, the DHP monomer is homologous to myoglobin containing the globin fold with eight helices and a heme prosthetic group ligated to the protein backbone via a proximal histidine (*5, 6*). The novelty of DHP lies in its ability to oxidatively dehalogenate haloaromatics found in its environment while simultaneously maintaining an oxygen storage function consistent with its hemoglobin structure (*7*−*9*).

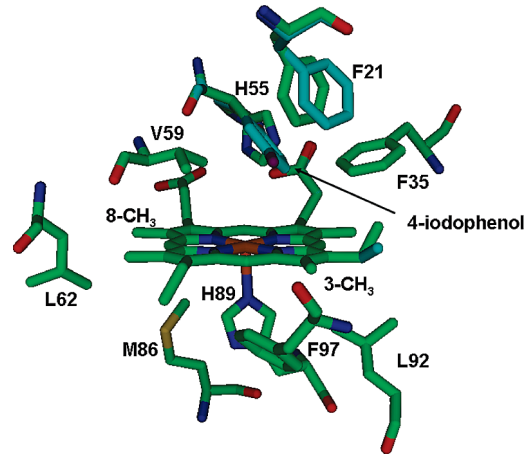

FIGURE 1: X-ray crystal structures of the local heme environment and substrate binding residues of DHP shown with (light blue) and without (green) bound substrate 4-iodophenol. Once the substrate binds, the 4-vinyl heme substituent shows slight changes in orientation. More predominant changes are observed in the orientations of His55 and Phe21.

DHP has the highest turnover rate for 2,4,6-trihalogentated phenols, which have been shown to be extremely toxic to marine life (*10, 11*).

The first X-ray crystal structure of substrate-bound DHP revealed that 4-iodophenol binds in the distal pocket but is not coordinated to the heme iron (Figure 1) (*5, 6*). This internal binding site distinguishes DHP not only from other

[†] This project was supported by Army Research Office Grant 52278-LS.

* To whom correspondence should be addressed. Phone: (919) 515-8915. Fax: (919) 515-8920. E-mail: Stefan_Franzen@ncsu.edu.

[‡] Department of Chemistry, North Carolina State University.

[§] Department of Molecular and Structural Biochemistry, North Carolina State University.

[||] Oberlin College.

[1] Abbreviations: Ap, ampicillin; 4-BP, 4-bromophenol; 2,4-DCP, 2,4-dichlorophenol; DHP, dehaloperoxidase; DHPCN, cyanide-ligated dehaloperoxidase; HRP, horseradish peroxidase; IPTG, isopropyl β-D-thiogalactopyranoside; 2,4,6-TBP, 2,4,6-tribromophenol; 2,4,6-TCP, 2,4,6-trichlorophenol; 2,4,6-TFP, 2,4,6-trifluorophenol.

10.1021/bi801568s CCC: $40.75
Published on Web 02/19/2009

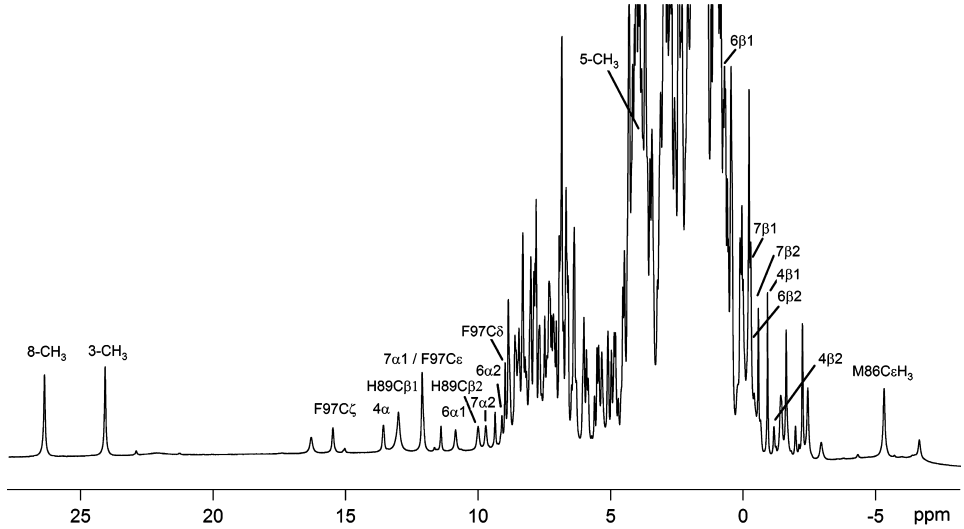

FIGURE 2: ^{1}H NMR spectrum of DHPCN. Spectrum taken at 298 K, 99.9% D_2O, 100 mM potassium phosphate, and pH 7.0. The assigned hyperfine-shifted resonances are labeled.

globins but also from other heme peroxidases that typically bind substrates on the heme periphery (*12*). According to this X-ray structure (Protein Data Bank entry 1EWA), the average occupancy of the substrate analogue 4-iodophenol in the internal binding site is only ~23% (*6*). Examination of the substrate-bound DHP crystal structure shows primary structural changes occurring solely at the heme and surrounding residues when substrate is bound. We have also confirmed by X-ray crystallography that para-halogenated (4-bromo- and 4-iodophenol) phenols can occupy this internal binding site (V. de Serrano and S. Franzen, unpublished data). However, 2,4-di- and 2,4,6-trichlorophenols do not readily enter the distal pocket in the crystal form. This is ironic considering the high turnover rate of 2,4,6-trihalophenols, which are the most active substrates for DHP. 2,4,6-Trifluorophenol (2,4,6-TFP) has been shown to enter the distal pocket of the metaquo and carbonmonoxy forms of DHP at low temperatures. We have recently shown that 2,4,6-TFP can displace the coordinated water molecule of the metaquo form at low temperature (*13*). However, it is apparently expelled from the distal pocket in the carbonmonoxy form at room temperature (*14*). The interaction of diatomic ligands and hydrogen peroxide, in the internal binding site is highly relevant to the function of DHP. The competition for binding in the distal pocket may involve the site occupied by 4-iodophenol in the 1EWA crystal structure.

We have used the carbonmonoxy form of DHP (DHPCO) as a model for the interaction of halogenated phenols and a heme-coordinated diatomic ligand in the distal pocket. 2,4,6-TFP has been observed to enter the distal pocket of the DHPCO at low temperatures at pH 5.5, but not at room temperature (*14*). We have recently shown that 2,4,6-TFP also binds to the DHPCO form at room temperature at pH 4.7 (*50*). The functional relevance of this binding is still not clear. Since trihalogenated substrates, such as 2,4,6-tribromophenol (2,4,6-TBP), exhibit the highest turnover rates, it is key from a functional perspective to determine whether oxidation of the substrate can occur in the internal site. The fact that the native substrate, 2,4,6-TBP, and other trihalophenols do not bind in that site under physiological conditions at room temperature and pH 7.4 presents a conundrum for DHP function. These data suggest that the internal binding site is not the active site. Therefore, the binding site for the native substrate, 2,4,6-TBP, has not yet been determined. The well-defined internal binding site for monohalogenated phenols, such as 4-bromophenol, may interfere with the binding of oxygen or hydrogen peroxide and could regulate either the hemoglobin or peroxidase function of DHP.

The X-ray crystal structure of DHP shows that the entire 4-iodophenol molecule binds within 6 Å of the iron center (*6*). The proximity of the internal molecular binding site to the heme permits the application of paramagnetic NMR experiments in elucidating specific structural changes near the heme iron when molecules bind in the internal binding pocket (*15*). NMR has been used extensively for active site characterization of high-spin ($S = {}^5/_2$) and low-spin ($S = {}^1/_2$) forms of many peroxidases and globins (*16*−*23*) and provides a sensitive method for probing structural details of the heme prosthetic group. Addition of a strong-field ligand, e.g., cyanide, to the ferric Fe(III) oxidation state of DHP creates a low-spin ($S = {}^1/_2$), paramagnetic species. This metcyano form is the focus of the current NMR study, as active site resonances are much sharper and less dispersed in the low-spin form than the high-spin, metaquo counterpart.

Herein, we report the first assignment and active site characterization of DHP using NMR spectroscopy and present evidence that there is both an internal and an external binding site for halogenated phenols. Assignment of the resonances was accomplished primarily through natural abundance ^{13}C−^{1}H HSQC (*24*) and WEFT-NOESY (*25*) experiments. Differential perturbation of certain active site resonances was observed upon titration of three different halogenated phenols chosen for their high water solubility: 4-bromophenol (4-BP), 2,4-dichlorophenol (2,4-DCP), and 2,4,6-trifluorophenol (2,4,6-TFP). The effects of substrate binding were also compared over a wide pH range.

MATERIALS AND METHODS

Protein Preparation. The pET 16b plasmid containing the 6XHisDHP4R DNA insert (*7*) was transformed into competent BL21(DE3) *Escherichia coli* cells, plated out on LB agar plates with 100 μg/mL ampicillin (Ap), and allowed to

grow at 37 °C for ~14 h. Single colonies were isolated, and starter growths were used to inoculate 6 L *E. coli* growths. The cells were incubated at 37 °C with shaking for 13 h. Expression of 6XHisDHP4R protein was not induced via addition of ITPG. Basal expression of the protein in the nonstringent BL21(DE3) cell line yielded significantly high levels of holoprotein. The cells were collected via centrifugation and then allowed to freeze overnight at −20 °C. The cells were resuspended in lysis buffer (2 mL/g of cell pellet) [50 mM NaH_2PO_4, 300 mM NaCl, and 10 mM imidazole (pH 6)], and lysozyme was added to a final concentration of 1 mg/mL. The cell slurry was allowed to stir at 4 °C for 1 h. The slurry was then sonicated for 30 min, and 200 μL of DNase I (16 mg/mL) and RNase A (10 mg/mL) were added. The cell slurry was again stirred at 4 °C for ~1 h before being frozen overnight at −20 °C. After rethawing, the cells were centrifuged at 18000 rpm for 45 min, and supernatant His-tagged DHP protein was collected. The crude His-DHP was applied to a Ni-NTA agarose column (Qiagen), washed with 50 mM NaH_2PO_4, 300 mM NaCl, 20 mM imidazole buffer (pH 6), and eluted with 50 mM NaH_2PO_4, 300 mM NaCl, 250 mM imidazole buffer (pH 6). The isolated His-DHP was buffer exchanged in 20 mM KH_2PO_4 (pH 6) using a Sephadex G-25 column. The protein was further purified on a CM 52 ion exchange column and was eluted stepwise between pH 6 with 20 mM KH_2PO_4 and pH 6 with 150 mM KH_2PO_4. The concentration of the protein was determined using the Soret band at 406 nm with a molar absorptivity of 116400 M^{-1} cm^{-1} (*26*). Final yields of purified wild-type (wt) DHP protein were approximately 20 mg/L of broth with A_{406}/A_{280} ratios greater than 4. Purified His-DHP was exchanged in 99.9% D_2O, 100 mM potassium phosphate buffer (pH 7). The reported pH values are left uncorrected for the deuterium isotope effect. The protein was concentrated to a final concentration of ~1−2 mM, and KCN was added to an approximately 10-fold excess.

^{1}H NMR Experiments. All ^{1}H NMR and ^{19}F NMR spectra were recorded on a either a 500 MHz AVANCE Bruker or 300 MHz Bruker NMR spectrometer. The one-dimensional (1D) NOE experiments were performed using a decoupling pulse to saturate the resonance of interest (*27*). Identical spectra were then collected with the decoupler slightly off-resonance. Difference spectra were generated by subtracting the on-resonance spectrum from the off-resonance spectrum. The magnitude of the NOE did not increase after 200 ms of resonance saturation via the decoupler. Thus, the 1D NOE data were collected in the steady state regime with a saturation time of 200 ms. The T_1 experiments were conducted using a standard inversion−recovery pulse sequence without a presaturation pulse. The τ values for the TFP relaxation experiments were 0.2, 0.4, 0.8, 1.6, 3.2, 6.4, 10, and 20 s, with a delay time, t, of 22 s. T_2 measurements were taken using a standard Carr−Purcell−Meiboom−Gill (CPMG) pulse sequence. The WEFT-NOESY data were collected utilizing a recovery delay of 300 ms and a mixing time of 100 ms. The ^{1}H−^{13}C HSQC experiments were recorded using a recycle time of 200 ms with a J of 200 Hz. Two-dimensional (2D) NOESY spectra incorporating a presaturation pulse were collected using a spectral width of 27000 Hz. Best results were obtained with a mixing time of 100 ms and a delay time of 1.2 s. Gradient-selective COSY spectra were also collected over a spectral width of 27000 Hz. A total of 2048 t_2 points and 512 t_1 blocks were collected with a delay time of 1.2 s.

Table 1: ^{1}H and ^{13}C NMR Assignments and T_1 Measurements for Selected Resonances of DHPCN at 25 °C and pH 7.0

	^{1}H δ (ppm)	^{13}C δ (ppm)	^{1}H T_1 (ms)	R_{Fe} (Å)[a]	R_{Fe} (Å)[b]
heme					
8-CH_3	26.8	−53.1	188	*c*	5.70
3-CH_3	24.5	−59.5	204	*c*	5.72
5-CH_3	4.3	−14.8	*d*	−	5.43
4α	14.0	52.8	149	5.43	5.68
4β_1	−1.1	not observed	*d*	−	6.75
4β_2	−1.5	not observed	303	6.1	6.75
6α1	13.4	84.4	−	−	5.8
6α2	9.4	84.4	−	−	6.29
6β1	1.2	not observed	*d*	−	6.23
6β2	0.3	not observed	*d*	−	7.56
7α1	12.5	−32.7	*d*	−	6.44
7α2	10.2	−32.7	213	5.76	5.83
7β1	0.4	118.8	*d*	−	6.27
7β2	−0.2	118.8	*d*	−	6.14
Phe97			−		
CζH	15.9	134.5	90	4.79	5.25
CεHs	12.6	132.6	*d*	−	5.45, 6.99
CδHs	9.4	132.2	*d*	−	7.27, 8.48
His89					
Nε_2H	19.9	not applicable	−	−	5.22
Cβ1H	13.4	24.5	*d*	−	6.45
Cβ2H	10.4	24.5	105	5.12	6.29

[a] Calculated using $R_{Fe}^i/R_{Fe}^j = (T_1^i/T_1^j)^{1/6}$. [b] Measurements taken from the X-ray structure (*5, 6*). [c] Not applicable due to contact shift contribution. [d] Not accurate measurements due to overlapping resonances.

UV−Vis Enzymatic Assays. For all experiments, the protein was exchanged into 100 mM potassium phosphate buffer (pH 7). The absorption data were collected using a Hewlett-Packard 8453 multiwavelength spectrometer. The spectra were collected every 5 s over a 60 s time frame. The conditions used for the assays were 5 μM DHP, 360 μM H_2O_2, and 120 μM substrate. Substrate turnover was monitored by the disappearance of substrate absorption bands (4-BP, 280 nm; 2,4-DCP, 284 nm; 2,4,6-TFP, 272 nm).

RESULTS

The low-spin metcyano form of DHP at pH 7.0 and 25 °C exhibits a wide dispersion of hyperfine-shifted heme and active site resonances, from −12 to 27 ppm as seen in Figure 2 and reported in Table 1. ^{13}C−^{1}H HSQC, WEFT-NOESY, gradient-selective COSY, 1D NOE difference, and presaturation NOESY spectra were used to assign the majority of active site resonances. The spectra of resonances pertinent to the substrate binding study are presented.

Examination of the X-ray structures shows that only the 3-CH_3 and 5-CH_3 heme methyls are within NOE distance of Phe side chains (*5, 6*), and only the former would have NOE connectivity to a vinyl substituent. The heme methyl at 24.5 ppm, assigned as the 3-CH_3 heme methyl, exhibits dipolar connectivity to a scalar coupled three-proton system at 14, −1.1, and −1.5 ppm, which is assigned as the vinyl 4αH and 4βH resonances, respectively (Figure 3), and dipolar connectivity to the CεH and CδH resonances of the well-resolved Phe97 side chain at 12.6 and 9.4 ppm (Table 1). The scalar coupled three-proton spin system was readily assigned as a heme vinyl group due to characteristic hyperfine shifting where the β-vinyl resonances are shifted to much lower frequencies than the α-resonance due to a large

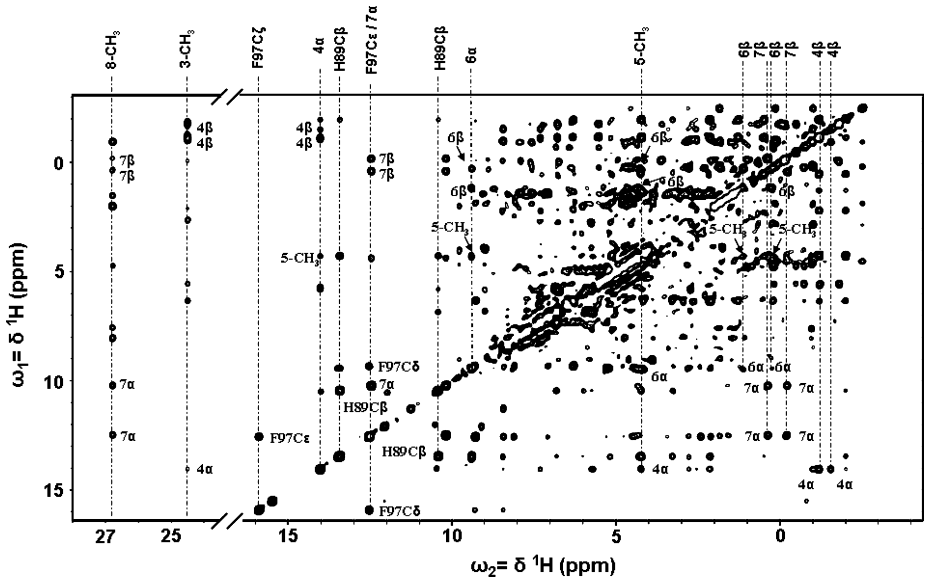

FIGURE 3: WEFT-NOESY map of metcyano DHP at 298 K, in 99.9% D_2O and 100 mM potassium phosphate, at pH 7.0. The mixing time was 100 ms. The labeled cross-peaks represent the observed ^1H dipolar connectivity.

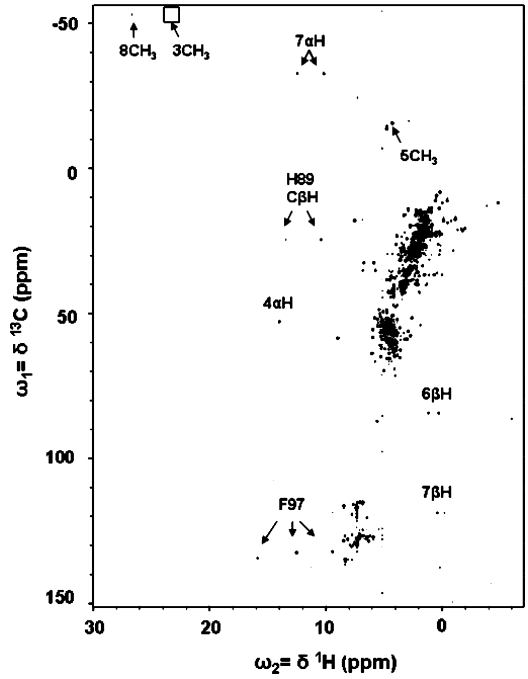

FIGURE 4: $^{13}C-^1H$ HSQC spectrum of DHPCN recorded at 298 K, in 99.9% D_2O with 100 mM potassium phosphate, at pH 7.0. Hyperfine-shifted resonances of the heme and local amino acids are labeled. The box indicates a cross-peak observed at higher contour levels.

Scheme 1: Axial Histidine Projection Angles As Shown in the X-ray Structures (A) and by the Relative Order of Heme Methyl Chemical Shifts (B)

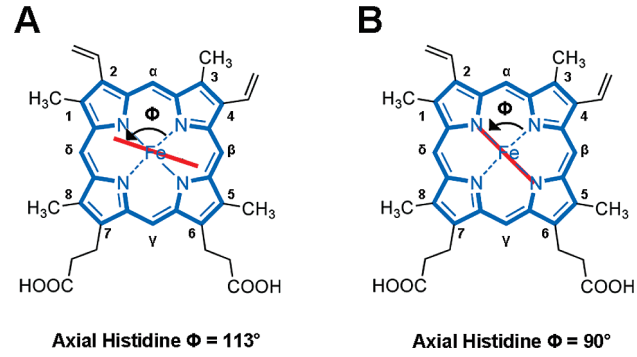

decrease in the contact shift contribution (*28*). While the 4β protons are not observed in the $^{13}C-^1H$ HSQC spectra (Figure 4), the 4α resonance was readily assigned at 14 (^1H) and 52.8 ppm (^{13}C). The Phe97 side chain was assigned by the natural abundance ^{13}C chemical shifts, CζH at 134.5, CεH at 132.6, and CεH at 132.2 ppm, and scalar coupling between the ring protons (Supporting Information).

The 4αH resonance also exhibits an NOE cross-peak to the 5-CH_3 heme methyl at 4.3 ppm. The 4.3 ppm resonance is assigned as the 5-CH_3 resonance due the degree of hyperfine shifting in the ^{13}C dimension (−14.8 ppm) and NOEs to a four-proton spin system indicative of the 6-propionate chain. This four-proton spin system at 11.3, 9.4, 1.2, and 0.3 ppm exhibits mutual dipolar coupling with the 5-CH_3 heme methyl. Only the two 6βH resonances of the propionate chain [1.2 and 0.3 ppm (84.4, ^{13}C)] were found in the $^{13}C-^1H$ HSQC map. NOESY cross-peaks of the two 6αH resonances (11.3 and 9.4 ppm) are observed at higher contour levels. Additional NOESY connectivity between the 6-propionate resonances can be found in the Supporting Information. The remaining downfield heme methyl at 26.8 ppm is assigned as the 8-CH_3 resonance on the basis of NOE connectivity to two hyperfine-shifted methylene groups at 12.5 and 10.2 ppm (−32.7, ^{13}C) and 0.4 and −0.2 ppm (118.8, ^{13}C) indicative of the 7-propionate chain. Inspection of the COSY data (Supporting Information) shows both methylene groups are scalar coupled, thus confirming their assignment as the 7αH and 7βH resonances, respectively.

The order of heme methyl shifts in metcyano DHP is 8 > 3 > 5 with the 1-CH_3 methyl not yet assigned. The 1-CH_3 methyl in low-spin metcyano heme proteins, at ambient temperatures, typically occurs at frequencies lower than those of the 5-CH_3 heme methyl. The relative order of heme methyl shifts is correlated to the angle, Φ, of the proximal histidine projection onto the $N_{II}-Fe-N_{IV}$ axis of the heme plane (*23, 29−33*). According to the X-ray structure of DHP, the axial histidine Φ is ∼113° as seen in Scheme 1A (*5, 6*). Models and experimental data have shown the 113° angle corresponds

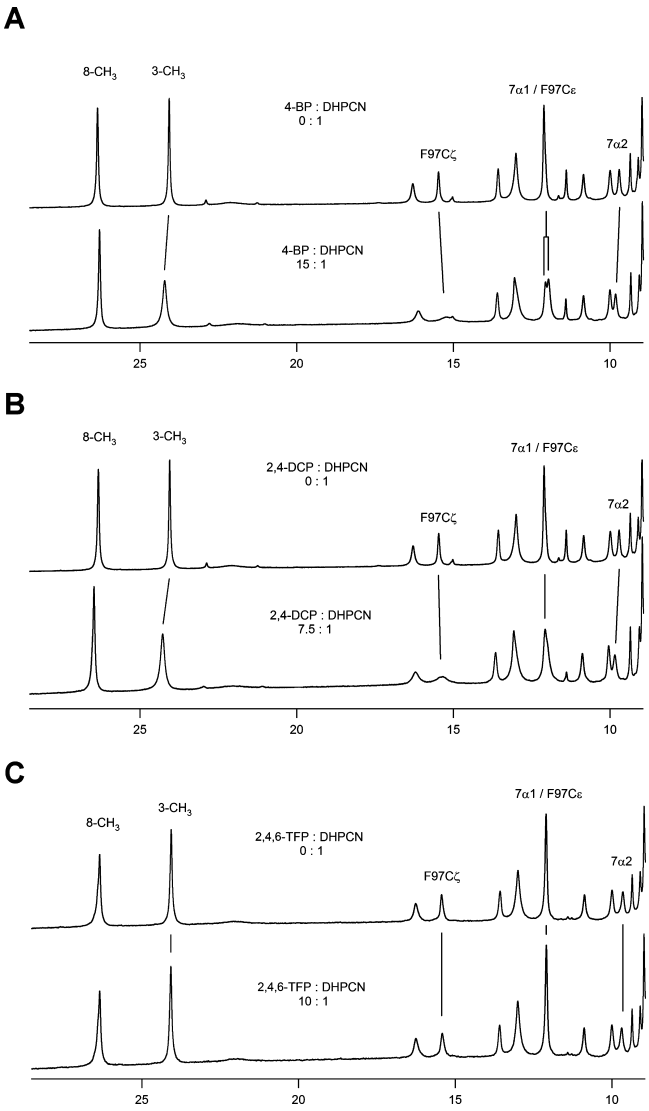

FIGURE 5: High-frequency hyperfine-shifted resonances of DHPCN in 100 mM potassium phosphate at pH 7.0 and 25 °C (A) without (top) and with (bottom) a 15-fold excess of 4-bromophenol, (B) without (top) and with (bottom) excess 2,4-dichlorophenol, and (C) without (top) and with (bottom) excess 2,4,6-trifluorophenol. Addition of either 4-BP or 2,4-DCP induces line broadening of the internal heme 3-CH_3 and Phe97 ring resonances, while the external 7α1H and 7α2H resonances show changes in their respective chemical shifts. Addition of 2,4,6-trifluorophenol does not effect any of the hyperfine-shifted resonances.

to a 3 > 8 > 5 > 1 order of heme methyls (*33*−*35*), which is not corroborated by the 8 > 3 > 5 > 1 order found in the ^{1}H NMR spectrum. Hence, the NMR data suggest the axial histidine in metcyano DHP is rotated by approximately −25° to ∼90° in solution, as seen in Scheme 1B.

Effects of Addition of Halogenated Phenols to DHPCN. The effects of three different substrates on the active site of DHPCN can be seen in Figure 5. The molecules 4-BP, 2,4-DCP, and 2,4,6-TFP were chosen for their high water solubility and/or structural similarities to substrates that have high rates of product turnover in DHP. The native substrate 2,4,6-TBP (*1*) and commonly used model substrate, 2,4,6-trichlorophenol (2,4,6-TCP) (*7*), cannot be used in the NMR binding studies due to their poor solubility. However, 4-BP is structurally comparable to 4-iodophenol, which was shown to bind in the internal distal cavity of DHP in current X-ray structures (*6*), while 2,4,6-TFP provides a comparison to the

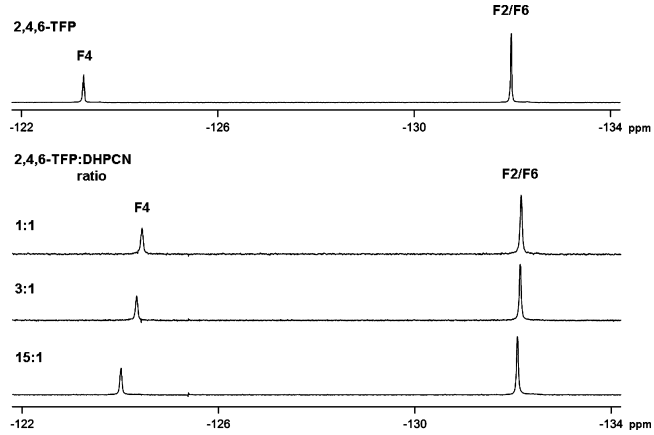

FIGURE 6: ^{19}F NMR spectra of the 2,4,6-TFP substrate analogue at pH 7 with 100 mM potassium phosphate and 99.9% D_2O buffer (top) and titration of this substrate to metcyano DHP at concentration ratios of 1:1, 3:1, and 15:1.

native substrate, 2,4,6-TBP, and the most active laboratory substrate, 2,4,6-TCP. Figure 5 shows there are two different effects induced by substrate binding. The mono- and dihalogenated 4-BP and 2,4-DCP cause similar effects within the active site of DHPCN. In both cases, the 3-CH_3 heme methyl and internal Phe97 exhibit significant line broadening when substrate is added in excess. The Phe97 side chain and heme 3-CH_3 methyl are separated by ∼4.5 Å according to the X-ray structures (*5, 6*), with the Phe side chain located slightly proximal to the 3-CH_3 heme methyl. Introduction of either 4-BP or 2,4-DCP also causes a slight change in the chemical shift of the 7α propionate resonances. The 8-CH_3 resonance exhibits a slight −0.2 ppm shift in the presence of 4-BP and a 0.1 ppm shift in the presence of 2,4-DCP. On the other hand, the interaction of 2,4,6-TFP with DHP does not create frequency perturbations and/or line broadening of active site resonances in DHPCN at the pH values studied. Comparing the effects of substrate titrations provides initial evidence for different modes of binding for substrates 2,4-DCP and 4-BP compared to 2,4,6-TFP. The differences in the nature of binding interactions are observed even when a significant molar excess of 2,4,6-TFP is used in DHPCN solutions (Supporting Information).

^{19}F NMR and Relaxation Data for Substrate 2,4,6-TFP in DHPCN. Utilization of ^{19}F NMR permits direct observation of the substrate as a probe of binding. In general, any binding interactions between the smaller 2,4,6-TFP substrate and DHP will result in a decrease in T_2 and, therefore, an increase in line width due to a slower molecular tumbling rate. Alternatively, depending on the rate of exchange, separate resonances may be visible for the fluorinated substrate, one for both the bound and free state of the substrate (*36, 37*).

Figure 6 shows the ^{19}F NMR spectra of substrate 2,4,6-TFP and titration of 2,4,6-TFP to the fully formed DHPCN complex. A significant change in chemical shift is observed in the para (F4) resonance as it is titrated to DHP. The F4 resonance of TFP, at −123.2 ppm, shifts to −124.4 ppm when the substrate is introduced at a 1:1 ratio. Additionally, the ortho (F2/F6) resonance shifts from −131.2 to −132.1 ppm. During the course of the titration, the F4 and F2/F6 resonances shift to slightly higher frequencies and approach the chemical shifts of 2,4,6-TFP without the presence of protein. Slight broadening of both resonances is observed at 1:1 and 3:1 ratios of 2,4,6-TFP to DHPCN. The F4 resonance

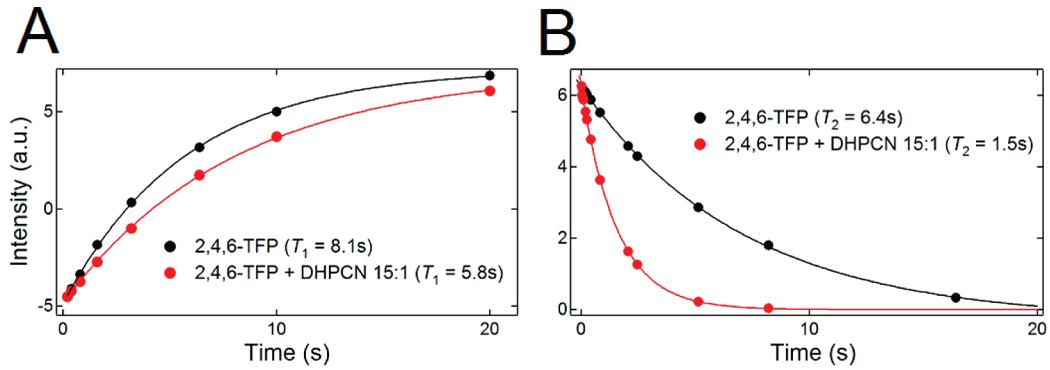

FIGURE 7: (A) T_1 relaxation curves and (B) T_2 relaxation curves for the meta protons of 2,4,6-trifluorophenol, alone (black), and in the presence of DHPCN (red) at a 15:1 molar ratio.

exhibits a 17% increase in line width (from 24 to 28 Hz), while the line width of the F2/F6 resonance increases by 33% (from 18 to 24 Hz) at a 1:1 ratio. Panels A and B of Figure 7 illustrate the change spin−lattice relaxation (T_1) and transverse relaxation (T_2) times of the 2,4,6-TFP meta protons when the molecule is added to DHPCN, respectively. The T_1 time decreased from 8.1 to 5.8 s and the T_2 time from 6.4 to 1.5 s when 2,4,6-TFP is added to DHPCN at a 15:1 molar ratio, respectively.

Enzymatic Activity Assay for Substrates 4-BP, 2,4-DCP, and 2,4,6-TFP. The hypothesis that there are two modes of binding is supported by the significant difference in the reactivity of the three phenols studied in enzymatic assays (see the Supporting Information). Using a standard DHP assay, we found that 4-BP has little or no activity. On the other hand, 2,4,6-TFP is a good substrate and shows turnover at rates that are comparable to that of the native substrate, 2,4,6-TBP (*49*). The rate of 2,4,6-TFP oxidation is approximately 3 times slower than that of the widely used test substrate, 2,4,6-TCP (*48, 49*). By contrast, 2,4-DCP shows significantly less activity than the 2,4,6-trihalophenols. There is also an increase in the baseline due to scattering when this substrate is used, which may be indicative of polymerization or other side reactions. Thus, the internal and external binding observed in the NMR signals is correlated with differences in substrate reactivity such that 4-BP and 2,4-DCP, which bind in the internal site, are not highly active and 2,4,6-TFP, which interacts with the protein at an external site, is active.

DISCUSSION

The dehalogenation of a variety of halogenated phenols, including bromo-, chloro-, and even fluorophenols, by DHP was first reported in 1996 (*2*). It was subsequently revealed that the original turnover numbers are not accurate (*8*). The X-ray crystal structure revealed the binding of 4-iodophenol in the distal pocket, which was assigned as the active site (*3*). The native substrate, however, is considered to be 2,4,6-TBP, and there has been no report of dehalogenation of 4-halophenols by DHP. This study uses soluble halogenated phenols to systematically test the differences in binding and correlated activity of three types of halogenated phenols. The molecules, 4-BP and 2,4-DCP, appear to bind or at least interact at an interior site in DHPCN and are poor substrates in a typical ferric DHP peroxidase assay using H_2O_2. On the other hand, 2,4,6-TFP interacts with the protein at an exterior site and has activity comparable to that of the native substrate, 2,4,6-TBP. In retrospect, this result is not surprising, since most known peroxidases have exterior substrate binding sites (*12*).

Binding of the monohalogenated (4-BP) and dihalogenated (2,4-DCP) substrates demonstrated comparable effects on the ^{1}H NMR spectrum of the metcyano adduct of DHP. The effects include perturbations along the internal heme edge near the 3-CH_3 heme methyl and Phe97 side chain. The broadening of these resonances appears to be greatest when the solution pH < pK_a of the substrate (Supporting Information). However, even at alkaline pH (pH 9.9), there is still observable broadening associated with the addition of 4-BP and 2,4-DCP. The effect of 4-BP and 2,4-DCP binding is localized to an internal region near the heme 3-CH_3 methyl and Phe97 residue. There is no broadening of other active site resonances, such as the 8-CH_3 methyl. Broadening of specific resonances of the heme and its substituents has been observed previously in substrate binding studies of horseradish peroxidase (HRP). Titration of the substrate benzohydroxamic acid to HRPCN resulted in significant broadening of the 8-CH_3 heme methyl and a 7α-propionate resonance, in a manner similar to the observed broadening of the 3-CH_3 and Phe97 resonances in DHPCN (*39*−*41*). Substrate binding is known to be external to the distal pocket in HRP. However, the 3-CH_3 and Phe97 resonances are more deeply buried than the 8-CH_3 heme methyl and 7α protons in DHP. Consequently, the binding interactions between 4-BP/2,4-DCP and DHPCN appear to occur at the internal site in the distal pocket. On the other hand, WEFT-NOESY and presaturation NOESY experiments did not reveal NOEs between DHPCN and the substrate analogues, 4-BP and 2,4,-DCP. The lack of NOEs may be due to fast exchange of the substrate between bound and free states. These experiments suggest that the binding of 4-BP and 2,4-DCP in the distal pocket of DHPCN may involve rapid exchange with solvent.

While the addition of 4-BP and 2,4-DCP induced observable changes in active site resonances, 2,4,6-TFP essentially had no effect on the ^{1}H NMR spectrum. The ^{19}F NMR data, however, show that the F2/F6 and F4 fluorine resonances of 2,4,6-TFP exhibit slight broadening and perturbations in chemical shifts when present at a 1:1 molar ratio with DHPCN. Resonance broadening and/or changes in chemical shift are commonly used to identify binding of small molecule protein ligands (*42*−*44*). The line width of the F2/F6 and F4 resonances at a 1:1 molar ratio of DHPCN to 2,4,6-TFP increases by 33 and 17%, respectively. This broadening translates to a decrease in the apparent transverse

relaxation time (T_2) from 17.7 to 13.3 ms for F2/F6 and from 13.3 to 11.4 ms for F4 (*45*) as discussed in the Supporting Information. The decrease in T_2 suggests a longer rotational correlation time (τ_c) of the molecule (*46*). On the basis of the Stokes−Einstein equation, $\tau_c = 34$ ns for DHPCN assuming that the radius $r = 20$ Å at a viscosity of 1 cP, whereas free 2,4,6-TFP would be expected to have a τ_c on the picosecond time scale (see the Supporting Information).

To elucidate the binding of 2,4,6-TFP to DHPCN, T_1 and T_2 relaxation experiments were used to observe changes in the rotational correlation time, τ_c. The T_1 relaxation time of the 2,4,6-TFP meta protons decreased from 8.1 to 5.8 s and the T_2 relaxation time of these same resonances from 6.4 to 1.5 s when 2,4,6-TFP was present at a 15:1 molar ratio (Figure 7). The high ratio of TFP to DHPCN was needed to fully resolve the 2,4,6-TFP signal over the background of the protein resonances. Because the same value for T_1 is consistent with two separate rotational correlation times in the limits $\omega_o\tau_c \ll 1$ and $\omega_o\tau_c \gg 1$, T_2 values were analyzed to determine whether the decrease in T_1 can be attributed to a significant decrease in the τ_c of 2,4,6-TFP in the presence of DHPCN (*47*). The analysis of the decrease in T_1 and T_2 times corresponds to a τ_c of ~35 ps for free 2,4,6-TFP and a τ_c of ~53 ns for 2,4,6-TFP in the presence of DHPCN. This increase in τ_c is in accord with the expected value for complexation of 2,4,6-TFP to DHPCN. Further details of the analysis are supplied in the Supporting Information. Although the analysis is based on a single dipolar interaction of a ^{19}F nucleus that is 2.47 Å from the meta hydrogen nucleus, we recognize that the relaxation may be more complicated in the bound state. The point of the analysis is to establish the 2,4,6-TFP binds at an external site and exhibits behavior different from that of the other two phenols studied, 4-BP and 2,4-DCP.

Although the relaxation data are consistent with an external binding site for 2,4,6-TFP, the location of that site has not been determined on the basis of the data obtained here. FTIR studies at cryogenic temperatures showed that 2,4,6-TFP can bind in the internal substrate binding pocket of the CO form of ferrous DHP, which is isoelectronic with DHPCN (*14*). However, at physiologically relevant pHs, there was no binding of 2,4,6-TFP above 260 K in the internal site (*14*). At room temperature, 2,4,6-TFP binding in the distal pocket is also observed in the CO form using FTIR, but only at pH <4.7 (*50*). It is difficult to study DHPCN at pH <5.0 to investigate the relevance of this observation using NMR due to the protonation of CN^- to form HCN. The ^{1}H NMR data corroborate the FTIR data in that no observable internal pocket perturbations are observed for the trihalogenated substrate at ambient temperatures in the pH range from 5.5 to 9.9.

The origin of the alteration of the axial histidine torsion angle shown in Scheme 1 requires further explanation. The value of the torsion angle (Φ) of ~113° shown in Scheme 1A was obtained by X-ray crystallography. The X-ray structures further indicate stabilization of the proximal histidine H89 by a strong hydrogen bond of the imidazole NH group to the carbonyl oxygen of L83 with a N···O distance of 2.74 Å (*5, 6*). The Φ value of ~90° in solution (Scheme 1B) is based on the well-established correlation of the ordering of heme methyl hyperfine shifts. The discrepancy in these data may arise from the dynamics of H89 and associated amino acid residues. The average thermal factors for amino acid residues 87−92, a region which includes the proximal histidine H89, were observed to be 50% larger than the average value in DHP as a whole (*5*). The region near H89 has the largest thermal motion in the molecule despite the fact that it is buried in the interior of the protein and bonded to the heme cofactor. The flexibility of H89 could be the reason for the decrease in the axial histidine torsion angle (Φ) from 113° to 90°, which was determined by the spacing and 8 > 3 > 5 > 1 order of heme methyl chemical shifts in the ^{1}H NMR spectrum. Similar deviations in the proximal histidine plane orientation between X-ray and solution structures have been observed in mouse neuroglobin (*38*), where higher thermal factors in the region of the proximal histidine indicated greater flexibility.

CONCLUSION

This study has shown that substrates interact with the six-coordinate DHPCN form in two different ways. Binding of both 4-BP and 2,4-DCP affects internal amino acid residues and heme group substituents in a pH-dependent manner, with the greatest affinity occurring under acidic conditions. The NMR data suggest that the binding has a strong and specific effect on the heme, which may result from an internal binding site where the substrate analogue is in rapid exchange with solvent. The molecules 4-BP and 2,4-DCP and greatly reduced in activity when compared to 2,4,6-trihalogenated phenols (*7, 48*), including 2,4,6-TFP (Supporting Information and ref *49*). Binding of 2,4,6-TFP, which is a structural homologue of the native substrate 2,4,6-TBP, did not induce effects on the internal amino acid residues, as indicated by ^{1}H NMR. However, broadening and chemical shift perturbations of the fluorine resonances are consistent with an external binding interaction. In the presence of DHPCN, the rotational correlation time of 2,4,6-TFP was found to increase from the picosecond to nanosecond time scale, consistent with the hypothesis that there is an external binding site. Although 2,4,6-TBP is not sufficiently soluble to permit a ^{1}H NMR study, the conclusion that 2,4,6-TFP binds at an external site clearly implies that the native substrate, 2,4,6-TBP, also binds at an external site. The similar reactivity of both of these substrates leads us to conclude that the active site for substrate oxidation in DHP is an external site, as observed in other heme peroxidases.

SUPPORTING INFORMATION AVAILABLE

1D NOE, gradient-selective COSY, presaturation NOESY data, variable-temperature ^{1}H NMR spectra, and hyperfine-shifted resonances in response to varying pH; additional titrations of substrate 2,4,6-TFP at alternative pHs; equations used for analysis of relaxation data; and spectroscopic data for enzyme assays of 4-BP, 2,4-DCP, and 2,4,6-TFP. This material is available free of charge via the Internet at http://pubs.acs.org.

REFERENCES

1. Han, K., Woodin, S. A., Lincoln, D. E., Fielman, K. T., and Ely, B. (2001) *Amphitrite ornata*, a marine worm, contains two dehaloperoxidase genes. *Mar. Biotechnol. 3*, 287–292.
2. Chen, Y. P., Woodin, S. A., Lincoln, D. E., and Lovell, C. R. (1996) An unusual dehalogenating peroxidase from the marine terebellid polychaete *Amphitrite ornata*. *J. Biol. Chem. 271*, 4609–4612.

3. Lebioda, L., LaCount, M. W., Zhang, E., Chen, Y. P., Han, K., Whitton, M. M., Lincoln, D. E., and Woodin, S. A. (1999) Protein structure: An enzymatic globin from a marine worm. *Nature 401*, 445.
4. Weber, R. E., Magnum, C. P., Steinman, H., Bonaventura, C., Sullivan, B., and Bonaventura, J. (1977) Hemoglobins of two terebellid polychaetes: *Enoplobranchus sanguineus* and *Amphitrite ornata*. *Comp. Biochem. Physiol. 56A*, 179–187.
5. de Serrano, V., Chen, Z., Davis, M. F., and Franzen, S. (2007) X-ray crystal structural analysis of the binding site in the ferric and oxyferrous forms of the recombinant heme dehaloperoxidase cloned from *Amphitrite ornata*. *Acta Crystallogr. D63*, 1094–1101.
6. Zhang, E., Chen, Y. P., Roach, M. P., Lincoln, D. E., Lovell, C. R., Woodin, S. A., Dawson, J. H., and Lebioda, L. (1996) Crystallization and initial spectroscopic characterization of the heme-containing dehaloperoxidase from the marine polychaete *Amphitrite ornata*. *Acta Crystallogr. D52*, 1191–1193.
7. Belyea, J., Gilvey, L. B., Davis, M. F., Godek, M., Sit, T. L., Lommel, S. A., and Franzen, S. (2005) Enzyme function of the globin dehaloperoxidase from *Amphitrite ornata* is activated by substrate binding. *Biochemistry 44*, 15637–15644.
8. Osborne, R. L., Taylor, L. O., Han, K. P., Ely, B., and Dawson, J. H. (2004) *Amphitrite ornata* dehaloperoxidase: Enhanced activity for the catalytically active globin using MCPBA. *Biochem. Biophys. Res. Commun. 324*, 1194–1198.
9. Lebioda, L. (2000) The honorary enzyme haemoglobin turns out to be a real enzyme. *Cell. Mol. Life Sci. 57*, 1817–1819.
10. Kishino, T., and Kobayashi, K. (1995) Relation between toxicity and accumulation of chlorophenols at various pH, and their absorption mechanism in fish. *Water Res. 29*, 431–442.
11. Allonier, A., Khalansk, M., Camel, V., and Bermond, A. (1999) Characterization of chlorination by-products in cooling effluents of coastal nuclear power stations. *Mar. Pollut. Bull. 38*, 1232–1241.
12. Ator, M. A., and Ortiz de Montellano, P. R. (1987) Protein control of prosthetic heme reactivity. Reaction of substrates with the heme edge of horseradish peroxidase. *J. Biol. Chem. 262*, 1542–1551.
13. Smirnova, T. I., Weber, R. T., Davis, M. F., and Franzen, S. (2008) Substrate binding triggers a switch in the iron coordination in dehaloperoxidase from *Amphitrite ornata*: HYSCORE experiments. *J. Am. Chem. Soc. 130*, 2128–2129.
14. Nienhaus, K., Deng, P. C., Belyea, J., Franzen, S., and Nienhaus, G. U. (2006) Spectroscopic study of substrate binding to the carbonmonoxy form of dehaloperoxidase from *Amphitrite ornata*. *J. Phys. Chem. B 110*, 13264–13276.
15. La Mar, G. N., and de Ropp, J. S. (1993) in *Biological Magnetic Resonance*, pp 1−73, Plenum Press, New York.
16. Emerson, S. D., and La Mar, G. N. (1990) Solution structural characterization of cyanometmyoglobin: Resonance assignment of heme cavity residues by two-dimensional NMR. *Biochemistry 29*, 1545–1556.
17. Banci, L., Bertini, I., Turano, P., Ferrer, J. C., and Mauk, A. G. (1991) Comparative ^{1}H NMR study of ferric low-spin cytochrome-c peroxidase and horseradish-peroxidase. *Inorg. Chem. 30*, 4510–4516.
18. Yu, L. P., La Mar, G. N., and Rajarathnam, K. (1990) ^{1}H NMR resonance assignments of the active site residues of paramagnetic proteins by 2D bond correlation spectroscopy: Metcyanomyoglobin. *J. Am. Chem. Soc. 112*, 9527–9534.
19. Yamamoto, Y., Iwafune, K., Nanai, N., Akemi, O., Chujo, R., and Suzuki, T. (1991) NMR study of *Galeorhinus japonicus* myoglobin. ^{1}H NMR study of molecular structure of the heme cavity. *Eur. J. Biochem. 198*, 299–306.
20. Bertini, I., Turano, P., and Vila, A. J. (1993) Nuclear magnetic resonance of paramagnetic metalloproteins. *Chem. Rev. 93*, 2833–2932.
21. Satterlee, J. D., and Erman, J. E. (1991) Proton NMR assignments of heme contacts and catalytically implicated amino acids in cyanide-ligated cytochrome c peroxidase determined from one- and two-dimensional nuclear overhauser effects. *Biochemistry 30*, 4398–4405.
22. Sukits, S. F., and Satterlee, J. D. (1996) Assignment of ^{1}H and ^{13}C hyperfine-shifted resonances for tuna ferricytochrome c. *Biophys. J. 71*, 2848–2856.
23. Shokhireva, T. Kh., Shokhirev, N. V., and Walker, F. A. (2003) Assignment of heme resonances and determination of the electronic structures of high- and low-spin nitrophorin 2 by ^{1}H and ^{13}C NMR spectroscopy: An explanation of the order of heme methyl resonances in high-spin ferriheme proteins. *Biochemistry 42*, 679–693.
24. Maudsley, A. A., and Ernst, R. R. (1977) Indirect detection of magnetic resonance by heteronuclear two-dimensional spectroscopy. *Chem. Phys. 50*, 368–372.
25. Patt, S. L., and Sykes, B. D. (1972) Water Eliminated Fourier Transform NMR Spectroscopy. *J. Chem. Phys. 56*, 3182–3184.
26. Osborne, R. L., Sumithran, S., Coggins, M. K., Chen, Y., Lincoln, D. E., and Dawson, J. H. (2006) Spectroscopic characterization of the ferric states of *Amphitrite ornata* dehaloperoxidase and *Notomastus lobatus* chloroperoxidase: His-ligated peroxidases with globin-like proximal and distal properties. *J. Inorg. Biochem. 100*, 1100–1108.
27. Satterlee, J. D., Erman, J. E., and DeRopp, J. S. (1987) Proton hyperfine resonance assignments in cyanide-ligated cytochrome *c* peroxidase using the nuclear Overhauser effect. *J. Biol. Chem. 262*, 11578–11583.
28. Alam, S. L., and Satterlee, J. D. (1994) Complete heme proton hyperfine resonance assignments of the *Glycera dibrachiata* component IV metcyano monomer hemoglobin. *Biochemistry 33*, 4008–4018.
29. Decatur, S. M., and Boxer, S. G. (1995) ^{1}H NMR characterization of myoglobins where exogenous ligand replace the proximal histidine. *Biochemistry 34*, 2122–2129.
30. Thanabal, V., de Ropp, J. S., and La Mar, G. N. (1987) ^{1}H NMR study of the electronic and molecular structure of the heme cavity in horseradish peroxidase. Complete heme resonance assignments based on saturation transfer and nuclear Overhauser effects. *J. Am. Chem. Soc. 109*, 265–272.
31. Yamamoto, Y., Nanai, N., Chujo, R., and Suzuki, T. (1990) Heme methyl hyperfine shift pattern as a probe for determining the orientation of the functionally relevent proximal histidyl imidazole with respect to the heme in hemoproteins. *FEBS Lett. 264*, 113–116.
32. Traylor, T. G., and Berzinis, A. P. (1980) Hemoprotein models: NMR of imidazole chelated protohemin cyanide complexes. *J. Am. Chem. Soc. 102*, 2844–2846.
33. Shokhirev, N. V., and Walker, F. A. (1998) The effect of axial ligand plane orientation on the contact and pseudocontact shifts of low-spin ferriheme proteins. *J. Biol. Inorg. Chem. 3*, 581–594.
34. ShiftPatterns. Heme methyl shift patterns, version 2, http://www.shokhirev.com/nikolai/programs/prgsciedu.html.
35. Banci, L., Bertini, I., Pierattelli, R., Tien, M., and Vila, A. J. (1995) Factoring of the hyperfine shifts in the cyanide adduct of lignin peroxidase from *P. chrysosporium*. *J. Am. Chem. Soc. 117*, 8659–8667.
36. Crull, G. B., Kennington, J. W., Garber, A. R., Ellis, P. D., and Dawson, J. H. (1989) ^{19}F nuclear magnetic resonance as a probe of the spatial relationship between the heme iron of cytochrome p-450 and its substrate. *J. Biol. Chem. 264*, 2649–2655.
37. Decatur, S. M., DePillis, G. D., and Boxer, S. G. (1996) Modulation of protein function by exogenous ligands in protein cavities: CO binding to a myoglobin cavity mutant containing unnatural proximal ligands. *Biochemistry 35*, 3925–3932.
38. Walker, F. A. (2006) The heme environment of mouse neuroglobin: Histidine plane orientations obtained from solution NMR and EPR spectroscopy as compared with X-ray crystallography. *J. Biol. Inorg. Chem. 11*, 391–397.
39. La Mar, G. N., Hernandez, G., and de Ropp, J. S. (1992) ^{1}H NMR investigation of the influence of interacting sites on the dynamics and thermodynamics of substrate and ligand binding to horseradish peroxidase. *Biochemistry 31*, 9158–9168.
40. Thanabal, V., de Ropp, J. S., and La Mar, G. N. (1987) Identification of the catalytically important amino acid residue resonances in ferric low-spin horseradish peroxidase with nuclear Overhauser effect measurements. *J. Am. Chem. Soc. 109*, 7516–7525.
41. de Ropp, J. S., Mandal, P. K., and La Mar, G. N. (1999) Solution ^{1}H NMR investigation of the heme cavity and substrate binding site in cyanide-inhibited horseradish peroxidase. *Biochemistry 38*, 1077–1086.
42. Reibarkh, M., Malia, T. J., and Wagner, G. (2006) NMR distinction of single- and multiple-mode binding of small-molecule protein ligands. *J. Am. Chem. Soc. 128*, 2160–2161.
43. Matsuo, H., Walters, K. J., Teruya, K., Tanaka, T., Gassner, G. T., Lippard, S. J., Kyogoku, Y., and Wagner, G. (1999) Identification by NMR spectroscopy of residues at contact surfaces in large,

slowly exchanging macromolecular complexes. *J. Am. Chem. Soc. 121*, 9903–9904.
44. Reibarkh, M., Malia, T. J., Hopkins, B. T., and Wagner, G. (2006) Identification of individual protein-ligand NOEs in the limit of intermediate exchange. *J. Biomol. NMR. 36*, 1–11.
45. Evans, J. N. S. (1995) in *Biomolecular NMR Spectroscopy*, pp 240, Oxford University Press, Oxford, U.K.
46. Tengel, T., Fex, T., Emtenäs, H., Almqvist, F., Sethson, I., and Kiflber, J. (2004) Use of ^{19}F NMR spectroscopy to screen chemical libraries for ligands that bind to proteins. *Org. Biomol. Chem. 2*, 725–731.
47. Carrington, A., and MacLachlan, A. D. (1967) in *Introduction to Magnetic Resonance*, pp 176203.
48. Franzen, S., Gilvey, L. B., and Belyea, J. (2007) The pH dependence of the activity of dehaloperoxidase from *Amphitrite ornata*. *Biochim. Biophys. Acta 1774*, 121–130.
49. Chaudhary, C. (2003) Point Mutagenesis and Spectroscopic Probing of Dehaloperoxidase: Characterizing the Mechanism and Activity of the Heme Active Site of the Native Protein, M.S. Thesis, North Carolina State University, Raleigh, NC.
50. Nienhaus, K., Nickel, E., Davis, M. F., Franzen, S., and Nienhaus, G. U. (2008) Determinants of substrate internalization in the distal pocket of dehaloperoxidase hemoglobin of *Amphitrite ornata*. *Biochemistry 47*, 12985–12994.

BI801568S

BIOCHEMISTRY
including biophysical chemistry & molecular biology
Article

Biochemistry **2010,** *49,* 1199–1206 1199
DOI: 10.1021/bi9018576

Determination of Separate Inhibitor and Substrate Binding Sites in the Dehaloperoxidase−Hemoglobin from *Amphitrite ornata*[†,‡]

Michael F. Davis,[§,#] Benjamin G. Bobay,[∥,⊥] and Stefan Franzen*[,§]

[§]*Departments of Chemistry, and* [∥]*Molecular and Structural Biochemistry, North Carolina State University, Raleigh, North Carolina 27606, and* [⊥]*North Carolina Research Campus, Kannapolis, North Carolina 28081.* [#]*Present address: Lineberger Comprehensive Cancer Center and Department of Biochemistry and Biophysics, University of North Carolina, Chapel Hill, NC 27599.*

Received October 29, 2009; Revised Manuscript Received January 11, 2010

ABSTRACT: Dehaloperoxidase−hemoglobin (DHP A) is a dual function protein found in the terrebellid polychaete *Amphitrite ornata*. *A. ornata* is an annelid, which inhabits estuary mudflats with other polychaetes that secrete a range of toxic brominated phenols. DHP A is capable of binding and oxidatively dehalogenating some of these compounds. DHP A possesses the ability to bind halophenols in a distinct, internal distal binding pocket. Since its discovery, the distal binding pocket has been reported as the sole binding location for halophenols; however, data herein suggest a distinction between inhibitor (monohalogenated phenol) and substrate (trihalogenated phenol) binding locations. Backbone $^{13}C\alpha$, $^{13}C\beta$, carbonyl ^{13}C, amide ^{1}H, and amide ^{15}N resonance assignments have been made, and various halophenols were titrated into the protein. $^{1}H-^{15}N$ HSQC experiments were collected at stoichiometric intervals during each titration, and binding locations specific for mono- and trihalogenated phenols have been identified. Titration of monohalogenated phenol induced primary changes around the distal binding pocket, while introduction of trihalogenated phenols created alterations of the distal histidine and the local area surrounding W120, a structural region that corresponds to a possible dimer interface region recently observed in X-ray crystal structures of DHP A.

The dehaloperoxidase−hemoglobin (DHP A)[1] is a globin with peroxidase activity found in the terebellid polychaete *Amphitrite ornata*. DHP A is one of two known proteins in *A. ornata* which contain the globin fold. Two isoforms of the dehaloperoxidase−hemoglobin are found in *A. ornata*, DHP A and DHP B (*1*). DHP B differs from DHP A by only five mutations (I9L, R32K, Y34N, N81S, and S91G) and has recently been cloned and expressed in *Escherichia coli* (*2*, *3*). Even though DHP A and DHP B are structurally homologous to typical myoglobins (Mbs) (*4*−*6*), DHP A was first isolated from *A. ornata* and characterized as a peroxidase (*7*). DHP A was later cloned into *E. coli*, expressed, and characterized as a function of pH (*8*, *9*). Site-directed mutations of the distal and proximal histidines, H55 and H89, respectively, have shown their essential nature in the catalytic mechanism of DHP A (*10*).

It has been known for more than a decade that DHP A has a unique ability to bind halogenated phenols in a distal pocket above the heme plane (*6*, *11*−*14*). We have recently demonstrated this internal binding site to be an inhibitor binding site favored by 4-halophenols, while the most active substrates, 2,4,6-trihalophenols, bind to an external active site (*13*, *15*). In addition to inhibition of peroxidase activity, a bound 4-halophenol in the distal cavity appears to interfere with the inherent role of globins in oxygen transport and NO scavenging (*11*, *12*, *15*, *16*). The role of 2,4,6-trihalophenol substrate binding is even more elusive since it is not directly observed in the X-ray crystal structure. Thus, there is a need for solution studies of both substrate and inhibitor binding to clarify the structural consequences of each binding event with DHP A.

A. ornata coinhabits estuary mudflats with other filter feeding marine polychaetes that secrete halophenols presumably for territorial protection (*17*−*19*). One of the coinhabitants, *Notomastus lobatus*, produces and excretes 4-bromophenol (4-BP), 2,4-dibromophenol (2,4-DBP), and 2,4,6-tribromophenol (2,4,6-TBP) to the surrounding sediment with a stoichiometric ratio of 1.8:0.9:1.0 (*20*). Brominated phenols are extremely toxic, particularly for aquatic organisms. The ability of DHP A to bind and oxidatively dehalogenate halophenols may therefore play an important role in the survival of *A. ornata*. Despite the globin fold, DHP A readily oxidizes various trihalogenated phenols, as illustrated in Scheme 1, with a total yield similar to that of horseradish peroxidase (HRP) (*8*−*10*, *21*). The oxidation rate, however, is ∼13 times less than HRP at pH 5 (*8*). Since HRP is a secretory peroxidase, it is optimized to function at pH 5. On the other hand, DHP A is optimized to function at pH 7.5, which is near the pH of cytosol. This value is consistent with the role of DHP A as a coelomic hemoglobin.

The internal binding pocket was initially thought to be the active site of DHP A, which was a reasonable assumption in the absence of detailed kinetic data and a structure of the external binding site (*6*). While the reactivity of DHP A toward

[†]This project was supported by Army Research Office Grant 52278-LS.

[‡]The DHPCN A magnetic coordinates have been deposited in the Biological Magnetic Resonance Data Bank (accession number 16401).

*To whom correspondence should be addressed. Phone: 919-515-8915. Fax: 919-515-8920. E-mail: Stefan_Franzen@ncsu.edu.

[1]Abbreviations: 4-BP, 4-bromophenol; 2,4,6-TBP, 2,4,6-tribromophenol; 2,4,6-TCP, 2,4,6-trichlorophenol; 2,4,6-TFP, 2,4,6-trifluorophenol; 2,6-DCQ, 2,6-dichloroquinone; Amp, ampicillin; CcP, cytochrome *c* peroxidase; DHP A, dehaloperoxidase−hemoglobin; DHPCN A, metcyano dehaloperoxidase−hemoglobin; HSQC, heteronuclear single-quantum coherence; HRP, horseradish peroxidase; IPTG, isopropyl β-D-thiogalactopyranoside.

Published on Web 01/12/2010

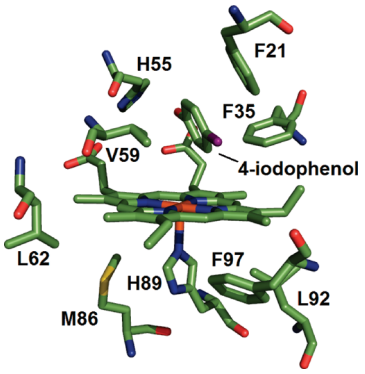

FIGURE 1: X-ray structure of the internal binding pocket of DHP A. The 1EWA X-ray structure illustrates binding of monohalogenated 4-IP in the distal pocket (*14*). The closest residues to bound 4-IP are F35, V59, and F21, respectively.

Scheme 1: DHP A Catalyzes the Oxidative Dehalogenation of Trihalophenol to the Corresponding Dihalogenated Quinone Product in the Presence of H_2O_2[a]

[a]The scheme represents the reaction at pH 6 where the substrate is in the phenol form.

2,4,6-trihalophenols is common in many peroxidases, the internal inhibitor binding pocket separates DHP A from any known globin or peroxidase. In fact, many of our early papers were based on this assumption that the internal binding pocket was the true substrate binding site. This led to a great deal of speculation about whether a one-electron or two-electron oxidation takes place in DHP A (*8*, *9*). However, the realization that an external site is the substrate binding site makes DHP A similar to other peroxidases and strongly suggests a one-electron oxidation mechanism. Inhibition of peroxidase activity, due to inhibitor binding in the distal pocket, is attributable to two main factors. The X-ray structure shown in Figure 1 illustrates bound 4-halophenol in the distal pocket (*14*). The close binding proximity of the inhibitor to the heme iron impedes access of H_2O_2 to the heme iron. H_2O_2 access is essential for formation of compound ES and subsequent peroxidase activity of the protein (*22*). Consequently, the steric interference of 4-halophenols provides one mechanism for inhibition. Second, the distal histidine is forced into a solvent-exposed position by the inhibitor. This conformational change results in DHP A inhibition because the distal histidine is the acid−base catalyst required for formation of the active compound ES.

At present, one of the major questions in DHP A function regards the structure of the true substrate binding site. Substrate binding is not observed in any of the X-ray crystal structures. While we can observe the binding of 4-iodo-, 4-bromo-, 4-chloro-, and 4-fluorophenol in the distal pocket, attempts to infuse 2,4,6-trihalophenols into crystals have not resulted in observed binding in a single X-ray crystal structure (*15*). We have treated the crystals with saturated solutions of 2,4,6-trihalophenols (substrates) exactly as we have done for 4-halophenols (inhibitors). Consequently, we turn to solution studies of DHP A in order to determine the conformation of the protein in response to substrate binding. The low water solubility of 2,4,6-trihalogenated phenols and apparent high K_D values make them poor choices for structural studies such as X-ray crystallography or NMR experiments. Of the active 2,4,6-trihalophenols only 2,4,6-trifluorophenol (2,4,6-TFP) and 2,4,6-trichlorophenol (2,4,6-TCP) have solubility greater than micromolar concentrations. 2,4,6-TCP is the closest analogue to the native substrate 2,4,6-TBP and is the best laboratory substrate due to its similar size and turnover rates. The most soluble trihalophenol, 2,4,6-TFP, has been used in cryogenic FT-IR, EPR, and HYSCORE studies to show binding at cryogenic temperature (< 260 K) but not at room temperature (*12*, *23*). Above 260 K the 2,4,6-TFP substrate leaves the distal binding pocket, and no other internal perturbations are observed (*12*). ^{19}F NMR and relaxation experiments provided initial evidence of an exterior binding site for 2,4,6-TFP at ambient temperatures (*13*). However, the exact location of 2,4,6-TFP binding has not been reported. Moreover, the use of 2,4,6-TFP as a substrate analogue may be a poor choice due to the relative size difference between fluorine and bromine or chlorine substituents.

In this report, assignments of the backbone $^{13}C\alpha$, $^{13}C\beta$, carbonyl ^{13}C, amide ^{1}H ,and amide ^{15}N resonances have been made using $^{13}C/^{15}N$ labeling and 3D NMR techniques. Paramagnetic low-spin metcyano DHP A was used in order to retain continuity with previous NMR investigations. Assignment of 92% of the backbone resonances allowed for observations of structural changes occurring throughout the protein upon introduction of various substrates or inhibitors. Titrations of inhibitor 4-BP and substrates 2,4,6-TCP/2,4,6-TFP were performed and monitored using $^{1}H-^{15}N$ HSQC experiments. Chemical shift deviations of backbone amide protons were observed for each substrate/inhibitor. The resonances exhibiting the greatest degree of change were then mapped onto current X-ray structures of the protein, and the local regions experiencing the largest deviations were analyzed.

MATERIALS AND METHODS

Protein Expression and Purification. The highly expressing His-DHP A 4R gene was inserted into the pET-16b vector and transformed into Rosetta (DE3) *E. coli* cells. The Rosetta cells were used for their slower growth cycle and additional chloramphenicol (Cam) resistance, not to supply tRNAs for poorly expressed *E. coli* codons. The cells were plated onto LB agar plates containing 100 μg/mL Amp and 34 μg/mL Cam and allowed to grow for ~18 h. Single colonies were isolated, and 2 mL starter growths in LB broth (100 μg/mL Amp, 34 μg/mL Cam) were allowed to grow at 37 °C overnight. One milliliter of the starter growth was then added to 1 L of Spectra 9-CN (Spectra Stable Isotopes, Inc.) medium with >98% ^{13}C and ^{15}N isotopes in the aforementioned Amp and Cam concentrations. The 1 L double-labeled growth was allowed to grow at 37 °C with shaking until an OD_{600} of 0.3 was reached. Isopropyl β-D-1-thiogalactopyranoside (IPTG) was added to a final concentration of 0.5 mM, and the growth temperature was reduced to 25 °C. The cells were then allowed to grow for 20 h before being collected via centrifugation. Cell lysis was performed as described previously (*13*) except that the cleared lysate was incubated with ~100 mg of hemin chloride dissolved in 1 mL of 0.2 M NaOH for 8 h with stirring at 4 °C. The protein was purified using affinity and ion-exchange chromatography as described elsewhere (*13*).

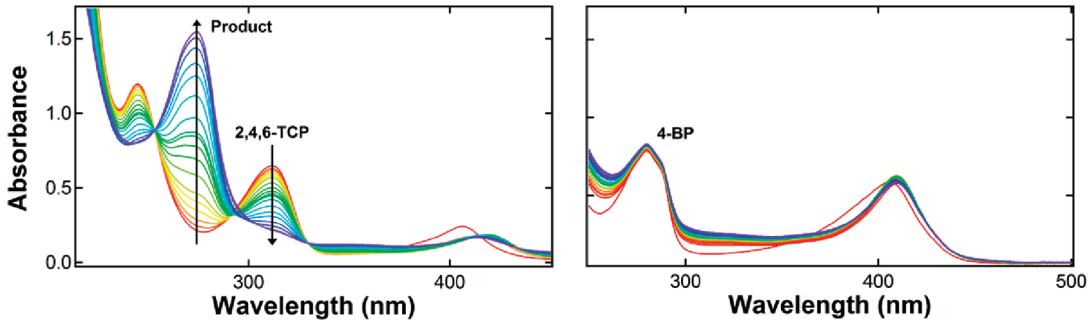

FIGURE 2: UV−vis enzymatic assay illustrating 2,4,6-TCP and 4-BP activity. The differences in activity between 2,4,6-TCP (left) and 4-BP (right) are shown. The figures represent a 600 s assay going from red (0 s) to blue (600 s). The 2,4,6-TCP molecule is completely converted to product 2,6-dichloro-1,4-benzoquinone (left) while the 4-BP molecule does not experience turnover (right).

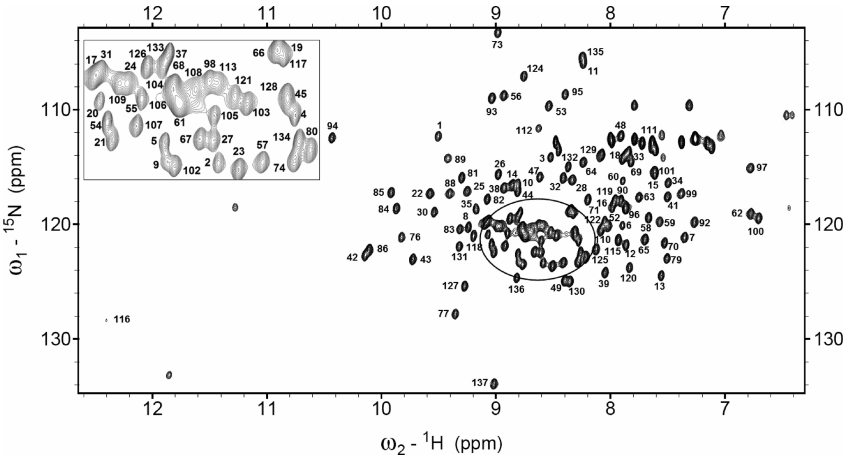

FIGURE 3: $^{1}H-^{15}N$ HSQC of DHPCN A collected at 298 K. The $^{1}H-^{15}N$ HSQC shows minimal overlap, and the crowded area of the spectrum (circled region) is shown in the inset for clarity. Backbone amide ^{1}H resonances are labeled.

Final yields of $^{13}C/^{15}N$-labeled DHP A were 24.5 mg/L using this protocol with A_{406}/A_{280} ratios greater than 4.

Sample Preparation and NMR Spectroscopy. All NMR samples were prepared using 90% H_2O/10% D_2O and 100 mM potassium phosphate buffer, pH 7. The protein was concentrated to 1.6 mM for all 3D NMR experiments, and KCN was added between 5× and 10× excess. All NMR experiments were collected on a Varian Inova 600 MHz spectrometer equipped with a Varian cryogenic $^{1}H/^{13}C/^{15}N$ triple resonance probe. For the 4-BP and 2,4,6-TFP titrations, a $^{1}H-^{15}N$ HSQC experiment was collected at 0:1, 1:1, 2:1, 3:1, 4:1, 5:1, 6:1, 7:1, 10:1, 12:1, and 15:1 halophenol to protein ratios. Only ratios of 0:1, 1:1, 2:1, 3:1, and 4:1 were feasible for the 2,4,6-TCP titration due to its poor water solubility. All NMR experiments were conducted at 298 K, processed via NMRPipe (*24*), and analyzed using Sparky (*25*).

UV−Vis Enzymatic Assays. For all experiments DHP A was oxidized via addition of excess $K_3Fe(CN)_6$. The excess ferricyanide was removed, and DHP A was buffer exchanged into 100 mM potassium phosphate, pH 7, using a Sephadex G-25 column. All absorption data were collected on a Hewlett-Packard 8453 multiwavelength spectrometer. Spectra were collected every 5 s over a 600 s time frame. The conditions used for the assays were ~2.5 μM DHP A, 120 μM H_2O_2, and 120 μM substrate or inhibitor. Turnover of the halophenols was determined by the disappearance of its respective absorption bands at pH 7 (4-BP, 280 nm; 2,4,6-TCP, 313 nm) and appearance of product absorption bands (2,6-dichloro-1,4-benzoquinone (2,6-DCQ), 272 nm).

RESULTS

Figure 2 illustrates the differences in activity between the monohalogenated 4-BP and trihalogenated 2,4,6-TCP. Upon addition of H_2O_2, complete conversion of 2,4,6-TCP to 2,6-DCQ is observed over the course of the assay (red = 0 s; blue = 600 s). The oxidation of 2,4,6-TCP can be seen by the decrease in absorption at 313 nm and the concomitant appearance of the 2,6-DCP product band at 273 nm. 4-BP, on the other hand, has been shown to be an efficient inhibitor of DHP A activity (*15*). Upon addition of H_2O_2 the 4-BP absorption band at 280 nm is not diminished, and during the 600s assay no detectable product band is observed.

Using $^{15}N-^{1}H$ HSQC, HNCO, HCACOCANH, HNCOCA, HNCA, and HNCACB, ~92% of the backbone $^{13}C\alpha$, $^{13}C\beta$, carbonyl ^{13}C, amide ^{1}H, and ^{15}N resonances were assigned in metcyano DHP A. The quality of the $^{15}N-^{1}H$ HSQC spectrum (Figure 3) shows good peak dispersion with minimal peak overlap, indicating a well-folded stable protein. The inset shows the crowded region between 9.2 and 8.2 ppm (^{1}H) for clarity. The cross-peaks at 11.8 (^{1}H), 133.0 ppm (^{15}N) and 11.2 (^{1}H), 118.5 ppm (^{15}N) arise from the nonbackbone W120 NεH and H55 NεH side chain resonances, respectively. DHP A contains one Trp (W120) and two His residues (H89, H55). The two His residues are the conserved proximal (H89) and distal (H55) histidines and are both susceptible to the paramagnetic effects of the CN-ligated heme iron. The exchangeable NεH of H89 exhibits considerable hyperfine shifting and was assigned in our previous work at 19.9 ppm (^{1}H) (*13*). In the ^{1}H NMR spectrum of

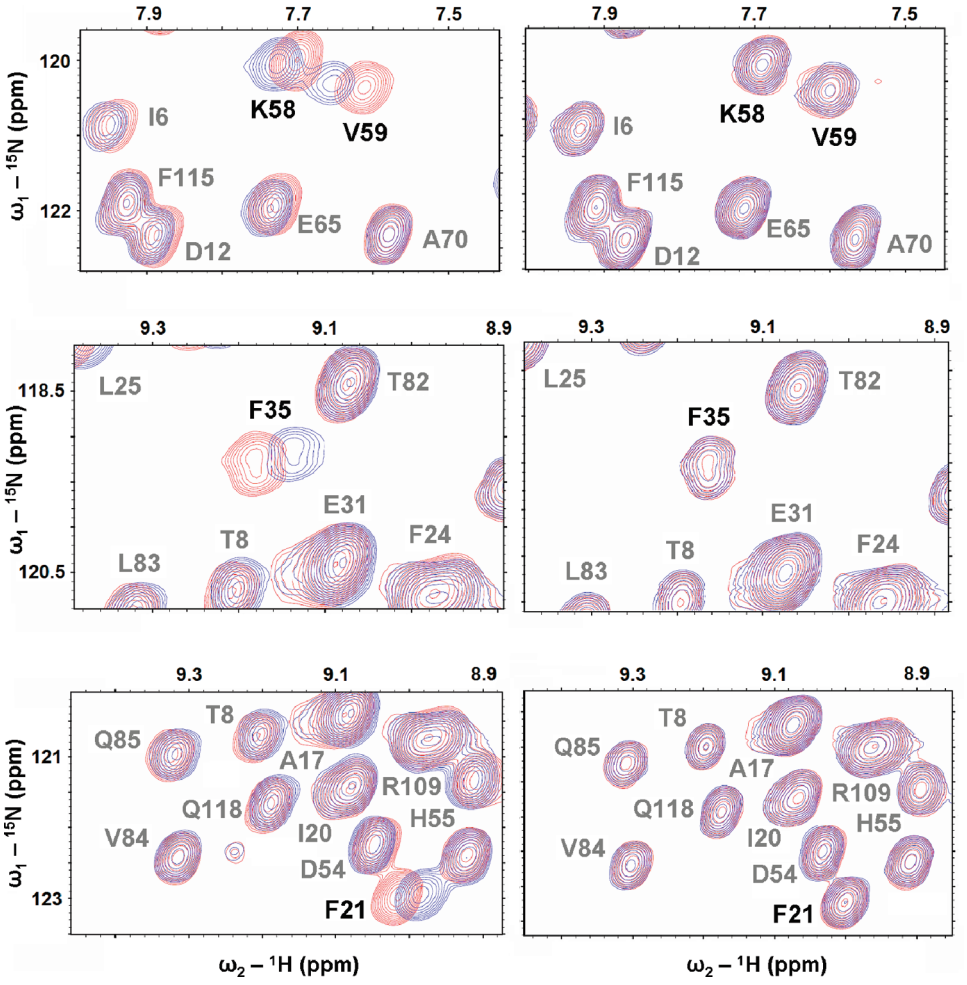

FIGURE 4: $^{1}H-^{15}N$ HSQC of DHPCN A titrated with 4-BP (left column) and 2,4,6-TCP (right column). The amide ^{1}H resonances which exhibit the greatest change in chemical shift upon addition of 4-BP are shown. Upon addition of 2,4,6-TCP these same resonances show no observable deviations.

a H55 V mutant, the hyperfine-shifted exchangeable at 11.2 ppm (H55 NεH) disappears while the other exchangeable at 11.8 ppm (W120 NεH) remains unchanged, confirming assignment of these resonances.

Amide proton chemical shift deviations upon introduction of inhibitor 4-BP and substrates 2,4,6-TCP and 2,4,6-TFP were quantified (eq 1) via a weighted chemical shift formula to account for the difference in backbone peak dispersion in the ^{15}N and ^{1}H dimensions (8.29-fold difference) (*26*, *27*).

$$\Delta\delta\ (\text{ppm}) = \sqrt{(^{1}\text{H}\ \delta\ (\text{ppm}))^2 + \frac{(^{15}\text{N}\ \delta\ (\text{ppm}))^2}{8.29}} \qquad (1)$$

Residues F60, F35, K99, R122, and V59 respectively represent the five largest deviations and V128, S42, G1, F21, and K58 respectively experience the next largest chemical shift alterations in the presence of 4-BP. Three of the top five (and five of the top ten) deviations occur in residues comprising the hydrophobic internal distal binding pocket: F21, F35, K58, V59, and F60. Current X-ray structures indicate that F35, V59, and F21 are the closest residues to bound 4-iodophenol (4-IP) having respective C−C distances of 2.98, 2.98, and 3.41 Å (*14*). The panels on the left in Figure 4 show these deviations in the presence of inhibitor 4-BP, while the panels on the right show responses of these same resonances upon addition of substrate 2,4,6-TCP. A large disparity was seen in the effects these two molecules had on the internal binding pocket, as no changes in chemical shift were observed in this local area upon addition of substrate 2,4,6-TCP. In addition to deviations in the distal pocket, 4-BP also induces changes in the local area near the dimer interface. These include perturbations of R122 and G1. Together, the internal binding pocket and dimer interface comprise 80% of the ten largest chemical shift changes in the presence of 4-BP.

The largest chemical shift deviations induced by the substrate 2,4,6-TCP occur in regions distinct from the internal binding pocket. The R122 amide proton and exchangeable side chain H55 NεH proton experience the largest degree of change in the presence of substrate 2,4,6-TCP. G1, S129, L76, Y34, E45, L100, D116, and N126 respectively experience the next eight largest chemical shift alterations when 2,4,6-TCP is titrated in. Some of the greatest deviations in the presence of 2,4,6-TCP can be observed in Figure 5. With the exception of the distal H55 NεH, the average weighted chemical shift deviation for 2,4,6-TCP was 11% lower than that of 4-BP. This may be attributed to the relatively low water solubility of the halophenols, as this permitted only a 4× excess of 2,4,6-TCP versus a 15× excess of 4-BP. 2,4,6-TFP was the only trihalogenated substrate soluble enough to reach a 15× excess concentration. While the smaller 2,4,6-TFP molecule is an active substrate, it is not as active as others such as 2,4,6-TCP or 2,4,6-TBP (*13*, *28*). With the addition of 2,4,6-TFP the greatest changes in chemical shift were observed in K99, Q4, H55 NεH, G1, M108, W120 NεH, L100, F60, F35, and E45, respectively (see Supporting Information). At a

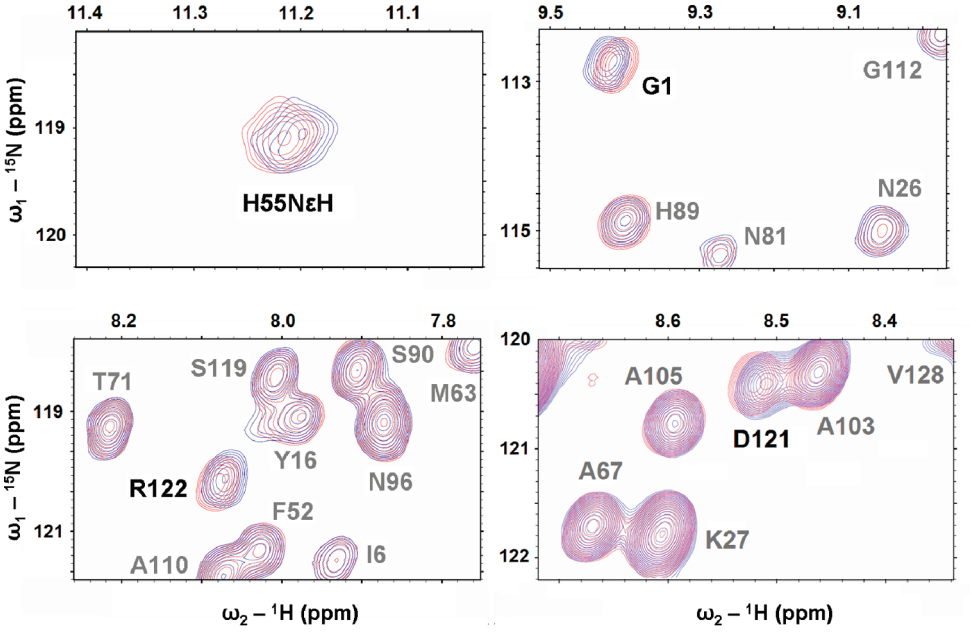

FIGURE 5: $^{1}H-^{15}N$ HSQC spectrum of DHPCN A titrated with 2,4,6-TCP. The amide ^{1}H resonances exhibiting some of the largest deviations are shown. These include the exchangeable distal histidine H55 NεH and amide protons of G1, R122, and D121.

15× excess of 2,4,6-TFP, the average chemical shift deviation was the lowest of the halophenols studied (72% lower than that of 4-BP). 2,4,6-TFP is believed to be the weakest binding trihalogenated phenol. In the monohalogenated phenol series, replacement of the chlorine substituent with a fluorine atom results in an increase in K_D from 1.7 to 3.7 mM (*15*). It is unclear if this decrease in binding affinity translates to the trihalogenated series. This assumption justifies the significantly lowered chemical shift deviations observed with 2,4,6-TFP.

DISCUSSION

The NMR backbone data presented here support the hypothesis that substrate and inhibitor have distinct binding sites in DHP A. The large effect of 4-bromophenol on binding pocket residues F21, F35, K58, V59, and F60 is consistent with internalization of the inhibitor in the distal pocket. The initial proposal that the internal site was the substrate binding site was reasonable on the grounds that such a well-defined site would be assumed to have a function (*6*, *14*). However, it is now clear that the function of binding in this site is to inhibit catalysis by steric interference at the heme iron (*15*). Steric interference both decreases the binding affinity of H_2O_2 at the heme iron and removes the acid−base catalyst, H55, from the distal pocket.

In order to extract structural information from the NMR data, the chemical shift perturbations caused by 4-BP, 2,4,6-TCP, and 2,4,6-TFP have been mapped onto the 2QFK X-ray structure of the protein (Figure 6) (*5*). The five largest deviations for each halophenol are shown in red, while the next five largest are shown in blue. The heme and W120 side chain are displayed in black. The heme and W120 sites serve as focal points for substrate binding analysis, because both are capable of retaining a reactive radical species necessary for the oxidation of 2,4,6-TCP or 2,4,6-TFP (*29*, *30*). The top panel in Figure 6 illustrates the effects of 4-BP addition. With the exception of R122, the most prominent changes (red) surround the internal binding pocket. The internal binding pocket residues F21, F35, K58, V59, and F60 exhibit large chemical shift deviations. However, it is not immediately apparent why residues near the dimer interface (R122 and G1) also exhibit significant perturbations. This could indicate either an allosteric effect or nonspecific binding interactions at the interface. Given the correlation between existing X-ray data and current $^{1}H-^{15}N$ HSQC data, there is little doubt regarding the

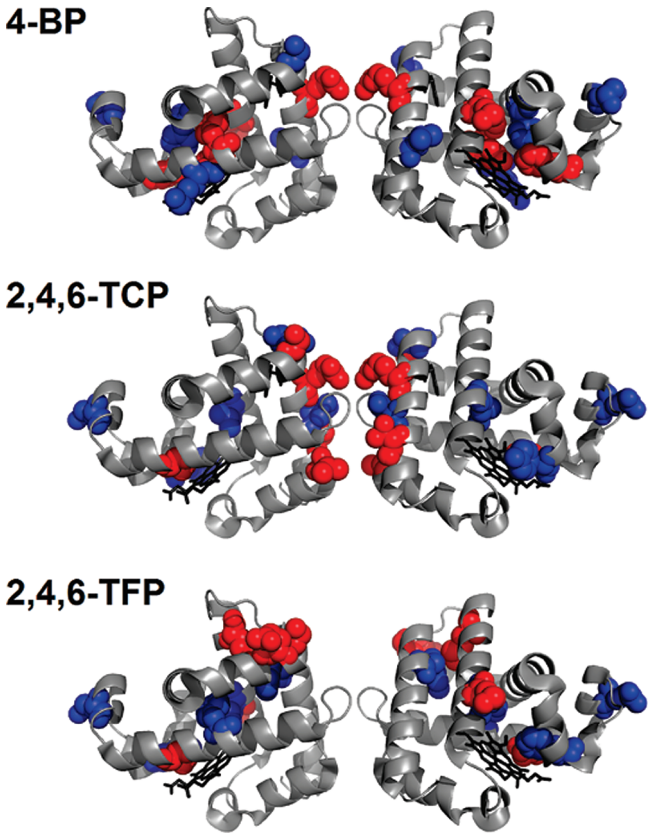

FIGURE 6: The residues experiencing the largest chemical shift deviations have been mapped onto the 2QFK X-ray structure (*5*). The side chains in red represent the five largest chemical shift changes, and the residues in blue represent the next five largest deviations. The heme and W120 residue (black) are provided as focal points. The panels display the largest deviations caused by addition of 4-BP, 2,4,6-TCP, and 2,4,6-TFP, respectively.

internalization of inhibitor 4-BP. However, since it has not been possible to obtain an X-ray structure of the bound substrate, and evidence points to an external site, $^{1}H-^{15}N$ HSQC data are one of the few current measurements that can be used to locate the binding site of substrates 2,4,6-TCP and 2,4,6-TFP under ambient conditions.

As can seen in Figure 4, in contrast to 4-BP, the internal pocket resonances do not exhibit a noticeable difference when titrated with the substrate 2,4,6-TCP. Instead, the local area surrounding the dimer interface shows four out of the five largest chemical shift perturbations (Figure 6). Of the five largest changes (R122, H55 NεH, G1, S129, and L76, respectively) only the distal histidine, H55 NεH, is not located near the interface. This result is surprising given the distal histidine is separated from the dimer interface by a distance of nearly 25 Å (*5*). Binding of substrate 2,4,6-TFP has aspects of contributions seen in both 4-BP and 2,4,6-TCP. As observed in Figure 6, alterations in chemical shift occurred near the internal pocket (F35, H55 NεH, and F60) and at a surface-exposed tryptophan near the interface (G1, Q4, M108, and W120). Previous NMR studies showed that internal heme substituents (most notably the 3-CH_3 heme methyl) were not affected by addition of 2,4,6-TFP but showed significant changes in the presence of 4-BP. These data indicate that the larger 4-BP has a much more pronounced effect in the distal pocket than 2,4,6-TFP (*13*). Thus, 2,4,6-TFP has some access to the distal pocket, but significantly less than 4-BP (*13*) and by extension other 4-halophenols (*15*). On the basis of these data we hypothesize that 2,4,6-TFP may act as both a substrate and a weakly bound inhibitor, which would explain the decreased activity of 2,4,6-TFP compared to 2,4,6-TCP (*13*, *28*).

The disparity in perturbations caused by monohalogenated inhibitor versus trihalogenated substrate indicates the importance of the 2- and 6-positions of the phenol in determining the binding site. In this study, the monohalogenated inhibitor primarily affects the internal distal pocket, while both trihalogenated substrates create perturbations externally near the heme edge (H55) and dimer interface region near W120. The presence of 2- and 6-position substituents on the phenol ring appears to be a decisive factor in controlling substrate and inhibitor binding locations. Steric and/or electrostatic effects of halogens at the 2- and 6-positions likely restrict substrate access to the internal distal binding pocket. While both substrates (2,4,6-TCP and 2,4,6-TFP) have a significant effect on the distal H55, both differ slightly in the perturbations induced near the dimer interface region (Figure 6, red spheres). Binding of the smaller 2,4,6-TFP substrate creates more localized deviations near W120, while 2,4,6-TCP binding appears to have a greater influence at the dimer interface. It is possible that the substrate binding site involves specific interactions with the halogens, and native 2,4,6-TBP may bind even more tightly than 2,4,6-TCP or 2,4,6-TFP. However, the low solubility of 2,4,6-TBP renders direct comparison impossible. Indeed, similar size dependencies were recently observed in various X-ray structures of bound monohalogenated phenol in the distal pocket (*15*). It was found that smaller monohalogated phenols (4-fluorophenol and 4-chlorophenol) bind with lower affinities and do not penetrate the internal pocket as efficiently when compared to larger monohalogenated phenols (4-bromophenol and 4-iodophenol).

In general, the NMR data indicate that binding of substrate may involve one of two possible scenarios. First, binding of the substrate may occur primarily on the external edge of the distal histidine, H55. This conclusion is reached on the basis that the second highest chemical shift change in 2,4,6-TCP, and third largest in 2,4,6-TFP, occurs at the distal H55 NεH. Earlier FT-IR experiments on the isoelectric, ferrous DHPCO A adduct indicated the orientation of H55 was in the "closed" conformation at pH 7, 290 K (*12*). If H55 is in the closed conformation, then the observed deviations of H55 NεH are likely the result of a perturbation in the Nε-H···NC hydrogen bond, where NC refers to bound cyanide. The lack of internal pocket deviations upon 2,4,6-TCP addition rules out binding of the molecule on the internal side of H55 (i.e., the distal 4-BP binding pocket). Binding of the molecule on the solvent-exposed, external side of H55 could be the cause for the deviation in the H55 NεH chemical shift. This scenario would place the substrate near the heme edge in an external fashion which is typical of other heme peroxidases, such as HRP. Peroxidases like HRP commonly perform substrate oxidation at the heme in an edge-on conformation (*29*). In addition, recent resonance Raman data on metaquo DHP A indicate an increase in 6-coordinate heme upon addition of 2,4,6-TCP consistent with a "push" of H55 toward the protein interior, adding credence to this mode of binding (*15*). There is also a long-standing precedent for allosteric changes at dimer interfaces as a result of axial ligand perturbations. Although cooperative binding and allosteric changes are typically related to tetrameric Hbs, many well-known studies have illustrated similar changes in more primitive, dimeric Hbs such as DHP A (*31*−*33*). Alterations in H55 NεH may affect the hydrogen bond between the H55 side chain and the axial ligand, ultimately resulting in allosteric communication via the dimer interface.

A second scenario involves direct binding of the substrate in the region near the interface. This scenario is highly plausible given the majority of residues with altered chemical shifts are located near a potentially redox-active tryptophan (W120). Upon inspection of the X-ray structures, this is the only residue in the interface area capable of acting as an oxidizing equivalent (i.e., a tryptophanyl radical). While the local shift deviations caused by 2,4,6-TCP appear evenly spread about the interface, the changes induced by 2,4,6-TFP are more localized near W120 (Figure 6). Many peroxidases, such as lignin peroxidase, manganese peroxidase, and versatile peroxidase, are known to bind and oxidize haloaromatics with high redox potentials near an exposed tryptophanyl radical (*34*−*36*). One of the most commonly studied peroxidases, cytochrome *c* peroxidase (CcP), is also known to generate a tryptophanyl radical (*37*). Upon addition of requisite cosubstrate H_2O_2, X-band EPR experiments do indicate the presence of a protein radical in DHP A that has tentatively been assigned as a tyrosyl radical (*22*). In fact, electronic similarities between the DHP A protein radical signature and the Trp191 radical species of CcP compound ES have led to naming this reactive intermediate "DHP A compound ES" (*22*). Although the EPR data reported for DHP A have been assigned to a tyrosyl radical when initially formed, analysis of the freeze-quenched radical signal at longer incubations times (> 12 s) led to the suggestion that the EPR signature could be a mixture of tyrosyl and tryptophanyl radicals (*22*). In structurally homologous sperm whale myglobin, there are three separate trappable protein radicals, including two tyrosyl (Y103 and Y151) and one tryptophanyl (W14) centered radical (*38*, *39*). In human hemoglobin up to four trappable radicals, including two tyrosyl (Y24 and Y42), one cysteinyl (C93), and one histidyl-based radical (H20), have been detected via the DMPO spin trap and subsequent MS analysis (*39*, *40*). Hence, there is precedent for formation of multiple protein radicals in structurally homolo-

gous globins, and there is no evidence that precludes the notion of radical hopping in DHP A. If tryptophanyl radical formation at W120 is a possibility, then a scenario involving 2,4,6-TCP or 2,4,6-TFP binding and oxidation near W120 should not be ruled out. Binding of the substrate at this site must however account for the change in H55 NεH. Because the heme edge and W120 are separated by nearly 9 Å, substrate binding near W120 must produce transferable long-range binding effects to the axial CN and likewise the H-bonded H55 NεH. Conducting enzymatic assays of various W120 mutants will help to determine any role W120 may have in substrate binding and overall protein activity.

The metcyano DHP adduct utilized in this study has been used previously to investigate halophenol binding interactions near the heme via 1D and 2D NMR experiments (*13*). Previous experiments demonstrated that DHPCN A exhibits a wide dispersion of chemical shifts (−12 to 27 ppm in the ^{1}H NMR spectra), with resonances of the heme and nearby residues being hyperfine-shifted out from under the diamagnetic envelope. The hyperfine shifts are due to a combination of contact, pseudocontact, and dipolar shift contributions arising from the $S = {}^1/_2$ paramagnetic heme center (*41*). Several resonances of nonligated residues experiencing large hyperfine shifts (i.e., proximal side F97 Cζ, Cε, and Cδ ring protons) were found to *lack* broadening and/or chemical shift deviations in the presence of substrate 2,4,6-TFP. This is significant as variations in dipolar contributions to the overall chemical shift are highly dependent on the orientation of the magnetic susceptibility tensor, χ, which is directly correlated to the Fe−CN tilt angle, β, from the heme normal (*42*−*44*). Chemical shift deviations in hyperfine-shifted resonances of nonligated residues, such as F97, would be expected if substrate binding induced structural rearrangements at or near the residue or if substrate binding altered the relative Fe−CN tilt angle, β. The Fe−CN tilt angle does not appear to be altered in the presence of active substrates like 2,4,6-TFP and suggests that chemical shift deviations observed in the distal H55NεH are not due to slight changes in the dipolar field. This rationale is supported by the lack of chemical shift deviations in other strongly paramagnetically influenced resonances, such as F97 CδHs, CεHs, and CζH and H89 Cβ Hs (*13*).

Deviations in the Fe−CN tilt angle cannot, however, be ruled out in the presence of inhibitor 4-BP. Previously reported NMR data indicated that resonances with large dipolar shifts (e.g., F97 ring protons) experience broadening and chemical shift deviations upon titration of 4-BP and not 2,4,6-TFP (*13*). Data from the current ^{1}H−^{15}N HSQC experiments indicate titration of 4-BP primarily results in alterations of *distal* side amide protons. In a previous report it was not fully understood why the ring protons of F97, a residue on the *proximal* side of the 3-CH_3 heme methyl, had such a sensitive response to the presence of 4-BP. One possible explanation could lie in a slight alteration of the Fe−CN tilt angle induced by steric interactions with inhibitor 4-BP in the distal pocket. This explanation is logical since NMR (*vide supra*) and X-ray data now indicate 4-BP bound in the distal pocket less than 4 Å from the heme iron (*14*, *15*).

CONCLUSION

The NMR study shows a distinct difference in the binding interactions of a 4-halophenol inhibitor and 2,4,6-trihalogenated phenol substrates. Binding of a 4-halophenol inhibitor, 4-BP, produced the greatest deviations in backbone chemical shifts in the distal binding pocket. Addition of trihalogenated substrate 2,4,6-TCP resulted in deviations largest at the distal H55 NεH and dimer interface. No significant changes were observed in internal binding pocket resonances upon addition of 2,4,6-TCP, clearly illustrating that binding of substrate 2,4,6-TCP is substantially different and separate from that of inhibitor 4-BP. Introduction of the smaller 2,4,6-TFP substrate showed a combination of the chemical shift changes observed for 4-BP and 2,4,6-TCP. These deviations include alterations at the internal pocket and surface tryptophan (W120) near the interface. Two scenarios were presented that may tie together the activity of 2,4,6-TCP and its observed binding perturbations. First, binding of the substrate on the external side of H55 could create allosteric changes at the dimer interface. This is in agreement with long-standing precedents relating allosteric changes at dimer interfaces to axial ligand perturbations. A second scenario involves direct binding near W120 itself. In both cases, the substrate molecule would be in favorable position for oxidation either along the heme edge or at a potential tryptophanyl radical, respectively. The NMR results have provided crucial insight into binding interactions between the protein and a highly active substrate, 2,4,6-TCP. Increased knowledge of the substrate binding site in DHP A will provide an understanding into toxic haloaromatic binding events in this bifunctional hemoglobin and possibly increase the opportunity to use DHP A for bioremediation processes beyond its native function that involves oxidation of 2,4,6-TBP.

SUPPORTING INFORMATION AVAILABLE

Full backbone chemical shift assignments and ^{1}H−^{15}N HSQC data upon titration of 2,4,6-TFP. This material is available free of charge via the Internet at http://pubs.acs.org.

REFERENCES

1. Han, K. P., Woodin, S. A., Lincoln, D. E., Fielman, K. T., and Ely, B. (2001) *Amphitrite ornata*, a marine worm, contains two dehaloperoxidase genes. *Mar. Biotechnol. 3*, 287–292.
2. de Serrano, V., D'Antonio, J., Thompson, M. K., Franzen, S., and Ghiladi, R. A. (2010) Crystal structure of dehaloperoxidase B at 1.58 Å and structural characterization of the A/B dimer from *Amphitrite ornata*, J. Biol. Chem. (submitted for publication).
3. D'Antonio, J., D'Antonio, E. L., Bowden, E. F., Smirnova, T. S., Franzen, S. F., and Ghiladi, R. A. (2010) Spectroscopic and mechanistic investigations of dehaloperoxidase B from *Amphitrite ornata*, J. Biol. Chem. (submitted for publication).
4. Chen, Z., De Serrano, V., Betts, L., and Franzen, S. (2009) Distal histidine conformational flexibility in dehaloperoxidase from *Amphitrite ornata*. *Acta Crystallogr., Sect. D: Biol. Crystallogr. 65*, 34–40.
5. de Serrano, V., Chen, Z. X., Davis, M. F., and Franzen, S. (2007) X-ray crystal structural analysis of the binding site in the ferric and oxyferrous forms of the recombinant heme dehaloperoxidase cloned from *Amphitrite ornata*. *Acta Crystallogr., Sect. D: Biol. Crystallogr. 63*, 1094–1101.
6. Lebioda, L., LaCount, M. W., Zhang, E., Chen, Y. P., Han, K., Whitton, M. M., Lincoln, D. E., and Woodin, S. A. (1999) An enzymatic globin from a marine worm. *Nature 401*, 445.
7. Weber, R. E., Mnum, C. P., Steinman, H., Bonaventura, C., Sullivan, B., and Bonaventura, J. (1977) Hemoglobins of two terebellid polychaetes: *Enoplobranchus sanuigneus* and *Amphitire ornata*. *Comp. Biochem. Physiol. 56A*, 179–187.
8. Belyea, J., Gilvey, L. B., Davis, M. F., Godek, M., Sit, T. L., Lommel, S. A., and Franzen, S. (2005) Enzyme function of the globin dehaloperoxidase from *Amphitrite ornata* is activated by substrate binding. *Biochemistry 44*, 15637–15644.
9. Franzen, S., Gilvey, L. B., and Belyea, J. L. (2007) The pH dependence of the activity of dehaloperoxidase from *Amphitrite ornata*. *Biochim. Biophys. Acta 1774*, 121–130.
10. Franzen, S., Chaudhary, C., Belyea, J., Gilvey, L., Davis, M. F., Sit, T. L., and Lommel, S. A. (2006) Proximal cavity, distal histidine and substrate hydrogen-bonding mutations modulate the acti-

vity of *Amphitrite ornata* dehaloperoxidase. *Biochemistry 45*, 9085–9094.
11. Nienhaus, K., Nickel, E., Davis, M. F., Franzen, S., and Nienhaus, G. U. (2008) Determinants of substrate internalization in the distal pocket of dehaloperoxidase hemoglobin of *Amphitrite ornata*. *Biochemistry 47*, 12985–12994.
12. Nienhaus, K., Deng, P. C., Belyea, J., Franzen, S., and Nienhaus, G. U. (2006) Spectroscopic study of substrate binding to the carbonmonoxy form of dehaloperoxidase from *Amphitrite ornata*. *J. Phys. Chem. B 110*, 13264–13276.
13. Davis, M. F., Gracz, H., Vendeix, F. A. P., de Serrano, V., Somasundaram, A., Decatur, S. M., and Franzen, S. (2009) Different modes of binding of mono-, di- and trihalogenated phenols to the hemoglobin dehaloperoxidase from *Amphitrite ornata*. *Biochemistry 48*, 2164–2172.
14. Zhang, E., Chen, Y. P., Roach, M. P., Lincoln, D. E., Lovell, C. R., Woodin, S. A., Dawson, J. H., and Lebioda, L. (1996) Crystallization and initial spectroscopic characterization of the heme-containing dehaloperoxidase from the marine polychaete *Amphitrite ornata*. *Acta Crystallogr., Sect. D 52*, 1191–1193.
15. Nicoletti, F. P., Thompson, M. K., Howes, B. D., Franzen, S., and Smulevich, G. (2010) New Insights into the Role of Distal Histidine Flexibility in Ligand Stabilization of Dehaloperoxidase-hemoglobin from *Amphitrite ornata*. *Biochemistry* (DOI: 10.1021/bi9020567).
16. Shikama, K. (2006) Nature of the FeO_2 bonding in myoglobin and hemoglobin: A new molecular paradigm. *Prog. Biophys. Mol. Biol. 91*, 83–162.
17. Fielman, K. T., Woodin, S. A., and Lincoln, D. E. (2001) Polychaete indicator species as a source of natural halogenated organic compounds in marine sediments. *Environ. Toxicol. Chem. 20*, 738–747.
18. Fielman, K. T., Woodin, S. A., Walla, M. D., and Lincoln, D. E. (1999) Widespread occurrence of natural halogenated organics among temperate marine infauna. *Mar. Ecol.: Prog. Ser. 181*, 1–12.
19. Woodin, S. A., Lindsay, S. M., and Lincoln, D. E. (1997) Biogenic bromophenols as negative recruitment cues. *Mar. Ecol.: Prog. Ser. 157*, 303–306.
20. Lincoln, D. E., Fielman, K. T., Marinelli, R. L., and Woodin, S. A. (2005) Bromophenol accumulation and sediment contamination by the marine annelids *Notomastus lobatus* and *Thelepus crispus*. *Biochem. Systemat. Ecol. 33*, 559–570.
21. Osborne, R. L., Taylor, L. O., Han, K. P., Ely, B., and Dawson, J. H. (2004) *Amphitrite ornata* dehaloperoxidase: Enhanced activity for the catalytically active globin using MCPBA. *Biochem. Biophys. Res. Commun. 324*, 1194–1198.
22. Feducia, J., Dumarieh, R., Gilvey, L. B. G., Smirnova, T., Franzen, S., and Ghiladi, R. A. (2009) Characterization of dehaloperoxidase compound ES and its reactivity with trihalophenols. *Biochemistry 48*, 995–1005.
23. Smirnova, T. I., Weber, R. T., Davis, M. F., and Franzen, S. (2008) Substrate binding triggers a switch in the iron coordination in dehaloperoxidase from *Amphitrite ornata*: HYSCORE experiments. *J. Am. Chem. Soc. 130*, 2128–2129.
24. Delaglio, F., Grzesiek, S., Vuister, G. W., Zhu, G., Pfeifer, J., and Bax, A. (1995) NMRPipe: A multidimensional spectral processing system based on UNIX pipes. *J. Biomol. NMR 6*, 277–293.
25. Goddard, T. D., and Kneller, D. G. SPARKY 3, University of California, San Francisco.
26. Kordys, D. R., Bobay, B. G., Thompson, R. J., Venters, R. A., and Cavanah, J. (2007) Peptide binding proclivities of calcium loaded calbindin-D28k. *FEBS Lett. 581*, 4778–4782.
27. Palmer, S. M., Schaller, M. D., and Campbell, S. L. (2008) Vinculin tail conformation and self-association is independent of pH and H906 protonation. *Biochemistry 47*, 12467–12475.
28. Chaudhary, C. (2003) Functional studies of the push-pull mechanism in dehaloperoxidase from *Amphitrite ornata*, Master's Thesis, North Carolina State University.
29. Ator, M. A., and Ortiz de Montellano, P. R. (1987) Protein control of prosthetic heme reactivity: Reaction of substrates with the heme edge of horseradish peroxidase. *J. Biol. Chem. 262*, 1542–1551.
30. Pogni, R., Baratto, M. C., Giansanti, S., Teutloff, C., Verdin, J., Valderrama, B., Lendzian, F., Lubitz, W., Vazquez-Duhalt, R., and Basosi, R. (2005) Tryptophan-based radical in the catalytic mechanism of versatile peroxidase from *Bjerkandera adusta*. *Biochemistry 44*, 4267–4274.
31. Royer, W. E., Hendrickson, W. A., and Chiancone, E. (1990) Structural transitions upon ligand-binding in a cooperative dimeric hemoglobin. *Science 249*, 518–521.
32. Royer, W. E., Pardanani, A., Gibson, Q. H., Peterson, E. S., and Friedman, J. M. (1996) Ordered water molecules as key allosteric mediators in a cooperative dimeric hemoglobin. *Proc. Natl. Acad. Sci. U.S.A. 93*, 14526–14531.
33. Knapp, J. E., Bonham, M. A., Gibson, Q. H., Nichols, J. C., and Royer, W. E. (2005) Residue F4 plays a key role in modulating oxygen affinity and cooperativity in *Scapharca* dimeric hemoglobin. *Biochemistry 44*, 14419–14430.
34. Doyle, W. A., Blodig, W., Veitch, N. C., Piontek, K., and Smith, A. T. (1998) Two substrate interaction sites in lignin peroxidase revealed by site-directed mutagenesis. *Biochemistry 37*, 15097–15105.
35. Perez-Boada, M., Ruiz-Duenas, F. J., Pogni, R., Basosi, R., Choinowski, T., Martinez, M. J., Piontek, K., and Martinez, A. T. (2005) Versatile peroxidase oxidation of high redox potential aromatic compounds: Site-directed mutagenesis, spectroscopic and crystallographic investigation of three long-range electron transfer pathways. *J. Mol. Biol. 354*, 385–402.
36. Ruiz-Duenas, F. J., Pogni, R., Morales, M., Giansanti, S., Mate, M. J., Romero, A., Martinez, M. J., Basosi, R., and Martinez, A. T. (2009) Protein radicals in fungal versatile peroxidase: Catalytic tryptophan radical in both compound I and compound II and studies on W164Y, W164H, and W164S variants. *J. Biol. Chem. 284*, 7986–7994.
37. Sivaraja, M., Goodin, D. B., Smith, M., and Hoffman, B. M. (1989) Identification by ENDOR of Trp191 as the free-radical site in cytochrome-*c* peroxidase compound ES. *Science 245*, 738–740.
38. Gunther, M. R. (2004) Probing the free radicals formed in the metmyoglobin-hydrogen peroxide reaction. *Free Radical Biol. Med. 36*, 1345–1354.
39. Mason, R. P. (2004) Using anti-5,5-dimethyl-1-pyrroline *N*-oxide to detect protein radicals in time and space with immuno-spin trapping. *Free Radical Biol. Med. 36*, 1214–1223.
40. Bhattacharjee, S., Deterding, L. J., Jiang, J., Bonini, M. G., Tomer, K. B., Ramirez, D. C., and Mason, R. P. (2007) Electron transfer between a tyrosyl radical and a cysteine residue in hemoproteins: Spin trapping analysis. *J. Am. Chem. Soc. 129*, 13493–13501.
41. La Mar, G. N., and de Ropp, J. S. (1993) in Biological Magnetic Resonance, pp 1−73, Plenum Press, New York.
42. La Mar, G. N. (2007) Application of the paramagnetic dipole field for solution NMR active site structure determination in low-spin, cyanide-inhibited ferric hemoproteins. *IUBMB Life 59*, 513–527.
43. La Mar, G. N., Chen, Z., Vyas, K., and McPherson, A. D. (1995) An interpretive bases of the hyperfine shifts in cyanide-inhibited horseradish peroxidase based on the magnetic axes and ligand tilt. Influence of substrate binding and extensions to other peroxidases. *J. Am. Chem. Soc. 117*, 411–419.
44. Zhu, W., Li, Y., Wang, J., Ortiz de Montellano, P. R., and La Mar, G. N. (2006) Solution NMR study of environmental effects on substrate seating in human heme oxygenase: Influence of polypeptide truncation, substrate modification and axial ligand. *J. Inorg. Biochem. 100*, 97–107.

BIOCHEMISTRY
including biophysical chemistry & molecular biology
Article

Biochemistry **2010,** *49,* 1903–1912 1903
DOI: 10.1021/bi9020567

New Insights into the Role of Distal Histidine Flexibility in Ligand Stabilization of Dehaloperoxidase−Hemoglobin from *Amphitrite ornata*[†]

Francesco P. Nicoletti,[‡] Matthew K. Thompson,[§] Barry D. Howes,[‡] Stefan Franzen,[§] and Giulietta Smulevich*[,‡]

[‡]*Dipartimento di Chimica, Università di Firenze, Via della Lastruccia 3, I-50019 Sesto Fiorentino (FI), Italy, and*
[§]*Department of Chemistry, North Carolina State University, 2620 Yarbrough Drive, Raleigh, North Carolina 27695*

Received December 2, 2009; Revised Manuscript Received January 14, 2010

ABSTRACT: The present work highlights the important role played by the distal histidine in controlling the binding of heme ligands in dehaloperoxidase (DHP) as compared to myoglobin and peroxidases. In DHP the distal histidine is highly mobile and undergoes a conformational change that places it within hydrogen-bonding distance of anionic ligands and water, where strong hydrogen bonding can occur. The detailed resonance Raman (RR) analysis at room temperature shows the presence of an equilibrium between a 5-coordinate and a 6-coordinate (aquo) high-spin form. The equilibrium shifts toward the aquo form at 12 K. These two forms are consistent with the existing X-ray structures where a closed conformation, with His55 positioned in the distal pocket and H-bonded with the distal water molecule (6-coordinate), and an open solvent-exposed conformation, with the His55 displaced from the distal pocket (5-coordinate form), are in equilibrium. Moreover, the comparison between the Raman data at 298 and 12 K and the results obtained by EPR of DHP in the presence of 4-iodophenol highlights the formation of a pure 5-coordinate high-spin form (open conformation). The data reported herein support the role of His55 in facilitating the interaction of substrate and inhibitor in the regulation of enzyme function, as previously suggested. The two conformations of His55 in equilibrium at room temperature provide a level of control that permits the distal histidine to act as both the acid−base catalyst in the peroxidase mechanism and the stabilizing amino acid for exogenous heme-coordinated ligands.

Dehaloperoxidase (DHP)[1] displays significant peroxidase activity under physiological conditions while having a globin fold (*1*). Peroxidases are typically characterized by an increased polarity of the distal cavity compared to globins. Accordingly, the postulated mechanism of hydrogen peroxide activation and heterolytic bond cleavage in peroxidases relies on the concerted role played by the conserved distal Arg and His (*2*) through direct hydrogen bonds and charge stabilization (*3*−*6*). However, unlike peroxidases, the distal cavity of DHP shows the presence of only a distal His, without an Arg (*7*−*9*). Therefore, it appears that the mechanism of hydrogen peroxide activation in DHP is controlled entirely by the distal His.

In general, heme pocket distal amino acid residues control ligand binding in heme proteins. However, while in hemoglobin and myoglobin the distal His tunes the ligand affinities via hydrogen bond stabilization involving its N_ε proton (*10*), the crystal structures and the spectroscopic study of the CN^-, NO, CO, and F^- adducts of peroxidases revealed that significant changes are induced in the distal cavity upon adduct formation, suggesting that the distal Arg and His residues are significantly perturbed (*11*, *12*). In addition, the comparison of the UV−vis and RR spectra of the fluoride and hydroxide complexes of various peroxidases and selected mutants has highlighted the complex mechanism of stabilization of anionic ligands exerted by the distal amino acids (*13*−*16*). This mechanism resembles that of compound I formation during peroxidase catalysis, where ligand stabilization by the distal arginine is coupled to protonation of the distal histidine (*12*, *17*). Both the distal Arg and His participate, in a concerted manner, in hydrogen-bonding interactions with the ligand. However, for cytochrome *c* peroxidase (CCP), it has been shown that the interaction between Arg48 and the anions is possible because the distal Arg undergoes a conformational change that places it within hydrogen-bonding distance of bound fluoride or hydrogen peroxide, which facilitates acid−base catalysis (*11*, *12*).

Since the specific interaction with Arg is missing in DHP, it is of interest to understand whether the different cavity characteristics of DHP, the globins, and peroxidases are also reflected in the binding of exogenous ligands. Therefore, we undertook a detailed spectroscopic investigation of the ferric−fluoride and hydroxide-ligated forms to highlight how the distal heme protein cavity interacts with the exogenous ligand in comparison with Mb and peroxidases.

The flexibility of the distal histidine is key for determining its ability to interact with heme-coordinated ligands. In many heme proteins, temperature, pH, and inhibitor or substrate binding in the distal pocket are all factors that regulate the conformation of the distal histidine (*18*, *19*). For native DHP, the room temperature

[†]This work was supported by the U.S. Army Research Office (Grant 52278-LS) and local Italian grants (ex60%).

*Corresponding author. Tel: +39 0554573083. Fax: +39 0554573077. E-mail: giulietta.smulevich@unifi.it.

[1]Abbreviations: DHP, dehaloperoxidase; DHP-CN, metcyano dehaloperoxidase; DHP-CO, carbonmonoxy dehaloperoxidase; CCP, cytochrome *c* peroxidase; Hb, hemoglobin; Mb, myoglobin; SWMb, sperm whale myoglobin; HHMb, horse heart myoglobin; HRP, horseradish peroxidase; DHP-F, dehaloperoxidase fluoride; DHP-OH, dehaloperoxidase hydroxide; 4CP, 4-chlorophenol; 4BP, 4-bromophenol; 4IP, 4-iodophenol; DCP, 2,4-dichlorophenol; TBP, 2,4,6-tribromophenol; TCP, 2,4,6-trichlorophenol; TFP, 2,4,6-trifluorophenol; RR, resonance Raman; EPR, electron paramagnetic resonance; 5c, 5-coordinate; 6c, 6-coordinate; HS, high-spin state.

Published on Web 01/14/2010

X-ray crystal structure showed that there are two conformations of the distal histidine at pH 6.0. Comparison with two X-ray crystal structures at 100 K suggests that these two conformations are associated with an unusual flexibility of the distal His55 (*7*−*9*). The 100 K structures consist of a closed conformation with His55 positioned in the distal pocket and H-bonded with the distal water molecule in the metaquo form (PDB 2QFK) and an open solvent-exposed conformation with the His55 displaced from the distal pocket in the 5-coordinate deoxy form (PDB 3DR9). The open form is also the only form observed when 4-iodophenol (4IP) binds in the internal binding site (*9*). The X-ray structural data suggest that His55 is stabilized in the closed conformation by hydrogen bonding to heme ligands (*7*). Unlike 4IP, no X-ray structure is available for DHP bound to a 2,4,6-trihalophenol. However, data are available in solution. In particular, 2,4,6-trifluorophenol (TFP) has been found to bind at low temperature (< 260 K) but not at room temperature by cryogenic FT-IR, EPR, and HYSCORE studies (*20*, *21*). In addition, ^{19}F NMR and relaxation experiments suggested that 2,4,6-TFP binds externally to the heme distal cavity at ambient temperature (*22*). Moreover, recent assignment of the backbone $^{13}C\alpha$, $^{13}C\beta$, carbonyl ^{13}C, amide ^{1}H, and amide ^{15}N resonances in DHP provides further evidence for the existence of distinct binding sites which allows to distinguish substrates and inhibitors. The substrates 2,4,6-TXP (X = Br, Cl, F) bind externally, and inhibitors 4-XP bind within the distal pocket. The NMR data show that shifts in the His55 position are coupled to binding of both the substrate and inhibitor. Hence, the flexibility of the distal histidine, His55, appears to have functional relevance for inhibition (*23*). The detailed spectroscopic investigation of the ferric form in the presence of different halogenated phenols undertaken in the present work further corroborates the unusual flexibility of the distal His55.

MATERIALS AND METHODS

Materials. DHP was expressed in *Escherichia coli* and purified as previously described (*24*). Purification using CM52 cation-exchange cellulose (Whatman, Clifton, NJ) in a 55 mL FLEXCOLUMN (Kimble/Kontes, Vineland, NJ) allowed us to completely remove imidazole contaminant. Isotopically enriched water ($H_2{}^{18}O$) (95%) and D_2O (99.8%) was purchased from Cambridge Isotope Laboratories (USA) and Merck AG (Darmstadt, Germany), respectively. The substrate analogues 4-iodophenol and 2,4,6-trifluorophenol were purchased from Acros (New Jersey). All the other chemicals were obtained from Merck AG (Darmstadt, Germany). All chemicals were of analytical or reagent grade and were used without further purification.

Sample Preparation. Ferric DHP samples were prepared in 150 mM potassium phosphate, pH 6.0. Completely oxidized DHP samples were prepared by oxidation of the significant amount of the oxy−ferrous form present, due to the high protein affinity for oxygen, using excess potassium hexacyanoferrate(III) followed by gel filtration on a Bio-Gel P-6DG column equilibrated with the 150 mM phosphate buffer at pH 6 to remove the oxidant. The DHP-F complex, in 150 mM potassium phosphate at pH 5.0, was prepared by adding a 0.018 M solution of NaF to the sample, giving a final concentration of 0.015 M. The samples at pH 5 were obtained by addition of citric acid to the samples at pH 6, reaching a final concentration of 110 mM. The DHP-OH sample was prepared in 150 mM potassium phosphate at pH 9.6. The hydroxyl complexes in isotopically enriched water were prepared by adding 5 μL of DHP, in 150 mM natural abundance potassium phosphate at pH 11, to 45 μL of D_2O and $H_2{}^{18}O$ to obtain a final pD 10 and pH 9.6, respectively. The 4IP-DHP (K_D 318 μM) sample was prepared by diluting a 200 μM, pH 6, DHP solution with a saturated 4IP solution (1 mM) in 150 mM potassium phosphate at pH 6 to yield final concentrations of 900 μM for 4IPh and 30 μM for DHP. The 4IP:DHP molar ratio of 30:1 was employed since titration of DHP with 4IP revealed progressive variations in the DHP absorption spectrum, reaching a final form for the 30:1 molar ratio (data not shown). The TFP-DHP samples were prepared by using a range from 10- to 320-fold excess of TFP with respect to DHP. The concentration of all the samples was between 15 and 200 μM. The sample concentration was determined using the molar absorptivity of 116.4 mM^{-1} cm^{-1} at 406 nm (*25*). All samples for low-temperature measurements were prepared in 150 mM phosphate and 30% (v/v) glycerol. It is noted that the room temperature UV−vis and RR spectra of corresponding samples in the presence and absence of glycerol were identical.

Spectroscopy. (*A*) *Room Temperature*. Electronic absorption spectra were measured with a double-beam Cary 5 spectrophotometer (Varian, Palo Alto, CA). The electronic absorption spectra were obtained using a 5 mm NMR tube or a 1 mm cuvette and a 600 nm/min scan rate. The RR spectra were obtained using a 5 mm NMR tube and by excitation with the 406.7 and 413.1 nm lines of a Kr^+ laser (Coherent, Innova 300 C, Santa Clara, CA) and the 514.5 nm line of an Ar^+ laser (Coherent, Innova 90/5, Santa Clara, CA). Backscattered light from a slowly rotating NMR tube was collected and focused into a triple spectrometer (consisting of two Acton Research SpectraPro 2300i and a SpectraPro 2500i in the final stage with a 3600 groove/mm grating) working in the subtractive mode, equipped with a liquid nitrogen-cooled CCD detector. It should be noted that the spectral resolution of the RR spectra cited in the figure captions is that calculated theoretically on the basis of the optical properties of the spectrometer. However, for the moderately broad experimental RR bands observed in the present study (ca. 10 cm^{-1}), the effective spectral resolution will in general be lower. All RR measurements were repeated several times under the same conditions to ensure reproducibility. To improve the signal/noise ratio, a number of spectra were accumulated and summed only if no spectral differences were noted. The RR spectra were calibrated with indene, CCl_4, and dimethyl sulfoxide as standards to an accuracy of ± 1 cm^{-1} for intense isolated bands. To determine peak intensities and positions a curve-fitting program (Lab Calc; Galactic) was used to simulate the spectra using a Lorentzian line shape with bandwidths between 10 and 13 cm^{-1}. In particular, 10 cm^{-1} has been used to fit the B_{1g} modes, 11 cm^{-1} for the vinyl modes, 12 cm^{-1} for the E_u modes, and 13 cm^{-1} for the A_{1g} and A_{2g} modes.

(*B*) *Low Temperature*. The low-temperature experiments were carried out using an Air Products Displex closed-cycle He refrigerator with automatic temperature control.

For the low-temperature RR measurements, 20 μL of the protein solution was deposited on the copper cold finger of the refrigerator at 90 K under a nitrogen flow. The temperature was then slowly decreased to 12 K under vacuum, and RR spectra were obtained at this temperature. The backscattered light was collected and focused into a computer-controlled double monochromator (Jobin-Yvon HG2S) equipped with a cooled photomultiplier (RCA C31034 A) and photon-counting electronics. The RR spectra were calibrated with indene as standard to an

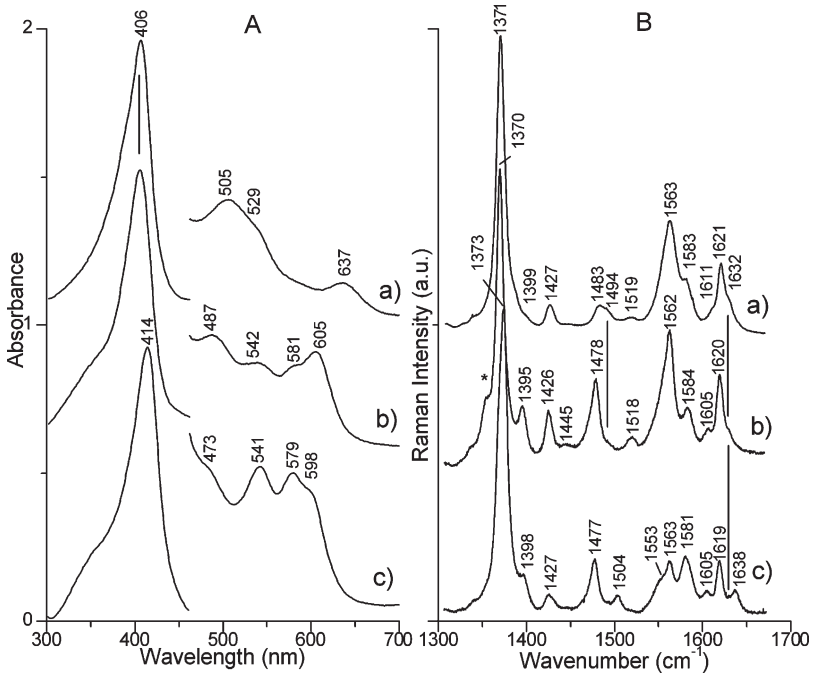

FIGURE 1: Electronic absorption spectra (panel A) and RR spectra (panel B) of (Fe^{3+})DHP at pH 6 (a), (Fe^{3+})DHP-F at pH 5 (b), and (Fe^{3+})-DHP-OH at pH 9.6 (c) in 0.15 M potassium phosphate. The 460−700 nm region (panel A) has been expanded by a factor of 5. Experimental conditions for panel B: (a) 406.7 nm excitation wavelength, 5 mW laser power at the sample, average of 6 spectra with 300 s integration time, 1.3 cm^{-1} spectral resolution; (b) 406.7 nm excitation wavelength, 5 mW laser power at the sample, average of 12 spectra with 300 s integration time, 1.3 cm^{-1} spectral resolution; the asterisk indicates the reduced form (1354 cm^{-1}); (c) 413.1 nm excitation wavelength, 6 mW laser power at the sample, average of 3 spectra with 600 s integration time, 1.2 cm^{-1} spectral resolution. The intensities are normalized to that of the ν_4 band. Spectra have been shifted along the ordinate axis to allow better visualization.

accuracy of ±1 cm^{-1} for intense isolated bands. The glycerol bands were subtracted from the RR spectra of the samples.

EPR spectra were recorded on a Bruker Elexys E500 instrument equipped with a microwave frequency counter. An Oxford Instruments ESR 900 cryostat was used to obtain low temperatures. The spectra were recorded under nonsaturating conditions at 5 K, 1 mW microwave power, and 1 mT modulation amplitude. The EPR simulation program used to determine the g values (Xsophe; Bruker) is appropriate for effective $S = {}^1/_2$ systems.

RESULTS

Room Temperature. (*A*) *Native Protein*. The absorption spectrum of metaquo DHP at pH 6.0 (Figure 1, panel A, trace a) is characterized by a Soret band at 406 nm, Q_1 and Q_0 bands at 505 and 529 nm, respectively, and the charge transfer (CT1) band (long wavelength, >600 nm porphyrin-to-metal charge transfer band) at 637 nm, very similar to the spectrum of metaquo Mb (*26*). Therefore, the spectrum, almost identical to those previously reported (*25*, *27*), is typical of a high-spin species. Accordingly, the corresponding RR spectrum (Figure 1, panel B, trace a) indicates an equilibrium between a predominant hexacoordinated high-spin species (6cHS) (ν_3 at 1483 cm^{-1}, ν_2 at 1563 cm^{-1}, and ν_{10} at 1611 cm^{-1}) and a pentacoordinated high-spin species (5cHS) (ν_3 at 1494 cm^{-1}). These two forms are consistent with the existing X-ray structures where a closed conformation with His55 positioned in the distal pocket (6-coordinate) and an open solvent-exposed conformation with the His55 displaced from the distal pocket (5-coordinate form) are in equilibrium (Figure 2, center top) (*9*). In a previous study, RR spectra showing a mixture of a high-spin and a low-spin species were obtained (*27*), the latter due to a bis-imidazole complex resulting from the presence of an imidazole impurity (see Materials and Methods).

Unlike Mb, which is characterized by two coincident $\nu_{(C=C)}$ stretching modes at 1621 cm^{-1} (*28*), on the basis of depolarization ratio measurements obtained by a curve-fitting analysis (Figure 3, panel A), two polarized bands (Table 1) are observed for DHP at 1621 and 1632 cm^{-1} which are therefore assigned to two vinyl stretching modes. A direct relationship between the $\nu_{(C=C)}$ stretching wavenumber and the orientations of the vinyl groups (i.e., their torsional angles), as induced by specific protein interactions, has been established for heme-containing peroxidases and myoglobin (*29*). Therefore, this result is consistent with the crystal structure of DHP (*8*) which shows two different torsional angles of −144° and 158° for 2- and 4-vinyl, respectively.

(*B*) *Binding of Anionic Ligands*. Upon addition of fluoride to the protein at pH 5.0 marked changes are observed in the UV−vis spectrum (Figure 1, panel A, trace b). In accord with previously reported results (*27*), the spectrum of the DHP-F adduct is characterized by a Soret band maximum at 406 nm and a CT1 band at 605 nm, which is 5 nm blue shifted compared to the corresponding band of the Mb−F complex (*16*). The corresponding RR spectrum is typical of a 6cHS form (Figure 1, panel B, trace b) with ν_3 at 1478 cm^{-1}, ν_2 at 1562 cm^{-1}, and ν_{10} at 1605 cm^{-1}. A small amount of a 5cHS unligated protein (ν_3 at 1494 cm^{-1}) is observed. As in the met form, but different from Mb, two $\nu_{(C=C)}$ vinyl stretching modes are observed at 1620 and 1632 cm^{-1} (Figure 3, panel B).

The UV−vis spectrum of DHP at alkaline pH (pH 9.6) (Figure 1, panel A, trace c) is characteristic of a mixture of 6-coordinate low-spin (6cLS) (maxima at 414, 541, and 579 nm) and 6cHS (CT at 473 and 598 nm) species with a hydroxyl group

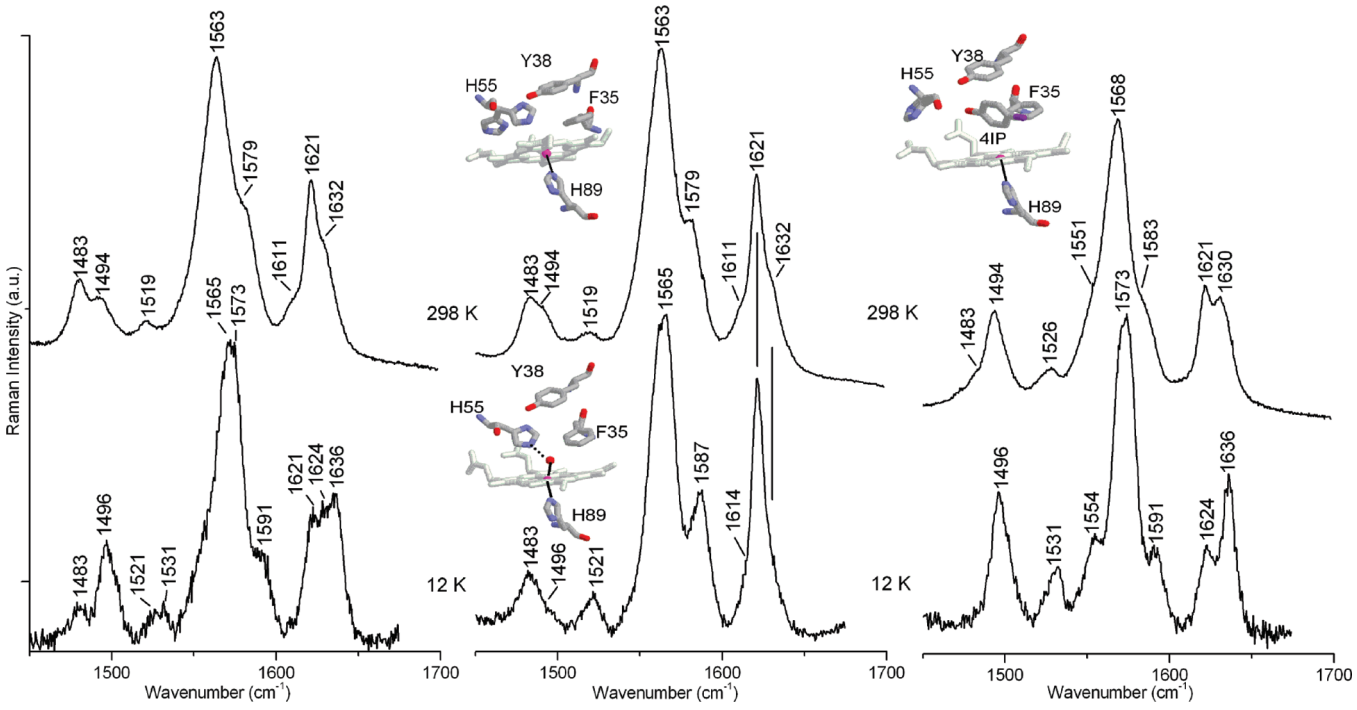

FIGURE 2: RR spectra of DHP (center), DHP-4IP (1:30 molar ratio) (right), and DHP-TFP (1:320 molar ratio) (left) at 298 K (top) and 12 K (bottom) at pH 6. Experimental conditions: λ_{exc} 406.7 nm, spectral resolution 1.3 cm^{-1} (298 K) and 5 cm^{-1} (12 K), power at the sample 5 mW (298 K) and 8 mW (12 K). DHP: average of 6 spectra with 300 s integration time (298 K), collection interval 8 s/0.5 cm^{-1} (12 K). 4IP: average of 6 spectra with 300 s integration time (298 K), collection interval 6 s/0.5 cm^{-1} (12 K). TFP: average of 3 spectra with 300 s integration time (298 K), collection interval 6 s/0.5 cm^{-1} (12 K). The intensities are normalized to that of the ν_4. Spectra have been shifted along the ordinate axis to allow better visualization. The existing heme cavity X-ray structures are also reported. Center top, structure at room temperature (PDB: 1EW6) (*9*); center bottom, 100 K structure (PDB: 2QFK) (*8*); right top, room temperature structure of DHP-4IP (PDB: 1EWA) (*9*).

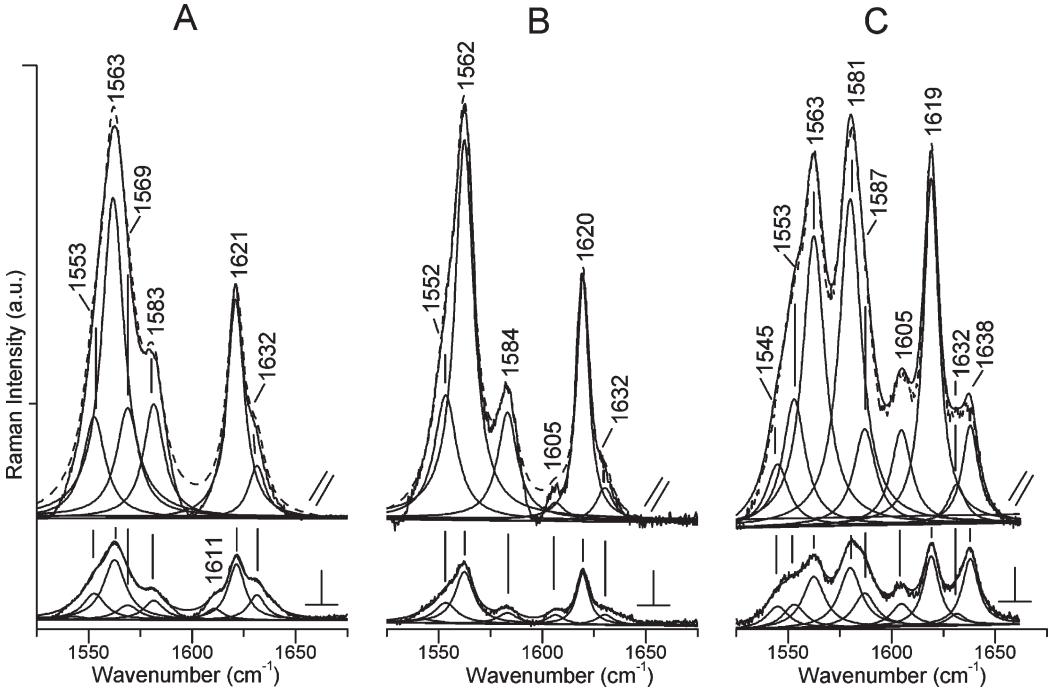

FIGURE 3: Curve fitting of the RR spectra of (Fe^{3+})DHP at pH 6 (A), (Fe^{3+})DHP-F at pH 5 (B), and (Fe^{3+})DHP-OH at pH 9.6 (C) in 0.15 M potassium phosphate for parallel (∥) and perpendicular (⊥) polarized light, taken with 406.7 nm (A and B) and 413.1 nm (C) excitation wavelengths.

bound to the heme iron, as previously observed (*20*, *27*). This behavior is similar to that of Mb except that the Soret and the CT1 bands are 1 and 2 nm blue shifted, respectively (*13*). The corresponding RR spectrum (Figure 1, panel B, trace c) indicates the presence of a 6cLS (ν_3 at 1504 cm^{-1}, ν_2 at 1581 cm^{-1}, and ν_{10} at 1638 cm^{-1}) and a 6cHS species (ν_3 at 1477 cm^{-1}, ν_2 at 1563 cm^{-1}). In addition, the bands at 1619 and 1632 cm^{-1} are assigned to the two $\nu_{(C=C)}$ vinyl stretches (Figure 3 panel C).

Table 1: RR Frequencies (in cm^{-1}) in the High Wavenumber Region of the Various Ferric DHP Species, Their Normal Mode Assignments, and Depolarization Ratios (ρ) (in Parentheses) Compared to Those of Mb[a]

		DHP								Mb			
		Fe^{3+}		+4IP		Fe^{3+}-F	Fe^{3+}-OH			Fe^{3+}[g]	$Fe^{3+}F$[h]	Fe^{3+}-OH[i]	
mode	sym	5cHS	*6cHS*	*5cHS*	6cHS	6cHS	*6cHS*		6cLS	6cHS	6cHS	*6cHS*	6cLS
ν_{21}	A_{2g}		1303[b]					1304[b]		1307			
ν_{41}	E_u		1340					1341		1341			
ν_4	A_{1g}		1371 (0.18)		1372 (0.16)	1370 (0.15)		1373 (0.17)		1371	1371	1373	
ν_{20}	A_{2g}		1399		1397	1395		1398		1401			
$\delta(CH_2)$			1427		1427	1426		1427		1426			
ν_{28}	B_{2g}					1445							
ν_3	A_{1g}	1494 (0.11)	1483 (0.15)	1494 (0.11)	1483 (0.11)	1478 (0.14)	1477 (0.16)		1504 (0.15)	1483	1482	1479	1504
ν_{38}	E_u		1519	1526		1518 (0.21)			1553 (0.22)	1511			
ν_{11}	B_{1g}		1548 (0.73)	1551		1552	1545			1544	1546	1545	
ν_2	A_{1g}		1563 (0.18)	1568 (0.13)		1562 (0.14)	1563 (0.17)		1581 (0.21)	1563	1556	1562	1583
ν_{19}	A_{2g}	1569 (∞)							1587				
ν_{37}	E_u		1583 (0.22)		1583 (0.22)	1584 (0.13)			1605 (0.24)	1583	1583		
$\nu_{(C=C)}$			1621 (0.24)		1622 (0.15)	1620 (0.19)		1619 (0.2)		1621	1619	1620	
$\nu_{(C=C)}$			1632[c]		overlapped[d]	1632 (0.33)		1632 (0.34)					
ν_{10}	B_{1g}	1632 (0.66)	1611[c]	1630[e]		1605			1638[f]			1607	1640

[a]The underlined frequencies are enhanced with the 514.5 nm excitation wavelength (data not shown). The species written in italics are the most predominant. [b]Not reported in the figures. [c]ρ cannot be determined due to the overlapping contribution of ν_{10} with the more intense $\nu_{(C=C)}$ band at 1621 cm^{-1}. [d]Overlapped with the ν_{10} at 1630 cm^{-1}. [e]ρ (0.42) cannot be precisely determined due to the overlapping contribution between this mode and the $\nu_{(C=C)}$ at about the same frequency. [f]ρ determined with 413.1 nm excitation wavelength. [g]Reference *28*. [h]Reference *30*. [i]Reference *13*.

A complete assignment of DHP, DHP-F, and DHP-OH in the high frequency region, compared to Mb, is reported in Table 1.

Figure 4 (panel A) compares the low-frequency RR spectra of WT-DHP and its adducts with fluoride and hydroxide. The DHP-F RR spectrum (Figure 4, trace b) shows a new band at 462 cm^{-1}, not present in the metaquo form (Figure 4, trace a). This band is assigned to the $\nu_{(Fe-F)}$ stretching mode by analogy with the corresponding band observed for Mb (*30*). The RR spectrum of DHP-OH shows new bands at 491 and 551 cm^{-1} (Figure 4, trace c) which are isotope sensitive. The band at 491 downshifts to 482 cm^{-1} in D_2O and to 471 cm^{-1} in $H_2{}^{18}O$, whereas the band at 551 cm^{-1} shifts to 542 cm^{-1} in D_2O and to 525 cm^{-1} in $H_2{}^{18}O$ (Figure 4, panel B). Therefore, they are assigned to the high-spin and low-spin Fe−OH stretching modes $\nu_{(Fe-OH)}$, respectively. Since the frequencies are identical to those previously reported for Mb (*13*), they indicate that the hydroxide derivative of DHP at room temperature exists in a thermal equilibrium between high- and low-spin states, as observed for myoglobin and other heme proteins.

The finding of two different $\nu_{(C=C)}$ vinyl stretching modes in all the ferric forms of DHP allows us to understand the slight difference observed in the electronic absorption spectra of the fluoride and hydroxyl complexes of DHP and Mb. In general, Soret and CT1 maxima shifts can occur when there are differences in the ligand field strength of the anionic ligand bound to the iron (*16*). However, the identity of the frequencies of the $\nu_{(Fe-F)}$ and $\nu_{(Fe-OH)}$ stretching modes between the two proteins allows us to exclude a different interaction between the exogenous ligand and the protein cavity. As a consequence, the blue shift of the Soret and CT1 bands between the complexes of DHP and Mb with anionic ligands derives from a different orientation of the two vinyl groups. The Soret band results from an electronic transition that involves π and π^* levels ($\pi \rightarrow \pi^*$), while the CT1 band is due to a transition from the $a_{2u}(\pi)$ porphyrin orbitals to $d\pi$ iron orbitals. The energy of the π orbitals depends on the coordination/spin state of the heme and the degree of conjugation between the heme group and its two vinyl substituents. Therefore, the electronic coupling between the vinyl groups and the porphyrin modulates the $\pi \rightarrow \pi^*$ and $a_{2u}(\pi) \rightarrow d\pi$ transitions and furnishes an enhancement mechanism for the vibrational modes of the vinyl groups in the RR spectra (*31*). In most cases, the vinyl substituents give rise to polarized bands around 1620−1630 cm^{-1}. A lower frequency is expected to correspond to a higher degree of conjugation between the vinyl group and the porphyrin π system. Increased conjugation with the vinyl group should shift the energy of the $\pi \rightarrow \pi^*$ and $a_{2u}(\pi) \rightarrow d\pi$ transitions to lower energy, thus shifting the Soret and CT1 maxima to the red. In Mb the two $\nu_{(C=C)}$ modes overlap at 1621 cm^{-1} (*28*). On the contrary, the RR spectra of DHP clearly show the presence of two vinyl stretching modes around 1620 and 1632 cm^{-1}. The presence of two vinyl bands in the spectra indicates that the protein matrix imposes different constraints on the two vinyl groups (*29*). The higher $\nu_{(C=C)}$ frequency in DHP, as compared to Mb, is consistent with a lower conjugation between the vinyl group and the porphyrin π system and, therefore, with the shift to higher energy of Soret and CT1.

The complete assignment of the high-frequency region RR modes of the WT-DHP and its complexes with small ligands and 4IP is reported in Table 1.

Binding of Halogenated Phenols. (*A*) *Room Temperature*. DHP has the capability to catalyze the peroxide-dependent dehalogenation of halogenated phenols (*1*). Contrasting results have been reported which suggest that substrate binding must precede H_2O_2 binding to optimize peroxidase activity (*24*) and vice versa (*32*). The DHP-4IP crystal structure (*9*) reveals that 4IP binds in an internal site of the distal heme cavity and forces H55 into a solvent-exposed position preventing coordination of the water molecule. Thus it is reasonable to hypothesize that the binding of this molecule affects the heme iron conformation and, therefore, its spin and coordination states. Figure 2 compares the RR spectra at pH 6 of WT-DHP (center), DHP-4IP (4IP:DHP = 30:1 molar ratio) (right), and DHP-TFP (TFP:DHP = 320:1 molar ratio) (left) complexes at room temperature (top spectra) and 12 K (bottom spectra). The existing X-ray heme cavity

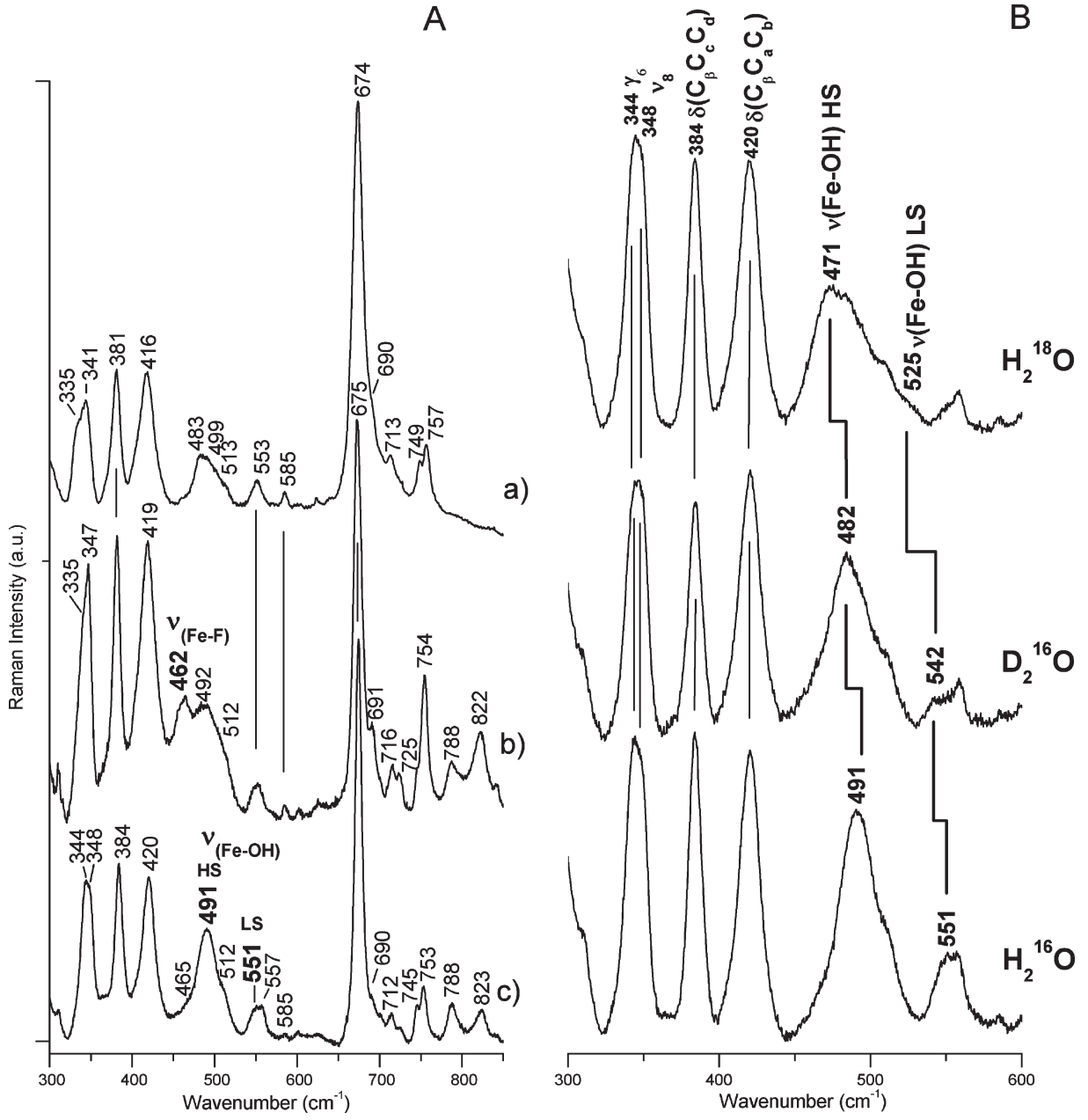

FIGURE 4: Panel A: RR spectra of (Fe^{3+})DHP at pH 6 (a), (Fe^{3+})DHP-F at pH 5 (b), and (Fe^{3+})DHP-OH at pH 9.6 (c) in 0.15 M potassium phosphate. Experimental conditions: (a) 406.7 nm excitation wavelength, 5 mW laser power at the sample, average of 9 spectra with 300 s integration time, 1.3 cm^{-1} spectral resolution; (b) 406.7 nm excitation wavelength, 5 mW laser power at the sample, average of 3 spectra with 600 s integration time, 1.3 cm^{-1} spectral resolution; (c) 413.1 nm excitation wavelength, 6 mW laser power at the sample, average of 3 spectra with 900 s integration time, 1.2 cm^{-1} spectral resolution. The intensities are normalized to that of the ν_7. Panel B: Low-frequency region RR spectra of (Fe^{3+})DHP-OH. Experimental conditions: excitation wavelength 413.1 nm, 6 mW laser power at the sample, 1.2 cm^{-1} spectral resolution. H_2O at pH 9.6 (average of 3 spectra with 900 s integration time), D_2O at pD 10.0 (average of 12 spectra with 900 s integration time), and $H_2{}^{18}O$ at pH 9.6 (average of 18 spectra with 900 s integration time). The intensities are normalized to that of ν_7 (not shown). Spectra have been shifted along the ordinate axis to allow better visualization.

structures are also shown. Upon binding 4IP, the predominant species changes from 6cHS (ν_3 at 1483 cm^{-1}, ν_{37} at 1583 cm^{-1}) to 5cHS (ν_3 at 1494 cm^{-1}, ν_2 at 1568 cm^{-1}, ν_{10} at 1630 cm^{-1}). Accordingly, the broadening and 6 nm blue shift of the Soret maximum (399 nm) together with the red shift of the CT1 (641 nm) (Figure S1, Supporting Information) are consistent with the formation of a 5cHS species, as previously suggested by the room temperature crystal structure of the DHP-4IP complex (*9*) (Figure 2, right). On the basis of depolarization studies (see Table 1) the frequencies of the vinyl stretches are observed to change slightly upon 4IP binding. In particular, one mode is identified at 1622 cm^{-1} while the second downshifts and overlaps with the ν_{10} mode at 1630 cm^{-1}. The shift in frequency of the vinyl stretching modes is in accord with the changes of the torsional angles estimated from the crystallographic data of the 4IP-DHP complex (*1*, *9*).

The binding of TFP to DHP has a quite different effect on the RR spectrum. In the presence of a 10-fold excess of TFP there are no significant differences at 298 K (and 12 K, see below) with respect to the wild-type form, while upon addition of a 40−320-fold excess of TFP at 298 K, a slight increase of 6cHS species is revealed by the intensification of the RR bands at 1483 cm^{-1} (ν_3) and 1611 cm^{-1} (ν_{10}) (Figure 2, left bottom, and Figure S2, Supporting Information).

(*B*) *Low Temperature*. The RR spectrum of WT-DHP at 12 K shows a markedly reduced amount of 5cHS, confirming the structural data obtained at 100 K by de Serrano et al. (*8*) in which the distal histidine is present only in the closed conformation (Figure 2, center bottom). These data are in agreement with the electronic absorption spectrum at 12 K, which shows a 3 nm red shift of the Soret band and 11 nm blue shift of the CT1 (data not shown). Unlike WT-DHP, the RR spectrum of the DHP-4IP complex at 12 K indicates the presence of a pure 5cHS species. The small amount of 6cHS (ν_3 at 1483 cm^{-1}) observed at 298 K disappears, indicating a higher affinity of 4IP for DHP at low temperature. As previously noted for other heme proteins at low temperature (*13*) an increased frequency (of about 2−6 cm^{-1}) of the 5cHS core size marker bands is observed at low temperature in the RR spectra as a consequence of a contraction of the heme cavity. The binding of TFP to DHP has a quite different effect on the RR spectrum. In the presence of a 10-fold excess of TFP there are no significant differences at both 298 and 12 K with respect to the wild-type form; however, the RR spectrum at 12 K of the DHP-TFP complex for a 40-fold excess of TFP shows an increase of the 5cHS population (ν_3 at 1496 cm^{-1}, ν_2 at 1573 cm^{-1}, and ν_{10} at 1636 cm^{-1}) (Figure S2, Supporting Information), which becomes the only species present for a 320-fold excess (Figure 2 left top). A possible explanation of this effect is that a large excess of TFP can cause nonspecific binding of the ligand due to the packing forces exerted by the lower temperature. However, a more plausible explanation is that at room temperature the binding mechanism of TFP is different from that of 4IP. Recently ^{1}H NMR, ^{19}F NMR, and relaxation data consistent with an external binding site for TFP have been reported, but the location of that site has not been determined (*22*). The RR data at 12 K suggest that TFP binds inside the distal cavity side, as 4IP, even if binding at the external site, which might induce allosteric changes to the protein matrix forcing the distal histidine into the open conformation, cannot be completely ruled out. However, binding of TFP at the internal site at 12 K is also in agreement with cryogenic FTIR (*20*) and EPR experiments (*21*), which had shown that the substrate affects the distal pocket of DHP at cryogenic temperatures. In particular, cryogenic HYSCORE measurements showed that at a 10-fold excess of TFP relative to DHP a heme-bound water molecule in the resting state of the ferric form is displaced when the substrate binds, resulting in a transition from 6- to 5-coordinated iron (*21*).

The corresponding EPR spectra of the DHP complexes with 4IP and TFP obtained at 5 K (Figure 5) are in overall agreement with the RR spectra at 12 K. WT-DHP is characterized by a mixture of 6cHS ($g_\perp$ 6.00, $g_{||}$ 2.00) and 5cHS (6.09, 5.54, 2.00) forms (Figure 5, trace a). The progressive addition of TFP (up to 320-fold excess) leads to an increasing proportion of 5cHS with respect to 6cHS species (Figure 5, traces b and c). Addition of 4IP (30-fold excess) leads to a pure 5cHS state, characterized by a more rhombic *g* tensor (6.22, 5.50, 1.99) (Figure 5, trace d) compared to DHP alone or in the presence of TFP. The EPR bandwidth is also greater in the presence of 4IP, indicating that there is *g*-strain at these HS sites probably resulting from some structural instability which gives a distribution of values.

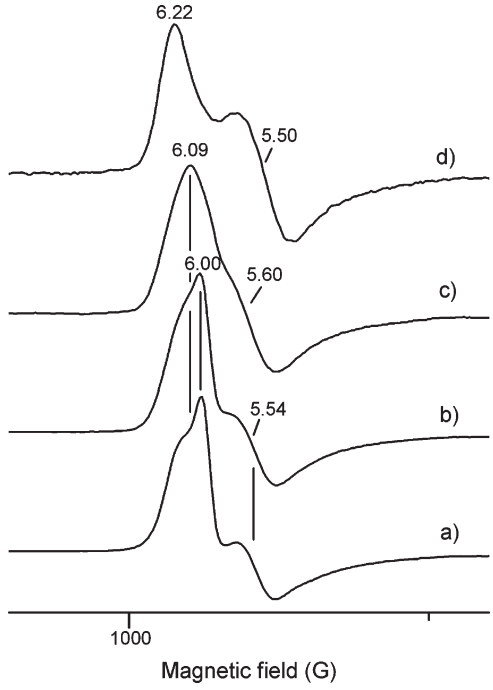

FIGURE 5: X-band EPR spectra showing the low-field $g_\perp$ region of DHP (a), DHP-TFP, 1:10 (b), and 1:320 molar ratio (c) and DHP-4IP (1:30 molar ratio) (d) at pH 6 in 0.15 M phosphate/glycerol, 30% (v/v). The spectra were recorded at 5 K, 1 mW microwave power, and 10 G modulation amplitude. Spectra have been shifted along the ordinate axis to allow better visualization.

DISCUSSION

Flexibility of the Distal Histidine in DHP. (*A*) *WT-(Fe^{3+})DHP*. The present spectroscopic characterization carried out in solution is in accord with the crystal structure at 298 K (*9*) in which His55 was observed to reside simultaneously in the open and closed conformations with nearly equal populations. In one of the two conformations His55 is located in the distal cavity, whereas in the second conformation it is positioned away from the distal pocket toward the solvent. The RR data clearly indicate that at room temperature the protein exists in equilibrium between the 6cHS and 5cHS states. In the 6cHS form a water molecule is coordinated to the iron and hydrogen-bonded to a distal histidine (His55), which is orientated toward the heme (closed conformation) whereas in the 5cHS state His55 is exposed to the solvent. Therefore, unlike the resting state of peroxidases, where the heme sixth coordination site is vacant or bound weakly to water (*12*), at pH 6 ferric wild-type DHP contains an metaquo 6cHS species with His55 located in the distal cavity and weakly hydrogen-bonded to the water molecule (closed conformation) (Figure 6) ($N_\delta-O_{H_2O}$ = 3.24 Å). Furthermore, at low temperature the equilibrium is shifted toward the 6cHS form (closed conformation), in perfect agreement with the recent structure obtained at 100 K which shows that, similar to the distance observed in myoglobin at neutral pH (*7*), the His55 is 0.75 Å closer to the heme iron than in the 298 K structure (*9*).

(*B*) *(Fe^{3+})DHP in the Presence Halogenated Phenols*. The internal binding site of DHP has been characterized by X-ray crystallography (*9*, *33*). The structure of the DHP-4IP complex shows that the monohalophenol binding pocket is surrounded largely by hydrophobic residues (F21, F24, F35, F52, V59, F60, and L100) as well as a tyrosine (Y38). The hydroxyl group of the 4IP substrate can act as a hydrogen bond acceptor for the hydroxyl group of Y38 (distance 3.7 Å), with the distal His positioned out of the cavity (open conformation) (*9*). As a consequence, no water molecule is observed in the close vicinity of the Fe atom, and accordingly, the RR spectra are characteristic of a mainly 5cHS heme. Moreover, as observed in the X-ray structure at room temperature, the RR data confirm the changes in the

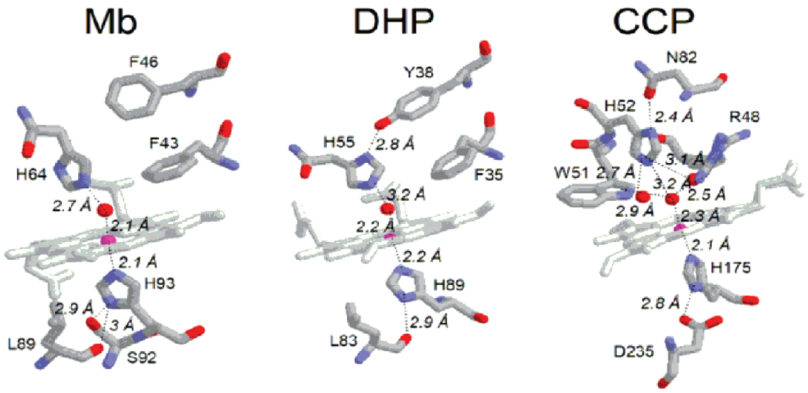

FIGURE 6: Comparison between the heme binding pockets of (Fe^{3+})Mb (PDB code 1A6K) (*36*), (Fe^{3+})DHP (PDB code 2QFK (subunit A)) (*8*), and (Fe^{3+})CCP (PDB code 1ZBY) (*42*), showing the key residues and water molecules in each case.

vinyl orientation upon 4IP binding. At low temperature, RR core size marker bands and EPR clearly indicate that only the 5cHS species exists. Therefore, at cryogenic temperature the equilibrium of distal histidine conformations shifts toward the open conformation, indicating the stabilization of 4IP in the distal pocket binding site at low temperature. Unlike 4IP, at room temperature TFP binds in an external binding site of the heme (*22*) maintaining the 6cHS coordination of the resting protein, while at 15 K an increased amount of 5cHS is observed, leading us to conclude, in agreement with previous reports (*20*, *21*), that TFP binds inside the distal cavity, as 4IP, forcing the distal histidine in the open conformation.

Push−*Pull Effect in* (Fe^{3+}) *DHP Compared to Peroxidases and Globins*. The heme enzyme DHP is a hemoglobin known to have excellent peroxidase activity under physiological conditions (*1*, *24*). For heme-containing peroxidases, the postulated mechanism of peroxide decomposition relies on the concerted roles played by the conserved proximal histidine and the distal histidine and arginine through H-bonds and charge stabilization (*12*). However, unlike peroxidases, DHP lacks some of the main features which determine the peroxidase activity: on the distal side of the heme in peroxidases, the conserved positively charged guanidinium of an arginine residue and an H-bond from the distal histidine N_δ atom to a nearby asparagine (2.4 Å in CCP, Figure 6, right) depress the histidine pK_a, constraining N_ε to act as a H-bond acceptor during the catalytic cycle (*34*). Although the Tyr38 residue of DHP has a strong interaction with H55 (Figure 6, middle), the pK_a of H55 is approximately 4.5, which is identical to that in Mb at room temperature (*35*). Moreover, the Y38F mutant appears to have a greater initial catalytic rate than wild type. Hence, in DHP there is no obvious analogue to the arginine interaction in peroxidases.

In general, the DHP secondary structure is very similar to that of SWMb (*36*) with the overall disposition of the key α-helices (B, C, D, E, and F) nearly identical. However, on the distal side, His55 in DHP has been reported at different distances from the heme iron, ranging from 5.4 Å (*9*) to 4.8 Å (*8*). While the first reported distance is more similar to the distal cavity of peroxidases than globins, the second structure reports a distance closer to that observed in other globins including SWMb, where the distal His64 is 4.3 Å from the heme iron and H-bonded to a distal water molecule (Figure 6, left). Nevertheless, the close similarity of the frequencies of the $\nu_{(Fe-F)}$ (462 cm^{-1}) and $\nu_{(Fe-OH)}$ (491 and 551 cm^{-1} for the HS and LS forms, respectively) stretching modes in the fluoride and hydroxyl adducts of DHP and Mb (*13*, *30*) but markedly different from the corresponding frequencies observed in peroxidases ($\nu_{(Fe-F)}$ at 385 cm^{-1} for HRP (*37*) and only a LS $\nu_{(Fe-OH)}$ around 500−507 cm^{-1} for various peroxidases (*13*, *38*−*40*)) clearly indicates that these ligands bind the heme iron in a similar manner in both DHP and Mb but quite different from that of peroxidases. In particular, in peroxidases, the Arg is determinant in controlling the ligand binding via a strong hydrogen bond between the positively charged guanidinium group and the anion (*13*, *15*, *16*, *41*). Recently, a high-resolution X-ray structure of resting state CCP revealed that the key residue for the formation of the catalytic intermediate compound, distal Arg48, occupies two positions: one "out" positioned close to the heme propionate and the other "in" positioned close to the heme iron. In the catalytic intermediate compound only the "in" position exists, which enables Arg48 to H-bond with the ferryl O ligand (*42*). The "in" position has been observed also in the CCP fluoride complex where the Arg48 guanidinium group moves about 2.5 Å toward the ligand to form a hydrogen bond with fluoride (*11*). Therefore, while in peroxidases the distal His contributes to the stability of the fluoride complex presumably by accepting a proton from HF and hydrogen bonding, through a water molecule, to the anion (*14*, *16*, *41*), in Mb it is the sole amino acid responsible for stabilization of the heme-coordinated ligand. The X-ray structure of the SWMb-F adduct has revealed that the fluoride anion, coordinated to the heme iron, is hydrogen-bonded to a water molecule (W195) which, in turn, is hydrogen-bonded to the N_ε of the distal histidine (*10*).

On the basis of the spectroscopic results and by analogy with Mb, we suggest that a hydrogen bond network may exist between the His55, a water molecule, and the fluoride in DHP. However, this conclusion implies that the distal His, similarly to Arg48 in CCP, may undergo a conformational change that places it within hydrogen-bonding distance of the anionic ligand. In analogy to the role played by the distal Arg in CCP (*41*) the spectroscopic data suggest that the movement of the distal His55 in DHP is determinant in stabilizing only the anionic ligand binding. In fact, when other ligands without an electrical charge, such as CO and NO, are bound to the heme iron, the interaction of the distal His with the heme-bound ligand is weaker than in myoglobins. In particular, CO is an excellent probe for investigating the distal cavity of heme proteins (*43*), since back-donation from the Fe dπ to the CO π^* orbitals is increased by polar interactions and formation of H-bonds between the bound CO and the distal protein residues. As a consequence, the Fe−C bond strengthens while the CO bond weakens, thereby increasing the $\nu_{(FeC)}$ vibrational frequencies and decreasing the $\nu_{(CO)}$ frequencies. A linear correlation with negative slope between the frequencies

of the $\nu_{(FeC)}$ and $\nu_{(CO)}$ stretching modes has been found for a large class of CO complexes of heme proteins containing imidazole as the fifth iron ligand. The $\nu_{(FeC)}/\nu_{(CO)}$ position along the correlation line reflects the type and strength of distal polar interactions. In the DHP-CO complex the slightly higher $\nu_{(CO)}$ (1950 vs 1947 cm^{-1}) and lower $\nu_{(FeC)}$ (499 vs 507 cm^{-1}) stretching frequencies than SWMb (*44*−*46*) (see Figure S3, Supporting Information) indicate a less polar environment around the CO ligand, possibly resulting from a larger distance between the CO and the imidazole. This is in agreement with the Fe−$N_{distal\ His}$ distance of 4.8−5.4 Å (*8*, *9*) vs 4.3 Å (*36*) observed in the X-ray structure of ferric DHP and Mb, respectively. In addition, recently it has been shown that the protein interactions with photolyzed NO are weaker in DHP than in the wild-type MbNO (for both SW and horse heart) (*47*).

The concerted interaction of the distal His and Arg with hydrogen peroxide bound to the heme has been called "the pull effect" (*48*−*50*). Therefore, the pull component in peroxidases is created by the distal histidine functioning as an acid/base in proton transfer to the leaving water molecule with the positively charged arginine stabilizing the developing negative charge (*48*, *50*). On the proximal side of peroxidases, the conserved H-bond between the N_δ atom of the imidazole fifth ligand and the carboxylate of an aspartic side chain, which acts as a H-bond acceptor, imparts an imidazolate character to the histidine ligand (*12*, *41*, *51*). The increased electron donation of the proximal imidazole ligand is called "the push effect" since it stabilizes the high oxidation state of the iron intermediate compound, leading to the rapid reaction of peroxidases with hydrogen peroxide (*52*).

In DHP the N_δ atom of the proximal His interacts with the carbonyl group of a Leu residue (Leu83). On the basis of the $\nu_{(Fe-Im)}$ stretching frequency of DHP (233 cm^{-1}), the authors concluded (*45*) that the H-bond appears to be stronger than in Mb (218−221 cm^{-1}) (*53*, *54*) but weaker than in peroxidases (*12*). However, a weaker imidazolate character of the proximal Fe ligand is not expected to impair the peroxidase activity of DHP (*55*). In fact, studies of proximal variants of various peroxidases clearly indicate that the "electron push" effect may not be so important for the activity since the strength of the proximal histidine−aspartate hydrogen bond can be modulated without serious effects on the peroxide cleavage step (*12*).

Therefore, the present results strongly support the view that for DHP the distal His is the only residue capable of performing proton shuttling in the active site. In the presence of negatively charged ligands, a conformational change places the distal His within hydrogen-bonding distance of the ligands, underlying its important role in anionic ligand stabilization.

CONCLUSION

In conclusion, the present work highlights the different stabilization mechanisms of heme−iron ligands exerted by the distal residues in DHP compared to Mb and peroxidases. For the latter proteins, the Arg is determinant in controlling the ligand binding via a strong hydrogen bond between the positively charged guanidinium group and the anion. The distal His accepts a proton and is hydrogen-bonded (probably through a water molecule) with the iron-coordinated ligand. For DHP (and Mb) the distal His is the only residue responsible for the stabilization of ligands coordinated to the heme iron. However, unlike Mb, in DHP the distal His is highly mobile and undergoes a conformational change to establish a strong hydrogen bond with ligands. At room temperature, in the ferric state, in the absence of a heme ligand, the distal histidine is in equilibrium between the open solvent-exposed position (5cHS) and the closed conformation (6cHS). The equilibrium shifts to the closed conformation at 12 K. The link between the histidine and heme iron coordination extends to the binding of phenols in the distal pocket. In fact, binding of 4IP in the distal heme cavity shifts the equilibrium toward the open conformation, as the protein is in a 5cHS state, while TFP binds externally to the distal side at room temperature (6cHS) but inside the heme cavity at low temperature. When considered in the light of the recent finding that there is an external substrate binding site in DHP (*22*), the movement of H55 appears to play a role in a regulatory mechanism in DHP function. The spectra presented here show that the flexibility of the distal histidine leads to the possibility of differing hydrogen bond strength for anionic and neutral ligands to the heme iron. This level of control may, in turn, be important in explaining how a single distal histidine can provide the peroxidase "pull" that is usually thought to require the concerted action of an arginine in proximity to the distal histidine.

ACKNOWLEDGMENT

We thank Dr. Maria Fittipaldi for provision of EPR facilities and assistance in recording the spectra.

SUPPORTING INFORMATION AVAILABLE

UV−vis spectra of (Fe^{3+})DHP and 4IP-(Fe^{3+})DHP at pH 6 in 0.15 M potassium phosphate, RR spectra of TFP-(Fe^{3+})DHP (40:1 molar ratio) at 298 and 12 K at pH 6 in 150 mM phosphate and 30% (v/v) glycerol, and a plot of the frequencies of the $\nu_{(FeC)}$ and $\nu_{(CO)}$ for DHP-CO at pH 7.0, Mb-CO at both pH 7.0 and 2.6, and Hb from *B. subtilis* at pH 7.0. This material is available free of charge via the Internet at http://pubs.acs.org.

REFERENCES

1. Chen, Y. P., Woodin, S. A., Lincoln, D. E., and Lovell, C. R. (1996) An unusual dehalogenating peroxidase from the marine terebellid polychaete *Amphitrite ornata*. *J. Biol. Chem. 271*, 4609–4612.
2. Welinder, K. G. (1992) Superfamily of plant, fungal and bacterial peroxidases. *Curr. Opin. Struct. Biol. 2*, 388–393.
3. Poulos, T. L., and Kraut, J. (1980) The stereochemistry of peroxidase catalysis. *J. Biol. Chem. 255*, 8199–8205.
4. Sitter, A. J., Reczek, C. M., and Terner, J. (1985) Heme-linked ionization of horseradish peroxidase compound II monitored by the resonance Raman Fe(IV)═O stretching vibration. *J. Biol. Chem. 260*, 7515–7522.
5. Smith, A. T., and Veitch, N. C. (1998) Substrate binding and catalysis in heme peroxidases. *Curr. Opin. Chem. Biol. 2*, 269–278.
6. Vitello, L. B., Erman, J. E., Miller, M. A., Wang, J., and Kraut, J. (1993) Effect of arginine-48 replacement on the reaction between cytochrome *c* peroxidase and hydrogen peroxide. *Biochemistry 32*, 9807–9818.
7. Chen, Z., de Serrano, V., Betts, L., and Franzen, S. (2009) Distal histidine conformational flexibility in dehaloperoxidase from *Amphitrite ornata*. *Acta Crystallogr., Sect. D: Biol. Crystallogr. 65*, 34–40.
8. de Serrano, V., Chen, Z., Davis, M. F., and Franzen, S. (2007) X-ray crystal structural analysis of the binding site in the ferric and oxyferrous forms of the recombinant heme dehaloperoxidase cloned from *Amphitrite ornata*. *Acta Crystallogr., Sect. D: Biol. Crystallogr. 63*, 1094–1101.
9. LaCount, M. W., Zhang, E., Chen, Y. P., Han, K., Whitton, M. M., Lincoln, D. E., Woodin, S. A., and Lebioda, L. (2000) The crystal structure and amino acid sequence of dehaloperoxidase from *Amphitrite ornata* indicate common ancestry with globins. *J. Biol. Chem. 275*, 18712–18716.
10. Aime, S., Fasano, M., Paoletti, S., Cutruzzola, F., Desideri, A., Bolognesi, M., Rizzi, M., and Ascenzi, P. (1996) Structural determinants of fluoride and formate binding to hemoglobin and myoglobin: crystallographic and ^{1}H-NMR relaxometric study. *Biophys. J. 70*, 482–488.

11. Edwards, S. L., and Poulos, T. L. (1990) Ligand binding and structural perturbations in cytochrome *c* peroxidase. A crystallographic study. *J. Biol. Chem. 265*, 2588–2595.
12. Smulevich, G., Feis, A., and Howes, B. D. (2005) Fifteen years of Raman spectroscopy of engineered heme containing peroxidases: what have we learned? *Acc. Chem. Res. 38*, 433–440.
13. Feis, A., Marzocchi, M. P., Paoli, M., and Smulevich, G. (1994) Spin state and axial ligand bonding in the hydroxide complexes of metmyoglobin, methemoglobin, and horseradish peroxidase at room and low temperatures. *Biochemistry 33*, 4577–4583.
14. Howes, B. D., Rodriguez-Lopez, J. N., Smith, A. T., and Smulevich, G. (1997) Mutation of distal residues of horseradish peroxidase: influence on substrate binding and cavity properties. *Biochemistry 36*, 1532–1543.
15. Neri, F., Indiani, C., Welinder, K. G., and Smulevich, G. (1998) Mutation of the distal arginine in *Coprinus cinereus* peroxidase—structural implications. *Eur. J. Biochem. 251*, 830–838.
16. Neri, F., Kok, D., Miller, M. A., and Smulevich, G. (1997) Fluoride binding in hemoproteins: the importance of the distal cavity structure. *Biochemistry 36*, 8947–8953.
17. Poulos, T. L., and Fenna, R. E. (1994) in Metal Ions in Biological Systems (Siegel, H., Ed.) pp 25−75, Marcel Dekker, New York.
18. Badyal, S. K., Metcalfe, C. L., Basran, J., Efimov, I., Moody, P. C., and Raven, E. L. (2008) Iron oxidation state modulates active site structure in a heme peroxidase. *Biochemistry 47*, 4403–4409.
19. Williams, P. A., Fulop, V., Garman, E. F., Saunders, N. F., Ferguson, S. J., and Hajdu, J. (1997) Haem-ligand switching during catalysis in crystals of a nitrogen-cycle enzyme. *Nature 389*, 406–412.
20. Nienhaus, K., Deng, P. C., Belyea, J., Franzen, S., and Nienhaus, G. U. (2006) Spectroscopic study of substrate binding to the carbomonoxy form of dehaloperoxidase from *Amphitrite ornata*. *J. Phys. Chem. 110*, 13264–13276.
21. Smirnova, T. I., Weber, R. T., Davis, M. F., and Franzen, S. (2008) Substrate binding triggers a switch in the iron coordination in dehaloperoxidase from *Amphitrite ornata*: HYSCORE experiments. *J. Am. Chem. Soc. 130*, 2128–2129.
22. Davis, M. F., Gracz, H., Vendeix, F. A., de Serrano, V., Somasundaram, A., Decatur, S. M., and Franzen, S. (2009) Different modes of binding of mono-, di-, and trihalogenated phenols to the hemoglobin dehaloperoxidase from *Amphitrite ornata*. *Biochemistry 48*, 2164–2172.
23. Davis, M. F., Bobay, B. G., and Franzen, S. (2010) Determination of separate inhibitor and substrate binding sites in the dehaloperoxidase-hemoglobin from *Amphitrite ornata*. *Biochemistry* (in press).
24. Belyea, J., Gilvey, L. B., Davis, M. F., Godek, M., Sit, T. L., Lommel, S. A., and Franzen, S. (2005) Enzyme function of the globin dehaloperoxidase from *Amphitrite ornata* is activated by substrate binding. *Biochemistry 44*, 15637–15644.
25. Osborne, R. L., Sumithran, S., Coggins, M. K., Chen, Y. P., Lincoln, D. E., and Dawson, J. H. (2006) Spectroscopic characterization of the ferric states of *Amphitrite ornata* dehaloperoxidase and Notomastus lobatus chloroperoxidase: His-ligated peroxidases with globin-like proximal and distal properties. *J. Inorg. Biochem. 100*, 1100–1108.
26. Eaton, W. A., and Hochstrasser, R. M. (1968) Single-crystal spectra of ferrimyoglobin complexes in polarized light. *J. Chem. Phys. 49*, 985–995.
27. Belyea, J., Belyea, C. M., Lappi, S., and Franzen, S. (2006) Resonance Raman study of ferric heme adducts of dehaloperoxidase from *Amphitrite ornata*. *Biochemistry 45*, 14275–14284.
28. Hu, S., Smith, K. M., and Spiro, T. G. (1996) Assignment of protoheme resonance Raman spectrum by heme labeling in myoglobin. *J. Am. Chem. Soc. 118*, 12638–12646.
29. Marzocchi, M. P., and Smulevich, G. (2003) Relationship between heme vinyl conformation and the protein matrix in peroxidases. *J. Raman Spectrosc. 34*, 725–736.
30. Desbois, A., Lutz, M., and Banerjee, R. (1979) Low-frequency vibrations in resonance Raman spectra of horse heart myoglobin. Iron-ligand and iron-nitrogen vibrational modes. *Biochemistry 18*, 1510–1518.
31. Spiro, T. G., and Li, X.-Y. (1988) in Biological Application of Raman Spectroscopy (Spiro, T. G., Ed.) Vol. *3*, pp 1−37, Wiley Interscience, New York.
32. Osborne, R. L., Coggins, M. K., Raner, G. M., Walla, M., and Dawson, J. H. (2009) The mechanism of oxidative halophenol dehalogenation by *Amphitrite ornata* dehaloperoxidase is initiated by H_2O_2 binding and involves two consecutive one-electron steps: role of ferryl intermediates. *Biochemistry 48*, 4231–4238.
33. de Serrano, V. S., Franzen, S., Thompson, M. K., Davis, M. F., Nicoletti, F. P., Howes, B. D., Smulevich, G. (2010) Two-site competitive inhibition in dehaloperoxidase-hemoglobin. Structures of the complexes of DHP with 4-fluoro- (3LB1), 4-chloro- (3LB2), 4-bromo- (3LB3), and 4-iodophenol (3LB4) have been deposited at the Protein Data Bank.
34. Smulevich, G., Miller, M. A., Kraut, J., and Spiro, T. G. (1991) Conformational change and histidine control of heme chemistry in cytochrome *c* peroxidase: resonance Raman evidence from Leu-52 and Gly-181 mutants of cytochrome *c* peroxidase. *Biochemistry 30*, 9546–9558.
35. Nienhaus, K., Nickel, E., Davis, M. F., Franzen, S., and Nienhaus, G. U. (2008) Determinants of substrate internalization in the distal pocket of dehaloperoxidase hemoglobin of *Amphitrite ornata*. *Biochemistry 47*, 12985–12994.
36. Vojtechovsky, J., Chu, K., Berendzen, J., Sweet, R. M., and Schlichting, I. (1999) Crystal structures of myoglobin-ligand complexes at near-atomic resolution. *Biophys. J. 77*, 2153–2174.
37. Yu, N. T. (1986) Resonance Raman studies of ligand binding. *Methods Enzymol. 130*, 350–409.
38. Nissum, M., Feis, A., and Smulevich, G. (1998) Characterization of soybean seed coat peroxidase: resonance Raman evidence for a structure-based classification of plant peroxidases. *Biospectroscopy 4*, 355–364.
39. Sitter, A. J., Shifflett, J. R., and Terner, J. (1988) Resonance Raman spectroscopic evidence for heme iron-hydroxide ligation in peroxidase alkaline forms. *J. Biol. Chem. 263*, 13032–13038.
40. Smulevich, G., Hu, S. Z., Rodgers, K. R., Goodin, D. B., Smith, K. M., and Spiro, T. G. (1996) Heme-protein interactions in cytochrome *c* peroxidase revealed by site-directed mutagenesis and resonance Raman spectra of isotopically labeled hemes. *Biospectroscopy 2*, 365–376.
41. Smulevich, G. (1998) Understanding heme cavity structure of peroxidases: comparison of electronic absorption and resonance Raman spectra with crystallographic results. *Biospectroscopy 4*, S3–S17.
42. Bonagura, C. A., Bhaskar, B., Shimizu, H., Li, H., Sundaramoorthy, M., McRee, D. E., Goodin, D. B., and Poulos, T. L. (2003) High-resolution crystal structures and spectroscopy of native and compound I cytochrome *c* peroxidase. *Biochemistry 42*, 5600–5608.
43. Spiro, T. G., and Wasbotten, I. H. (2005) CO as a vibrational probe of heme protein active sites. *J. Inorg. Biochem. 99*, 34–44.
44. Anderton, C. L., Hester, R. E., and Moore, J. N. (1997) A chemometric analysis of the resonance Raman spectra of mutant carbonmonoxy-myoglobins reveals the effects of polarity. *Biochim. Biophys. Acta 1338*, 107–120.
45. Franzen, S., Roach, M. P., Chen, Y.-P., Dyer, R. B., Woodruff, W. H., and Dawson, J. H. (1998) The unusual reactivities of *Amphitrite ornata Notomastus lobatus* chloroperoxidase do not imidazolate proximal heme iron ligand. *J. Am. Chem. Soc. 120*, 4658–4661.
46. Tsubaki, M., Srivastava, R. B., and Yu, N. T. (1982) Resonance Raman investigation of carbon monoxide bonding in (carbon monoxy)hemoglobin and -myoglobin: detection of Fe-CO stretching and Fe-C-O bending vibrations and influence of the quaternary structure change. *Biochemistry 21*, 1132–1140.
47. Franzen, S., Jasaitis, A., Belyea, J., Brewer, S. H., Casey, R., MacFarlane, A. W. t., Stanley, R. J., Vos, M. H., and Martin, J. L. (2006) Hydrophobic distal pocket affects NO-heme geminate recombination dynamics in dehaloperoxidase and H64V myoglobin. *J. Phys. Chem. B 110*, 14483–14493.
48. Dawson, J. H. (1988) Probing structure-function relations in heme-containing oxygenases and peroxidases. *Science 240*, 433–439.
49. Erman, J. E., Vitello, L. B., Miller, M. A., Shaw, A., Brown, K. A., and Kraut, J. (1993) Histidine 52 is a critical residue for rapid formation of cytochrome *c* peroxidase compound I. *Biochemistry 32*, 9798–9806.
50. Poulos, T. L. (1988) Heme enzyme crystal structures. *Adv. Inorg. Biochem. 7*, 1–36.
51. Smulevich, G., Mauro, J. M., Fishel, L. A., English, A. M., Kraut, J., and Spiro, T. G. (1988) Heme pocket interactions in cytochrome *c* peroxidase studied by site-directed mutagenesis and resonance Raman spectroscopy. *Biochemistry 27*, 5477–5485.
52. Finzel, B. C., Poulos, T. L., and Kraut, J. (1984) Crystal structure of yeast cytochrome *c* peroxidase refined at 1.7-Å resolution. *J. Biol. Chem. 259*, 13027–13036.
53. Argade, P. V., Sassaroli, M., Rousseau, D. L., Inubushi, T., Ikeda-Saito, M., and Lapidot, A. (1984) Confirmation of the assignment of the iron-histidine stretching mode in myoglobin. *J. Am. Chem. Soc. 106*, 6593–6596.
54. Teraoka, J., and Kitagawa, T. (1981) Structural implication of the heme-linked ionization of horseradish peroxidase probed by the Fe-histidine stretching Raman line. *J. Biol. Chem. 256*, 3969–3977.
55. Franzen, S. (2001) Effect of a charge relay on the vibrational frequencies of carbonmonoxy iron porphine adducts: the coupling of changes in axial ligand bond strength and porphine core size. *J. Am. Chem. Soc. 123*, 12578–12589.

Acta Crystallographica Section D
Biological Crystallography
ISSN 0907-4449
Editors: **E. N. Baker and Z. Dauter**

X-ray structure of the metcyano form of dehaloperoxidase from *Amphitrite ornata*: evidence for photoreductive dissociation of the iron–cyanide bond

V. S. de Serrano, M. F. Davis, J. F. Gaff, Qi Zhang, Z. Chen, E. L. D'Antonio, E. F. Bowden, R. Rose and S. Franzen

Acta Cryst. (2010). D**66**, 770–782

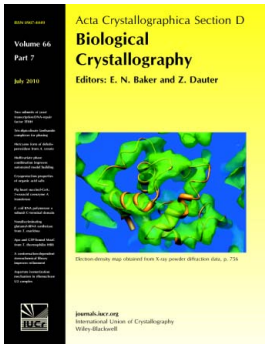

Acta Crystallographica Section D: Biological Crystallography welcomes the submission of papers covering any aspect of structural biology, with a particular emphasis on the structures of biological macromolecules and the methods used to determine them. Reports on new protein structures are particularly encouraged, as are structure–function papers that could include crystallographic binding studies, or structural analysis of mutants or other modified forms of a known protein structure. The key criterion is that such papers should present new insights into biology, chemistry or structure. Papers on crystallographic methods should be oriented towards biological crystallography, and may include new approaches to any aspect of structure determination or analysis.

Acta Crystallographica Section D
Biological Crystallography
ISSN 0907-4449

X-ray structure of the metcyano form of dehaloperoxidase from *Amphitrite ornata*: evidence for photoreductive dissociation of the iron–cyanide bond

V. S. de Serrano,[a] M. F. Davis,[a] J. F. Gaff,[a] Qi Zhang,[a] Z. Chen,[a] E. L. D'Antonio,[a] E. F. Bowden,[a] R. Rose[b] and S. Franzen[a]*

[a]Department of Chemistry, North Carolina State University, Raleigh, NC 27695, USA, and [b]Department of Biochemistry, North Carolina State University, Raleigh, NC 27695, USA

Correspondence e-mail: stefan_franzen@ncsu.edu

Received 27 January 2010
Accepted 20 April 2010

PDB References: metcyano form of dehaloperoxidase, wild type, 3kun; C73S mutant, 3kuo.

X-ray crystal structures of the metcyano form of dehaloperoxidase-hemoglobin (DHP A) from *Amphitrite ornata* (DHPCN) and the C73S mutant of DHP A (C73SCN) were determined using synchrotron radiation in order to further investigate the geometry of diatomic ligands coordinated to the heme iron. The DHPCN structure was also determined using a rotating-anode source. The structures show evidence of photoreduction of the iron accompanied by dissociation of bound cyanide ion (CN^-) that depend on the intensity of the X-ray radiation and the exposure time. The electron density is consistent with diatomic molecules located in two sites in the distal pocket of DHPCN. However, the identities of the diatomic ligands at these two sites are not uniquely determined by the electron-density map. Consequently, density functional theory calculations were conducted in order to determine whether the bond lengths, angles and dissociation energies are consistent with bound CN^- or O_2 in the iron-bound site. In addition, molecular-dynamics simulations were carried out in order to determine whether the dynamics are consistent with trapped CN^- or O_2 in the second site of the distal pocket. Based on these calculations and comparison with a previously determined X-ray crystal structure of the C73S–O_2 form of DHP [de Serrano *et al.* (2007), *Acta Cryst.* D**63**, 1094–1101], it is concluded that CN^- is gradually replaced by O_2 as crystalline DHP is photoreduced at 100 K. The ease of photoreduction of DHP A is consistent with the reduction potential, but suggests an alternative activation mechanism for DHP A compared with other peroxidases, which typically have reduction potentials that are 0.5 V more negative. The lability of CN^- at 100 K suggests that the distal pocket of DHP A has greater flexibility than most other hemoglobins.

1. Introduction

Dehaloperoxidase (DHP A) is a truncated hemoglobin originally isolated from the terebellid polychaete *Amphitrite ornata* that has been cloned and expressed in *Escherichia coli* (Belyea *et al.*, 2005). DHP A is unique within the globin family because it is bifunctional, with both O_2-transport and peroxidase activities, which are regulated by external substrate binding and internal inhibitor binding (Thompson *et al.*, 2010). Two genes code for dehaloperoxidase-hemoglobins in *A. ornata*: *dhpA* and *dhpB* (Han *et al.*, 2001). We have recently cloned the protein product of the second gene, DHP B, which has a higher peroxidase activity than DHP A (de Serrano *et al.*,

2010). In this study, we continue our investigation of the ligand-binding properties of DHP A by determining cyanide-adduct structures under conditions where photoreduction may be taking place. The activity of peroxidases is related to the reduction potential of the active-site Fe. For O_2 transport, globins maintain the ferrous Fe^{II} state, while the resting state for peroxidases is the ferric Fe^{III} state. Photoreduction of ferric heme proteins is often observed in the high flux of synchrotron radiation. Here, we have compared the use of high-flux and low-flux X-ray sources combined with molecular modeling in order to understand the effect of Fe reduction on the active-site ligation and structure.

DHP A catalyzes the oxidative dehalogenation of 2,4,6-trihalophenols, according to Fig. 1, leading to the formation of the corresponding 2,4-dihaloquinones (Chen *et al.*, 1996; Belyea *et al.*, 2005, 2006; Franzen *et al.*, 2007; Feducia *et al.*, 2009). The dehaloperoxidase reactivity of DHP A shown in Fig. 1 is believed to be an important function in *A. ornata* (Chen *et al.*, 1996; Lincoln *et al.*, 2005), in addition to the oxygen-transport function that is common to hemoglobins (Hbs). Despite the apparent simplicity of the globin structure, the structure–function relationships of DHP A have only begun to be elucidated. The mutually exclusive binding of inhibitor and substrate to DHP has recently been studied by NMR and X-ray crystallography (Davis *et al.*, 2009; Thompson *et al.*, 2010).

The X-ray crystal structures of the metaquo (PDB code 2qfk), oxy (PDB code 2qfn) and deoxy (PDB code 3dr9) forms of DHP show that there is a correlation between the position of the distal histidine His55 and the coordination state of the heme iron (de Serrano *et al.*, 2007; Chen *et al.*, 2009). In five-coordinate high-spin (5cHS) adducts His55 is observed in a solvent-exposed or open conformation, as in the 100 K deoxy structure (PDB code 3dr9). However, in six-coordinate high-spin (6cHS) adducts His55 is in an internal or closed conformation in hydrogen-bonding contact with heme-bound H_2O or O_2 (PDB codes 2qfk and 2qfn, respectively). Complete understanding of the binding to the heme iron requires further study of the dependence of the histidine conformation on the coordination state of the heme iron.

The CN^- adduct is a useful probe of the active-site geometry of heme-containing enzymes and oxygen carriers (Bolognesi *et al.*, 1999; Edwards & Poulos, 1990; Fukuyama & Okada, 2007; Fedorov *et al.*, 2003; Furtmüller *et al.*, 2006; Sugishima *et al.*, 2003). CN^- binds to the ferric form of heme proteins and inhibits both enzymatic activity and oxygen transport (Chance, 1943). The metcyano form of DHP has proven to be useful for solution structural studies using ^1H hyperfine NMR spectroscopy, which have probed the interactions of halogenated phenols with the protein in solution (Davis *et al.*, 2009). The X-ray crystal structures of the CN^- adducts of many heme proteins have provided detailed insight into the interaction of the diatomic ligand with the amino-acid side chains in the distal pocket. Although model systems have an Fe—C—N angle of nearly 180°, there are examples of smaller Fe—C—N angles that are caused by interaction with the amino acids in the distal cavity (Sugishima *et al.*, 2003). CN^- and H_2O_2 have similar binding dependencies. For example, in human myeloperoxidase it was postulated that CN^- provides a model for the intermediate Compound I (Blair-Johnson *et al.*, 2001).

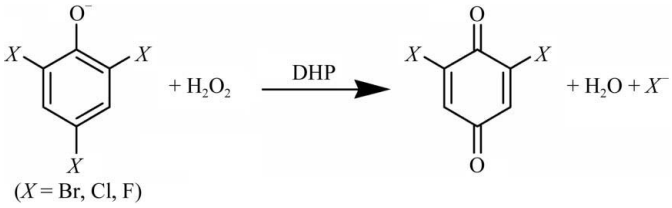

Figure 1
Oxidative dehalogenation of 2,4,6-trihalophenols catalyzed by DHPA.

Hemoglobins and myoglobins have provided unique information on the dynamics of diatomic ligands as they move through the protein on their way to or from the heme iron. The carbonmonoxy adduct DHPCO is isoelectronic with the metcyano adduct DHPCN, providing comparisons by using Fourier transform infrared (FTIR) spectroscopy to determine the effects of amino-acid interactions with the heme-iron-bound CO. We are particularly interested in understanding the relationship between DHPCN and metcyano myoglobin (MbCN) in order to elucidate the significance of the CO trajectories in both proteins that have been measured using temperature-derivative spectroscopy (TDS; Nienhaus *et al.*, 2006, 2008). Hence, the questions addressed by an X-ray structure of DHPCN pertain not only to the binding of CN^- but also to the protein dynamics that accompany ligand photodissociation. The observed electron density in the distal pocket indicates a ligand trajectory since there is density at a site not coordinated to the heme iron. This observation may be important in a dual-function protein that binds both O_2 and H_2O_2 in a manner that requires ligand exchange for function.

Here, we report that the CN^- ligand dissociates from the heme iron of DHPCN during the X-ray experiment owing to photoreduction of the iron from the ferric to the ferrous state. We have compared the structural results obtained using synchrotron radiation with those from a rotating-anode X-ray source, both of which show evidence that the Fe—CN bond is broken during the course of data collection at 100 K. The significance of this comparison is that we have attempted to determine the effect of the radiation dose on the yield of photoreduction of Fe^{III} to Fe^{II}. The crystals studied were approximately 100 µm in each dimension, which permits the absorbed doses to be estimated as 7×10^6 and 0.3×10^6 Gy (where 1 Gy = 1 J kg^{-1}) for the synchrotron and in-house rotating-anode sources, respectively. To obtain these values, the appropriate fluxes for each source were used (see §2) and the assumption was made that 2% of the incident X-ray flux was absorbed by the crystal (Murray *et al.*, 2005). Although the doses differ by a factor of ∼20, the flux is ∼380 times larger for synchrotron radiation. In order to avoid beam damage, the typical synchrotron exposure times used were 19 times shorter than those for the rotating-anode source. Photoreduction and photolysis of a ligand can depend strongly on the flux. As a

result of the greater flux and perhaps also the total dose, both photoreduction of metcyano heme proteins and photolysis of ligands are observed (Keilin & Hartree, 1955); the photoreduction phenomenon has been observed previously during structure determination of heme proteins using synchrotron radiation (Chance *et al.*, 1980; George *et al.*, 2008).

Accordingly, in a previous study we found that *in situ* photoreduction of Fe^{III} in the C73S mutant of DHP by the X-ray beam leads to the binding of O_2 to the heme iron (de Serrano *et al.*, 2007). The C73S mutant was originally investigated in order to eliminate the possibility of reactions involving the surface cysteine Cys73. In the present study, the diatomic ligand in both the C73S (C73SCN) and wild-type (DHPCN) structures resides in two positions in the distal pocket whose relative populations appear to depend on the X-ray beam exposure. However, the fact that the initial ligand is CN^- required more extensive study in order to explain the fate of the photoreduction and dissociation processes in the DHPCN and C73SCN crystals at 100 K. Because of the difficulties in making a definitive assignment of the electron density in the distal pocket, we have studied the bonding and protein dynamics associated with this process using both density functional theory (DFT) calculations and molecular-dynamics (MD) simulations. The combination of calculations and experimental data elucidate the factors that govern the loss of the CN^- ligand during X-ray exposure in these crystal structures. The trajectory of CN^- provides insight into the motions of O_2 and H_2O_2 in the distal pocket, which are key determinants of function in DHP A.

2. Materials and methods

2.1. Preparation of crystals of CN^--bound complexes

Wild-type DHP and C73S mutant protein were expressed in Rosetta(DE3)pLysS cells (Novagen, Madison, Wisconsin, USA) and purified as described previously (de Serrano *et al.*, 2007). DHPCN complexes were prepared by incubating 8 mg ml^{-1} protein in 20 m*M* sodium cacodylate buffer pH 6.5 with 10 m*M* KCN for 30 min on ice prior to crystallization setup. The crystallization conditions were similar to those described for DHP in the absence of any added ligands (de Serrano *et al.*, 2007). Crystals were grown by the hanging-drop vapor-diffusion method, with reservoir solution containing unbuffered 0.2 *M* ammonium sulfate and PEG 4000 at a concentration in the range 28–34%(*w*/*v*). Diffraction-quality crystals grew within one week at 277 K.

2.2. Data collection, processing and refinement

Diffraction data were collected at 100 K on the SER-CAT 22-BM beamline at the Advanced Photon Source (Argonne, Illinois, USA) using an X-ray wavelength of 1.0 Å. Both DHPCN and C73SCN crystals diffracted to 1.26 Å resolution on a MAR 225 detector. A data set for DHPCN was also collected on a Rigaku MicroMax-007 HF copper rotating-anode X-ray generator (λ = 1.54 Å). The DHPCN crystal diffracted to 1.72 Å resolution on an R-AXIS IV^{++} image-plate detector. The 22-BM beamline, with a photon flux of 3×10^{13} photons s^{-1} mm^{-2} and an average exposure of 5 s per frame (120 frames in total) at an energy of 12 keV (λ = 1 Å), delivers an X-ray dose to a crystal that is approximately an order of magnitude larger than an in-house Micromax-007 HF Cu rotating-anode X-ray generator with a flux of 7.8×10^{10} photons s^{-1} mm^{-2} and 180 s exposure per frame (90 frames in total) at an energy of 8 keV (λ = 1.54 Å).

The diffraction data were processed using *DENZO* and *SCALEPACK* (Otwinowski & Minor, 1997). The CN-complex crystals belonged to the primitive orthorhombic space group $P2_12_12_1$, analogous to C73S mutant and wild-type protein crystals that do not contain added ligand, and have very similar unit-cell parameters: $a = 57.2$, $b = 66.6$, $c = 68.7$ Å for the wild-type complex and $a = 57.7$, $b = 66.5$, $c = 68.2$ Å for the C73S mutant complex, respectively (de Serrano *et al.*, 2007). The 1.62 Å resolution structure of metaquo DHP determined at 100 K was used as the starting model for molecular replacement with *Phaser* (McCoy *et al.*, 2005) and subsequent refinement steps were carried out using the *CCP*4 suite of programs (Collaborative Computational Project, Number 4, 1994). In the refinement procedures, model bias was eliminated by constructing OMIT maps with the *CNS* program (Brünger *et al.*, 1998), omitting the relevant residues or heme-bound ligand from the map calculations. With the resolution of 1.26 Å for each crystal form, we were able to model approximately one third of the residues in each subunit of each structure in two conformations. Notably, the distal histidine residue (His55) was modeled in two conformations within the distal pocket, as were the aromatic residues defining the distal pocket hydrophobic cavity. The alternative occupancies of the ligand were defined by the appearance of a second alternative conformation of CN^- in the distal pocket during acquisition of the X-ray diffraction data set. These conformations of CN^- may in fact be a consequence of O_2 entering the distal pocket following photoreduction of Fe^{III}. This hypothesis was examined using model calculations. Furthermore, in order to evaluate the effect of X-ray exposure on the development of the electron density attributed to the alternative CN^- conformation, we have grouped and scaled the collected data set to include only a set of the first and/or last collected diffraction images of the data set.

Final models were obtained by iterative cycles of model building in *Coot* (Emsley & Cowtan, 2004) using $2F_o - F_c$ (contoured at the 1σ level) and $F_o - F_c$ (contoured at the 3σ level) electron-density maps and positional and anisotropic *B*-factor structure refinement using *REFMAC*5 (Murshudov *et al.*, 1997) from the *CCP*4 suite of programs (Collaborative Computational Project, Number 4, 1994) and *CNS* (Brünger *et al.*, 1998). Simulated-annealing and composite OMIT maps were constructed with the *CNS* program. Structural figures were prepared using *PyMOL* (DeLano, 2002).

The final models of the DHPCN and C73SCN structures refined to R/R_{free} values of 15.7/18.7% and 17.7/19.8%, respectively, for the synchrotron-radiation data sets. The models contained two polypeptide chains, two CN^- ions, two sulfate ions and 352 or 324 water molecules for DHPCN and

Table 1
Data-collection and refinement statistics.

Values in parentheses are for the highest resolution shell. The sixth coordination ligand of heme Fe is a CN^- ion; data are compiled for the first 90 diffraction images (of the 120 collected) for the data sets obtained at the synchrotron.

	Wild-type, recombinant, CN complex	C73S mutant, CN complex	Wild-type, recombinant, CN complex
PDB code	3kun	3kuo	
Source	Synchrotron	Synchrotron	Rotating anode
Data collection			
Wavelength (Å)	1.0	1.0	1.5418
Space group	$P2_12_12_1$	$P2_12_12_1$	$P2_12_12_1$
Unit-cell parameters			
a (Å)	57.2	57.7	58.8
b (Å)	66.6	66.5	67.7
c (Å)	68.7	68.2	67.7
Resolution (Å)	35.0–1.26 (1.29–1.26)	35.0–1.26 (1.29–1.26)	37.1–1.72 (1.77–1.72)
Unique reflections	67355 (4633)	66582 (4665)	27852 (2037)
Completeness (%)	97.2 (96.5)	96.3 (94.8)	99.3 (100.0)
R_{merge}† (%)	5.3 (32.4)	5.2 (53.6)	5.7 (53.2)
$I/\sigma(I)$	21.9 (2.6)	25.4 (2.0)	26.3 (2.3)
Redundancy	3.5 (3.3)	3.3 (2.9)	3.4 (3.3)
Refinement			
R_{work}‡ (%)	15.7	17.6	18.8
R_{free}§ (%)	18.7	19.8	23.0
Average *B* factor (Å^2)			
All atoms	12.0	13.4	18.0
Protein	10.4	12.0	17.3
Water	24.2	25.1	25.6
No. of protein atoms	2896	2966	2815
No. of solvent atoms	352	324	255
R.m.s.d. from ideal geometry			
Bond lengths (Å)	0.006	0.007	0.008
Bond angles (°)	1.02	1.08	1.11
Ramachandran plot¶ (%)			
Most favored region	94.8	94.8	95.2
Additional allowed region	5.2	5.2	4.8

† $R_{merge} = \sum_{hkl}\sum_i |I_i(hkl) - \langle I(hkl)\rangle| / \sum_{hkl}\sum_i I_i(hkl)$, where $I_i(hkl)$ is the *i*th measurement and $\langle I(hkl)\rangle$ is the weighted mean of all measurements of $I(hkl)$. ‡ $R_{work} = \sum_{hkl} ||F_{obs}| - |F_{calc}|| / \sum_{hkl} |F_{obs}|$, where F_{obs} are the observed and F_{calc} are the calculated structure factors. § R_{free} is the *R* factor for a subset (5%) of reflections selected before and not included in refinement. ¶ Calculated using *PROCHECK* (Laskowski *et al.*, 1993).

C73SCN, respectively. The data-collection and model statistics for the X-ray data sets are summarized in Table 1.

2.3. Binding-constant determination

KCN titrations were conducted in 50 m*M* phosphate buffer pH 6.5 and 100 m*M* NaCl. The pH was chosen to be the same as that of the crystallization buffer. The binding constants were measured at ambient temperature. Titrations were performed in a cuvette in a Hewlett–Packard 8453 diode-array spectrophotometer. Changes in the absorbance at the wavelength of the Soret maximum were measured and converted into relative populations of the cyanide and metaquo forms as described elsewhere (Thompson *et al.*, 2010).

2.4. Spectroelectrochemical determination of formal reduction potentials

Spectroelectrochemistry (SEC) experiments were carried out in 100 m*M* potassium phosphate buffer at pH 7.00 ± 0.02 in an air-tight UV–visible cell that utilized an optically transparent thin-layer electrode, namely indium–tin oxide (ITO). The ITO electrode was thoroughly cleaned before use by 10 min successive sonications in 1%(*v*/*v*) Contrex solution (Decon Labs Inc.), 95% ethanol and twice in deionized water. The SEC cell was stored in a nitrogen-atmosphere drybox for at least 8 h prior to experimentation. UV–visible spectra were recorded using a Hewlett–Packard 8453 spectrophotometer and the applied potentials were controlled with a Model 273A Princeton Applied Research potentiostat. The SEC cell made use of an Ag/AgCl (saturated KCl) reference electrode (Microelectrodes Inc.) and a platinum-wire auxiliary electrode (Alfa Aesar). The reduction potential of C73S-DHP is referenced to the standard hydrogen electrode (SHE). The electron-transfer mediators tetramethyl *p*-phenylenediamine (TMPD; Sigma) and tris (ethylenediamine)ruthenium(II) tetrachlorozincate, $[Ru(en)_3]^{2+}$, which we synthesized using a previously described procedure (Smolenaers & Beattie, 1979), were used to facilitate electron transfer between DHP and the electrode. The ratio of DHP to mediators was 2:1.

2.5. Density functional theory (DFT) calculation of potential energy surfaces

DFT calculations of the potential energy surfaces were used to model the bond strength and possible dissociation of the cyanide from different spin and oxidation states of the iron. Geometry optimizations were performed for heme in the low-spin state for both ferric and ferrous oxidation states with either the O_2 or CN^- ligand. All calculations were implemented using the electronic structure package *DMol*^{3} (Delley, 1990, 2000). The generalized gradient approximation of the BLYP (Becke, 1988; Lee *et al.*, 1988) density functional is utilized in the ground-state energy calculation, using a double numeric basis set with one polarization function. Optimized geometries were obtained using the conjugate-gradient method constrained to an energy difference of 10^{-6} Hartrees (1 Hartree = 27.2 eV). Potential energy surfaces were calculated implementing the thermal treatment (Weinert & Davenport, 1992) of the density functional. The grand canonical calculation was carried out at a finite temperature of 0.02 Hartrees. The system used to model the heme in geometry optimizations consists of an imidazole bound to the central iron in porphine (FeP), with both CN^- and O_2 ligands initially bound *trans* to the imidazole.

2.6. Molecular-dynamics (MD) simulations

MD simulations were employed in order to determine the trajectory of the dissociated ligand for comparison with the

Table 2
Comparison of heme iron and ligand distances for metcyano adducts.

The values are tabulated for subunit *A* of the asymmetric unit.

Protein form	Wild type†	C73S†	Wild type‡	
Source	Synchrotron	Synchrotron	Rotating anode	
			Chain *A*	Chain *B*
Fe—His89 $N^{\varepsilon 2}$ (Å)	2.17	2.13	2.16	2.15
Fe—His55*a*§ $N^{\varepsilon 2}$ (Å)	5.01	5.02	5.43	5.62
Fe—His55*b*§ $N^{\varepsilon 2}$ (Å)	5.38	5.32	5.23	5.08
Fe—His55*c* ND1 (Å)	—	—	8.19	7.92
Outside distal pocket				
Fe–ligand¶ (CN1) (Å)	2.05	2.16	2.29	2.19
Fe–ligand¶ (CN2) (Å)	3.11	3.20	—	—
Ligand–His55††				
CN1 N—His55*a* $N^{\varepsilon 2}$ (Å)	3.40	3.56	2.82	3.38
CN2 N—His55*a* $N^{\varepsilon 2}$ (Å)	2.84	2.87	—	—
Fe–pyrrole N plane (Å)	0.05	0.05	0.08	0.1
Fe–ligand bend angle‡‡ (°)				
CN1	125	117§§	154	127
CN2	175	158		
Fe–ligand tilt angle¶¶ (°)				
CN1	6	7	11	14
CN2	14	19		

† Structures of wild-type recombinant and C73S mutant protein in complex with cyanide ion. ‡ Values for both chains *A* and *B* in the asymmetric unit are tabulated since there are differences in the ligand geometries in the two molecules. § There are two conformers of His55 present in the distal cavity, designated *a* and *b*. ¶ Distances from heme iron to CN present in two alternative orientations in the distal pocket, designated CN1 and CN2 (see text). †† Distances of the N atom of CN1 and CN2 to His55*a* are shown. The distances to H55*b* are similar and are discussed in the text. ‡‡ The bend angle is defined as the Fe—C—N angle. §§ The bend angles in subunit *B* of the C73S mutant protein are 123° for CN1 and 163° for CN2. ¶¶ The tilt angle is defined as the angle between the heme perpendicular and the Fe—C bond (Vangberg *et al.*, 1997).

Table 3
Comparison of resolution, completeness and redundancy for various frames of the C73SCN X-ray data set collected using synchrotron radiation.

Values for the completeness and redundancy are obtained from the log files of the respective *SCALEPACK* truncations of the collected data sets.

Group	Frames	Resolution (Å)	Completeness (%)	Redundancy
Total	120	1.31	97.3	4.2
Initial† *A*	60	1.26	92.1	2.3
Initial† *B*	45	1.26	83.5	1.9
Final‡ *A*	60	1.45	74.7	2.6
Final‡ *B*	45	1.45	72.5	1.9

† Initial refers to the first set of 60 (group *A*) or 45 (group *B*) data frames of the total 120 data frames collected that were used to construct electron-density maps. ‡ Final refers to the last set of 60 (group *A*) or 45 (group *B*) data frames of the total 120 frames collected that were used to construct electron-density maps.

crystallographic results. The DHP A crystal structure deposited as PDB entry 2qfk was employed in the computational study. The monomeric form of DHP A was used with a spherical boundary condition. This procedure is justified by the weak contacts between the two monomers (de Serrano *et al.*, 2007; Chen *et al.*, 2009). The bound water in the original metaquo form was replaced by a CN^- ligand. The simulation system was then constructed using the program suite *VMD* (Humphrey *et al.*, 1996). H atoms were added to the protein, which was then solvated with a 26 Å water sphere and charge-balanced with NaCl. The solvated system contained 4900 atoms, of which 1136 were protein atoms. Simulations were carried out using *NAMD* (Phillips *et al.*, 2005) with the modified PARAM27 version of the CHARMM force fields. Spherical boundary conditions were implemented using a constant temperature of 100 K. The constant temperature was maintained using Langevin dynamics with a damping coefficient of 5 ps^{-1}. The initial structure was minimized for 10 000 steps of 0.02 ns and equilibrated in either 1 or 2 ns (5×10^5 or 10^6 steps, respectively) intervals depending on the model system. After each restart the structure was minimized for an additional 5000 steps. Nonbonded interactions were truncated after 12.0 Å and a switching cutoff distance of 10.0 Å for Lennard–Jones parameters was used.

Topology and parameter files were modified to account for both the ferrous and ferric oxidation states of the heme iron, with and without bound ligand, based on density functional theory calculations. Atomic charges and the force constant for free O_2 are provided in the force field supplied by the *NAMD* simulation package.

3. Results

The structures of DHPCN and C73SCN were determined at 100 K at a resolution of 1.26 Å and refined to $R/R_{\rm free}$ factors of 15.7/18.7% and 17.7/19.8%, respectively (Table 1). The main-chain atoms of the two monomers in the asymmetric unit (de Serrano *et al.*, 2007; Chen *et al.*, 2009) superimpose with an r.m.s.d. of 0.448 Å for the wild-type DHP and 0.437 Å for the C73S mutant. Overall, the structure of the DHPCN complex is very similar to the structures of the metaquo DHP and C73S oxy forms, both of which were determined at a resolution of 1.62 Å using a rotating-anode source (de Serrano *et al.*, 2007).

We have observed that ferric metaquo DHP is prone to reduction in the X-ray beam during data collection even using a rotating copper-anode source (de Serrano *et al.*, 2007). Because the samples were prepared in the cyanide-bound form and cooled to 100 K, we assumed that the electron density at the shortest times of observation can be accounted for by CN^-. However, it is not clear that the electron density observed at the first possible observation time in the X-ray beam corresponds to CN^-. Based on the $2F_o - F_c$ maps, both the DHPCN and C73SCN display electron density that can accommodate two distinct conformations of a diatomic ligand: one bound and one at a nonbonding distance from iron. In the first site, designated CN1, the diatomic ligand is coordinated to the heme iron with a distance from iron to the C atom of CN^- of 2.08 Å in the wild-type protein and 2.16 Å in the C73S mutant protein (Table 2). In this first site, CN1, the diatomic ligand has a bent conformation, with an Fe—*X*—*Y* angle of 126° (124° in subunit *B*) in the wild-type DHP adduct. In the C73SCN adduct the angle is 117° (123° in subunit *B*). The second conformation, CN2, is observed at a site about 3.0 Å from the heme iron in a conformation nearly perpendicular to the heme plane. The structure obtained using a rotating-anode source has Fe—C—N angles of 154° and 127° in subunits *A* and *B*, respectively. Hence, the Fe—*X*—*Y* (or Fe—C—N) bond angle in CN1 is not consistent with the perpendicular

geometry expected for a CN^- adduct with ferric heme in any of the structures. Moreover, the appearance of the electron density above the heme iron strongly resembles the C73S structure (PDB code 2qfn; not shown). In the C73S structure the heme was initially in the metaquo form (de Serrano *et al.*, 2007), but is observed to bind O_2 following photoreduction. Comparison of the two structures suggests that photoreduction of Fe^{III} to Fe^{II} by the X-ray beam followed by dissociation of CN^- may have occurred in the structures presented here.

In order to assess the photoreduction phenomenon and the dose-dependence of the electron density in the distal pocket, we analyzed the data sets obtained using synchrotron radiation as the data acquisition progressed. The collected data sets comprising 120 diffraction images (collected at 1° oscillation range) were separated and processed in the groups shown in Table 3. Fig. 2 shows an OMIT map for the ligand to the heme iron for the first and last sets of 60 images acquired from the C73S crystal. The electron density in the distal position, CN2, which is about 3 Å from the heme Fe, is observed to increase as X-ray data collection progresses (Bellelli *et al.*, 1990). Based on a comparison of these changes with the C73S–O_2 structure (PDB code 2qfn), we contemplated the possibility that the electron density arises from CN^-, HCN or O_2 or from a progressive replacement of CN^- by either HCN or O_2. We include HCN in our consideration since protonation of CN^- is possible in the distal pocket following dissociation given that the pK_a of HCN is ∼9.2 and the crystal buffer is at pH 6.5. It is difficult to assess the meaning of pH in a crystal at 100 K, but we consider the possibility that proton transfer occurs to dissociated CN^- to yield HCN.

Regardless of the identity of the diatomic ligand, the electron density in this site may be regarded as a trapped state, which can be compared with the B state of photolyzed Mb*CO (Schlichting *et al.*, 1994; Teng *et al.*, 1994; Srajer *et al.*, 1996; Hartmann *et al.*, 1996; Schotte *et al.*, 2003). The B state for photodissociated CO has been extensively studied by cryogenic and time-resolved X-ray crystallography. However, the conformation of the CN2 molecule is clearly not the same as that of CO in the B state of Mb*CO. Fig. 3 indicates that the diatomic molecule in CN2 is stabilized by hydrogen bonding to the $N^{\varepsilon 2}$ atom of His55 (see Table 2). In contrast, CO in the B state is more nearly parallel to the heme plane. Fig. 3(*a*) shows the structure of PDB entry 3kun (nominally metcyano DHP A) compared with 2qfn (nominally metaquo DHP A; de Serrano *et al.*, 2007). Although CN1 and CN2 are indicated in Fig. 3(*a*), the point of our study is to determine the identity of the molecules that occupy this electron density. A similar electron density can be obtained starting from the metaquo form of the C73S mutant of DHP A. In this structure (2qfn) we assigned the electron density to a diatomic oxygen molecule, which replaced water during the course of X-ray data collection. Fig. 4 shows that a different electron density can be obtained starting from the metcyano form by collecting data

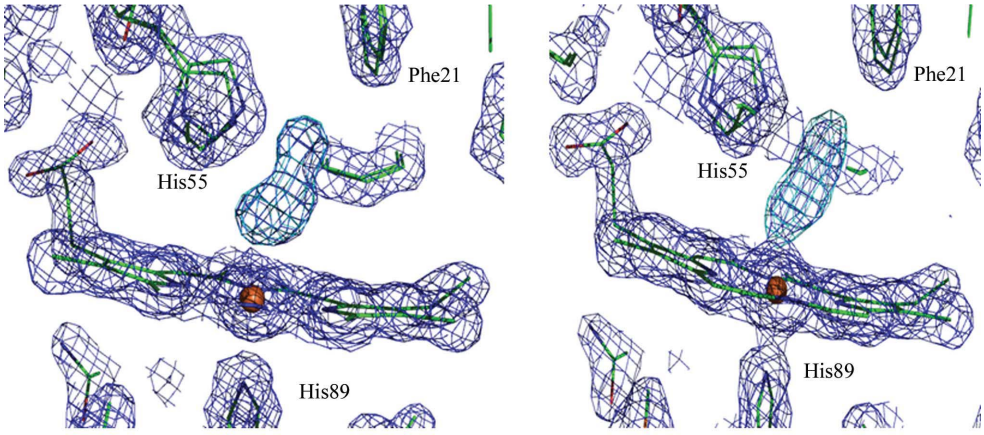

Figure 2
Changes in the ligand electron density during the course of X-ray exposure. The CN^- complex structure is shown for the distal side of the C73S mutant. Electron-density maps, calculated with the ligand omitted, are computed from (*a*) the first 60 and (*b*) the last 60 of the total of 120 collected diffraction images ($2F_o - F_c$ maps contoured at 1.2σ, $F_o - F_c$ maps contoured at 4σ).

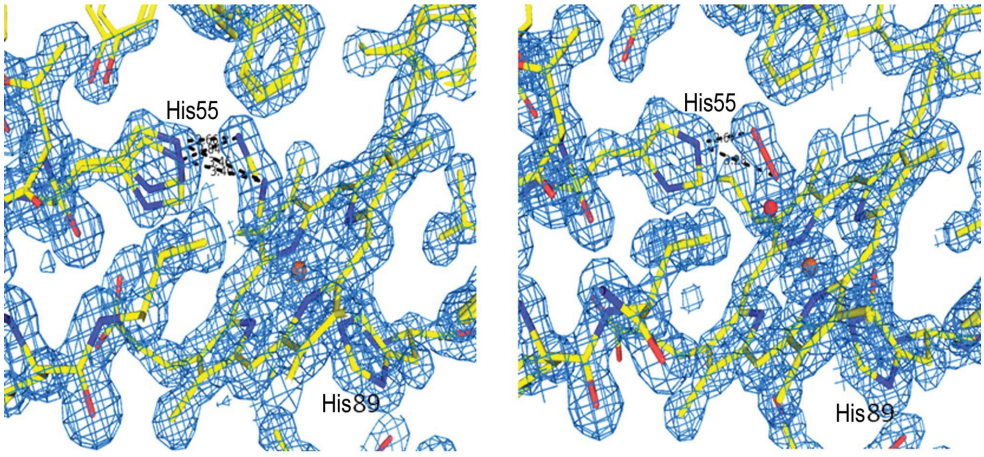

Figure 3
Electron-density maps ($2F_o - F_c$), from data collected on the 22-BM beamline, of wild-type DHP A in complex with cyanide (*a*) and metaquo wild-type protein (*b*). The maps are contoured at the 1.2σ level. The hydrogen bonding of cyanide in two discrete positions with His55 conformers is indicated in the maps, as is the hydrogen bonding of the oxygen molecule and His55 in the wild-type unligated structure. In the distal pocket of the metaquo structure a water molecule and an alternate oxygen molecule are colored red.

Table 4
Comparison of experimental and simulation distances.

	CN ligand (wild type)†	CN ligand (HSD‡)	O_2 ligand (HSD‡)	O_2 ligand (HSE‡)	HCN ligand (HSD‡)
Fe—His89 $N^{\varepsilon 2}$ (Å)	2.16	1.65	1.96	1.96	1.59
Fe—His55*a* $N^{\varepsilon 2}$ (Å)	5.03	6.40	n/a§	n/a§	n/a§
Fe—His55*b* $N^{\varepsilon 2}$ (Å)	5.38	6.60	5.70	5.00	6.38
Fe–ligand (CN1) (Å)	2.08	1.89	2.08	2.08	n/a
Fe–ligand (CN2) (Å)	3.12	10.5	3.76	4.20/6.50¶	4.80
Ligand–His55 (Å)					
CN1 N–H55*a* $N^{\varepsilon 2}$	3.39	4.40	4.33	4.33	n/a
CN2 N–His55*a* $N^{\epsilon 2}$	2.85	>4.50††	3.29	3.50/4.50	4.40
Fe–ligand bend angle (°)					
CN1	126.2	179.5	124.8	124.8	n/a
CN2	173.3	n/a††	90.0	90.0/130.0¶	153.8

† Experimental distances tabulated for chain *A* of the wild-type DHPCN data set. ‡ HSD refers to the His55 tautomer protonated at the δ-nitrogen; HSE refers to the His55 tautomer protonated at the ε-nitrogen. § No evidence of a second His55 conformation. ¶ Distance of the second occupation site for the O_2 HSE simulation. †† Simulations suggest immediate exit of the CN ligand.

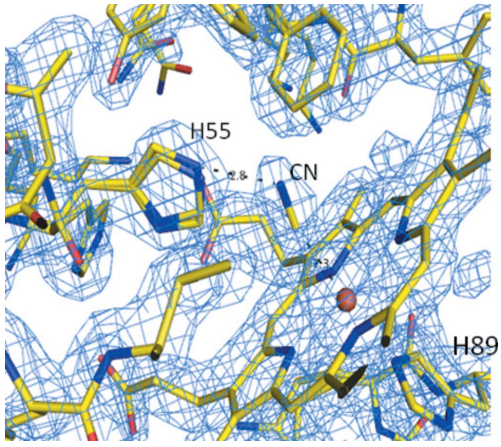

Figure 4
Electron-density maps ($2F_o - F_c$), from data collected using the in-house X-ray generator, of wild-type DHP A in complex with cyanide. The maps are contoured at the 1.2σ level as in Fig. 3. The CN molecule is not coordinated to the heme Fe, but is observed at a distance of 2.3 Å.

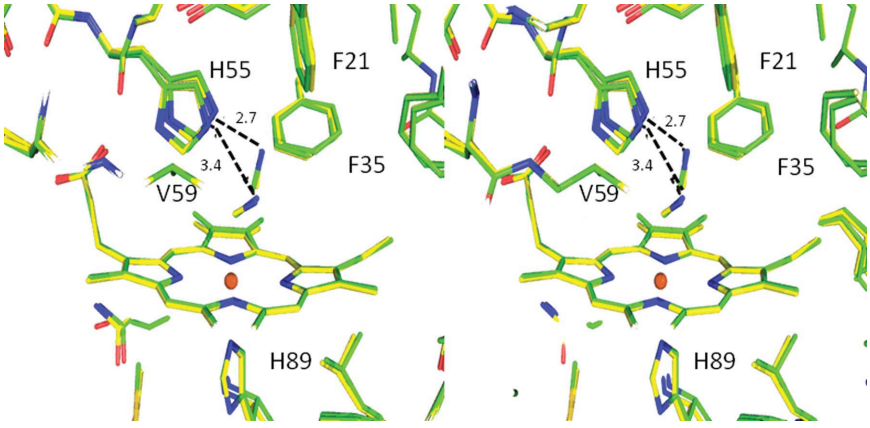

Figure 5
Structural features of the binding of cyanide to the ferric form of DHP. The overlay of the distal sites of wild-type (green) and C73S mutant (yellow) DHP is shown and marker residues of the pocket are labeled. The hydrogen bonding of cyanide to conformers of distal histidine in the wild-type structure is also shown (dashed lines).

at lower X-ray flux and dose using an in-house copper rotating-anode source. The excess density in the 3kun and 3kuo structures may arise from dissociated CN^-, O_2 replacement or some amount of H_2O that associates with these diatomic ligands in the distal pocket. DFT calculated and MD simulations were conducted to obtain models that were consistent with the observed electron density (see below).

3.1. Heme conformation in the DHPCN structure

The conformations of the heme in the DHPCN structures presented here are similar to that in the C73S–O_2 structure, which is consistent with the idea that C73S–O_2 was also formed by photoreduction of the heme iron by synchrotron radiation. The structure of the heme shows relatively minor structural changes in the various frames studied. In both structures there is a heme rotation of 3.6° about the α,γ *meso*-carbon axis. This rotation also helps to position the propionates closer to the positive charge of Lys51. The displacements of iron from the heme pyrrole plane are 0.05 Å in the DHPCN and C73SCN structures and 0.04 Å in the metaquo DHP adduct (Table 2; de Serrano *et al.*, 2007).

3.2. Conformation of the distal histidine His55

In previous work, we established that His55 is present in two orientations, called internal and external. The internal orientation with His55 in the distal pocket is observed in the metaquo and oxyferrous (C73S–O_2) six-coordinate DHP structures (2qfk and 2qfn, respectively). The solvent-exposed or external orientation is observed in the five-coordinate deoxy form (PDB code 3dr9; de Serrano *et al.*, 2007; Chen *et al.*, 2009). The presence of two orientations of the distal histidine has also been observed in high-resolution structures of myoglobin (Vojtechovsky *et al.*, 1999). The flexibility of His55 was also noted in the room-temperature DHP A met(aquo) structure, where there is an equilibrium between the internal and external orientations of this critical residue (LaCount *et al.*, 2000). In the 3kun and 3kuo structures presented in Figs. 3(*a*) and 4, respectively, there are two His55 conformers that are both observed in the internal orientation such that their $N^{\varepsilon 2}$ atom is located close to the bound ligand and their $N^{\delta 1}$ atom is pointing outwards into the solvent. The $N^{\varepsilon 2}$ atom is located at a distance of 5.03 and 5.38 Å from the heme iron in subunits *A* and *B*, respectively, as shown in Table 2. The two conformations most closely resemble the His55 conforma-

Table 5
Potential energies (kJ mol^{-1}) of binding for both ferrous and ferric FeP–CN.

FeP–CN is the Fe porphine model in complex with CN ligand used in geometry optimization and in simulations. LS denotes the low-spin state of the heme iron, whereas HS refers to the high-spin state of the heme iron.

	Q_p = 0.0		Q_p = 0.2		Q_p = 0.4	
	LS	HS	LS	HS	LS	HS
Fe^{II}	−197.5	−74.7	−155.9	−34.7	−91.5	0
Fe^{III}	−282.5	−106.4	−241.2	−69.1	−188.1	−34.7

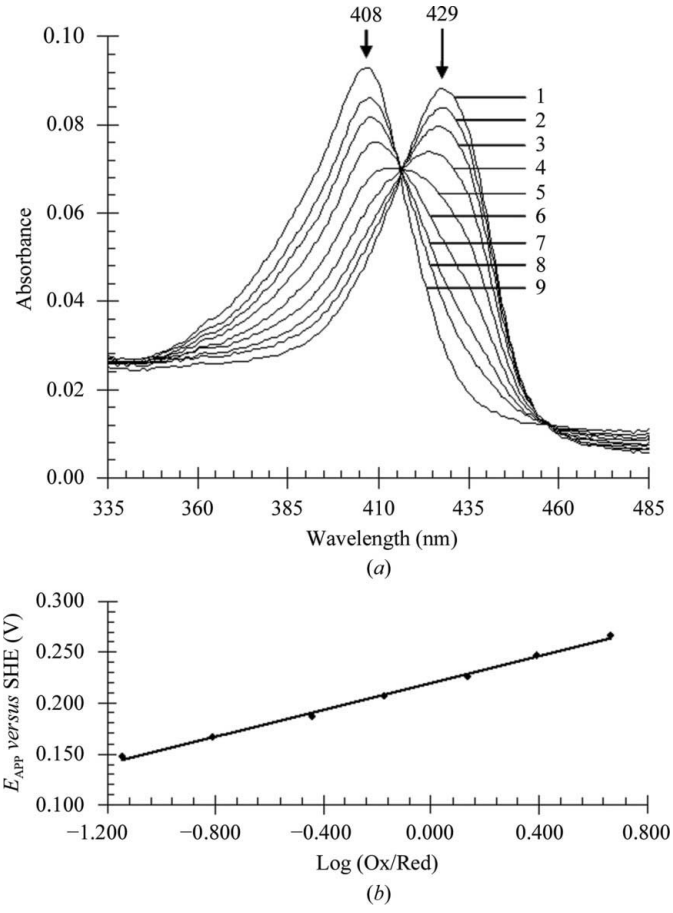

Figure 6
(*a*) UV–visible thin-layer spectroelectrochemical plot for C73S-DHP A in 100 m*M* potassium phosphate buffer pH 7.0; the mediators were $[Ru(en)_3]^{2+}$ and TMPD. Applied potentials (E_{APP} *versus* SHE): (1) −0.103, (2) +0.147, (3) +0.167, (4) +0.187, (5) +0.207, (6) +0.227, (7) +0.247, (8) +0.267 and (9) +0.497 V. (*b*) The Nernst plot for C73S-DHP A.

tions in the C73S–O_2 structure (de Serrano *et al.*, 2007), which are also internal owing to the hydrogen-bonding interaction with the O_2 coordinated to the heme iron. A second conformation is observed for a number of other residues within the distal pocket, which is consistent with the existence of two ligand conformations. This may also in part be a consequence of the higher resolution of this structure compared with previous structures (LaCount *et al.*, 2000; de Serrano *et al.*, 2007). The hydrogen bonding of each of the His55 conformers to the CN1 and CN2 diatomic ligands is shown in Fig. 5.

3.3. Determination of the CN^- dissociation constant of the Fe^{III} and Fe^{II} forms

The photoreduction of Fe^{III} to Fe^{II} leads to a reduced affinity for CN^- binding. We determined the dissociation constant K_d for the binding of CN^- to DHP in the Fe^{III} and Fe^{II} forms by titrating the corresponding protein solution with KCN solution and showed that the Fe^{III} protein form has a much higher affinity for CN^- than the Fe^{II} protein. The K_d values are 6.3×10^{-6} and 0.43 *M* for Fe^{III} and Fe^{II}, respectively, at pH 6.5. This property of DHP compares very closely with that of myoglobin, which has a K_d of 4.4×10^{-6} *M* for the Fe^{III} form at pH 6.6 and 0.4 *M* at pH 9.3 for the Fe^{II} form of the protein (Cox & Hollaway, 1977; Bellelli *et al.*, 1990).

3.4. Determination of the formal reduction potential

Spectroelectrochemical data for the C73S mutation of DHP are shown in Fig. 6. The Soret bands of the metaquo and deoxy forms are observed at 406 and 430 nm, respectively. Similar spectra were obtained for wild-type DHP (D'Antonio *et al.*, 2010). The clear isosbestic point indicates that there are two species present during the experiment: the Fe^{III} and Fe^{II} forms. The solution formal reduction potential of the Fe^{III}/Fe^{II} couple is +0.214 ± 0.006 V *versus* SHE for C73S-DHP A. In comparison, we determined that the reduction potential of horse heart myoglobin was +0.042 ± 0.006 V, which agrees well with the values determined elsewhere (D'Antonio *et al.*, 2010; Heineman *et al.*, 1979).

3.5. DFT calculations of heme structure and potential energy surfaces

DFT geometry optimization of an Fe porphine (FeP) model with axial imidazole (Im) and CN^- or O_2 ligands provides a structure that can be compared with the observed geometry. Geometry-optimized low-spin FeP–CN and FeP–O_2 exhibit angles of 180° and 125°, respectively (Fig. 7). These angles can be compared with the experimental extremes of 154.0° and 126.5° for CN1 and CN2 (Table 4). For DHP, the Fe—O—O angle is 144° (PDB code 2qfn; de Serrano *et al.*, 2007) and for MbO_2 the Fe—O—O angle is 123° (PDC code 1a6m; Vojtechovsky *et al.*, 1999). The calculated Fe—C and Fe—O bond lengths are 1.89 and 2.08 Å (Table 4), respectively, compared with an observed Fe–ligand distance of 2.08 Å for CN1 (Table 2).

Fig. 8 shows the potential energy surfaces for FeP–CN in both the ferric and ferrous oxidation states. Surfaces were calculated for both low-spin (S = 1/2 and S = 0) and high-spin (S = 5/2 and S = 2) configurations for Fe^{III} and Fe^{II} oxidation states, respectively. The calculations were carried out at three values of Q_p, a coordinate that represents the iron out-of-plane distance relative to the plane of the pyrrole N atoms of the heme. For Q_p = 0.0 Å, where the iron is entirely in plane with the heme, the binding energies are −197.5 and

−282.5 kJ mol^{-1} for low-spin Fe^{II} and Fe^{III}. As the iron changes from a low-spin state to a high-spin state, the Fe—CN binding energy decreases for the ferric and ferrous oxidation states by 176 and 123 kJ mol^{-1}, respectively. As the iron is displaced out of the heme plane, *i.e.* as Q_p increases, there is a decrease in the Fe—CN binding energy of ∼35 kJ mol^{-1} for a corresponding increase in Q_p of 0.2 Å. High-spin ferrous iron with a heme displacement of 0.4 Å corresponds to the geometry of deoxy heme. This has been found to be a dissociative state (Franzen, 2002). All others surfaces correspond to bound states. Table 5 gives a summary of the calculated binding energies, which are in agreement with the dissociation constants determined experimentally, as discussed above.

3.6. Molecular-dynamics trajectories for models of coordination ligands

MD simulations were carried out to further clarify the identity of the diatomic ligand in the distal pocket after X-ray-induced reduction of Fe^{III} to Fe^{II}. Simulations were performed on three ligands: free O_2, HCN and CN^-. In addition, in order to further examine the identity of the ligand, O_2 simulations were carried out for the δ- and ε-tautomers of His55, where the N^{δ}—H and N^{ε}—H tautomers are named HSD and HSE, respectively. In all simulations, the heme Fe was in the ferrous oxidation state and the simulations were carried out using the same force field, with the exception of the force-field terms that apply to the diatomic ligand. The major difference in the simulations is the charge on the ligand, since CN^- carries a charge of −1 and HCN and O_2 are both neutral molecules. In the DHPCN simulation the overall neutrality of the system was satisfied by

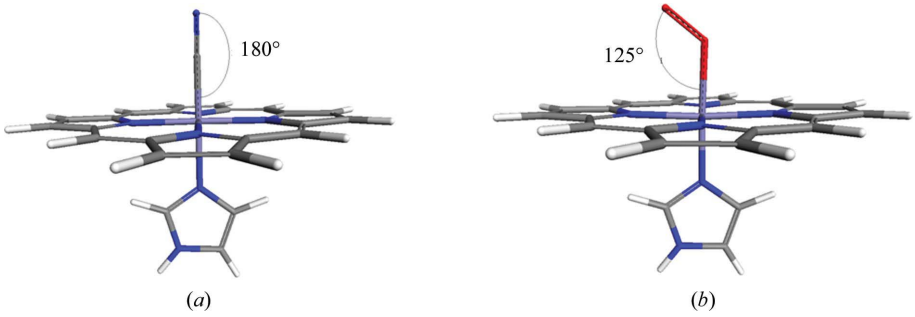

Figure 7
Optimized geometry of the ferric form of heme displaying the bond angle for (*a*) Fe^{III}P–CN and (*b*) Fe^{III}P–O_2. The DFT method was used for the iron-porphine model of the heme as described in the text.

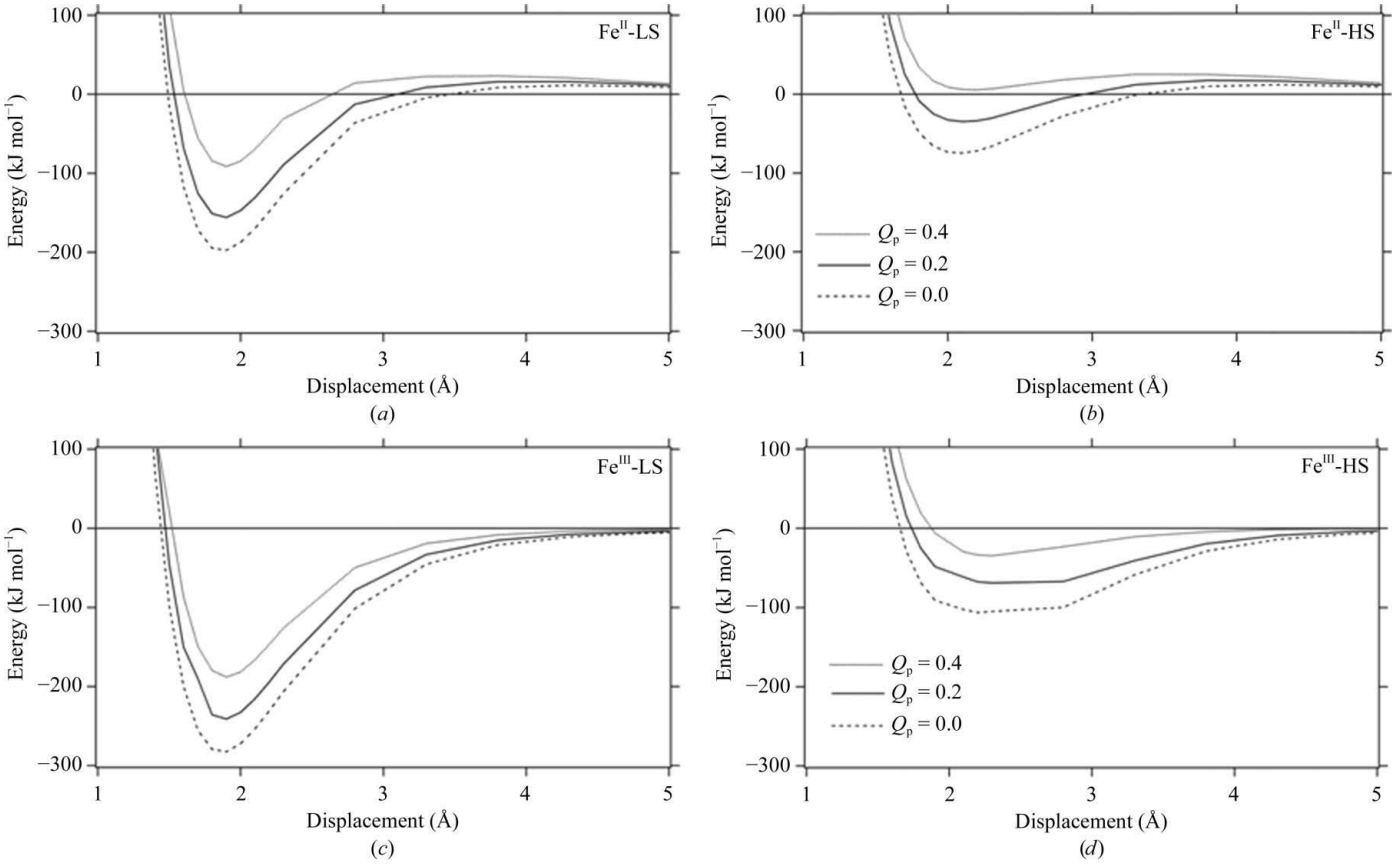

Figure 8
Calculated potential energy surfaces for FeP–CN. (*a*) Surface for ferrous iron, low spin. (*b*) Surface for ferrous iron, high spin. (*c*) Surface for ferric iron, low spin. (*d*) Surface for ferric iron, high spin. Q_p denotes the iron distance from the heme plane.

introducing one Na^+ ion into the water sphere surrounding the protein. The CN^- starting geometry was normal to the heme plane and the N atom is observed at distances of 2.8 and 3.5 Å from the N^ε atoms of His55 and Fe, respectively. In O_2 simulations, both tautomeric forms started with the free ligand in the same position: normal to the heme plane. The distal O atom is positioned 2.8 and 3.5 Å away from N^ε and Fe, respectively. HCN was also positioned normal to the heme plane, with the N atom at distances of 3.2 and 1.8 Å from His55 N^ε and Fe, respectively. In all cases, the His55 starting conformation was closed (inside the distal pocket).

3.7. CN^- ligand

Simulations involving the CN^- ligand were carried out for 4.30 ns. At the start of the simulation, the Fe–CN iron–nitrogen distance was 3.5 Å. Within 0.02 ns of the start of the simulation, the CN^- ligand migrates out of the distal pocket and into the solvation sphere. The iron–nitrogen distance increases to 8.0 Å (by approximately 4.5 Å) and then further to 10 Å for the remainder of the simulation (data not shown). This behavior is attributed to electrostatic interactions between the negatively charged CN^- ligand and the amino acids that make up the distal cavity. At the start of the simulation the distance between His55 N^ε and CN^- is 3.8 Å and it increases to 4.4 Å as CN^- exits the pocket and enters the solvation sphere. As the ligand starts to migrate out of the pocket and approaches His55, this amino acid can be seen to move to a more solvent-exposed position. Originally 6.4 Å, the Fe—N^ε distance increases by 0.2 Å as ligand migration begins, while the dihedral angle between the imidazole and the backbone of His55 changes by 30° (from 105° to 75°). Owing to this concerted motion between His55 and CN^-, the distance between the ligand and N^ε remained constant at 4.5 Å throughout the remainder of the simulation.

3.8. O_2 ligand

Simulations involving the O_2 ligand for both tautomers of His55 were performed for 8.0 ns; longer times were used than the CN^- simulation times owing to the observation that the O_2 ligand remains within the distal pocket. A shorter simulation time was possible for CN^- since it was observed to rapidly exit the pocket.

3.8.1. HSD tautomer. For the full 8.0 ns, O_2 remains stationary within the distal pocket. The O_2 molecule rests parallel to the heme plane at a distance of 3.8 Å from the heme iron, maintaining a constant iron–ligand (Fe—O_2) bend angle of ∼90°. For bound ligand (state CN1) the distance to His55, O_2—N^ε, was 4.3 Å and for the free ligand (state CN2) this distance decreased to 3.3 Å. This difference is not a result of the two His55 conformations shown in Fig. 3(*a*). Rather, the effect arises from the ability of the unbound diatomic ligand to position itself at a close hydrogen-bonding distance to His55. Fluctuations of 0.20 Å were observed in the N^ε—O1 distance throughout the 8.0 ns for O_2 in the CN2 state and were attributed to the rotation of the free ligand above the heme plane. The Fe—N^ε distance remained constant at a distance of 5.7 Å for the duration of the simulation.

3.8.2. HSE tautomer. Similar to the HSD simulation, O_2 remains inside in the distal pocket for the full 8.0 ns of simulation time. However, O_2 occupies two different sites within the pocket in the HSE simulation. Initially 4.2 Å, the Fe—O_2 distance increases to 6.5 Å within 0.2 ns (Fig. 9*a*). The O_2—N^ε distance fluctuates between 3.5 and 4.5 Å when O_2 moves from site 1 to site 2. His55 is positioned more deeply in the distal pocket in the HSE tautomer than in the HSD tautomer. A difference of 0.7 Å is observed between the two Fe—N^ε distances, with the protonated N^ε of HSE at 5.0 Å and the unprotonated N^ε being positioned 5.7 Å away from the heme Fe. In addition, the Fe—O_2 bend angle varies randomly between 90° and 130° during the course of ligand migration throughout the 8.0 ns simulation run.

3.9. HCN ligand

We also investigated the possibility that the observed electron density in the crystal structure corresponded to HCN. As with O_2, HCN remained inside the distal pocket throughout 8.0 ns of simulation time. Simulation results show that HCN hydrogen bonds to the heme iron and remains

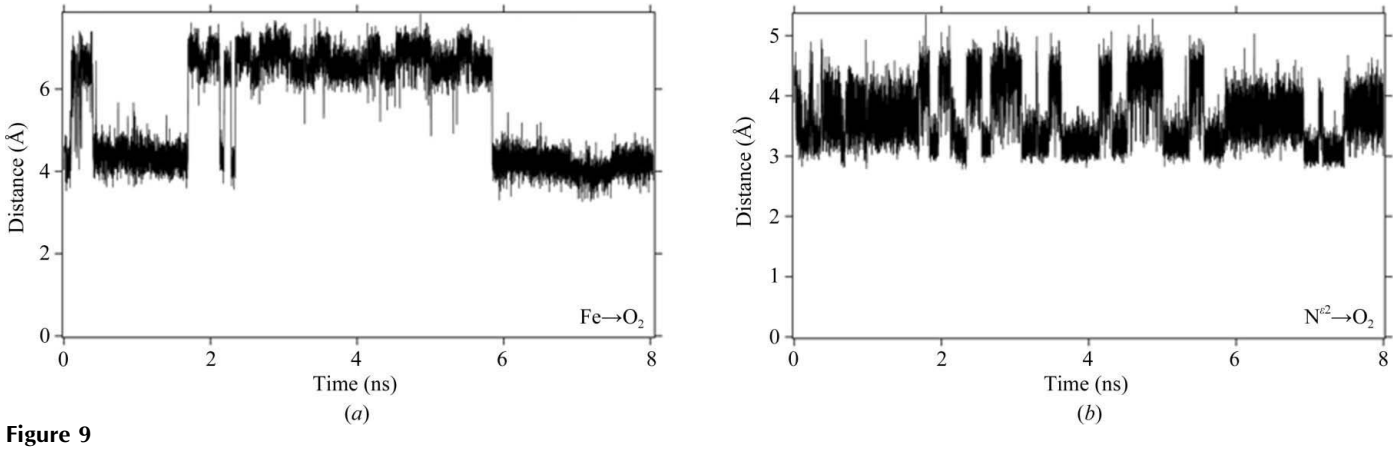

Figure 9
Distance *versus* time for the O_2 HSE simulation results. The arrow depicts the distance being measured. (*a*) Iron–O_2 ligand distance for the HSD tautomer. (*b*) O_2—His55 N^ε distance. Both distances are represented as an arrow between iron and the ligand at the bottom of the figure. The migration of the ligand within the distal pocket is depicted by the fluctuations in distance for the respective measurement.

stationary above the heme plane with no change in orientation. As a result, the iron–ligand distance is reported as the Fe—C distance (the C atom in this instance being oriented away from the iron), not the Fe—N distance as was performed in the CN^- simulation. This distance remained constant at 3.8 Å. The Fe—N^{ε} distance and Fe–ligand bend angle also remained constant at 6.4 Å and 154°, respectively.

4. Discussion

The presence of two alternate conformations of a diatomic ligand in the distal pocket of heme is attributed to photoreduction of Fe^{III}–CN to Fe^{II}–CN followed by dissociation of the Fe^{II}—CN bond. We have investigated this hypothesis by measurement of the CN^--dissociation constant for the Fe^{III} and Fe^{II} forms of DHPCN, measurement of the formal reduction potential, DFT and MD calculations. These studies are relevant for X-ray crystallographic studies of ferric heme proteins in general where photoreduction is an inherent side-effect of data collection, particularly using synchrotron radiation. DHP A is an interesting case because its reduction potential is the highest known for any Hb (with the exception of the giant Hb of *Lumbricus*; Harrington *et al.*, 2007) and thus it is more prone to photoreduction. The functional significance of the higher redox potential is still not clear, but it may provide a means for DHP A to cycle between two functions by favoring reduction of the heme iron under conditions where H_2O_2 is not present. Thus, it is possible that the dual function of DHP A is maintained by the local environment in the coelom of *A. ornata*. The C73S mutant has a 0.012 V higher reduction potential than wild-type DHP A, which is consistent with the observation that photoreduction is more facile in the C73S mutant than in wild-type DHP A. Cys73 is a surface cysteine that is located near the dimer interface in the X-ray crystal structure (PDB code 2qfn). The mutation C73S has no major effect on protein structure, but may play a role in protein–protein interactions in solution. The functional consequence of the high reduction potential of DHP A remains to be explained since it is nearly 0.5 V more positive than that of HRP (Battistuzzi *et al.*, 2002). This fact suggests that activation of H_2O_2 (or possibly O_2) in DHP A occurs by a different mechanism from that in typical peroxidases.

Photoreduction can lead to dissociation provided that there is a change in the ligation strength that depends on the oxidation state of the heme iron. Equilibrium binding studies of CN^- provide a means to test the relative stability of the Fe^{II}–CN and Fe^{III}–CN adducts. The experimentally observed difference in binding constant corresponds to a loss in stabilization free energy of the Fe–CN adduct of 27.3 kJ mol^{-1} upon reduction from Fe^{III} to Fe^{II}. Consistent with this loss of stabilization, spectroscopic studies of the dithionite reduction of the Fe^{III}–CN adduct of myoglobin (MbCN) provide evidence for the transient formation of an unstable Fe^{II} MbCN intermediate in the process of forming the final product, deoxy Mb (Cox & Hollaway, 1977; Bellelli *et al.*, 1990). Ligand destabilization upon chemical reduction was not observed for the metMb adducts of other ligands such as SCN^-, N_3^- and F^-. These observations support the hypothesis that photoreduction will destabilize CN^- coordination to the heme iron.

While the data are consistent with facile photoreduction in DHP A, it is more difficult to discern the identity of the molecule that occupies the extra electron density in the distal pocket of DHP A shown in Figs. 2 and 3, which is associated with an apparent second conformation of a diatomic ligand. The evolution of the geometry of the DHPCN structure can be explained by the dissociation and migration of the CN^- ligand. We consider below the possibility that the identity of the diatomic ligand changes during the course of X-ray data collection. However, first we consider the evidence that the change in the Fe—C—N angle over time is the result of CN^- dissociation. Since CN^- is isoelectronic with CO, the Fe—C—N angle in FeP–CN should be similar to the angle of 179° found for Fe—C—O in MbCO (Lim *et al.*, 1995) and as observed in model porphyrin–CO complexes (Peng & Ibers, 1976). Early studies of MbCN suggested that the Fe—C—N is nearly linear (Deatherage *et al.*, 1976) but slightly tilted from the heme normal. High-resolution X-ray diffraction and XANES structural studies agree that the Fe—C—N angle is 166–170° in MbCN (PDB codes 1ebc and 2jho; Bolognesi *et al.*, 1999; Arcovito *et al.*, 2007). However, at room temperature photoreduction and photolysis was observed that gave rise to an Fe—C—N angle of approximately 90°, as observed in photolyzed Fe-CO (Schlichting *et al.*, 1994; Teng *et al.*, 1994; Hartmann *et al.*, 1996; Srajer *et al.*, 1996; Schotte *et al.*, 2004). Consistent with these precedents, the Fe—C—N angle observed in the DHPCN structure has a maximum value of ∼154° and decreases progressively thoughout data collection to a value of ∼126°. Our interpretation of the fact that the largest angle is 154°, rather than the 170° found in the 1ebc or 2jho structures, is that Fe^{III} is reduced so readily in the DHPCN structure that some amount of Fe reduction has occurred even in the shortest possible time frames in our data collection, which is best modeled by a single CN^- displaced from the linear conformation.

The fate of the dissociated CN^- ligand could be either to remain in the distal pocket and possibly to be protonated to form HCN or to escape and be replaced by O_2. The phenomenon of reduction of the heme iron center and concomitant dissociation of CN^- is reminiscent of the phenomenon of photolysis of carbon monoxide from the MbCO complex and subsequent entrapment of CO in the 'Xe' binding sites (Schlichting *et al.*, 1994; Teng *et al.*, 1994; Hartmann *et al.*, 1996; Srajer *et al.*, 1996; Schotte *et al.*, 2004). However, the negative charge on CN^- may have an effect on the conformation assumed in the distal pocket and possibly on the escape trajectory. In the C73S mutant metaquo structure (PDB code 2qfn), Fe^{III}–OH_2 was replaced by Fe^{II}–O_2 during the course of data collection as a result of reduction of the heme iron center (de Serrano *et al.*, 2007). The OMIT-map electron density in the C73S–O_2 structure is similar to the apparent OMIT-map electron density in the C73SCN and DHPCN structures, leading to the suggestion that O_2 is able to diffuse into the distal pocket and replace CN^- under the conditions of both experiments.

Given the difficulty in identifying the diatomic ligand in the X-ray crystal structures, we employed DFT calculations of the ImFeP–CN and ImFeP–O_2 structures and MD simulations of the respective ligand trajectories to provide support for the model that O_2 replaces CN^- during data collection. Firstly, geometry optimizations of $ImFe^{III}$–CN and $ImFe^{II}$–O_2 suggest that the electron density observed in the CN1 state is that of O_2. The reported Fe–CN bend angle is 126°. Calculations show that this bend angle does not agree with the calculated Fe^{III}–CN bend angle of 180°, but corresponds to bound O_2 with a calculated angle of 125° (Table 4). The experimental Fe–ligand bond length is 2.1 Å, corresponding to the calculated Fe—O bond length of 2.08 Å, not the Fe—C bond length of 1.89 Å. However, XANES provides evidence for a significantly shorter Fe—CN bond (Arcovito *et al.*, 2007) so that the comparison of bond lengths is only valid in a relative sense. Secondly, potential energy surfaces were generated to study the binding energies of FeP–CN for various spin and oxidation states. Taking into account all possible spin states and out-of-plane conformations (spin S = 0 and 2 for Fe^{II} or S = 1/2 and 5/2 for Fe^{III} and Q_p = 0.0, 0.2 or 0.4 Å), only one dissociative state was observed, high-spin Fe^{II}, in which the iron was displaced 0.4 Å out of the heme plane. DFT results suggest that heme undergoes photoreduction from the ferric to the ferrous form, with a decrease in calculated Fe–CN binding energy of ΔE = 85 kJ mol^{-1}, which may be accompanied by cleavage of the Fe—CN bond when the iron heme experiences a rapid out-of-plane motion. The magnitude of the calculated free-energy change (85 kJ mol^{-1}) is larger than the measured change based on the difference in Fe–CN dissociation constants (27 kJ mol^{-1}); this is most likely to be a consequence of the additional interactions of the diatomic ligand with His55, which were not included in the calculation.

Several molecular-dynamic simulations were performed to further elucidate the identity of the electron density observed in the $2F_o - F_c$ map. As mentioned above, possible candidates for this density included CN^-, HCN and O_2. The results of the MD simulations propose that the observed electron density was neither CN^- nor HCN. The CN^- ligand was observed to immediately exit the distal pocket and migrate into the solvation sphere, which is consistent with loss of CN^- from the distal pocket. The simulations show HCN hydrogen bonding to the heme iron. This orientation is contrary to the observed electron density, which is consistent with two conformations: one that is bound to the iron (not hydrogen bonded) and a second that is stabilized within the pocket by forming a hydrogen bond to His55. Simulations of the DHP–O_2 system yielded the closest agreement with the experimental data. Both tautomeric forms of His55 (HSD and HSE) were studied in order to obtain a more precise model of the conformation of O_2. The HSD results exhibited the best agreement with the experimental distances (all within 1.0 Å). However, the HSE tautomer showed the closest agreement with the Fe-O_2 bend angle for dissociated O_2, *i.e.* the CN2 conformation. The experimental Fe—O—O angle for CN2 is 173°, while the calculated angle is 90° and 130° for the HSD and HSE tautomers, respectively. Moreover, the O_2 ligand moves from ~4 to ~7 Å in the HSE simulation, which corresponds to migration into the Xe4 binding site (Nienhaus *et al.*, 2006). We have recently confirmed by X-ray crystallography that a similar Xe-binding site also exists in DHP A (de Serrano *et al.*, manuscript in preparation). In summary, it appears that some combination of the HSD and HSE simulations gives agreement with the experimental electron density if O_2 is the ligand.

5. Conclusions

We have observed photoreduction of the ferric heme iron from Fe^{III} to Fe^{II}, which appears to lead to dissociation of CN^- originally bound to the heme iron. The photoreduction depends on the duration of exposure to X-ray radiation. The ease of photoreduction is consistent with the high reduction potential of the heme Fe in DHP A relative to other Hbs. The reduction potential is completely outside the normal range for peroxidases, suggesting that DHP A may activate H_2O_2, or even O_2, by a different mechanism, such as electron transfer from an as yet unidentified cofactor. The OMIT-map electron density, dissociation constant and potential energy surfaces calculated by DFT methods are consistent with dissociation of CN^- from Fe^{II}. MD simulations provide evidence for the replacement of CN^- by O_2 in the distal cavity at 100 K. Based on the comparison of MD trajectories with the structure, His55 appears to play a role in stabilizing O_2 in the distal pocket by hydrogen-bond formation. The ease of ligand substitution in the distal pocket is consistent with our previous X-ray crystal structures (PDB codes 3dr9 and 2qfk), which show that His55 is unusually flexible in DHP A. The significant role played by hydrogen bonding of His55 to O_2 further supports the proposed role of His55 as an acid–base catalyst in the heterolytic cleavage of hydrogen peroxide and removal of the generated water molecule, which are both essential elements of the peroxidase mechanism.

We would like to thank Gerald Guanga and Dr Greg Buhrman of the Department of Molecular and Structural Biochemistry at North Carolina State University for collecting data on the SER-CAT synchrotron beamline at the Advanced Photon Source in Argonne, Illinois. Use of the Advanced Photon Source was supported by the US Department of Energy, Office of Science, Office of Basic Energy Sciences under Contract No. W-31-109-Eng-38. SF and EFB acknowledge support from the Army Research Office through grants 52278-LS and 51432-CH-SR, respectively.

References

Arcovito, A., Benfatto, M., Cianci, M., Hasnain, S. S., Nienhaus, K., Nienhaus, U., Savino, C., Strange, R. W., Vallone, B. & Della Longa, S. (2007). *Proc. Natl Acad. Sci. USA*, **104**, 6211–6216.

Battistuzzi, G., Borsari, M., Ranieri, A. & Sola, M. (2002). *J. Am. Chem. Soc.* **124**, 26–27.

Becke, A. D. (1988). *Phys. Rev. A*, **38**, 3098–3100.

Bellelli, A., Antonini, G., Brunori, M., Springer, B. A. & Sligar, S. G. (1990). *J. Biol. Chem.* **265**, 18898–18901.

Belyea, J., Belyea, C. M., Lappi, S. E. & Franzen, S. (2006). *Biochemistry*, **45**, 14275–14284.

Belyea, J., Gilvey, L. B., Davis, M. F., Godek, M., Sit, T. L., Lommel, S. A. & Franzen, S. (2005). *Biochemistry*, **44**, 15637–15644.

Blair-Johnson, M., Fiedler, T. & Fenna, R. (2001). *Biochemistry*, **40**, 13990–13997.

Bolognesi, M., Rosano, C., Losso, R., Borassi, A., Rizzi, M., Wittenberg, J. B., Boffi, A. & Ascenzi, P. (1999). *Biophys. J.* **77**, 1093–1099.

Brünger, A. T., Adams, P. D., Clore, G. M., DeLano, W. L., Gros, P., Grosse-Kunstleve, R. W., Jiang, J.-S., Kuszewski, J., Nilges, M., Pannu, N. S., Read, R. J., Rice, L. M., Simonson, T. & Warren, G. L. (1998). *Acta Cryst.* D**54**, 905–921.

Chance, B. (1943). *J. Biol. Chem.* **179**, 1299–1309.

Chance, B., Angiolillo, P., Yang, E. K. & Powers, L. (1980). *FEBS Lett.* **112**, 178–182.

Chen, Y. P., Woodin, S. A., Lincoln, D. E. & Lovell, C. R. (1996). *J. Biol. Chem.* **271**, 4609–4612.

Chen, Z., de Serrano, V., Betts, L. & Franzen, S. (2009). *Acta Cryst.* D**65**, 34–40.

Collaborative Computational Project, Number 4 (1994). *Acta Cryst.* D**50**, 760–763.

Cox, R. P. & Hollaway, M. R. (1977). *Eur. J. Biochem.* **74**, 575–587.

D'Antonio, E., Bowden, E. & Franzen, S. (2010). Submitted.

Davis, M. F., Gracz, H., Vendeix, F. A. P., de Serrano, V., Somasundaram, A., Decatur, S. M. & Franzen, S. (2009). *Biochemistry*, **48**, 2164–2172.

Deatherage, J. F., Loe, R. S., Anderson, C. M. & Moffat, K. (1976). *J. Mol. Biol.* **104**, 687–706.

DeLano, W. L. (2002). *The PyMOL Molecular Graphics System.* DeLano Scientific, San Carlos, California, USA.

Delley, B. (1990). *J. Chem. Phys.* **92**, 508–517.

Delley, B. (2000). *J. Chem. Phys.* **113**, 7756–7764.

Edwards, S. L. & Poulos, T. L. (1990). *J. Biol. Chem.* **265**, 2588–2595.

Emsley, P. & Cowtan, K. (2004). *Acta Cryst.* D**60**, 2126–2132.

Fedorov, R., Ghosh, D. K. & Schlichting, I. (2003). *Arch. Biochem. Biophys.* **409**, 25–31.

Feducia, J., Dumarieh, R., Gilvey, L. B. G., Smirnova, T., Franzen, S. & Ghiladi, R. A. (2009). *Biochemistry*, **48**, 995–1005.

Franzen, S. (2002). *Proc. Natl Acad. Sci. USA*, **99**, 16754–16759.

Franzen, S., Gilvey, L. B. & Belyea, J. (2007). *Biochim. Biophys. Acta*, **1774**, 121–131.

Fukuyama, K. & Okada, T. (2007). *Acta Cryst.* D**63**, 472–477.

Furtmüller, P. G., Zederbauer, M., Jantschko, W., Helm, J., Bogner, M., Jakopitsch, C. & Obinger, C. (2006). *Arch. Biochem. Biophys.* **445**, 199–213.

George, S. J., Fu, J., Guo, Y., Drury, O. B., Friedrich, S., Rauchfuss, T., Volkers, P. I., Peters, J. C., Scott, V., Brown, S. D., Thomas, C. M., Cramer, S. P. (2008). *Inorg. Chim. Acta*, **361**, 1157–1165.

Han, K. P., Woodin, S. A., Lincoln, D. E., Fielman, K. T. & Ely, B. (2001). *Mar. Biotechnol.* **3**, 287–292.

Harrington, J. P., Kobayashi, S., Dorman, S. C., Zito, S. L. & Hirsh, R. E. (2007). *Artif. Cells Blood Substit. Immobil. Biotechnol.* **35**, 53–67.

Hartmann, H., Zinser, S., Komninos, P., Schneider, R. T., Nienhaus, G. U. & Parak, F. (1996). *Proc. Natl Acad. Sci. USA*, **93**, 7013–7016.

Heineman, W. R., Meckstroth, M. L., Norris, B. J. & Su, C. (1979). *J. Electroanal. Chem.* **104**, 577–585.

Humphrey, W., Dalke, A. & Schulten, K. (1996). *J. Mol. Graph.* **14**, 33–38.

Keilin, D. & Hartree, E. F. (1955). *Biochem. J.* **61**, 153–171.

LaCount, M. W., Zhang, E., Chen, Y. P., Han, K., Whitton, M. M., Lincoln, D. E., Woodin, S. A. & Lebioda, L. (2000). *J. Biol. Chem.* **275**, 18712–18716.

Laskowski, R. A., MacArthur, M. W., Moss, D. S. & Thornton, J. M. (1993). *J. Appl. Cryst.* **26**, 283–291.

Lee, C. T., Yang, W. T. & Parr, R. G. (1988). *Phys. Rev. B*, **37**, 785–789.

Lim, M., Jackson, T. A. & Anfinrud, P. A. (1995). *Science*, **269**, 962–966.

Lincoln, D. E., Fielman, K. T., Marinelli, R. L. & Woodin, S. A. (2005). *Biochem. Syst. Ecol.* **33**, 559–570.

McCoy, A. J., Grosse-Kunstleve, R. W., Storoni, L. C. & Read, R. J. (2005). *Acta Cryst.* D**61**, 458–464.

Murshudov, G. N., Vagin, A. A. & Dodson, E. J. (1997). *Acta Cryst.* D**53**, 240–255.

Murray, J. W., Rudiño-Piñera, E., Owen, R. L., Grininger, M., Ravelli, R. B. G. & Garman, E. F. (2005). *J. Synchrotron Rad.* **12**, 268–275.

Nienhaus, K., Deng, P. C., Belyea, J., Franzen, S. & Nienhaus, G. U. (2006). *J. Phys. Chem. B*, **110**, 13264–13276.

Nienhaus, K., Nickel, E., Davis, M. F., Franzen, S. & Nienhaus, G. U. (2008). *Biochemistry*, **47**, 12985–12994.

Otwinowski, Z. & Minor, W. (1997). *Methods Enzymol.* **276**, 307–326.

Peng, S.-M. & Ibers, J. A. (1976). *J. Am. Chem. Soc.* **98**, 8032–8036.

Phillips, J. C., Braun, R., Wang, W., Gumbart, J., Tajkhorshid, E., Villa, E., Chipot, C., Skeel, R. D., Kale, L. & Schulten, K. (2005). *J. Comput. Chem.* **26**, 1781–1802.

Sanctis, D. de, Ascenzi, P., Bocedi, A., Dewilde, S., Burmester, T., Hankeln, T., Moens, L. & Bolognesi, M. (2006). *Biochemistry*, **45**, 10054–10061.

Schlichting, I., Berendzen, J., Philips, G. N. Jr & Sweet, R. M. (1994). *Nature (London)*, **371**, 808–812.

Schotte, F., Lim, M. H., Jackson, T. A., Smirnov, A. V., Soman, J., Olson, J. S., Phillips, G. N., Wulff, M. & Anfinrud, P. A. (2003). *Science*, **300**, 1944–1947.

Schotte, F., Soman, J., Olson, J. S., Wulff, M. & Anfinrud, P. A. (2004). *J. Struct. Biol.* **147**, 235–246.

Serrano, V. de, Chen, Z., Davis, M. F. & Franzen, S. (2007). *Acta Cryst.* D**63**, 1094–1101.

Serrano, V. de, D'Antonio, J., Thompson, M., Franzen, S. & Ghiladi, R. A. (2010). Submitted.

Smolenaers, P. J. & Beattie, J. K. (1979). *Inorg. Synth.* **19**, 117–121.

Srajer, V., Teng, T.-Y., Ursby, T., Pradervand, C., Ren, Z., Adachi, S.-I., Schildkamp, W., Bourgeois, D., Wulff, M. & Moffat, K. (1996). *Science*, **274**, 1726–1729.

Sugishima, M., Sakamoto, H., Noguchi, M. & Fukuyama, K. (2003). *Biochemistry*, **42**, 9898–9905.

Teng, T.-Y., Srajer, V. & Moffat, K. (1994). *Nature Struct. Biol.* **1**, 701–705.

Thompson, M. K., Davis, M. F., de Serrano, V., Nicoletti, F. P., Howes, B. D., Smulevich, G. & Franzen, S. (2010). In the press.

Vangberg, T., Bocian, D. F. & Ghosh, A. (1997). *J. Biol. Inorg. Chem.* **2**, 526–530.

Vojtechovsky, J., Chu, K., Berendzen, J., Sweet, R. M. & Schlichting, I. (1999). *Biophys. J.* **77**, 2153–2174.

Weinert, M. & Davenport, J. W. (1992). *Phys. Rev. B*, **45**, 13709–13712.

Acta Crystallographica Section D
Biological Crystallography
ISSN 0907-4449

Structure of dehaloperoxidase B at 1.58 Å resolution and structural characterization of the AB dimer from *Amphitrite ornata*

Vesna de Serrano, Jennifer D'Antonio, Stefan Franzen and Reza A. Ghiladi*

North Carolina State University, USA

Correspondence e-mail: reza_ghiladi@ncsu.edu

Received 4 January 2010
Accepted 8 February 2010

PDB Reference: dehaloperoxidase B, 3ixf.

As members of the globin superfamily, dehaloperoxidase (DHP) isoenzymes A and B from the marine annelid *Amphitrite ornata* possess hemoglobin function, but they also exhibit a biologically relevant peroxidase activity that is capable of converting 2,4,6-trihalophenols to the corresponding 2,6-dihaloquinones in the presence of hydrogen peroxide. Here, a comprehensive structural study of recombinant DHP B, both by itself and cocrystallized with isoenzyme A, using X-ray diffraction is presented. The structure of DHP B refined to 1.58 Å resolution exhibits the same distal histidine (His55) conformational flexibility as that observed in isoenzyme A, as well as additional changes to the distal and proximal hydrogen-bonding networks. Furthermore, preliminary characterization of the DHP AB heterodimer is presented, which exhibits differences in the AB interface that are not observed in the A-only or B-only homodimers. These structural investigations of DHP B provide insights that may relate to the mechanistic details of the H_2O_2-dependent oxidative dehalogenation reaction catalyzed by dehaloperoxidase, present a clearer description of the function of specific residues in DHP at the molecular level and lead to a better understanding of the paradigms of globin structure–function relationships.

1. Introduction

Spanning all kingdoms of life, the globin superfamily is comprised of a vast number of proteins which exhibit a diverse array of functions. Although defined by the presence of a characteristic protein fold, namely the canonical 3/3 α-helical structure most commonly associated with myoglobin (Mb), the sequence homology between globins from different phyla may be as low as 10%. Thus, the combination of a highly conserved structural motif with a relatively low sequence homology, coupled with the diverse number of roles which globins fulfill, has been the driving force behind new research into understanding the nuances of globin structure–function relationships that enable specific discrete functions.

As an example of a globin found in marine organisms, structural and mechanistic investigations of the enzyme dehaloperoxidase (DHP) may reveal new insights into the structure–function paradigms of the globin superfamily. DHP is a bifunctional hemoprotein which acts as both the O_2-transport protein and as a peroxidase in the terebellid polychaete *Amphitrite ornata* (LaCount *et al.*, 2000; Chen *et al.*, 1996), although how DHP performs these dual roles remains unclear at the present time. DHP has been shown to be a homodimer consisting of two identical subunits of ~15.5 kDa

in the asymmetric unit, each of which contains a heme protoporphyrin IX cofactor and eight α-helices (de Serrano *et al.*, 2007; Zhang *et al.*, 1996). These subunits are connected through an interface mainly comprised of salt bridges from acidic and basic amino-acid residues on the protein surface, specifically between Asp72 of one subunit and the side-chain groups of Arg122 and Asn126 of the other subunit (Lebioda *et al.*, 1999; Chen *et al.*, 2009). There is also a hydrophobic interaction between the Val74 residues of the two subunits (LaCount *et al.*, 2000). The only cysteine present in DHP, Cys73, is located in close proximity to this interface. However, the distance between the S atoms within the dimer subunits is not sufficiently short to make a potential disulfide bond between the subunits likely.

Since the seminal work of Lebioda and coworkers revealed a small-molecule-binding pocket in close proximity to the heme active site (Lebioda *et al.*, 1999), several studies have focused on the specifics of substrate localization in DHP (Davis *et al.*, 2009; Smirnova *et al.*, 2008; Nienhaus *et al.*, 2008; Belyea *et al.*, 2005), a feature that is unique to dehaloperoxidase among all known globins. More recently, it has been postulated that both external and internal small-molecule-binding sites may exist, with regulatory implications that may govern how DHP switches between its hemoglobin and peroxidase activities (Chen *et al.*, 2009; Davis *et al.*, 2009; Smirnova *et al.*, 2008). One intriguing possibility is that the distal histidine His55, which has been observed in distinct 'open' and 'closed' conformations, mediates either H_2O or O_2 displacement from the heme in the presence of (tri)halophenol substrate, possibly serving as a trigger for peroxidase function (Chen *et al.*, 2009). It has been hypothesized that the 'open' and 'closed' conformations are the consequence of an equilibrium between five-coordinate and six-coordinate (metaquo) forms of DHP at room temperature, respectively (Chen *et al.*, 2009; Lebioda *et al.*, 1999). Specifically, in the open conformation His55 is swung out of the distal pocket and solvent-exposed, with a heme Fe$-$N$_{His}$ distance of $\sim$9 Å, and for this reason is unable to participate in hydrogen-bonding interactions that would stabilize the presence of a sixth axial heme ligand. The open conformation is not unique to DHP; it has been observed previously in myoglobin (Mb) at low pH (Tian *et al.*, 1993; Zhu *et al.*, 1992; Sage *et al.*, 1991). In contrast, the 'closed' conformation of DHP, with His55 swung into the distal pocket, exhibits a heme Fe$-$N$_{His}$ distance of 5.4 Å and represents a more reasonable distance for associating with the sixth heme ligand (*i.e.* water or dioxygen) *via* hydrogen-bonding interactions (de Serrano *et al.*, 2007). This is clearly shown in the structure of oxyferrous DHP, in which a bent bonding geometry for the Fe$-$O(1)$-$O(2) adduct was observed, yielding a 2.8 Å hydrogen bond between O(2), the second O atom of molecular oxygen bound to the heme iron, and the N$^{\varepsilon}$ atom of the distal histidine His55 (de Serrano *et al.*, 2007). A similar closed conformation of the distal histidine in Mb has also been shown to exist under basic conditions (Tian *et al.*, 1993; Zhu *et al.*, 1992).

To date, X-ray diffraction studies of dehaloperoxidase have been limited to one isoenzyme (DHP A; Chen *et al.*, 2009; de Serrano *et al.*, 2007; LaCount *et al.*, 2000; Zhang *et al.*, 1996; Lebioda *et al.*, 1999). However, two isoforms of dehaloperoxidase, termed DHP A and DHP B, occur in *A. ornata* and are encoded by two separate genes (*dhpA* and *dhpB*; Han *et al.*, 2001). Both have been shown to catalyze the oxidative dehalogenation of 2,4,6-trihalogenated phenols to the corresponding 2,6-dihalo-1,4-benzoquinones in the presence of hydrogen peroxide (Feducia *et al.*, 2009; D'Antonio *et al.*, 2010). Although they share 96% sequence identity (DHP B differs from DHP A at five positions: I9L, R32K, Y34N, N81S and S91G), significant spectroscopic and mechanistic differences between dehaloperoxidase isoenzymes A and B have recently been elucidated (D'Antonio *et al.*, 2010). These include the observations that DHP B is twofold to fourfold more active than DHP A (depending on the trihalophenol substrate), that it forms a Compound RH intermediate which exhibits different reactivity to the analogous species in DHP A and that DHP B exhibits a greater extent of substrate inhibition than DHP A. Furthermore, an interesting parallel may be drawn between DHP A and B and the α and β chains of Hb: two globin chains which are structurally homologous yet exhibit altered chemical reactivity (Feducia *et al.*, 2009; D'Antonio *et al.*, 2010). Given this, a number of interesting questions can be posed. For example, what are the structural features of DHP B and what are the differences when compared with DHP A? Will DHP B exhibit the same conformational flexibility of the distal histidine (His55) as DHP A? How does the S91G substitution in DHP B alter the proximal histidine (His89) binding? Is the small-molecule-binding pocket maintained in DHP B? Will DHP A and B form an $\alpha\beta$ dimer or an $\alpha_2\beta_2$ tetramer reminiscent of that found in hemoglobin (Hb) and will cooperative effects on O_2-binding or peroxidase activity be observed? To begin to address these and other questions, here we present a structural study of recombinant DHP B both by itself and with isoenzyme A using X-ray diffraction. Such investigations of DHP B may provide critical insight that may help in understanding the mechanistic details of the H_2O_2-dependent oxidative dehalogenation reaction catalyzed by dehaloperoxidase and may advance our knowledge of how globins acquired such an enzymatic function. Our structural findings on DHP B are presented in the light of our recent mechanistic investigations on both isoenzymes (Feducia *et al.*, 2009; D'Antonio *et al.*, 2010) and together provide a clearer description of the function of DHP at the molecular level.

2. Materials and methods

2.1. Protein purification, characterization and crystallization

Buffer salts were purchased from Fisher Scientific. All other reagents and biochemicals, unless otherwise specified, were of the highest grade available from Sigma–Aldrich. The QIAprep Spin Miniprep Kit was from Qiagen Sciences (Valencia, California, USA) and the QuikChange II site-directed mutagenesis kit was purchased from Stratagene (La Jolla, California, USA). The required oligonucleotides were

synthesized by IDT DNA Technologies Inc. Optical spectra were recorded using quartz microcuvettes (1 cm path length) on a Cary 50 UV–visible spectrophotometer equipped with thermostatted cell holders at 298 K.

For protein crystallization, the polyhistidine purification tag was removed from the 5′-end of the template plasmid pDHPB(6×His), which encodes the DHP B isoenzyme, using the QuikChange II site-directed mutagenesis kit. Mutagenesis [melting (368 K, 50 s), annealing (333 K, 50 s) and extension (341 K, 6 min)] was performed for 18 cycles using the mutagenic primers 5′-AGG AGA TAT ACC ATG GGG TTT AAA CAA GAT-3′ (sense) and 5′-ATC TTG TTT AAA CCC CAT GGT ATA TCT CCT-3′ (antisense). The plasmid was extracted using the QIAprep Spin Miniprep Kit and DNA sequencing of the resulting plasmid pDHPB(-6×-His) bearing the *dhpB* gene confirmed the success of the His-tag deletion and the absence of secondary mutations. Recombinant DHP B lacking the polyhistidine tag was subsequently overexpressed in Rosetta *Escherichia coli* cells (DE3 strain) and purified using the procedures established for the purification of DHP A (de Serrano *et al.*, 2007). DHP A (non-His-tagged) was also expressed and purified as described previously (Davis *et al.*, 2009) with only minor modification. The purification strategy (ammonium sulfate fractionation followed by ion-exchange and size-exclusion chromatography) resulted in protein that was of satisfactory purity for crystallization. As has previously been noted for dehaloperoxidase (Roach *et al.*, 1997), the enzyme was initially isolated as a mixture of the ferric and oxyferrous forms. Enzyme in the purely ferric state was prepared by treatment with an excess of potassium ferricyanide as described elsewhere (de Serrano *et al.*, 2007; D'Antonio *et al.*, 2010). Only protein samples that exhibited Reinheitzahl values (R_z) of greater than 4.0 were utilized in this study. The concentration of DHP B was determined spectrophotometrically (ε_{406} = 117.6 mM^{-1} cm^{-1}; D'Antonio *et al.*, 2010). Dehaloperoxidase activity assays of the enzyme preparations used here for crystallization confirmed proper enzymatic function (Feducia *et al.*, 2009; D'Antonio *et al.*, 2010).

The crystal structure of DHP B was determined for the protein in the ferric oxidation state and was confirmed by UV–visible spectroscopy, which showed the characteristic 406 nm Soret band absorption of the ferric protein (Feducia *et al.*, 2009; D'Antonio *et al.*, 2010). All crystallizations were carried out at 277 K using the hanging-drop vapor-diffusion method. For DHP B, the protein (9 mg ml^{-1}) in 20 m*M* sodium cacodylate buffer pH 6.5 was mixed with an equal volume of crystallization solution and equilibrated against 600 µl crystallization solution [0.2 *M* ammonium sulfate and PEG 4000 in the concentration range 30–36%(*w*/*v*)]. Crystals initially grew in twinned clusters that appeared after 3 d of incubation and were subsequently improved by two rounds of microseeding. The crystals were allowed to grow for 7 d after microseeding and were harvested into mother liquor supplemented with 15% PEG 400 as a cryoprotectant and flash-frozen at 100 K for data collection. A diffraction data set was collected using Cu *Kα* radiation and was refined to a resolution of 1.58 Å with an *R* factor of 17.0% ($R_{\rm free}$ = 21.4%). To grow crystals from a mixture of DHP A and B, the two proteins were combined in a 1:1 molar ratio (11 mg ml^{-1} final protein concentration), followed by mixing the protein solution with an equal volume of crystallization solution and incubating the mixture in a hanging drop over a 600 µl reservoir of crystallization solution as described above. The best diffraction-quality DHP AB crystals grew from 0.2 *M* ammonium sulfate and 32% PEG 4000.

2.2. X-ray data collection and structure refinement

X-ray diffraction data were collected from the DHP B crystals using a Rigaku MicroMax007 HF copper rotating-anode generator (λ = 1.5418 Å) equipped with VariMax HF optics and a Rigaku R-AXIS IV^{++} image-plate detector (Biomolecular X-ray Crystallography Core Facility, University of North Carolina at Chapel Hill). The data set was collected from a single crystal at a crystal-to-detector distance of 85 mm using a 1° oscillation range and an exposure time of 3 min per image. The diffraction data for the DHP AB crystals were collected on the SER-CAT 22-BM beamline at the Advanced Photon Source (Argonne, Illinois, USA) using a wavelength of 0.91339 Å, a 1° oscillation range and a crystal-to-detector distance of 120 mm. The diffraction data were reduced and scaled using the *HKL*-2000 suite (Otwinowski & Minor, 1997). The crystals of both DHP B and DHP AB belonged to space group $P2_12_12_1$, as do the crystals of DHP A, and had unit-cell parameters a = 60.65, b = 67.42, c = 67.48 Å and a = 60.165, b = 67.387, c = 67.653 Å, respectively, which are very similar to the unit-cell parameters of the DHP A crystals (de Serrano *et al.*, 2007). The crystals of DHP B diffracted to a resolution of 1.58 Å and those of DHP AB diffracted to a resolution of 1.52 Å.

The structures of DHP B and DHP AB were determined by molecular replacement with *Phaser* (McCoy *et al.*, 2005) using the metaquo structure of DHP A (PDB entry 2qfk; de Serrano *et al.*, 2007) as a search model. Cycles of refinement and map calculation were carried out with *REFMAC*5 from the *CCP*4 suite of programs (Collaborative Computational Project, Number 4, 1994) and were iterated with model building using the *Coot* program (Emsley & Cowtan, 2004). All occupancies were refined manually. The final model of DHP B refined to an *R* factor of 17.0% ($R_{\rm free}$ = 21.4%) and contained two protein molecules, with 94.0% of the residues in the most favored regions of the Ramachandran plot and the remaining 6.0% in allowed regions, whereas that of DHP AB refined to $R_{\rm work}$ and $R_{\rm free}$ values of 17.6% and 21.9%, respectively, with 93.6% of the residues in the most favored region and 6.4% of the residues in the allowed region of the Ramachandran plot. Under the conditions employed, DHP B crystallized with two molecules in the asymmetric unit; the main-chain atoms of the two molecules superposed with an average displacement of 0.289 Å. These findings are analogous to those for DHP A, which also was found to crystallize as a homodimer (de Serrano *et al.*, 2007; LaCount *et al.*, 2000). Data-collection and refinement statistics are summarized in Table 1. The structural coordinates for DHP B have been deposited in the Research

Collaboratory for Structural Bioinformatics (RCSB) Protein Data Bank under accession code 3ixf.

Table 1
Data-collection and refinement statistics for DHP B.

Values in parentheses are for the highest resolution shell.

	DHP B	DHP AB complex†
Data collection		
Space group	$P2_12_12_1$	$P2_12_12_1$
Unit-cell parameters		
a (Å)	60.65	60.17
b (Å)	67.42	67.39
c (Å)	67.48	67.65
$\alpha = \beta = \gamma$ (°)	90	90,
Temperature (K)	100	100
Wavelength (Å)	1.54	0.913
Resolution (Å)	30.17–1.58 (1.62–1.58)	40.00–1.52 (1.56–1.52)
R_{merge}‡	9.7 (54.7)	7.9 (62.8)
$I/\sigma(I)$	21.9 (2.5)	19.3 (2.7)
Completeness (%)	99.7 (99.9)	97.0 (98.9)
Redundancy	4.8 (4.8)	4.9 (4.7)
Refinement		
No. of reflections	36546 (2665)	39585 (2934)
R_{work}/R_{free}§ (%)	17.0/21.4	17.6/21.9
Average B factor (Å^2)		
All atoms	13.82	10.13
Protein	12.52	9.07
Water	23.84	20.63
No. of atoms		
Protein	3002	3139
Water	373	287
R.m.s.d.¶ from ideal		
Bond lengths (Å)	0.024	0.011
Bond angles (°)	2.197	1.365
Ramachandran plot†† (%)		
Most favored	94.0	93.6
Allowed	6.0	6.4

† Protein crystallized using a 1:1 ratio of DHP A and DHP B. ‡ $R_{merge} = \sum_{hkl}\sum_i |I_i(hkl) - \langle I(hkl)\rangle| / \sum_{hkl}\sum_i I_i(hkl)$, where $I_i(hkl)$ is the ith measurement of $I(hkl)$ and $\langle I(hkl)\rangle$ is the weighted mean of all measurements of $I(hkl)$. § $R_{work} = \sum_{hkl} ||F_{obs}| - |F_{calc}|| / \sum_{hkl} |F_{obs}|$, where F_{obs} are the observed and F_{calc} are the calculated structure factors; R_{free} is the R factor for a subset (5%) of reflections selected before and not included in the refinement. ¶ Root-mean-square deviation. †† Calculated using *PROCHECK* (Laskowski *et al.*, 1993).

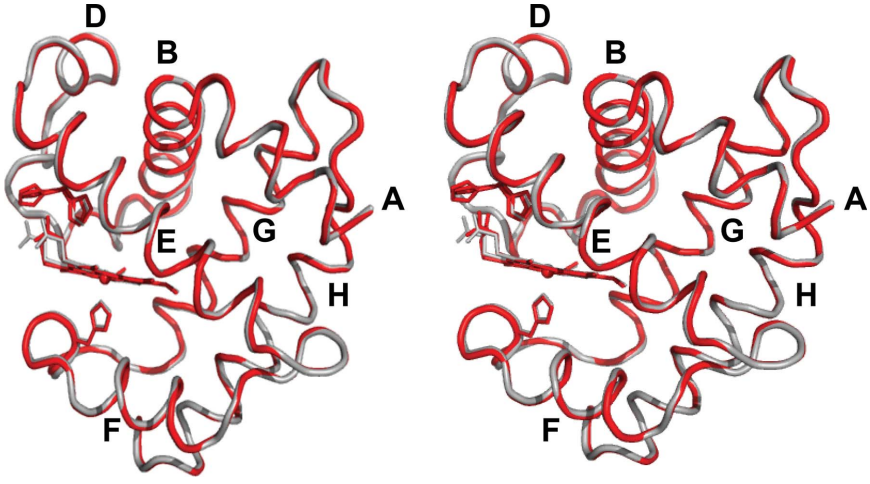

Figure 1
Stereo ribbon diagram of the overlay of the C$^\alpha$ trace of DHP B (red) and DHP A (grey; PDB code 2qfk). The heme cofactor and the distal (His55; both conformations) and proximal (His89) histidines are shown in stick representation. Helices are labeled *A*–*H* and one (chain *A*) of the two subunits in the asymmetric unit is shown throughout.

3. Results and discussion

3.1. Overall DHP B protein structure

DHP B exhibits the canonical myoglobin fold consisting of eight helices (Phillips, 2001) identified by the letters *A*–*H* (of which the segments Pro29–Asn34, Lys36–Tyr38 and Lys87–His89 assume 3_{10}-helical conformations). As shown by the superposition of their backbone main-chain traces (Fig. 1), the structure of DHP B is nearly identical to that of isoenzyme A. Superposition of the main-chain atoms of the two dimeric molecules of DHP B with the equivalent chains of DHP A gives similar statistics for the coordinate r.m.s.d.: 0.257 Å for the *A* chains of DHP A and B and 0.236 Å for the *B* chains. The structural variations between DHP B and A are essentially limited to the amino-acid differences between the two isoenzymes, which cluster in the regions of the distal (R32K and Y34N; Fig. 2*a*) and proximal (N81S and S91G; Fig. 2*b*) sides of the heme cavity, with one additional substitution, I9L (Fig. 2*c*), that is located in a hydrophobic region enclosed by residues Tyr16, Ile20, Phe115, Trp120, Phe60, Met64, Val104, Phe107 and Met108. However, it is apparent from backbone-superposition calculations that these amino-acid differences do not perturb the overall structural fold of DHP but are limited to hydrogen-bonding and nonbonding interactions within the molecule and with symmetry-related molecules.

Specifically, the amino-acid differences in the distal pocket (Fig. 2*a*) introduce new hydrogen bonds, notably between the NH_2 group of one of the Lys32 conformers and the backbone carbonyl O atom of Leu25 (2.80 Å) as well as between the NH_2 group of one of the Asn34 conformers and the backbone carbonyl O atom of Glu31 (2.73 Å). The conformations of the intervening residues, as well as the residues participating in the formation of the distal pocket (*e.g.* phenylalanines 21, 24 and 35), are thus affected. In addition, the replacement of tyrosine in position 34 with asparagine affects the hydrogen-bonding interactions related to these two residues (Fig. 3). In DHP A Tyr34 forms only one weak hydrogen bond involving its hydroxyl group and the side chain of Asn96 (de Serrano *et al.*, 2007). Upon the substitution of this tyrosine with asparagine in DHP B this hydrogen bond is lost, but Asn34 is capable of forming a much stronger hydrogen bond to the carbonyl O atom of Glu31 as well as a couple of very weak ionic interactions with the side chains of Glu31 and Asn96. Thus, since Tyr34 has been implicated as one possible site of radical formation in DHP B Compound ES (Feducia *et al.*, 2009), its replacement by a redox-inactive asparagine residue may affect either the site of radical formation in DHP B Compound ES or may alter the pathway for the migration of this radical out of the active site. Furthermore, the substitution-induced differences in the distal pocket of DHP B *versus* DHP A directly affect both the conformations of critical

active-site residues and the hydrogen-bonding networks that encompass the region putatively ascribed as the internal binding site, which may play a role in radical stabilization and radical migration and may also contribute to the differences in enzymatic activity (*i.e.* substrate specificity) observed between the two isoenzymes (D'Antonio *et al.*, 2010).

On the proximal side of the heme pocket (Fig. 2*b*), the differences between the two isoenzymes have a pronounced effect on the hydrogen-bonding network present and may also alter the bonding of the proximal histidine to the heme cofactor. The substitution of Asn81 in DHP A by a serine residue in DHP B places one of the Ser81 conformers in a position to establish a new hydrogen bond to one of the Gln85 NH_2 conformers, thus possibly affecting the hydrogen bonding of Leu83 to His89 (the proximal histidine), as well as allowing the hydrogen bonding of Gln88 to the propionate A side chain of the heme cofactor. Additionally, the substitution of Ser91 by a glycine residue affords greater flexibility to the region surrounding the proximal histidine His89, possibly affecting the strength of the Fe—N_{His} bond and thus the electronics of the heme cofactor related to hydrogen peroxide activation. The increased mobility of Gly91 in DHP B is apparent from the resulting alternate backbone conformations of this residue (Fig. 2*b*).

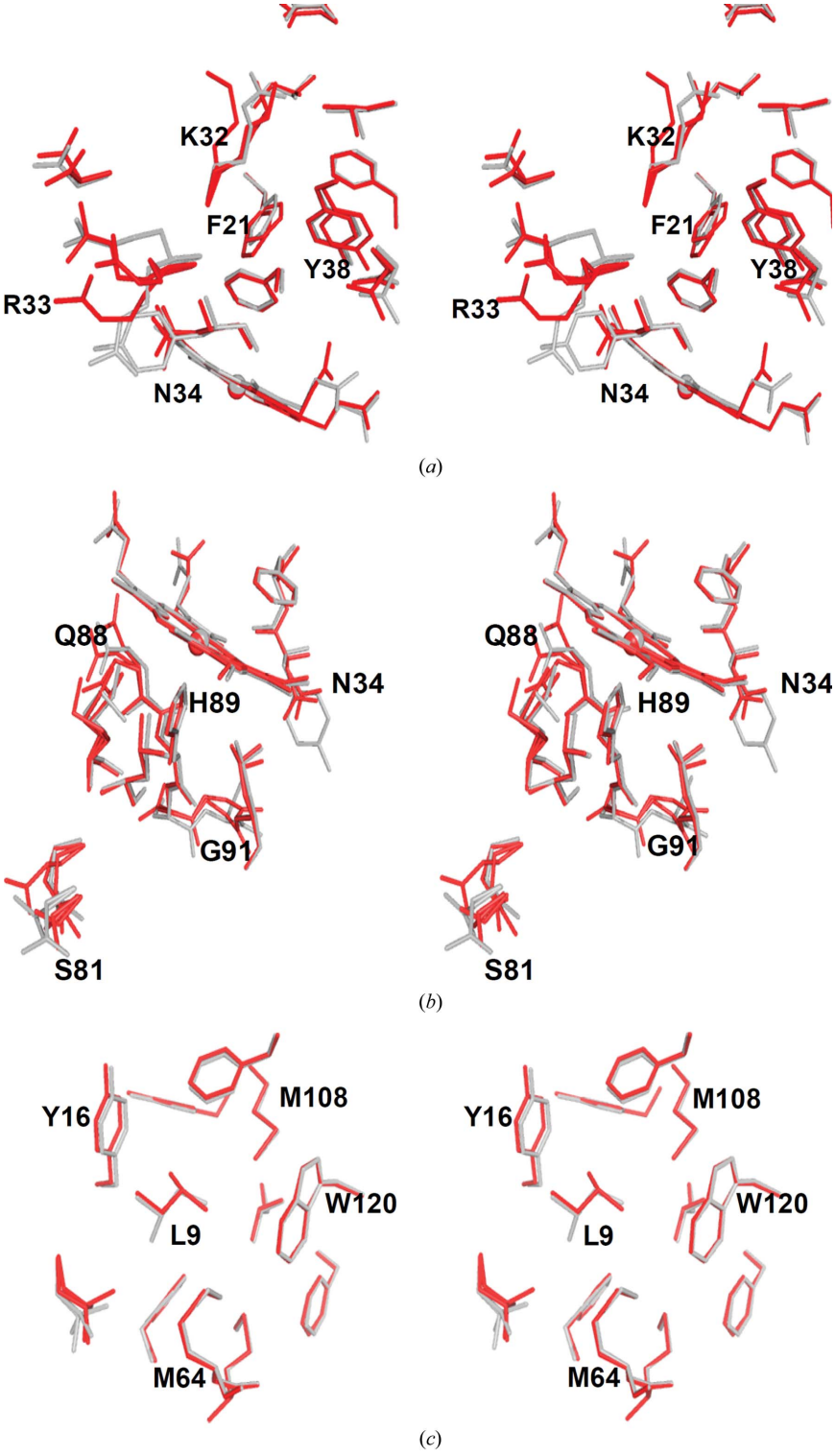

3.2. Heme–Fe ligation and conformations of the distal histidine

The active-site region, which includes the heme cofactor as well as the proximal and distal histidine residues, is identically located in the tertiary structure of the protein fold in both DHP isoenzymes (Figs. 1, 3 and 4). We have previously established that the binding of a ligand to the heme iron in DHP A is a crucial determinant of the conformation of the distal histidine His55 (Chen *et al.*, 2009; Davis *et al.*, 2009; Smirnova *et al.*, 2008). For example, in the structure determined at 100 K a water molecule is bound to the heme iron as the sixth coordination ligand for DHP A in its ferric form (de Serrano *et al.*, 2007). The presence of such a ligand stabilizes His55 in the 'closed' conformation by allowing the formation of a hydrogen-bonding interaction between the histidine $N^{\varepsilon 2}$ atom and the sixth ligand. This hydrogen bonding stabilizes both the ligand and the histidine

Figure 2
Superposition of the DHP isoenzymes showing the three regions of structural changes affected by the amino-acid substitutions. (*a*) Distal side of the heme cavity. Isoenzyme differences are noted at positions 32 (lysine in DHP B and arginine in DHP A) and 34 (asparagine in DHP B and tyrosine in DHP A). (*b*) Proximal side of the heme cavity. The relevant isoenzyme substitutions are at positions 81 (serine in DHP B and asparagine in DHP A) and 91 (glycine in DHP B and serine in DHP A). (*c*) Overlay of the region containing the residue at position 9 (leucine in DHP B and isoleucine in DHP A). The side chains are shown in red for DHP B and gray for DHP A. Residues are only labeled for DHP B.

conformation as being swung inside the distal pocket (*i.e.* 'closed'). This pattern of ligand binding leading to a 'closed' conformation of the distal histidine also seems to occur in DHP B, as chain *A* exhibits a water molecule bound to the heme cofactor concomitant with His55 being swung inside the distal pocket, together with the presence of a hydrogen bond between the two at 3.12 Å (a virtually identical distance to that observed in DHP A; de Serrano *et al.*, 2007). Moreover, the water molecule that is bound to heme iron as the sixth coordination ligand in DHP B is also located at a similar distance from the iron to that observed in the DHP A structure (Table 2 and Fig. 4; de Serrano *et al.*, 2007).

With respect to the heme active site, the structures and distances noted are very similar for the two isoenzymes of DHP regardless of the amino-acid substitutions that affect the distal and proximal heme environments. One noteworthy difference between DHP B and DHP A, however, is that the two proteins differ in the extent of ligand occupancy present in their respective crystal structures. Whereas the water molecule in DHP A is bound at a 1:1 ligand:protein ratio (taking into account a small percentage of molecular oxygen that is present; see below; de Serrano *et al.*, 2007), the crystal structure of DHP B (chain *A*) exhibits only 45% ligand occupancy, with 34% of the ligand occupancy being water and 9% being molecular oxygen. Accordingly, His55 exhibits both the open and closed conformations in the same proportions as the sixth-ligand occupancy (Table 2). Specifically, the closed conformation (Fe—$N^{\varepsilon 2}$ distance of 5.48 Å) was observed with 45% occupancy, whereas the open conformation (Fe—$N^{\varepsilon 2}$ distance of ∼10 Å) was present with 55% occupancy.

The presence of only 45% occupancy of the sixth axial ligand in the structure of DHP B is possibly the consequence of partial photoreduction of the heme iron (de Serrano *et al.*, 2007), leading to dissociation of the bound water molecule, which preferentially binds to heme in the Fe^{III} oxidation state. This phenomenon of photoreduction of DHP B was more pronounced in chain *B*, in which the iron had undergone complete reduction and which resembled the structure of dithionite-reduced DHP A (PDB entry 3dr9; de Serrano *et al.*, 2007), where the distal histidine is present only in the solvent-exposed open conformation owing to the absence of the sixth ligand with which to establish hydrogen bonds. Interestingly, in wild-type DHP A we did not observe any photoreduction of the heme iron in the metaquo form of the protein using Cu *Kα* X-ray radiation (de Serrano *et al.*, 2007), whereas the DHP(C73S) mutant of this protein underwent complete reduction using this radiation source. The partially reduced iron in WT DHP B signifies that this form of the protein is reduced more easily than WT DHP A under these conditions and represents an apparent inconsistency as our spectroelectrochemical study of these two isoenzymes suggested that they had nearly identical reduction potentials (D'Antonio *et al.*, 2010).

The displacement of the heme Fe relative to the heme pyrrole plane also supports the interpretation of partial ligand occupancy concomitant with the distal histidine His55 in both the open and closed conformations. In the hexacoordinate metaquo form of WT DHP A (de Serrano *et al.*, 2007) the Fe is 0.04 Å below the heme plane (Table 2). In the structure of DHP B presented here the iron is located 0.21 Å below the pyrrole heme plane, which is more similar to the iron displacement observed in the reduced form of DHP A (de Serrano *et al.*, 2007) and signifies that a major fraction of the heme iron is in the pentacoordinate state owing to dissociation of the water ligand upon reduction of the heme iron center.

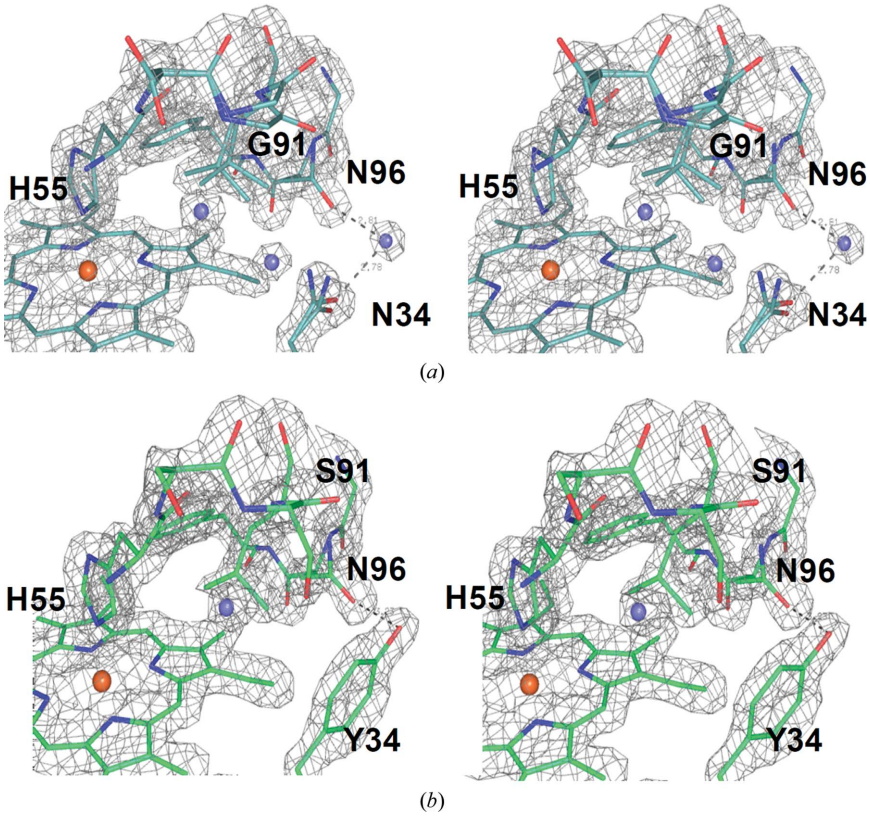

Figure 3
Stereoview of the proximal side of the heme cavity showing the $2F_o - F_c$ electron-density maps of (*a*) DHP B and (*b*) DHP A contoured at the 1.2σ level. Water molecules are represented as blue spheres. The differences in the region shown are limited to residue 34 (asparagine in DHP B and tyrosine in DHP A) and residue 91 (glycine in DHP B and serine in DHP A). The effect of the substitution of the tyrosine residue at position 34 by asparagine is most evident in the changes in the hydrogen-bonding interactions of these residues: Tyr34 (DHP A) makes a weak hydrogen-bonding contact (3.2 Å) to Asn96, whereas the Asn34 (DHP B) hydrogen-bonding interactions with Asn96 are mediated by a water molecule (distances of 2.78 and 2.81 Å, respectively) as illustrated.

3.3. Overall DHP AB cocrystal protein structure

The structure of the DHP AB heterodimer complex, which was crystallized at a

Table 2
Comparison of heme-ligand parameters for DHP A and B.

Only the values for molecule *A* of the asymmetric unit are listed for both structures.

	DHP B	DHP A
Fe—His89 $N^{\varepsilon 2}$ (Å)	2.16	2.09
Fe—His55 $N^{\varepsilon 2}$† (Å)		
Inside conformation (Å)	5.48 (5.41)‡	4.8
Outside conformation (Å)	9.8 (10.26)	—
Fe—water§ (Å)	2.15	2.2
Fe to pyrrole N plane (Å)	0.21	0.04
Fe–ligand tilt angle¶ (°)	15.4	10.8

† In the DHP B structure the distal histidine is present in conformations both inside and outside the pocket, whereas in the metaquo structure of DHP A (PDB entry 2qfk) it is only found in the conformation inside the pocket. ‡ In the DHP B structure the distal histidine assumes two conformations when oriented both inside and outside the pocket. § Distances for water as the sixth coordination ligand of heme Fe are listed (see text). ¶ The tilt angle is defined as the angle between the heme perpendicular and the Fe—O bond (Vangberg *et al.*, 1997).

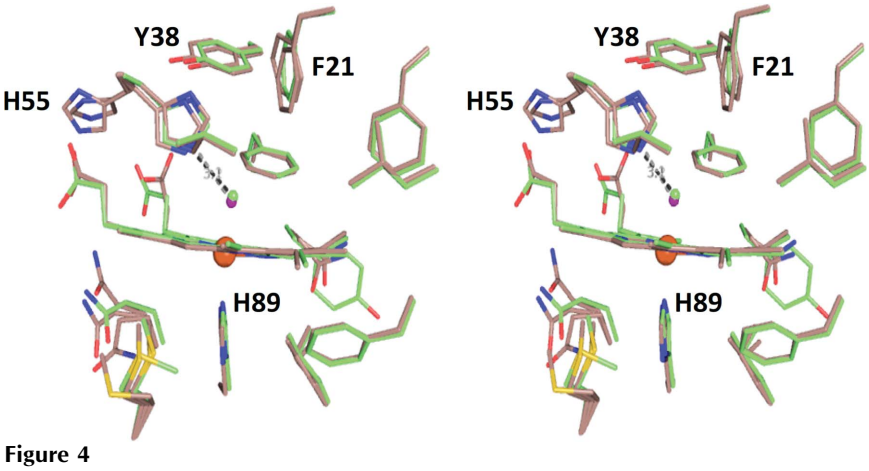

Figure 4
Stereoview of the superposition of the distal pocket regions of DHP B (beige) and DHP A (green). Note the differences in the conformation of the distal histidine His55 in these two structures. A water molecule is coordinated to the heme iron of both structures. A hydrogen bond (3.12 Å) between the $N^{\varepsilon 2}$ atom of His55 (closed conformation) and the heme-bound water molecule is indicated.

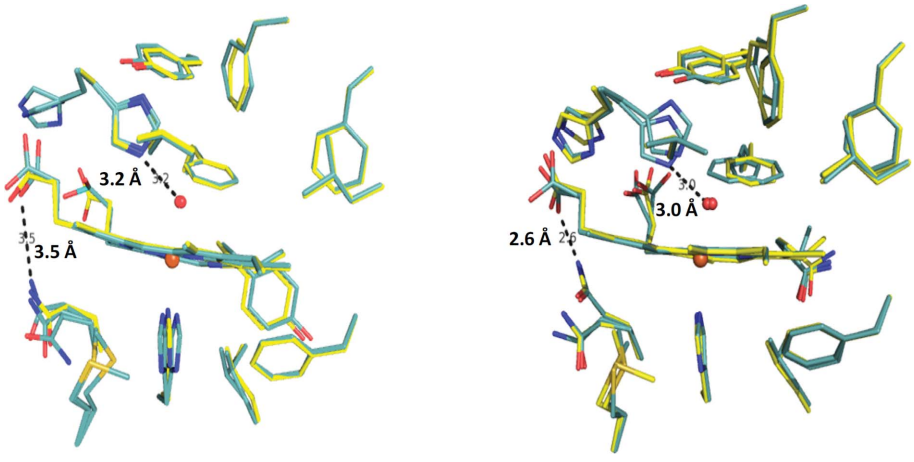

Figure 5
Superposition of the active site of DHP AB with the active sites of DHP A and DHP B. (*a*) Chain *A* of the DHP AB complex (blue) best superposes with the active site of chain *A* of DHP A (PDB entry 2qfk; yellow). (*b*) Chain *B* of the DHP AB complex (blue) best matches the active site of chain *B* of DHP B (yellow). Distances for the hydrogen bond between the distal histidine (His55) and the water coordinated to the heme iron and for that between Gln88 and the heme propionate A are also indicated.

1:1 DHP A:DHP B molar ratio, was determined at 1.52 Å resolution and refined to an *R* factor of 17.6% ($R_{\rm free}$ = 21.4%). The protein complex showed the symmetry of orthorhombic space group $P2_12_12_1$, which is also the space group in which both DHP A (de Serrano *et al.*, 2007) and DHP B crystallize under similar experimental conditions.

The results of molecular replacement with *Phaser* clearly demonstrate the presence of only two protomers in the asymmetric unit, with chain *A* mostly consisting of DHP A (approximately 80% DHP A and 20% DHP B, as assessed from the occupancies of the amino acids that differ between these two isoenzymes) and chain *B* predominantly derived from DHP B (approximately 70% of chain *B* is DHP B and 30% is DHP A). The main-chain atoms of chain *A* from the DHP AB structure superpose with those of chain *A* from the DHP A homodimer (average displacement of 0.159 Å), whereas the main-chain atoms of chain *B* in DHP AB superpose with chain *B* of the DHP B homodimer (average displacement of 0.158 Å).

As shown in Fig. 5, the superposition of the side chains is also very close. Specifically, the active sites are shown for chain *A* of the DHP AB heterodimer superposed with chain *A* of DHP A (Fig. 5*a*) as well as for chain *B* of DHP AB superposed with chain *B* of DHP B (Fig. 5*b*). Moreover, according to both its distance from the iron and the length of its hydrogen-bonding interaction with the distal histidine (His55), the heme-bound water molecule is positioned identically in the overlaid structures, further supporting the identities of the overlaid heme-pocket structures. However, one notable difference between the chains is the proximity of the Gln88 side chain to the carboxylate of heme propionate A (Fig. 5). The $N^{\varepsilon 2}$ atom of one of the conformers of Gln88 is at a hydrogen-bonding distance of 2.6 Å in both DHP B and chain *B* of DHP AB but is elongated to 3.5 Å in both DHP A (de Serrano *et al.*, 2007) and chain *A* of DHP AB; it is not known at this time whether this difference in the hydrogen-bonding distance has a functional significance.

Interestingly, *PISA* analysis (*Protein Interfaces, Surfaces and Assemblies*; Krissinel & Henrick, 2007) of the state of assembly and interfaces of the two chains of the DHP AB heterodimer suggests that they are most likely to be present as monomers in the asymmetric unit and hence are not predicted to form a complex in solution. However,

examination of the chain interfaces for all three structures (DHP A, DHP B and DHP AB) reveals differences in the distances of relevant residues involved in these interfacial interactions which may have ramifications beyond the *PISA* analysis. In particular, one of the major interfaces involving residues Asp72 and Arg122 from both chains in DHP AB is shown in Fig. 6(*c*) and is contrasted with those of the two chains of DHP A (Fig. 6*a*) and DHP B (Fig. 6*b*). The interfacial hydrogen-bonding distances of 2.4 Å between these two pairs of residues in the DHP AB heterodimer is indicative of a very strong interaction between the side chains involved. These hydrogen bonds are weaker in the DHP B homodimer (2.5–3.1 Å; Fig. 6*b*) and are further elongated to 3.2–3.4 Å in the DHP A homodimeric structure (Fig. 6*a*; de Serrano *et al.*, 2007). Therefore, there appears to be a trend in the strength of the interaction between the two chains of this interface, with DHP AB being the strongest, DHP B somewhat weaker and the weakest interaction being that found in the DHP A structure. As a whole, there may be a preference in chain assembly for the asymmetric unit of the DHP AB complex over that of either the DHP A or DHP B homodimers, as well as a difference in the strength of the interaction of the residues involved in the chain interfaces, but these interactions and their significance require further investigation by other means.

3.4. Structure–function relationship of DHP

Across the superfamily, globins have been shown to perform a diverse number of roles that include O_2 transport, small-molecule sensing or scavenging, redox chemistry and, as discussed here, peroxidase activity. This range of biomolecular processes is remarkable given the highly conserved structural motif that defines globins despite their relatively low sequence homologies. In light of the structural constraints of the canonical 3/3 globin fold, understanding the nuances of globin structure that enable their specific and functionally unique activities is paramount to establishing the paradigms of globin structure–function relationships. Within this context, our recent focus has been the elucidation of the molecular details that enable both O_2-transport and peroxidase functions in the globin dehaloperoxidase from the terebellid polychaete *A. ornata*. In addition to being the coelomic hemoglobin of this marine worm (Weber *et al.*, 1977), DHP possesses a biologically relevant peroxidase activity in that it catalyzes the oxidative degradation of trihalophenols to dihaloquinones (Chen *et al.*, 1996). Whereas *A. ornata* has been shown to possess two genes, *dhpA* and *dhpB* (Han *et al.*, 2001), that encode dehaloperoxidase isoenzymes A and B, respectively, only isoenzyme A has been characterized structurally. Thus, in order to support recent and ongoing detailed mechanistic investigations (Feducia *et al.*, 2009; D'Antonio *et al.*, 2010; Osborne *et al.*, 2009) and to provide further insight into the molecular details of the protein environment that support a bifunctional heme active site, we present here the structural characterization of DHP B both as a homodimer and as a heterodimer crystallized with isoenzyme A.

The single-crystal X-ray diffraction study of the DHP B homodimer at 1.58 Å resolution revealed a protein structure that was similar overall to that previously observed for the homodimer of DHP A (LaCount *et al.*, 2000; Lebioda *et al.*, 1999; de Serrano *et al.*, 2007). The superposition of the backbone trace of isoenzyme B with that of isoenzyme A showed that the primary differences between the two structures were limited to regions surrounding the five amino-acid substitutions that distinguish these two isoenzymes and can be clustered into three distinct regions: (i) the distal cavity (R32K and Y34N), (ii) the proximal cavity (N81S and S91G) and (iii) the hydrophobic region in proximity to I9L. While the effects of the latter are mitigated by the relatively small structural difference between isoleucine and leucine, the former two regions lead to differences that are much more significant. Specifically, both the N81S and S91G substitutions impact on the bonding character of the proximal histidine His89. Compared with DHP A, the Fe—N_{His} bond is elongated by 0.07 Å

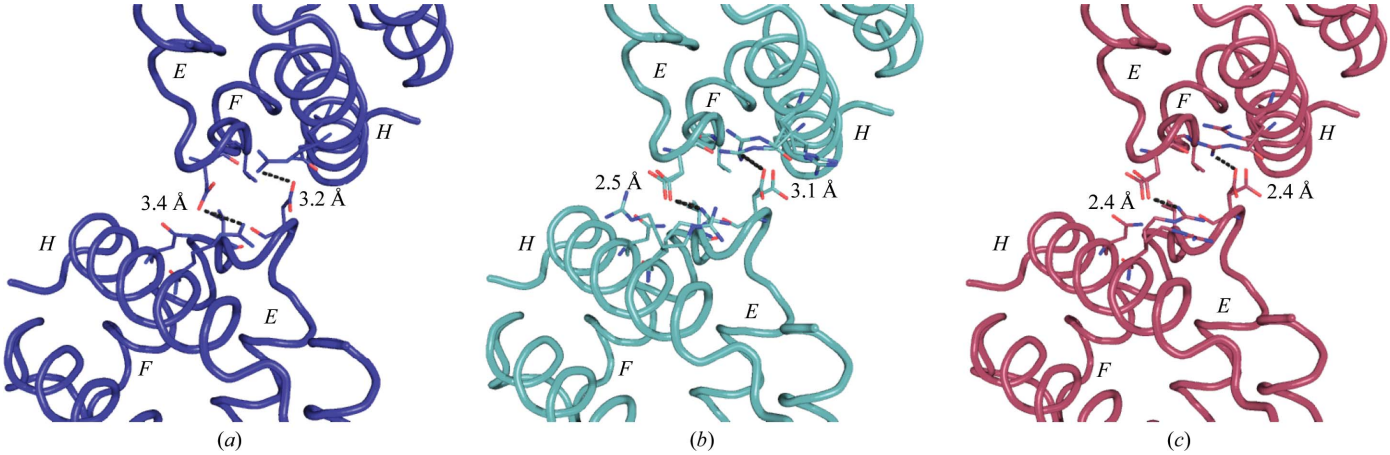

Figure 6
Interface of chain *A* (bottom chain) and chain *B* (top chain) located in the asymmetric unit of DHP. The ribbon diagram of the C^{α} trace is shown for (*a*) DHP A (PDB entry 2qfk; dark blue), (*b*) DHP B (cyan) and (*c*) DHP AB at a 1:1 protein ratio (pink). The residues involved in the interface interactions, Asp72, Arg122, Asn126 and Val74 of both chains, are displayed in stick representation and the relevant hydrogen-bonding distances are indicated. The *E*, *F* and *H* helices involved in these interactions are also indicated.

in DHP B. Based on the Fe—N_{His} vibrational frequency, previous resonance Raman spectroscopic studies have shown that DHP exhibits an imidazolate character that is weaker than in peroxidases but stronger than in globins (Belyea *et al.*, 2006). In the monofunctional peroxidases (*e.g.* cytochrome *c* peroxidase and horseradish peroxidase), the strength of this bond has been implicated as a contributing factor in the 'push–pull' effect, which has been hypothesized to play an essential role in facilitating the requisite O—O bond-cleavage step needed to generate Compound I (or ES), the catalytically active species of the Poulos–Kraut mechanism (Poulos & Kraut, 1980). Generally, the Asp–His–Fe catalytic triad typical of peroxidases consists of a series of electronic interactions that results in a charge relay to the imidazole ring of the proximal histidine (Goodin & McRee, 1993; Poulos & Kraut, 1980). This localization of charge is responsible for an electronic 'push' of electron density into the O–O bond which aids its cleavage. Interestingly, DHP does not have an Asp–His–Fe catalytic triad but instead contains a Leu83–His89–Fe triad, in which there is a strong hydrogen-bond interaction between the N^{δ} atom of His89 and the backbone carbonyl of Leu83. This interaction is weak when compared with the Asp–His interaction in peroxidases, but has been shown to provide polarization of the proximal histidine that is stronger than in typical globins (Franzen, 2001). The Ser→Gly substitution at position 91 affords greater flexibility to His89 and may be one of the contributing factors behind the elongation of the Fe—N_{His} bond in DHP B compared with isoenzyme A. Similarly, the Asn→Ser substitution at position 81 alters the proximal hydrogen-bonding network, which includes Gln85, Leu83, the proximal histidine His89 and Gln88 as well as the heme propionate A and may either contribute to this bond elongation or potentially affect (de)protonation events during catalytic turnover. It has also been hypothesized that the lone pairs of the S atom of Met86, one of which is in contact with the proximal His89, could aid the 'push' effect through charge transfer (Belyea *et al.*, 2006). The weakening of the Fe—N_{His} bond compared with typical monofunctional peroxidases may be related to the fact that DHP functions both as a hemoglobin and as a peroxidase. However, further studies of the proximal cavity, coupled with additional investigations on the distal residues involved in the 'pull' effect, will be necessary to deconvolute the factors that contribute to this observation.

The distal cavity substitutions R32K and Y34N comprise the other major region in which structural differences are observed between DHP B and DHP A. As Tyr34 has been implicated as one of the possible sites of radical formation in DHP A Compound ES (Feducia *et al.*, 2009), its substitution by asparagine in DHP B rules out radical formation at this position in this case. Tyr34 also participates in a weak hydrogen bond between its hydroxyl group and the side chain of Asn96. This hydrogen bond is lost on the substitution of tyrosine by asparagine, but Asn34 forms a much stronger hydrogen bond to the carbonyl O atom of Glu31, as well as a couple of very weak ionic interactions with the Glu31 and Asn96 side chains. The Arg→Lys substitution at position 32 also introduces new hydrogen bonds, notably between the NH_2 group of one of the Lys32 conformers and the backbone carbonyl O atom of Leu25. Interestingly, the findings from our previous EPR spectroscopic studies (Feducia *et al.*, 2009; D'Antonio *et al.*, 2010) of the radical(s) present in the Compound ES intermediates of DHP A and B may be related to substitution-induced hydrogen-bonding differences present at the sites of radical formation between these two isoenzymes. The EPR spectroscopic study (D'Antonio *et al.*, 2010) of the Compound ES intermediate of DHP B at pH 7 showed that this signal was strikingly similar to that observed for DHP A at pH 5 (Feducia *et al.*, 2009) but dissimilar to that observed at pH 7. Furthermore, we noted time-dependent changes in the DHP B Compound ES radical signal (but not in that of DHP A; Feducia *et al.*, 2009; D'Antonio *et al.*, 2010) and hypothesized a pathway-dependent radical migration out of the active site that was pH-specific. Thus, the structural evidence here supports the hypothesis that the DHP B amino-acid substitutions may affect the hydrogen-bonding networks that originate at these two critical positions in the distal pocket, which may play an important role in the formation, stabilization and/or migration of the Compound ES radical formed during catalytic turnover.

Although some chain heterogeneity was observed, the structure of the DHP AB heterodimer also demonstrates how the DHP A and B monomers may preferentially interact with each other. Examination of the chain interfaces for all three structures (DHP A, DHP B and DHP AB) reveals differences in the distances of residues involved in interfacial hydrogen bonding, specifically between residues Asp72 and Arg122, which may suggest a preference for a heterodimeric complex over a purely homodimeric one should the A and B monomers interact in solution. However, outside the interfacial regions the overall structures of the two chains in DHP AB closely resemble those of the homodimers of DHP A and DHP B for both main-chain and side-chain superposition. The one notable exception is that the hydrogen-bonding interaction between the $N^{\varepsilon 2}$ atom of one of the conformers of Gln88 and the heme propionate A differs between the two chains in DHP AB, with that in chain *B* being 2.6 Å whereas that in chain *A* is 3.5 Å. The consequence, if any, of this elongation of nearly 1 Å is not known at this time. One possibility, however, is that these interfacial interactions lead to the formation of *A. ornata* erythrocruorin, a giant hemoglobin found in the vascular system of the marine worm (Chiancone *et al.*, 1980). Although speculation at this point, future study of both DHP A and DHP B in the presence of conditions known to stabilize erythrocruorin may lead to its formation and is currently under investigation (Chiancone *et al.*, 1981).

4. Conclusion

We have been able to show that although dehaloperoxidase B is structurally very similar to DHP A there are distinct differences between the two that may manifest themselves in the different catalytic activities exhibited by these isoenzymes. Subtle alterations in the active-site hydrogen-bonding network as well as the substitution of a critical active-site tyrosine

residue are likely to be the structural factors behind the spectroscopic differences noted for the radical in DHP B Compound ES when compared with that of isoenzyme A (D'Antonio *et al.*, 2010) and suggest that 'fine-tuning' of the active site can lead to profound differences in the mechanism of action between these two isoenzymes. Furthermore, despite having been observed in other globins, the extent of the conformational flexibility of the distal histidine appears to be a hallmark of dehaloperoxidases and may function as a molecular trigger that serves to discriminate between peroxidase and hemoglobin function that is dependent upon the type of halophenol (monohalophenol *versus* trihalophenol) present. In light of the structural findings presented here, a firmer understanding of the structure–function relationship in dehaloperoxidase is rapidly emerging and may have potential implications for future studies involving globin protein engineering or directed evolution of DHP for bioremediation.

We would like to thank the NCSU Molecular Biotechnology Training Program for an NIH T32 Biotechnology Traineeship grant (JD), the Army Research Office for grant 52278-LS (SF) and the North Carolina State University (RG) for their financial support of this research. We would also like to thank Dr Zhongmin Jin at SER-CAT (Advanced Photon Source) for synchrotron data collection. The Advanced Photon Source is supported by the US Department of Energy, Office of Science, Office of Basic Energy Sciences under Contract No. W-31-109-Eng-38. We acknowledge Dr Robert Rose (NC State University) for his insight into the interpretation of the structural data.

References

Belyea, J., Belyea, C. M., Lappi, S. & Franzen, S. (2006). *Biochemistry*, **45**, 14275–14284.
Belyea, J., Gilvey, L. B., Davis, M. F., Godek, M., Sit, T. L., Lommel, S. A. & Franzen, S. (2005). *Biochemistry*, **44**, 15637–15644.
Chen, Y. P., Woodin, S. A., Lincoln, D. E. & Lovell, C. R. (1996). *J. Biol. Chem.* **271**, 4609–4612.
Chen, Z., de Serrano, V., Betts, L. & Franzen, S. (2009). *Acta Cryst.* D**65**, 34–40.
Chiancone, E., Brenowitz, M., Ascoli, F., Bonaventura, C. & Bonaventura, J. (1980). *Biochim. Biophys. Acta*, **623**, 146–162.
Chiancone, E., Ferruzzi, G., Bonaventura, C. & Bonaventura, J. (1981). *Biochim. Biophys. Acta*, **670**, 84–92.
Collaborative Computational Project, Number 4 (1994). *Acta Cryst.* D**50**, 760–763.
D'Antonio, J., D'Antonio, E. L., Bowden, E. F., Smirnova, T., Franzen, S. & Ghiladi, R. A. (2010). Submitted.
Davis, M. F., Gracz, H., Vendeix, F. A., de Serrano, V., Somasundaram, A., Decatur, S. M. & Franzen, S. (2009). *Biochemistry*, **48**, 2164–2172.
Emsley, P. & Cowtan, K. (2004). *Acta Cryst.* D**60**, 2126–2132.
Feducia, J., Dumarieh, R., Gilvey, L. B., Smirnova, T., Franzen, S. & Ghiladi, R. A. (2009). *Biochemistry*, **48**, 995–1005.
Franzen, S. (2001). *J. Am. Chem. Soc.* **123**, 12578–12589.
Goodin, D. B. & McRee, D. E. (1993). *Biochemistry*, **32**, 3313-3324.
Han, K., Woodin, S. A., Lincoln, D. E., Fielman, K. T. & Ely, B. (2001). *Mar. Biotechnol.* **3**, 287–292.
Krissinel, E. & Henrick, K. (2007). *J. Mol. Biol.* **372**, 774–797.
LaCount, M. W., Zhang, E., Chen, Y. P., Han, K., Whitton, M. M., Lincoln, D. E., Woodin, S. A. & Lebioda, L. (2000). *J. Biol. Chem.* **275**, 18712–18716.
Laskowski, R. A., MacArthur, M. W., Moss, D. S. & Thornton, J. M. (1993). *J. Appl. Cryst.* **26**, 283–291.
Lebioda, L., LaCount, M. W., Zhang, E., Chen, Y. P., Han, K., Whitton, M. M., Lincoln, D. E. & Woodin, S. A. (1999). *Nature (London)*, **401**, 445.
McCoy, A. J., Grosse-Kunstleve, R. W., Storoni, L. C. & Read, R. J. (2005). *Acta Cryst.* D**61**, 458–464.
Nienhaus, K., Nickel, E., Davis, M. F., Franzen, S. & Nienhaus, G. U. (2008). *Biochemistry*, **47**, 12985–12994.
Osborne, R. L., Coggins, M. K., Raner, G. M., Walla, M. & Dawson, J. H. (2009). *Biochemistry*, **48**, 4231–4238.
Otwinowski, Z. & Minor, W. (1997). *Methods Enzymol.* **276**, 307–326.
Phillips, G. N. (2001). *Handbook of Metalloproteins*, edited by A. Messerschmidt, R. Huber, T. L. Poulos & K. Weighardt, vol. 1, pp. 5–15. Chichester: John Wiley & Sons.
Poulos, T. L. & Kraut, J. (1980). *J. Biol. Chem.* **255**, 8199–8205.
Roach, M. P., Chen, Y. P., Woodin, S. A., Lincoln, D. E., Lovell, C. R. & Dawson, J. H. (1997). *Biochemistry*, **36**, 2197–2202.
Sage, J. T., Morikis, D. & Champion, P. M. (1991). *Biochemistry*, **30**, 1227–1237.
Serrano, V. de, Chen, Z., Davis, M. F. & Franzen, S. (2007). *Acta Cryst.* D**63**, 1094–1101.
Smirnova, T. I., Weber, R. T., Davis, M. F. & Franzen, S. (2008). *J. Am. Chem. Soc.* **130**, 2128–2129.
Tian, W. D., Sage, J. T. & Champion, P. M. (1993). *J. Mol. Biol.* **233**, 155–166.
Vangberg, T., Bocian, D. F. & Ghosh, A. (1997). *J. Biol. Inorg. Chem.* **2**, 526–530.
Weber, R. E., Mangum, C., Steinman, H., Bonaventura, C., Sullivan, B. & Bonaventura, J. (1977). *Comp. Biochem. Physiol. A Comp. Physiol.* **56**, 179–187.
Zhang, E., Chen, Y. P., Roach, M. P., Lincoln, D. E., Lovell, C. R., Woodin, S. A., Dawson, J. H. & Lebioda, L. (1996). *Acta Cryst.* D**52**, 1191–1193.
Zhu, L., Sage, J. T., Rigos, A. A., Morikis, D. & Champion, P. M. (1992). *J. Mol. Biol.* **224**, 207–215.

6600 *Biochemistry* **2010,** *49,* 6600–6616
DOI: 10.1021/bi100407v

BIOCHEMISTRY
including biophysical chemistry & molecular biology
Article

Spectroscopic and Mechanistic Investigations of Dehaloperoxidase B from *Amphitrite ornata*[†]

Jennifer D'Antonio, Edward L. D'Antonio, Matthew K. Thompson, Edmond F. Bowden, Stefan Franzen, Tatyana Smirnova, and Reza A. Ghiladi*

Department of Chemistry, North Carolina State University, Raleigh, North Carolina 27695-8204

Received March 16, 2010; Revised Manuscript Received June 9, 2010

ABSTRACT: Dehaloperoxidase (DHP) from the terebellid polychaete *Amphitrite ornata* is a bifunctional enzyme that possesses both hemoglobin and peroxidase activities. Of the two DHP isoenzymes identified to date, much of the recent focus has been on DHP A, whereas very little is known pertaining to the activity, substrate specificity, mechanism of function, or spectroscopic properties of DHP B. Herein, we report the recombinant expression and purification of DHP B, as well as the details of our investigations into its catalytic cycle using biochemical assays, stopped-flow UV−visible, resonance Raman, and rapid freeze-quench electron paramagnetic resonance spectroscopies, and spectroelectrochemistry. Our experimental design reveals mechanistic insights and kinetic descriptions of the dehaloperoxidase mechanism which have not been previously reported for isoenzyme A. Namely, we demonstrate a novel reaction pathway in which the products of the oxidative dehalogenation of trihalophenols (dihaloquinones) are themselves capable of inducing formation of oxyferrous DHP B, and an updated catalytic cycle for DHP is proposed. We further demonstrate that, unlike the traditional monofunctional peroxidases, the oxyferrous state in DHP is a peroxidase-competent starting species, which suggests that the ferric oxidation state may not be an obligatory starting point for the enzyme. The data presented herein provide a link between the peroxidase and oxygen transport activities which furthers our understanding of how this bifunctional enzyme is able to unite its two inherent functions in one system.

The "metalloproteome" contains a number of enzymes which possess more than one inherent catalytic function. Dehaloperoxidase (DHP),[1] the coelomic oxygen-transport hemoglobin from the terebellid polychaete *Amphitrite ornata* (*1*), is the first globin identified to possess a biologically relevant peroxidase activity (*2*). In the benthic ecosystems in which *A. ornata* is commonly found, DHP functions both as the O_2-transport protein and to protect this marine worm against biogenically produced halometabolites which act as repellents secreted by other organisms. As the monomeric (noncooperative) intracellular coelomic hemoglobin, DHP binds dioxygen (P_{50} = 2.8 Torr) that is delivered to the coelom by the extracellular, multisubunit vascular erythrocruorin (P_{50} = 11 Torr) (*1*, *3*). Hemoglobin (Hb) phylogeny reveals a common genetic ancestry across species from bacteria to plants and animals extending back 1.8 billion years (*4*−*6*). However, despite DHP being categorized as a globin according to the Structural Classification of Proteins (SCOP) database (*7*), DHP has little sequence homology to other known Hbs. Moreover, DHP bears little resemblance to the fold of cytochrome *c* peroxidase (C*c*P), the prototype for the heme peroxidase family (*8*). Thus, as a representative of globins found in marine organisms, its relationship to other Hbs and peroxidases may aid in establishing the scientific foundation and new paradigms of protein structure−function relationships specific to bi/multifunctional proteins.

A number of sediment-dwelling marine polychaetes and hemichordates employ haloperoxidases to produce high levels of volatile brominated secondary metabolites as defense mechanisms (*9*, *10*). Examples include *Notomastus lobatus* (polychaeta) (*11*−*13*), which contaminates the sediments with mono-, di-, and tribromophenols and mono- and dibromovinylphenols, and *Saccoglossus kowalevskii* (hemichordata) (*14*, *15*), which also produces bromopyrroles. Thus, environmental sediments that are contaminated with this diverse array of toxic haloaromatic compounds represent a significant challenge to other infaunal organisms that coinhabit these coastal mudflats. One such annelid, *A. ornata*, is able to oxidize a wide variety of mono-, di-, and trisubstituted halophenols that possess bromine, chlorine, or fluorine substituents (*2*).

[†]This project was supported by the North Carolina State University Molecular Biotechnology Training Program through an NIH T32 Biotechnology Traineeship grant (J.D.), the Army Research Office Grant 52278-LS (S.F.) and Grant 51432-CH-SR (E.F.B.), and the North Carolina State University Department of Chemistry (R.A.G.).

*To whom correspondence should be addressed: (919) 513-0680 (phone); (919) 515-8920 (fax); Reza_Ghiladi@ncsu.edu (e-mail).

[1]Abbreviations: DHP, dehaloperoxidase; Hb, hemoglobin; Mb, myoglobin; DCP, 2,4-dichlorophenol; TBP, 2,4,6-tribromophenol; TCP, 2,4,6-trichlorophenol; TFP, 2,4,6-trifluorophenol; TXP, trihalophenol; DXQ, dihalophenol; RFQ-CW-EPR, rapid freeze-quench continuous wave electron paramagnetic resonance; compound I, two-electron-oxidized heme center when compared to the ferric form, commonly as an Fe^{IV}=O porphyrin π-cation radical; compound II, one-electron-oxidized heme center when compared to the ferric form, commonly as an Fe^{IV}=O or Fe^{IV}−OH; compound III, oxyferrous [$Fe^{II}-O_2$ or $Fe^{III}-(O_2^-)$] state of the enzyme; compound ES, two-electron-oxidized state containing both a ferryl center [Fe^{IV}=O] and an amino acid (tryptophanyl or tyrosyl) radical, analogous to compound ES in cytochrome *c* peroxidase; compound RH, "reversible heme" state of dehaloperoxidase, formed from the decay of compound ES in the absence of cosubstrate; compound P426, state of DHP B formed upon reduction of compound ES with $Na_2S_2O_4$; 5cHS, five-coordinate high-spin heme; 6cHS, six-coordinate high-spin heme; 6cLS, six-coordinate low-spin heme.

 Published on Web 06/14/2010

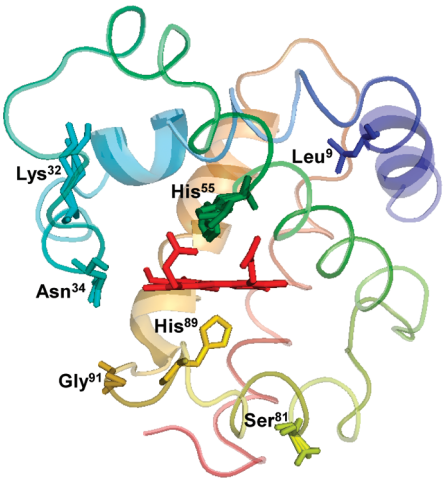

FIGURE 1: Crystal structure of DHP B (PDB accession code 3ixf). The locations of the five residues (Leu[9], Lys[32], Asn[34], Ser[81], and Gly[91]) relative to the heme active site that differ in DHP A are shown, as well as the proximal (His[89]) and distal (His[55]) histidines.

A. ornata is exposed to these contaminants on two fronts, by contact upon burrowing into the sediments and through ingestion as a deposit feeder consuming contaminated surface deposits, yet survives due to the production of dehalogenating enzymes that allow it to tolerate such environmental haloaromatic toxins. One such enzyme is dehaloperoxidase, a dual-function hemoprotein that, in addition to being the coelomic hemoglobin of *A. ornata* (*1*, *16*, *17*), possesses a broad substrate specificity for the oxidation of the aforementioned trihalophenols (*2*, *18*). The dehaloperoxidase function of this hemoglobin was first determined by fractionation of the *A. ornata* proteome to determine which component of the organism was capable of degrading bromophenols (*2*). The high specific activity of the purified protein signified that DHP was solely responsible for the observed oxidative dehalogenation reaction, and recombinant expression of the protein further indicated that such enzymatic activity is intrinsic to DHP (*18*). Soon thereafter, Ely and co-workers identified and characterized two separate genes (*dhpA* and *dhpB*) that encoded for a pair of DHP isoenzymes, termed DHP A and DHP B (*19*). Both enzymes were found to contain 137 amino acid residues, but DHP B differs from DHP A at five positions: I9L, R32K, Y34N, N81S, and S91G (Figure 1). It was hypothesized at that time that the differences between DHP A and B may result in altered cosubstrate specificity, but no follow up studies were conducted. Thus, while DHP A has been the focus of many studies for well over a decade, DHP B has received minimal attention.

DHP catalyzes the oxidative degradation of 2,4,6-trihalogenated phenols to the corresponding 2,6-dihalo-1,4-benzoquinones in the presence of hydrogen peroxide (see insert). Several recent studies have focused on the characterization of DHP, as well as elucidating the mechanism of this reaction (*18*, *20*−*34*). Using stopped-flow UV−visible and rapid freeze-quench EPR spectroscopic methods, we have previously demonstrated that ferric DHP reacts with hydrogen peroxide to yield compound ES, an iron(IV)−oxo heme center with an amino acid radical (*20*). The catalytic competency of that intermediate in oxidizing the cosubstrate 2,4,6-trichlorophenol (TCP) was also shown, and we proposed a peroxidase-like catalytic cycle for DHP at that time. It was also found that in the absence of cosubstrate there is the formation of a new species named as compound RH, which is unique to dehaloperoxidase and has not been found in any other globin. With regard to cosubstrate oxidation, Dawson and co-workers have recently reported that the overall two-electron oxidation of TCP by DHP proceeds through discrete one-electron steps (*31*), which is consistent with the hypothesis that the trihalogenated cosubstrate likely binds at an external site similar to other peroxidases (*22*). However, despite the fact that these and a number of other studies on DHP (*20*, *26*, *31*, *35*) have helped to elucidate its mechanistic pathways, it is still not understood how this bifunctional protein can act as both a hemoglobin and a peroxidase, and a number of questions still remain.

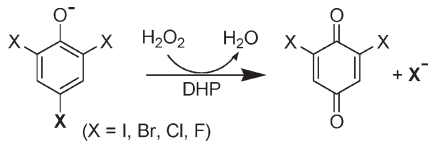

The primary focus of this report is to provide a detailed picture of the chemistry of DHP B (Scheme 1) with results and experimental details *not* previously described for either isoenzyme: (a) dichloroquinone (DCQ), the purported product of trihalophenol dehalogenation, further reacts with the putative oxidant compound ES leading to oxyferrous DHP; (b) DCQ reacts with ferric DHP also leading to oxyferrous DHP formation; (c) oxyferrous DHP catalyzes the oxidative dehalogenation of TCP in the presence of hydrogen peroxide; (d) 4-bromophenol, a presumed cosubstrate known to bind in the distal cavity of the heme active site (*36*), is an inhibitor of 2,4,6-trichlorophenol dehalogenation; (e) spectroelectrochemistry of DHP B reveals an unusually high redox potential for this globin peroxidase. As investigations of isoenzyme B may also provide important clues and significant advances in understanding the catalytic mechanism of both isoforms of DHP, the secondary focus of this report is to present additional spectroscopic studies of DHP B, including resonance Raman, stopped-flow UV−visible, and rapid freeze-quench electron paramagnetic resonance spectroscopies, which when coupled with biochemical assays provide further evidence in support of the proposed catalytic cycle (Scheme 1). While the secondary focus parallels our recent study of isoenzyme A (*20*), our experimental design in this report differs and reveals new mechanistic insights and kinetic descriptions of the intermediates in DHP B which have not been previously reported for DHP A. When interpreted in light of our recent X-ray crystallographic study of DHP B which demonstrates a mechanistic role for the conformational flexibility of the distal histidine (His[55]) (*37*), the results presented herein advance our understanding of how DHP as a bifunctional enzyme is able to concurrently perform its two inherent peroxidase and oxygen transport activities in one system.

MATERIALS AND METHODS

Materials. Buffer salts were purchased from Fisher Scientific. All other reagents and biochemicals, unless otherwise specified, were of the highest grade available from Sigma Aldrich. The QIAprep spin miniprep kit was from Qiagen Sciences (Valencia, CA), and the Quikchange II site-directed mutagenesis kit was purchased from Stratagene (La Jolla, CA). The required oligonucleotides were synthesized by IDT DNA Technologies, Inc. *N*,*N*,*N*′,*N*′-tetramethyl-*p*-phenylenediamine (TMPD) was

Scheme 1: Proposed Catalytic Cycle for Dehaloperoxidase B

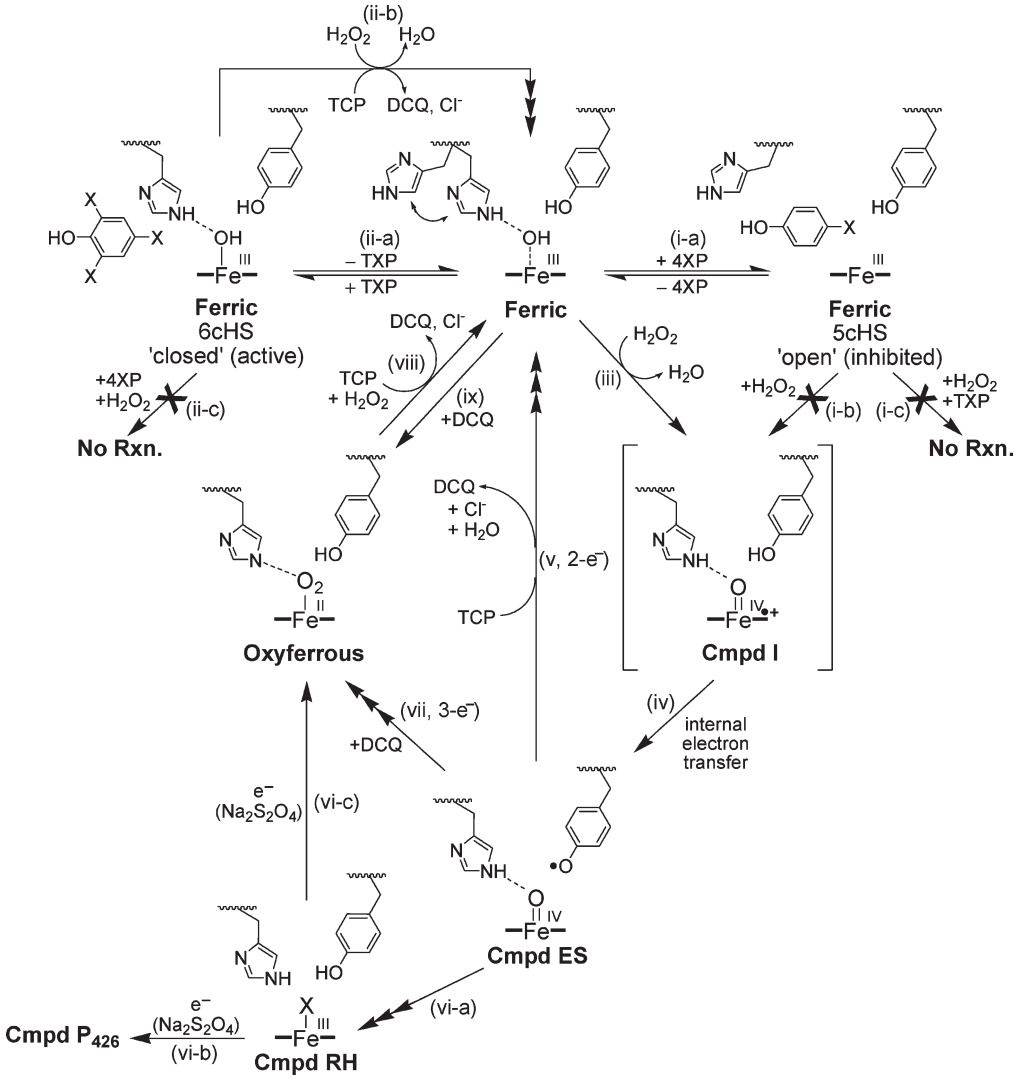

purchased from Sigma, $[Ru(en)_3][ZnCl_4]$ was synthesized according to previously reported methods (*38*−*40*), and the reagents (i.e., $RuCl_3$, ethylenediamine, and zinc dust) for its reaction were also purchased from Sigma. EPR tubes were purchased from Norell (Landisville, NJ). Solutions of trihalogenated phenols were freshly prepared prior to each experiment in 100 mM potassium phosphate (KP_i) buffer, pH 7, and kept at 4 °C and protected against light. UV−visible spectra were recorded periodically to ensure that the cosubstrate had not degraded by monitoring its absorbance: trifluorophenol, 270 nm (1027 M^{-1} cm^{-1}); trichlorophenol, 312 nm (3752 M^{-1} cm^{-1}) (*20*); tribromophenol, 316 nm (5055 $M^{-1}cm^{-1}$). Hydrogen peroxide stock solutions were also freshly prepared daily prior to each experiment and maintained at 4 °C. The hydrogen peroxide stability was monitored by UV−visible spectroscopic analysis at 240 nm (ε_{240} = 43.6 M^{-1} cm^{-1}) (*41*). The stock H_2O_2 solution was diluted to the corresponding premixing concentrations for each experiment.

Plasmid Preparation, Protein Expression, and Purification. All of the mutations were generated with the Quikchange II site-directed mutagenesis kit. Mutagenesis [melt (95 °C, 50 s), anneal (60 °C, 50 s), and extension (68 °C, 6 min)] was performed for 18 cycles. The plasmid encoding wild-type (WT) DHP A (His tag) was used as a template to generate the mutation pDHPA (R32K/Y34N) using the mutagenic primers [5′-G AAT AAG TAT CCG GAC GAG **AAA** CGC **AAC** TTC AAA AAC TAT GTC-3′ (sense) and 5′-GAC ATA GTT TTT GAA **GTT** GCG **TTT** CTC GTC CGG ATA CTT ATT C- 3′ (antisense)]. The resulting plasmid was then subsequently utilized to generate the triple mutant DHPA (R32K/Y34N/S91G) using the primers [5′-G ATG AAA CAG CAT TCC **GGC** CTG ACG ACT GGA AAC-3′ (sense) and 5′-GTT TCC AGT CGT CAG **GCC** GGA ATG CTG TTT CAT C-3′ (antisense)]. The R32K/Y34N/S91G plasmid was then employed for the mutation pDHPA-(R32K/Y34N/S91G/I9L) using 5′-CAA GAT ATT GCC ACC **CTC** CGC GGT GAT CTC CGC-3′ (sense) and 5′-GCG GAG ATC ACC GCG **GAG** GGT GGC AAT ATC TTG-3′ (antisense). Finally, the template R32K/Y34N/S91G/I9L was used to generate the plasmid pDHPA(R32K/Y34N/S91G/I9L/N81S), also referred to as pDHPB, with 5′-CTT GCG TCC GAC GCC **AGC** ACA CTC GTC CAG ATG-3′ (sense) and 5′-CAT CTG GAC GAG TGT **GCT** GGC GTC GGA CGC AAG-3′ (antisense). The plasmids were extracted using the QIAprep spin miniprep kit after each round of mutagenesis, and the presence of the desired mutations and lack of secondary mutations were confirmed by sequencing. Wild-type DHP B and DHP A (6× His-tagged proteins) were expressed and purified as previously described (*20*, *22*) with only minor modification.

Molecular Weight Determination. The molecular weight of DHP B was determined by a 6210 LC-TOF mass spectrometer in positive ion electrospray ionization (Agilent Technologies, Santa Clara, CA). The protein sample was in 50 mM ammonium acetate buffer, pH 7.0. The mobile phase consisted of HPLC grade solvents: water + 0.1% formic acid (v/v) and water: acetonitrile (5:95) + 0.1% formic acid (v/v). The injection volume was 5 μL, and the flow rate was 300 μL/min.

Preparation of Ferric DHP. DHP B was treated with an excess of potassium ferricyanide in order to obtain a homogeneous solution of the enzyme in the ferric state. Ferri/ferrocyanide was removed using a PD-10 desalting column prepacked with Sephadex G-25 medium. The protein was concentrated using an Amicon Ultra centrifugal filter equipped with a 10 kDa cutoff molecular weight membrane, and the purity of DHP was determined as previously published (*20*, *22*). Only protein samples that exhibited Reinheitzahl values (R_z) greater than 4.0 were utilized in this study. Protoheme content was measured by the pyridine hemochrome assay using $\Delta\varepsilon_{557}$ = 20.7 mM^{-1} cm^{-1} (reduced minus oxidized) for iron protoporphyrin IX (*42*, *43*), leading to a molar absorptivity for DHP B of 117.6 mM^{-1} cm^{-1} (λ_{max} = 407 nm), in good agreement with that of DHP A (ε_{406} = 116.4 mM^{-1} cm^{-1}) (*18*).

Preparation of DHP B Complexes for UV−Visible Spectroscopic Studies. Optical spectra were recorded using quartz microcuvettes (1 cm path length) on a Cary 50 UV−visible spectrophotometer equipped with thermostated cell holders at 25 °C. Complexes of DHP B (10 μM final concentration) were prepared in 100 mM KP_i buffer (pH 7). The ferric−CN complex was generated upon addition of NaCN (50 mM final concentration) to ferric DHP B. Oxyferrous DHP B was obtained by the aerobic addition of either 2 equiv of the reducing agent tris(2-carboxyethyl)phosphine (TCEP) or ascorbic acid to a solution of ferric DHP B, followed by application of the enzyme over a PD-10 desalting column. Ferrous DHP B was prepared by mixing the ferric enzyme with sodium dithionite anaerobically using standard Schlenk techniques. Ferrous DHP B prepared thusly was then exposed to CO gas to yield the DHP B ferrous−CO complex.

Mono- and trihalophenol complexes of DHP B were obtained upon the addition of stock solutions of the halophenols to a solution of DHP B in 100 mM KP_i buffer (pH 7). Final concentrations were as follows: DHP B, 8 μM; 2,4,6-trifluorophenol, 4 mM; 2,4,6-trichlorophenol, 2 mM or 300 μM; 2,4,6-tribromophenol, 255 μM; phenol, 4-fluorophenol, 4-chlorophenol, 4-bromophenol, 8 mM; 4-iodophenol, 850 μM.

Preparation of Oxyferrous DHP B. Oxyferrous DHP B was generated through incubation of the ferric enzyme with 5 equiv of ascorbic acid in 100 mM potassium phosphate buffer (pH 7). The formation of the oxyferrous species was monitored by its UV−visible spectrum [418 (Soret), 542, 578 nm]. Excess reducing agent was removed by using a PD-10 desalting column prepacked with Sephadex G-25 medium. The protein was concentrated using an Amicon Ultra centrifugal device equipped with a 10 kDa cutoff molecular weight membrane. The oxyferrous form of DHP B was found to be stable for at least 2 weeks when prepared in this fashion and stored at 4 °C.

UV−Visible Spectroscopic Studies and Dehaloperoxidase Activity Assays. Optical spectra were recorded using quartz microcuvettes (1 cm path length) on a Cary 50 UV−visible spectrophotometer equipped with thermostated cell holders at 25 °C. The apparent values of K_m and k_{cat} for DHP B for various concentrations of hydrogen peroxide at a fixed saturating concentration of the trihalophenol cosubstrate were calculated by triplicate measurements of initial rate at each H_2O_2 concentration. The experimental data were fitted to the Michaelis−Menten model using the enzyme kinetics software GraFit (Erithacus Software). The enzymatic activity was assayed on the basis of the disappearance of cosubstrate (trichlorophenol, 312 nm; tribromophenol, 316 nm) or formation of product (difluoroquinone, 330 nm) monitored for 2 min at 25 °C. The 1 mL reaction mixture contained 0.5 μM enzyme (ferric or oxyferrous), 150 μM trihalophenol, and varying H_2O_2 concentrations in 100 mM potassium phosphate buffer at pH 7.

Stopped-Flow UV−Visible Spectrophotometric Studies. Experiments were performed on a Bio-Logic SFM-400 triple-mixing stopped-flow instrument equipped with a diode array UV−visible spectrophotometer and were carried out at 20 °C in 100 mM KP_i buffer, pH 7. Constant temperature was maintained using a circulating water bath. Data were collected (900 scans total) over three time-domain regimes (2., 25, and 250 ms; 300 scans each) using the Bio Kinet32 software package (Bio-Logic). Single-mixing experiments were performed as follows: (i) ferric DHP B at a final concentration of 10 μM was reacted with 2.5−25 equivalents of H_2O_2 or (ii) 10 μM ferric DHP B was reacted with 5, 25, 70, and 100 μM DCQ (all final concentrations). Experiments were performed in double-mixing mode using an aging line prior to the second mixing step. The design of the experiments allowed for the mixing of DHP B with either TCP/DCQ or H_2O_2 for various aging times, followed by the second mix with the remaining (co)substrate: (i) DHP B + TCP/DCQ → delay → $+H_2O_2$ or (ii) DHP B + H_2O_2 → delay → +TCP/DCQ. Concentrations after mixing were $[DHP\ B]_f$ = 10 μM, $[H_2O_2]_f$ = 100 μM, and $[TCP]_f$ = 300 μM or [DHP B] = 10 μM, $[H_2O_2]$ = 25 μM, and [DCQ] = 70 μM. All data were evaluated using the Specfit Global Analysis System software package (Spectrum Software Associates) and fit with SVD analysis as either one-step, two species or two-step, three species irreversible mechanisms, where applicable. Kinetic data were baseline corrected using the Specfit autozero function.

Preparation of Reaction Intermediates by Freeze-Quench Methods. Rapid freeze-quench experiments were performed with a BioLogic SFM 400 freeze-quench apparatus by mixing a 50 μM enzyme solution (final concentration) with a 10-fold excess of H_2O_2 solution in 100 mM potassium phosphate buffer (pH 7) at 25 °C. Reaction times were as follows: 100 ms, 300 ms, 500 ms, 800 ms, 2 s, 38.25 s, and 60 s. The dead time of the instrument as configured was 10 ms. A standard 4 mm OD quartz EPR tube was connected to a Teflon funnel, and both the tube and the funnel were completely immersed in an isopentane bath at −110 °C. The reaction mixtures were quenched by spraying them into cold isopentane, and the frozen material so obtained was packed at the bottom of the quartz tube using a packing rod equipped with a Teflon plunger. In this manner, a packing factor of 60 ± 2% was consistently achieved. Samples were then transferred to a liquid nitrogen storage dewar until analyzed.

X-band EPR Spectroscopy. EPR spectra were recorded with an X-band (9 GHz) Varian E-9 EPR spectrometer (Varian, El Paso, CA). A standard 4 mm OD quartz EPR tube containing sample was placed into a quartz finger dewar insert filled with liquid nitrogen. The temperature of the samples was maintained at 77 K for the duration of the data acquisition, which required periodic refilling of the dewar due to the evaporation of the liquid nitrogen during longer acquisition runs. The typical spectrometer

settings were as follows: field sweep 200 G, scan rate 3.33 G/s, modulation frequency 100 kHz, modulation amplitude 4.0 G, and microwave power 2 mW. The exact resonant frequency of each EPR experiment was measured by an EIP-578 (Phase-Matrix, San Jose, CA) in-line microwave frequency counter. Typically, 20−200 individual scans were averaged to achieve sufficient signal-to-noise ratio for the spectra obtained at short-quench and long-quench times, respectively.

Spectroelectrochemistry (*SEC*). For a given experiment, a solution of ferric DHP B at a concentration of 100−200 μM [$\varepsilon_{406\ nm}$: 117600 $M^{-1}cm^{-1}$ (*18*)] was prepared in a supporting electrolyte of 100 mM KP_i, pH 7.0. SEC was carried out in a previously designed anaerobic UV−visible spectroelectrochemical cell made of cast acrylic (Small Parts, Inc.) that utilized an optically transparent thin-layer electrode (OTTLE) of antimony−tin oxide (ATO; Delta Technologies, Limited) (*44*). The path length for the cell was maintained at 0.1 mm by use of Teflon-coated fiberglass tape (Small Parts, Inc.). The ATO electrode was thoroughly cleaned before use by 10 min successive sonications in 1% (v/v) Contrex solution (Decon Laboratories, Inc.), 95% ethanol, and twice in deionized water. The SEC cell was stored in a nitrogen atmosphere drybox (Vacuum Atmospheres Co.; H_2O < 1 ppm, O_2 < 1 ppm) for at least 8 h prior to experimentation. Electronic spectra were recorded with a Hewlett-Packard 8453 spectrophotometer, and applied potentials were controlled with a Model 273 Princeton Applied Research potentiostat. The SEC cell made use of an Ag/AgCl (saturated KCl) reference electrode (Microelectrodes, Inc.) and a platinum wire auxiliary electrode (Alfa Aesar). All formal reduction potentials are referenced to the standard hydrogen electrode (SHE). Electron transfer mediators such as TMPD and $[Ru(en)_3]^{2+}$ were used to facilitate electron transfer between DHP B and the working electrode. The formal reduction potentials for TMPD and $[Ru(en)_3]^{2+}$ as determined by cyclic voltammetry were +0.250 and +0.111 V vs SHE, respectively. The ratio of DHP B to mediators was 2 to 1.

Resonance Raman Spectroscopy. Protein samples (~100 μM) were prepared in 100 mM KP_i buffer at pH 7. Para-halogenated phenols were introduced to final concentrations of 8 mM for 4-BP, 4-CP, 4-FP, and phenol and to 1 mM for 4-IP. 2,4,6-Trihalophenols were added to final concentrations of 4 mM for TFP, 3 mM for TCP, and 200 μM for TBP. The samples were placed into 5 mm diameter glass NMR tubes and stored on ice until used.

Resonance Raman spectra were obtained by Soret band excitation using a Coherent Mira 900 titanium sapphire (Ti:sapphire) laser. The Ti:sapphire laser was pumped using a Coherent Verdi 10 frequency doubled diode pumped Nd:vanadate (Nd:VO_4) laser generating 10 W at 532 nm. The beam generated from the Ti:sapphire was sent through a Coherent 5-050 doubler to generate a normal working range of 400−430 nm for Soret band excitation of each of the DHP complexes. The beam was collimated and cylindrically focused to a vertical line of ~0.5 mm on the sample. Laser power at the sample was 60 mW. Scattered light was collected with a Spex 1877 triple spectrometer equipped with a liquid nitrogen-cooled CCD detector controlled by Spectramax software.

Kinetics of 4-Bromophenol Inhibition of the DHP B Catalyzed Oxidation of TCP. Inhibition assays were conducted in 100 mM KP_i buffer at pH 7 using an Agilent 8453 UV−visible spectrometer equipped with temperature control and Hewlett-Packard UV−visible Chemstation software set to kinetic mode. The concentration of DHP and TCP in each sample was 2.5 μM and 125 μM, respectively. Temperature was equilibrated to 20 °C before initiation. A 100-fold excess of H_2O_2 (250 μM) was added to the cuvette to initiate the assay. Electronic absorption spectra were taken every 2 s for 2 min, monitoring the 273 nm peak of the 2,6-dichloro-1,4-dibenzoquinone product (2,4-DCQ). This process was repeated with the addition of 250 μM 4-BP to serve as the inhibitor.

Table 1: UV−Visible Spectroscopic Data for DHP B Complexes at pH 7

	λ_{max} (nm)	
	Soret	visible
ferric	407	508, 633
ferric−CN	423	544
ferrous	433	554
ferrous−CO	422	537, 567
oxyferrous	417	542, 578

RESULTS

Overexpression, Purification, and Characterization of DHP B. The plasmid encoding wild-type DHP A with an N-terminal poly-His tag (pDHPA) was subjected to four successive rounds of PCR amplification using mutagenic primers. DNA sequencing of the entire resulting *dhpB* gene (pDHPB) confirmed the success of the site-directed mutagenesis and the absence of secondary mutations. Recombinant DHP B was obtained by expression in *Escherichia coli* and resulted in a protein yield of ~9 mg/L of culture. The two-part purification strategy (immobilized metal affinity followed by ion-exchange chromatographies) resulted in purification levels >95% homogeneity, with DHP B being indistinguishable by SDS−PAGE gel from DHP A. As was found for isoenzyme A, DHP B was initially isolated as a mixture of the ferric and oxyferrous forms, but subsequent treatment with an excess of potassium ferricyanide permitted the isolation of the ferric form. The optical purity ratio (Reinheitzahl or R_z, defined as A_{Soret}/A_{280}) for WT DHP B was found to be 4.1, in good agreement with the literature value for DHP A. The monomeric molecular weight of DHP B was determined by electrospray ionization MS to be 16274.38 g/mol, which agrees with the theoretical expected value (16274.37 g/mol).

UV−Visible Characterization of DHP B. The electronic absorption spectra of different heme states of DHP B at pH 7 are presented in Figure SD1 and Table 1. Ferric metaquo DHP B at pH 7 exhibits electronic absorption features typical of a high-spin ferric heme [UV−visible: 407 (Soret), 508, 633 nm] and similar to those previously observed for DHP A under identical conditions (*18*, *20*). Addition of cyanide, a strong field ligand, led to a red shift of the Soret band [UV−visible: 423 (Soret), 544 nm], suggestive of the presence of a 6cLS ferric heme. Reduction of ferric DHP B with sodium dithionite yielded an absorption spectrum typical of a 5cHS ferrous heme [UV−visible: 433 (Soret), 554 nm] (*27*), which blue shifted in the presence of carbon monoxide [UV−visible: 422 (Soret), 537, 567 nm] and dioxygen [UV−visible: 417 (Soret), 542, 578 nm] to give the ferrous−CO and oxyferrous complexes, respectively, both of which are 6cLS hemes (*24*, *27*). Structural studies of the ferric [1ewa and 1ew6 (*45*), 2qfk (*27*), 3ixf (*37*)], deoxy (*21*), and oxyferrous (*27*) analogues of DHP A and B further support these spectroscopic assignments here. Periodic recording of the optical spectrum of the oxyferrous form of DHP B found it to be stable for at least 2 weeks (when stored at 4 °C).

Table 2: UV−Visible Spectroscopic Data for DHP B Halophenol Complexes at pH 7

	λ_{max} (nm)	A_{Soret}/A_{380}
ferric DHP B	407, 508, 540 (sh), 633	1.81
+phenol	406, 503, 538 (sh), 612	1.70
+4-fluorophenol	404, 502, 538 (sh), 612	1.53
+4-chlorophenol	404, 503, 538 (sh), 624	1.54
+4-bromophenol	404, 504, 538 (sh), 640 (sh)	1.39
+4-iodophenol	402, 503, 538 (sh), 640 (sh)	1.35
+trifluorophenol	406, 500, 536 (sh), 617	1.80
+trichlorophenol[a]	406, 503, 536 (sh), 624	1.57
+trichlorophenol[b]	406, 504, 536 (sh), 619	1.81
+tribromophenol	407, 506, 536 (sh), 623	1.74

[a]2 mM. [b]300 μM.

Mono- and Trihalophenol Binding in DHP B. The UV−visible spectra of ferric DHP B and its mono- and trihalophenol complexes at pH 7 are shown in Figure SD2, and relevant spectral features and analysis can be found in Table 2. In general, examination of a hemoprotein electronic absorption spectrum reveals the relative populations of 6cHS vs 5cHS heme species present: overall, 5cHS hemes exhibit a slightly blue-shifted and lower extinction coefficient Soret band than their 6cHS counterparts, as well as a shoulder at 380 nm (*46*). Furthermore, the charge transfer band denoted as CT1 in a 5cHS heme is found at ~640 nm (or higher), while that of a 6cHS heme is generally closer to 630 nm. LS heme systems exhibit a red-shifted Soret, the absence of a CT1 feature, and visible features at ~540 and 580 nm. Here, the effect of (tri)halophenol binding on DHP B was demonstrated by following specifically the A_{Soret}/A_{380} ratio (*47*, *48*). In the presence of phenol, the A_{Soret}/A_{380} ratio decreases from 1.81 for ferric DHP B to 1.70, indicative of an increase in 5cHS heme upon increasing occupancy of the distal active site binding pocket (Figure SD2A). Phenols bearing 4-halo substituents led to a progressive decrease in this ratio (1.53, 1.54, 1.39, and 1.35) which correlates well with the periodicity of the halogen (F, Cl, Br, and I, respectively). These findings suggested an increase in the relative population of 5cHS heme as one moves down the periodic table. We interpret these results as an increase in the binding affinity of the monohalophenol based upon the size of the substituent present, which in turn displaces the heme-bound water ligand and leads to a greater population of the "open" conformation (5cHS) of the distal histidine, His^{55} (*21*) (Scheme 1, step i-a).

In contrast to the above results obtained for the monohalophenol complexes, none of the trihalophenol complexes exhibited a significant decrease in the A_{Soret}/A_{380} ratio (Table 2 and Figure SD2B). As it is unlikely that the exogenously added trihalophenol and distal histidine are able to occupy the internal binding pocket simultaneously, the data suggest that trihalophenols are simply excluded from entering the distal cavity in DHP B due to their bulky size, precluding them from both displacing the heme-bound water ligand and generating a sufficient quantity of the 5cHS species as to affect the A_{Soret}/A_{380} ratio. In light of the X-ray crystallographic evidence for the binding of monohalogenated phenols at an internal site (*36*), as well as evidence for a trihalophenol external binding site (*22*, *25*, *49*), we suggest that our findings here support the latter supposition that trihalophenols bind externally (predominantly, although we cannot rule out exclusively) and monohalophenols bind internally. Further evidence is provided by our resonance Raman study (*vide infra*).

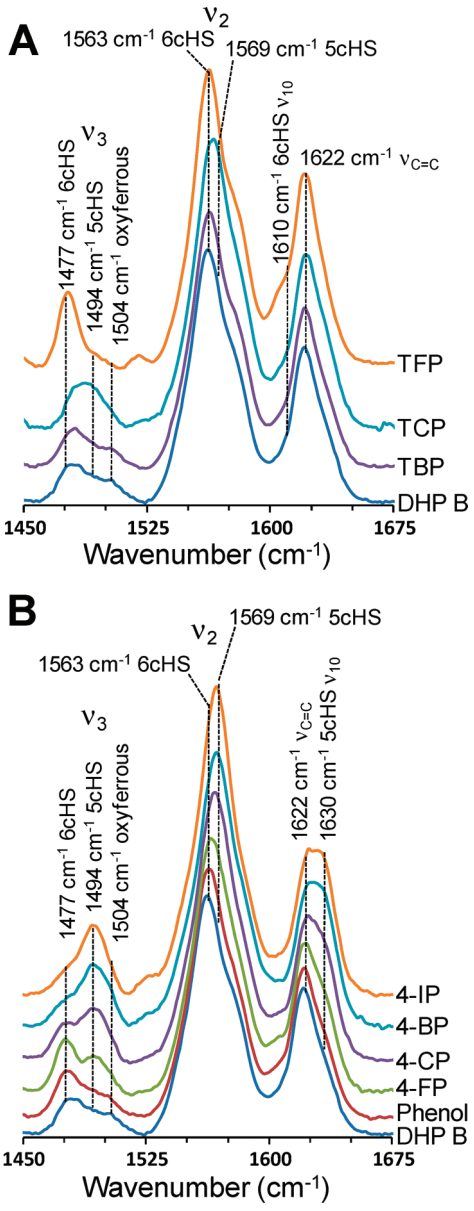

FIGURE 2: Resonance Raman spectra of halophenol complexes of DHP B (100 μM) at pH 7.0. (A) Trihalophenol complexes of TFP (4 mM), TCP (3 mM), and TBP (200 μM). (B) Monohalophenol complexes of 4-FP (8 mM), 4-CP (8 mM), 4-BP (8 mM), 4-IP (1 mM), and phenol (8 mM).

Resonance Raman Spectroscopy of DHP B and Its (Tri)halophenol Complexes. The high-frequency heme vibrational modes were investigated for DHP B at pH 7 using resonance Raman spectroscopy, and the results are presented in Figure 2. These resonance Raman spectroscopic results provide a complementary approach to our electronic absorption study with respect to elucidating the electronics of the heme cofactor. Binding of monohalogenated phenols to DHP B yielded the same trend as that observed in our electronic absorption study above. Specifically, a systematic shift to 5cHS heme resulted from the internal binding of the monohalophenols and followed the halogen series (5cHS heme population: I > Br > Cl > F), concomitant with the distal histidine assuming an open conformation. Internal binding is indicated by the loss of the 6cHS heme population (ν_3, 1477 cm^{-1}; ν_2, 1563 cm^{-1}) and gain of the 5cHS heme population (ν_3, 1494 cm^{-1}; ν_2, 1569 cm^{-1}; ν_{10}, 1630 cm^{-1}) (Figure 2B). These findings are in excellent

Table 3: Kinetic Data for the Oxidative Catalytic Reaction of Different Cosubstrates, TCP, TBP, and TFP, with 0.5 μM DHP B and 150 μM Corresponding Cosubstrates and Varying H_2O_2 Concentrations in 100 mM KP_i, pH 7

	DHP B				DHP A			
cosubstrate	$K_m^{H_2O_2}$ (μM)	K_m^{TXP} (μM)	k_{cat} (s^{-1})	$k_{cat}/K_m^{H_2O_2}$ (μM^{-1} s^{-1})	$K_m^{H_2O_2}$ (μM)	k_{cat} (s^{-1})	$k_{cat}/K_m^{H_2O_2}$ (μM^{-1} s^{-1})	ratio[c] k_{cat}(B)/k_{cat}(A)
TFP[a]	96 ± 18	N/A[d]	N/A	N/A	59 ± 10	N/A	N/A	2.1
TCP[a]	22 ± 2	210 ± 23	1.53 ± 0.03	0.070	23 ± 1	0.61 ± 0.01	0.027	2.6
TCP[b]	35 ± 6	N/A	1.17 ± 0.05	0.034	16 ± 1	0.57 ± 0.01	0.036	2.1
TBP[a]	63 ± 15	315 ± 11	1.3 ± 0.1	0.021	11 ± 1	0.30 ± 0.01	0.027	4.3

[a]Ferric starting oxidation state. [b]Oxyferrous starting oxidation state. [c]As ratio of initial rate. [d]N/A = not available.

agreement with those observed previously for DHP A under similar conditions (*50*).

In contrast, the binding of trihalophenols resulted in an increase of 6cHS heme population (ν_3, 1477 cm^{-1}; ν_2, 1563 cm^{-1}; ν_{10}, 1607 cm^{-1}) (Figure 2A). While the effect is more limited for TBP and TCP, the binding of TFP to DHP B resulted in nearly complete production of 6cHS heme. We attribute the increase in 6cHS population to the movement of the distal histidine into the closed conformation upon external trihalophenol binding, thereby stabilizing the heme-coordinated water molecule (Scheme 1, step ii-a). However, the data differ slightly from those observed for DHP A, which showed that although TBP and TCP were excluded from binding internally, TFP was able to do so, albeit not to the same extent as for the monohalophenols. We surmise that the subtle structural differences between these two isoforms give rise to the greater active site accessibility in DHP A vs B for TFP, the smallest of the three trihalophenols examined. We rule out a contamination of free fluoride ion in the TFP solution as the cause of these changes in DHP B given that the same solution did not produce an identical spectrum in DHP A (*50*).

In the above resonance Raman studies, a minor population of 6cLS heme was observed, as denoted by the ferrous heme vibrational mode at 1504 cm^{-1} (Figure 2). We attribute this to the presence of oxyferrous DHP B, which we presume is formed from the autoreduction of the ferric enzyme (*vide infra*). The oxyferrous low-spin heme component was also observed, albeit not in all spectra, as a minor feature in the above UV−visible study at ~576 nm. Interestingly, internal binding of monohalogenated phenols did not appear to affect the oxyferrous component of the enzyme (i.e., the signal intensity present in the monohalophenol-free sample remained upon 4XP binding), whereas external binding of trihalophenols led to loss of the 6cLS heme. This suggests that monohalophenols either do not enter the distal cavity of the oxyferrous enzyme or, if they do, they are present in the cavity along with the heme-ligated O_2 molecule. Why external binding of the trihalophenol would displace the O_2 molecule, while internal binding of monohalophenols does not, remains a question of interest. We surmise that this action might contribute in some way to the trigger mechanism that switches the function of the enzyme from globin to peroxidase. Evidence for this supposition is derived from our UV−visible spectroscopic study which shows that oxyferrous DHP B does not form the catalytically competent compound ES intermediate in the presence of H_2O_2 (as ferric DHP does) when trihalophenols are absent, but oxyferrous DHP does exhibit catalytic activity when trihalophenols and hydrogen peroxide are present concurrently. This functional-switch triggering event predicated upon cosubstrate binding is discussed in more detail below.

Enzymatic Activity of DHP B. The hydrogen peroxide-dependent oxidative dehalogenation of 2,4,6-trihalogenated phenols (TXP) catalyzed by DHP B at pH 7 was monitored by UV−visible spectroscopy (Figure SD3). Three TXP cosubstrates were examined (X = F, Cl, Br), and the reaction mixture yielded the corresponding 2,6-dihalo-1,4-benzoquinone (DXQ) products as expected. The enzymatic reaction was initiated by the addition of H_2O_2 as the substrate. Both enzyme and TXP cosubstrate concentrations were held constant while H_2O_2 concentration was varied. For the reactions employing TCP or TBP, cosubstrate loss was monitored. In the case of TFP, however, the reaction was monitored using product formation [2,6-difluoro-1,4-benzoquinone (DFQ), λ_{max} = 330 nm] due to the lack of a clear absorption maximum for the TFP cosubstrate (Figure SD3A). In the absence of DHP (nonenzymatic control), no product was observed under the conditions examined, in agreement with previous reports that showed a requirement for the enzyme (*18*, *20*).

Kinetic parameters (k_{cat}, K_m, and catalytic efficiency, k_{cat}/K_m) for the dehaloperoxidase activity of DHP B are presented in Table 3, together with those determined for DHP A under the same conditions of fixed trihalophenol cosubstrate concentration and varied hydrogen peroxide substrate concentration. Both isoenzymes exhibited saturable dehaloperoxidase activity under the conditions employed, and the data were fit to standard Michaelis−Menten kinetics using the method of initial rates. For the reactions with TBP and TCP, d[S]/dt was computed using the known ε values for these two cosubstrates, thus allowing for the determination of k_{cat}. For TFP, however, neither −d[S]/dt nor d[P]/dt were determined as the cosubstrate absorption maximum underwent a shift during catalytic turnover, and the molar absorptivity of the product is unknown. Thus, while initial rates for the oxidation of TFP could be determined by following product formation (Figure SD3A), the corresponding k_{cat} value could not be determined. Comparison of the enzymatic activity between DHP B and DHP A was therefore based on the ratio of their corresponding k_{cat} (TCP, TBP) or initial rate (TFP) values as listed in Table 3.

When starting from the ferric form, DHP B exhibited a consistently higher catalytic rate than DHP A for the three different cosubstrates examined in this study (Scheme 1, step ii-b). We observed the general trend of an increased rate of reaction as the periodicity of the halogen substituent was increased. Specifically, DHP B is able to dehalogenate TFP, TCP, and TBP 2.1-, 2.6-, and 4.3-fold faster than DHP A. The fastest rate of conversion was found for the brominated cosubstrate and is not surprising since TBP has been reported to be the natural cosubstrate for DHP under physiological conditions (*2*). Interestingly, the K_m values for DHP B were 2−6-fold higher than for DHP A for the substrate H_2O_2, leading to comparable catalytic efficiencies (k_{cat}/K_m) between the two isoenzymes.

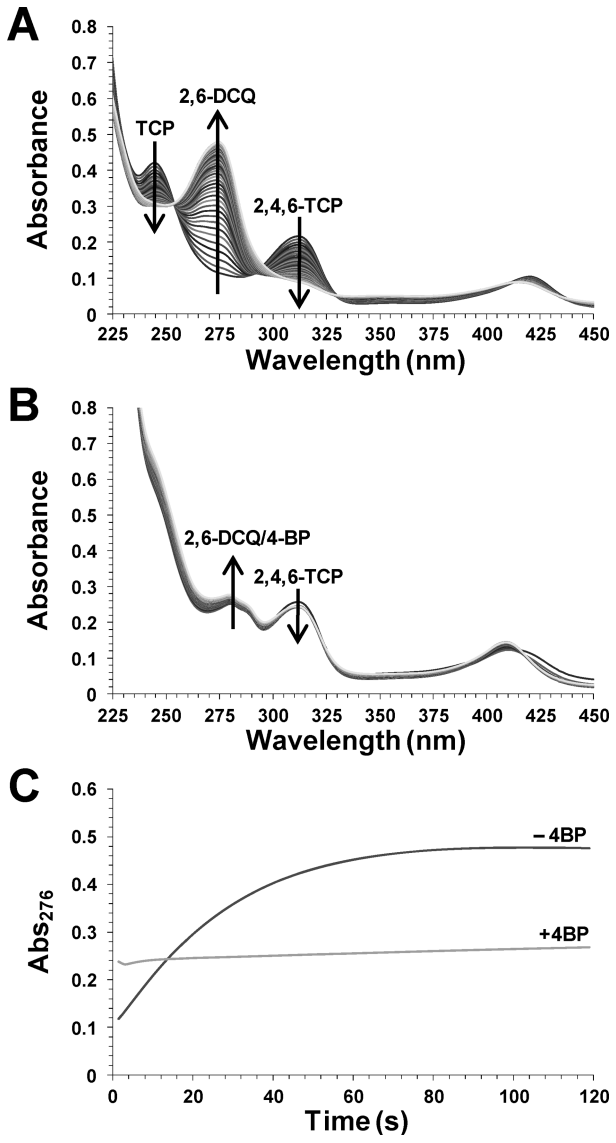

FIGURE 3: Oxidative dehalogenation of 2,4,6-trichlorophenol (125 μM) as catalyzed by DHP (2.5 μM) and hydrogen peroxide (250 μM) in the absence (A) and presence (B) of 4-bromophenol (250 μM). The formation 2,6-dichloroquinone was monitored at 276 nm (C).

The above study was repeated for the cosubstrate 2,4,6-TCP using oxyferrous DHP as the starting oxidation state rather than the ferric form of the enzyme (Scheme 1, step viii). Oxyferrous DHP B exhibited a catalytic efficiency that was only 2-fold lower than that observed for ferric DHP, whereas it was found that oxyferrous DHP A had a k_{cat}/K_m value 1.3 times greater than that of the ferric enzyme. Overall, these values for k_{cat} and K_m between the two different starting oxidation states (ferric and oxyferrous) are virtually the same despite having started in the former from what is the traditional peroxidase resting state and in the latter from what is normally a catalytically inactive state for peroxidases. Given the similarity of kinetic parameters, it reasons that although the first turnover may be initiated from either of the two oxidations states, subsequent turnovers proceed through a common pathway (i.e., a traditional peroxidase mechanism).

Inhibition of Trichlorophenol Oxidation by 4-BP. The kinetics of 2,4,6-TCP oxidation in the absence (Figure 3A) and presence (Figure 3B) of 4-bromophenol (4-BP) are shown. The binding affinity of 4-halophenols to DHP A follows the trend I > Br > Cl > F > H, with apparent dissociation constants of 0.536,

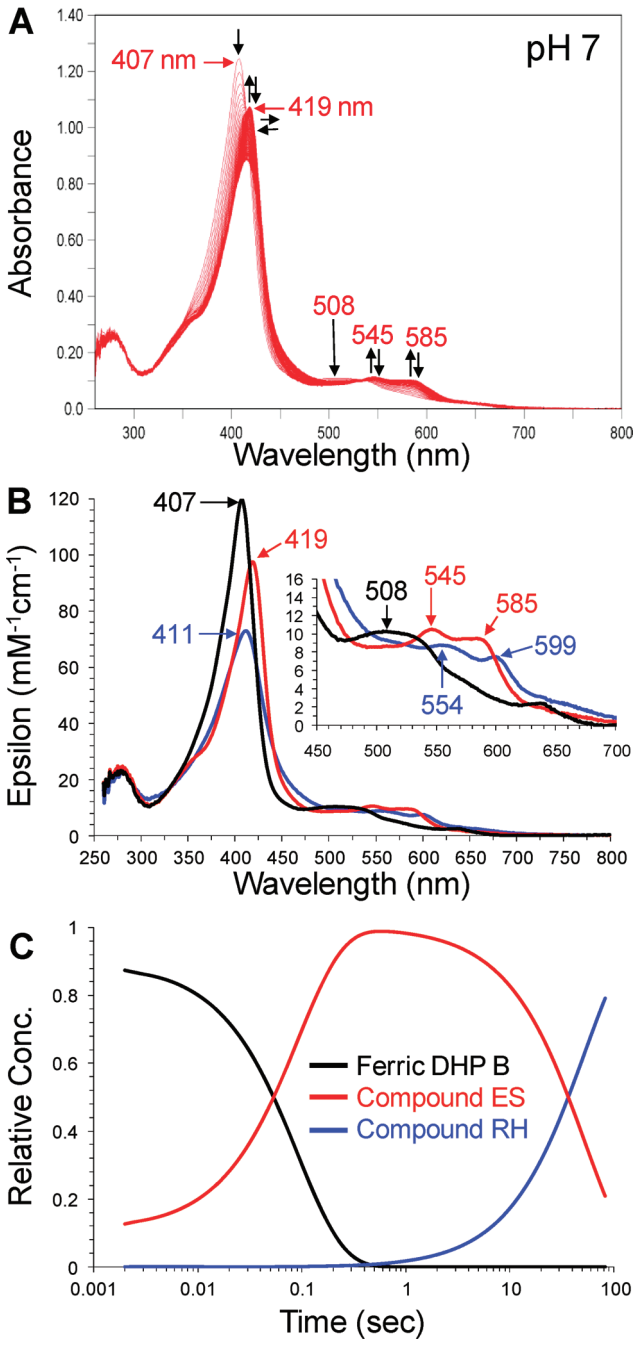

FIGURE 4: (A) Stopped-flow UV−visible spectroscopic monitoring (900 scans, 85 s) of the reaction between ferric DHP B (10 μM) and a 10-fold excess of H_2O_2 at pH 7. See Materials and Methods for details. (B) Calculated UV−visible spectra for ferric (black), compound ES (red), and compound RH (blue) DHP B are shown; the rapid-scanning data from panel A were compiled and fitted to a two-step, three species sequential irreversible model using the Specfit global analysis program. (C) Relative concentration profile determined from the three-component fit used in panel B.

1.15, 1.78, 3.72, and 10.0 mM, respectively (*51*). In agreement with our recent observations for DHP A (*51*), the presence of 4-monohalophenols led to a significant attenuation of the rate of trihalophenol oxidation as catalyzed by DHP B when compared to the absence of 4-bromophenol. The effect was observed regardless of whether the formation of 2,6-dichloroquinone (DCQ, 276 nm) (Figure 3C) or the loss of TCP (312 nm; data not shown) was followed. The kinetic results are interpreted as internal monohalophenol binding (confirmed above by resonance

Table 4: UV−Visible Spectroscopic Data and Kinetic Parameters for Oxidized Intermediates of DHP B and DHP A at pH 7

	DHP B		DHP A	
	λ_{max} (nm)	k_{obs}[a]	λ_{max} (nm)	k_{obs}[a]
ferric	407, 508, 633	not applicable	407, 504, 538, 635	not applicable
compound ES	419, 545, 585	$(1.08 \pm 0.02) \times 10^5$	420, 545, 585	$(3.56 \pm 0.02) \times 10^4$
compound RH	411, 554, 599	$(1.9 \pm 0.1) \times 10^{-2}$	411, 530, 564	$(1.7 \pm 0.03) \times 10^{-2}$
oxyferrous	417, 541, 577	not determined	417, 542, 578	not determined

[a] M^{-1} s^{-1} and s^{-1} for compounds ES and RH, respectively.

Raman spectroscopy) which precludes the activation of hydrogen peroxide due to the distal histidine His^{55} being swung out of the active site (Scheme 1, step i-c). In this "open" conformation, His^{55} is unable to facilitate the O−O bond cleavage necessary for compound ES formation. In support of this supposition, the control experiment showed no reaction between ferric DHP B (10 μM) and H_2O_2 (100 μM) when 30 equiv of 4-BP was present (data not shown) (Scheme 1, step i-b). Additionally, inhibition was observed regardless as to whether the monohalophenol inhibitor was added to DHP before (Scheme 1, step i-c) or after (Scheme 1, step ii-c) the trihalophenol cosubstrate.

Stopped-Flow UV−Visible Characterization of DHP B Compounds ES and RH. Formation of DHP B transient species was investigated by single-mixing stopped-flow UV−visible spectroscopy at pH 7. Upon rapid mixing (2 ms) of a ferric DHP B solution [UV−visible spectrum: 407 (Soret), 508, 633 nm] with H_2O_2 (Scheme 1, steps iii and iv), a new species was observed (Figure 4 and Table 4) whose spectral features [UV−visible: 419 (Soret), 545, 585 nm] we attributed to the ferryl-containing DHP B intermediate compound ES based upon our previous assignment of this reaction intermediate in DHP A (*20*, *26*, *29*, *35*) as well as the spectroscopic properties of other Fe(IV)−oxo species commonly found in hemoproteins. Specifically, non-globin peroxidases (e.g., HRP (*52*, *53*), CcP (*54*−*56*), APX (*57*, *58*), and others) exhibit a red-shifted Soret feature (~417−422 nm) and characteristic visible bands (~530, ~560 nm) for compound ES/II, whereas globins, such as myoglobin (*59*, *60*) and hemoglobin (*61*, *62*), display a similar red-shifted Soret feature but have visible bands that appear at lower energy, generally 540−545 and 580−590 nm. Not surprisingly, DHP exhibits features for compound ES that are similar to those observed for ferrylglobins. Assignment of this species as a traditional compound I intermediate was ruled out based on the lack of hypochromicity and absence of a strong red shift of the Soret band that is typical for an iron(IV)−oxo porphyrin π-cation radical (*52*, *57*, *58*). Compound 0 (ferric hydroperoxide) was also ruled out due to timescale considerations (*63*, *64*) and the lack of an observed hyperporphyrin spectrum (*65*, *66*). As compound ES and compound II, both ferryl-containing intermediates, are not distinguishable by UV−visible spectroscopy, our assignment for the intermediate described here as compound ES is based upon the results of our EPR spectroscopic study (*vide infra*). The experimental values of k_{obs} for compound ES formation varied linearly with hydrogen peroxide concentration in the range of 2.5−25 mol equiv (Figure SD4). From this dependence, the bimolecular rate constant was determined to be $(1.29 \pm 0.11) \times 10^5$ M^{-1} s^{-1} and is approximately 3.6-fold greater in DHP B than in DHP A. At higher peroxide concentrations (> 1 mM), heme bleaching was noted (data not shown).

In the absence of cosubstrate, DHP B compound ES was found to be unstable and converted to a new species [UV−visible: 411 (Soret), 554, 599 nm; $k_{obs} = 0.010 \pm 0.001$ s^{-1}] (Scheme 1, step vi-a). We have termed this stable end point in the DHP B catalytic cycle as compound RH based upon analogy to a similar, but not identical, species observed in DHP A (*20*). Both compound RH species form from compound ES but have different UV−visible spectroscopic properties and different chemical reactivity (*vide infra*).

Reaction of Preformed Compound ES with TCP Cosubstrate. Double-mixing stopped-flow UV−visible spectroscopic methods were used to investigate the reaction of preformed DHP B compound ES with TCP cosubstrate. The results of the UV−visible and resonance Raman studies suggest that TCP binds at an external binding site under the conditions employed in these stopped-flow studies reported herein, although such an assumption does not directly affect the interpretation of the results presented. Ferric DHP B was reacted with 10 mol equiv of H_2O_2 at pH 7, incubated for 500 ms to allow for the maximum accumulation of compound ES (see Figure 4C), and subsequently mixed with 30 mol equiv of TCP, which resulted in the regeneration of ferric DHP B (Figure SD5) after 18.5 s (Scheme 1, step v). The disappearance of compound ES was concomitant with the formation of the DCQ product. Furthermore, no compound RH was observed here, and the final spectrum [UV−visible: 409 (Soret), 502, 538, 576 nm] suggested the presence of a mixture of ferric and oxyferrous DHP B (*vide infra*). Additionally, varying the concentration of TCP cosubstrate (5 and 15 equiv; data not shown) in an attempt to determine the second-order rate constant for the reduction of compound ES by TCP was also investigated. However, while the reaction employing lower equivalents of TCP was qualitatively the same with respect to the formation of ferric DHP B (and subsequently oxyferrous DHP B) as to that observed for 30 equiv of cosubstrate, the reaction kinetics were poorly behaved and did not allow for a quantitative determination of the bimolecular rate constant. We attribute this to the multiple reactions (i.e., steps v, vii, and ix of Scheme 1) that may be occurring both sequentially and concurrently that give rise to the overall observed transition of compound ES to oxyferrous DHP B.

Repetition of the above double-mixing experiment with increasingly longer incubation times (800 ms−5 min) that allowed for the conversion of compound ES to RH exhibited progressively less cosubstrate loss (312 nm) and less product (275 nm) formation (Figure SD6). Shorter incubation times (100 and 300 ms) that did not allow for complete formation of compound ES still exhibited the same amount of TCP loss and DCQ formation as was observed for when compound ES was maximally formed. Thus, the extent of product formation is directly correlated with the amount of compound ES present or capable of being formed, strongly indicating that this intermediate is an active oxidant in DHP. Interestingly, DHP B still retained a small fraction of activity even after 5 min of preincubation (as

evidenced by both cosubstrate loss and product formation) at which point our component analysis indicates only compound RH and no compound ES present (Figure 4C). DHP A compound RH exhibited no such activity under identical experimental conditions (*20*).

In Situ DHP B Compound ES Formation in the Presence of TCP. Double-mixing stopped-flow UV−visible spectroscopic methods were employed to allow for preincubation of ferric DHP B with TCP (30 mol equiv, 500 ms incubation), followed by the addition of a 10-fold excess of H_2O_2 (Figure SD7). This set of conditions allowed for the *in situ* formation of compound ES in the presence of TCP, as opposed to the above experiments in which compound ES was preformed. DCQ product formation (275 nm) was observed and exhibited a pseudo-first-order rate constant (k_{obs}) of 0.19 ± 0.03 s^{-1} at pH 7. However, the amount of product formation was significantly less than when compound ES was preformed and then reacted with TCP (Figure SD6). This observation contrasts with DHP A which showed identical amounts of DCQ generated regardless of whether preformed or *in situ* formed compound ES was employed (*20*). In order to explore this chemistry further, the incubation time for ferric DHP B and TCP was varied from 0.1 to 60 s (Figure SD8). Interestingly, while the data do not support a clear temporal dependence on the amount of product formed or cosubstrate reacted, they do show an attenuation of the dehaloperoxidase reaction which is possibly indicative of cosubstrate inhibition, but this chemistry was not further explored.

DHP B compound ES was not observed under these conditions and is likely indicative of its immediate reduction in the presence of TCP cosubstrate. DHP A, however, did yield an observable *in situ* formed compound ES at pH 7, but not pH 5, and we attribute this difference to the higher activity of DHP B when compared to DHP A. Of significant note, however, was the observation of an electronic absorption spectrum that did not match that of ferric DHP B at the conclusion of this experiment (Figure SD7; 83 s). The spectral features [UV−visible: 410 (Soret), 541, 577 nm] were more similar to those of oxyferrous DHP B (Table 1), particularly with respect to the visible absorption features at ~541/577 nm and were also similar to what was observed in the reaction of preformed compound ES with TCP (Figure SD5). We interpret this spectrum to be a mixture of both oxyferrous and ferric DHP B based primarily on these data and our further investigations on the reaction between DCQ product and ferric DHP (*vide infra*).

Characterization of Protein Radicals in DHP B Compound ES. In order to confirm the presence of a protein radical in DHP B compound ES, continuous wave (CW) EPR spectroscopy was employed to probe the intermediate of the reaction of ferric DHP B and a 10-fold excess of H_2O_2 at pH 7 using rapid freeze-quench (RFQ) techniques. The X-band RFQ-CW-EPR spectra for DHP B compound ES with quench times of 100 ms, 300 ms, 500 ms, 800 ms, and 2 s are presented in Figure 5. The position of the signal is characterized by an effective *g*-value of 2.0057, and the shape of the signal is best described as an anisotropic septet, although both the shape and intensity of the signal change as a function of quench time. At the longest quench time (60 s), when our component analysis (Figure 4C) suggests little to no remaining compound ES present by UV−visible spectroscopy, the signal intensity dropped significantly, and it was not possible to resolve the hyperfine structure. Previously, we observed that the protein radical in DHP A compound ES exhibited an anisotropic quintet at pH 7 and an anisotropic

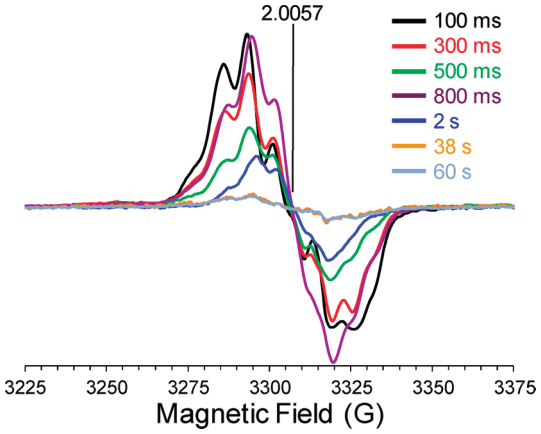

FIGURE 5: EPR spectra of the radical(s) in DHP B compound ES at pH 7. Rapid freeze-quench samples were prepared from the reaction of ferric DHP B (50 μM final concentration) with a 10-fold molar excess of H_2O_2 at 25 °C and rapidly frozen in an isopentane slurry. Spectra were recorded at 77 K using the spectrometer settings described in the Materials and Methods section. The cavity resonant frequency was 9.28005 GHz.

septet at pH 5 (both at $g = 2.0058$) (*20*). Thus, the DHP B signal collected here at pH 7 more closely resembles that observed for DHP A at pH 5. Furthermore, while their intensities decreased as a function of quench time, neither signal for DHP A exhibited the variation in line shape observed here for DHP B. We tentatively assign the EPR signal observed here at short quench times (100−800 ms) as a tyrosyl radical based on the obtained *g*-value and the partially resolved hyperfine structure with a peak-to-peak line width of approximately 21 G (*67*, *68*).

While we are able to demonstrate its presence, the low *g* factor spectral resolution of these RFQ-CW X-band experiments here prevents an unequivocal identification of the radical species based solely upon the observed magnetic parameters. However, in a separate report on DHP A (*69*), the assignment of the compound ES radical location was performed using the aid of the tyrosyl radical spectra simulation algorithm (TRSSA) (*68*). In this method, two input parameters, the phenoxyl ring rotation angle (θ) and the spin density on atom C1 of the radical (ρ_{C1}), were used to calculate 12 different EPR spectral simulation parameters ($g_{x,y,z}$, $A^{\beta 1}{}_{x,y,z}$, $A^{\beta 2}{}_{x,y,z}$, and $\Delta H_{x,y,z}$) using semiempirical dependences. These TRSSA-derived simulation parameters were combined with another 18 (ϕ and $A_{x,y,z}$ for C3, C5, C2, and C6; $\phi^{\beta 1}$ and $\phi^{\beta 2}$) that are set invariant in the algorithm for all tyrosyl radicals and were then used to simulate the EPR spectra of compound ES using Simpow6 (*70*). The derived θ-value that led to an accurate simulation was then compared to tyrosine residues with similar θ angles using the phenol ring rotation angle database (*71*), which when correlated with the known geometries of all the tyrosine residues from the available crystal structure of DHP led to an assignment of the tyrosine candidate(s) likely to host the radical. Using this approach for DHP A, two different radicals were identified as being both present in compound ES, a primary tyrosyl radical that is characterized by a phenoxyl ring rotation angle of 45° or 75° and was suggested to correspond to either Tyr^{34} or Tyr^{28} and a secondary radical that was suggested to reside on Tyr^{38}. Furthermore, spin quantification revealed that the Tyr^{34} radical is formed with a very high relative yield (almost 100% of heme), atypical of other globins. By extending this interpretation to the observed heterogeneity of the EPR line shape in DHP B, which lacks a tyrosine at position 34, we suggest

that the radical initially forms on Tyr^{28} and Tyr^{38}. Although tentative, these assignments are in good agreement with our preliminary mutagenesis studies (R. Dumarieh, J. D'Antonio, D. A. Svistunenko, R. A. Ghiladi, unpublished results) in which the mutation of these residues leads to compound I formation (see below). However, in light of the limitations of simulating the poorly resolved hyperfine splitting at low field, it will be necessary to utilize high-field EPR spectroscopic measurements in tandem with this site-directed mutagenesis study in order to unambiguously assign the nature of the protein radical in DHP B compound ES.

EPR spectroscopic characterization of DHP compound ES at liquid helium temperature has also been reported (*69*). In that study, the kinetic dependences of the ferric heme state and the free radical concentrations were investigated at low microwave power. Upon addition of hydrogen peroxide to ferric DHP, a nearly quantitative loss of the HS ferric heme signal (upon formation of the EPR-silent ferryl state of compound ES) was observed at pH 7, concomitant with the nearly quantitative formation of the tyrosyl radical signal. Moreover, the recovery of the ferric heme signal was noted to begin after 1 min, which coincides with the formation of compound RH from ES. Overall, the reported results strongly support the proposed mechanism in Scheme 1 in which the formation of a tyrosyl radical and ferryl heme occurs upon the two-electron oxidation of ferric DHP by hydrogen peroxide.

Reactivity of Compound ES with DCQ. To explore the possibility that DHP B compound ES could react directly with the product DCQ (Scheme 1, step vii), the reaction of preformed compound ES with 7 equiv of DCQ was monitored by double-mixing stopped-flow UV−visible spectroscopy at pH 7. Compound ES was first formed upon rapid mixing of a solution of ferric DHP B with 2.5 equiv of H_2O_2, allowed to incubate for 800 ms to ensure its full formation, and subsequently mixed with a solution of DCQ (7-fold excess). As shown in Figure 6, loss of DCQ (275 nm) was observed, concomitant with the conversion of compound ES [UV−visible spectrum: 420 (Soret), 546, 588 nm] to a new species [UV−visible spectrum: 415 (Soret), 541, 577 nm] whose spectral features closely resemble those observed for oxyferrous DHP B, particularly with respect to the visible absorption features at ~541/577 nm. We interpret this spectrum to be a mixture of both oxyferrous and ferric DHP B. Under these conditions, no compound RH was observed, strongly suggesting that compound ES was reduced in the presence of DCQ. Varying concentrations of DCQ (data not shown) were also employed in an attempt to determine the bimolecular rate constant for the reduction of compound ES by DCQ. Again, although the reactions were qualitatively the same, the kinetics were poorly behaved, likely indicative of several reactions with varying dependencies on DCQ concentration occurring in step vii of Scheme 1, and the quantitative determination of the second-order rate constant was not possible.

To examine the effect of DCQ preincubation on *in situ* formed compound ES, the above experiment was repeated by first incubating ferric DHP B with 7 equiv of DCQ for 500 ms, followed by the addition of 2.5 equiv of H_2O_2 (Figure SD9). The first spectrum observed exhibited spectral features that matched those of a mixture of oxyferrous and ferric DHP B [UV−visible spectrum: 408 (Soret), 508, 541 (sh), 577 (sh) nm]. This spectrum converted cleanly to DHP B compound ES [UV−visible spectrum: 419 (Soret), 546, 588 nm], before returning once again to a ferric/oxyferrous mixture [UV−visible spectrum: 413 (Soret), 541, 577 nm]. As was noted above, DCQ loss during this experiment was observed. Furthermore, it was possible to observe formation of the compound ES intermediate here *in situ* in the presence of DCQ (as a cosubstrate), whereas this was not possible when TCP was employed as cosubstrate. Overall, the reaction chemistry with DCQ, regardless of whether compound ES is preformed or generated *in situ*, leads to the reduction of this intermediate and the formation of oxyferrous DHP, likely through a transiently formed deoxyferrous species.

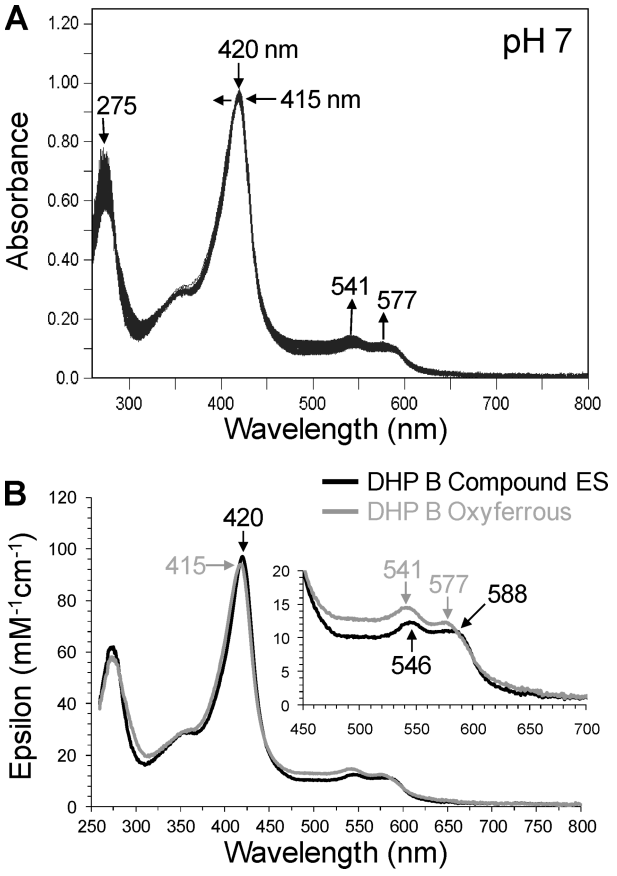

FIGURE 6: (A) Stopped-flow UV−visible spectroscopic monitoring (900 scans, 85 s) of the double-mixing reaction between preformed DHP B compound ES (10 μM, 500 ms) and a 7-fold molar excess of DCQ at pH 7. (B) Calculated UV−visible spectra for compound ES (black) and a ferric/oxyferrous DHP B mixture (gray) are shown; the rapid-scanning data from panel A were compiled and fitted to a one-step, two species sequential irreversible model using the Specfit global analysis program.

Incubation of DCQ with Ferric DHP B. As noted in the previous double-mixing experiment in which ferric DHP B was preincubated with DCQ prior to their reaction with H_2O_2, a mixture of oxyferrous and ferric DHP B was initially observed. As the hydrogen peroxide chemistry described herein has been shown to yield compound ES, and not oxyferrous DHP, the reaction between ferric DHP B and DCQ in the absence of H_2O_2 (Scheme 1, step ix) was investigated using single-mixing stopped-flow techniques in order to further elucidate the origin of formation of the oxyferrous species shown in Figures SD5 and SD7 and Figure 6. The reaction initiated upon rapid mixing of ferric DHP B with 0.5−10 equiv of DCQ was monitored by UV−visible spectroscopy over 85 (Figure SD10) and 800 s (Figure 7) at pH 7. The data exhibited saturable kinetics with a clear formation of oxyferrous DHP B [UV−visible spectrum: 413−5 (Soret), 541, 577 nm; $k_{cat} = (8.49 \pm 0.26) \times 10^{-2}$ s^{-1};

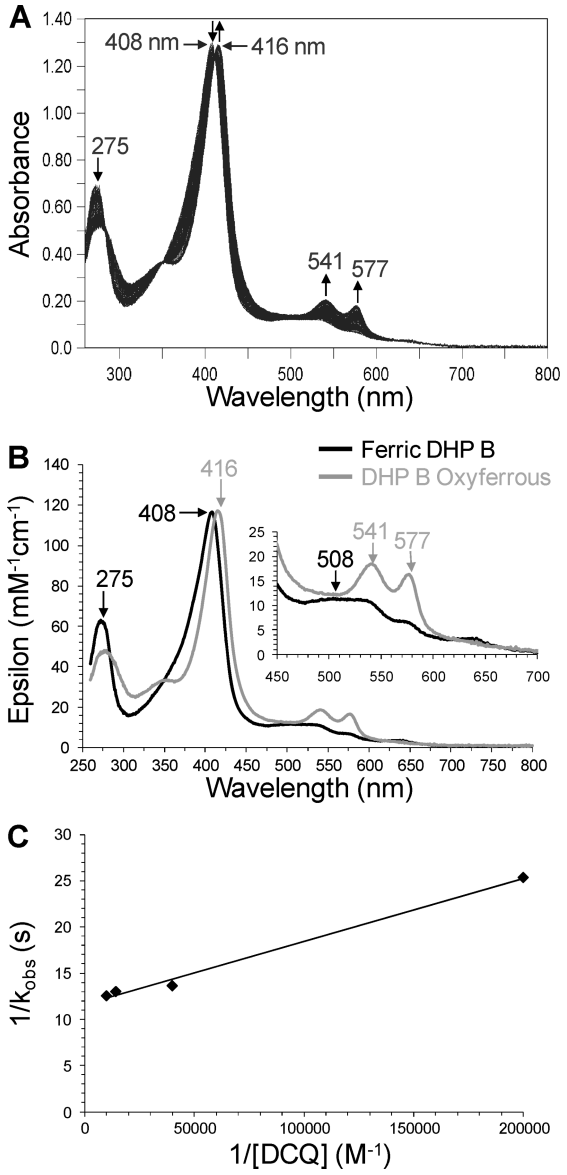

FIGURE 7: (A) Stopped-flow UV−visible spectroscopic monitoring (900 scans, 800 s) of the reaction between ferric DHP B (10 μM) and a 7-fold excess of DCQ at pH 7. (B) Calculated UV−visible spectra for ferric (black) and the ferric/oxyferrous DHP B mixture (gray) are shown; the rapid-scanning data from panel A were compiled and fitted to a one-step, two species sequential irreversible model using the Specfit global analysis program. (C) Double-reciprocal plot.

K_m = 5.4 ± 0.9 μM], with concomitant loss of the DCQ feature (275 nm). In a separate nonenzymatic control experiment (data not shown), DCQ loss due to autoxidation was observed to be less than 1% over 5 min at pH 7, indicative of a DCQ degradation pathway under the conditions employed in this study, but one which is not relevant to the time scale of the stopped-flow experiment. Thus, it appears that DCQ itself may be able to reduce ferric DHP B in the presence of dioxygen to generate the observed oxyferrous complex. Although outside of the scope of this current study, it is not clear at this time what the products of DCQ degradation are in the presence and absence of ferric DHP B, and these questions will be addressed separately in future experiments. The reactivity of DCQ demonstrated here complicates the determination of a DXQ binding affinity for ferric DHP B.

Spectroelectrochemistry of DHP B. The reduction potential of DHP B at pH 7 was determined by spectroelectrochemistry.

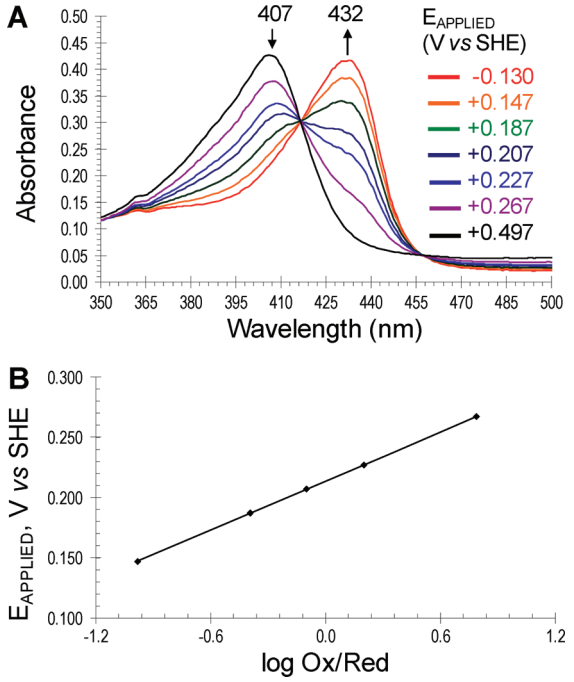

FIGURE 8: Spectroelectrochemical determination of the formal reduction potential of the ferric/ferrous couple in DHP B. (A) The UV−visible spectroelectrochemical plots of DHP B at various applied potentials ($E_{applied}$ versus SHE) are shown. In the absence of dioxygen, ferric DHP B (λ_{max} = 407 nm) converted to the ferrous enzyme (λ_{max} = 432 nm) as the applied reduction potential was lowered from 497 to −130 mV. (B) The corresponding Nernst plot of the data in panel A.

The UV−visible spectroelectrochemical plot of DHP B at various applied potentials ($E_{applied}$ versus SHE) are shown in Figure 8A. In the absence of dioxygen, ferric DHP B (λ_{max} = 407 nm) converted to the ferrous enzyme (λ_{max} = 432 nm) as the applied reduction potential was lowered from 497 to −130 mV. The corresponding Nernst plot (Figure 8B) reveals a formal reduction potential of 206 ± 6 mV (vs SHE), with a slope of 72 ± 5 mV consistent with an n = 1 process. The spectroelectrochemical measurement for obtaining the reduction potential was found to be reversible when the electrochemical stepping procedure (titration) was initiated from either the fully oxidized (ferric) or fully reduced (deoxyferrous) state (results not shown). The observed formal reduction potential for DHP B is nearly identical to that of DHP A (202 ± 6 mV) (*72*) and suggests that the five mutations between these two isoenzymes do not strongly influence their electrochemical properties. The relatively high reduction potential of this oxygen-transport globin may be a contributing factor as to why the reaction of DCQ with ferric DHP B yields the oxyferrous enzyme.

Compound RH Formation and Chemical Reactivity. Previously, we observed that DHP A compound RH was able to be reduced in the presence of sodium dithionite at pH 7 to subsequently form the oxyferrous complex (*20*), providing a possible link between the two activities (oxygen carrier and peroxidase) of this bifunctional hemoprotein. To explore whether this chemistry was possible with DHP B compound RH, this species was formed as described above from the decay of DHP B compound ES, itself formed from the reaction of the ferric enzyme with 10 equiv of H_2O_2 at pH 7. Upon its full formation (as confirmed by UV−visible spectroscopy), catalase was then added to remove any unreacted hydrogen peroxide, yielding

compound RH. Neither excess sodium dithionite nor ascorbate was able to generate the (oxy)ferrous enzyme within 15 min. Rather, a new species was observed (Scheme 1, step vi-b) which exhibited a Soret band maximum at 426 nm and no distinct visible bands (Figure SD11). For discussion within this report, we have termed this new species compound P_{426}.

By contrast, when the above experiment was repeated using compound RH that was formed from 2.5 equiv of H_2O_2 rather than the 10 equiv employed previously, treatment with catalase followed by addition of excess sodium dithionite did reveal the formation of ferrous DHP B (Figure SD12), which then converted to the oxyferrous complex upon consumption of the excess reductant (Scheme 1, step vi-c). Thus, the extent of the formation of the 426 nm species is dependent upon the amount of H_2O_2 used to generate the precursor compound RH. Given the conditions needed to form it, there is a high likelihood that compound P_{426} is a nonphysiologically relevant species, and its chemistry was not explored further.

DISCUSSION

The terebellid polychaete *A. ornata* has been shown to possess two genes, *dhpA* and *dhpB* (*19*), which encode for dehaloperoxidase isoenzymes A and B, respectively. While the molecular details of the dehaloperoxidase catalytic cycle have been investigated for some time for isoenzyme A, no such mechanistic studies have been performed for DHP B. The primary focus of this report is to provide the details of dehaloperoxidase chemistry which have yet to be reported for either isoenzyme and to augment that with a full study of dehaloperoxidase B.

The activity studies presented herein demonstrate that dehaloperoxidase B is able to catalyze the oxidative dehalogenation of 2,4,6-trihalogenated phenols to their corresponding 2,6-dihalo-1,4-benzoquinones in the presence of hydrogen peroxide. As brominated aromatics are the most abundant halometabolites present in the environment of *A. ornata* (*10*), it was surprising that 2,4,6-tribromophenol was found to be oxidized with the lowest catalytic efficiency under the conditions examined, a result that differs from that reported previously for DHP A (*2*). Overall, DHP B exhibits a higher catalytic rate for all cosubstrates (TFP, TCP, and TBP) examined when compared to DHP A under identical conditions. However, the catalytic efficiencies for the dehalogenation of these cosubstrates are similar between the two isoenzymes due to the higher K_m for hydrogen peroxide binding in DHP B over that determined for DHP A. K_m for trihalophenol cosubstrate was determined to be in the high micromolar range. In the absence of data regarding protein expression levels *in vivo*, it is not possible to speculate whether the differences in activity relate to selective isoenzyme expression under conditions of high oxidative or excessive trihalophenol stresses.

Enzymatic activity was observed regardless of whether the catalytic cycle was initiated from the ferric or oxyferrous states. As DHP is a globin peroxidase, this is of critical importance given that the two inherent functions of the enzyme traditionally require different iron oxidation states: ferrous for O_2 transport, ferric for peroxidase activity. Furthermore, the oxyferrous state is normally a catalytically incompetent species for monofunctional peroxidases (*73*), which makes this observation even more unique to DHP. Thus, we surmise that dehaloperoxidase may have evolved its peroxidase function to begin from the oxyferrous state, which is the normal oxidation state for this hemoglobin in *A. ornata*. How the enzyme accomplishes this and functions as both an O_2-carrier and a peroxidase may be linked to the highly unusual conformational flexibility of the distal histidine in dehaloperoxidase. Typically, the Fe−His $N^{\varepsilon 2}$ distances in globins range between 4.1−4.6 Å and 5.5−6.0 Å for peroxidases (*74*−*77*). By comparison, in dehaloperoxidase the Fe−His $N^{\varepsilon 2}$ distance in ferric DHP B is 5.5 Å (*37*) and between 4.8 and 5.5 Å in DHP A (*27*, *36*, *45*) for when the distal histidine is in the closed position. Although not available for DHP B, the Fe−His $N^{\varepsilon 2}$ distance in oxyferrous DHP A is 5.1 Å. Thus, the distal histidine-to-heme distance in dehaloperoxidase, being intermediate between those found in globins and peroxidases, is well positioned to function both as a stabilizer of the bound dioxygen ligand in the former and as the general acid/base that facilitates both the deprotonation and heterolytic O−O bond cleavage of hydrogen peroxide in the latter. Interestingly, using site-directed mutagenesis Watanabe and co-workers repositioned the distal histidine in sperm whale myoglobin from 4.3 Å in the wild-type protein to 5.7 Å in the F43H/H64L Mb mutant, effectively converting Mb from an oxygen transport protein to a peroxidase (*74*). They concluded that the interaction of the closer distal histidine in wild-type Mb with both oxygen atoms of an iron-bound peroxide would not facilitate the charge separation that is necessary for heterolysis, whereas the repositioned distal histidine in the F43H/H64L mutant, being further from the iron-bound oxygen atom, was suggested to interact exclusively with the terminal oxygen atom, thereby leading to the heterolytic O−O bond cleavage necessary in peroxidases. With His^{55}−O(1) (iron-bound) and His^{55}−O(2) (terminal) distances of 3.2 and 2.8 Å (*27*), respectively, oxyferrous DHP exhibits similarities to wild-type Mb in that the distal histidine interacts with both of the oxygen atoms of the end-on bound dioxygen ligand, while at the same time ferric DHP has a longer Fe−His $N^{\varepsilon 2}$ distance that more resembles those of peroxidases. Taken together, these characteristics that are particular to the highly flexible distal histidine in dehaloperoxidase are likely vital to answering the larger question of how DHP performs its dual functions.

Stopped-flow UV−visible spectroscopic studies were employed to monitor the reaction of ferric DHP with hydrogen peroxide (the putative physiological oxidant) in the absence of cosubstrate. Similar to DHP A, the first intermediate observed exhibited spectral features which matched those for a ferryl-containing species that lacked a porphyrin π-cation radical (*20*), suggestive of the formation of compound ES or compound II. We interpret this result as the transient formation of compound I upon heterolysis of the O−O bond of hydrogen peroxide, followed by rapid endogenous electron transfer yielding the observed compound ES intermediate. An alternative explanation as to the lack of an identifiable compound I intermediate under the conditions explored is that the reaction with hydrogen peroxide proceeds homolytically, thereby directly generating the observed ferryl species. However, several lines of evidence argue against this. First, the observation of the protein radical in compound ES concomitant with the ferryl state favors a two-electron oxidation process (i.e., heterolytic cleavage). Second, compound I has been identified as a transient species in myoglobin (*66*, *78*), and it is likely that dehaloperoxidase, being a globin itself, proceeds through similar reaction chemistry. Third, a recent report from Dawson and co-workers demonstrated a significant amount of heterolytic O−O bond cleavage of cumene hydroperoxide upon its reaction with DHP A, consistent with the formation of a transient compound I species (*31*). Finally, our preliminary characterization of mutants of DHP A and B which

lack both Tyr^{34} and Tyr^{38} exhibits by optical spectroscopy an intermediate that possesses the spectral features of compound I (R. Dumarieh, J. D'Antonio, D. A. Svistunenko, and R. A. Ghiladi, unpublished results).

In the presence of cosubstrate, the disappearance of compound ES was observed in parallel with the formation of the quinone product; however, differences were noted between preformed and *in situ* generated compound ES. Specifically, the amount of product formed when compound ES was generated *in situ* was less than one-third of that produced by preformed compound ES. These results for DHP B differ from the observation reported previously for DHP A, where equivalent amounts of product were generated regardless of how compound ES was formed (*20*). One possible interpretation of the results here is that the binding of a small molecule to DHP B interferes with the subsequent activation of H_2O_2 at the heme center. This may occur if the small molecule binding sterically blocks access of the hydrogen peroxide to the heme iron. Also of note is that both reactions involving either preformed or *in situ* generated compound ES yielded oxyferrous DHP B in the presence of cosubstrate; these results differ from DHP A in which both methods for forming compound ES yielded ferric enzyme upon reduction with cosubstrate (*20*). While it is tempting to suggest that these results may represent two different reaction pathways for cosubstrate oxidation, i.e., the reactivity of a transiently formed compound I versus that of preformed compound ES, our findings regarding the reactivity of DCQ with ferric DHP B (*vide infra*) point to a second reaction which was not known when DHP A was first being investigated.

In the absence of cosubstrate, DHP B compound ES was found to decay to a new, stable species termed compound RH. Again, differences with DHP A were observed. First, the electronic absorption spectrum of DHP B compound RH differs from that observed in isoenzyme A (*20*), possibly indicative of a different electronic structure present. Moreover, whereas the oxyferrous enzyme could be regenerated from DHP A compound RH upon reduction, providing a link between peroxidase and O_2-transport functions, DHP B compound RH cannot. Rather, a new species unique to DHP B was observed. The formation of "compound P_{426}", so termed for the absorption maximum of the Soret band, was found to be dependent on the amount of hydrogen peroxide used to first generate the precursors, compounds ES and RH, with increasing amounts of H_2O_2 leading to full formation of this species. The significance of compound P_{426} in the dehaloperoxidase catalytic cycle, if any, is not known at this time.

Our findings point to DHP B compound ES as a catalytically competent species in the dehaloperoxidase reaction cycle. Dichloroquinone product formation may result from either a single two-electron oxidation of the trichlorophenol cosubstrate by compound ES or two sequential one-electron oxidations, both pathways being indistinguishable under the multiple-turnover conditions examined here. However, Dawson and co-workers (*31*) recently reported evidence supporting a peroxidase cycle for DHP A involving two sequential one-electron oxidations of TCP to yield DCQ when preformed compound ES was employed. Thus, it is likely that the same reaction pathway with respect to cosubstrate oxidation may be occurring here for DHP B. Our data also show significantly attenuated rates of cosubstrate loss and product formation when compound ES is allowed to decay to compound RH, either partially or fully, prior to the addition of cosubstrate. The implication here is that compound RH is not a catalytically relevant species in the DHP reaction cycle, although it does appear to possess a very low level of activity.

RFQ-CW-EPR spectroscopic studies were employed to confirm the presence of the protein radical in DHP B compound ES. The absence of an observable compound I species under the conditions employed here suggests the presence of an endogenous reductant which we have tentatively ascribed to as a tyrosine side chain (*20*), yielding the EPR-observable tyrosyl radical. Indeed, we have demonstrated the presence of such a carbon-centered signal here for DHP B compound ES at pH 7 based upon our analysis of the signal *g*-factor, partially resolved hyperfine structure, and peak-to-peak line width (~21 G). Of the four tyrosine residues in DHP B (Tyr^{16}, Tyr^{28}, Tyr^{38}, and Tyr^{107}), Tyr^{28} and Tyr^{38} are the most likely candidates for the initial site of radical formation given their relative proximity of 10.24 and 7.57 Å, respectively, to the heme edge, while the remaining two tyrosine residues are > 15 Å distant. The time-dependent changes observed in the protein radical signal, which are more pronounced for DHP B than for DHP A, may suggest a migration of the radical out of the active site to other redox active protein side chains (including Trp^{120}, 10.47 Å distant from the heme edge) upon decay of the compound ES intermediate (*20*). Thus, we highlight that there may be a difference between the site of initial radical formation and that of the observed radical in compound ES. With respect to the EPR parameters (*g*-value, hyperfine splitting), a comparison of the radical signal observed here for DHP B at pH 7 reveals that it is more similar to that signal noted for DHP A at pH 5 rather than at pH 7 (*20*). Given that the Tyr^{34} residue present in DHP A is absent in DHP B (replaced with a redox inactive asparagine), we rule out that the location of the radical observed in DHP A at pH 5 given the persistence of the similar signal in DHP B, albeit at the higher pH value. One possible explanation for this pH-dependent observation is that the mutations in DHP B provide an alternative electron-transfer pathway between the heme center and the putative external cosubstrate binding site, thus giving rise to EPR signals that originate from different redox active amino acid residues.

The reactivity of dichloroquinone, the presumed end product of TCP oxidative dehalogenation, with either *in situ* generated or preformed DHP B compound ES was also investigated by double-mixing stopped-flow UV−visible spectroscopy. Under the conditions examined, these studies revealed that compound ES, regardless of how it was generated, reacted with DCQ to ultimately yield oxyferrous DHP B. Thus, in a novel reaction pathway not previously observed for DHP A, the two-electron-oxidized compound ES intermediate was reduced by three electrons in the presence of DCQ, itself already two electrons oxidized compared to the starting cosubstrate TCP. Although the mechanistic details of this highly unusual reaction will require a separate full study, one possible explanation is that DCQ is further oxidized, perhaps yielding a polymeric species in solution, and thus presumably able to reduce compound ES, although one might rather expect a return to the resting ferric state in this case. Even more significant, however, was the finding that ferric DHP B alone was capable of reacting with DCQ to also generate the oxyferrous complex. Here, we hypothesize that the inherent instability of DCQ in solution, as evidenced by its degradation in our nonenzymatic and oxidant-free control reaction, leads to the production of species, possibly radical in nature, that reduce ferric DHP B to ferrous in the presence of dioxygen to yield the observed oxyferrous complex. This would also account for the

above formation of oxyferrous DHP B in the reaction of compound ES with DCQ if one invoked a ferric species in that pathway. The unusually high reduction potential for a peroxidase, as deduced by our spectroelectrochemistry study, likely facilitates reactions that favor reduction of the heme and formation of oxyferrous DHP B. Thus, the dichloroquinone chemistry explored herein may represent a link between the two activities of the bifunctional dehaloperoxidase by allowing for the ferric state to initiate a peroxidase pathway in the presence of TCP and H_2O_2 or enabling O_2-transport capability by forming the oxyferrous complex in the presence of DCQ (itself generated from the aforementioned peroxidase pathway).

The UV−visible and resonance Raman spectroscopic studies presented here also provide a picture of how small molecule binding affects the electronic structure of the heme active site in DHP B. As inferred from their effect on the relative populations of five- and six-coordinate high-spin heme (*50*), a clear difference between internal (*36*) and external (*22*, *25*, *49*) small molecule binding was observed. In particular, monohalophenol binding led to a greater population of 5cHS heme, which we interpret as internal binding leading to the displacement of the heme-bound axial water ligand and locking the distal histidine His^{55} in the "open" conformation (*37*, *50*). Biophysical studies and molecular dynamics simulations on both oxyferrous and carbonmonoxy Mb illustrate the conformational flexibility of the distal histidine in globins (*79*−*81*). In particular, the molecular dynamics simulations on the His^{64} $N_\delta H$ tautomer in Mb showed it to exist in both "open" and "closed" conformations (*80*), and we envision a similar scenario in dehaloperoxidase B. In the "open" conformation, a channel between the solvent and the heme active site is formed (*37*), allowing for monohalophenol to enter and sterically block the distal histidine from assuming the "closed" conformation. Trihalophenol binding, however, led to a greater population of 6cHS, which we interpret as external binding where the heme-bound water molecule is stabilized by this "closed" conformation of the distal histidine (*50*). The findings presented herein for DHP B are in good agreement with previous studies from which one can surmise internal and external binding sites in DHP A (*22*, *25*, *36*, *49*). The conformational flexibility of the distal histidine in DHP may be critical in understanding how this hemoprotein functions as both a peroxidase and an oxygen-transport globin (*21*, *37*), as activation of hydrogen peroxide is predicated upon the ability of the distal histidine to facilitate O−O bond cleavage (i.e., the "pull" of the push−pull mechanism). Presumably, monohalophenol binding would preclude the distal histidine from participating in the activation of hydrogen peroxide due to it being locked into the "open" conformation (Scheme 1, step i-a), leading to an attenuation of the oxidative dehalogenation reaction as catalyzed by DHP B. Indeed, in agreement with this supposition are the results of our inhibition study here which strongly suggest that 4-bromophenol is an inhibitor of the oxidation of 2,4,6-trichlorophenol. If correct, then other factors pertaining to the *in vivo* biological relevance of monohalophenols, which are outside the scope of this *in vitro* study, need to be elucidated in order to better understand the role of monohalophenols in the environment of *A. ornata*.

In light of the spectroscopic and biochemical findings presented here, we propose the following updated mechanism for the *in vitro* peroxide-dependent oxidation of ferric DHP B from *A. ornata* in the presence and absence of trihalophenol and dichloroquinone (Scheme 1): In the presence of a monohalophenol, ferric DHP forms a 5cHS inhibited complex with the distal histidine (His^{55}) in the open conformation (step i-a). This inhibited form of the enzyme is unreactive toward H_2O_2 alone (i-b) or in the presence of TXP (i-c). When trihalophenol is present, ferric DHP forms a 6cHS active species with the distal histidine in the closed conformation (ii-a). If H_2O_2 is added to this active complex, catalytic turnover results (ii-b). However, if a monohalophenol is added prior to the addition of H_2O_2, then the complex is again inhibited (ii-c).

In the absence of (tri)halophenol, ferric DHP B reacts with 1 equiv of H_2O_2, yielding a putative compound I intermediate (step iii), which then undergoes rapid endogenous electron transfer from an amino acid side chain to generate the observed compound ES and a protein radical (iv). From this intermediate, we suggest three possible pathways that are cosubstrate and/or product dependent. In the presence of trichlorophenol, compound ES is reduced by two electrons [likely in two separate one-electron reduction steps as described by Dawson and coworkers (*31*)], regenerating the ferric state and forming dichloroquinone, chloride, and water as products (v). The DCQ product thus formed, either due to its inherent instability or as an alternative cosubstrate for the enzyme, leads to the reduction of the ferric state to the ferrous, generating oxyferrous DHP B in the presence of dioxygen (ix). Alternatively, compound ES may directly react with DCQ as a cosubstrate, leading to the generation of the oxyferrous complex (vii). In the absence of cosubstrate, DHP B compound ES was found to form compound RH (vi-a), which upon reduction yields either oxyferrous DHP B (vi-c) or the novel compound P_{426} state (vi-b), depending on the number of oxidizing equivalents that went into first forming compound RH. Critically, oxyferrous DHP B is a catalytically competent starting state for the oxidative dehalogenation of TCP in the presence of H_2O_2 (viii).

CONCLUSION

The chemistry reported herein furthers our understanding of the mechanism of dehaloperoxidase. That oxyferrous DHP is a competent starting oxidation state for enzymatic turnover and that the presumed products of trihalophenol oxidation, namely, dihaloquinones, are themselves cosubstrates for the ferric enzyme that lead to oxyferrous DHP are two notable observations which suggest how this globin peroxidase is able to reconcile its two activities, each with a distinctive oxidation state, in one system. An intriguing interpretation of the results is that the ferric state may not be the only functionally relevant starting oxidation state for the peroxidase activity of DHP in vivo. Additionally, the conformation flexibility of the distal histidine appears to serve as a functional trigger between active and inhibited states of the enzyme, dependent upon the type of halophenol, mono vs tri, present. While DHP B does exhibit some differences between its reactivity and that observed for DHP A, the most significant findings provide the necessary link between the peroxidase and O_2-transport activities present in this bifunctional hemoprotein. The new insights provided by our findings *in vitro* help to rationalize how dehaloperoxidase may maintain both of these roles *in vivo*, although additional questions still need to be addressed. For example, it is still not known why *A. ornata* possesses two dehaloperoxidase isoenzymes. Given the parallels between hemoglobin and DHP, one intriguing possibility is that DHP A and B form a cooperative dimer or tetramer, similar to the $\alpha_2\beta_2$ structure of Hb, and future studies employing mixtures of DHP A/B are planned. Additionally, the spectroscopic findings

presented here, when viewed in the context of our recent structural investigations of DHP, provide a clearer picture of the structure−function relationship in dehaloperoxidase and may have potential implications for globin protein engineering or directed evolution of DHP for bioremediation.

SUPPORTING INFORMATION AVAILABLE

UV−visible spectra of different heme states of DHP B (10 μM) at pH 7.0 (Figure SD1); UV−visible spectra of the (tri)halophenol complexes of DHP B (Figure SD2); UV−visible spectroscopic monitoring of the oxidative dehalogenation of trihalophenols as catalyzed by DHP B in the presence of hydrogen peroxide (Figure SD3); dependence of k_{obs} for the reaction between ferric DHP B with hydrogen peroxide (2.5−25 equivalents) at pH 7 yielding compound ES (Figure SD4); stopped-flow UV−visible spectroscopic monitoring of (Figure SD5) and DCQ product formation and TCP cosubstrate loss for (Figure SD6) the double-mixing reaction between preformed DHP B compound ES and TCP at pH 7; stopped-flow UV−visible spectroscopic monitoring of (Figure SD7) and DCQ product formation and TCP cosubstrate loss for (Figure SD8) the double-mixing reaction between ferric DHP B preincubated with TCP for 500 ms prior to its reaction with a 10-fold excess of H_2O_2 (*in situ* generated compound ES) at pH 7; stopped-flow UV−visible spectroscopic monitoring of the double-mixing reaction between ferric DHP B preincubated with a 7-fold molar excess of DCQ for 500 ms prior to its reaction with a 2.5-fold excess of H_2O_2 (*in situ* generated compound ES) (Figure SD9); stopped-flow UV−visible spectroscopic monitoring of the reaction between ferric DHP B and a 7-fold excess of DCQ at pH 7 (Figure SD10); reduction of compound RH yielding compound P_{426} (Figure SD11); reduction of compound RH yielding oxyferrous DHP B (Figure SD12). This material is available free of charge via the Internet at http://pubs.acs.org.

REFERENCES

1. Weber, R. E., Mangum, C., Steinman, H., Bonaventura, C., Sullivan, B., and Bonaventura, J. (1977) Hemoglobins of two terebellid polychaetes: *Enoplobranchus sanguineus* and *Amphitrite ornata*. *Comp. Biochem. Physiol., Part A: Comp. Physiol. 56*, 179–187.
2. Chen, Y. P., Woodin, S. A., Lincoln, D. E., and Lovell, C. R. (1996) An unusual dehalogenating peroxidase from the marine terebellid polychaete *Amphitrite ornata*. *J. Biol. Chem. 271*, 4609–4612.
3. Weber, R. E., and Vinogradov, S. N. (2001) Nonvertebrate hemoglobins: functions and molecular adaptations. *Physiol. Rev. 81*, 569–628.
4. Hardison, R. (1998) Hemoglobins from bacteria to man: evolution of different patterns of gene expression. *J. Exp. Biol. 201*, 1099–1117.
5. Bailly, X., Chabasse, C., Hourdez, S., Dewilde, S., Martial, S., Moens, L., and Zal, F. (2007) Globin gene family evolution and functional diversification in annelids. *FEBS J. 274*, 2641–2652.
6. Chabasse, C., Bailly, X., Sanchez, S., Rousselot, M., and Zal, F. (2006) Gene structure and molecular phylogeny of the linker chains from the giant annelid hexagonal bilayer hemoglobins. *J. Mol. Evol. 63*, 365–374.
7. Murzin, A. G., Brenner, S. E., Hubbard, T., and Chothia, C. (1995) SCOP: a structural classification of proteins database for the investigation of sequences and structures. *J. Mol. Biol. 247*, 536–540.
8. Poulos, T. L., and Kraut, J. (1980) A hypothetical model of the cytochrome *c* peroxidase·cytochrome *c* electron transfer complex. *J. Biol. Chem. 255*, 10322–10330.
9. Woodin, S. A. (1991) Recruitment of infauna—positive or negative cues. *Am. Zool. 31*, 797–807.
10. Woodin, S. A., Walla, M. D., and Lincoln, D. E. (1987) Occurrence of brominated compounds in soft-bottom benthic organisms. *J. Exp. Mar. Biol. Ecol. 107*, 209–217.
11. Chen, Y. P., Lincoln, D. E., Woodin, S. A., and Lovell, C. R. (1991) Purification and properties of a unique flavin-containing chloroperoxidase from the capitellid polychaete *Notomastus lobatus*. *J. Biol. Chem. 266*, 23909–23915.
12. Roach, M. P., Chen, Y. P., Woodin, S. A., Lincoln, D. E., Lovell, C. R., and Dawson, J. H. (1997) *Notomastus lobatus* chloroperoxidase and *Amphitrite ornata* dehaloperoxidase both contain histidine as their proximal heme iron ligand. *Biochemistry 36*, 2197–2202.
13. Lincoln, D. E., Fielman, K. T., Marinelli, R. L., and Woodin, S. A. (2005) Bromophenol accumulation and sediment contamination by the marine annelids *Notomastus lobatus* and *Thelepus crispus*. *Biochem. Syst. Ecol. 33*, 559–570.
14. King, G. M. (1986) Inhibition of microbial activity in marine sediments by a bromophenol from a hemichordate. *Nature 323*, 257–259.
15. Fielman, K. T., and Targett, N. M. (1995) Variation of 2,3,4-tribromopyrrole and its sodium sulfamate salt in the hemichordate *Saccoglossus kowalevskii*. *Mar. Ecol.: Prog. Ser. 116*, 125–136.
16. Chiancone, E., Ferruzzi, G., Bonaventura, C., and Bonaventura, J. (1981) *Amphitrite ornata* erythrocruorin. 2. Molecular controls of function. *Biochim. Biophys. Acta 670*, 84–92.
17. Chiancone, E., Brenowitz, M., Ascoli, F., Bonaventura, C., and Bonaventura, J. (1980) *Amphitrite ornata* erythrocruorin. 1. Structural properties and characterization of subunit interactions. *Biochim. Biophys. Acta 623*, 146–162.
18. Osborne, R. L., Taylor, L. O., Han, K. P., Ely, B., and Dawson, J. H. (2004) *Amphitrite ornata* dehaloperoxidase: enhanced activity for the catalytically active globin using MCPBA. *Biochem. Biophys. Res. Commun. 324*, 1194–1198.
19. Han, K., Woodin, S. A., Lincoln, D. E., Fielman, K. T., and Ely, B. (2001) *Amphitrite ornata*, a marine worm, contains two dehaloperoxidase genes. *Mar. Biotechnol. (New York) 3*, 287–292.
20. Feducia, J., Dumarieh, R., Gilvey, L. B., Smirnova, T., Franzen, S., and Ghiladi, R. A. (2009) Characterization of dehaloperoxidase compound ES and its reactivity with trihalophenols. *Biochemistry 48*, 995–1005.
21. Chen, Z., de Serrano, V., Betts, L., and Franzen, S. (2009) Distal histidine conformational flexibility in dehaloperoxidase from *Amphitrite ornata*. *Acta Crystallogr., Sect. D: Biol. Crystallogr. 65*, 34–40.
22. Davis, M. F., Gracz, H., Vendeix, F. A., de Serrano, V., Somasundaram, A., Decatur, S. M., and Franzen, S. (2009) Different modes of binding of mono-, di-, and trihalogenated phenols to the hemoglobin dehaloperoxidase from *Amphitrite ornata*. *Biochemistry 48*, 2164–2172.
23. Smirnova, T. I., Weber, R. T., Davis, M. F., and Franzen, S. (2008) Substrate binding triggers a switch in the iron coordination in dehaloperoxidase from *Amphitrite ornata*: HYSCORE experiments. *J. Am. Chem. Soc. 130*, 2128–2129.
24. Miksovska, J., Horsa, S., Davis, M. F., and Franzen, S. (2008) Conformational dynamics associated with photodissociation of CO from dehaloperoxidase studied using photoacoustic calorimetry. *Biochemistry 47*, 11510–11517.
25. Nienhaus, K., Nickel, E., Davis, M. F., Franzen, S., and Nienhaus, G. U. (2008) Determinants of substrate internalization in the distal pocket of dehaloperoxidase hemoglobin of *Amphitrite ornata*. *Biochemistry 47*, 12985–12994.
26. Franzen, S., Gilvey, L. B., and Belyea, J. L. (2007) The pH dependence of the activity of dehaloperoxidase from *Amphitrite ornata*. *Biochim. Biophys. Acta 1774*, 121–130.
27. de Serrano, V., Chen, Z., Davis, M. F., and Franzen, S. (2007) X-ray crystal structural analysis of the binding site in the ferric and oxyferrous forms of the recombinant heme dehaloperoxidase cloned from *Amphitrite ornata*. *Acta Crystallogr., Sect. D: Biol. Crystallogr. 63*, 1094–1101.
28. Franzen, S., Jasaitis, A., Belyea, J., Brewer, S. H., Casey, R., MacFarlane, A. W. t., Stanley, R. J., Vos, M. H., and Martin, J. L. (2006) Hydrophobic distal pocket affects NO-heme geminate recombination dynamics in dehaloperoxidase and H64V myoglobin. *J. Phys. Chem. B 110*, 14483–14493.
29. Franzen, S., Belyea, J., Gilvey, L. B., Davis, M. F., Chaudhary, C. E., Sit, T. L., and Lommel, S. A. (2006) Proximal cavity, distal histidine, and substrate hydrogen-bonding mutations modulate the activity of *Amphitrite ornata* dehaloperoxidase. *Biochemistry 45*, 9085–9094.
30. Belyea, J., Belyea, C. M., Lappi, S., and Franzen, S. (2006) Resonance Raman study of ferric heme adducts of dehaloperoxidase from *Amphitrite ornata*. *Biochemistry 45*, 14275–14284.
31. Osborne, R. L., Coggins, M. K., Raner, G. M., Walla, M., and Dawson, J. H. (2009) The mechanism of oxidative halophenol dehalogenation by *Amphitrite ornata* dehaloperoxidase is initiated by H_2O_2 binding and involves two consecutive one-electron steps: role of ferryl intermediates. *Biochemistry 48*, 4231–4238.
32. Osborne, R. L., Coggins, M. K., Walla, M., and Dawson, J. H. (2007) Horse heart myoglobin catalyzes the H_2O_2-dependent oxidative dehalogenation of chlorophenols to DNA-binding radicals and quinones. *Biochemistry 46*, 9823–9829.

33. Osborne, R. L., Raner, G. M., Hager, L. P., and Dawson, J. H. (2006) *C. fumago* chloroperoxidase is also a dehaloperoxidase: oxidative dehalogenation of halophenols. *J. Am. Chem. Soc. 128*, 1036–1037.
34. Osborne, R. L., Sumithran, S., Coggins, M. K., Chen, Y. P., Lincoln, D. E., and Dawson, J. H. (2006) Spectroscopic characterization of the ferric states of *Amphitrite ornata* dehaloperoxidase and *Notomastus lobatus* chloroperoxidase: His-ligated peroxidases with globin-like proximal and distal properties. *J. Inorg. Biochem. 100*, 1100–1108.
35. Belyea, J., Gilvey, L. B., Davis, M. F., Godek, M., Sit, T. L., Lommel, S. A., and Franzen, S. (2005) Enzyme function of the globin dehaloperoxidase from *Amphitrite ornata* is activated by substrate binding. *Biochemistry 44*, 15637–15644.
36. Lebioda, L., LaCount, M. W., Zhang, E., Chen, Y. P., Han, K., Whitton, M. M., Lincoln, D. E., and Woodin, S. A. (1999) An enzymatic globin from a marine worm. *Nature 401*, 445.
37. de Serrano, V., D'Antonio, J., Franzen, S., and Ghiladi, R. A. (2010) Structure of dehaloperoxidase B at 1.58 Å resolution and structural characterization of the AB dimer from *Amphitrite ornata*. *Acta Crystallogr., Sect. D: Biol. Crystallogr. 66*, 529–538.
38. Meyer, T. J. (1967) Stanford University.
39. Smolenaers, P. J., and Beattie, J. K. (1979) *Inorg. Synth. 19*, 117–121.
40. Smolenaers, P. J., Beattie, J. K., and Hutchinson, N. D. (1981) Crystal and molecular structure of racemic tris(ethylenediamine)ruthenium-(II) tetrachlorozincate(II). *Inorg. Chem. 20*, 2202–2206.
41. Beers, R. F., Jr., and Sizer, I. W. (1952) A spectrophotometric method for measuring the breakdown of hydrogen peroxide by catalase. *J. Biol. Chem. 195*, 133–140.
42. Falk, J. E. (1964) Haems. I. Determination as pyridine hemochromes, in Porphyrins and Metalloporphyrins: Their General, Physical, and Coordination Chemistry and Laboratory Methods, pp 181−188, Elsevier Publishing, New York.
43. Fuhrhop, J. H., and Smith, K. M. (1975) Laboratory Methods, in Porphyrins and Metalloporphyrins (Smith, K. M., Ed.) pp 804−807, Elsevier Publishing, New York.
44. Bowden, E. F., Cohen, D. J., and Hawkridge, F. M. (1982) Anaerobic thin-layer electrochemical cell for planar optically transparent electrodes. *Anal. Chem. 54*, 1005–1008.
45. LaCount, M. W., Zhang, E., Chen, Y. P., Han, K., Whitton, M. M., Lincoln, D. E., Woodin, S. A., and Lebioda, L. (2000) The crystal structure and amino acid sequence of dehaloperoxidase from *Amphitrite ornata* indicate common ancestry with globins. *J. Biol. Chem. 275*, 18712–18716.
46. Gouterman, M. (1978) Optical spectra and electronic structure of porphyrins and related rings, in The Porphyrins (Dolphin, D., Ed.) pp 1−165, Academic Press, New York.
47. Chouchane, S., Girotto, S., Kapetanaki, S., Schelvis, J. P., Yu, S., and Magliozzo, R. S. (2003) Analysis of heme structural heterogeneity in *Mycobacterium tuberculosis* catalase-peroxidase (KatG). *J. Biol. Chem. 278*, 8154–8162.
48. Ghiladi, R. A., Knudsen, G. M., Medzihradszky, K. F., and Ortiz de Montellano, P. R. (2005) The Met-Tyr-Trp cross-link in *Mycobacterium tuberculosis* catalase-peroxidase (KatG): autocatalytic formation and effect on enzyme catalysis and spectroscopic properties. *J. Biol. Chem. 280*, 22651–22663.
49. Nienhaus, K., Deng, P., Belyea, J., Franzen, S., and Nienhaus, G. U. (2006) Spectroscopic study of substrate binding to the carbonmonoxy form of dehaloperoxidase from *Amphitrite ornata*. *J. Phys. Chem. B 110*, 13264–13276.
50. Nicoletti, F. P., Thompson, M. K., Howes, B. D., Franzen, S., and Smulevich, G. (2010) New insights into the role of distal histidine flexibility in ligand stabilization of dehaloperoxidase-hemoglobin from *Amphitrite ornata*. *Biochemistry 49*, 1903–1912.
51. Thompson, M. K., Davis, M. F., De Serrano, V., Nicoletti, F. P., Howes, B. D., Smulevich, G., and Franzen, S. (2010) Internal binding of halogenated phenols in dehaloperoxidase-hemoglobin inhibits peroxidase function. Biophys. J. (in press).
52. Hewson, W. D., and Hager, L. P. (1979) Oxidation of horseradish peroxidase compound II to compound I. *J. Biol. Chem. 254*, 3182–3186.
53. Blumberg, W. E., Peisach, J., Wittenberg, B. A., and Wittenberg, J. B. (1968) The electronic structure of protoheme proteins. I. An electron paramagnetic resonance and optical study of horseradish peroxidase and its derivatives. *J. Biol. Chem. 243*, 1854–1862.
54. Wittenberg, B. A., Kampa, L., Wittenberg, J. B., Blumberg, W. E., and Peisach, J. (1968) The electronic structure of protoheme proteins. II. An electron paramagnetic resonance and optical study of cytochrome *c* peroxidase and its derivatives. *J. Biol. Chem. 243*, 1863–1870.
55. Balny, C., Anni, H., and Yonetani, T. (1987) A stopped-flow study of the reaction of cytochrome *c* peroxidase with hydroperoxides. *FEBS Lett. 221*, 349–354.
56. Coulson, A. F., Erman, J. E., and Yonetani, T. (1971) Studies on cytochrome *c* peroxidase. XVII. Stoichiometry and mechanism of the reaction of compound ES with donors. *J. Biol. Chem. 246*, 917–924.
57. Marquez, L. A., Quitoriano, M., Zilinskas, B. A., and Dunford, H. B. (1996) Kinetic and spectral properties of pea cytosolic ascorbate peroxidase. *FEBS Lett. 389*, 153–156.
58. Yadav, R. K., Dolai, S., Pal, S., and Adak, S. (2008) Role of tryptophan-208 residue in cytochrome *c* oxidation by ascorbate peroxidase from *Leishmania major*—kinetic studies on Trp208Phe mutant and wild type enzyme. *Biochim. Biophys. Acta 1784*, 863–871.
59. Lardinois, O. M., and Ortiz de Montellano, P. R. (2004) Autoreduction of ferryl myoglobin: discrimination among the three tyrosine and two tryptophan residues as electron donors. *Biochemistry 43*, 4601–4610.
60. Giulivi, C., and Cadenas, E. (1994) Ferrylmyoglobin: formation and chemical reactivity toward electron-donating compounds. *Methods Enzymol. 233*, 189–202.
61. Herold, S., and Rehmann, F. J. (2003) Kinetics of the reactions of nitrogen monoxide and nitrite with ferryl hemoglobin. *Free Radical Biol. Med. 34*, 531–545.
62. Giulivi, C., and Davies, K. J. (1994) Hydrogen peroxide-mediated ferrylhemoglobin generation in vitro and in red blood cells. *Methods Enzymol. 231*, 490–496.
63. Belevich, I., Borisov, V. B., and Verkhovsky, M. I. (2007) Discovery of the true peroxy intermediate in the catalytic cycle of terminal oxidases by real-time measurement. *J. Biol. Chem. 282*, 28514–28519.
64. Shintaku, M., Matsuura, K., Yoshioka, S., Takahashi, S., Ishimori, K., and Morishima, I. (2005) Absence of a detectable intermediate in the compound I formation of horseradish peroxidase at ambient temperature. *J. Biol. Chem. 280*, 40934–40938.
65. Baek, H. K., and Van Wart, H. E. (1989) Elementary steps in the formation of horseradish peroxidase compound I: direct observation of compound 0, a new intermediate with a hyperporphyrin spectrum. *Biochemistry 28*, 5714–5719.
66. Egawa, T., Yoshioka, S., Takahashi, S., Hori, H., Nagano, S., Shimada, H., Ishimori, K., Morishima, I., Suematsu, M., and Ishimura, Y. (2003) Kinetic and spectroscopic characterization of a hydroperoxy compound in the reaction of native myoglobin with hydrogen peroxide. *J. Biol. Chem. 278*, 41597–41606.
67. Svistunenko, D. A. (2005) Reaction of haem containing proteins and enzymes with hydroperoxides: the radical view. *Biochim. Biophys. Acta 1707*, 127–155.
68. Svistunenko, D. A., and Cooper, C. E. (2004) A new method of identifying the site of tyrosyl radicals in proteins. *Biophys. J. 87*, 582–595.
69. Thompson, M. K., Franzen, S., Ghiladi, R. A., Reeder, B. J., and Svistunenko, D. A. (2010) Free radical mechanism of hydrogen peroxide induced activation of dehaloperoxidase-hemoglobin from *Amphitrite ornata* (submitted for publication).
70. Nilges, M. SimPow6. Illinois EPR Research Center (http://ierc.scs.uiuc.edu/~nilges/software.html).
71. Svistunenko, D. A. (2004) Tyrosine residues in different proteins: phenol ring rotation angle database (http://privatewww.essex.ac.uk/~svist/lev1/tyrdb/home.shtml).
72. D'Antonio, E. L., Franzen, S., and Bowden, E. F. (2010) The Fe(III)/Fe(II) reduction potential of dehaloperoxidase-hemoglobin (submitted for publication).
73. Dunford, H. B. (1999) Heme Peroxidases, Wiley-VCH, New York.
74. Matsui, T., Ozaki, S., Liong, E., Phillips, G. N., Jr., and Watanabe, Y. (1999) Effects of the location of distal histidine in the reaction of myoglobin with hydrogen peroxide. *J. Biol. Chem. 274*, 2838–2844.
75. Finzel, B. C., Poulos, T. L., and Kraut, J. (1984) Crystal structure of yeast cytochrome *c* peroxidase refined at 1.7-Å resolution. *J. Biol. Chem. 259*, 13027–13036.
76. Phillips, G. N., Jr., Arduini, R. M., Springer, B. A., and Sligar, S. G. (1990) Crystal structure of myoglobin from a synthetic gene. *Proteins 7*, 358–365.
77. Gajhede, M., Schuller, D. J., Henriksen, A., Smith, A. T., and Poulos, T. L. (1997) Crystal structure of horseradish peroxidase C at 2.15 Å resolution. *Nat. Struct. Biol. 4*, 1032–1038.
78. Egawa, T., Shimada, H., and Ishimura, Y. (2000) Formation of compound I in the reaction of native myoglobins with hydrogen peroxide. *J. Biol. Chem. 275*, 34858–34866.
79. Olson, J. S., and Phillips, G. N., Jr. (1996) Kinetic pathways and barriers for ligand binding to myoglobin. *J. Biol. Chem. 271*, 17593–17596.
80. Jewsbury, P., and Kitagawa, T. (1994) The distal residue-CO interaction in carbonmonoxy myoglobins: a molecular dynamics study of two distal histidine tautomers. *Biophys. J. 67*, 2236–2250.
81. Perutz, M. F. (1989) Myoglobin and haemoglobin: role of distal residues in reactions with haem ligands. *Trends Biochem. Sci. 14*, 42–44.

Internal Binding of Halogenated Phenols in Dehaloperoxidase-Hemoglobin Inhibits Peroxidase Function

Matthew K. Thompson,[†] Michael F. Davis,[†‡§] Vesna de Serrano,[†] Francesco P. Nicoletti,[¶] Barry D. Howes,[¶] Giulietta Smulevich,[¶] and Stefan Franzen[†*]

[†]Department of Chemistry, North Carolina State University, Raleigh, North Carolina; [‡]Lineberger Comprehensive Cancer Center, [§]Department of Biochemistry and Biophysics, University of North Carolina, Chapel Hill, North Carolina; and [¶]Dipartimento di Chimica, Università di Firenze, Sesto Fiorentino, Italy

ABSTRACT Dehaloperoxidase (DHP) from the annelid *Amphitrite ornata* is a catalytically active hemoglobin-peroxidase that possesses a unique internal binding cavity in the distal pocket above the heme. The previously published crystal structure of DHP shows 4-iodophenol bound internally. This led to the proposal that the internal binding site is the active site for phenol oxidation. However, the native substrate for DHP is 2,4,6-tribromophenol, and all attempts to bind 2,4,6-tribromophenol in the internal site under physiological conditions have failed. Herein, we show that the binding of 4-halophenols in the internal pocket inhibits enzymatic function. Furthermore, we demonstrate that DHP has a unique two-site competitive binding mechanism in which the internal and external binding sites communicate through two conformations of the distal histidine of the enzyme, resulting in nonclassical competitive inhibition. The same distal histidine conformations involved in DHP function regulate oxygen binding and release during transport and storage by hemoglobins and myoglobins. This work provides further support for the hypothesis that DHP possesses an external binding site for substrate oxidation, as is typical for the peroxidase family of enzymes.

INTRODUCTION

The two dehaloperoxidase (DHP) hemoglobins (Hbs) from *Amphitrite ornate*, DHP A and DHP B, are the first characterized Hbs that have natural peroxidase function (1–6). Hbs, including DHP, are readily identified by their characteristic 3/3 α-helical protein structure. Although Hbs are primarily associated with O_2 storage and transport, the characteristic globin fold actually encodes a diversity of protein functions. In addition to allosteric regulation of oxygen uptake, globins minimize the autooxidation rate of the heme iron, discriminate against CO binding, and carry out other natural functions such as NO binding and oxidation to nitrate. DHP brings this functional diversity to a new level by combining the seemingly contradictory functions of reversible oxygen binding (globin) and hydrogen peroxide activation (peroxidase).

Although Hbs and heme peroxidases are structurally distinct and perform different functions, they have a common heme cofactor and iron-binding site, with a histidine residue positioned on each side (Fig. 1). The proximal histidine is coordinated to the heme iron and provides a charge relay that supports either the ferrous (Fe^{2+}) or ferric (Fe^{3+}) iron oxidation state (7,8) depending on the local environment of globins or peroxidases, respectively. In myoglobins (Mbs) and Hbs, the distal histidine stabilizes diatomic oxygen during uptake and transport, whereas in peroxidases, the distal histidine serves as the acid-base catalyst necessary for heterolytic O-O bond cleavage, which constitutes the activation of bound hydrogen peroxide. Allostery in Hb is vital for the proper uptake of oxygen in the lungs and release of oxygen to respiring tissues (9). Whereas allostery may modify a binding constant or facilitate communication between multimers in cooperative proteins such as Hb, allosteric inhibition in heme peroxidases is an off-switch that can cause the enzyme to become completely inactive (10–12). The significance of both allostery and inhibition is more complex in a dual-function protein like DHP because the regulation involves not only each individual function, but also the switch between functions.

The first x-ray crystal structures of DHP A (Protein Data Bank (PDB) 1EW6 and 1EWA), obtained at room temperature, showed two features that are unique in the Hb superfamily (1). First, the distal histidine was observed in two conformations at pH 6, identified as open or closed. The closed conformation is the commonly observed conformation shown in Fig. 2 *a*, in which the histidine is in the distal pocket and interacts with a ligand coordinated to the heme iron (13). In the open conformation (Fig. 2 *b*), the distal histidine (H55) has swung out to a solvent-exposed position (14). Although the open conformation is known in sperm whale Mb, it is only observed below pH 4.5 when the distal histidine is protonated (15). We previously showed by a comparison of x-ray crystal structures (3DR9 and 2QFK) at 100 K that the open and closed conformations in DHP A are correlated with the 5-coordinate (5c) and 6-coordinate (6c) forms of the heme iron, respectively (13,14). Furthermore, the unique flexibility of the distal histidine has been shown to play an important role in heme-coordinated ligand stabilization (16). The second unprecedented observation in the initial x-ray crystal structure of DHP A was the presence of a substrate analog,

Submitted March 4, 2010, and accepted for publication May 17, 2010.

*Correspondence: Stefan_Franzen@ncsu.edu

Editor: Patrick Loria.

0006-3495/10/09/1586/10 $2.00

doi: 10.1016/j.bpj.2010.05.041

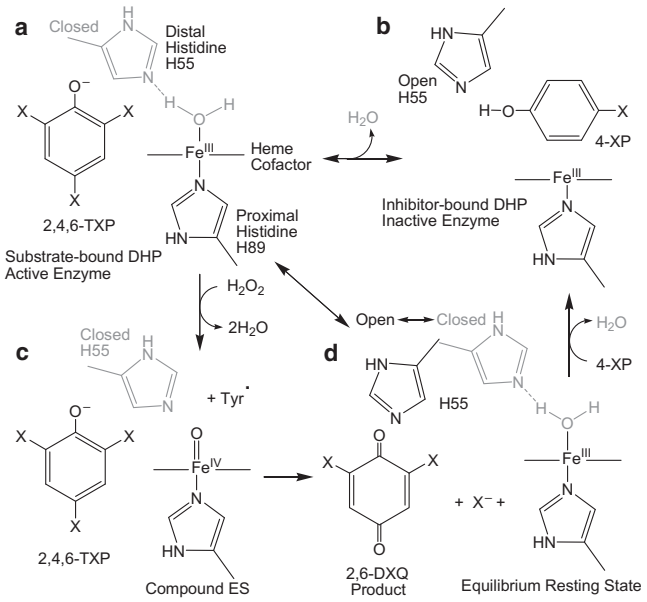

FIGURE 1 Reaction scheme emphasizing the conformation of the distal histidine, H55, in response to binding of the substrate, 2,4,6-TXP, and inhibitor, 4-XP. (*a*) Active enzyme: DHP with TXP substrate bound external to the heme pocket. The protein is 6cHS (aquo) with the distal H55 in a closed position. (*b*) When an inhibitor (4-XP) binds in the internal pocket of DHP, H_2O is displaced (5cHS) and the distal H55 is pushed to the open position. The resulting conformation leads to inactivation of the enzyme. (*c*) Addition of H_2O_2 leads to the formation of compound ES (39), the high-valent iron-oxo protein (Tyr) radical intermediate, which can lead to formation of the product 2,6-DXQ by two-electron oxidation. Compound ES cannot be formed in the inhibitor-bound state because the Fe^{III} site is blocked by 4-XP binding in the distal cavity. (*d*) In the resting state of DHP the distal histidine exists in two conformations, known as open (*black*) and closed (*gray*). H_2O is bound to the heme iron only in the closed conformation.

4-iodophenol, in a well-defined position in the distal pocket of the globin but not coordinated to the heme iron (1). This unusual mode of binding in an Hb led to the suggestion that the internal binding site is the substrate-binding site (1). We have systematically investigated this hypothesis and found that the 4-halogenated phenols (4-XP) that bind internally are inhibitors rather than substrates. The active site for oxidation of substrates such as 2,4,6-tribromophenol (2,4,6-TBP), 2,4,6,-trichlorophenol (2,4,6-TCP), and 2,4,6,-trifluorophenol (2,4,6-TFP) is external (17). The possibility that an external substrate-binding site is located on DHP A was recently established via backbone NMR experiments (18). Given the extensive data available on DHP A relative to the more recently characterized DHP B, the remainder of this study will focus on DHP A, which will be referred to as DHP for brevity.

In this work, we provide detailed evidence that internal binding of 4-XPs inhibits the peroxidase function of DHP. This result is contradictory to the previous hypothesis that the distal pocket binding site for 4-XP is the substrate-binding site for phenol oxidation. This work builds on a number of observations that support the existence of distinct binding sites for 4-BP and 2,4,6-TBP, and demonstrates that these distinct sites are involved in inhibition of a competitive nature. Normally, competitive inhibition implies that the substrate and inhibitor compete for the same binding site. However, the structural and kinetic evidence presented below suggests that DHP exhibits a form of competitive inhibition (formally known as allosteric or nonclassical competitive inhibition (19–22)) in which the inhibitor binds remote to the active site and creates a conformational change in the enzyme that prevents the substrate from binding. The x-ray crystallographic, resonance Raman (RR), and kinetic data presented here are consistent with competitive inhibition between the internal and external sites mediated by the distal histidine (H55). The proposed functional role for the distal histidine, as the switch that leads to peroxidase inhibition (open) and activation (closed), underlies the regulation of oxygen-binding affinity by the same histidine in the open (low affinity) and closed (high affinity) conformations traditionally observed in globins (15,23,24).

MATERIALS AND METHODS

Materials

Buffer salts were purchased from Fisher Scientific (Waltham, MA). All other reagents were purchased from Sigma-Aldrich (St. Louis, MO) and used without further purification.

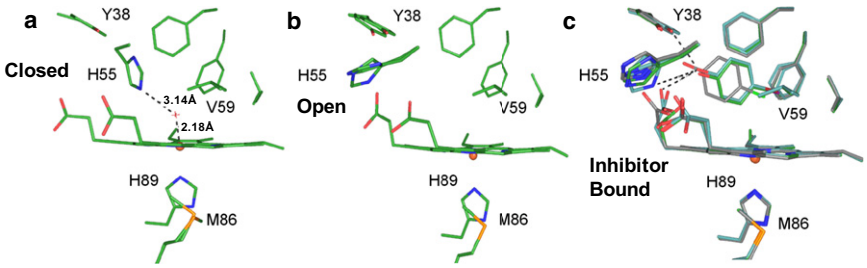

FIGURE 2 X-ray crystal structures of DHP at 100 K. (*a*) The metaquo form shows a hydrogen-bond interaction between the distal histidine (H55) and the water molecule coordinated to the ferric heme iron (PDB 2QFK; closed conformation). (*b*) The deoxy form has a pentacoordinate heme iron. Two rotamers of H55 are observed in which H55 appears exclusively in a solvent-exposed conformation (PDB 3DR9). This His conformer corresponds to the open form observed in Mb at pH 4.5 (15). (*c*) The three structures of 4-IP (3LB1, *green*), 4-BP (3LB2, *light blue*), and 4-CP (3LB3, *gray*) bound in the distal pocket of DHP are superimposed. 4-FP (3LB4) is not shown in the figure (see text).

TABLE 1 Data collection and refinement statistics

	I*	Br*	Cl*	F*
PDB code	3LB1	3LB2	3LB3	3LB4
Space group	$P2_12_12_1$	$P2_12_12_1$	$P2_12_12_1$	$P2_12_12_1$
Unit-cell parameters				
a (Å)	57.84	58.01	58.20	59.78
b (Å)	67.25	67.36	67.21	67.49
c (Å)	69.13	69.42	68.72	67.84
Data collection				
Temperature (K)	100	100	100	100
Wavelength (Å)	1.5000	0.91942	1.0000	1.0000
Resolution (Å)	35.0–1.76 (1.81–1.76)†	35.0–1.06 (1.09–1.06)†	35.0–1.85 (1.90–1.85)†	35.0–1.56 (1.60–1.56)†
Unique reflections	25737(1737)†	121970(8490)†	22277(15730)†	33583(2740)†
Completeness (%)	94.24(87.82)†	98.67(93.80)†	94.25(92.91)†	94.03(95.34)†
R_{merge}‡ (%)	4.1(9.8)	5.2(31.8)	10.1(32.2)	6.1(38.3)
I/σI	37.9(13.2)†	22.5(3.8)†	7.9(3.4)†	10.9(3.9)†
Redundancy	3.5(3.4)†	4.0(3.3)†	3.4(3.4)†	3.1(3.3)†
Refinement				
R_{work}/R_{free} (%)§	18.6/22.7	16.8/18.3	18.7/24.3	19.5/23.5
Average B factor (Å^2)				
All atoms	12.73	10.16	19.13	17.19
Protein	11.81	8.98	18.55	15.19
Water	21.59	20.21	30.35	28.75
No. of atoms				
Protein	2658	3122	2192	2849
Water	268	356	213	299
RMSD from ideal				
Bond length (Å)	0.008	0.006	0.008	0.011
Bond angle (deg)	1.124	1.170	1.157	1.377
Ramachandran plot¶ (%)				
Most favored	94.4	94.4	94.4	94.8
Allowed	5.6	5.6	5.6	5.2

*Crystal containing 4-halophenol in complex with WT DHP; the letter specifies the halogen substituent.
†Values in parentheses are the highest-resolution shell.
‡$R_{merge} = (\Sigma_h\Sigma_i\{\} \times 100\%$, where I_i is the ith measurement and <I(h)> is the weighted mean of all measurements of I(h).
§$R_{work} = \Sigma|F_o - F_c|/\Sigma F_o \times 100\%$, where F_o and F_c are observed and calculated structure factors, respectively; R_{free} is R factor for the subset (5%) of reflections selected before, and not included in the refinement.
¶Calculated using PROCHECK.

Crystallization, data collection, and processing

Recombinant wild-type (WT) protein was expressed in *E. coli*, purified, and characterized as previously described (13). To obtain crystals of DHP complexed with substrate analogs, the protein, at a concentration of 8 mg/mL dissolved in 10 mM Na cacodylate pH 6.5, was incubated on ice for 30 min with the parahalogenated phenols (1.5 mM 4-IP, 10 mM 4-BP, or 10 mM 4-CP, respectively) and crystallized using the hanging drop vapor diffusion method, with the reservoir solution containing unbuffered 0.2 M ammonium sulfate and 32% PEG 4000 (w/v) as described previously (13,14). The crystals were cryoprotected in a solution containing 0.2 M ammonium sulfate, 35% PEG 4000 (w/v), and 15% PEG 400 as the cryoprotectant. Data were collected at 100 K on the SER-CAT 22-ID beamline at the APS synchrotron facility using a wavelength of 1 Å for crystals derivatized with 4-chloro- and 4-fluorophenol, 0.91942 Å for crystals derivatized with 4-bromophenol, and 1.5 Å for crystals derivatized with 4-iodophenol. The latter two wavelengths were chosen so that two data sets could be collected in a single-wavelength anomalous dispersion mode to correctly orient the halogenated phenol in its electron density. The collected diffraction data sets were processed using the HKL2000 program suite (25). The new crystals belong to the same space group ($P2_12_12_1$) as the ferric water-ligated (metaquo) form (PDB entry 2QFK), and the structures were solved by molecular replacement using 2QFK coordinates as a starting model in the Phaser molecular replacement program (26). Structure determination and refinement calculations were performed using the CCP4 suite of programs (27,28), and visualization and manual model building were conducted using *Coot* model building software (29). Waters were placed with the Coot routine Find Waters using $2F_o$-F_c contoured at the 1σ level, and F_o-F_c maps at the 3σ level. The occupancies were refined manually until no residual F_o-F_c density remained. Final models were obtained by iterative cycles of model building in *Coot* using $2F_o$-F_c (contoured at the 1σ level) and F_o-F_c electron density maps (contoured at the 3σ level), and positional and anisotropic B factor structure refinement using Refmac5 (30) in the CCP4 suite of programs (31) and CNS (32). Simulated annealing and composite omit maps were constructed with the CNS program. All of the figures were prepared using VMD (33). The refinement statistics of the four x-ray crystal structures (3LB1, 3LB2, 3LB3, and 3LB4) are given in Table 1.

Electronic absorption spectroscopy and kinetic assays

Recombinant his-tagged WT protein was expressed in *Escherichia coli* and purified as previously described (17,18). Initial inhibition experiments were conducted in 100 mM potassium phosphate buffer at pH 7 using an Agilent

8453 UV-vis spectrometer equipped with a temperature control and Hewlett Packard UV-Visible Chemstation software set to kinetics mode. The concentration of DHP in each sample was ~2.4 μM and the temperature was equilibrated to 20°C. A 100-fold excess of H_2O_2 (240 μM) was added to the cuvette to initiate the assay. Electronic absorption spectra were taken every 2 s for 2 min, monitoring the 273 nm peak of the 2,6-dichloro-1,4-dibenzoquinone (2,4-DCQ) product. The assays were repeated with the addition of 250 μM 4-bromophenol in each sample to demonstrate the inhibition effect.

Inhibition assays for Michaelis-Menten analysis were conducted on a Cary 100 UV-vis equipped with a Cary temperature control system and an Applied Photophysics RX2000 rapid kinetics spectrometer accessory. The Applied Photophysics premixing chambers were temperature-controlled with a Fisher Scientific Isotemp 3006S set to 25°C. Instruments were controlled by Cary WinUV software in kinetics mode set to monitor the 273 2,4-DCQ peak every 0.1 s for 60 s. Assay conditions were 2 μM DHP initiated with 2 mM H_2O_2 in 100 mM potassium phosphate buffer at pH 7. Eight assays were completed at each of the 2,4,6-TCP concentrations. The assays were then repeated at each of the 2,4,6-TCP concentrations with the presence of 125, 250, and 500 μM 4-BP. The initial velocity, V_o, of enzyme turnover was obtained for each concentration of the 2,4,6-TCP substrate and the 2,4,6-TCP substrate with inhibitor. The V_o versus 2,4,6-TCP concentration data were fit independently to the Michaelis-Menten equation using nonlinear least squares in Igor Pro 5.0.

RR spectroscopy

All protein samples used in the RR experiments were purified as above and maintained in 150 mM potassium phosphate buffer, pH 6. The final protein concentration for all RR samples was 100 μM. Parahalogenated substrate analogs were introduced to final concentrations of 8 mM for 4-BP, 4-CP, 4-FP, and phenol, and to 1 mM for 4-IP (the concentration of 4-IP is limited by its low solubility at 25°C). The samples were placed into 5-mm-diameter glass NMR tubes and stored on ice until used.

RR spectra were obtained by Soret band excitation using a Coherent Mira 900 titanium sapphire (Ti:sapphire) laser. The Ti:sapphire laser was pumped using a Coherent Verdi 10 frequency-doubled diode-pumped Nd:vanadate laser generating 10 W at 532 nm. The beam generated from the Ti:sapphire is tunable through ~700–1000 nm, and was sent through a Coherent 5-050 doubler to generate a normal working range of 400–430 nm for Soret band excitation. The beam was collimated and cylindrically focused to a vertical line of ~0.5 mm on the sample. Scattered light was collected with a Spex 1877 triple spectrometer (2400 grooves/mm final stage grating) equipped with an ISA SPEX liquid nitrogen-cooled CCD at ~1.7 cm^{-1} resolution. Computer acquisition of the data was accomplished with SpectraMax 2.0 software. The spectra were calibrated using known peaks from indene, toluene, and carbon tetrachloride standards.

Binding isotherm analysis

A titration data set for each inhibitor binding to DHP was collected via a series of RR spectra. Each sample contained 100 μM DHP in 150 mM potassium phosphate buffer at pH 6, with concentrations of the inhibitor from 0 to 8 mM (0–1 mM for 4-IP only). Singular value decomposition (SVD) was performed on the spectral data set with the use of Igor Pro 5.0. The SVD analysis yields one-dimensional column and row eigenvectors, with columns corresponding to changes with respect to wavenumber, and rows corresponding to changes with respect to concentration. The SVD row eigenvectors representing the intensity changes and the peak shifts of the Raman data set were fit using nonlinear least-squares to the single-site binding equation

$$\theta = \frac{[I]}{K_d + [I]}$$

to determine apparent substrate dissociation constants, K_d, where θ is the fraction 5c high spin (5cHS) protein and $[I]$ is the concentration of inhibitor.

RESULTS

Crystallography

Previously published x-ray crystal structures (13,14) and spectroscopic data (16) strongly suggest a role for distal histidine flexibility in DHP. Fig. 2, *a* (closed) and *b* (open), shows PDB structures 2QFK and 3DR9, respectively. As mentioned above, in the metaquo form, the distal His is stabilized in the closed conformation by hydrogen bonding to the heme-coordinated water molecule (Fig. 2 *a*), and the heme iron is 6c high spin (6cHS). However, unlike other Hb structures (34–36), in the 5c deoxy form, the His is observed in the open conformation (Fig. 2 *b*). Therefore, the open and closed conformations in DHP are correlated with the 5c and 6c forms of the heme iron. Fig. 2 *c* shows an overlay of the new heme pocket structures of DHP cocrystallized with 4-IP (3LB1), 4-BP (3LB2), and 4-CP (3LB3) following established protocols (13). The 4-XPs bind in a conformation close to that originally reported for 4-IP (1). The occupancy of the 4-IP, 4-BP, and 4-CP molecules is >90% in all three structures. The structure of DHP with 4-FP (3LB4) is not shown, due to its low occupancy (<50%) and for clarity of the figure. Upon binding of these molecules in the internal site, the heme-coordinated water molecule is displaced and the histidine is pushed into the open conformation; thus, the iron is 5cHS (see also Fig. 1 for a schematic). The secondary structure of DHP A exhibits remarkably little change when 4-XPs bind in the distal pocket. The backbone root mean-square deviations (RMSDs) from the metaquo structure are ~≤0.4 Å, and the pairwise main-chain differences between the complexed structures are on the order of 0.1–0.2 Å. On the other hand, superposition of the structures shows that as the size of the parahalogen atom increases, the position of the 4-XP molecules bound in the distal pocket shifts slightly toward the heme-7-propionate and the solvent-exposed distal histidine.

Binding of parahalogenated phenols

In this study, the x-ray crystal structures provided meaningful insight into DHP in the solid state, whereas RR spectroscopy revealed the solution-state properties of halophenol binding. Fig. 3 *a* compares the RR spectra of WT-DHP with those obtained upon addition of phenol, and the 4-XP molecules (X = F, Cl, Br, I). The 5cHS core size marker band frequencies (ν_3 at 1494 cm^{-1}, ν_2 at 1568 cm^{-1}, and ν_{10} at 1632 cm^{-1}) systematically become more intense at the expense of the aquo 6cHS heme state (ν_3 at 1481 cm^{-1}, ν_2 at 1562 cm^{-1}, and ν_{10} at 1611 cm^{-1}) for the series of 4-XP bound DHP relative to WT-DHP. Similar systematic changes are also observed in the corresponding electronic absorption spectra. The Soret maximum undergoes

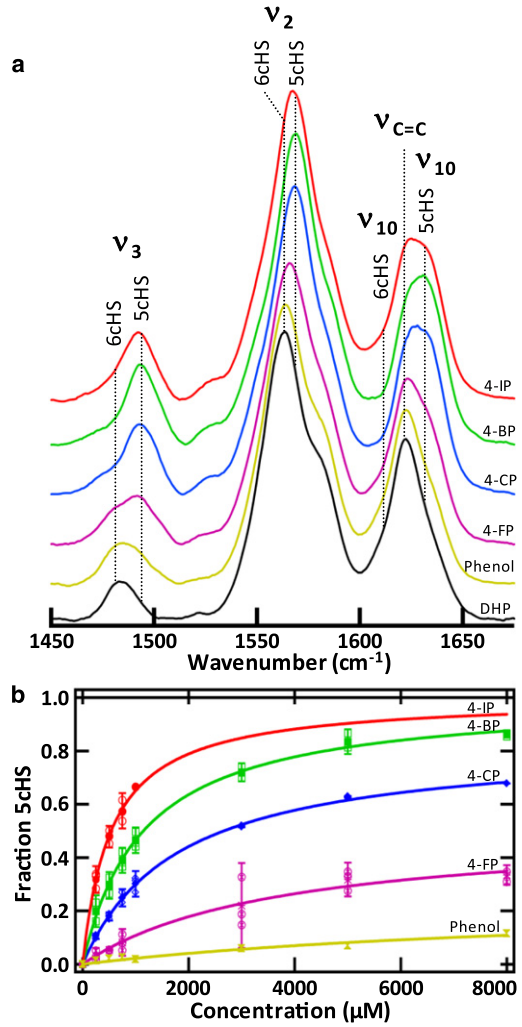

FIGURE 3 Determination of internal binding affinity. (*a*) RR core size marker band region for WT-DHP (*black*), DHP with phenol (*yellow*), DHP with 4-FP (*purple*), DHP with 4-CP (*blue*), DHP with 4-BP (*green*), and DHP with 4-IP (*red*). The ν_2, ν_3, and ν_{10} frequencies are consistent with the increase of a 5cHS iron upon addition of the inhibitors. The final concentration of 4-IP was 1 mM (maximum solubility), and the final concentration of 4-BP, 4-CP, 4-FP, and phenol was 8 mM. Protein concentration: 100 μM; excitation wavelength: 406 nm; resolution: 1.7 cm^{-1}; laser power at the sample: 60 mW; acquisition time: 300 s. (*b*) Binding isotherms for 4-IP (*red*), 4-BP (*green*), 4-CP (*blue*), 4-FP (*purple*), and phenol (*yellow*). The isotherms clearly establish that the affinity of DHP for 4-XP inhibitors follows the pattern 4-IP > 4-BP > 4-CP > 4-FP, > phenol at pH 6.

a systematic blue shift as the substrate halogen is changed and follows the halogen series (see Fig. S1 in the Supporting Material). Therefore, in agreement with the x-ray crystal structures, binding of 4-XP in the internal pocket is consistent with the loss of the 6cHS population and subsequent movement of the distal His to the open, solvent-exposed position. Fig. 3 *b* shows that 4-halophenols bind in the distal pocket with a binding affinity that follows the trend I > Br > Cl > F > H, with apparent dissociation constants of 0.536, 1.15, 1.78, 3.72, and 10.0 mM, respectively. We use the term "apparent dissociation constant" because the binding isotherms represent the fraction of enzyme that is converted to 5cHS, which does not necessarily reflect total binding to the enzyme. The relative binding affinity of 4-FP reflects its low occupancy in the crystal structure. The binding isotherms were determined using the change in relative intensities and the frequency shifts of the core size heme vibrational modes measured by RR spectroscopy and obtained from the data shown in Fig. 3 *a* by SVD (as shown in Fig. S2).

Binding of trihalogenated phenols

In contrast to the binding of 4-XPs, binding of 2,4,6-TXP substrates produces an increase of the 6cHS species. Fig. 4 shows the change of the RR core size marker bands, indicating the formation of a predominantly 6cHS heme (ν_3 at 1481 cm^{-1}, ν_2 at 1562 cm^{-1}, and ν_{10} at 1611 cm^{-1}) when 2,4,6-TBP and 2,4,6-TCP bind to DHP. Although the binding of 2,4,6-TFP also produces predominantly 6cHS heme, an appreciable amount of 5cHS (ν_3 at 1494 cm^{-1},

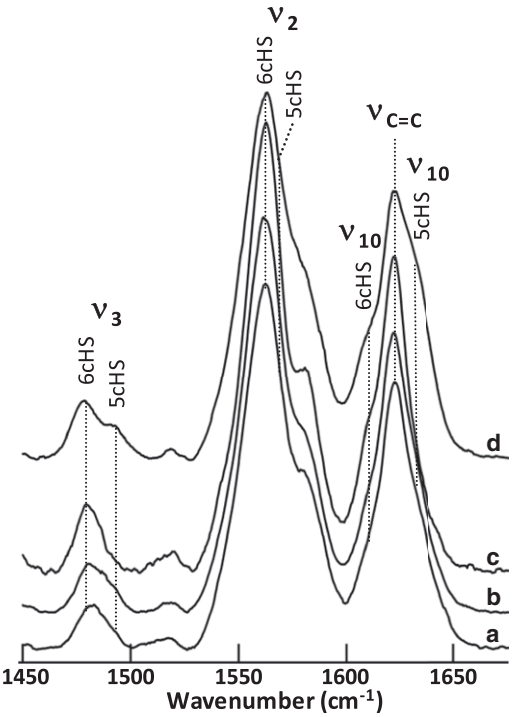

FIGURE 4 Evidence of external binding. RR core size marker band region for WT-DHP (*a*), DHP with 2,4,6-TBP (*b*), DHP with 2,4,6-TCP (*c*), and DHP with 2,4,6-TFP (*d*). The ν_2, ν_3, and ν_{10} frequencies shift to predominantly 6cHS upon addition of the TXP substrates. The 5cHS population observed upon addition of 2,4,6-TFP may indicate that 2,4,6-TFP does enter the distal pocket to some degree, in agreement with cryogenic experiments (16,37,38). The final concentration of 2,4,6-TBP was 200 μM, and the final concentrations of 2,4,6-TCP and 2,4,6-TFP were 4 mM in 150 mM potassium phosphate buffer, pH 6. Excitation wavelength: 406 nm; resolution: 1.7 cm^{-1}; laser power at the sample: 60 mW; acquisition time: 300 s.

ν_2 at 1568 cm^{-1}, and ν_{10} at 1632 cm^{-1}) is also formed, indicating that, unlike 2,4,6-TCP or 2,4,6-TBP, 2,4,6-TFP binds either externally or internally. This result is in agreement with previous studies of DHP showing that 2,4,6-TFP binds internally at cryogenic temperatures (16,37,38) but binds nonspecifically to both sites at room temperature (16,18). The corresponding electronic absorption spectra of 2,4,6-TXP binding (Fig. S3) change accordingly. Of greater importance, we can control the distal histidine and force DHP to adopt either the 5cHS or 6cHS state by changing the concentrations of 4-BP and 2,4,6-TCP present in solution. Fig. S4 shows that the same ratio of 5cHS/6cHS heme is achieved by first adding DHP to 2,4,6-TCP and then adding 4-BP, or by first adding DHP to 4-BP and then adding 2,4,6-TCP. The result demonstrates that 2,4,6-TCP and 4-BP compete for their respective binding locations until an equilibrium between the two states is attained. The x-ray crystal structures show the mutual exclusivity of the closed conformation of the distal histidine and the binding of 4-XP in the distal pocket. Since binding of 2,4,6-TCP forces the distal histidine into the closed position, it must also effectively remove 4-BP from the distal pocket. Thus, by correlation of the x-ray crystal structures and the RR data, we conclude that binding at the internal site and binding at the external site are mutually exclusive events.

Enzyme inhibition by parahalogenated phenols

Davis et al. (18) confirmed the existence of two distinct binding sites for 2,4,6-TCP and 4-BP, and showed that DHP has little activity toward 4-BP compared to 2,4,6-TCP. We therefore tested the effect of internal binding of 4-XP on the turnover of 2,4,6-TCP. Fig. 5 provides kinetic evidence that the oxidation of 2,4,6-TCP is in fact inhibited by internal binding of 4-halophenols. The substrate (2,4,6-TCP) is readily converted to product (2,6-DCQ) when DHP is activated with excess H_2O_2 (Fig. 5 *a*). However, in the presence of even a 2:1 ratio of 4-XP/2,4,6-TCP, little turnover of 2,4,6-TCP to 2,6-DCQ is observed (Fig. 5, *b–e*). In fact, the only appreciable turnover is observed in the presence of 4-FP, in agreement with the binding isotherms from Fig. 2 *b* that suggest only a small fraction of 4-FP binds internally. Since the 4-XP molecules bind internally and force the distal histidine to adopt the open conformation, it is likely that they prevent the formation of compound ES (39), the H_2O_2 activated protein radical form of DHP that is analogous to compound I of cytochrome *c* peroxidase (40) (see Fig. 1 *c*). Indeed, Fig. 5 *f* shows that increasing the concentration of 4-BP systematically blocks the formation of compound ES.

Michaelis-Menten inhibition/kinetic analysis

Since the unique internal binding of 4-XPs inhibits the peroxidase function of DHP at a remote external site, it is of interest to determine the type of inhibition that occurs between the two sites. The solubility of the native substrate, 2,4,6-TBP, is relatively low (~200 μM), which limits its usefulness for kinetic studies. However, 2,4,6-TCP is an excellent substrate and has higher solubility than 2,4,6-TBP. Therefore, we used 2,4,6-TCP rather than 2,4,6-TBP for the subsequent kinetic studies to demonstrate enzymatic

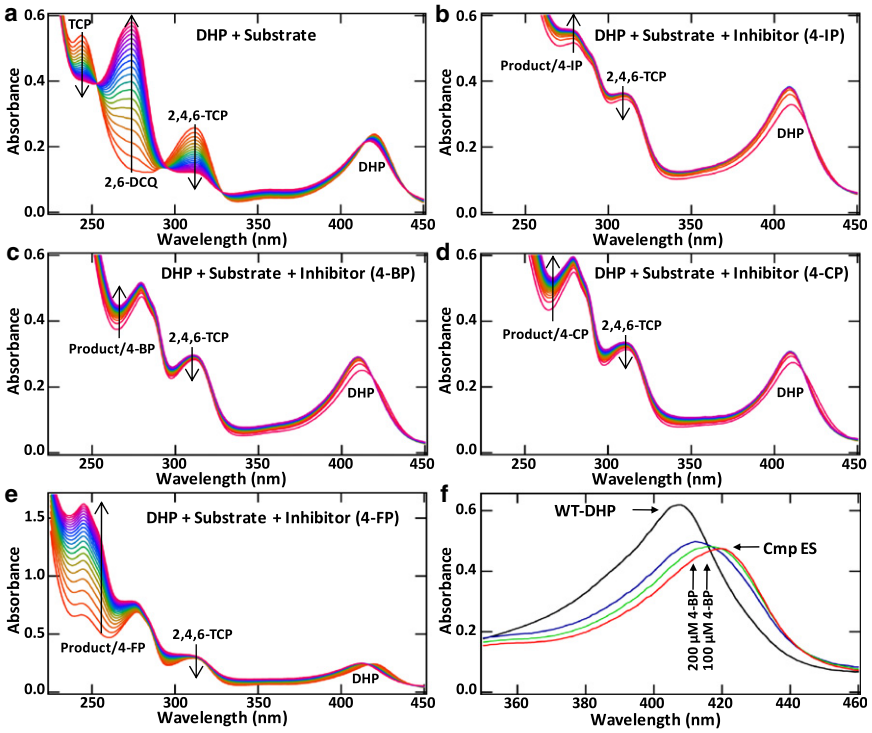

FIGURE 5 Kinetic assays showing inhibition by internally bound 4-XPs. (*a–e*) Time-dependent UV-Vis spectra from 0 s (*red*) to 120 s (*purple*). In the absence of 4-XP (*a*), the TCP substrate (312 nm) is converted to the DCQ product (273 nm). In the presence of 4-IP, 4-BP, and 4-CP (*b–d*), little product is formed, with no significant decrease in the substrate band. In the presence of 4-FP (*e*) some turnover is observed, in agreement with the lower affinity of 4-FP to bind internally. (*f*) Inhibition of compound ES formation (λ_{max} (Soret) = 420 nm) in ferric DHP at pH 7 due to increasing concentrations of 4-BP.

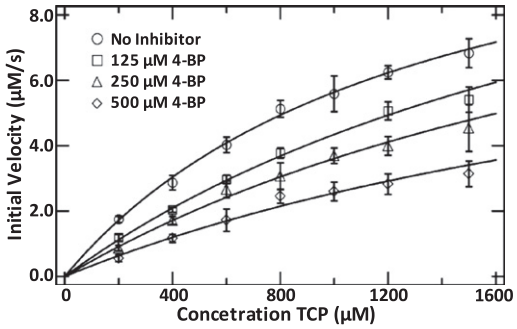

FIGURE 6 Michaelis-Menten analysis of inhibition, showing the initial reaction velocity versus substrate (2,4,6-TCP) concentration. Assays were conducted on WT-DHP without the presence of inhibitor, WT-DHP with 125 μM 4-BP, WT-DHP with 250 μM 4-BP, and WT-DHP with 500 μM 4-BP. The Michaelis-Menten fit parameters are given in Table 2.

inhibition by 4-BP (Fig. 6). The data obtained with and without 4-BP were fit independently to a Michaelis-Menten kinetic model. The fit parameters for the kinetic data are summarized in Table 2. K_M increases as the concentration of inhibitor increases, but V_{max} is essentially unchanged within the limits of the fitting errors. Ideally, one would use substrate concentrations several times greater than K_M, i.e., $[S]_{max} >> K_M$, but even when 2,4,6-TCP is used, the substrate solubility remains the limiting factor. Thus, errors in the fit data arise as K_M becomes greater than $[S]_{max}$. Although we recognize this limitation, the relative effect of the inhibitor is clearly observed. Based on these data, the substrate/inhibitor pair exhibits competitive inhibition in DHP. Although results of this type cannot be demonstrated for 2,4,6-TBP because of its limited solubility, kinetic assays of 2,4,6-TBP with 4-BP under conditions identical to those used for 2,4,6-TCP with 4-BP yield the same complete inhibition effect (Fig. S5).

DISCUSSION

The shifts in the relative position of 4-XPs bound in the distal pocket of DHP suggest that there are two driving forces that stabilize the molecule. First, the parahalogen atom fills a cavity in the protein. Previous studies have examined cavities in Mb by determining Xe binding sites using x-ray crystallography (41). The cavity within DHP that is filled by the parahalogen is surrounded by hydrophobic residues (Fig. S6) and resembles the Xe4 binding site in sperm whale Mb (41). The second factor is the interaction of the hydroxyl group with Y38, heme-7-propionate, and, to a lesser extent, H55 (Fig. 2 *c*). As the atomic radius of the halogen decreases, the hydroxyl group moves into closer contact with H55, Y38, and the heme propionate. Therefore, as shown in Figs. 2 and 3, a single atom, the parahalogen X in 4-XP, determines the binding affinity of the molecule in the distal pocket. Since the bound 4-XP displaces the water coordinated to the heme iron, one can also expect that it prevents the coordination of H_2O_2 and thereby inhibits peroxidase activity. The finding that increased concentrations of 4-BP systematically block the formation of the radical enzymatic intermediate (compound ES (39); see Fig. 1) in ferric DHP at pH 7 supports this hypothesis. Moreover, in accord with this hypothesis, the H55V mutation effectively eliminates the enzymatic activity of DHP (42).

TABLE 2 Mechaelis-Menten fit parameters

	V_{max} (μM/s)	K_M (mM)
No inhibitor	13.1 ± 1.32	1.32 ± 2.11
125 μM 4-BP	15.3 ± 2.94	2.53 ± 6.11
250 μM 4-BP	13.7 ± 4.12	2.80 ± 1.06
500 μM 4-BP	10.4 ± 4.58	3.08 ± 1.71

On the basis of these results, and in agreement with the known mechanism for the peroxidase family members, we propose that enzymatic oxidation of substrates such as 2,4,6-TXP (X = I, Br, Cl, F) occurs at an external site. Recent $^{1}H^{-15}N$ HSQC experiments on $^{13}C/^{15}N$-labeled DHP clearly indicate different binding interactions between 4-BP inhibitor and 2,4,6-TCP substrate (18). 4-BP binding causes deviations in the internal binding pocket residues (F24, F35, F21, H55, and V59; see Fig. S7), whereas 2,4,6-TCP binding affects the distal H55 and amino acids residing at the protein dimer interface (R122, G1, S129, and L76; see Fig. S8) (18). Of interest, the common amino acid that is affected by either binding event, as observed by NMR, is the distal H55. The combination of RR and NMR strongly supports the existence of an external substrate-binding site. Consistent with these observations, every attempt to infuse 2,4,6-TXPs into the distal pocket in crystals of DHP under conditions identical to those used for the 4-XP x-ray structures resulted in no observable binding.

It appears from the RR data in Fig. 4 that 2,4,6-TFP binds both externally and internally, which implies that it acts as substrate and inhibitor, respectively. It is not possible to directly measure whether 2,4,6-TFP inhibits itself (i.e., whether autoinhibition is occurring). However, 2,4,6-TFP is a poor substrate for DHP compared with 2,4,6-TCP or 2,4,6-TBP, which may be in part due to its propensity to bind as an inhibitor. Fig. S9 provides a kinetic summary of the inhibition of 2,4,6-TCP by 2,4,6-TFP. It is clear from the data that 2,4,6-TFP does in fact inhibit 2,4,6-TCP oxidation. The sigmoidal shape of the 2,6-DCQ product formation suggests that 2,4,6-TFP is oxidized until its concentration is reduced such that it no longer acts as an inhibitor to 2,4,6-TCP oxidation. Several previous binding studies (16,37,38) used 2,4,6-TFP as a model for the native substrate because of its high solubility and similar substitution pattern.

The proposed external active site is consistent with pH-dependent studies of enzyme activity. The greatest activity of DHP for oxidation of 2,4,6-TCP was observed at pH 7.5

(43). Since at this pH, 2,4,6-TCP (pKa 6.4 (44)) is in the phenolate form, it is unlikely that it would be able to enter the distal pocket. On the other hand, the pKa of 4-BP is 9.3 (45), so the inhibitor would be protonated and hence neutral at pH 7.5. It is well known that buried charges are not stable in proteins. Attempts to place a buried charge in Mb by the mutation V68D resulted in ligation of the negatively charged carboxylate to the ferric heme iron, thus neutralizing the charge (46). Hence, neither the structural nor the functional observations of enzymatic activity are consistent with substrate binding in the distal pocket, but the same considerations are consistent with the internal binding of 4-bromophenol as an inhibitor. In line with this reasoning, the pKa of 2,4,6-TFP is ~7.2 (47), the highest of all of the TXPs studied. Thus 2,4,6-TFP would have the highest percentage of the phenol form at physiological pH, and therefore the greatest propensity to enter the distal cavity of the enzyme.

The correlation of the x-ray structural and RR data elucidates the key role played by the flexibility of the distal histidine. The x-ray crystal structure of Lebioda et al. (1) (PDB 1EW6) shows that H55 is in equilibrium between the open and closed conformations at room temperature. Nicoletti et al. (16) showed that the ν_3 band of the RR spectrum displays an ~40:60 ratio of 5cHS and 6cHS forms. Binding of 4-XP to DHP forces the distal H55 and H_2O out of the distal pocket (Figs. 1 *b*, 2 *c*, and 3 *a*). Accordingly, the RR spectra in the presence of 4-XP are typical of 5cHS heme, indicating that the water molecule has been expelled. Conversely, the RR spectroscopic data in Fig. 4 and the UV-vis data in Fig. S3 show that binding of 2,4,6-TXP increases the population of aquo 6cHS heme. Thus, external binding of a 2,4,6-TXP substrate forces the distal H55 into the closed position, stabilizing the heme iron-coordinated water molecule (Fig. 1 *a*). Substrate binding, then, enforces the closed H55 conformation, which strengthens H_2O_2 coordination to the heme iron and positions H55 to serve as the acid-base catalyst in the peroxidase mechanism. Furthermore, we have demonstrated that the 5cHS/6cHS ratio can be driven to either extreme by varying the concentrations of inhibitor and substrate (Fig. S4), indicating mutual exclusivity between their respective binding sites.

The kinetic data presented in Fig. 6 and Table 2 demonstrate the competitive nature of the inhibition that occurs between the substrate-inhibitor pair. The structural and spectroscopic data presented herein indicate that this unique mechanism involves two independent but concerted competitive binding events. The first arises from the steric interactions of 4-XP binding in the distal pocket preventing ligation of H_2O_2 to the heme iron. The second is allosteric communication by movement of the distal histidine resulting in two-site competitive binding between the substrate and inhibitor pair. Thus, inhibition by 4-XP appears to involve three simultaneous effects: 1), H_2O_2 coordination to the heme iron is impeded; 2), the distal H55, which is the acid-base catalyst in the peroxidase mechanism (48–50), is displaced out of the cavity; and 3), the external binding site is subsequently rearranged by the solvent-exposed (open) distal H55 conformation. Therefore, DHP exhibits a nonclassical two-site competitive inhibition in which the inhibitor and substrate have mutually exclusive binding interactions. When the substrate is bound, the distal histidine is in the internal, or active, conformation (6cHS), and the inhibitor cannot access the internal site (see Fig. 1 *a*). On the contrary, when the inhibitor is bound, the distal histidine is in the solvent-exposed, or inactive, conformation (5cHS), and the substrate cannot access the external site (see Fig. 1 *b*). The two-site competitive inhibition is driven by the same open/closed conformational change that has been studied for many years in Mb (15,24).

CONCLUSIONS

Since the x-ray crystal structure of DHP showing the substrate analog 4-IP bound in the distal pocket (PDB 1EWA) was the first observation of internal binding, it was reasonable to consider that the internal site may serve as the active site (1). However, structural, functional, and spectroscopic studies have repeatedly contradicted that assumption (17,18,37,38,43,51). The finding that 4-BP and 2,4,6-TBP act as an inhibitor and a substrate, respectively, for DHP is noteworthy because both molecules are present in benthic ecosystems (52). However, since 4-BP is not an oxidation product of 2,4,6-TBP, this inhibitor-substrate pair is not part of a feedback system for this enzyme. Organisms such as *Notomastus lobatus* (among many others) synthesize 4-BP and 2,4,6-TBP, but this does not appear to be the case for *A. ornata* (3,53). Instead, DHP, which is the most abundant protein in *A. ornata*, oxidizes 2,4,6-TBP to 2,6-dibromo-1,4-benzoquinone (Fig. 1). The substrate 2,4,6-TBP acts as both a repellent, protecting marine organisms from predators, and a potentially lethal toxin. Therefore, the degradation of 2,4,6-TBP must be a protective function that minimizes the concentration of the highly toxic molecule in *A. ornata* (52). Although the reason for the inhibition of 2,4,6-TBP oxidation by 4-BP is not known, it is clear that DHP is a finely tuned enzyme that has an unusual mechanism for inhibitor specificity.

SUPPORTING MATERIAL

Nine figures and two references are available at http://www.biophysj.org/biophysj/supplemental/S0006-3495(10)00716-2.

We thank R. Ghiladi for a technical critique of the manuscript, and E. Ison for use of the Cary 100.

This work was supported by the U.S. Army Research Office (grant 52278-LS) and Italian grant ex60%.

The atomic coordinates and structure factors for the reported crystal structures have been deposited with the Protein Data Bank under accession codes 3LB1, 3LB2, 3LB3, and 3LB4.

REFERENCES

1. Lebioda, L., M. W. LaCount, …, S. A. Woodin. 1999. An enzymatic globin from a marine worm. *Nature.* 401:445.
2. Weber, R. E., C. Mangum, …, J. Bonaventura. 1977. Hemoglobins of two terebellid polychaetes: *Enoplobranchus sanguineus* and *Amphitrite ornata*. *Comp. Biochem. Physiol. Comp. Physiol.* 56:179–187.
3. Chen, Y. P., S. A. Woodin, …, C. R. Lovell. 1996. An unusual dehalogenating peroxidase from the marine terebellid polychaete Amphitrite ornata. *J. Biol. Chem.* 271:4609–4612.
4. Reference deleted in proof.
5. Han, K., S. A. Woodin, …, B. Ely. 2001. *Amphitrite ornata*, a marine worm, contains two dehaloperoxidase genes. *Mar. Biotechnol.* 3: 287–292.
6. de Sorrano, V., J. D'Antonio, …, R. A. Ghiladi. 2010. Crystal structure of dehaloperoxidase B at 1.58 A and characterization of the A/B dimer from *Amphitrite ornata*. *Acta Crystallogr. D Biol. Crystallogr.* 66: 529–538.
7. Goodin, D. B., and D. E. McRee. 1993. The Asp-His-Fe triad of cytochrome c peroxidase controls the reduction potential, electronic structure, and coupling of the tryptophan free radical to the heme. *Biochemistry.* 32:3313–3324.
8. Spiro, T. G., G. Smulevich, and C. Su. 1990. Probing protein structure and dynamics with resonance Raman spectroscopy: cytochrome c peroxidase and hemoglobin. *Biochemistry.* 29:4497–4508.
9. Perutz, M. F., A. J. Wilkinson, …, G. G. Dodson. 1998. The stereochemical mechanism of the cooperative effects in hemoglobin revisited. *Annu. Rev. Biophys. Biomol. Struct.* 27:1–34.
10. Chen, Y. R., L. J. Deterding, …, R. P. Mason. 2000. Nature of the inhibition of horseradish peroxidase and mitochondrial cytochrome c oxidase by cyanyl radical. *Biochemistry.* 39:4415–4422.
11. Zatón, A. M., and E. Ochoa de Aspuru. 1995. Horseradish peroxidase inhibition by thiouracils. *FEBS Lett.* 374:192–194.
12. Ziemys, A., and J. Kulys. 2005. Heme peroxidase clothing and inhibition with polyphenolic substances revealed by molecular modeling. *Comput. Biol. Chem.* 29:83–90.
13. de Serrano, V., Z. Chen, …, S. Franzen. 2007. X-ray crystal structural analysis of the binding site in the ferric and oxyferrous forms of the recombinant heme dehaloperoxidase cloned from *Amphitrite ornata*. *Acta Crystallogr. D Biol. Crystallogr.* 63:1094–1101.
14. Chen, Z., V. de Serrano, …, S. Franzen. 2009. Distal histidine conformational flexibility in dehaloperoxidase from *Amphitrite ornata*. *Acta Crystallogr. D Biol. Crystallogr.* 65:34–40.
15. Yang, F., and G. N. Phillips, Jr. 1996. Crystal structures of CO-, deoxy- and met-myoglobins at various pH values. *J. Mol. Biol.* 256:762–774.
16. Nicoletti, F. P., M. K. Thompson, …, G. Smulevich. 2010. New insights into the role of distal histidine flexibility in ligand stabilization of dehaloperoxidase-hemoglobin from *Amphitrite ornata*. *Biochemistry.* 49:1903–1912.
17. Davis, M. F., H. Gracz, …, S. Franzen. 2009. Different modes of binding of mono-, di-, and trihalogenated phenols to the hemoglobin dehaloperoxidase from *Amphitrite ornata*. *Biochemistry.* 48: 2164–2172.
18. Davis, M. F., B. G. Bobay, and S. Franzen. 2010. Determination of separate inhibitor and substrate binding sites in the dehaloperoxidase-hemoglobin from *Amphitrite ornata*. *Biochemistry.* 49: 1199–1206.
19. Tippett, P. S., and K. E. Neet. 1982. An allosteric model for the inhibition of glucokinase by long chain acyl coenzyme A. *J. Biol. Chem.* 257:12846–12852.
20. Hu, D. D., C. A. White, …, J. W. Smith. 1999. A new model of dual interacting ligand binding sites on integrin αIIbβ3. *J. Biol. Chem.* 274:4633–4639.
21. Tran, K. L., P. A. Aronov, …, C. Morisseau. 2005. Lipid sulfates and sulfonates are allosteric competitive inhibitors of the N-terminal phosphatase activity of the mammalian soluble epoxide hydrolase. *Biochemistry.* 44:12179–12187.
22. Horton, H. R., L. A. Morton, …, D. Rawn. 2006. Principles of Biochemistry. Pearson Prentice Hall, Upper Saddle River, NJ.
23. Johnson, J. B., D. C. Lamb, …, R. D. Young. 1996. Ligand binding to heme proteins. VI. Interconversion of taxonomic substates in carbonmonoxymyoglobin. *Biophys. J.* 71:1563–1573.
24. Tian, W. D., J. T. Sage, and P. M. Champion. 1993. Investigations of ligand association and dissociation rates in the "open" and "closed" states of myoglobin. *J. Mol. Biol.* 233:155–166.
25. Otwinowski, Z., and W. Minor. 1997. Processing of x-ray diffraction data collected in oscillation mode. *Methods Enzymol.* 276:307–326.
26. McCoy, A. J., R. W. Grosse-Kunstleve, …, R. J. Read. 2007. Phaser crystallographic software. *J. Appl. Cryst.* 40:658–674.
27. Krissinel, E. B., M. D. Winn, …, P. Emsley. 2004. The new CCP4 Coordinate Library as a toolkit for the design of coordinate-related applications in protein crystallography. *Acta Crystallogr. D Biol. Crystallogr.* 60:2250–2255.
28. Potterton, L., S. McNicholas, …, M. Noble. 2004. Developments in the CCP4 molecular-graphics project. *Acta Crystallogr. D Biol. Crystallogr.* 60:2288–2294.
29. Emsley, P., and K. Cowtan. 2004. Coot: model-building tools for molecular graphics. *Acta Crystallogr. D Biol. Crystallogr.* 60: 2126–2132.
30. Murshudov, G. N., A. A. Vagin, and E. J. Dodson. 1997. Refinement of macromolecular structures by the maximum-likelihood method. *Acta Crystallogr. D Biol. Crystallogr.* 53:240–255.
31. Collaborative Computational Project, Project Number 4. 1994. The CCP4 suite: programs for protein crystallography. *Acta Crystallogr. D Biol. Crystallogr.* 50:760–763.
32. Brünger, A. T., P. D. Adams, …, G. L. Warren. 1998. Crystallography & NMR system: a new software suite for macromolecular structure determination. *Acta Crystallogr. D Biol. Crystallogr.* 54:905–921.
33. Humphrey, W., A. Dalke, and K. Schulten. 1996. VMD—Visual Molecular Dynamics. *J. Mol. Graph.* 14:33–38.
34. Fermi, G., M. F. Perutz, …, R. Fourme. 1984. The crystal structure of human deoxyhaemoglobin at 1.74 A resolution. *J. Mol. Biol.* 175: 159–174.
35. Harrington, D. J., K. Adachi, and W. E. Royer, Jr. 1997. The high resolution crystal structure of deoxyhemoglobin S. *J. Mol. Biol.* 272: 398–407.
36. Schlichting, I., J. Berendzen, …, R. M. Sweet. 1994. Crystal structure of photolysed carbonmonoxy-myoglobin. *Nature.* 371:808–812.
37. Nienhaus, K., P. Deng, …, G. U. Nienhaus. 2006. Spectroscopic study of substrate binding to the carbonmonoxy form of dehaloperoxidase from *Amphitrite ornata*. *J. Phys. Chem. B.* 110:13264–13276.
38. Smirnova, T. I., R. T. Weber, …, S. Franzen. 2008. Substrate binding triggers a switch in the iron coordination in dehaloperoxidase from *Amphitrite ornata*: HYSCORE experiments. *J. Am. Chem. Soc.* 130: 2128–2129.
39. Feducia, J., R. Dumarieh, …, R. A. Ghiladi. 2009. Characterization of dehaloperoxidase compound ES and its reactivity with trihalophenols. *Biochemistry.* 48:995–1005.
40. Sivaraja, M., D. B. Goodin, …, B. M. Hoffman. 1989. Identification by ENDOR of Trp191 as the free-radical site in cytochrome c peroxidase compound ES. *Science.* 245:738–740.
41. Tilton, Jr., R. F., I. D. Kuntz, Jr., and G. A. Petsko. 1984. Cavities in proteins: structure of a metmyoglobin-xenon complex solved to 1.9 A. *Biochemistry.* 23:2849–2857.
42. Franzen, S., J. Belyea, …, S. A. Lommel. 2006. Proximal cavity, distal histidine, and substrate hydrogen-bonding mutations modulate the activity of *Amphitrite ornata* dehaloperoxidase. *Biochemistry.* 45:9085–9094.

43. Franzen, S., L. B. Gilvey, and J. L. Belyea. 2007. The pH dependence of the activity of dehaloperoxidase from *Amphitrite ornata*. *Biochim. Biophys. Acta.* 1774:121–130.

44. Dodgson, K. S., J. N. Smith, and R. T. Williams. 1950. Studies in detoxication. 29. The orientation of glucuronic acid conjugation in chloroquinol. *Biochem. J.* 46:124–128.

45. Kortum, G., W. Vogel, and K. Andrussow. 1961. Dissociation constants of organic acids in aqueous solution. *Pure Appl. Chem.* 1:190–536.

46. Varadarajan, R., T. E. Zewert, …, S. G. Boxer. 1989. Effects of buried ionizable amino acids on the reduction potential of recombinant myoglobin. *Science.* 243:69–72.

47. Gilvey, L. B. 2006. Kinetic studies of dehaloperoxidase-hemoglobin from *Amphitrite ornata*. MS thesis. North Carolina State University, Raleigh, North Carolina.

48. Dawson, J. H. 1988. Probing structure-function relations in heme-containing oxygenases and peroxidases. *Science.* 240:433–439.

49. Poulos, T. L. 1988. Heme enzyme crystal structures. *Adv. Inorg. Biochem.* 7:1–36.

50. Poulos, T. L., and J. Kraut. 1980. The stereochemistry of peroxidase catalysis. *J. Biol. Chem.* 255:8199–8205.

51. Belyea, J., L. B. Gilvey, …, S. Franzen. 2005. Enzyme function of the globin dehaloperoxidase from *Amphitrite ornata* is activated by substrate binding. *Biochemistry.* 44:15637–15644.

52. Lincoln, D. E., K. T. Fielman, …, S. A. Woodin. 2005. Bromophenol accumulation and sediment contamination by the marine annelids *Notomastus lobatus* and *Thelepus crispus*. *Biochem. Syst. Ecol.* 33: 559–570.

53. Chen, Y. P., D. E. Lincoln, …, C. R. Lovell. 1991. Purification and properties of a unique flavin-containing chloroperoxidase from the capitellid polychaete *Notomastus lobatus*. *J. Biol. Chem.* 266: 23909–23915.

Kinetic Analysis of a Naturally Occurring Bioremediation Enzyme: Dehaloperoxidase-Hemoglobin from *Amphitrite ornata*

Huan Ma,[†,‡] Matthew K. Thompson,[†] John Gaff,[†] and Stefan Franzen*[,†,‡]

Department of Chemistry, North Carolina State University, Raleigh, North Carolina 27695, and Department of Chemistry, Zhejiang University, Hangzhou, China

Received: February 16, 2010; Revised Manuscript Received: August 24, 2010

The temperature dependence of the rate constant for substrate oxidation by the dehaloperoxidase-hemoglobin (DHP) of *Amphitrite ornata* has been measured from 278 to 308 K. The rate constant is observed to increase over this range by approximately a factor of 2 for each 10 °C temperature increment. An analysis of the initial rates using a phenomenological approach that expresses the peroxidase ping-pong mechanism in the form of the Michaelis−Menten equation leads to an interpretation of the effects in terms of the fundamental rate constants. The analysis of kinetic data considers a combination of diffusion rate constants for substrate and H_2O_2, elementary steps involving activation and heterolysis of the O−O bond of H_2O_2, and two electron transfers from the substrate to the iron. To complete the analysis from the perspective of turnover of substrate into product, density function theory (DFT) calculations were used to address the fate of phenoxy radical intermediates. The analysis suggests a dominant role for diffusion in the kinetics of DHP.

Introduction

The dehaloperoxidase-hemoglobin (DHP) from *Amphitrite ornata* has recently been shown to have a unique peroxidase enzyme mechanism that may be characterized as nonclassical competitive inhibition.[1] In the nonclassical model, the inhibitor binds remotely to the active site and causes a conformational change in the enzyme that prevents substrate binding. In DHP, the substrate binds at an external site, and the inhibitor binds in the distal pocket above the heme iron. There are multiple X-ray crystal structures of 4-halophenols binding in the internal site.[1,2] The location of the external site has been characterized by spectroscopic measurements. NMR spectroscopy indicates that there is an interaction between the substrate and the distal histidine, H55.[3] Resonance Raman spectroscopy confirms this interaction, using the observation that the distal histidine (H55) position appears to correlate with water in the metaquo form such that H55 in the internal position stabilizes the 6-coordinate high spin state and H55 in the external position gives rise to the 5-coordinate high spin state.[1,4−6] Models of these structures are shown in Figure 1. There are two isoforms of DHP in *A. ornata*.[7] All previous studies that referred to DHP implicitly referenced DHP A. We have recently cloned and expressed the B isoform of DHP, DHP B,[8,9] so that we now distinguish the specific experiments conducted on DHP A in this study from general features that apply to both isoforms of DHP. The two isoforms are structurally homologous but differ by five amino acids: I9L, R32K, Y34N, N81S, and S91G. Although there is slight variation in the amino acid sequence, both isoforms are capable of performing the dehalogenation function.

The external substrate binding site in DHP is related to external binding in peroxidases[10,11] in that electron transfer from the substrate to the heme edge (or alternatively to an amino acid radical)[12] is the key step in substrate oxidation as shown in Figure 2. Similar considerations apply to myoglobin mutants that have peroxidase activity.[13−16] Amino acid radicals, which are formed in myoglobin as well as peroxidases, may act as a conduit for electron transfer or might result in protein cross-linking.[13,17−19] The oxidized phenol rapidly deprotonates to form the corresponding phenoxy radical.[20,21] The standard peroxidase mechanism involves disproportionation of the radical to form the phenoxy radical cation and phenolate as shown on the left side of Figure 2. Disproportionation is self-electron transfer in this case. Attack by water could occur on either the radical (right side) or the cation (left side). If attack by water occurs on the radical (right side of Figure 2), then electron transfer occurs subsequently. While the order of electron transfer and attack by water is difficult to ascertain with certainty in a kinetic experiment, it can be addressed using density functional theory (DFT) calculations.

Kinetic analysis is needed to understand the implication of the various possible pathways for one-electron activation implicit in the external binding site.[22] Substrate binding and oxidation under physiological conditions are the basic physical phenomena required for application of DHP as a bioremediation enzyme. One can regard DHP as a bioremediation enzyme since its natural function is to oxidize 2,4,6-tribromophenol (2,4,6-TBP).[23] While 2,4,6-TBP is a natural pollutant made by organisms such as *Notomastus lobatus* and *Thelepus crispus* in benthic ecosystems,[23] 2,4,6-trichlorophenol (2,4,6-TCP) is a man-made pollutant that is widely dispersed.[24] 2,4,6-TCP and related polysubstituted chlorinated phenols are substrates for DHP, while, as we have recently shown, 4-chlorophenols are inhibitors. Since 2,4,6-TCP is an excellent substrate, as well as a bioremediation target, the present study serves as a baseline for future comparison of a range of substrates in DHP and its mutants.[25] Herein, we focus on the kinetics of the uninhibited reaction using an Arrhenius analysis of the rate constants based on kinetic

* To whom correspondence should be addressed: Stefan Franzen, Department of Chemistry, North Carolina State University, Raleigh, NC 27695. E-mail: stefan_franzen@ncsu.edu. Phone: 919-515-8915.
† North Carolina State University.
‡ Zhejiang University.

10.1021/jp1014516
Published on Web 10/08/2010

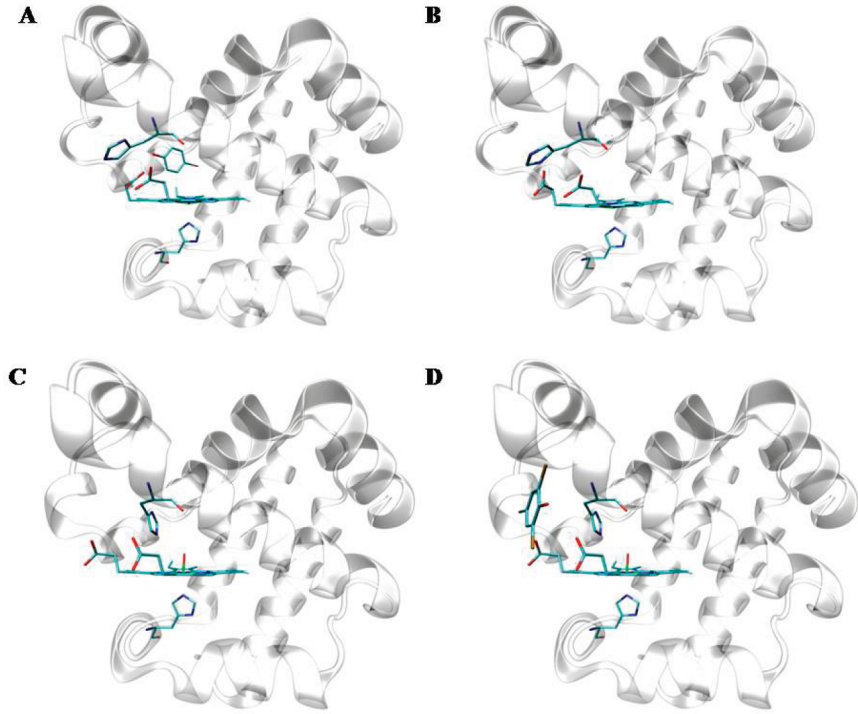

Figure 1. Structures of DHP A with substrate and inhibitor bound to the enzyme. (A) Metaquo form with inhibitor bound (3LB1 is shown, but 3LB2, 3BL3, and 3LB4 are similar in structure); H55 open. (B) Deoxy form of DHP (3DR9); H55 open. (C) Metaquo form of DHP (2QFK); H55 closed. (D) Metaquo form with the substrate at proposed external substrate binding site; H55 closed.

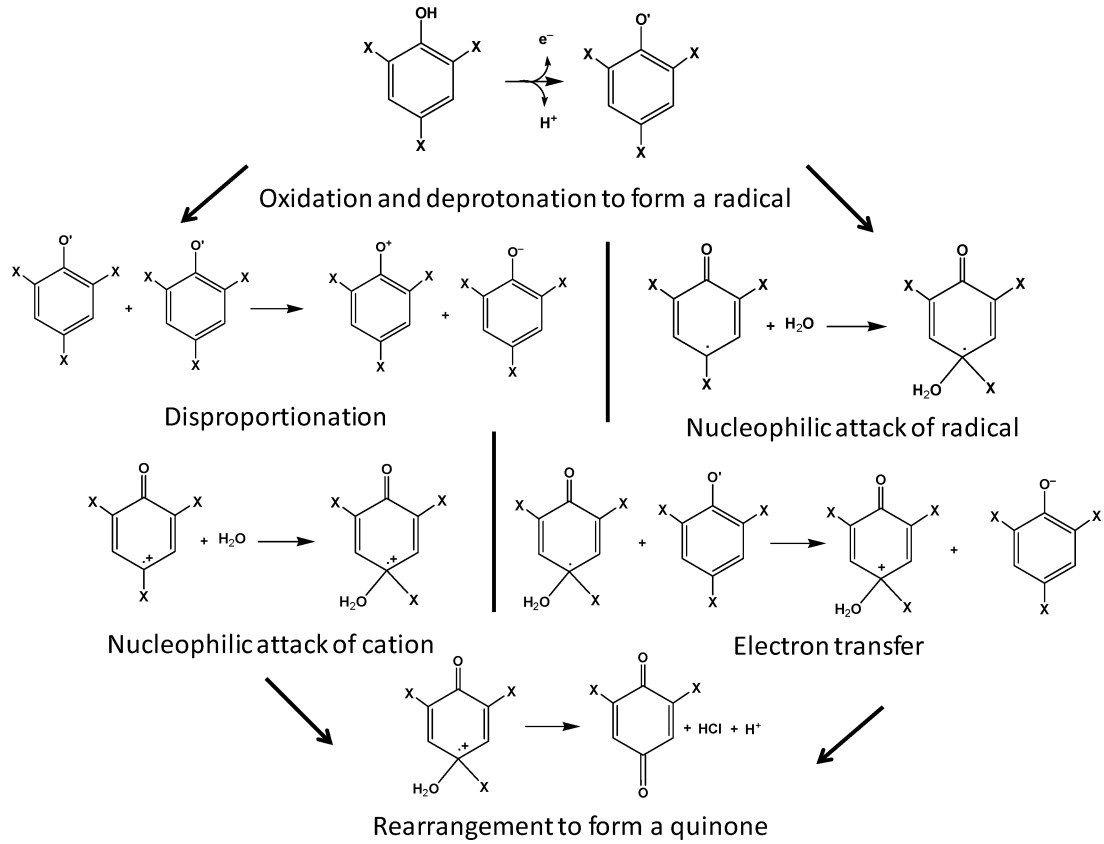

Figure 2. Possible routes from phenol to quinone subsequent electron transfer to the heme oxoferryl intermediates of the DHP A enzyme. These structures were used for DFT calculations described in the text.

models of the ping-pong mechanism.[26] We show that a phenomenological model permits fit to an equation that has the form of the Michaelis−Menten equation but ultimately has an interpretation in terms of the fundamental rate constants for peroxidase kinetics.[26] Finally, we consider the fate of the radical generated by the oxidation reactions of DHP. Since this process is not directly probed by the spectroscopic assay, DFT calculations are needed to deter-

mine whether the barrier height corresponds to the measured kinetic parameters using an Arrhenius approach.

Materials and Methods

DHP A Protein Growth. A pET-16b plasmid containing the 6XHis-tagged DHP A DNA insert was transformed into competent BL21(DE3) *Escherichia coli* cells and then plated with 100 μg/mL ampicillin and allowed to grow at 37 °C for about 14 h. Single colonies were isolated and transferred to 2 mL starter growths of 2xYT broth containing 75 μg/mL of ampicillin at 37 °C with shaking for about 8 h. A portion of 1 mL of each starter growth was then used to inoculate six 1 L flasks of 2xYT broth containing 75 μg/mL of ampicillin. The 6 L *E. coli* growth was incubated at 37 °C with shaking for about 15 h. The cells were collected via centrifugation at 7000 rpm, at 4 °C for 20 min.

Purification of 6XHisDHP A. The *E. coli* cell pellet was resuspended in 2 mL/(gram cell pellet) of lysis buffer (50 mM NaH_2PO_4, 300 mM NaCl, 10 mM imidazole, pH 8), and lysozyme was added to a final concentration of 1 mg/mL. The cell slurry was stirred at 4 °C for an hour and then sonicated for 30 min, and 500 μL of DNase I (10 mg/mL) and RNase A (16 mg/mL) were added. The cell slurry was then stirred again at 4 °C for 1 h before freezing overnight at −20 °C. After rethawing, the cells were centrifuged at 18 000 rpm for half an hour, and the supernatant containing the 6XHisDHP A was collected. The crude DHP A solution was applied to a Ni-NTA agarose column (5 Prime Perfect Pro), washed with washing buffer (50 mM NaH_2PO_4 300 mM NaCl, 20 mM imidazole, pH 8), and eluted using elution buffer (50 mM NaH_2PO_4, 300 mM NaCl, 250 mM imidazole, pH 8). The isolated 6XHis DHP A from the column was oxidized by excess 10 mM $K_3[Fe(CN)_6]$. Excess $K_3[Fe(CN)_6]$ was removed by gel filtration on a Sephadex G-25 column, which permitted simultaneous buffer exchange into 20 mM KH_2PO_4 pH 6 buffer. The oxidized protein was loaded onto a CM-52 column for further purification. Once loaded onto the column, the 6XHis DHP A was washed with 20 mM KH_2PO_4 pH 6 and eluted form the column with 150 mM KH_2PO_4 pH 7 buffer. The concentration of the ferric DHP A was determined using the Soret absorption intensity at 406 nm with a molar absorptivity of 116 400 M^{-1} cm^{-1}. The purified 6XHisDHP A was stored at 4 °C for future use.

Sample Preparation. Purified 6XHisDHP A was oxidized in the presence of 10 mM $K_3[Fe(CN)_6]$, separated from excess $K_3[Fe(CN)_6]$ by gel filtration on Sephadex G-25, and further purified on CM-52 (as above) prior to each experiment. For kinetic assays the elution buffer was 150 mM KH_2PO_4 buffer at pH 7.0. A portion of 98% 2,4,6-tricholorophenol from Acros Organics (Lot No. A0245137) was dissolved in 150 mM KH_2PO_4, pH 7 buffer with a final concentration of 3 mM and stored at 4 °C until use. The H_2O_2 solution was prepared from 30% reagent grade H_2O_2 solution from Fisher Chemicals in 150 mM KH_2PO_4, pH 7 buffer to a final concentration of 17.6 mM for the stock solution. The H_2O_2 solution was prepared freshly before use and stored at 4 °C during the course of a series of experiments.

Kinetic Assays. The kinetic assays were conducted in a 0.4 cm path length quartz cuvette with a total volume of 1500 μL. The final concentration of ferric DHP A in the cuvette was $[E]_T \sim 2.4$ μM, and substrate, 2,4,6-TCP, concentrations were varied from 100 to 1900 μM. Spectra were obtained using a photodiode UV−vis spectrometer (Agilent 8453) equipped with a Peltier temperature controller using benchtop mixing of the reagents. To reach thermal equilibrium, DHP A and 2,4,6-TCP (150 mM KH_2PO_4, pH = 7 buffer) were allowed to incubate for 5 min in the cuvette placed in the thermal cell. The H_2O_2 solution, with a final concentration of 500 times DHP A, was injected into the cuvette within one second of initiation of data collection. The data were measured over the wavelength range from 200 to 700 nm with a time resolution of 3.1 s. The wavelength monitored during kinetic measurements was 273 nm, the peak of the product absorption band. For 2,6-DCQ, ε_{273} is 14 130 M^{-1} cm^{-1} at pH 7. Data were extracted using an Excel spreadsheet and analyzed using Igor Pro 5.0.

Kinetic Analysis. The purpose of this kinetic assay is to study the relationship between enzymatic reaction initial velocity and temperature. The obtained data were first fit to a linear function to get the initial reaction velocity at a given substrate concentration. Then those initial velocities of different substrate concentrations were fit to the Michaelis−Menten equation to obtain relevant parameters k_{cat} and K_M. Finally, the relationship between these parameters and temperature was analyzed using a phenomenological Arrhenius equation. The enzyme-substrate (ES) complex is formed reversibly in the Michaelis−Menten mechanism. However, in peroxidase chemistry there are two complexes, one with the substrate, 2,4,6-TCP, and one with H_2O_2. According to the standard enzyme kinetic scheme, the binding of H_2O_2 leads to formation of compound I and is not reversible. We have recently shown that compound I is not observed in DHP A and that compound ES is rapidly formed.[12] We recently confirmed similar observations for DHP B.[9] Both compound I and compound ES consist of a Fe(IV)═O species and a cation radical. The difference is that the radical resides on the heme ring in compound I but on an aromatic amino acid in comound ES. We have further shown that the radical is located on one of the five tyrosines in DHP A.[12] Since compound ES formation appears to be rapid in DHP, we present the peroxidase rate scheme with a compound ES intermediate. The compound ES is reduced in two one-electron steps by a substrate, XAOH, which is 2,4,6-TCP in the present study. The sequential oxidation of two substrates by two different processes with rate constants k_2 and k_3 is known as the ping-pong mechanism.

The kinetic model for this rate scheme is given by:

$$V_o = \frac{V_{max}[XAOH]}{K_m + [XAOH]}$$

$$V_{max} = k_1[H_2O_2][E]_o \qquad K_m = \left(\frac{1}{k_2} + \frac{1}{k_3}\right)k_1[H_2O_2] \tag{1}$$

Dunford does not recommend the use of the Michaelis−Menten model since $k_1 \gg k_2$ for well-studied peroxidases such as HRP.[26] Consequently, compound I (Cmp I) is rapidly formed and can build up to an appreciable concentration in these peroxidases for a period of minutes or even longer in very pure preparations. According to eq 1, the dependence of V_o on [XAOH] is linear for $k_1 \gg k_2$, and saturation should not be observed.[26] However, DHP A does not behave like HRP in this regard.[27,28] If we consider that compound ES plays the role of compound I in DHP A,[12] then k_1 and k_2 are not vastly different in magnitude in DHP A. Accordingly, the results presented in this study show that saturation is observed in DHP A. These observations justify the parametrization in eq 1. The product is formed by disproportionation of the radical intermediate A•. The H_2O_2 concen-

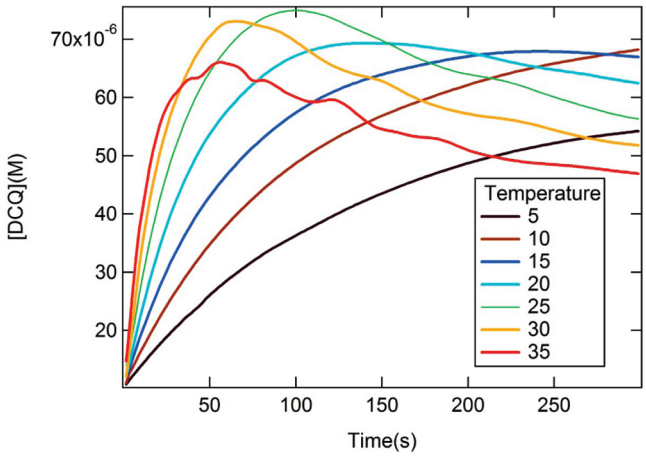

Figure 3. Single wavelength kinetics at 273 nm of the oxidation reaction of TCP by DHP as a function of time and product DCQ concentration obtained using a UV−vis spectrometer. Assay conditions were [ferric DHP] ~2 μM, [TCP] ~150 μM, [H_2O_2] ~150 μM, pH 7 KP buffer.

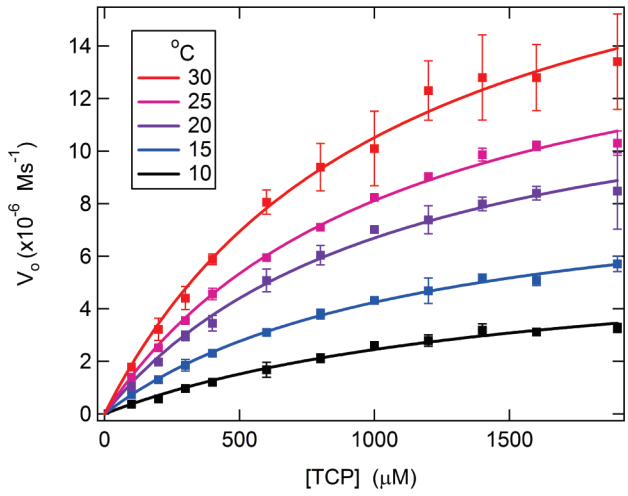

Figure 4. Single wavelength kinetics of oxidation of TCP by DHP as a function of substrate TCP concentration and enzymatic reaction initial velocity. The assay conditions were ferric DHP ~2 μM, 150 μM TCP M, H_2O_2, 150 μM pH 7 KB buffer.

tration was held constant at 1.2 mM in this study so that only the substrate concentration, [XAOH], is considered here.

DFT Calculations. Substrates involved in the two pathways, Figure 2, were constructed using the software package Materials Studio (Accelrys). All quantum chemical calculations were performed in a water environment with the electronic structure package DMol.[3,30−33] Ground state geometries of the substrates (without the protein) were optimized using the conjugate gradient method constrained to an energy difference of $<10^{-6}$ Ha, the Perdew−Burke−Ernzerhof (PBE)[29] density functional, and with a double numeric basis set with one polarization function. To achieve self-consistent field energy convergence for each optimization cycle the thermal treatment of electron occupancy[34] with an electronic temperature of 0.02 Hartrees was implemented. To incorporate solvent effects, the COSMO (dielectric screening model) module employed by DMol[3] was also implemented. For the solvent used in this study, water, the dielectric constant adopted was $\varepsilon = 80.4$.[35]

Results

Kinetic data were obtained as both time-dependent spectra and single-wavelength kinetics. The single wavelength kinetics were analyzed first to determine the appropriate temperature range for spectral measurement.

The single wavelength (273 nm) kinetics shown in Figure 3 give the change in the concentration of the product 2,6-dichlorophenol-1,4-benzoquinone (2,6-DCQ) at seven different temperatures. The change in the product concentration is assumed to be proportional to the enzymatic rate. However, the concentration of 2,6-DCQ reaches a maximum and begins to decrease at longer times when the temperature is greater than 20 °C. The decrease in absorbance on time scales of 50 s and longer is due to secondary hydrolysis reactions of the 2,6-DCQ product.[36] Because of the secondary reaction, only the short time kinetics were used to estimate the catalytic rate for the process. This choice is consistent with the common practice of confining analysis of Michaelis−Menten kinetics to the initial rates.

The initial rates of appearance of the product 2,6-DCQ at 273 nm at five different temperatures are shown in Figure 4 as a function of substrate, 2,4,6-TCP, concentration. As expected, on the basis of the kinetics in Figure 3, Figure 4 shows that the initial rate of the enzyme reaction between DHP A and 2,4,6-TCP at pH 7 has a strong temperature dependence. The initial rate data were fit to eq 1, and from the curve fitting, we can determine the phenomenological Michaelis constant and the catalytic constant, K_M and k_{cat}, respectively. Table 1 provides a summary of the Michaelis−Menten fit parameters for the initial rate data.

TABLE 1: Kinetic Parameters from the Curve Fitting to the Phenomenological Michaelis−Menten Equation

T/K	V_{max}/μM s^{-1}	k_{cat}/s^{-1}	K_M/mM
283	6.32	2.68	1.58
288	9.16	3.88	1.16
293	14.2	6.00	1.13
298	16.9	7.16	1.08
303	21.7	9.19	1.06

Using the phenomenological Michaelis−Menten equation, the turnover number is $k_{cat} = V_{max}/[E]_T = k_1[H_2O_2]$. According to the parametrization presented in eq 1, the phenomenological k_{cat} is a pseudofirst order rate constant (i.e., $[H_2O_2]$ is constant) that represents the activation of the heme iron to form compound ES. Figure 5 presents an analysis of k_{cat} as a function of temperature based on the Arrhenius equation, $k = Ae^{-E_a/RT}$. The fit shown in Figure 5 is from the linearized form $\ln k = -E_a/RT + \ln A$. Here the parameter A is defined as the pre-exponential or Arrhenius factor. E_a is called the activation energy, and R is the universal gas constant. Figure 5 shows that the plot of $\ln k$ against $1/T$ is reasonably approximated by a straight line with slope equal to $-E_a/R$ and intercept equal to $\ln A$. The slope of the line found from the fit corresponds to an activation energy of $E_a = 44$ kJ/mol.

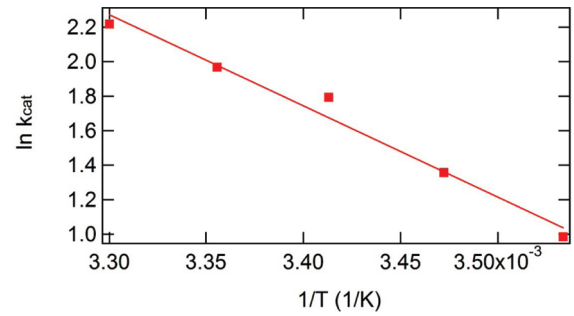

Figure 5. Plot of $\ln(k_{cat})$ vs $1/T$ with a fit to a line according to the Arrhenius equation $\ln k_{cat} = -E_a/RT + \ln A$. k_{cat} was obtained from the fit of the initial velocity data to eq 1.

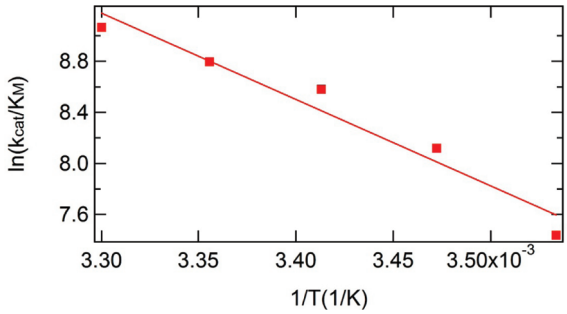

Figure 6. Linear fit of $\ln(k_{cat}/K_M)$ vs $1/T$ according to Arrhenius equation (Table 1). k_{cat}/K_M is sometimes called the efficiency of the enzyme.

TABLE 2: Calculated Gibbs Free Energies

compound	$G_{r,M}$ (kJ/mol)
Disproportionation	
TCPR	−93.696
TCP^+	−94.036
TCP^-	−94.156
Nucleophilic Attack of Radical	
TCPR	−93.642
TCPR + H_2O	−106.80
Nucleophilic Attack of Cation	
TCPRC	−93.889
TCPRC + H_2O	−104.64
Formation of Quinone	
DCQ	−91.377
HCl	−47.081
H_2O	−48.173

Figure 6 shows a plot of the logarithm of $\ln(k_{cat}/K_M)$ as a function of $1/T$. Although k_{cat}/K_M in the Michaelis−Menten scheme is a second-order rate constant related to enzymatic efficiency when substrate concentration is high, the phenomenological expression according to eq 1 is proportional to $k_2k_3/(k_2 + k_3)$, which represents the combined rate constant for substrate oxidation. Figure 6 shows that the activation energy for this process is $E_a = 56.3$ kJ/mol.

Using DFT calculations, the change in Gibbs free energy for each step of the two pathways shown in Figure 2 were calculated. Table 2 provides the calculated Gibbs free energy for each of the reaction participants in the proposed mechanism. According to the reactions, the first mechanism after the formation of a radical involves disproportionation (−0.8 kJ/mol) followed by nucleophilic attack of a cation by water (+37.4 kJ/mol). The second mechanism involves nucleophilic attack of a radical by water (+35.0 kJ/mol) followed by electron transfer (+1.7 kJ/mol). Thus, the net combined barrier height is calculated to be +36.6 and +36.7 kJ/mol for the left and right side pathways shown in Figure 2, respectively. The final step involving rearrangement to form the product 2,6-DCQ is exergonic with $\Delta_{quinone}G^o = -33.8$ kJ/mol.

Discussion

The analysis of the temperature dependence of the rate constants in the peroxidase scheme provides activation energies and mechanistic information on the steps leading to catalysis in DHP A. We have used 2,4,6-TCP as a substrate because it is more soluble than the native substrate, 2,4,6-TBP. First we consider secondary reactions that occur subsequent to the rate constants analyzed here. Second, we will discuss the interpretation of the activation energies of the rate constants, k_1, k_2, and k_3 in the peroxidase kinetic scheme. Next, we will discuss 2,6-DCQ product formation via a radical pathway, which appears to be rapid compared to any subsequent secondary reactions, and finally we present DFT calculations to address the mechanism of the disproportion of radicals to give the product.

SCHEME 1: Rate Scheme for Peroxidase Catalysis

$$DHP + H_2O_2 \xrightarrow{k_1} Cmp\ ES + H_2O$$

$$Cmp\ ES + XAOH \xrightarrow{k_2} Cmp\ II + A^{\cdot}$$

$$Cmp\ II + XAOH \xrightarrow{k_3} DHP + A^{\cdot}$$

We have identified a second reaction on longer time scales, which depletes the product 2,6-DCQ. This reaction is highly activated and has a negligible rate below 20 °C. It is approximately one order of magnitude slower than product formation even at the highest temperature. It has been shown elsewhere, and we have independently confirmed, that the second process is the reaction of 2,6-DCQ with H_2O_2 to produce 3-hydroxy-2,6,-DCQ, which proceeds even uncatalyzed in solution.[36] Although the further reactions of 2,6-DCQ do not interfere with the analysis presented here, they are of interest as steps on the path to the total dechlorination of 2,4,6-TCP and will be considered elsewhere. Figure 3 shows that these processes are significant only at $T > 20$ °C. However, since the initial rate constant for 2,4,6-TCP oxidation also increases over this same temperature range, the separation of time scales between the first and the subsequent steps is maintained such that the initial rate approximation still holds for the determination of the enzyme kinetic parameters. The formation of a less active form of DHP A, known as compound RH, is a second process that occurs on a slower time scale.[12] The inactivation of catalyst has also been considered in a kinetic model for oxidation of 2,4,6-TCP by Fe(III) meso-tetra(4-sulfonatophenyl)porphine that has strong parallels with DHP A catalysis.[36] Specifically, there is a slow process (conversion to RH) that alters catalytic efficiency of the catalyst without necessarily completely abolishing that activity.

The phenomenological analysis in terms of a Michaelis−Menten kinetic scheme provides insight into the two fundamental processes required for catalysis by DHP. The catalytic rate constant, k_{cat}, is apparently proportional to k_1, the rate constant for formation of compound ES, the first active species. The efficiency, k_{cat}/K_M, is proportional to the overall substrate oxidation rate constant $k_2k_3/(k_2 + k_3)$. The oxidized substrate rapidly loses H^+ to become a 2,4,6-trichlorophenoxy radical (2,4,6-TCPR). The radical can react by disproportionation to form 2,4,6-TCP and 2,4,6-trichlorophenoxy radical cation (2,4,6-TCPRC). Here we do not consider the possibility that a second electron transfer to the heme iron by 2,4,6-TCPR immediately leads to product but rather follows the well-established precedent in the peroxidase literature shown in Scheme 1 that the mechanism consists of two one-electron processes similar to the peroxidase family of enzymes.[37] Previous consideration of a two-electron model for DHP was an attempt to rationalize the hypothesis that the substrate binding site is in the distal pocket.[27,28] However, we now know that the distal pocket is an inhibitor binding site and the substrate binding site is external as is commonly observed in peroxidases.[1,3,38−40]

According to the mechanism in Scheme 1, the rate constant, k_1, is a bimolecular rate constant for the formation of compound

ES. The temperature dependence of the pseudofirst-order rate constant, $k_1[H_2O_2]$, arises primarily from the H_2O_2 binding and activation steps required to break the O−O bond. The distal histidine, H55, acts as an acid−base catalyst for these steps. The energy barrier of 44 kJ/mol determined from the Arrhenius analysis applies to the bond-breaking step.

The rate constants k_2 and k_3 are bimolecular rate constants that represent the combination of the diffusion rate constant, k_d, for formation of the enzyme−substrate complex and the electron transfer rate constant, $k_{ET}^{ES,II}$, from substrate to compounds ES and II, respectively.[41]

$$k_{2,3} = k_d/(1 + K_D k_d/k_{ET}^{ES,II}) \quad (2)$$

Here, K_D is the dissociation equilibrium constant, where $K_D = k_{-d}/k_d$. The electron transfer barrier height has a major contribution from the outer sphere reorganization energy, λ, which has been estimated to be in the range of 0.5−1.25 eV for peroxidases.[41,42] If the electron transfer driving force were $\varepsilon = 0$ and the reorganization energy were 1.25 eV, then the barrier height would be $E = (\lambda - \varepsilon)^2/4\lambda = 0.375$ eV. This is a maximal value since smaller values of the energy gap, ε, or reorganization energy, λ, will decrease E. On the basis of this estimate, electron transfer can only account for part of the 0.58 eV (56 kJ/mol) barrier height obtained from the kinetic analysis of the Michaelis−Menten equations, and the diffusion rate constant, k_d, may be rate limiting. However, it is reasonable to assume that k_d increases with temperature. Hence, the origin of the kinetic effect is likely to arise from subsequent diffusion-controlled steps such as disproportionation and attack by water to produce the quinone product (Figure 2).

The unusual oxidation kinetics of 2,4,6-TCP by metalloporphyrins arise from the fact that the catalyst concentration determines the amount of oxidized product but not the rate of oxidation.[36] This type of behavior also suggests that the electron transfer from substrate to catalyst (i.e., heme iron or tyrosine) is not rate limiting. The catalyst concentration may be a limiting reagent due to diffusion control as well as other factors such as inactivation by conversion to a less active form. This type of process is not entirely unexpected for reactions involving strong oxidants such as H_2O_2. Nonetheless, it is consistent with rate-limiting steps elsewhere in the sequence of steps that lead to product.

Figure 2 shows two pathways that involve attack by H_2O, either on the radical or the radical cation, to displace chloride. DFT calculations have been employed to determine which of the reaction pathways in Figure 2 occurs by calculating the change in Gibbs free energy for each step. First, the analysis for the disproportionation reaction yields $\Delta_{disprop}G^o = -0.8$ kJ/mol followed by an attack on the cation radical, $\Delta_{phenoxy\_cat}G^o = +37.4$, to lead to an overall energy barrier of +36.6 kJ/mol shown as the blue pathway in the energy level diagram in Figure 7. The alternative pathway consists of attack on the phenoxy radical by a water with a free energy change of $\Delta_{phenoxy\_rad}G^o = +35.0$ kJ/mol followed by electron transfer, $\Delta_{elec\_trans}G^o = +1.7$ kJ/mol, to give an overall energy barrier of +36.7 kJ/mol (shown as the red pathway in Figure 7. Although the overall barrier heights are so similar that the two pathways appear equally likely, Figure 7 makes it clear that disproportionation will dominate in a thermodynamic sense. Since water is present in a much greater concentration than the substrate, required for the bimolecular disproportionation, there is still a kinetic issue to consider. Given the consideration above, the electron transfer

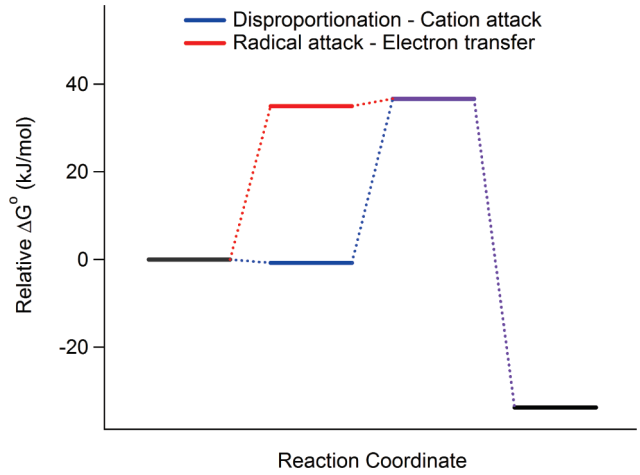

Figure 7. Energy level diagram based on DFT calculations.

from the heme (or amino acid radicals in the protein) is unlikely to account for the measured barrier heights in the Arrhenius kinetic analysis. Therefore, we suggest that the calculated barrier height of 36.6 kJ/mol is the dominant contribution to the measured barrier height of 56 kJ/mol for k_{cat}/K_M. Finally, we propose the hypothesis that the solution portion of the reaction consists of a disproportionation followed by attack of a phenoxy cation by water. Although we have given a complete analysis of the fundamental rate constants in terms of a pseudo-Michaelis−Menten scheme and demonstrated saturation, our analysis suggests that the rate-limiting steps for product formation may occur apart from the enzyme itself.

Conclusion

DHP is a unique dual function enzyme. Since it functions as both a hemoglobin and a dehaloperoxidase, it has features that distinguish it from other peroxidases. Two specific unique features are the internal binding site and a switch in function that may be linked to the flexibility of H55. To understand the activation energy for the various steps in the oxidation of substrate, we have measured the temperature dependence of the oxidation of 2,4,6-TCP to 2,6-DCQ. We applied the analysis of Dunford[26] and compared it to a Michaelis−Menten analysis to show that the rate constants, k_1, k_2, and k_3, of the ping-pong mechanism can be understood in a mechanism that gives saturation of the rate at a high substrate concentration. This type of kinetic result, which is valid for DHP, is distinct from enzymes such as HRP, which have very large k_1 and do not exhibit saturation. On the basis of the fit to an Arrhenius model, we were able to understand the temperature dependence of phenomenological k_{cat} and k_{cat}/K_M, which correspond to $k_1[H_2O_2]$ and $k_2k_3/(k_2 + k_3)$, respectively. The activation energies are 44 and 56 kJ/mol, respectively, for these two processes. The rate-limiting process is $k_2k_3/(k_2 + k_3)$, which has an activation energy that is fairly typical for chemical reactions. An anecdotal rule of thumb suggests that the rate constant for many diffusion-controlled reactions increases by a factor of 2 for each 10 °C, which corresponds to an activation energy of 54 kJ/mol. The rate constant for substrate oxidation in DHP is close to that value, probably because of the diffusion-controlled nature of the solution reactions involving the radical XAO• that leads to product formation.

We have analyzed the mechanism of the respective steps to understand the origins of the activation energy. The rate constant for the formation of the compound ES, $k_1[H_2O_2]$, reflects the rate-limiting step in the catalytic rearrangement of H_2O_2 bound

to the heme iron followed by electron transfer from a tyrosine. The second and third processes, $k_2k_3/(k_2 + k_3)$, both result in oxidation of substrate but involve both diffusion to the active site and electron transfer. Although k_2 and k_3 are nominally electron transfer steps that generate the radical intermediate, the observed rate constant appears to be dominated by the diffusional dissociation from the binding site and subsequent attack water. The analysis suggests a dominant role for a bimolecular solution component in the kinetics of substrate oxidation by DHP and has implications for the mechanism of the entire peroxidase family.

Acknowledgment. S.F. and M.K.T. were supported by Army Research Office Grant 52278-LS. H.M. thanks North Carolina State University for financial assistance. We thank Accelrys, Inc. for use of the DMol3 DFT code.

Supporting Information Available: Derivation of eq 1. This material is available free of charge via the Internet at http://pubs.acs.org.

References and Notes

(1) Thompson, M. K.; Davis, M. F.; de Sorrano, V.; Howes, B. D.; Smulevich, G.; Franzen, S. *Biophys. J.* **2010**, *99*, 1586−1595.
(2) LaCount, M. W.; Zhang, E.; Chen, Y. P.; Han, K.; Whitton, M. M.; Lincoln, D. E.; Woodin, S. A.; Lebioda, L. *J. Biol. Chem.* **2000**, *275*, 18712.
(3) Davis, M. F.; Bobay, B. G.; Franzen, S. *Biochemistry* **2010**, *49*, 1199.
(4) de Serrano, V.; Chen, Z.; Davis, M. F.; Franzen, S. *Acta Crystallogr., Sect. D: Biol. Crystallogr.* **2007**, *D63*, 1094.
(5) Chen, Z.; De Serrano, V.; Betts, L.; Franzen, S. *Acta Crystallogr., Sect. D: Biol. Crystallogr.* **2009**, *65*, 34.
(6) Nicoletti, F. P.; Thompson, M. K.; Howes, B. D.; Franzen, S.; Smulevich, G. *Biochemistry* **2010**, *49*, 1903.
(7) Han, K.; Woodin, S. A.; Lincoln, D. E.; Fielman, K. T.; Ely, B. *Mar. Biotechnol.* **2001**, *3*, 287.
(8) de Serrano, V.; D'Antonio, J.; Franzen, S.; Ghiladi, R. A. *Acta Crystallogr., Sect. D: Biol. Crystallogr.* **2010**, *66*, 529.
(9) D'Antonio, J.; D'Antonio, E. L.; Thompson, M. K.; Bowden, E. F.; Smirnova, T.; Franzen, S.; Ghiladi, R. A. *Biochemistry* **2010**, *49*, 6600.
(10) Ator, M. A.; Montellano, O. D. *J. Biol. Chem.* **1987**, *262*, 1542.
(11) Sharp, K. H.; Moody, P. C. E.; Brown, K. A.; Raven, E. L. *Biochemistry* **2004**, *43*, 8644.
(12) Feducia, J.; Dumarieh, R.; Gilvey, L. B. G.; Smirnova, T.; Franzen, S.; Ghiladi, R. A. *Biochemistry* **2009**, *48*, 995.
(13) Witting, P. K.; Mauk, A. G.; Lay, P. A. *Biochemistry* **2002**, *41*, 11495.
(14) Hildebrand, D. P.; Lim, K. Y.; Rosell, F. I.; Twitchett, M. B.; Wan, L. G.; Mauk, A. G. *J. Inorg. Biochem.* **1998**, *70*, 11.
(15) Wan, L. L.; Twitchett, M. B.; Eltis, L. D.; Mauk, A. G.; Smith, M. *Proc. Natl. Acad. Sci. U.S.A.* **1998**, *95*, 12825.
(16) Matsui, T.; Ozaki, S.; Watanabe, Y. *J. Am. Chem. Soc.* **1999**, *121*, 9952.
(17) Lardinois, O. M.; de Montellano, P. R. O. *J. Biol. Chem.* **2001**, *276*, 23186.
(18) Tsaprailis, G.; English, A. M. *J. Biol. Inorg. Chem.* **2003**, *8*, 248.
(19) Wright, P. J.; English, A. M. *J. Am. Chem. Soc.* **2003**, *125*, 8655.
(20) Harvey, P. J.; Floris, R.; Lundell, T.; Palmer, J. M.; Schoemaker, H. E.; Wever, R. *Biochem. Soc. Trans.* **1992**, *20*, 345.
(21) Yamada, K.; Shibuya, T.; Noda, M.; Uchiyama, N.; Kashiwada, A.; Matsuda, K.; Hirata, M. *Biosci. Biotechnol. Biochem.* **2007**, *71*, 2503.
(22) Dunford, H. B. *Xenobiotica* **1995**, *25*, 725.
(23) Lincoln, D. E.; Fielman, K. T.; Marinelli, R. L.; Woodin, S. A. *Biochem. Syst. Ecol.* **2005**, *33*, 559.
(24) Davidenko, T. I.; Oseychuk, O. V.; Sevastyanov, O. V.; Romanovskaya, I. I. *Appl. Biochem. Microbiol.* **2004**, *40*, 542.
(25) Franzen, S.; Chaudhary, C.; Belyea, J.; Gilvey, L.; Davis, M. F.; Sit, T. L.; Lommel, S. A. *Biochemistry* **2006**, *45*, 9085.
(26) Dunford, B. H. *Heme Peroxidases*; John Wiley and Sons: New York, 1999.
(27) Belyea, J.; Gilvey, L. B.; Davis, M. F.; Godek, M.; Sit, T. L.; Lommel, S. A.; Franzen, S. *Biochemistry* **2005**, *44*, 15637.
(28) Franzen, S.; Gilvey, L. B.; Belyea, J. L. *Biochim. Biophys. Acta* **2007**, *1774*, 121.
(29) Perdew, J. P.; Burke, K.; Ernzerhof, M. *Phys. Rev. Lett.* **1996**, *77*, 3865.
(30) Andzelm, J.; King-Smith, R. D.; Fitzgerald, G. *Chem. Phys. Lett.* **2001**, *335*, 321.
(31) Baker, J.; Kessi, A.; Delley, B. *J. Chem. Phys.* **1996**, *105*, 192.
(32) Delley, B. *J. Chem. Phys.* **1990**, *92*, 508.
(33) Delley, B. *J. Chem. Phys.* **2000**, *113*, 7756.
(34) Weinert, M.; Davenport, J. W. *Phys. Rev. B* **1992**, *45*, 13709.
(35) Andzelm, J.; Kolmel, C.; Klamt, A. *J. Chem. Phys.* **1995**, *103*, 9312.
(36) Lente, G.; Espenson, J. H. *Int. J. Chem. Kinet.* **2004**, *36*, 449.
(37) Dunford, H. B. *J. Biol. Inorg. Chem.* **2001**, *6*, 819.
(38) Davis, M. F.; Gracz, H.; Vendeix, F. A. P.; de Serrano, V.; Somasundaram, A.; Decatur, S. M.; Franzen, S. *Biochemistry* **2009**, *48*, 2164.
(39) Nienhaus, K.; Nickel, E.; Davis, M. F.; Franzen, S.; Nienhaus, G. U. *Biochemistry* **2008**, *47*, 12985.
(40) Smirnova, T. I.; Weber, R. T.; Davis, M. F.; Franzen, S. *J. Am. Chem. Soc.* **2008**, *130*, 2128.
(41) Khopde, S. M.; Priyadarsini, K. I. *Biophys. Chem.* **2000**, *88*, 103.
(42) Folkes, L. K.; Candeias, L. P. *FEBS Lett.* **1997**, *412*, 305.

JP1014516

J|A|C|S
ARTICLES

Published on Web 11/22/2010

Compound ES of Dehaloperoxidase Decays via Two Alternative Pathways Depending on the Conformation of the Distal Histidine

Matthew K. Thompson,[†] Stefan Franzen,[†] Reza A. Ghiladi,[†] Brandon J. Reeder,[¶] and Dimitri A. Svistunenko*[,¶]

Department of Chemistry, North Carolina State University, Box 8204, Raleigh, North Carolina 27695-8204, United States, and Department of Biological Sciences, University of Essex, Colchester CO4 3SQ, United Kingdom

Received July 26, 2010; E-mail: svist@essex.ac.uk

Abstract: Dehaloperoxidase (DHP) is a respiratory hemoglobin (Hb) that has been shown to catalyze the conversion of trihalophenols to dihaloquinones in the presence of hydrogen peroxide. Ferric heme states of the resting DHP and the free radical intermediates formed under H_2O_2 treatment were studied by low-temperature electron paramagnetic resonance spectroscopy in the range of reaction times from 50 ms to 2 min at three different pH values. Two high-spin ferric heme forms were identified in the resting enzyme and assigned to the open and closed conformations of the distal histidine, His55. Two free radicals were found in DHP activated by H_2O_2: the radical associated with Compound ES (the enzyme with the heme in the oxoferryl state and a radical on the polypeptide chain) has been assigned to Tyr34, and the other radical has been assigned to Tyr38. The Tyr34 radical is formed with a very high relative yield (almost 100% of heme), atypical of other globins. High-performance liquid chromatography analysis of the reaction products showed a pH-dependent formation of covalent heme-to-protein cross-links. The stable DHP Compound RH, formed under H_2O_2 in the absence of the trihalophenol substrates, is proposed to be a state with the ferric heme covalently cross-linked to Tyr34. A kinetic model of the experimental data suggests that formation of Compound RH and formation of the Tyr38 radical are two alternative routes of Compound ES decay. Which route is taken depends on the conformation of His55: in the less populated closed conformation, the Tyr38 radical is formed, but in the major open conformation, Compound ES decays, yielding Compound RH, a product of safe termination of the two oxidizing equivalents of H_2O_2 when no substrate is available.

1. Introduction

Dehaloperoxidase hemoglobin (DHP), originally isolated from the terebellid polychaete *Amphitrite ornata*, is the first characterized hemoglobin known to have natural peroxidase function. When activated with hydrogen peroxide, DHP catalyzes the overall two-electron oxidation of 2,4,6-trihalophenol (2,4,6-TXP) to the corresponding 2,6-dihaloquinone (Scheme 1).[1] *A. ornata* cohabits benthic ecosystems with organisms such as *Thelespus crispis* and *Notomastus lobatus* that secrete brominated aromatics as predatory defense mechanisms.[2−4] To survive the toxic buildup, the coelomic oxygen-binding hemoglobin in *A. ornata* has evolved to perform a dehaloperoxidase function that results in a decrease in the concentration of toxic 2,4,6-TXP. DHP has a typical globin fold but a low amino acid sequence homology with other members of the globin family.[5] Two isoforms of DHP are found in *A. ornata* (DHP A and DHP B), both of which can bind oxygen reversibly.[6] The occurrence of globins in annelids is known to occur in two general contexts. First, a monomeric hemoglobin is observed in the coelom. Second, a giant hemoglobin is found in the tentacles and other compartments outside the coelom.[7] As a peroxidase, DHP acts 2 orders of magnitude faster than myoglobin (Mb)[8] and only an order of magnitude slower than horseradish peroxidase (HRP).[9] Thus, DHP lies in a unique median, sharing structural homology with globins and peroxidase activity with HRP.

Six available X-ray structures of DHP[5,10−12] demonstrate that the distal histidine, His55, may adopt an open (outside the distal pocket) or closed (inside the pocket) conformation. This high flexibility of the distal histidine has been implicated in the mechanism of switching between oxygen storing and peroxidase activity.[11] The first X-ray crystal structure of DHP showed the substrate analogue 4-iodophenol bound in the distal pocket with His55 pushed into the open conformation.[5] This led to the proposal that the distal pocket is the substrate-binding site.

Scheme 1

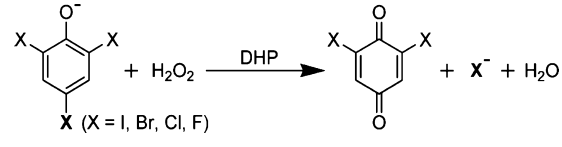

[†] North Carolina State University.
[¶] University of Essex.

(1) Chen, Y. P.; Woodin, S. A.; Lincoln, D. E.; Lovell, C. R. *J. Biol. Chem.* **1996**, *271*, 4609–4612.

However, structural, spectroscopic, and kinetic data[13−15] suggest the existence of an external binding site, while binding in the internal site, in fact, inhibits peroxidase function. Recently, Thompson et al. demonstrated that DHP exhibits nonclassical competitive inhibition, in which the inhibitor and substrate pair communicate between the internal and external binding sites, respectively, through two conformations of the distal histidine.[16]

Upon activation by H_2O_2, DHP is converted to the oxoferryl heme state, with a free radical on the globin assigned to a tyrosine.[17] This state of DHP was interpreted as Compound ES by analogy with cytochrome *c* peroxidase (C*c*P)[18] and was implicated in substrate oxidation. In the absence of trihalophenol substrates, Compound ES evolves stoichiometrically into a new optically detectable stable species termed Compound RH (*reversible heme* intermediate). This compound has not been reported for other heme proteins. It has an optical spectrum more characteristic of the ferric state of the heme, rather than the oxoferryl, but with a red shift of the Soret band.[17] Interestingly, Compound RH can be reduced by external reductants to completely functional ferrous DHP, which combines with oxygen to give Compound III (an oxyferrous state).[17]

The electron paramagnetic resonance (EPR) spectra of the radical associated with Compound ES were shown to be different when the activation was conducted at pH 5 and pH 7.[17] This raises the question of whether the structural properties of Compound ES change with pH or a parallel process is leading to formation of a different free radical on the enzyme. This paper is aimed at elucidation of the mechanism of free radical formation on DHP when the enzyme is treated with H_2O_2. Herein we show that two different tyrosyl radicals, Tyr34$^{\bullet}$ and Tyr38$^{\bullet}$, are responsible for the pH dependence of the free radical EPR spectrum, but only the Tyr34$^{\bullet}$ radical is associated with Compound ES. The other radical is formed during one of the two alternative routes of Compound ES decay.

2. Experimental Section

2.1. Materials. Buffer salts were purchased from Fisher Scientific. All other reagents were purchased from Sigma-Aldrich and used without further purification. DHP A[6] was studied in this paper.

2.2. 6XHis-Tagged DHP A Growth and Purification. Recombinant his-tagged wild-type DHP protein was expressed in *Escherichia coli* and purified as previously described.[14] All experiments in this report were conducted in 100 mM potassium phosphate buffer.

2.3. Hydrogen Peroxide Solutions. The H_2O_2 solution was prepared from a 30% reagent grade H_2O_2 solution from Fisher Chemicals to a final concentration of 15 mM for the stock solution. Aliquots of 15 mM H_2O_2 stock solution in 100 mM potassium phosphate buffer at pH 7 were stored in cryotubes at liquid nitrogen temperature. The cryotubes were thawed and diluted in 100 mM potassium phosphate buffer shortly before use. One cryotube was used for making no more than three or four freeze-quenched samples, which normally took no longer than 1 h. This protocol was followed in order to maintain the peroxide concentration constant during several hours of sample preparation sessions.

2.4. EPR Sample Preparation. Wilmad SQ EPR tubes (Wilmad Glass, Buena, NJ) were used for EPR samples. To minimize the effect that slightly different tube sizes might have on the quantitative results, only tubes with outer diameter 4.05 ± 0.07 mm and inner diameter 3.12 ± 0.04 mm (mean $\pm$ range) were selected for use. When a set of samples was prepared by freezing the same protein solution in the selected Wilmad SQ tubes, the random error in the EPR signal intensities was determined to be very low (1−3%).

The rapid freeze-quenching (RFQ) of the EPR samples was performed by a combined use of an Update Instrument (Madison, WI) mixing machine and a home-built apparatus for freezing the ejected mixtures on the surface of a rapidly rotating aluminum disk kept at liquid nitrogen temperature (see Supporting Information, SI.Methods.1). The freezing time achievable by this apparatus was calibrated by the method described elsewhere[19] based on azide binding to horse metmyoglobin (metMb), where the rate constant of the binding was determined optically by an Applied Photophysics SX18MV diode array spectrophotometer. DHP and H_2O_2 solutions were kept at 4 °C in the Update Instrument freeze-quenching apparatus and were mixed in the mixing chamber kept just outside the ice bath (at ca. 15 °C). The samples corresponding to the time points in the range of 50−300 ms were made using aging hoses of variable length. For longer reaction times, a delay was used between two pushes of the ram of the freeze-quenching apparatus. The sample frozen on the cold disk was transferred to a funnel attached to an EPR tube and packed with a Teflon-tipped stainless steel rod. The packing factor was found to be persistently close to 50% ($\pm$4%). The freeze-quenched samples, when packed, were of variable length, sometimes shorter than the active zone of the resonators. This affected the intensity of the EPR signals. To make a correction for this effect, we used the sample length-specific coefficients obtained as described in the Supporting Information (SI.Methods.2).

2.5. EPR Spectra Measurement and Processing. All EPR spectra were measured on a Bruker EMX EPR spectrometer (X-band) at a modulation frequency of 100 kHz. Accurate *g*-values were obtained using the built-in microwave frequency counter and a 2,2-diphenyl-1-picrylhydrazyl powder standard, the *g*-value for which is $g = 2.0037 \pm 0.0002$.[20] A spherical high-quality Bruker resonator SP9703 and an Oxford Instruments liquid helium system

(2) Woodin, S. A.; Marinelli, R. L.; Lincoln, D. E. *J. Chem. Ecol.* **1993**, *19*, 517–530.
(3) Fielman, K. T.; Woodin, S. A.; Walla, M. D.; Lincoln, D. E. *Mar. Ecol.: Prog. Ser.* **1999**, *181*, 1–12.
(4) Lincoln, D. E.; Fielman, K. T.; Marinelli, R. L.; Woodin, S. A. *Biochem. Systemat. Ecol.* **2005**, *33*, 559–570.
(5) LaCount, M. W.; Zhang, E.; Chen, Y. P.; Han, K.; Whitton, M. M.; Lincoln, D. E.; Woodin, S. A.; Lebioda, L. *J. Biol. Chem.* **2000**, *275*, 18712–18716.
(6) Han, K.; Woodin, S. A.; Lincoln, D. E.; Fielman, K. T.; Ely, B. *Mar. Biotechnol. (NY)* **2001**, *3*, 287–292.
(7) Mangum, C. P.; Woodin, B. R.; Bonaventura, C.; Sullivan, B.; Bonaventura, J. *Comp. Biochem. Physiol.* **1975**, *51A*, 281–294.
(8) Osborne, R. L.; Coggins, M. K.; Walla, M.; Dawson, J. H. *Biochemistry* **2007**, *46*, 9823–9829.
(9) Belyea, J.; Gilvey, L. B.; Davis, M. F.; Godek, M.; Sit, T. L.; Lommel, S. A.; Franzen, S. *Biochemistry* **2005**, *44*, 15637–15644.
(10) de Serrano, V.; Chen, Z.; Davis, M. F.; Franzen, S. *Acta Crystallogr. D: Biol. Crystallogr.* **2007**, *63*, 1094–1101.
(11) Chen, Z.; de Serrano, V.; Betts, L.; Franzen, S. *Acta Crystallogr. D: Biol. Crystallogr.* **2009**, *65*, 34–40.
(12) de Serrano, V.; D'Antonio, J.; Franzen, S.; Ghiladi, R. A. *Acta Crystallogr. D: Biol. Crystallogr.* **2010**, *66*, 529–238.
(13) Nienhaus, K.; Nickel, E.; Davis, M. F.; Franzen, S.; Nienhaus, G. U. *Biochemistry* **2008**, *47*, 12985–12994.
(14) Davis, M. F.; Gracz, H.; Vendeix, F. A.; de Serrano, V.; Somasundaram, A.; Decatur, S. M.; Franzen, S. *Biochemistry* **2009**, *48*, 2164–2172.
(15) Davis, M. F.; Bobay, B. G.; Franzen, S. *Biochemistry* **2010**, *49*, 1199–206.
(16) Thompson, M. K.; Davis, M. F.; de Serrano, V.; Nicoletti, F. P.; Howes, B. D.; Smulevich, G.; Franzen, S. *Biophys. J.* **2010**, *99*, 1586–1595.
(17) Feducia, J.; Dumarieh, R.; Gilvey, L. B.; Smirnova, T.; Franzen, S.; Ghiladi, R. A. *Biochemistry* **2009**, *48*, 995–1005.
(18) Sivaraja, M.; Goodin, D. B.; Smith, M.; Hoffman, B. M. *Science* **1989**, *245*, 738–740.
(19) Cherepanov, A. V.; De Vries, S. *Biochim. Biophys. Acta* **2004**, *1656*, 1–31.
(20) Weil, J. A.; Bolton, J. R.; Wertz, J. E. *Electron paramagnetic resonance: Elementary theory and practical applications*; John Wiley & Sons, Inc.: New York, 1994.

were used to measure the low-temperature EPR spectra. The EPR spectra of the blank samples (frozen water) were subtracted from the EPR spectra of the enzyme samples to eliminate the baseline caused by the resonator's walls, quartz insert, or quartz EPR tube.

The freeze-quenched control samples were obtained by mixing a DHP solution with buffer. The $g_{||} = 2$ component of the high-spin (HS) ferric heme signal, obtained from the DHP control samples, has been subtracted from the EPR spectra of the protein radicals formed under peroxide treatment using individual coefficients of subtraction for each spectrum as described elsewhere.[21] Thus, the free radical spectra presented in this paper are not contaminated with the HS ferric heme DHP EPR signal.

To measure intensities of overlapping EPR signals in a composite EPR spectrum, the procedure of spectral subtraction with a variable coefficient was used.[22,23] Different EPR samples are measured at slightly different microwave frequencies because of the variation in the physical characteristics of the EPR tubes. Therefore, the same EPR signal in two different EPR samples can appear at slightly different values of the magnetic field. To increase the accuracy of the spectral subtraction, this error has been corrected by shifting each experimental spectrum to the left or to the right along the magnetic field in accordance with the difference between the frequency used to record an individual spectrum and a frequency value chosen as a standard for the whole array of experimental spectra. Thus, a good alignment of all EPR spectra on the magnetic field axis has been achieved. Figure S5 (Supporting Information, SI.Methods.3) illustrates the effect of the spectral shifting procedure on a set of spectra obtained from different samples. It should be noted that the spectral position correction based on the microwave frequency value will not have an accurate outcome (e.g., as shown in Figure S5) if the magnetic field is drifting. It normally takes several hours for the EMX spectrometer to achieve stable magnetic field characteristics. Therefore, all our EPR experiments were performed after the spectrometer had a considerable warm-up time (2−3 days).

2.6. EPR Spectra Simulation. Tyrosyl radical EPR spectra were simulated using SimPow6.[24] The Tyrosyl Radical Spectra Simulation Algorithm (TRSSA)[25] was used to generate the EPR spectral simulation parameters on an input of only two parameters, the phenoxyl ring rotation angle and the spin density on atom C1 of the radical.

2.7. Assignment of Tyrosyl Radicals to Specific Tyrosine Residues. The Phenol Ring Rotation Angle Database[26] has been used to identify the tyrosine residues in DHP with the same, or similar, rotational conformation of the phenol group (the ring rotation angle) as the conformation determined from the simulation of the tyrosyl radical EPR spectrum.

2.8. Kinetic Modeling. Time dependences of the concentration of total ferric heme state and total free radical, at three different pH values, were modeled using Microsoft Office Excel 2007, while the Excel Solver tool was used to optimize the rate constants by finding the minimum of the average distance between experimental and calculated values. Three average distance parameters attributable to different pH value series were added together to a single value which has been minimized during global optimization.

2.9. Reverse-Phase HPLC. The reverse-phase HPLC method for the identification of heme-protein cross-links was adapted from that of Osawa and Korzekwa.[27] DHP (80 μM) was reacted with H_2O_2 (0−1600 μM) in 15 mM sodium acetate buffer (pH 5.0) or sodium phosphate buffer (pH 6.0 or 7.0). The reaction was allowed to stand for at least 2 h prior to HPLC analysis. Samples were analyzed on an Agilent HP1100 HPLC equipped with a diode array spectrophotometer and fitted with a Zorbax StableBond 300 C3 column (250 mm × 4.6 mm) with a 12 mm × 4.6 mm guard column. Solvents were (A) water containing 0.1% trifluoroacetic acid (TFA) and (B) acetonitrile containing 0.1% TFA. The gradient was initially 35% solvent B, stable for 10 min, increasing to 37% solvent B over 5 min. This was increased to 40% solvent B over 1 min and then to 43% solvent B over 10 min. The flow rate was 1 mL min^{-1}, and the temperature was 25 °C. The concentration of heme-to-protein cross-linking was determined by integrating the heme-to-protein cross-linked HPLC peak at 400 nm and comparing the area to a standard.

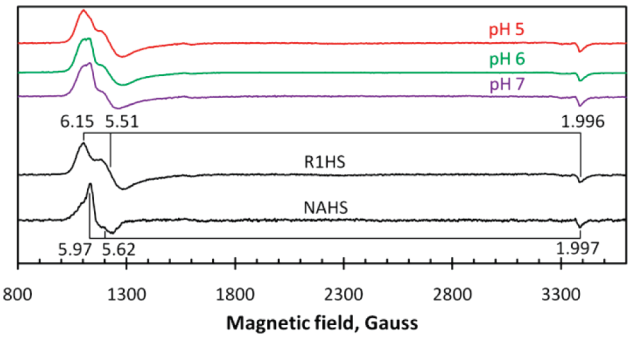

Figure 1. EPR spectra of ferric DHP at different pH values and the result of their deconvolution into two individual HS ferric heme EPR signals, rhombic type 1 (R1HS) and nearly axial (NAHS). The spectra were obtained at 10 K from the samples made by freeze-quenching 80 μM DHP at the indicated pH values mixed with equal volumes of buffer to give a final concentration of 40 μM. All spectra are plotted at similar amplitudes for comparative viewing. The instrumental conditions were as follows: microwave frequency $\nu_{MW} = 9.471$ GHz, microwave power $P = 3.18$ mW, modulation frequency $\nu_m = 100$ kHz, modulation amplitude $A_m = 5$ G, time constant $\tau = 82$ ms, scan rate $\upsilon = 22.6$ G s^{-1}, number of scans per spectrum NS = 1. The principal g-factors of the signals R1HS and NAHS are indicated.

3. Results

3.1. Heme States in the Resting (Ferric) Enzyme. The EPR spectra of rapidly freeze-quenched DHP in the resting (ferric) state at three different pH values are shown in Figure 1. While no low-spin ferric heme forms are seen in the spectra, the EPR signal of the HS form in the $g = 6$ region shows a slightly different line shape at pH 5, 6, and 7. The differences were used to deconvolute the signal into two components: a rhombic component, with the g-values g_1 and g_2 well separated (R1HS, rhombic type 1 high spin), and a nearly axial component, i.e., when the difference between g_1 and g_2 is small (NAHS, nearly axial high spin). The R1HS EPR signal ($g_1 = 6.15$, $g_2 = 5.51$, $g_3 = 1.996$) was obtained as a difference spectrum, R1HS = (pH 5) − 0.38(pH 7). The NAHS signal ($g_1 = 5.97$, $g_2 = 5.62$, $g_3 = 1.997$) was constructed as NAHS = (pH 7) − 0.69(pH 5). The coefficients of the subtractions were determined empirically to yield the best pure line shapes of the individual EPR signals.

The relative concentrations of the heme states responsible for the two signals, R1HS and NAHS, were estimated by measuring the relative intensities of the signals in the DHP spectra at pH 5, 6, and 7 and expressing them in common units

(21) Svistunenko, D. A.; Reeder, B. J.; Wankasi, M. M.; Silaghi-Dumitrescu, R.-L.; Cooper, C. E.; Rinaldo, S.; Cutruzzolà, F.; Wilson, M. T. *Dalton Trans.* **2007**, 840–850.
(22) Svistunenko, D. A. *Biochim. Biophys. Acta* **2005**, *1707*, 127–155.
(23) Svistunenko, D. A.; Davies, N.; Brealey, D.; Singer, M.; Cooper, C. E. *Biochim. Biophys. Acta* **2006**, *1757*, 262–272.
(24) Nilges, M. J.; Matteson, K.; Bedford, R. L. In *ESR Spectroscopy in Membrane Biophysics*; Hemminga, M. A., Berliner, L., Eds.; Biological Magnetic Resonance *27*; Springer: New York, 2007; Appendix 2.
(25) Svistunenko, D. A.; Cooper, C. E. *Biophys. J.* **2004**, *87*, 582–595.
(26) Svistunenko, D., 2004, http://privatewww.essex.ac.uk/~svist/lev1/tyrdb/home.shtml.
(27) Osawa, Y.; Korzekwa, K. *Proc. Natl. Acad. Sci. U.S.A.* **1991**, *88*, 7081–7085.

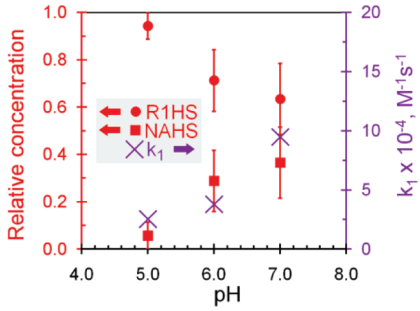

Figure 2. Relative concentration (left axis) of the two HS ferric heme forms in DHP, rhombic type 1 (R1HS) and nearly axial (NAHS), at three different pH values. The error bars indicate maximal deviation from the average determined on the basis of three independent measurements. The concentration units are normalized to give the total concentration equal to unity. Also shown are the values of the rate constants k_1 (Compound ES formation, right axis) that have been obtained from the kinetic model described in section 3.2.5.

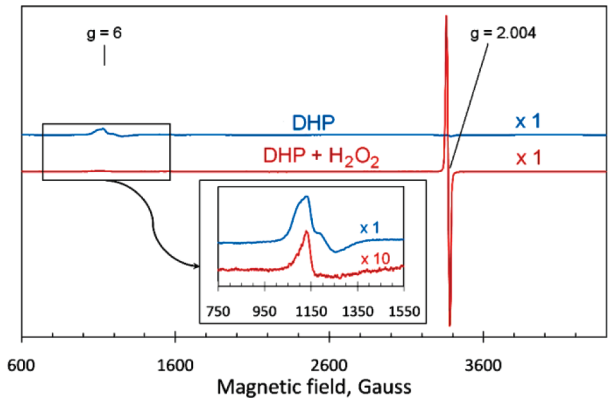

Figure 3. EPR spectra of 40 μM DHP reacted with 150 μM H_2O_2 and freeze-quenched 0.5 s after mixing (all concentrations are final, pH 7). The control sample was obtained by mixing equal volumes of 80 μM DHP and pH 7 buffer and freeze-quenching 50 ms after mixing. Inset shows the g = 6 area in greater detail, with the H_2O_2-treated spectrum magnified by a factor of 10. The spectra were recorded at 10 K at the same instrumental conditions as specified in the Figure 1 legend.

when the values of second integrals of R1HS and NAHS were taken into account. The result is presented in Figure 2, which shows a stoichiometric transition of R1HS into NAHS as pH increases.

3.2. DHP Reacting with H_2O_2. When hydrogen peroxide is added to DHP, the paramagnetic ferric heme state is transformed to the EPR-silent oxoferryl form, leading to a decrease of the g = 6 signal intensity in the EPR spectrum. At the same time, a protein-bound free radical is formed, resulting in the appearance of a g = 2.004 EPR signal (Figure 3). This state of DHP with a protein-bound free radical was first observed by Feducia et al. and interpreted as Compound ES.[17]

3.2.1. Concentration of the Ferric Heme and the Free Radicals as a Function of Reaction Time. Kinetic dependences of the ferric heme state and the free radical concentrations were studied in DHP reacting with H_2O_2 at three different pH values (Figures 4 and 5).

The concentrations of the ferric heme state were measured from the intensities of the HS ferric heme EPR signal and, in the absence of detectable low-spin forms, were assumed to reflect the total ferric heme concentration. The average intensity of the HS ferric heme EPR signals in the control samples (freeze-quenched on mixing with buffer containing no peroxide)

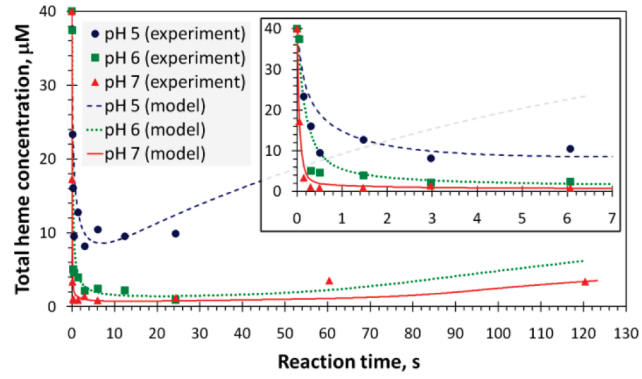

Figure 4. Kinetic dependences of total ferric heme state concentration in the course of the reaction of 40 μM ferric DHP with 120 μM H_2O_2, at pH 5, 6, and 7 (both concentrations are final). The ferric heme concentrations (symbols) were determined by EPR spectroscopy in the samples prepared by the RFQ method as described in the text. The lines are calculated from the kinetic model described in section 3.2.5.

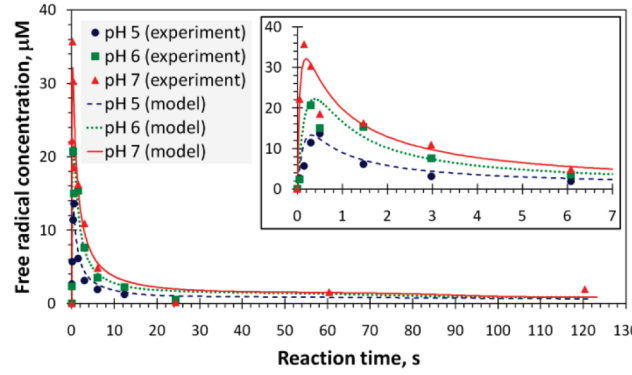

Figure 5. Kinetic dependences of total free radical concentration in the three pH series referred to in Figure 4. The EPR spectra of the free radicals detected in these series are given in Figure S6 (Supporting Information). Symbols represent the experimental results; the lines are generated by the same kinetic model used to plot the curves in Figure 4 (see section 3.2.5 for details).

was thus normalized to the initial ferric enzyme concentration determined optically (40 μM after 2-fold dilution). The small changes in the proportion of R1HS and NAHS (see section 3.2.2) were ignored in the measurements.

The total free radical concentrations were determined in common units of the second integral of the EPR spectra (Supporting Information, Figure S6, SI.Results.1), measured at low microwave power, after the g = 2 component of the HS ferric heme state (measured in the control, i.e., when no H_2O_2 was added) was subtracted as described elsewhere.[21] The subtraction coefficients for each spectrum were found from the kinetics of the HS forms shown in Figure 4. The integral values were then corrected for variable sample size, as described in section 2.4, and normalized to absolute concentration values using a Cu^{2+} concentration standard.

While reporting the "total free radical concentration" in Figure 5, we should note that the radical composition was not uniform in the series studied. The line shape of the free radical EPR signals was different in the different pH series. The line shape also changed during the reaction time. Generally, the resolution of the hyperfine structure in the free radical EPR spectrum becomes poorer as time progresses (Figure S6). In different pH series, the initial line shape persisted for different lengths of reaction time, i.e., for 0.5 s at pH 5, for 3 s at pH 6, and for 6 s at pH 7.

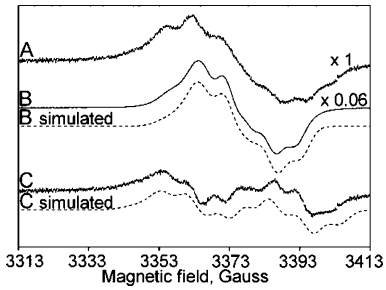

Figure 6. Line shapes of the free radical EPR spectra of the freeze-quenched samples of 40 μM DHP treated with 120 μM H_2O_2: (A) pH 5, 50 ms after mixing and (B) pH 7, 300 ms after mixing, multiplied by a factor of 0.06. The factor 0.06 was chosen empirically to construct a pure line shape of the signal C = A − B. Both the principal radical (B) and pH 5 radical (C) EPR signals were simulated as neutral tyrosyl radical spectra (dotted lines). The parameters of the simulation (Supporting Information, Tables S1 and S2) were found by TRSSA.[25]

The experimental kinetic dependences of the ferric heme and free radical at pH 5, 6, and 7 have been fitted by the dependences computed from a kinetic model (Figures 4 and 5). The model is described in section 3.2.5.

3.2.2. High-Spin Ferric Heme after H_2O_2 Addition. Although a significant decrease in the concentration of the HS ferric heme forms is seen during the reaction of DHP with H_2O_2, the relative proportion of the rhombic (R1HS) and nearly axial (NAHS) ferric heme forms after the addition of H_2O_2 is similar to the relative proportion before the addition of H_2O_2. This indicates that the two forms might be in a fast equilibrium. Two small but noticeable effects should be noted though. First, the relative concentration of the axial form is slightly higher in the samples of DHP reacting with H_2O_2 than in the resting (control) samples. Second, when the ferric heme starts to recover from the EPR-invisible oxoferryl form (e.g., 1 min after mixing, pH 7, Figure 4), a weak signal of a new rhombic HS ferric heme (type 2, R2HS) can be seen in the spectrum. It shows a slightly greater degree of rhombicity than R1HS and is characterized by the g-factors $g_1 = 6.39$ and $g_2 = 5.42$ (Supporting Information, Figure S7).

3.2.3. Identification of Two Different Hydrogen-Bonded Tyrosyl Radicals. Figure S6 demonstrates that the line shapes of the free radical EPR spectra of DHP treated with H_2O_2 are different at different pH values. The difference is particularly evident when the pH 5 and pH 7 series are compared. We used the procedure of spectral subtraction with a variable coefficient[22,23] to identify two different free radical EPR signals (Figure 6). One is present at all pH values studied and is particularly strong in the pH 7 spectra. We will refer to this EPR signal as that originating from *the principal free radical*. The other signal is generally of a much weaker intensity and is observable at pH 5 (henceforth referred to as the *pH 5 radical* signal).

The two EPR signals have been simulated as tyrosyl radical EPR spectra (Figure 6). The simulation parameters are given in the Supporting Information, Tables S1 and S2. Each of these two sets of 30 parameters has been found by TRSSA[22,25,28] when only two input parameters of the algorithm were varied. The optimal values of these two parameters for the two radicals are specified in Table 1.

Table 1. TRSSA[a] Input Parameters for the Simulation of the Tyrosyl Radical EPR Signals in Figure 6

	McConnell spin density on atom C1, ρ_{C1}	phenoxyl ring rotation angle θ, degrees[b]
principal radical (B)	0.400	45 (or 75)
pH 5 radical (C)	0.420	−8 (or −52)

[a] Tyrosyl Radical Spectra Simulation Algorithm. [b] There are always two values of rotation angle θ that give identical sets of simulation parameters.[25,29] See Supporting Information (SI.Results.2) for details.

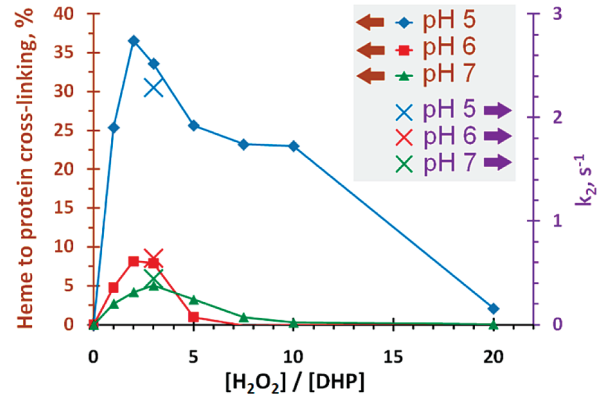

Figure 7. Effect of H_2O_2 molar excess over heme on the extent of heme-to-protein cross-link formation in 80 μM DHP (curves, left axis). The concentration of the heme-to-protein cross-links was determined by HPLC, and dependences at three different pH values are presented. Three crosses are related to the right axis and represent the rate constant k_2 of Compound ES to Compound RH conversion at the three pH values, as found from the kinetic model described in section 3.2.5.

The values of the spin density on C1 for the two radicals are both in the upper part of the range of values (0.35−0.42) for other protein-bound tyrosyl radicals.[25] This means that both tyrosyl radicals are hydrogen bonded. In fact, the value of 0.42 for the pH 5 radical is at the top of the range and indicates that the H-bond engaging this radical must be strong.

The principal tyrosyl radical, found in all three pH series, is characterized by the phenoxyl ring rotation angle of 45° or 75°. This angle in the pH 5 tyrosyl radical is either −8° or −52°. By using the Phenol Ring Rotation Angle Database,[26] an assignment of the radicals has been performed. The most likely site of the principal radical is either Tyr28 or Tyr34, and the most likely site of the pH 5 radical is Tyr38. For details of the analysis leading to this conclusion, see the Supporting Information, SI.Results.2.

3.2.4. Formation of Heme-to-Protein Cross-Links. Reverse-phase HPLC was employed to study the oxidation of the heme prosthetic group in the reaction of DHP with H_2O_2 (Supporting Information, Figure S8). The chromatograms obtained and the optical properties of the eluted fractions (Supporting Information, Figure S9) allowed identification of a DHP form in which the heme is covalently cross-linked to the globin. The H_2O_2 concentration profile of the cross-link formation is pH dependent, as shown in Figure 7.

3.2.5. Kinetic Model. The time dependences of the concentrations of total ferric heme and total free radical have been modeled (Figures 4 and 5) by calculating a kinetic evolution of ferric DHP reacting with H_2O_2. A set of 10 chemical reactions involving six reaction components was postulated:

$$\mathrm{Fe(III)} + \mathrm{H_2O_2} \xrightarrow{k_1} \bullet\mathrm{Fe(IV)} \qquad (1)$$

(28) Svistunenko, D. A.; Jones, G. A. *Phys. Chem. Chem. Phys.* **2009**, *11*, 6600–6613.
(29) Svistunenko, D. A.; Wilson, M. T.; Cooper, C. E. *Biochim. Biophys. Acta* **2004**, *1655*, 372–380.

$$\bullet\text{Fe(IV)} \xrightarrow{k_2} \text{Fe(III)} \quad (2)$$

$$\bullet\text{Fe(IV)} \xrightarrow{k_3} \bullet\text{Fe(III)}\bullet \quad (3)$$

$$\text{Fe(IV)} \xrightarrow{k_4} \bullet\text{Fe(III)} \quad (4)$$

$$\bullet\text{Fe(IV)} + \bullet\text{Fe(IV)} \xrightarrow{k_5} \text{Fe(IV)} + \text{Fe(IV)} \quad (5)$$

$$\bullet\text{Fe(IV)} + \bullet\text{Fe(III)} \xrightarrow{k_6} \text{Fe(IV)} + \text{Fe(III)} \quad (6)$$

$$\bullet\text{Fe(IV)} + \bullet\text{Fe(III)}\bullet \xrightarrow{k_7} \text{Fe(IV)} + \bullet\text{Fe(III)} \quad (7)$$

$$\bullet\text{Fe(III)} + \bullet\text{Fe(III)} \xrightarrow{k_8} \text{Fe(III)} + \text{Fe(III)} \quad (8)$$

$$\bullet\text{Fe(III)} + \bullet\text{Fe(III)}\bullet \xrightarrow{k_9} \text{Fe(III)} + \bullet\text{Fe(III)} \quad (9)$$

$$\bullet\text{Fe(III)}\bullet + \bullet\text{Fe(III)}\bullet \xrightarrow{k_{10}} \bullet\text{Fe(III)} + \bullet\text{Fe(III)} \quad (10)$$

The rationales behind postulating these reactions, together with a number of assumptions made, are given in the Supporting Information, SI.Results.3. Briefly, reaction 1 describes formation of Compound ES. The latter decays via two alternative reactions, 2 and 3. Reaction 4 is a decay of the ferryl heme state into the "ferric + radical" state. Reactions 5−10 are six radical recombination reactions that can take place between three types of radical species in the model: a radical on DHP in the ferric heme state •Fe(III), a radical when DHP is in the ferryl state •Fe(IV), and a biradical DHP when the heme is ferric •Fe(III)•. For a time point of the evolution, the derivatives by time of the concentrations (rates) for each component were formulated via the rate constants and the components' concentrations. The concentration dependences on time (t) were then obtained by stepwise integration of the derivatives over the time range of choice (see details in Supporting Information, SI.Results.3 and the Excel file). The graphs showing the time dependences of the total free radical concentration and the total ferric heme state were combined as follows:

$$[\text{Total free radical}](t) = \bullet\text{Fe(III)}(t) + 2\bullet\text{Fe(III)}\bullet(t) + \bullet\text{Fe(IV)}(t)$$

$$[\text{Total ferric heme}](t) = \text{Fe(III)}(t) + \bullet\text{Fe(III)}(t) + \bullet\text{Fe(III)}\bullet(t)$$

The Excel file available in the Supporting Information allows visual monitoring of all constructed kinetic dependences on one screen. A change in any one of the 32 parameters (ten rate constants × three pH values + $[DHP]_0$ + $[H_2O_2]_0$) instantly produces change(s) in the calculated kinetic dependences. The initial DHP and H_2O_2 concentrations were not varied during the fitting process. The fitting procedure was based on minimizing the "target" parameters, the average absolute difference between experimental and calculated concentration values, defined for each pH series (T_{pH5}, T_{pH6}, and T_{pH7}) and for all three sets of data when optimizing the rate constants globally ($T = T_{pH5} + T_{pH6} + T_{pH7}$) (see details in Supporting Information, SI.Results.3). The constraints imposed on the rate constants have allowed diminishing of the 30D variable space down to 13 variables (see SI.Results.3). Table 2 presents the optimized values of the 30 rate constants that were used to plot the continuous lines in Figures 4 and 5. This set of rate constants produces the T parameter equal to 12.73 μM, which is, on average, 2.1 μM for each of the six experimental kinetic dependences modeled. We consider this a good accuracy of fitting for the case of total protein concentration of 40 μM. It is rather difficult to estimate classical errors of the rate constants in Table 2 because of uncertainty in the confidence level one might want to assume for a range of values for each k_i (i = 1, 2, ..., 10). It is possible, however, to determine the ranges of k_i values around their optimal points for which the target parameter T would be greater than $T_{optimal}$ by not more than a conventional value. Table 2 thus reports the ranges of k values that correspond to a maximal increase of T by 1 μM from the optimal value of 12.73 μM (see details in Supporting Information). These ranges of k values are given for the rate constants that have been varied during the optimization (k_1, k_2, k_4, and k_5), all other rate constants being their algebraic functions.

Table 2. Optimized Rate Constants of the Reactions Included in the Kinetic Model[a]

	pH 5	pH 6	pH 7
k_1, M^{-1} s^{-1}	$(2.53 \pm 0.18) \times 10^4$	$(3.78 \pm 2.46) \times 10^4$	$(9.47 \pm 0.94) \times 10^4$
k_2, s^{-1}	2.29 ± 0.09	0.64 ± 0.05	0.44 ± 0.79
k_3, s^{-1}	0.093	0.017	0.005
k_4, s^{-1}	0.009 ± 0.003	0.002 ± 0.002	0.001 ± 0.001
k_5, M^{-1} s^{-1}	$(14.52 \pm 1.94) \times 10^4$	$(5.11 \pm 1.17) \times 10^4$	$(2.81 \pm 2.68) \times 10^4$
k_6, M^{-1} s^{-1}	19.36×10^4	6.81×10^4	3.75×10^4
k_7, M^{-1} s^{-1}	38.72×10^4	13.63×10^4	7.50×10^4
k_8, M^{-1} s^{-1}	25.81×10^4	9.08×10^4	5.00×10^4
k_9, M^{-1} s^{-1}	51.63×10^4	18.17×10^4	10.01×10^4
k_{10}, M^{-1} s^{-1}	103.3×10^4	36.33×10^4	20.01×10^4

[a] The ranges of values are given for the rate constants varied during optimization, k_1, k_2, k_4 and k_5. Constants k_6-k_{10} are calculated as direct proportions of k_5; constants k_3 are calculated as k_2/Ak_1 where A is a constant.

4. Discussion

The enzyme activation can be represented as a sequence of transformations (Scheme 2) when the intermediates are the species detectable by optical and/or EPR spectroscopy. We now consider in detail the individual intermediates presented in Scheme 2 from the perspective of their spectroscopic properties.

4.1. Resting DHP: Relation between the Two HS Forms and the His55 in Open and Closed Conformations. We have found two HS ferric heme forms in the resting enzyme: a "nearly axial" signal and a rhombic one (NAHS and R1HS, Figure 1). These two forms are in a pH-dependent equilibrium, with R1HS being the acidic component and NAHS the alkaline component (Figure 2). The axial HS ferric heme state in the globins, such as Mb and Hb, has a water molecule coordinated by the distal histidine.[30−32] Therefore, we suggest that NAHS is a six-coordinate HS ferric heme state (6cHS) of DHP when the distal His55 is in the closed conformation coordinating a water molecule. Recently, Nicoletti et al. showed that binding of

(30) Peisach, J.; Blumberg, W. E.; Wittenberg, B. A.; Wittenberg, J. B. *J. Biol. Chem.* **1968**, *243*, 1871–1880.
(31) Peisach, J.; Blumberg, W. E.; Wittenberg, B. A.; Wittenberg, J. B.; Kampa, L. *Proc. Natl. Acad. Sci. U.S.A.* **1969**, *63*, 934–939.
(32) Svistunenko, D. A.; Sharpe, M. A.; Nicholls, P.; Blenkinsop, C.; Davies, N. A.; Dunne, J.; Wilson, M. T.; Cooper, C. E. *Biochem. J.* **2000**, *351*, 595–605.

Scheme 2

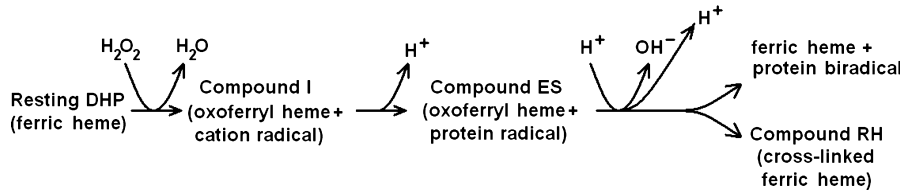

4-iodophenol to DHP produces a rhombic-type EPR line shape with g-values $g_1 = 6.22$, $g_2 = 5.50$, and $g_3 = 1.99$,[33] similar to the resting state R1HS shown in Figure 1 and Figure S7. Binding of 4-iodophenol in the distal heme side results in the distal His55 being pushed out of the pocket to the open conformation.[5] Therefore, we can assign R1HS to a five-coordinate HS ferric heme state (5cHS) of DHP in the open His55 conformation.

The forms R1HS (5cHS, open) and NAHS (6cHS, closed) are in a fast pH-dependent equilibrium in the resting state. The correlation of the His55 position and heme coordination has been observed by X-ray crystallography and nuclear magnetic resonance and resonance Raman spectroscopies.[10,11,14,15,33] The equilibrium is shifted toward R1HS as the pH is lowered (Figure 2) because of increasing protonation of the distal His55, which leads to the disruption of the hydrogen bonding to the water molecule in the sixth position of the heme iron. This displaces the distal His55 toward the open conformation, thus producing a 5cHS heme state. Another way to rationalize the effect of pH on the open/closed equilibrium is to think that one excessive positive charge on the histidine (at lower pH) makes it harder for the residue to approach the positively charged heme iron.

The equilibrium between the R1HS and NAHS ferric heme states seems to be slightly affected after the reaction starts: the decrease of R1HS upon H_2O_2 addition is marginally greater than the decrease of NAHS. In fact, the EPR spectra of the RFQ samples sometimes showed a complete disappearance of the R1HS form just 50 ms after mixing, leaving just a small-intensity axial HS ferric heme EPR signal (not shown). We suggest that the reaction with H_2O_2 starts when the distal His55 is in the closed conformation. It is known that if a heme protein lacks a histidine in the distal side of the heme, the reaction can still be initiated, but Compound 0 (a transient complex of H_2O_2 and the ferric heme) is formed as the first intermediate.[21,34] Since no Compound 0 has been observed in DHP upon reaction with H_2O_2, it appears feasible that peroxide reacts with the heme iron when His55 is in the closed conformation. It is also known that the open, 5cHS, form of DHP is inactive and does not convert to compound ES.[16]

Once the oxoferryl heme state starts to be reduced in the course of the reaction, a new rhombic ferric species, R2HS, is formed with a slightly stronger rhombic distortion of the heme than in R1HS (Figure S7). This is likely to be an open His55 conformation of DHP, similar to R1HS but modified due to a peroxide-induced change in the heme geometry.

4.2. Compound I, Compound ES, and the Substrate Oxidation Site. Compound I is a term commonly used to describe the two-electron-oxidized form of a heme protein, in which one oxidizing equivalent originates from the ferric iron, resulting in the oxoferryl heme state, and the other comes from the π-system of the porphyrin, yielding a π-cation radical.

Compound I has not been reported in DHP. Instead, the oxidation state of DHP formed shortly after mixing with H_2O_2 has been interpreted as Compound ES[17] by analogy with C*c*P,[18] in which the heme is oxidized to the oxoferryl state and a free radical is formed on an amino acid. H_2O_2 reacting with respiratory heme proteins, such as Mbs and Hbs, also produces an oxoferryl heme state and a protein-bound radical. However, an essential difference with Compound ES in C*c*P is in the amount of the free radical produced. The apparent yield of the protein-bound free radical in the globins is never greater than a few percent.[22] We show now that in DHP the free radical concentration is nearly quantitative with respect to the enzyme concentration (a ~93% yield at 150 ms, pH 7, Figure 5). This fact makes the "oxoferryl + radical" oxidation state of DHP more like classical Compound ES in C*c*P rather than the "oxoferryl + radical" state in the globins.

We have assigned the Compound ES radical (the "principal radical") to either Tyr28 or Tyr34 on the basis of its EPR spectrum simulation (section 3.2.3). These two residues are both solvent-exposed and provide possible sites for electron transfer from the halogenated substrate. Of the two radical sites, Tyr34 is closer to the heme, and it makes a direct van der Waals contact with the heme porphyrin (Figure 8). This is one reason to suggest that the observed radical is on Tyr34. However, the other, more important reason is the fact that Tyr34 in DHP A is a conserved tyrosine residue in a number of globins, and structural homologues of this residue — Tyr103 in horse Mb, sperm whale Mb, and human Mb and Tyr42 in the α-subunit of human Hb — all are reportedly the sites of free radical formation when these globins react with H_2O_2.[22,35−38]

4.3. Effects of pH on the Reactivity of the Oxoferryl Heme. The oxoferryl heme must be in a dynamic equilibrium with its protonated state, which can be represented as the resonance hybrid boxed in Scheme 3.

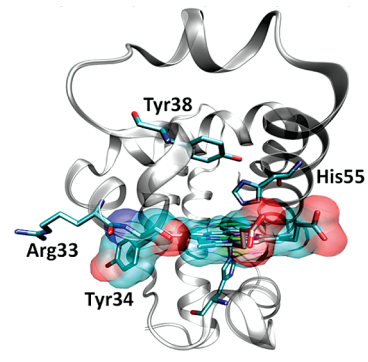

Figure 8. Selected residues in the heme environment of DHP. Tyr34, the site suggested to host the principal radical, is in van der Waals interaction with the heme porphyrin. Arg33 is in close proximity and might play a role in substrate binding. The pH 5 radical is proposed to be located on Tyr38, which can make a strong hydrogen bond with the distal His55. The PDB structure file 2QFK[10] was used to generate the figure.

(33) Nicoletti, F. P.; Thompson, M. K.; Howes, B. D.; Franzen, S.; Smulevich, G. *Biochemistry* **2010**, *49*, 1903–1912.
(34) Brittain, T.; Baker, A. R.; Butler, C. S.; Little, R. H.; Lowe, D. J.; Greenwood, C.; Watmough, N. J. *Biochem. J.* **1997**, *326*, 109–115.

Scheme 3

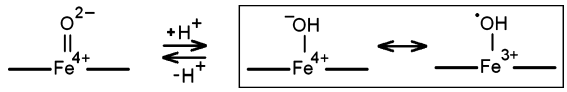

A direct correlation of Hb and Mb ferryl reactivity with their ferryl protonation status ($pK_a = 4.7$) has been demonstrated.[39] A value close to the pK_a for this equilibrium might be expected in DHP. Indeed, the state of the oxoferryl heme in DHP at pH 7 has been assessed by cryoreduction of DHP Compound ES with γ-radiation and was concluded to be a deprotonated $Fe^{4+}{=}O^{2-}$ state.[40]

The high oxoferryl reactivity in the protonated state can be understood from its electronic equivalence to a ferric heme iron coordinated by a hydroxyl radical (Scheme 3), the strongest oxidation agent known. The deprotonated oxoferryl heme, on the other hand, can be stable for hours.[41]

4.4. Hypothesis: Two Alternative Routes of the Reduction of the Protonated Oxoferryl Heme of Compound ES. The oxoferryl heme state, which is part of Compound ES, is chemically reactive and can be converted to the resting ferric state if it is protonated. It is electronically equivalent to a ferric heme iron coordinated by a hydroxyl radical (Scheme 3), which is a highly reactive oxidant. Therefore, we suggest that what happens after the oxoferryl is protonated depends on whether His55 is in the closed or open conformation.

If His55 is in the open conformation (higher population at the lower pH values, Figure 2), the protonated oxoferryl would abstract a hydrogen atom from the nearest target to be oxidized, the porphyrin (possibly in two steps, $-e^-$ and $-H^+$, as shown in the animation available for the open form in the Supporting Information). This would leave the porphyrin in a transient neutral free radical state, ready to recombine with the nearby neutral Tyr34 radical (principal radical), thus yielding a covalent cross-link between the tyrosine and the heme. Indeed, our HPLC data show the formation of a cross-link between the heme and the globin (Figures S8 and S9). Tyr34 is very close to the heme, and it is likely that it could form a cross-link. A homologous residue, Tyr103, in horse Mb treated with H_2O_2 was reported to form a cross-link with the heme,[42] although this assignment has been challenged.[43] Furthermore, an autocatalytic formation of a similar cross-link under H_2O_2 treatment has been demonstrated in ascorbate peroxidase in which a tyrosine has been engineered close to the heme edge.[44] The yield of the cross-link in DHP is higher at lower pH values (Figure 7), which is in agreement with a higher concentration of the protonated ferryl form of the heme and a higher concentration of the open His55 conformation. Therefore, we put forward a hypothesis that Compound RH is a ferric-type heme with the porphyrin covalently cross-linked to Tyr34. An important question is whether the formation of such a cross-link might be reversible, since it is known that Compound RH can be reduced by external reductants to the ferrous form of DHP.[17] The possibility that such a link in DHP can be reduced is supported by the fact that similar heme-to-protein cross-links in horse heart Mb[45] are partially reversible when sodium dithionite is used as a reductant (our unpublished data).

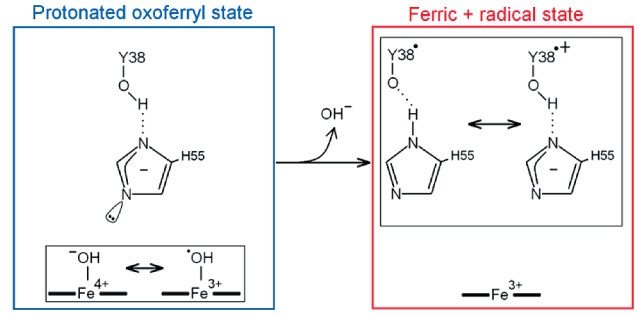

Figure 9. Conversion of the protonated oxoferryl heme to a "ferric heme + protein radical" state when the distal His55 is in the closed conformation. The Tyr38• radical is formed (the pH 5 radical), which might be in an equilibrium with its protonated form, the cation radical.

If, however, His55 is in the closed conformation (see the animation in the Supporting Information), which in terms of population is a much smaller fraction, the protonated ferryl would certainly attack the distal His55, likely by subtracting an electron from the lone pair of the imidazole's nitrogen (Figure 9). As a result, a hydroxyl anion will be liberated, the heme will be left in the ferric state, and a neutral radical will be formed on His55. What will happen next? We have assigned the EPR signal of the pH 5 radical to the neutral radical on Tyr38 (see section 3.2.3) on the basis of the EPR signal simulation and the DHP structure. We also concluded that the pH 5 radical must be strongly hydrogen bonded. Tyr38 is indeed very close to His55 when it is in the closed conformation (Figure 8) and can make a strong hydrogen bond with the nitrogen of the imidazole group.[10] Thus, it is reasonable to expect that the Tyr38 radical is formed instantly upon His55 oxidation by the protonated oxoferryl (Figure 9). A neutral Tyr38 radical might be in resonance with its cation radical when the proton is shared between the histidine and the tyrosyl radical, but the population of the latter state must be much smaller than the population of the neutral radical, which we observe as the pH 5 radical.

Thus, it appears that the dual functionality of DHP might be linked to changes in the enzyme's environment, particularly to the changes in the environment's oxidizing or reducing capacity. At decreased O_2 concentrations, the environment becomes more reducing and the ferrous heme fraction is increased. This shifts the DHP function toward oxygen binding. As oxygen becomes more abundant in the environment, spontaneous heme oxidation increases the ferric state DHP fraction, which can be seen as a shift toward the peroxidase function. This is useful in an oxidative environment, as such reactive oxygen species as H_2O_2 will be eliminated, and the trihalophenols will be converted to

(35) Fenwick, C. W.; English, A. M. *J. Am. Chem. Soc.* **1996**, *118*, 12236–12237.
(36) Harris, M. N.; Burchiel, S. W.; Winyard, P. G.; Engen, J. R.; Mobarak, C. D.; Timmins, G. S. *Chem. Res. Toxicol.* **2002**, *15*, 1589–1594.
(37) Gunther, M. R.; Sturgeon, B. E.; Mason, R. P. *Free Radic. Biol. Med.* **2000**, *28*, 709–719.
(38) Reeder, B. J.; Grey, M.; Silaghi-Dumitrescu, R. L.; Svistunenko, D. A.; Bulow, L.; Cooper, C. E.; Wilson, M. T. *J. Biol. Chem.* **2008**, *283*, 30780–30787.
(39) Silaghi-Dumitrescu, R.; Reeder, B. J.; Nicholls, P.; Cooper, C. E.; Wilson, M. T. *Biochem. J.* **2007**, *403*, 391–395.
(40) Davydov, R.; Osborne, R. L.; Kim, S. H.; Dawson, J. H.; Hoffman, B. M. *Biochemistry* **2008**, *47*, 5147–5155.
(41) Reeder, B. J.; Wilson, M. T. *Free Radic. Biol. Med.* **2001**, *30*, 1311–1318.
(42) Catalano, C. E.; Choe, Y. S.; Ortiz de Montellano, P. R. *J. Biol. Chem.* **1989**, *264*, 10534–10541.
(43) Reeder, B. J.; Cutruzzolà, F.; Bigotti, M. G.; Watmough, N. J.; Wilson, M. T. *IUBMB Life* **2007**, *59*, 477–489.
(44) Pipirou, Z.; Bottrill, A. R.; Svistunenko, D. A.; Efimov, I.; Basran, J.; Mistry, S. C.; Cooper, C. E.; Raven, E. L. *Biochemistry* **2007**, *46*, 13269–13278.
(45) Reeder, B. J.; Svistunenko, D. A.; Sharpe, M. A.; Wilson, M. T. *Biochemistry* **2002**, *41*, 367–375.

dihaloquinones on the way. However, if there are no trihalophenols in the environment, the two potentially damaging oxidative equivalents formed on DHP in the reaction with H_2O_2 recombine to form a safe heme-to-protein cross-link state, which is seen optically as Compound RH. According to this hypothesis, compound RH formation avoids a biradical state of DHP that would be highly reactive and potentially damaging. The yield of such a state is kept persistently low due to a low fraction of the His55 in the closed conformation at the low pH and to a low oxoferryl reactivity at the high pH values. Therefore, Compound RH is the state of DHP in an oxidative medium in the absence of substrates to oxidize. Once the environment becomes reducing again, the covalent link is reduced and Compound RH is transformed into oxyferrous heme DHP (Compound III).

Interestingly, whereas Compound RH has the heme in the ferric state, it cannot be further oxidized by H_2O_2.[17] This might be explained by suggesting that His55 is arrested in the open conformation in Compound RH, which makes it hardly possible for a H_2O_2 molecule to react with the heme.

Thus, DHP appears to be an oxygen-binding hemoglobin that becomes a peroxidase when oxygen concentration is increased. Alternatively, we could say that DHP is a peroxidase that switches to oxygen binding when the concentration of oxygen is decreased.

4.5. Analysis of the Optimized Rate Constants. The kinetic model used to fit experimental time dependences of the total free radical and total ferric heme states, at three different pH values, holds the following assumptions made on the basis of the experimental results obtained in this work:

(a) Formation of Compound ES takes place only when His55 is in the closed conformation.

(b) Open/closed His55 equilibrium is governed by a single protonation event.

(c) Compound ES decays only if the ferryl heme iron is protonated (although the *principal radical* associated with Compound ES can recombine with another radical in the system, independently of the heme oxidation state, thus turning Compound ES into a nonradical ferryl heme species).

(d) The ratio of the rates of the two alternative routes of the Compound ES decay directly depends on the open/closed His55 conformation: Compound RH is formed in the open conformation, but a second, *pH 5 radical* is formed in the closed conformation. Thus, the partial weight of these two routes of reaction (k_2/k_3) should have the same pH profile as the rate constant k_1 that reflects the pH dependence of Compound ES formation via reaction 1; that is, k_2/k_3k_1 is a constant at pH 5, 6, and 7.

When the kinetic model is optimized with the constraints imposed by the above assumptions, the calculated time dependences are found in satisfactory proximity to the experimental data points (Figures 4 and 5). The conclusions that follow from the analysis of the optimized rate constants further support the feasibility of the kinetic model and the molecular mechanism of the reaction.

Figure 10 shows the pH dependences of the optimized rate constants (Table 2). The k_1 dependence on pH is in agreement with the EPR data on the pH dependence of the R1HS and NAHS equilibrium (Figure 2). Also, the values of k_1 obtained from the model are in agreement with the Compound ES formation rate constants determined for pH 5 and pH 7 by optical spectroscopy (2.78×10^4 and 3.56×10^4 M^{-1} s^{-1} at pH 5 and 7, respectively[17]). An estimate of the pK_a value from the *Step* parameter defined from the three k_1 values optimized for pH 5, pH 6, and pH 7 (SI.Results.3) give a value of 6.9. Interestingly, a similar equilibrium between the 5cHS (open) and 6cHS (closed) heme states in Mb, which is characterized by orders of magnitude lower peroxidase activity, is observed at a significantly lower pK_a of 4.5.[46]

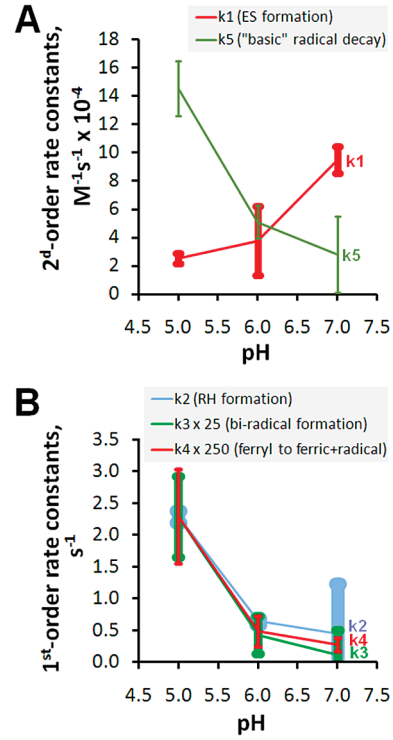

Figure 10. Optimized values of the second-order (A) and first-order (B) rate constants used in the kinetic model (see section 3.2.5) plotted as functions of pH. For comparative viewing, k_3 and k_4 dependences (B) are multiplied by the factors of 25 and 250, respectively, to bring the pH 5 data point to a similar position on the graph. Rate constants k_6–k_{10} are set in the model to be proportional to k_5, and therefore they have pH dependences identical in shape to that of k_5 and are not shown. The error bars indicate how much the rate constants should be changed (individually, while keeping the other constants at the optimized values) in order to produce a 1 μM increase in the global "target" optimization parameter *T*.

We interpret Compound RH of DHP as a ferric heme state with the heme covalently bound to the globin. In agreement with this, the rate constants k_2 of Compound RH formation at the three pH values (Figure 10B) correlate with the yield of the heme-to-protein cross-links (Figure 7). The values of k_2 obtained from the model are approximately 30 times greater than the rates of Compound RH formation determined optically (0.0701 s^{-1} at pH 5 and 0.0167 s^{-1} at pH 7),[17] although both sets of data have similar pH trends. If these differences are confirmed in future experiments under common reaction conditions, it might indicate that what we see kinetically as the principal radical disappearance linked to the ferric heme state formation is not formation of Compound RH but rather formation of its precursor, which then transforms to Compound RH with an approximately 30-fold slower rate.

The radical decay rate constants, as determined from the model (Figure 10A), decrease with increasing pH (with a formal pK_a = 5.2 estimated from the *Step* parameter for the three "basic" radical decay rate constants k_5; see SI.Results.3 for

(46) Yang, F.; Phillips, G. N., Jr. *J. Mol. Biol.* **1996**, *256*, 762–774.

details). This is in agreement with a faster loss of the hyperfine structure in the free radical EPR spectrum at the lower pH values (see section 3.2.1). Even quantitative comparison shows a good correlation: while $k_5^{pH6}/k_5^{pH7} = 1.8$, the rate of loss of the hyperfine structure in the EPR spectra (estimated as inverse time of the line shape preservation; see section 3.2.1) is 2 times greater at pH 6 than at pH 7; also, while $k_5^{pH5}/k_5^{pH6} = 2.8$, the rate of loss of the hyperfine structure at pH 5 is 6 times greater than at pH 6. We think that such a good quantitative agreement is remarkable, particularly since no information about the free radical spectra line shape is present the kinetic model.

Finally, the overall rate of the oxoferryl heme decay ($k_2 + k_3 + k_4$) has a pH profile consistent with $pK_a = 4.4$ (see Excel file in Supporting Information), a value which is very close to the $pK_a = 4.7$ for the globins' oxoferryl heme protonation.[39] Reaction 4, however, contributes very little to the overall sum (0.2−0.4%; note that the k_4 dependence is multiplied by a factor of 250 in Figure 10B).

Overall, the kinetic model that satisfactorily describes the experimental data is dependent on three pK_a values roughly estimated from the triads of the rate constants optimized at pH 5, pH 6, and pH 7. The first one, $pK_a = 6.9$, is related to the His55 protonation and thus governs its open/closed conformations. The second, $pK_a = 4.4$, defines if the oxoferryl heme is protonated and therefore redox active. The third one, $pK_a = 5.2$, governs the radical decay and is suggested to reflect the radical-transfer dependence on the pH.

5. Conclusions

1. Two HS ferric heme forms are found in the resting enzyme and assigned to the 6cHS (aquo) heme with the distal His55 in the closed conformation and the 5cHS heme with His55 in the open conformation.

2. Two free radicals are identified in DHP activated by H_2O_2. The one associated with Compound ES has been assigned to the on-surface residue, Tyr34. The other radical, better detectable at lower pH values, has been assigned to Tyr38, which is well situated to make a strong hydrogen bond with the distal histidine, His55.

3. Covalent heme-to-protein cross-links are found in DHP treated with H_2O_2.

4. A pH-dependent mechanism of DHP activation by H_2O_2 is proposed and tested by kinetic modeling. A good correspondence between the model and the experimental data, at a range of pH values, allows the following interpretation of the results obtained. The formation of Compound ES is pH dependent, reflecting the pH dependence of the equilibrium of the distal His55 in the open and closed conformations. Once formed, Compound ES may enter one of the two alternative paths of further transformation. This depends again on whether His55 is in the closed or in the open conformation. In the less populated closed conformation, the Tyr38 radical is formed, but in the major open conformation, if no trihalophenol substrates are available, the protonated oxoferryl produces a transient porphyrin radical, which recombines with Tyr34$^{\bullet}$ and makes a heme-to-protein cross-link. This cross-link might be the Compound RH characterized previously by optical spectroscopy, or it might be its precursor. Formation of Compound RH is therefore interpreted as the enzyme's means to terminate the two oxidizing equivalents in a safe way, producing a cross-linked heme, which can be further reduced in a controlled way. Thus, the ability of H_2O_2-activated DHP to be transformed into a safe state of Compound RH might be important in avoiding unwanted radical propagation in the absence of trihalophenol substrates.

Acknowledgment. D.A.S. acknowledges the BBSRC grant BB/E02355X/1 "Advanced sample making tools for electron paramagnetic resonance spectroscopy". S.F. and M.K.T. acknowledge support by the Army Research Office grant 52278-LS.

Supporting Information Available: Details of new freeze-quenching apparatus, EPR spectra correction for variable length of EPR samples, spectra shifting in accordance with the microwave frequency, and assignment of radicals to specific tyrosine residues; supporting figures and tables; kinetic model Excel file; Quicktime animations of electron and proton transfer in open and closed His55 conformations. This material is available free of charge via the Internet at http://pubs.acs.org.

JA106620Q